

# UNCLASSIFIED

AD NUMBER
AD824482
NEW LIMITATION CHANGE
TO Approved for public release, distribution unlimited
FROM Distribution authorized to U.S. Gov't. agencies and their contractors; Administrative/Operational Use; DEC 1967. Other requests shall be referred to Air Force Flight Dynamics Laboratory, Attn: FDDA, Wright-Patterson AFB, OH 45433.
AUTHORITY
AFFDL ltr, 29 Oct 1973

THIS PAGE IS UNCLASSIFIED

AD 824482

AFFDL-TR-67-70

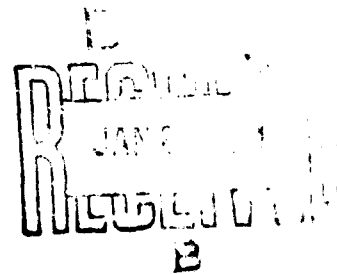
## THE RESPONSE OF SIMPLE PANELS TO TURBULENT BOUNDARY LAYER EXCITATION

JOHN F. WILBY

UNIVERSITY OF SOUTHAMPTON  
HAMPSHIRE, ENGLAND

TECHNICAL REPORT AFFDL-TR-67-70

OCTOBER 1967



This document is subject to special export controls and each transmittal to foreign governments or foreign nationals may be made only with prior approval of AFFDL (FDDA).

AIR FORCE FLIGHT DYNAMICS LABORATORY  
RESEARCH AND TECHNOLOGY DIVISION  
AIR FORCE SYSTEMS COMMAND  
WRIGHT-PATTERSON AIR FORCE BASE, OHIO

# NOTICES

When Government drawings, specifications, or other data are used for any purpose other than in connection with a definitely related Government procurement operation, the United States Government thereby incurs no responsibility nor any obligation whatsoever; and the fact that the Government may have formulated, furnished, or in any way supplied the said drawings, specifications, or other data, is not to be regarded by implication or otherwise as in any manner licensing the holder or any other person or corporation, or conveying any rights or permission to manufacture, use, or sell any patented invention that may in any way be related thereto.

ACCESSION NO.		
OPSTI	WHITE SECTION	<input type="checkbox"/>
DDC	DIFF. SECTION	<input checked="" type="checkbox"/>
UNANNOUNCED		<input type="checkbox"/>
JUSTIFICATION		
BY		
DISTRIBUTION/AVAILABILITY CODES		
DISC.	AVAIL.	and/or SPECIAL
2		

Copies of this report should not be returned to the Air Force Flight Dynamics Laboratory unless return is required by security considerations, contractual obligations, or notice on a special document.

# **THE RESPONSE OF SIMPLE PANELS TO TURBULENT BOUNDARY LAYER EXCITATION**

**JOHN F. WILBY**

This document is subject to special export controls and each transmittal to foreign governments or foreign nationals may be made only with prior approval of AFFDL (FDDA).



## FOREWORD


This report was prepared by the Institute of Sound and Vibration Research at the University of Southampton, England, for the Aero-Acoustics Branch, Vehicle Dynamics Division, Air Force Flight Dynamics Laboratory, Wright-Patterson Air Force Base, Ohio under contract number AF 61(052)-756. This research is part of a continuing effort to obtain advanced data and techniques for defining vibration and acoustic phenomena in flight vehicles under the Air Force System Command's exploratory development program. The Project Number is 1471 "Aero-Acoustic Problems," and Task Number 147102 "Prediction and Control of Noise." Mr. P. H. Hermes and later Mr. D. L. Smith of the Aero-Acoustics Branch were task engineers.

The contract was administrated by the Air Force Flight Dynamics Laboratory through the European Office of Aerospace Research (OAR), United States Air Force.

The period covered by this contract is from 1 November 1963 to 30 November 1966. This report which discusses a complete phase of the research work is one of two reports generated under the contract. These reports conclude the work on Contract AF 61(052)-756. The assistance of Professor E. J. Richards, the Contract Supervisor, and Dr. D. J. Mead during the investigation is gratefully acknowledged.

The manuscript of this report was released by the authors on 30 December 1966 for publication as an AFFDL Technical Report.

This technical report has been reviewed and is approved.

  
HOWARD A. MAGRATH  
Chief, Vehicle Dynamics Division  
AF Flight Dynamics Laboratory

## ABSTRACT

The response of a series of single, fully-fixed, panels to turbulent boundary layer excitation has been measured in a subsonic wind tunnel for flow velocities of 329 ft/sec and 540 ft/sec, and boundary layer thicknesses in the range 0.4 inch to 1.4 inches. When the results are compared with theoretical predictions based on simply supported mode shapes, the magnitude of the displacement is overestimated but the effects of boundary layer thickness, pressure field convection direction, panel aspect ratio and static pressure differential are well predicted. The effect of flow velocity is not predicted accurately.

The boundary layer thickness affects the panel vibration mainly through the pressure spectrum, the modal response increasing to a maximum when the spectral density at the natural frequency reaches a maximum. The overall displacement is determined by the dominant low order modes and reaches a maximum for thick boundary layers.

The maximum response in some modes of a panel can occur at an angle of convection  $0^\circ < \theta < 90^\circ$ , but in other modes the maximum occurs at  $\theta = 0^\circ$  or  $90^\circ$ . The angle of convection has only a small effect on the (1-1) mode. The static pressure differential increases the panel natural frequencies and decreases the response, the latter change being due mainly to the change in the panel stiffness.

The theory overestimates the effect of flow velocity near coincidence and underestimates the effect elsewhere. The error may be caused by the assumed theoretical mode shape but more experimental data is required.

Random techniques are used to measure the panel damping in the presence of an airflow, and the results show a general increase over the zero airflow values. In several cases the change is small, but restrictions on the use of the methods prevent a detailed investigation.

## CONTENTS

	<u>Page</u>
Chapter 1    Review of Previous Work and the Aims of the Investigation	1
1.1    Introduction to the General Problem	1
1.2    Review of Previous Work	1
1.3    Extension of Previous work	12
1.4    Summary	16
Chapter 2    Theoretical Response to Boundary Layer Excitation	18
2.1    Introduction	18
2.2    General Theory	18
2.3    Displacement Power Spectral Density Function	23
2.4    Acceptance Terms	34
2.5    Simplification for Acoustic Excitation	38
2.6    Evaluation of Joint Acceptance Terms	40
2.7    Direction of Convection of the Pressure Field	48
2.8    Cross Acceptance	54
2.9    Summary	57
Chapter 3    Experimental Equipment	61
3.1    Wind Tunnel	61
3.2    Siren Tunnel	64
3.3    Experimental Panels	65
3.4    Displacement Measuring Probe	67
3.5    Signal Analysis	72
3.6    Pressure Equalising System	72
3.7    Background Vibration and Equipment Noise	74

## CONTENTS (Cont.)

	<u>Page</u>
Chapter 4    Panel Damping	76
4.1    Introduction	76
4.2    Discrete Frequency Excitation Methods	77
4.3    Damping Measurements using Discrete Frequency Excitation	81
4.4    Random Excitation Methods	89
4.5    Damping Measurements using Random Techniques	100
4.6    Summary	109
 Chapter 5    Measured Response to Boundary Layer Excitation	 110
5.1    Introduction	110
5.2    Root Mean Square Displacement	114
5.3    Displacement Spectra	116
5.4    Effect of Boundary Layer Thickness	119
5.5    Effect of Flow Velocity	125
5.6    Angle of Convection	128
5.7    Static Pressure Differential	129
5.8    General Discussion	132
5.9    Summary	133
 Chapter 6    Measured Response to Acoustic Excitation	 137
6.1    Introduction	137
6.2    Root Mean Square Displacement	137
6.3    Displacement Spectra	139
6.4    Angle of Convection	144
6.5    Summary	145
 Chapter 7    Conclusions	 146

CONTENTS (Cont.)		<u>Page</u>
Appendix A	Excitation Fields	152
A.1	Type of Excitation	152
A.2	Narrow Band Cross Correlation Coefficient	152
A.3	Boundary Layer Excitation	155
A.4	Acoustic Excitation	158
A.5	Summary	160
Appendix B	Effects of Filter Bandwidth in Spectral Analysis	162
B.1	Introduction	162
B.2	Single Degree of Freedom System	163
B.3	Multi Degree of Freedom System	167
B.4	Bandwidth of Resonant Peaks	170
B.5	Summary	171
Appendix C	Panel Natural Frequencies and Mode Shapes	172
C.1	Material Properties	172
C.2	Estimation of Natural Frequencies and Mode Shapes	172
C.3	Measured Natural Frequencies	176
C.4	Measured Mode Shapes	180
C.5	Summary	181
Appendix D	Panel Root Mean Square Displacement	183
D.1	Introduction	183
D.2	Theoretical R.M.S. Displacement	183
D.3	Measured R.M.S. Displacement	186
References		196

## PLATES

<u>Plate</u>		<u>Page</u>
3.1	Boundary layer wind tunnel.	202
3.2	Experimental panels.	203
3.3	Capacitance probe calibration equipment.	204
3.4	Traversing unit and wind tunnel side plate.	205
3.5	Wind tunnel side plate in the siren tunnel.	206
3.6	Traversing unit mounted on the wind tunnel.	207
3.7	Carrier plug with pressure equalising box.	208
4.1	Equipment for free-space damping measurements.	209
C.1	Modal patterns for the 3.5in x 3.5in panel.	210
C.2	Modal patterns for the 4.0in x 2.75in panel.	211
C.3	Modal patterns for the 4.0in x 2.0in and 4.0in x 1.0in panels.	212

## ILLUSTRATIONS

<u>Figure</u>		<u>Page</u>
2.1	Longitudinal joint acceptance valid for $\frac{\omega \delta^*}{U_c} \geq 0.37$ .	213
2.2	Effect of $\alpha_1$ on joint acceptance : $m = 1$ .	214
2.3	Effect of $\alpha_1$ on joint acceptance : $m = 2$ .	215
2.4	Effect of $\alpha_1$ on joint acceptance : $m = 3$ .	216
2.5	Effect of $\alpha_1$ on joint acceptance : $m = 4$ .	217
2.6	Longitudinal joint acceptance as function of boundary layer displacement thickness : $m = 1$	218
2.7	Longitudinal joint acceptance as function of boundary layer displacement thickness : $m = 2$ .	219
2.8	Longitudinal joint acceptance as function of boundary layer displacement thickness : $m = 3$ .	220
2.9	Longitudinal joint acceptance as function of boundary layer displacement thickness : $m = 1$ .	221
2.10	Longitudinal joint acceptance as function of boundary layer displacement thickness : $m = 2$ .	222
2.11	Effect of lateral correlation coefficient on panel joint acceptance; simple form : $m = 1, 2$ .	223
2.12	Effect of lateral correlation coefficient on panel joint acceptance; simple form : $m = 3, 4$ .	224
2.13	Lateral joint acceptance for boundary layer excitation.	225
2.14	Lateral joint acceptances for different forms of correlation coefficient.	226
2.15	Effect of pressure field convection direction on panel joint acceptance : mode 1-1.	227
2.16	Effect of pressure field convection direction on panel joint acceptance : mode 2-2.	228
2.17	Effect of pressure field convection direction on panel joint acceptance : mode 3-1.	229
2.18	Effect of pressure field convection direction and panel aspect ratio on the joint acceptance.	230
2.19	Effect of acoustic wave direction on panel joint acceptance : mod 1-1.	231
2.20	Effect of acoustic wave direction on panel joint acceptance : mode 2-2.	231

## ILLUSTRATIONS (Cont.)

<u>Figure</u>		<u>Page</u>
2.21	Real part of longitudinal cross acceptance calculated for panel 5 under boundary layer excitation.	233
2.22	Imaginary part of longitudinal cross acceptance calculated for panel 5 under boundary layer excitation.	234
2.23	Real part of lateral cross acceptance calculated for panel 5 under boundary layer excitation.	235
2.24	Predicted contribution of cross terms to response spectrum for boundary layer excitation : (m+r) odd.	236
2.25	Predicted contribution of cross terms to response spectrum for boundary layer excitation : (m+r) even.	237
3.1	General arrangement of 9in x 6in boundary layer wind tunnel.	238
3.2	Background noise in the boundary layer wind tunnel.	239
3.3	Block diagram of the apparatus for the measurement of panel response to acoustic excitation.	240
3.4	Construction of an experimental panel.	241
3.5	Details of construction of the equipment for the calibration of the Wayne Kerr capacitance probes.	242
3.6	Block diagram of the apparatus for the calibration of the Wayne Kerr capacitance probes.	243
3.7	Calibration curve for Wayne Kerr capacitance probes.	244
3.8	Effect of distance between probe and panel on Wayne Kerr probe calibration.	245
3.9	Vibrating surface inclined to probe face.	246
3.10	Traversing unit for the vibration-measuring probe.	247
3.11	Details of the pressure equalising box and probe holder.	248
3.12	Diagram of pressure equalising system.	249
3.13	Background vibration and equipment noise : boundary layer excitation.	250
3.14	Background vibration and equipment noise : boundary layer and siren excitations.	251
4.1	Correction term for estimation of true half-power point.	252
4.2	Block diagram of the apparatus for the measurement of panel damping using discrete frequency excitation.	253
4.3	Block diagram of the apparatus for the measurement of panel damping using cross correlation techniques.	254



# ILLUSTRATIONS (Cont.)

<u>Figure</u>		<u>Page</u>
4.4	Effect of D.C. current on excitation-response cross correlation coefficient.	255
4.5	Autocorrelation decay caused by tape recorder speed variations.	256
4.6	Effect of excitation bandwidth on cross correlation between excitation and response.	257
4.7	Cross correlation between excitation and response for lightly damped mode.	258
4.8	Typical panel response autocorrelation curves.	259
4.9	Panel damping in the presence of airflow : Panel 4.	260
4.10	Panel damping in the presence of airflow : Panels 2, 5.	261
5.1	Co-ordinate system for panels in the boundary layer and siren tunnels.	262
5.2(a)(b)	Panel r.m.s. displacement at measuring positions.	263/264
5.3	Root mean square displacement in individual modes : Panel 4.	265
5.4	Root mean square displacement in individual modes : Panels 2, 6.	266
5.5	Response of panel 2 to boundary layer excitation : $M_o = 0.3$	267
5.6	Response of panel 3 to boundary layer excitation : $M_o = 0.3$	268
5.7	Response of panel 4 to boundary layer excitation : $M_o = 0.3$	269
5.8	Response of panel 5 to boundary layer excitation : $M_o = 0.3$	270
5.9	Response of panel 6 to boundary layer excitation : $M_o = 0.3$	271
5.10	Response of panels 1 and 7 to boundary layer excitation : $M_o = 0.3$ .	272
5.11	Response of panel 3 to boundary layer excitation : $M_o = 0.5$	273
5.12	Response of panel 4 to boundary layer excitation : $M_o = 0.5$	274
5.13	Response of panel 5 to boundary layer excitation : $M_o = 0.5$	275
5.14	Effect of flow velocity on panel response spectra.	276
5.15	Variation of modal response at natural frequencies with boundary layer thickness : Panel 4, $M_o = 0.3$ .	277
5.16	Variation of modal response at natural frequencies with boundary layer thickness : Panel 2, $M_o = 0.3$ .	278
5.17	Variation of modal response at natural frequencies with boundary layer thickness : Panel 3, $M_o = 0.3$ .	279

# ILLUSTRATIONS (Cont.)

<u>Figure</u>		<u>Page</u>
5.18	Variation of modal response at natural frequencies with boundary layer thickness : Panel 4, $M_o = 0.3$ .	280
5.19	Variation of modal response at natural frequencies with boundary layer thickness : Panel 5, $M_o = 0.3$ .	281
5.20	Variation of modal response at natural frequencies with boundary layer thickness : Panel 6, $M_o = 0.5$ .	282
5.21	Variation of modal response at natural frequencies with boundary layer thickness : Panel 3, $M_o = 0.5$ .	283
5.22 (a)(b)	Variation of modal response at natural frequencies with boundary layer thickness : Panel 4, $M_o = 0.5$ .	284/285
5.23	Variation of modal response at natural frequencies with boundary layer thickness : Panel 5, $M_o = 0.5$ .	286
5.24	Response to unit excitation at natural frequencies as a function of boundary layer thickness : Panel 4, $M_o = 0.3, 0.5$ .	287
5.25	Response to unit excitation at natural frequencies as a function of boundary layer thickness : Panel 5, $M_o = 0.3, 0.5$ .	288
5.26	Curves for $\frac{\omega \delta^*}{U_c} = 0.37$ .	289
5.27	Variation of modal response at natural frequencies with flow velocity : Panel 3.	290
5.28	Variation of modal response at natural frequencies with flow velocity : Panel 4.	291
5.29	Variation of modal response at natural frequencies with flow velocity : Panel 5.	292
5.30 (a)(b)	Effect of angle of convection on response of panel 5 to boundary layer excitation.	293/294
5.31	Effect of static pressure differential on measured response of panel 4 to boundary layer excitation.	295
5.32	Effect of static pressure differential on measured response of panel 5 to boundary layer excitation.	296
5.33	Effect of pressure differential in wind tunnel on natural frequencies of panel 4.	297
5.34	Effect of pressure differential in wind tunnel on natural frequencies of panel 5.	298
5.35	Variation of modal response at natural frequencies with static pressure differential : Panel 4.	299
5.36	Variation of modal response at natural frequencies with static pressure differential : Panel 5.	300

## ILLUSTRATIONS (Cont.)

<u>Figure</u>		<u>Page</u>
6.1	Response of panel 2 to acoustic excitation.	301
6.2	Response of panel 3 to acoustic excitation.	302
6.3	Response of panel 4 to acoustic excitation.	303
6.4	Response of panel 5 to acoustic excitation.	304
6.5	Response of panel 6 to acoustic excitation.	305
6.6	Response to siren excitation : effect of angle of propagation.	306
A.1	Similarity of corrected frequency spectra of wall pressure fluctuations under various flow conditions.	307
A.2	Turbulent boundary layer spectra at panel positions.	308
A.3	Amplitude of narrow band longitudinal space-time correlations of the wall pressure field.	309
A.4	Low frequency value of narrow band longitudinal pressure correlation amplitudes.	310
A.5	Amplitude of narrow band lateral space-time correlations of the wall pressure field.	311
A.6	Low frequency values of narrow band lateral pressure correlation amplitudes.	312
A.7	Convection velocities derived from narrow band longitudinal space-time correlations of the wall pressure field.	313
A.8	Siren tunnel noise spectra.	314
A.9	Excitation spectrum in the siren tunnel.	315
B.1	Effect of filter bandwidth on response spectra : Loss Factor = 0.012.	316
B.2	Effect of filter bandwidth on response spectra : Loss Factor = 0.002.	317
B.3	Spectrum resolution corrections for filter with 1.2% bandwidth.	318
B.4	Spectrum resolution corrections for filter with 2.0% bandwidth.	319
B.5	Spectrum resolution correction at the natural frequency of a system in presence of background vibration : 1.2% filter bandwidth.	320
B.6	Spectrum resolution correction at the natural frequency of a system in presence of background vibration : 2.0% filter bandwidth.	321
B.7	Relationship between true and measured bandwidths at half-power point.	322

## ILLUSTRATIONS (Cont.)

<u>Figure</u>		<u>Page</u>
C.1	Panel static deflection due to permanent magnetism of the exciter.	323
C.2 (a)(b)	Mode shapes for 3.5in x 3.5in x 0.015in panel.	324/325
C.3 (a)(b)	Mode shapes for 4.0in x 2.75in x 0.015in panel.	326/327
C.4 (a)(b)	Mode shapes for 4.0in x 2.0in x 0.015in panel.	328/329

## TABLES

		Page
3.1	Summary of Experimental Conditions	63
4.1	Average measured loss factors for zero airflow (2 pages)	86
4.2	Effect of pressure equalising system on 4.0in x 2.75in x 0.015in panel	88
4.3	Mean loss factors measured in the siren tunnel	90
4.4	Effect of airflow on damping loss factor (Mean Values)	108
5.1	Dimensions of the experimental panels	111
5.2	Ratio of theoretical to measured displacement power spectral density (boundary layer excitation)	122
5.3	Value of non-dimensional panel length at natural frequencies (boundary layer excitation)	124
6.1	Overall root-mean-square displacement at probe measuring position (siren excitation)	138
6.2	Ratio of theoretical to measured displacement power spectral density (siren excitation)	141
6.3	Values of non-dimensional panel length at natural frequencies (siren excitation)	143
B.1	The effect of filter bandwidth on the measured peaks in the displacement spectra	169
C.1	Properties of panel materials	173
C.2	Panel natural frequencies (3 pages)	177
D.1	Modal R.M.S. Displacement: Panel 3, $M_0=0.3$	188
D.2	Modal R.M.S. Displacement: Panel 4, $M_0=0.3$	189
D.3	Modal R.M.S. Displacement: Panel 5, $M_0=0.3$	190
D.4	Modal R.M.S. Displacement: Panels 2 and 6, $M_0=0.3$	191
D.5	Modal R.M.S. Displacement: Panel 3, $M_0=0.5$	192
D.6	Modal R.M.S. Displacement: Panel 4, $M_0=0.5$	193
D.7	Modal R.M.S. Displacement: Panel 5, $M_0=0.5$	194
D.8	Modal R.M.S. Displacement: Panels 2 and 6, $M_0=0.5$	195

## SYMBOLS

$a$	Correlation exponential decay parameter; equation (2.53).
$a_1, a_2$	Longitudinal correlation decay parameters; equations (2.83) (2.84).
$a_3, a_4$	Lateral correlation decay parameters; equation (2.54).
$a_1'$	Longitudinal correlation decay parameter for inclined flow; equation (2.91).
$a_3'$	Lateral correlation decay parameter for inclined flow; equation (2.91).
$A$	Area of structure. For panel $A = L_1 L_3$ .
$b$	Typical excitation wave number $b = \omega/U_c(\omega)$ .
$b_1$	Longitudinal wave number for inclined flow; $b_1 = b \cos \theta$
$b_3$	Lateral wave number for inclined flow; $b_3 = b \sin \theta$
$B$	Defined by equation (A.4).
$c$	Lateral correlation term; equation (2.54).
$c_o$	Speed of sound.
$C$	Viscous damping rate.
$C_a$	Generalised damping coefficient in $\alpha^{th}$ mode.
$C_{ae}$	Effective viscous damping coefficient in terms of the hysteretic damping; $C_{ae} = \frac{K_a v_a}{\omega}$ .
$C_p(\underline{x}', \underline{x}'', \omega)$	Real part of cross power spectral density function $S_p(\underline{x}', \underline{x}'', \omega)$
$C_{p1}(x_1', x_1'', \omega)$	Real part of longitudinal cross power spectral density function $S_{p1}(x_1', x_1'', \omega)$ .
$C_{p3}(x_3', x_3'', \omega)$	Real part of lateral cross power spectral density function $S_{p3}(x_3', x_3'', \omega)$ .
$C_p(\xi_1, \xi_3, \omega)$	$= C_p(\underline{x}', \underline{x}'', \omega)$ for homogeneous pressure field
$C_v$	Displacement probe capacitance.
$\bar{C}_v$	Probe capacitance for parallel surfaces separated by distance $\bar{y}$ .
$d$	Lateral correlation term; equation (2.54).
$d_m$	Defined by equation (2.57).
$d_{mr}$	Defined by equation (2.66).

# SYMBOLS (Cont.)

$d'_{ns}(a)$	Defined by equation (2.59).
$D$	Flexural rigidity of a plate.
$D(\tau)$	Weighting function in the computation of $S'(p(\underline{x}'), w(\underline{x}'), \omega)$ ; equation (4.21).
$D_{\alpha\beta}$	Defined by equation (4.32).
$D_{\alpha\beta}^*$	Complex conjugate of $D_{\alpha\beta}$ .
$D_{\alpha\beta}^r$	Real part of $D_{\alpha\beta}$ ; equation (4.32).
$D_{\alpha\beta}^i$	Imaginary part of $D_{\alpha\beta}$ ; equation (4.32).
$E_m$	Young's modulus for the panel material, in $x_1$ direction.
$E_n$	Young's modulus for the panel material, in $x_3$ direction.
$f, f', f''$	Frequency in cycles per second.
$f_r$	Natural frequency of mode of order $r$ for one-dimensional system.
$f_\alpha \equiv f_{m,n}$	Natural frequency of mode of order $\alpha = m, n$ for two-dimensional system.
$f_F$	Centre frequency of analysing filter.
$\Delta f_F$	Filter bandwidth at the half-power point.
$\Delta f_M$	Measured bandwidth of a resonance peak.
$\Delta f_T$	True bandwidth of a resonance peak.
$F_p$	Excitation force amplitude.
$F(\frac{\omega \xi_1}{U_c}, \frac{\omega \xi_2}{U_c})$	Defined by equation (A.9).
$g$	Defined by equation (2.24).
$G(f)$	Single-sided spectral density function measured in practice $G(f) = 2\pi G(\omega)$ .
$G(\omega)$	Single-sided spectral density function in terms of $\omega$ $G(\omega) = 2 S(\omega)$ .
$G_d(f)$	Panel displacement spectral density function.
$G_d^!(f)$	Measured panel displacement spectral density function uncorrected for resolution loss.
$G_E(f)$	Equivalent displacement spectral density function representation of background vibration, equipment noise, etc.

# SYMBOLS (Cont.)

$h_{\alpha}(\tau)$	Impulse response function for mode of order $\alpha$ .
$h_{\alpha\beta}$	Defined by equation (2.24).
$H_{\alpha}(\omega)$	Complex response function for mode of order $\alpha$ ; equation (2.16).
$H_{\alpha}^{*}(\omega)$	Complex conjugate of $H_{\alpha}(\omega)$ .
$H_1(f)$	Complex response function.
$H_2(f)$	Complex response function of an analysing filter.
$i$	$= \sqrt{-1}$
$I_{\alpha\beta}(\omega)$	Defined by equation (2.21).
$I_{\alpha\beta}'(\underline{x}', \underline{x}'')$	Defined by equation (4.28).
$j_{mm}(\omega)$	Joint acceptance term in $x_1$ direction ( $m=r$ ).
$j_{mr}(\omega)$	Real part of cross acceptance term in $x_1$ direction; equation (2.42).
$j_{nn}'(\omega)$	Joint acceptance term in $x_3$ direction ( $n=s$ ).
$j_{ns}'(\omega)$	Real part of cross acceptance term in $x_3$ direction; equation (2.43).
$J_{\alpha\alpha}(\omega)$	Displacement joint acceptance for mode $\alpha$ ; equation (2.20).
$J_{\alpha\beta}(\omega)$	Displacement cross acceptance for mode $\alpha$ ; equation (2.20).
$k$	Constant of proportionality.
$k'$	Defined by equation (C.4).
$k_1$	Range boundary for excitation longitudinal narrow band correlation coefficient (Section A.5).
$k_3$	Range boundary for excitation lateral narrow band correlation coefficient (Section A.5).
$k_{mr}(\omega)$	Imaginary part of cross acceptance in $x_1$ direction; equation (2.44).
$K_r, K_{\alpha}$	Generalised stiffness in modes of order $r$ and $\alpha$ respectively.
$K', K''$	Constants defined by equations (B.5) and (B.14).
$l$	Arc length for function $S(p(\underline{x}'), w(\underline{x}''), \omega)$ .
$L$	Typical structural length.
$L_1$	Panel length in $x_1$ direction.
$L_3$	Panel length in $x_3$ direction.
$L_{\alpha}$	Generalised external force in mode of order $\alpha$ ; equation (2.4).
$m$	Mode order in $x_1$ direction, denoting the number of modal half-wavelengths.
$M$	Mass per unit area.
$M_r, M_{\alpha}$	Generalised mass in modes of order $r$ and $\alpha$ respectively. equation (2.4)
$M_0$	Free stream Mach number.



# SYMBOLS (Cont.)

$n$	Mode order in $x_3$ direction, denoting the number of modal half-wavelengths.
$N$	Number of periods in autocorrelation function; $N = f\tau$ .
$p = p(\underline{x}, t)$	Pressure at point $\underline{x}$ and time $t$ .
$\bar{p}^2 = \langle p^2 \rangle$	Mean square pressure.
$p_m$	Defined by equation (2.57).
$p_{mr}$	Defined by equation (2.66).
$p'_n(a)$	Defined by equation (2.59).
$p'_{ns}$	Defined by equation (2.68).
$\Delta p$	Static pressure differential.
$q_0$	Free stream dynamic pressure.
$q_m$	Defined by equation (2.57).
$q_{mr}$	Defined by equation (2.66).
$q'_n(a)$	Defined by equation (2.59).
$q'_{ns}$	Defined by equation (2.68).
$q_\alpha(t)$	Generalised co-ordinate of mode of order $\alpha$
$Q(\underline{x}', \underline{x}'', \omega)$	Complex part of $S^*(\underline{x}', \underline{x}'', \omega)$ .
$Q_{p_1}(\underline{x}_1', \underline{x}_1'', \omega)$	Complex part of $S^*_{p_1}(\underline{x}_1', \underline{x}_1'', \omega)$ .
$Q_{p_3}(\underline{x}_3', \underline{x}_3'', \omega)$	Complex part of $S^*_{p_3}(\underline{x}_3', \underline{x}_3'', \omega)$ .
$r$	Mode order in $x_1$ direction, denoting the number of modal half-wavelengths. Alternatively, radius of displacement probe element.
$R$	Outer radius of displacement probe guard ring.
$R(p(\underline{x}'), w(\underline{x}'')_\tau)$	Cross correlation function between pressure $p(\underline{x}', t)$ and displacement $w(\underline{x}'', t)$ ; equation (4.14).
$R_d(\tau)$	Displacement autocorrelation function; equation (2.10).
$R_p(\underline{x}', \underline{x}'', \tau)$	Pressure cross correlation function; equation (2.12).
$R_{p_1 \Delta \omega}(\xi_1, \xi_3, \tau; \omega)$	Filtered pressure cross correlation function defined in equation (A.1).
$s$	Mode order in $x_3$ direction, denoting the number of modal half-wavelengths.
$S(p(\underline{x}'), w(\underline{x}''), \omega)$	Cross power spectral density function between excitation pressure $p(\underline{x}', t)$ and displacement $w(\underline{x}'', t)$ ; equation (4.14).
$S'(p(\underline{x}'), w(\underline{x}''), \omega)$	Value of $S(p(\underline{x}'), w(\underline{x}''), \omega)$ computed from cross correlation function; equation (4.21).

# SYMBOLS (Cont.)

$S_d(\omega)$	Displacement power spectral density function; equation (2.14).
$S_p(\omega)$	Pressure power spectral density function.
$S_p(\underline{x}', \underline{x}'', \omega)$	Pressure cross-power spectral density function; equation (2.15).
$S_p^*(\underline{x}', \underline{x}'', \omega)$	Complex conjugate of $S_p(\underline{x}', \underline{x}'', \omega)$ .
$S_p(\underline{\xi}, \omega) \equiv S_p(\xi_1, \xi_3, \omega)$	Alternative form of $S_p(\underline{x}', \underline{x}'', \omega)$ for homogeneous pressure field.
$S_{p1}(x_1', x_1'', \omega)$	Longitudinal pressure cross-power spectral density function; equation (2.29).
$S_{p3}(x_3', x_3'', \omega)$	Lateral pressure cross-power spectral density function; equation (2.29).
$S_\alpha^r$	Defined by equation (4.31).
$S_\alpha^l$	Defined by equation (4.31).
$t, T$	Time parameters.
$U_o$	Free stream velocity.
$U_1$	Local flow velocity in $x_1$ direction.
$\bar{U}_c$	Overall convection velocity of boundary layer pressure field.
$U_c \equiv U_c(\omega)$	Narrow band pressure field convection velocity at frequency $\omega$ .
$v$	Tape recorder speed
$w(\underline{x}, t)$	Structural displacement.
$\bar{w}$	Displacement amplitude.
$w'$	Measured amplitude in multidegree of freedom system.
$w_r$	Displacement of single degree of freedom system at $\omega = \omega_r$ .
$w_r'$	Measured displacement at $\omega = \omega_r$ .
$w_1'$	Measured displacement at half-power point.
$x$	Distance measured along tunnel working section, in downstream direction.
$\underline{x}$	$\equiv (x_1, x_3)$ . Distance vector in $(x_1, x_3)$ plane.
$x_1, x_2, x_3$	Rectangular co-ordinates with panel in $(x_1, x_3)$ plane and positive $x_1, x_3$ directions parallel to the panel axes. $x_1$ in flow direction when $\theta = 0$ .
$y$	Distance between probe face and structure.
$\bar{y}$	Mean distance between probe face and structure.
$y'$	Indicated distance between probe face and structure; equation (3.4).

# SYMBOLS (Cont)

$y'_s$	Value of $y'$ when probe guard ring touches the structure.
$\bar{y}_s$	Value of $\bar{y}$ when probe guard ring touches the structure.
$\Delta y$	$= \bar{y} - y'$ . Difference between mean and measured separations.
$y_1, y_3$	Rectangular coordinates in plane of panel, positive $y_1$ direction in the flow direction.
$Y_\alpha(\omega)$	Complex impedance of the structure.
$Y_\alpha^*(\omega)$	Complex conjugate of $Y_\alpha(\omega)$ .
$z$	Defined by equation (3.3).
$Z_\alpha$	Constant; equation (4.38) et seq.
$Z_1(\omega), Z_2(\omega)$	Frequency response functions of analysing filters.
$Z_1^*(\omega)$	Complex conjugate of $Z_1(\omega)$ .
$\alpha$	Two-dimensional mode order $\alpha \equiv (m, n)$ .
$\alpha_1, \alpha_2$	Constant coefficients in longitudinal narrow band pressure cross correlation coefficient; equations (A.19), (A.20).
$\alpha_3, \alpha_4$	Constant coefficients in lateral narrow band pressure cross correlation coefficient; equations (A.21), (A.22).
$\alpha_5$	Constant coefficient in narrow band convection velocity function; equation (A.23).
$\beta$	Two-dimensional mode order $\beta \equiv (r, s)$ .
$\gamma$	Measure of inverse radius of turbulence component.
$\gamma_m$	Eigenvalue corresponding to the free vibration of the $m^{\text{th}}$ order mode of a string.
$\gamma_1'$	Defined by equation (C.2).
$\gamma_2'$	Defined by equation (C.3).
$\gamma_3'$	Defined by equation (C.4).
$\Gamma$	Measure of correlation area of the pressure field; $\Gamma = \frac{2\pi}{\gamma^2}$
$\delta$	Boundary layer thickness.
$\delta^*$	Boundary layer displacement thickness.
$\delta_\alpha$	Viscous damping factor in mode of order $\alpha$ .
$\Lambda_m$	Defined by equation (2.57).
$\epsilon$	$= X/ w_r $
$\epsilon_s$	Standard deviation error for $G(f)$ ; Section B.1.
$\zeta$	Pressure correlation length defined by $\cos \frac{\omega \zeta}{U_c} = 0$ .

# SYMBOLS (Cont.)

$\zeta_{m,n}$	Value of $\zeta$ at $f = f_{m,n}$ .
$\underline{n} \equiv (\eta_1, \eta_3)$	Separation in $\underline{y} \equiv (y_1, y_3)$ direction.
$\theta$	Angle between positive $x_1$ direction and flow direction, i.e. angle between positive $x_1$ and $y_1$ directions.
$\theta_t$	Mean statistical lifetime of an eddy.
$\Theta(f)$	Defined by equation (B.10).
$\kappa_1, \kappa_2$	Constant coefficients in narrow band convection velocity function; equation (A.23).
$\kappa_\alpha(\underline{x}', \underline{x}'')$	$= \psi_\alpha(\underline{x}'')\Lambda(\underline{x}')$ .
$\lambda$	Excitation wave length.
$\lambda_m$	Modal wavelength $= 2L_1/m$ .
$\Lambda_\alpha(\underline{x})$	Defined by equation (4.20).
$\mu = \mu(\underline{x})$	Panel mass per unit area.
$\nu_r \nu_\alpha$	Hysteretic damping factor, or loss factor, for modes of order $r$ and $\alpha$ respectively. Defined in terms of the complex stiffness $K(1 + i\nu)$ .
$\underline{\xi} \equiv (\xi_1, \xi_3)$	Separation in $\underline{x}$ direction.
$\rho$	Density.
$\rho_0$	Free stream density.
$\rho_\ell$	Radius of curvature of $S(p(\underline{x}'), w(\underline{x}''), \omega)$ .
$\rho(\tau)$	Autocorrelation coefficient.
$\rho_p(\xi_1, \xi_3, \tau; \omega)$	Narrow band pressure cross-correlation coefficient; equation (A.5).
$\sigma$	Poisson's ratio for the material of the panel.
$\tau$	Time delay.
$T_r$	$\tau_r^2 = 1 + \nu_r^2$ ; equation (B.9).
$\phi$	Angle of inclination between displacement probe face and structure.
$\phi(f)$	Defined by equation (B.10).
$\phi_D(\omega - \omega')$	Defined by equation (4.23).
$x$	Off-resonant contribution to vibration in the neighbourhood of a natural frequency.
$x_M$	Measured displacement at a frequency removed from any natural frequency.
$\bar{x}_M$	Mean value of $x_M$ from values either side of a natural frequency.

# SYMBOLS (Cont)

$\psi_m(x_1), \psi_r(x_1)$	Mode shapes of order m and r in the $x_1$ direction.
$\psi_n(x_3), \psi_s(x_3)$	Mode shapes of order n and s in the $x_3$ direction.
$\psi_\alpha(\underline{x}), \psi_\beta(\underline{x})$	Panel mode shapes of order $\alpha$ and $\beta$ .
$\Psi(r)$	Defined by equation (B.10).
$\omega, \omega'$	Angular frequency, radians per second.
$\omega_1, \omega_2$	Angular frequencies at half-power points.
$\omega_r, \omega_\alpha$	Angular frequencies of modes of order r and $\alpha$ .
$\Delta\omega$	Angular frequency bandwidth.
$\Omega(\frac{-\omega}{U}, \xi_3, 0)$	Defined by equation (A.9).
$\langle \quad \rangle$	Mean value.
$ \quad $	Modulus.

## CHAPTER 1

### Review of Previous Work and the Aims of the Investigation

#### 1.1 Introduction to the General Problem

The study of the response of flexible structures to turbulent boundary layer excitation became important with the advent of high speed subsonic passenger carrying aircraft, but the problem has applications also in the design of missiles and in underwater investigations. The response of the structure is of direct interest because the turbulent boundary layer might induce disturbing vibration levels in the neighbourhood of sensitive equipment or might create levels of vibration which, although not very high, could produce or accelerate structural fatigue because of the long term exposure. The vibration is of interest also because of the transducer action in converting the hydrodynamic fluctuations in the boundary layer into acoustical energy which is radiated into the interior of the body or into the surrounding fluid. The efficiency of the structure as a transducer will depend on the response to boundary layer excitation and on the radiation efficiency of the structure. A study of the vibration of structures exposed to turbulent boundary layer excitation is essential, therefore, in understanding the fatigue and noise radiation problems.

#### 1.2 Review of Previous Work

##### 1.2.1 General Review

The response of structures to random excitation has been studied theoretically by a number of authors, for a range of excitation conditions and for structures ranging from strings to panel arrays. In some cases the aim of the investigation has been the prediction of structural vibration, whilst in others the work has been extended to include the estimation of the acoustic radiation from the structure. Experimental investigations are much smaller in number and the more important ones have been reported during the progress of the present work. In only two or three cases has there been any attempt to compare the measured vibration with that predicted and in two

cases the work was concerned largely with the occurrence of running waves in the experimental panels.

In the following review of work by other authors it is intended to restrict discussion to only the more important published results, and to omit discussion on the acoustic radiation problem.

#### 1.2.2 Theoretical Investigations

The theoretical investigations considered have one common assumption, that there is no interaction between the plate vibration and the excitation field. This means that it is assumed that the excitation field is identical to that on a rigid surface and, for example, instabilities such as panel flutter cannot occur. With two exceptions the structures are all of finite size and are in the form of strings, beams, single panels, or panel arrays. The exceptions are the structures considered by Ribner (1956) and Corcos and Liepmann (1956) which are infinitely large plates, Corcos and Liepmann claiming that the assumption is valid since the mean square acceleration, integrated over the panel area, does not depend significantly on the boundary conditions. When considering the local vibration the assumption is not necessarily a valid one and the infinite model does not provide a good representation of practical structures. For obvious reasons the infinite panel response spectra will not contain resonance peaks. Kraichnan (1957) assumed initially that the structure was a semi-infinite plane but, when considering the structural vibration, he divided the plane into a series of independent square panels so that the analysis was essentially that of a finite structure. In all analyses except that of Dyer (1958) it was assumed that the vibrating structure was bounded on each side by a semi-infinite space, and even then the case of a panel radiating into a closed box was considered by Dyer only as a special radiation case.

The analysis of the finite structure was carried out in all investigations by the use of the normal mode approach and the majority of authors assumed that the structural boundaries satisfied the conditions for simple supports. This assumption does not affect the main conclusions

of the investigations, but it simplifies the theoretical analysis. Bozich (1964) has compared results for simply-supported and fully fixed plates subjected to acoustic excitation and has shown that, except for a very rapidly decaying excitation field, the assumption of simply-supported boundaries overestimates the response by a factor of up to two. However, the variation of response with frequency is similar for the two edge conditions.

The derivation of the structural response function differs from author to author but it is possible to separate the methods into two general classes in which the response is expressed in either the frequency or the time domain. The two alternatives are in fact equivalent because the analysis can be transformed from one domain to the other by Fourier transformation, but differences do arise in the specification of the excitation function. In the time domain the excitation is defined in terms of the overall pressure cross-correlation function  $R_p(\xi_1, \xi_3, \tau)$  and in the frequency domain in terms of the pressure cross-power spectral density function  $S_p(\xi_1, \xi_3, \omega)$ . The theoretical investigations contain several types of random excitation but interest in the present discussion is centred primarily on acoustic and turbulent boundary layer pressure fields. In some investigations, particularly the early work of Ribner (1956), Corcos and Liepmann (1956), Lyon (1956) and Kraichnan (1957), there were only simple attempts at representing the boundary layer pressure field and the results were published in general terms using non-dimensional parameters. Later work contained attempts to represent the pressure fluctuations in a more realistic manner but, following the lead of Dyer (1958), complications in analysis were reduced by adopting a delta function representation of the boundary layer cross-correlation function. This simplification was restricted to the spatial terms except in the work of Eringen (1957) who used a delta function also in the time domain. Usually it was assumed that the correlation coefficient decayed exponentially with time. Thus the boundary layer pressure cross-correlation function proposed by Dyer (1958)

$$\langle p(x_1, x_3, t) p(x_1 + \xi_1, x_3 + \xi_3, t + \tau) \rangle = \langle p^2 \rangle \exp \left( -\gamma \sqrt{((\xi_1 - \bar{U}_c \tau)^2 + \xi_3^2)} - \frac{|\tau|}{\theta_t} \right) \dots (1.1)$$



was reduced by Dyer, and later by other authors, to the form

$$\langle p(x_1, x_3, t) p(x_1 + \xi_1, x_3 + \xi_3, t + \tau) \rangle = \langle p^2 \rangle \Gamma \delta(\xi_1 - \bar{U}_c \tau) \delta(\xi_3) e^{-\frac{|\tau|}{\theta_t}} \quad \dots (1.2)$$

where  $\frac{1}{\gamma}$  is a measure of the radius of a turbulence "eddy",  $\theta_t$  is the mean statistical lifetime of the turbulence,  $\langle p^2 \rangle$  is the mean square boundary layer pressure fluctuation,  $\Gamma = \frac{2\pi}{\gamma^2}$  is defined to be a measure of the correlation area of the pressure field, and  $\bar{U}_c$  is the overall convection velocity.

The parameters  $\Gamma$ ,  $\gamma$ ,  $\theta_t$  and  $\bar{U}_c$  in equation (1.2) are overall values and are independent of frequency, but  $\theta_t$  and  $\gamma$  (and hence  $\Gamma$ ) can be expressed, empirically, in terms of the boundary layer displacement thickness  $\delta^*$ . For simplicity the overall convection velocity  $\bar{U}_c$  is assumed to be independent of  $\xi_1$ , although boundary layer measurements (e.g. Bull (1963)) show this to be incorrect. The assumption of a constant velocity  $\bar{U}_c$  can be interpreted to imply that pressure eddies are convected at a speed which is independent of frequency, again in contradiction to measurements (Figure A.7).

In the frequency domain the pressure cross-power spectral density function  $S_p(\xi_1, \xi_3, \omega)$  has not been measured directly but it can be replaced by the product of the power spectral density function  $S_p(\omega)$  and the narrow band cross correlation function, both of which have been measured. Tack and Lambert (1962) adopted a system which lies between the frequency and time domain methods and is not legitimate in a strict sense. The analysis was carried out in the time domain but in the final results it was assumed that  $\Gamma$  and  $\theta_t$  in equation (1.2) were frequency dependent and corresponding empirical values were inserted. However, by definition, the right hand sides of equations (1.1) and (1.2) are independent of frequency.

Working in the frequency domain Powell (1958a) expressed the displacement power spectral density function for a single panel in terms of a double summation of the normal modes of order  $\alpha$  and  $\beta$ . The summation was

separated in two parts,  $\alpha = \beta$  and  $\alpha \neq \beta$ , and the associated terms were identified by Powell as the joint acceptance and cross acceptance respectively. Powell did not substitute particular representations for the excitation but showed that, in general, the cross terms could be neglected if the damping was sufficiently small, and that if the response was averaged over the panel surface, the cross terms would have a zero contribution due to the orthogonality property of the modes. In later work, Powell (1958b) used the general displacement power spectral density function to consider the vibration of strings under various random loads, and discussed the application to aircraft structures excited by jet noise. Nash (1961) obtained a displacement power spectral density function similar to that of Powell (1958a) but the method of derivation differed in that the analysis was carried out initially in the time domain and then was transformed to the frequency domain. Nash did not take the analysis much further than Powell, extending it only to consider the case of an excitation cross-correlation function separable in the time and space co-ordinates. He applied it in particular to a spatially uniform load in which the excitation space correlation coefficient was constant, and thus was not representative of a boundary layer pressure field.

The work of Powell was repeated by White (1962) for the case of strings with fixed or flexible supports, the excitation being in the form of sinusoidal components convected with a velocity independent of frequency. The flexible supports were introduced as an approximation to the type of supports achieved in practical structures. The results of White illustrate how the effect of the cross terms depends on the position along the beam, and show the importance of coincidence between the mode and excitation. White shows that coincidence occurs when the excitation convection velocity and the flexural velocity in the structure are equal and when the ratio of the string length  $L$  to the excitation wavelength  $\lambda$  is given approximately by

$$\frac{L}{\lambda} = \frac{\gamma_m L}{2\pi}$$

where  $\gamma_m$  is the eigenvalue corresponding to the free vibration in the  $m^{\text{th}}$  order modes. For a fixed end string  $\gamma_m = \frac{m\pi}{L}$  and  $\frac{L}{\lambda} = \frac{m}{2}$  which corresponds to results in Chapter 2.

Similar work was carried out on beams by Barnoski (1965) in an analysis of the response of single degree of freedom and continuous systems to deterministic and random excitation. Barnoski did not consider the case of a convected excitation field but proposed the reduction of a continuous spatially correlated loading into a set of correlated discrete loadings, as an approximate solution in the case of complex mode shapes and spatial correlation functions. This method does not seem to have application in boundary layer induced vibration problems.

An extension of the analysis to include a multi-support system was carried out by Mercer (1965) when the response spectrum was considered for a nine bay beam exposed to a convected excitation field similar in form to boundary layer turbulence. The variation of response with convection speed was illustrated and the relative magnitudes of the joint and cross terms were compared showing that in general the cross term contributions were not significant for the lightly damped structures. The response was calculated for the first band of nine modes bounded by the first order stringer torsion and bending modes, and the results showed trends similar to those for a single panel. This was particularly true for the stringer torsion mode which corresponds to the 9<sup>th</sup> order mode of a simply supported single beam. However, the single beam and the multi-beam do differ in one respect. Within one pair of bounding modes, the modal wavelength increases with natural frequency from a wavelength equal to two bay lengths to an effective wavelength equal to twice the overall length of the array. Thus there is a much greater opportunity for one mode to be near coincidence than in the case of a single beam where modal wavelength always decreases as frequency increases.

In time domain analysis, Lyon (1956) investigated the mean square modal response of a string exposed to several forms of random excitation including decaying turbulence convected along the string at a constant speed. It was assumed that the pressure field was purely random in space so that a correlation function with a delta function spatial term was used. The results show the occurrence of coincidence but this was apparent only when the excitation did not decay significantly whilst being convected a distance

equal to a modal wavelength. The disappearance of the wavelength matching peaks in the joint acceptance terms, to be discussed in Chapter 2, is shown in work by Bozich (1964) when the excitation decays very rapidly.

The analysis of Lyon was extended to two dimensions by Dyer (1958) and this investigation, with the work of Powell (1958a,b) has been the basis of the majority of subsequent investigations. Dyer used the Green's function technique, which is equivalent to the use of the impulse response function, to determine the displacement cross correlation function in terms of the panel normal modes. Initially proposing an exponential form of excitation cross correlation function (equation (1.1)), Dyer reduced the spatial terms to delta functions as shown in equation (1.2), before carrying out the response analysis.

The use of the delta function representation introduces several errors but Maidanik (1960) has shown that in certain cases of convected turbulence the errors may be small. The form of the cross correlation function in equation (1.2) implies that the pressure field is uncorrelated in the  $x_3$  direction but is highly correlated, because of convection, in the  $x_1$  direction. The uncorrelated lateral component implies that there will be no statistical coupling of modes  $(m-n)$  and  $(r-s)$  when  $n \neq s$ , but statistical coupling is possible in the longitudinal direction. However, Dyer assumed further that  $U_c \theta_t \ll L_1$ , i.e. that a turbulent eddy decays whilst travelling a distance which is small relative to the panel length, and the conclusions drawn by Dyer refer to a system which is effectively uncorrelated in space. Thus the predicted response does not include the statistical coupling of modes. The assumption  $U_c \theta_t \ll L_1$  is not valid for the experimental conditions discussed by the author in later chapters. A further disadvantage of the delta function representation is the implication of infinite energy, the excitation pressure power spectral density having a constant value at all frequencies. The panel displacement cross correlation function derived by Dyer was used by Baroudi (1964) and Maestrello (1965b) to indicate the presence of running waves in experimental panels.

For zero time delay, the results of Dyer give the mean square modal

response of the panel and under these conditions the effect of "hydrodynamic" coincidence was studied, in a given mode, when the component of the convection velocity in the direction of the standing wave on the plate matched the bending wave velocity.

Following the work of Dyer, the response of a beam to turbulent boundary layer excitation was studied by Tack and Lambert (1962). The delta function representation of the excitation cross correlation function shown in equation (1.2) was used as a basis, and the beam was assumed to have simply-supported mode shapes. The theoretical results were compared with measurements of the mean square modal response of a beam exposed to the turbulent boundary layer of an air flow with free stream Mach numbers up to  $M_0 = 0.3$ . However, in the final analysis the overall correlation area  $\Gamma$  and the eddy lifetime  $\theta_t$  in equation (1.2) were replaced by empirical frequency dependent parameters. The measured and predicted mean square displacements of the beam showed good agreement but the use of the empirical parameters makes it difficult to assess the reliability of the method. Measurements by Tack and Lambert suggested that, in the wind tunnel used for the experiments, the boundary layer convection velocity was almost equal to the free stream velocity, and the latter value was used in place of the convection velocity. This result differs from other investigations, where the convection velocities were 70% to 80% of the free stream values.

When estimating the radiation sound field of a rectangular panel excited by a turbulent boundary layer, Davies (1964) assumes the excitation correlation function shown in equation (1.1). However, for simplification in the analysis Davies introduces assumptions which effectively reduce the representation to the delta function form of equation (1.2). In a further assumption, that the turbulence lifetime is very short, the convected pressure field is effectively replaced by a non-convected field, and the final panel vibration results apply only to a very restricted form of excitation. The analysis of the structural vibrations is a combination of the work of Powell (1958a) and Dyer (1958) since both the frequency domain (joint and cross acceptances) and the time domain (Fourier transforms of the acceptances) are used. The choice of domain can depend on whether

the available information for the boundary layer turbulence is in the form of a spectral density function or a correlation function. Also, if numerical integration is used, the choice of function may be determined by the associated rate of decrease of the function with frequency or time.

The method of analysis of Kraichnan (1957) differs from that of other authors because of the use of the complete Fourier transform in the wave number-frequency domain, other investigators having used the partial transform in the space-frequency domain. However, the work of Kraichnan is similar to that of Powell and Dyer, the semi-infinite plane under the boundary layer being subdivided into a series of independently vibrating square panels with simply supported boundaries. The boundary layer pressure field was assumed to have a rigidly convected pattern and Kraichnan assumed an idealised wave number-frequency spectrum for the pressure fluctuations. The form of the spectrum was based on purely theoretical reasoning and does not provide a reasonable representation of later measurements. As the use of the assumed spectrum shape is implicit in subsequent analysis, the results are difficult to modify for alternative excitation functions.

### 1.2.3 Experimental Investigations

Experimental investigations of the response of simple structures to turbulent boundary layer excitation have been carried out by several authors but little attempt has been made to compare the measured response with theoretical estimates. The work has been confined primarily to controlled laboratory experiments with air or water as the excitation fluid, and there is a very limited amount of data published for in-flight measurements. Initially the experimental structures were simple panels of square or rectangular planform but recent investigations by Maestrello (1965) and McNulty (see Richards, Wilby and McNulty (1965)) have included panel arrays where the individual panels are separated by stringers. The vibration of the panels has been measured in the form of accelerations, strains, or displacements, the latter method having the advantage that the measuring probes could be of the non-contacting type and could be traversed over the panel surface.

Response spectra for single panels have been measured in subsonic wind tunnels by Baroudi (1964) and Maestrello (1965a,b,c) and in a water tunnel by Stevenson, Saltus and Taggart (1961). Baroudi used clamped panels which were 11 inches square and had thicknesses in the range of 0.0015 inch to 0.008 inch. These were exposed to airflow velocities of up to 190 ft/sec. Maestrello measured the response of 12" x 7" and 36" x 6.5" panels with thicknesses in the range of 0.02 inch to 0.08 inch, and airspeeds of up to 700 ft/sec. The airflow in the experiments conducted by Baroudi was fully developed pipe flow, and in the work of Maestrello the flow had a boundary layer with a displacement thickness of  $\delta^*$  where  $0.155 \text{ inch} < \delta^* < 0.180 \text{ inch}$ . In both investigations the measurements were influenced by background noise in the wind tunnel and, as in the present investigation, low frequency results had to be rejected. This limitation has a negligible effect on the results presented by Maestrello (1965a) and by the present author because the experimental panels were designed to have the lowest natural frequencies above the interference range. However, the panels used by Baroudi were very flexible so that a measurable response could be obtained at the low flow velocities. The lower natural frequencies of the panels were within the interference band, and rejection of the low frequency results implied a rejection of useful information. A further disadvantage of the very thin panels used by Baroudi was the presence of the "oil-can" effect and the panels were exposed to a slight static pressure differential to overcome the phenomenon. In addition to the above laboratory experiments, the vibration of an 8" x 6" x 0.018" experimental panel was measured in flight at Mach numbers up to  $M_0 = 1.6$ , by Webb, Keeler and Allen (1962), but it is difficult to interpret the results.

The spectral data in the four investigations is limited in scope and only Baroudi (1964) made a comparison between the measurements and the theoretical predictions. The response was calculated by use of the idealised delta function representation of the boundary layer pressure field proposed by Dyer (1958) and there was little agreement between experiment and theory. Spectral measurements by Maestrello (1965b) showed the presence of modes of unit order only in the lateral direction. This restriction is not observed

in the results presented by the author, modes of higher order being present in the measured and predicted spectra.

The mean square displacement of the panels has been measured by Maestrello (1965c) and he showed that there was a relationship between the displacement and the free stream velocity which varied from  $U_0^{2.0}$  to  $U_0^{4.7}$ . Maestrello compared this dependency with a similar one for the radiated acoustic power, the relationship varying from  $U_0^{2.3}$  to  $U_0^{8.0}$ . Similar measurements by Ludwig (1962) using the same equipment as that used by Baroudi, showed the acoustic power to be proportional to  $U_0^5$  for the thinner panels and  $U_0^6$  to  $U_0^8$  for the thickest panels. With the wide divergence of these results it becomes obvious that neither the mean square panel displacement, nor the radiated acoustic power, can be represented by the velocity term alone.

Using displacement cross-correlation techniques, Maestrello (1965b,c) and Baroudi (1964) investigated the occurrence of running flexural waves in the panels, and they were able to relate the measurements to theoretical predictions using the method of Dyer (1958). Maestrello showed that the waves occurred primarily in the thinner panels and at the higher flow speeds, and suggested that the change from standing waves to running waves was responsible for the change in the acoustic radiation laws. The change from standing to running waves could alter the radiation efficiency of the panels but this is responsible, probably, for only part of the change in the radiation laws. An alternative solution to that proposed by Maestrello (or more probably, the complete solution is a combination of the various suggestions) is given by the joint acceptance curves shown in Chapter 2. On this basis the mean square displacement law, which Maestrello associates with the acoustic radiation power law, changes when the condition of coincidence is reached for the dominant modes. When the flow velocity increases from a value below that for coincidence, the joint acceptance for a given mode increases, but further velocity increases above coincidence result in decreases in the joint acceptance. The coincident state may be associated with running waves but this is not necessarily true for all modes.



The existence of the running waves will depend upon the lifetime of the pressure fluctuations and on the damping present in the structure. When the lifetime is short relative to the time for convection over the panel surface, or when the damping in the structure is high, the waves in the panel will suffer negligible reflection at the panel boundaries. In such circumstances it will be difficult to set up a standing wave system and the vibration of the structure will be composed essentially of running waves. The condition of coincidence will occur independently of whether the vibration is composed of standing waves or of running waves. Coincidence will arise when there is wavelength and frequency matching between the excitation and the structure, and is of importance when it occurs in the neighbourhood of a panel natural frequency.

Running waves have been observed by Bies (1965) in a circular panel excited by the turbulent boundary layer in supersonic flow up to a Mach number  $M_0 = 3.5$ . The panel was designed to have a high degree of damping so that wave reflection at the boundaries was a minimum, and was subjected to a small tension to maintain a flat surface and to prevent the "oil-can" effect. The analysis of the panel vibration was carried out in octave frequency bands in a frequency range of high modal density and qualitative, but not quantitative, agreement was claimed between the measured and predicted results.

### 1.3 Extension of Previous Work.

#### 1.3.1 Requirements

In the review of previous theoretical investigations of the response of structures to random excitation it was seen that the work was restricted to simple structures and to simple representations of the excitation field. In particular there was a negligible amount of work in which realistic representations of the statistical characteristics of a turbulent boundary layer were used. This omission was the result partly of the absence of detailed information when the investigations were carried out, and partly as a result of the desire to reduce the complexity of the theoretical analysis. As a more detailed knowledge of the excitation field in a

boundary layer is now available, the theoretical studies can be extended using analytical forms of the pressure field which are more realistic representations of the physical phenomenon. The effect of aerodynamic parameters such as flow velocity, boundary layer thickness and pressure gradient, in addition to the effects of the structural parameters, can be investigated theoretically.

The review has shown also that, apart from the two contemporary investigations which were reported during the period covered by the current work, there were virtually no measurements of the response of structures excited by turbulent boundary layers. Thus there was a requirement for experimental data which could be used to test the reliability of the theoretical predictions. The comparison between theory and experiment was needed for two reasons: firstly to investigate the variation of the structural response with the aerodynamic and structural parameters, and secondly to compare the absolute magnitudes of the predicted and measured response. However, due to the random nature of the systems, it was not expected that close numerical agreement could be achieved. The work published since the start of this investigation has helped to provide a basis for comparison between theoretical and experimental results in certain cases but further work is required.

#### 1.3.2 Present Investigation

A specially designed boundary layer wind tunnel with low noise and vibration characteristics has been built at the University of Southampton, and this tunnel was used to provide the turbulent boundary layer excitation for the experimental investigation.

The wall pressure field in the wind tunnel has been studied in detail by Bull (1963) for a zero pressure gradient, and this information can be used in the prediction of the response of structures placed in the wall of the tunnel working section. Thus a comparison can be made between measured and predicted results. The design of the tunnel, with flow control being achieved using single position liners, limits the variation of tunnel speed and the present construction permits only two operating conditions. However the subsonic working section is sufficiently long to allow a range of boundary

layer thicknesses to be used. The method of construction of the panels permitted measurements to be made of the effect of flow direction. The effects of pressure gradient and supersonic flow are not discussed but a limited range of flow parameters is available for a comparison to be made between measured and estimated vibration levels.

For structural simplicity the experimental specimens were constructed in the form of single square or rectangular panels, with the intention that the programme could be extended to more complex panel-stringer combinations in subsequent investigations. The single panels are not representative of many practical structures but their use as experimental structures is essential at the beginning of an investigation of this nature, so that the number of possible variables is not too large. A series of experimental panels was used in order that the effects of panel dimensions, aspect ratio and natural frequency could be observed.

The design of the wind tunnel is such that the static pressure in the tunnel working section is below ambient and under normal running conditions there is a static pressure differential across the walls of the tunnel. The pressure differential is experienced also by the experimental panels and a pressure equalising system had to be constructed to eliminate the differential. This caused additional complications in the panel vibration measurements but there was partial compensation because the effect of a static pressure differential on the panel vibration could be measured.

In addition to the boundary layer wind tunnel, experimental equipment available at the University of Southampton enabled comparative response measurements to be made when specimens were exposed to grazing incidence acoustic waves in a siren tunnel, or to acoustic waves with non-zero angles of incidence in the near or far field of a cold air jet. Air jet excitation was used in early measurements using thin panels and the panel vibration results were similar to those obtained in the siren tunnel, as shown by Wilby (1963) and Bull, Wilby and Blackman (1963). The measurements are not presented here because the panels were accidentally destroyed before the investigation was completed, and later measurements were confined

to the siren and boundary layer tunnels.

The main investigation carried out by the author was supplemented by subsidiary investigations which arose from the limitations of the available equipment. One such problem was associated with the requirement for analysing filters with very narrow bandwidths. The filters available had bandwidths which were comparable to, or greater than, the bandwidths of the peaks in the panel response spectra. A method is presented for the estimation of the spectral resolution loss due to the finite bandwidth of the filters but the filter bandwidths were too wide to permit reasonable estimation of the panel damping in the presence of an airflow. Alternative methods using random techniques were employed with only limited success and the application of these techniques is discussed in Chapter 4.

The basic aims of the investigation can now be stated. They were primarily the measurement of the vibration of structures exposed to turbulent boundary layers in flows with zero pressure gradient, studying the variation of response with boundary layer thickness, flow velocity, panel orientation relative to flow direction, and static pressure differential. The experimental panels were to be exposed to alternative forms of convected, random excitation. The experimental programme was to be carried out in association with a theoretical investigation using a realistic representation of the pressure field so that the measured and predicted response variation with the aerodynamic parameters could be compared. The comparison would also indicate the accuracy with which the magnitude of the response could be predicted. Subsidiary investigations into the effect of filter bandwidth on the spectrum resolution of the measurements, and into the effect of flow velocity on the panel damping, would be necessary for the completion of the main programme. The programme, although restricted to simple panels, provides experimental and theoretical data on the effect of several parameters which have not been studied previously, only flow velocity having been varied in other investigations.

The form of the experimental panels was chosen for several reasons.

As has been stated previously, it was desirable that the number of structural parameters should be restricted so that the theoretical and experimental analysis would not become too complicated initially. The size and shape of the panels was determined from practical considerations which are discussed in section 3.3. Because of these restrictions the direct application of the results will be limited but it was decided that this was preferable until the reliability of the experimental and theoretical method was established. The work could then be extended, as is being done now by McNulty (see Richards, Wilby and McNulty (1965)) to more complicated panel arrays which resemble practical structures more closely.

The results of the investigation will be of direct use in the estimation of the level of boundary layer induced vibration at different positions on the structure of a moving body. The estimation of the response is required in the prediction of fatigue damage but it will provide also an indication of the variation of acoustic radiation with the aerodynamic parameters investigated. Detailed analysis of the noise radiation problem cannot be completed, however, until measurements have been made of the panel displacement cross-correlation function. Application of the results will be restricted in the first instance to structures which vibrate as a series of independent panels, but this may be extended following further investigations into the vibration of multi-panel arrays.

#### 1.4 Summary

The survey of the published theoretical studies of the response of simple structures to random excitation has shown that the basic modal approach, following Powell (1958a) or Dyer (1958), for finite structures is well established but that there has been little attempt to use a realistic representation of the statistical properties of a turbulent boundary layer in the estimation of the response of structures to boundary layer excitation. In many cases the investigations were not intended to include boundary layer excitation and in others, due to the lack of alternative information or to the need for simplification, only simplified representations of the boundary layer pressure field were used. From available data it is possible now to

use realistic representations of the boundary layer pressure field and to calculate the associated panel response. Thus a theoretical study of the effect of aerodynamic and structural parameters can be carried out in the present investigation.

With the exception of two investigations reported during the period covered by the present work, there is a negligible amount of experimental data which refers to the vibration of boundary layer excited structures. Even when the recently published results are considered, the effect of several parameters is excluded and there is no systematic comparison between theoretical and experimental results. Thus the combined experimental and theoretical programme which has been outlined in the preceding section and which is described in detail in the succeeding chapters, covers aspects of the problem which are not contained in earlier or contemporary investigations.

## CHAPTER 2

### Theoretical Response to Boundary Layer Excitation

#### 2.1 Introduction

In the review of other theoretical investigations in Chapter 1, it was seen that the normal mode method was used for all work on finite structures, and that the wave approach was used for infinite structures. In the present analysis it is assumed that the excitation pressure pattern is correlated, in a moving frame of reference, over distances which are of the same order of magnitude as the panel dimensions. This assumption is justified by the experimental results of Bull (1963). Thus the normal mode approach will be used in the prediction of panel response to boundary layer and acoustic excitation. The displacement power spectral density function will be derived from the impulse response function, a method similar to that of Dyer (1958), but the resulting equation for the spectral density function will be directly comparable to the result of Powell (1958a).

It will be assumed initially that the panel is a flat plate in bending, and that there is negligible interaction between the panel and the excitation field. The vibration will be assumed to be adequately represented by a series of normal modes, with no modal coupling due to damping. At a later stage of the analysis, further assumptions will be introduced regarding separability in the co-ordinate directions and the form of the mode shapes. For ease of computation simply supported mode shapes will be used, but other forms can be used if necessary.

#### 2.2 General Theory

The displacement  $w(\underline{x}, t)$  of a vibrating plate is assumed to obey the thin-plate equation

$$M\nabla^4 w + C\dot{w} + D\nabla^2 w = p(\underline{x}, t) \quad \dots (2.1)$$

where  $M$  is the mass per unit area,  $C$  the damping,  $D$  the flexural rigidity and  $p(\underline{x}, t)$  the exciting force. The solution to equation (2.1) can be expressed in terms of a linear sum of the normal modes

$$w(\underline{x}, t) = \sum_{\alpha=1}^{\infty} q_{\alpha}(t) \psi_{\alpha}(\underline{x}) \quad \dots (2.2)$$

where  $q_{\alpha}(t)$  is the generalised co-ordinate for the  $\alpha^{\text{th}}$  mode, and  $\psi_{\alpha}(\underline{x})$  is the mode shape function. In practice the infinite sum can be reduced, for a sufficient degree of accuracy, to a summation over a finite range of  $\alpha$ .

From Lagrange's equation, the motion in the  $\alpha^{\text{th}}$  mode is given by the equation

$$M_{\alpha} \ddot{q}_{\alpha}(t) + C_{\alpha} \dot{q}_{\alpha}(t) + K_{\alpha} q_{\alpha}(t) = L_{\alpha}(t) \quad \dots (2.3)$$

where  $M_{\alpha}$ ,  $C_{\alpha}$ ,  $K_{\alpha}$  and  $L_{\alpha}$  are, respectively, the generalised mass, damping, stiffness and external force in the  $\alpha^{\text{th}}$  mode, and, in particular,  $M_{\alpha}$  and  $L_{\alpha}$  are defined by

$$\begin{aligned} M_{\alpha} &= \int_A \mu(\underline{x}) \psi_{\alpha}^2(\underline{x}) d\underline{x} \\ L_{\alpha} &= \int_A p(\underline{x}, t) \psi_{\alpha}(\underline{x}) d\underline{x} \end{aligned} \quad \dots (2.4)$$

where  $\mu(\underline{x})$  is the panel surface density and where the notation  $\int_A d\underline{x}$  is an abbreviated form of the double integral  $\int_{x_1} \int_{x_3} dx_1 dx_3$  over the structural area  $A$ . The frame of reference is the three-dimensional rectangular Cartesian system  $(x_1, x_2, x_3)$  and the undisturbed panel neutral plane is assumed to lie in the  $(x_1, x_3)$  plane. The natural frequency of the mode is defined to be  $\omega_{\alpha} = \sqrt{K_{\alpha}/M_{\alpha}}$

The equation of motion in the  $\alpha^{\text{th}}$  mode can be written in the form of equation (2.3) only if it is assumed that the modal coupling due to damping effects is negligible.



The form of equation (2.3) implies that the damping in that mode is of the viscous type, the damping coefficient being  $\delta_\alpha = \frac{C_\alpha}{2\sqrt{M_\alpha K_\alpha}}$ .

Similar Lagrange equations can be obtained for hysteretic damping when the concept of a complex stiffness  $K_\alpha(1 + i\nu_\alpha)$  is used. The equation of motion is

$$M_\alpha \ddot{q}_\alpha(t) + K_\alpha(1 + i\nu_\alpha) q_\alpha(t) = L_\alpha(t) \quad \dots (2.5)$$

Strictly, the solutions of equation (2.5) are restricted to be complex exponential in form, and hysteretic damping has to be used carefully when the loading is random. The problems associated with the use of hysteretic damping for random vibration are discussed in Chapter 4, and it is suggested that equation (2.5) be written in the form

$$M_\alpha \ddot{q}_\alpha(t) + \frac{K_\alpha \nu_\alpha}{\omega} \dot{q}_\alpha(t) + K_\alpha q_\alpha(t) = L_\alpha(t) \quad \dots (2.6)$$

which is valid for harmonic solutions. Equation (2.6) can now be written in the equivalent viscous form

$$M_\alpha \ddot{q}_\alpha(t) + C_{\alpha e} \dot{q}_\alpha(t) + K_\alpha q_\alpha(t) = L_\alpha(t) \quad \dots (2.7)$$

where  $C_{\alpha e} = \frac{K_\alpha \nu_\alpha}{\omega}$  represents an "effective" viscous damper. Solutions of equation (2.7) can be obtained for viscous damping, and hysteretic damping then reintroduced. Thus the theoretical analysis of random vibration will assume initially that the damping is viscous.

The solution of equation (2.3) can be obtained in terms of the "impulse response function"  $h_\alpha(\tau)$

$$\begin{aligned} q_\alpha(t) &= \int_{-\infty}^{\infty} L_\alpha(\tau) h_\alpha(t - \tau) d\tau \\ &= \int_{-\infty}^{\infty} L_\alpha(t - \tau) h_\alpha(\tau) d\tau \end{aligned} \quad \dots (2.8)$$

where  $h_\alpha(\tau) = 0$  for  $\tau < 0$ .

Substituting equations (2.4) and (2.8) in equation (2.2)

$$w(\underline{x}, t) = \sum_{\alpha} \psi_{\alpha}(\underline{x}) \int_{-\infty}^{\infty} \int_A \psi_{\alpha}(\underline{x}') p(\underline{x}', t - \tau_1) h_{\alpha}(\tau_1) d\underline{x}' d\tau_1 \quad \dots (2.9)$$

The response autocorrelation function is, by definition,

$$R_d(\tau) = \lim_{T \rightarrow \infty} \frac{1}{2T} \int_{-T}^{+T} w(\underline{x}, t) w(\underline{x}, t + \tau) dt \quad \dots (2.10)$$

and from equation (2.9)

$$R_d(\tau) = \sum_{\alpha} \sum_{\beta} \psi_{\alpha}(\underline{x}) \psi_{\beta}(\underline{x}) \int_A \int_A \psi_{\alpha}(\underline{x}') \psi_{\beta}(\underline{x}'') \int_{-\infty}^{\infty} \int_{-\infty}^{\infty} h_{\alpha}(\tau_1) h_{\beta}(\tau_2) \\ \times \lim_{T \rightarrow \infty} \frac{1}{2T} \int_{-T}^T p(\underline{x}', t - \tau_1) p(\underline{x}'', t + \tau - \tau_2) dt d\tau_1 d\tau_2 d\underline{x}' d\underline{x}'' \quad \dots (2.11)$$

where it is assumed that the appropriate integrals are uniformly convergent so that the change in the order of integration is valid.

Now the excitation cross-correlation function is

$$R_p(\underline{x}; \underline{x}'', \tau) = \lim_{T \rightarrow \infty} \frac{1}{2T} \int_{-T}^{+T} p(\underline{x}; t) p(\underline{x}'', t + \tau) dt \quad \dots (2.12)$$

Therefore, from equations (2.11) and (2.12)

$$R_d(\tau) = \sum_{\alpha} \sum_{\beta} \psi_{\alpha}(\underline{x}) \psi_{\beta}(\underline{x}) \int_A \int_A \psi_{\alpha}(\underline{x}') \psi_{\beta}(\underline{x}'') \int_{-\infty}^{\infty} \int_{-\infty}^{\infty} h_{\alpha}(\tau_1) h_{\beta}(\tau_2) \\ \times R_p(\underline{x}', \underline{x}'', \tau + \tau_1 - \tau_2) d\tau_1 d\tau_2 d\underline{x}' d\underline{x}'' \quad \dots (2.13)$$

The response power spectral density function  $S_d(\omega)$  can be obtained

from equation (2.13) by the Wiener-Khinchin relations.

$$\begin{aligned} R_d(\tau) &= \int_{-\infty}^{\infty} S_d(\omega) e^{i\omega\tau} d\omega \\ S_d(\omega) &= \frac{1}{2\pi} \int_{-\infty}^{\infty} R_d(\tau) e^{-i\omega\tau} d\tau \end{aligned} \quad \dots (2.14)$$

Thus the displacement power spectral density function is, from equations (2.13) and (2.14),

$$\begin{aligned} S_d(\omega) &= \sum_{\alpha} \sum_{\beta} \psi_{\alpha}(\underline{x}) \psi_{\beta}(\underline{x}) \int_A \int_A \psi_{\alpha}(\underline{x}') \psi_{\beta}(\underline{x}'') \int_{-\infty}^{\infty} \int_{-\infty}^{\infty} h_{\alpha}(\tau_1) h_{\beta}(\tau_2) \\ &\quad \times \frac{1}{2\pi} \int_{-\infty}^{\infty} R_p(\underline{x}', \underline{x}'', \tau + \tau_1 - \tau_2) e^{-i\omega\tau} d\tau d\tau_1 d\tau_2 d\underline{x}' d\underline{x}'' \\ &= \sum_{\alpha} \sum_{\beta} \psi_{\alpha}(\underline{x}) \psi_{\beta}(\underline{x}) H_{\alpha}^*(\omega) H_{\beta}(\omega) \int_A \int_A \psi_{\alpha}(\underline{x}') \psi_{\beta}(\underline{x}'') S_p(\underline{x}', \underline{x}'', \omega) d\underline{x}' d\underline{x}'' \end{aligned} \quad \dots (2.15)$$

where  $S_p(\underline{x}', \underline{x}'', \omega) = \frac{1}{2\pi} \int_{-\infty}^{\infty} R_p(\underline{x}', \underline{x}'', \tau) e^{-i\omega\tau} d\tau$  is the excitation cross-power spectral density function and  $H_{\alpha}(\omega)$  is the complex response function or receptance, which is related to the impulse response function by the Fourier transform pair

$$\begin{aligned} h_{\alpha}(\tau) &= \frac{1}{2\pi} \int_{-\infty}^{\infty} H_{\alpha}(\omega) e^{i\omega\tau} d\omega \\ H_{\alpha}(\omega) &= \int_{-\infty}^{\infty} h_{\alpha}(\tau) e^{-i\omega\tau} d\tau \end{aligned} \quad \dots (2.16)$$

$H_{\alpha}(\omega)$  is also the reciprocal of the complex impedance  $Y_{\alpha}(\omega)$ . The complex conjugate of  $H_{\alpha}(\omega)$  is denoted by  $H_{\alpha}^*(\omega)$ .

From the definitions in equations (2.10) and (2.14), it can be shown

that the cross-power spectral density function has the property

$$\begin{aligned} S(\underline{x}', \underline{x}'', \omega) &= S^*(\underline{x}', \underline{x}'', -\omega) \\ &= S^*(\underline{x}'', \underline{x}', \omega) \end{aligned} \quad \dots (2.17)$$

where the asterisk again denotes a complex conjugate.

$$\text{Writing } S(\underline{x}', \underline{x}'', \omega) = C(\underline{x}', \underline{x}'', \omega) - iQ(\underline{x}', \underline{x}'', \omega) \quad \dots (2.18)$$

where  $C(\underline{x}', \underline{x}'', \omega)$  and  $Q(\underline{x}', \underline{x}'', \omega)$  are functions of  $\omega$  with real coefficients, then, from equation (2.17)

$$\begin{aligned} C(\underline{x}', \underline{x}'', \omega) &= C(\underline{x}', \underline{x}'', -\omega) = C(\underline{x}'', \underline{x}', \omega) \\ Q(\underline{x}', \underline{x}'', \omega) &= -Q(\underline{x}', \underline{x}'', -\omega) = -Q(\underline{x}'', \underline{x}', \omega) \end{aligned} \quad \dots (2.19)$$

Equation (2.15) can be used as a basis for the calculation of the response of a structure subjected to a spatially distributed random excitation, and is similar to the response spectral density equation derived by Powell (1958a).

"Joint acceptance"  $J_{\alpha\alpha}(\omega)$  and "cross acceptance"  $J_{\alpha\beta}(\omega)$  terms can be defined by

$$\begin{aligned} J_{\alpha\alpha}(\omega) &= \frac{4}{A^2 S_p(\omega)} \int_A \int_A \psi_\alpha(\underline{x}') \psi_\alpha(\underline{x}'') S_p(\underline{x}', \underline{x}'', \omega) d\underline{x}' d\underline{x}'' \\ \text{and } J_{\alpha\beta}(\omega) &= \frac{4}{A^2 S_p(\omega)} \int_A \int_A \psi_\alpha(\underline{x}') \psi_\beta(\underline{x}'') S_p(\underline{x}', \underline{x}'', \omega) d\underline{x}' d\underline{x}'' \end{aligned} \quad \dots (2.20)$$

where  $S_p(\omega)$  is the excitation power spectral density function.

## 2.3 Displacement Power Spectral Density Function

### 2.3.1 Elimination of Imaginary Term

The form of the displacement power spectral density function in equation (2.15) can be investigated further without too great a loss of

generality.

Consider the double integral term in equation (2.15)

$$\begin{aligned}
 I_{\alpha\beta}(\omega) &= \frac{A^2}{4} S_p(\omega) J_{\alpha\beta}(\omega) \\
 &= \int_A \int_A \psi_\alpha(\underline{x}') \psi_\beta(\underline{x}'') S_p(\underline{x}', \underline{x}'', \omega) d\underline{x}' d\underline{x}'' \\
 &= \int_A \int_A \psi_\alpha(\underline{x}'') \psi_\beta(\underline{x}') S_p(\underline{x}'', \underline{x}', \omega) d\underline{x}'' d\underline{x}' \text{ on interchanging } \underline{x}' \text{ and } \underline{x}'' \\
 &= \int_A \int_A \psi_\alpha(\underline{x}'') \psi_\beta(\underline{x}') S_p^*(\underline{x}', \underline{x}'', \omega) d\underline{x}' d\underline{x}'' \quad \dots (2.21)
 \end{aligned}$$

when the order of integration is changed and the properties of equation (2.17) are used. For the case  $\alpha = \beta$ , equation (2.21) gives

$$\begin{aligned}
 I_{\alpha\alpha}(\omega) &= \int_A \int_A \psi_\alpha(\underline{x}') \psi_\alpha(\underline{x}'') S_p(\underline{x}', \underline{x}'', \omega) d\underline{x}' d\underline{x}'' \\
 &= \int_A \int_A \psi_\alpha(\underline{x}') \psi_\alpha(\underline{x}'') S_p^*(\underline{x}', \underline{x}'', \omega) d\underline{x}' d\underline{x}''
 \end{aligned}$$

and, equating the imaginary parts

$$\int_A \int_A \psi_\alpha(\underline{x}') \psi_\alpha(\underline{x}'') Q_p(\underline{x}', \underline{x}'', \omega) d\underline{x}' d\underline{x}'' = 0 \quad \dots (2.22)$$

Further, for reasons similar to the above,

$$\begin{aligned}
 &H_\alpha^*(\omega) H_\beta(\omega) I_{\alpha\beta}(\omega) + H_\alpha(\omega) H_\beta^*(\omega) I_{\beta\alpha}(\omega) \\
 &= \int_A \int_A \psi_\alpha(\underline{x}') \psi_\beta(\underline{x}'') \{H_\alpha^*(\omega) H_\beta(\omega) S_p(\underline{x}', \underline{x}'', \omega) + H_\alpha(\omega) H_\beta^*(\omega) S_p^*(\underline{x}', \underline{x}'', \omega)\} d\underline{x}' d\underline{x}'' \\
 &= 2 \int_A \int_A \psi_\alpha(\underline{x}') \psi_\beta(\underline{x}'') \operatorname{Re} |H_\alpha^*(\omega) H_\beta(\omega) S_p(\underline{x}', \underline{x}'', \omega)| d\underline{x}' d\underline{x}'' \quad \dots (2.23)
 \end{aligned}$$

where the symbol 'Re' denotes "real part of".

If the complex impedance product  $Y_{\alpha}^*(\omega) Y_{\beta}(\omega)$  is denoted by

$$Y_{\alpha}^*(\omega) Y_{\beta}(\omega) = M_{\alpha} M_{\beta} (g_{\alpha\beta} - i h_{\alpha\beta}) = \frac{1}{H_{\alpha}^*(\omega) H_{\beta}(\omega)} \quad \dots (2.24)$$

then from equations (2.18) and (2.24)

$$\operatorname{Re} (H_{\alpha}^*(\omega) H_{\beta}(\omega) S_p(\underline{x}', \underline{x}'', \omega)) = \frac{g_{\alpha\beta} C_p(\underline{x}', \underline{x}'', \omega) + h_{\alpha\beta} Q_p(\underline{x}', \underline{x}'', \omega)}{M_{\alpha} M_{\beta} (g_{\alpha\beta}^2 + h_{\alpha\beta}^2)} \quad \dots (2.25)$$

Combining equations (2.15), (2.18), (2.22), (2.23) and (2.25), the displacement power spectral density function becomes

$$\begin{aligned} S_d(\omega) = & \int_{\alpha} \psi_{\alpha}^2(\underline{x}) |H_{\alpha}(\omega)|^2 \int_A \int_A \psi_{\alpha}(\underline{x}') \psi_{\alpha}(\underline{x}'') C_p(\underline{x}', \underline{x}'', \omega) d\underline{x}' d\underline{x}'' \\ & + 2 \sum_{\substack{\alpha \neq \beta \\ \alpha \neq \beta}} \int_{\alpha} \psi_{\alpha}(\underline{x}) \psi_{\beta}(\underline{x}) \int_A \int_A \psi_{\alpha}(\underline{x}') \psi_{\beta}(\underline{x}'') \frac{g_{\alpha\beta} C_p(\underline{x}', \underline{x}'', \omega) + h_{\alpha\beta} Q_p(\underline{x}', \underline{x}'', \omega)}{M_{\alpha} M_{\beta} (g_{\alpha\beta}^2 + h_{\alpha\beta}^2)} d\underline{x}' d\underline{x}'' \end{aligned} \quad \dots (2.26)$$

where the pair  $(\alpha, \beta)$  is counted only once.

The right-hand side of equation (2.26) is real, which is to be expected because from physical arguments  $S_d(\omega)$  is real.

### 2.3.2 Forms Separable in $x$ Coordinates

In many cases it is possible to express the mode shape  $\psi_{\alpha}(\underline{x})$  in an exact or approximate form which is separable in the  $(x_1, x_3)$  directions.

$$\begin{aligned} \text{Let } \psi_{\alpha}(\underline{x}) &= \psi_m(x_1) \psi_n(x_3) & m, n &= 1, 2, \dots \\ \text{and } \psi_{\beta}(\underline{x}) &= \psi_r(x_1) \psi_s(x_3) & r, s &= 1, 2, \dots \end{aligned} \quad \dots (2.27)$$

where the suffices  $m, n, r, s$  denote the number of modal half-wavelengths in the  $x_k$  directions. When expressed in the form of equation (2.27) the

mode forms have the property that for a uniform rectangular structure bounded by  $0 \leq x_k \leq L_k$

$$\psi_j(x_k) = (-1)^{j+1} \psi_j(L_k - x_k) \quad \dots (2.28)$$

Assume now that the excitation cross power spectral density function can be expressed also in a form which is separable in the co-ordinate directions

$$S_p(\underline{x}', \underline{x}'', \omega) = S_{p_1}(x_1', x_1'', \omega) S_{p_3}(x_3', x_3'', \omega)$$

$$\text{where } S_{p_1}(x_1', x_1'', \omega) = C_{p_1}(x_1', x_1'', \omega) - iQ_{p_1}(x_1', x_1'', \omega) \quad \dots (2.29)$$

$$\text{and } S_{p_3}(x_3', x_3'', \omega) = C_{p_3}(x_3', x_3'', \omega) - iQ_{p_3}(x_3', x_3'', \omega)$$

$S_{p_1}(x_1', x_1'', \omega)$  and  $S_{p_3}(x_3', x_3'', \omega)$  will satisfy conditions similar to those of equation (2.17). Comparing equations (2.18) and (2.29)

$$C_p(\underline{x}', \underline{x}'', \omega) = C_{p_1}(x_1', x_1'', \omega) C_{p_3}(x_3', x_3'', \omega) - Q_{p_1}(x_1', x_1'', \omega) Q_{p_3}(x_3', x_3'', \omega)$$

and

$$Q_p(\underline{x}', \underline{x}'', \omega) = C_{p_1}(x_1', x_1'', \omega) Q_{p_3}(x_3', x_3'', \omega) + C_{p_3}(x_3', x_3'', \omega) Q_{p_1}(x_1', x_1'', \omega)$$

$\dots (2.30)$

For a homogeneous and stationary forcing field the power spectral density function is independent of position  $\underline{x}'$  and is a function only of the separation  $\underline{\xi} = \underline{x}'' - \underline{x}'$ . Thus the function  $S_p(\underline{x}', \underline{x}'', \omega)$  can be written as

$$S_p(\underline{x}', \underline{x}'', \omega) \equiv S_p(\underline{\xi}, \omega) \equiv S_p(\xi_1, \xi_3, \omega)$$

and it can then be shown, from equations (2.27), (2.28), (2.29) and (2.30), that, for a structure with dimensions  $L_1, L_3$ ,

$$\begin{aligned}
 & \int_A \int_A \psi_\alpha(\underline{x}') \psi_\beta(\underline{x}'') C_p(\underline{x}', \underline{x}'', \omega) d\underline{x}' d\underline{x}'' \\
 &= \int_0^{L_1} \int_0^{L_3} \int_0^{x_1''} \int_0^{x_3''} \psi_\alpha(x_1', x_3') \psi_\beta(x_1'', x_3'') \\
 & \quad \{ (1+(-1)^{m+r})(1+(-1)^{n+s}) C_p(\xi_1, 0, \omega) C_p(0, \xi_3, \omega) \\
 & \quad - (1-(-1)^{m+r})(1-(-1)^{n+s}) Q_p(\xi_1, 0, \omega) Q_p(0, \xi_3, \omega) \} dx_3' dx_1' dx_3'' dx_1'' \\
 & \quad \dots (2.31)
 \end{aligned}$$

where  $C_p(x_1', x_1'', \omega)$  is now written

$$C_{p1}(x_1', x_1'', \omega) = C_p(\xi_1, 0, \omega)$$

$$\text{similarly } C_{p3}(x_3', x_3'', \omega) = C_p(0, \xi_3, \omega)$$

$$Q_{p1}(x_1', x_1'', \omega) = Q_p(\xi_1, 0, \omega)$$

$$\text{and } Q_{p3}(x_3', x_3'', \omega) = Q_p(0, \xi_3, \omega)$$

$$= 4 \int_0^{L_1} \int_0^{L_3} \int_0^{x_1''} \int_0^{x_3''} \psi_\alpha(x_1', x_3') \psi_\beta(x_1'', x_3'') C_p(\xi_1, 0, \omega) C_p(0, \xi_3, \omega) dx_3' dx_1' dx_3'' dx_1''$$

when  $m+r$  and  $n+s$  even

$$= -4 \int_0^{L_1} \int_0^{L_3} \int_0^{x_1''} \int_0^{x_3''} \psi_\alpha(x_1', x_3') \psi_\beta(x_1'', x_3'') Q_p(\xi_1, 0, \omega) Q_p(0, \xi_3, \omega) dx_3' dx_1' dx_3'' dx_1''$$

when  $m+r$  and  $n+s$  odd

$$= 0 \quad \text{when } m+r \text{ even and } n+s \text{ odd}$$

or  $m+r$  odd and  $n+s$  even.

... (2.32)



Similarly

$$\begin{aligned}
& \int_A \int_A \psi_\alpha(\underline{x}') \psi_\beta(\underline{x}'') Q_p(\underline{x}', \underline{x}'', \omega) d\underline{x}' d\underline{x}'' \\
&= - \int_0^{L_1} \int_0^{L_3} \int_0^{x_1''} \int_0^{x_3''} \psi_\alpha(x_1', x_3') \psi_\beta(x_1'', x_3'') \\
&\quad \{ (1+(-1)^{m+r})(1-(-1)^{n+s}) C_p(\xi_1, 0, \omega) Q_p(0, \xi_3, \omega) \\
&\quad + (1-(-1)^{m+r})(1+(-1)^{n+s}) C_p(0, \xi_3, \omega) Q_p(\xi_1, 0, \omega) \} dx_3' dx_1' dx_3'' dx_1'' \\
&\quad \dots (2.33) \\
&= -4 \int_0^{L_1} \int_0^{L_3} \int_0^{x_1''} \int_0^{x_3''} \psi_\alpha(x_1', x_3') \psi_\beta(x_1'', x_3'') C_p(\xi_1, 0, \omega) Q_p(0, \xi_3, \omega) dx_3' dx_1' dx_3'' dx_1'' \\
&\quad \text{when } m+r \text{ even and } n+s \text{ odd} \\
&= -4 \int_0^{L_1} \int_0^{L_3} \int_0^{x_1''} \int_0^{x_3''} \psi_\alpha(x_1', x_3') \psi_\beta(x_1'', x_3'') C_p(0, \xi_3, \omega) Q_p(\xi_1, 0, \omega) dx_3' dx_1' dx_3'' dx_1'' \\
&\quad \text{when } m+r \text{ odd and } n+s \text{ even} \\
&= 0 \text{ when } m+r \text{ and } n+s \text{ even} \\
&\quad \text{or } m+r \text{ and } n+s \text{ odd} \dots (2.34)
\end{aligned}$$

From equations (2.32) and (2.34) it is seen that at least one double integral of the pair

$$\int_A \int_A \psi_\alpha(\underline{x}') \psi_\beta(\underline{x}'') C_p(\underline{x}', \underline{x}'', \omega) d\underline{x}' d\underline{x}''$$

$$\text{and } \int_A \int_A \psi_\alpha(\underline{x}') \psi_\beta(\underline{x}'') Q_p(\underline{x}', \underline{x}'', \omega) d\underline{x}' d\underline{x}''$$

must be zero for a given mode pair  $(\alpha, \beta)$ . This simplifies the computation since only one term has to be considered for a particular mode combination.

Further reduction of the double integral terms depends on the form of the excitation cross-power spectral density function, or alternatively on the narrow band cross correlation coefficient  $\rho_p(\xi_1, \xi_3, \tau; \omega)$ .

From Appendix A, it can be shown that

$$\begin{aligned} S_p(\xi, \omega) &\equiv S_p(\xi_1, \xi_3, \omega) = |S_p(\xi_1, \xi_3, \omega)| e^{-ib\xi_1} \\ &= |\rho_p(\xi_1, \xi_3, \tau; \omega)| S_p(\omega) e^{-ib\xi_1} \quad \dots (2.35) \end{aligned}$$

where it is assumed that the pressure field is convected in the positive  $x$ , direction with velocity  $U_c$  and where

$$b = \frac{\omega}{U_c} \quad \dots (2.36)$$

Written in this form the right hand side of equation (2.35) appears to be a time dependent function but, from equation (A.5) it is seen that

$$|\rho_p(\xi_1, \xi_3, \tau; \omega)| \equiv |\rho_p(\xi_1, \xi_3, 0; \omega)| \quad \dots (2.37)$$

which is independent of  $\tau$ .

From equations (2.18) and (2.35) it is obvious that

$$\begin{aligned} C_p(\xi_1, \xi_3, \omega) &= S_p(\omega) |\rho_p(\xi_1, \xi_3, \tau; \omega)| \cos b \xi_1 \\ Q_p(\xi_1, \xi_3, \omega) &= S_p(\omega) |\rho_p(\xi_1, \xi_3, \tau; \omega)| \sin b \xi_1 \quad \dots (2.38) \end{aligned}$$

The assumption in equation (2.29) that

$$S_p(\xi_1, \xi_3, \omega) = S_p(\xi_1, 0, \omega) \cdot S_p(0, \xi_3, \omega)$$

now implies that a similar representation is true for the narrow band cross-correlation coefficient,

$$\text{i.e. } |\rho_p(\xi_1, \xi_3, \tau; \omega)| = |\rho_p(\xi_1, 0, \tau; \omega)| \cdot |\rho_p(0, \xi_3, \tau; \omega)| \quad \dots (2.39)$$

and, from equation (2.35)

$$S_p(\xi_1, \xi_3, \omega) = S_p(\omega) |\rho_p(\xi_1, 0, \tau; \omega)| \cdot |\rho_p(0, \xi_3, \tau; \omega)| e^{-ib\xi_1} \quad \dots (2.40)$$

Comparing equations (2.29) and (2.40)

$$Q_p(0, \xi_3, \omega) = 0 \quad \dots (2.41)$$

Substitution of equation (2.41) into equations (2.32) and (2.34) reduces the number of possible forms of solution to those equations. When equation (2.41) is satisfied, functions of  $j_{mr}(\omega)$ ,  $j'_{ns}(\omega)$  and  $k_{mr}(\omega)$  can be defined.

$$\text{Let } \int_A \int_A \psi_\alpha(\underline{x}') \psi_\beta(\underline{x}'') C_p(\xi_1, \xi_3, \omega) d\underline{x}', d\underline{x}'' = \frac{A^2}{4} S_p(\omega) j_{mr}(\omega) j'_{ns}(\omega)$$

$$\begin{aligned} \text{where } j_{mr}(\omega) &= \frac{2}{L_1^2} \int_0^L \int_0^L \psi_m(x_1') \psi_r(x_1'') |\rho_p(\xi_1, 0, \tau; \omega)| \cos b\xi_1 dx_1' dx_1'' \\ &= \frac{4}{L_1^2} \int_0^L \int_0^L \psi_m(x_1') \psi_r(x_1'') |\rho_p(\xi_1, 0, \tau; \omega)| \cos b\xi_1 dx_1' dx_1'' \\ &\quad \text{when } m+r \text{ even} \\ &= 0 \text{ when } m+r \text{ odd.} \end{aligned}$$

$\dots (2.42)$

$$\begin{aligned} \text{and } j'_{ns}(\omega) &= \frac{2}{L_3^2} \int_0^L \int_0^L \psi_n(x_3') \psi_s(x_3'') |\rho_p(0, \xi_3, \tau; \omega)| dx_3' dx_3'' \\ &= \frac{4}{L_3^2} \int_0^L \int_0^L \psi_n(x_3') \psi_s(x_3'') |\rho_p(0, \xi_3, \tau; \omega)| dx_3' dx_3'' \\ &\quad \text{when } n+s \text{ even} \\ &= 0 \text{ when } n+s \text{ odd} \end{aligned}$$

$\dots (2.43)$

Also let

$$\int_A \int_A \psi_\alpha(\underline{x}') \psi_\beta(\underline{x}'') Q_p(\xi_1, \xi_3, \omega) d\underline{x}', d\underline{x}'' = \frac{A^2}{4} S_p(\omega) j'_{ns}(\omega) k_{mr}(\omega)$$

$$\begin{aligned} \text{where } k_{mr}(\omega) &= \frac{2}{L_1^2} \int_0^L \int_0^L \psi_m(x_1') \psi_r(x_1'') |\rho_p(\xi_1, 0, \tau; \omega)| \sin b\xi_1 dx_1' dx_1'' \\ &\quad \text{when } m+r \text{ odd} \\ &= 0 \text{ when } m+r \text{ even} \end{aligned}$$

$\dots (2.44)$

Substitution of equations (2.42), (2.43) and (2.44) into equation (2.26) yields

$$S_d(\omega) = \frac{A^2}{4} S_p(\omega) \sum_{\alpha} \psi_{\alpha}^2(\underline{x}) |H_{\alpha}(\omega)|^2 j_{mm}(\omega) j'_{nn}(\omega) \\ + \frac{A^2}{2} S_p(\omega) \sum_{\substack{\alpha \neq \beta}} \frac{\psi_{\alpha}(\underline{x}) \psi_{\beta}(\underline{x}) j'_{ns}(\omega)}{M_{\alpha} M_{\beta}} \cdot \frac{g_{\alpha\beta} j_{mr}(\omega) + h_{\alpha\beta} k_{mr}(\omega)}{g_{\alpha\beta}^2 + h_{\alpha\beta}^2} \dots (2.45)$$

where the pair  $(\alpha, \beta)$  are counted once only,  
and where  $j_{mr}(\omega) = 0$  when  $m+r$  is odd  
 $j'_{ns}(\omega) = 0$  when  $n+s$  is odd  
 $k_{mr}(\omega) = 0$  when  $m+r$  is even.

### 2.3.3 Panel Characteristics

Further discussion of the response power spectral density function can now be restricted to the vibration of single panels. For simplicity in computation it will be assumed that the panels are simply supported on all edges. The mode shapes of equation (2.27) can then take the form

$$\psi_m(x_1) = \sin\left(\frac{m\pi x_1}{L_1}\right), \quad \psi_r(x_1) = \sin\left(\frac{r\pi x_1}{L_1}\right) \\ \psi_n(x_3) = \sin\left(\frac{n\pi x_3}{L_3}\right), \quad \psi_s(x_3) = \sin\left(\frac{s\pi x_3}{L_3}\right) \dots (2.46)$$

From equations (2.4) and (2.46), when the surface density  $\mu(\underline{x})$  is assumed to be constant, the generalised mass in the  $\alpha^{\text{th}}$  mode is

$$M_{\alpha} = \int_0^{L_1} \int_0^{L_3} \mu \sin^2\left(\frac{m\pi x_1}{L_1}\right) \sin^2\left(\frac{n\pi x_3}{L_3}\right) dx_1 dx_3 \\ = \frac{\mu L_1 L_3}{4} = \frac{\mu A}{4} \dots (2.47)$$

A similar generalised mass can be calculated for a fully fixed panel, using mode shapes of the type given by equation (C.4), normalised to have a maximum value of unity. A comparison of the results for the (1-1) mode shows that the generalised mass of a simply supported panel is greater than that for a fully fixed panel, by a factor of approximately 1.46. The factor decreases as the mode order increases, and reaches an asymptotic value of 1.30.

From equation (2.3) the form of the complex receptance  $H_\alpha(\omega)$  is

$$H_\alpha(\omega) = \frac{1}{(K_\alpha - M_\alpha \omega^2) + iC_\alpha \omega} \quad \dots (2.48)$$

$$= \frac{1}{M_\alpha \{(\omega_\alpha^2 - \omega^2) + 2i\delta_\alpha \omega \omega_\alpha\}}$$

Alternatively, if the Lagrange equation has the form of equation (2.7),  $H_\alpha(\omega)$  can be written in terms of the hysteretic loss factor  $\nu_\alpha$

$$H_\alpha(\omega) = \frac{1}{M_\alpha \{(\omega_\alpha^2 - \omega^2) + i\nu_\alpha \omega_\alpha^2\}} \quad \dots (2.49)$$

The two forms of  $H_\alpha(\omega)$  in equations (2.48) and (2.49) will give similar results when  $\delta_\alpha$  and  $\nu_\alpha$  are small.

Assuming the hysteretic form of damping, substitution for  $M_\alpha$  from equation (2.47) yields

$$H_\alpha(\omega) = \frac{h}{A\mu \{(\omega_\alpha^2 - \omega^2) + i\nu_\alpha \omega_\alpha^2\}} \quad \dots (2.50)$$

and, from equation (2.24)

$$g_{\alpha\beta} = (\omega_\alpha^2 - \omega^2)(\omega_\beta^2 - \omega^2) + \nu_\alpha \nu_\beta \omega_\alpha^2 \omega_\beta^2$$

$$h_{\alpha\beta} = \nu_\alpha \omega_\alpha^2 (\omega_\beta^2 - \omega^2) - \nu_\beta \omega_\beta^2 (\omega_\alpha^2 - \omega^2) \quad \dots (2.51)$$

#### 2.3.4 Excitation Field

It has been assumed in equation (2.35) that the excitation has the form of a fluctuating pressure field which is convected in the positive  $x_1$  direction. If the convection velocity is in the direction of  $x_1$  decreasing, then equation (2.45) is valid if  $k_{mr}(\omega)$  is replaced by  $k_{mr}'(\omega) = -k_{mr}(\omega)$ .

From the results of several experimental investigations of turbulent boundary layer pressure fluctuations, the excitation narrow band cross correlation coefficients can be represented approximately by inverse exponential functions of the form

$$|\rho_p(\xi, 0, \tau; \omega)| = e^{-a|\xi|} \quad \dots (2.52)$$

where  $\xi = x'' - x'$ . This form can be used as an approximate representation of other convected pressure fields, for example acoustic plane waves at grazing or inclined incidence, and jet noise, and permits the integrals in equations (2.42), (2.43) and (2.44) to be evaluated in closed form. A more detailed study of the statistical properties of the excitation is contained in Appendix A.

Based on the experimental results for turbulent boundary layers, measured by Bull (1963), the  $x_1$  longitudinal component of the excitation narrow band cross correlation coefficient is assumed to be

$$|\rho_p(\xi_1, 0, \tau; \omega)| = e^{-a|\xi_1|} \text{ where } \xi_1 = x_1'' - x_1' \quad \dots (2.53)$$

The lateral, or  $x_3$ , component has the assumed form, for reasons given in Appendix A,

$$\begin{aligned} |\rho_p(0, \xi_3, \tau; \omega)| &= e^{-a_3|\xi_3|} \quad \text{for } |\xi_3| \geq k_3 \\ &= c + de^{-a_4|\xi_3|} \quad \text{for } |\xi_3| < k_3 \end{aligned} \quad \dots (2.54)$$

where  $\xi_3 = x_3'' - x_3'$ , and  $k_3$  is a function of  $\omega$  and  $\xi_3$ .

## 2.4 Acceptance Terms

### 2.4.1 Joint Acceptance Terms

The acceptance terms are of particular importance because they estimate the degree of coupling between the excitation and the structure, and they will be studied in detail. It is possible, with the assumed mode shapes and excitation correlation coefficients, to evaluate the definite integrals  $j_{mr}(\omega)$ ,  $j'_{ns}(\omega)$  and  $k_{mr}(\omega)$  in closed form. Considering the case  $\alpha = \beta$ , by analogy with equation (2.20),  $j_{mm}(\omega)$  and  $j'_{nn}(\omega)$  can be called the "longitudinal" and "lateral" joint acceptances respectively. From the excitation field assumptions of stationarity, homogeneity and a separable form of  $S_p(\underline{x}', \underline{x}'', \omega)$  used in the derivation of  $j_{mm}(\omega)$  and  $j'_{nn}(\omega)$ , and from the condition given by equation (2.41), it can be shown that

$$J_{\alpha\alpha}(\omega) = j_{mm}(\omega) \cdot j'_{nn}(\omega) \quad \dots (2.55)$$

Substituting equations (2.46), (2.53) and (2.54) into equations (2.42) and (2.43), it can be shown that

$$\begin{aligned} j_{mm}(\omega) &= \frac{2}{L_1^2} \int_0^{L_1} \int_0^{L_1} \psi_m(x_1') \psi_m(x_1'') |\rho_p(\xi_1, 0, \tau; \omega)| \cos b\xi_1 \, dx_1' \, dx_1'' \\ &= \frac{4}{m^2 \pi^2 \Delta_m^2} \{ p_m (1 - (-1)^m e^{-aL_1} \cos bL_1) + (-1)^m q_m e^{-aL_1} \sin bL_1 + \frac{m\pi d}{2} \Delta_m \} \end{aligned}$$

... (2.56)

$$\begin{aligned} \text{where } \Delta_m &= \left( 1 + \left( \frac{aL_1}{m\pi} \right)^2 + \left( \frac{bL_1}{m\pi} \right)^2 \right)^2 - 4 \left( \frac{bL_1}{m\pi} \right)^2 \\ p_m &= \left( 1 + \left( \frac{aL_1}{m\pi} \right)^2 - \left( \frac{bL_1}{m\pi} \right)^2 \right)^2 - 4 \left( \frac{aL_1}{m\pi} \right)^2 \left( \frac{bL_1}{m\pi} \right)^2 \\ q_m &= \left( \frac{aL_1}{m\pi} \right) \left( \frac{bL_1}{m\pi} \right) \left( 1 + \left( \frac{aL_1}{m\pi} \right)^2 - \left( \frac{bL_1}{m\pi} \right)^2 \right) \\ d_m &= \left( \frac{aL_1}{m\pi} \right) \left( 1 + \left( \frac{aL_1}{m\pi} \right)^2 + \left( \frac{bL_1}{m\pi} \right)^2 \right) \end{aligned}$$

... (2.57)

$$\begin{aligned}
j'_{nn}(\omega) &= \frac{2}{L_3^2} \int_0^{L_3} \int_0^{L_3} \psi_n(x_3') \psi_n(x_3'') [\rho_p(0, k_3, \omega)] dx_3' dx_3'' \\
&= \frac{2}{n^2 \pi^2} \left\{ \left( \frac{p'_n(a_3) e^{-a_3 k_3}}{d'_{nn}(a_3)} - \frac{p'_n(a_4) e^{-a_4 k_4}}{d'_{nn}(a_4)} - 2c \right) \cos \frac{n \pi k_3}{L_3} \right. \\
&\quad + \left( \frac{q'_n(a_3) e^{-a_3 k_3}}{d'_{nn}(a_3)} - \frac{q'_n(a_4) e^{-a_4 k_4}}{d'_{nn}(a_4)} - c \left( \frac{L_3 - k_3}{L_3} \right) n \pi \right) \sin \frac{n \pi k_3}{L_3} \\
&\quad \left. - \left( \frac{2(-1)^n e^{-a_3 L_3}}{d'_{nn}(a_3)} - d \frac{2 + a_4 L_3 \left( 1 + \left( \frac{a_4 L_3}{n} \right)^2 \right)}{d'_{nn}(a_4)} - 2c \right) \right\} \dots (2.58)
\end{aligned}$$

where  $p'_n(a) = a(L_3 - k_3) \left( 1 + \left( \frac{a L_3}{n \pi} \right)^2 \right) + 2$

$$q'_n(a) = 2 \left( \frac{a L_3}{n \pi} \right) + \left( \frac{a L_3}{n \pi} - \left( \frac{L_3 - k_3}{L_3} \right) n \pi \right) \left( 1 + \left( \frac{a L_3}{n \pi} \right)^2 \right) \dots (2.59)$$

$$d'_{ns}(a) = \left( 1 + \left( \frac{a L_3}{n \pi} \right)^2 \right) \left( 1 + \left( \frac{a L_3}{s \pi} \right)^2 \right)$$

In the special cases when  $k_3 \leq 0$  or  $k_3 \geq L_3$ ,  $j'_{nn}(\omega)$  has the simpler forms:-

$$j'_{nn}(\omega) = \frac{4}{n^2 \pi^2} \left( \frac{1 - (-1)^n e^{-a_3 L_3}}{d'_{nn}(a_3)} + \frac{a_3 L_3}{2 \sqrt{d'_{nn}(a_3)}} \right) \text{ for } k_3 \leq 0 \dots (2.60)$$

$$= \frac{4}{n^2 \pi^2} \left\{ d \left( \frac{1 - (-1)^n e^{-a_4 L_3}}{d'_{nn}(a_4)} + \frac{a_4 L_3}{2 \sqrt{d'_{nn}(a_4)}} \right) + c(1 - (-1)^n) \right\} \text{ for } k_3 \geq L \dots (2.61)$$

#### 2.4.2 Cross Acceptance Terms

When  $\alpha \neq \beta$ , the "cross acceptance" has been defined in equation (2.20)

by

$$J_{\alpha\beta}(\omega) = \frac{4}{A^2 S_p(\omega)} \int_A \int_A \psi_\alpha(\underline{x}') \psi_\beta(\underline{x}'') S_p(\underline{x}', \underline{x}'', \omega) d\underline{x}' d\underline{x}'' \dots (2.62)$$



With assumptions again of a stationary and homogeneous excitation, a separable form of  $S_p(\underline{x}', \underline{x}'', \omega)$ , and the condition given by equation (2.41), it can be shown that

$$J_{\alpha\beta}(\omega) = j_{ns}'(\omega) (j_{mr}(\omega) + i k_{mr}(\omega)) \quad \dots (2.63)$$

where  $j_{mr}(\omega)$ ,  $j_{ns}'(\omega)$  and  $k_{mr}(\omega)$  are given by equations (2.42), (2.43), and (2.44) respectively. By analogy with the joint acceptances,  $j_{mr}(\omega)$  and  $k_{mr}(\omega)$  can be called the real and imaginary components of the longitudinal cross acceptance, and  $j_{ns}'(\omega)$  is the real component of the lateral cross acceptance (the imaginary component being zero as a result of equation (2.41)).

From equations (2.42), (2.46) and (2.53) it can be shown that, for the assumed excitation correlation form,

$$j_{mr}(\omega) = \frac{4}{mr\pi^2 \Delta_m \Delta_r} \left\{ p_{mr} (1 - (-1)^m e^{-aL_1} \cos bL_1) + (-1)^m 2(q_{mr} + q_{rm}) e^{-aL_1} \sin bL_1 \right\}$$

for  $m+r$  even

$$= 0 \quad \text{for } m+r \text{ odd}$$

\dots (2.64)

and, from equations (2.44), (2.46) and (2.53)

$$k_{mr}(\omega) = \frac{4}{mr\pi^2 \Delta_m \Delta_r} \left\{ (-1)^m 2(q_{mr} + q_{rm}) e^{-aL_1} \cos bL_1 + (-1)^m p_{mr} e^{-aL_1} \sin bL_1 \right.$$

$$\left. + \frac{2mr}{m-r} (d_{mr} + d_{rm}) \right\}$$

for  $m+r$  odd

$$= 0 \quad \text{for } m+r \text{ even}$$

\dots (2.65)

where  $\epsilon_m$  is given by equation (2.57)

$$\begin{aligned} p_{mr} &= \left(1 + \left(\frac{aL_1}{m\pi}\right)^2 - \left(\frac{bL_1}{m\pi}\right)^2\right) \left(1 + \left(\frac{aL_1}{r\pi}\right)^2 - \left(\frac{bL_1}{r\pi}\right)^2\right) - 4\left(\frac{aL_1}{m\pi}\right)\left(\frac{aL_1}{r\pi}\right)\left(\frac{bL_1}{m\pi}\right)\left(\frac{bL_1}{r\pi}\right) \\ q_{mr} &= \left(\frac{aL_1}{r\pi}\right)\left(\frac{bL_1}{r\pi}\right) \left(1 + \left(\frac{aL_1}{m\pi}\right)^2 - \left(\frac{bL_1}{m\pi}\right)^2\right) \\ d_{mr} &= \left(\frac{r}{m}\right) \Delta_r \left(\frac{aL_1}{m\pi}\right)\left(\frac{bL_1}{m\pi}\right) \end{aligned} \quad \dots (2.66)$$

The lateral cross acceptance component  $j'_{ns}(\omega)$  is, from equations (2.43), (2.46) and (2.54)

$$\begin{aligned} j'_{ns}(\omega) &= \frac{4}{ns\pi^2} \left\{ \left( p'_{ns} \cos \frac{n\pi k_3}{L_3} + p'_{sn} \cos \frac{s\pi k_3}{L_3} \right) + \left( q'_{ns} \sin \frac{n\pi k_3}{L_3} + q'_{sn} \sin \frac{s\pi k_3}{L_3} \right) \right. \\ &\quad \left. + \left( c + \frac{d}{d'_{ns}(a_4)} - \frac{(-1)^n e^{-a_3 L_3}}{d'_{ns}(a_3)} \right) \right\} \text{ for } n+s \text{ even} \\ &= 0 \text{ for } n+s \text{ odd.} \end{aligned} \quad \dots (2.67)$$

$$\begin{aligned} \text{where } p'_{ns} &= \left( \frac{s^2}{n^2 - s^2} \right) \left( \frac{d e^{-a_4 k_3}}{d'_{nn}(a_4)} - \frac{e^{-a_3 k_3}}{d'_{nn}(a_3)} + c \right) \\ q'_{ns} &= \left( \frac{s^2}{n^2 - s^2} \right) \left( \frac{\left( \frac{a_4 L_3}{n\pi} \right) d e^{-a_4 k_3}}{d'_{nn}(a_4)} - \frac{\left( \frac{a_3 L_3}{n\pi} \right) e^{-a_3 k_3}}{d'_{nn}(a_3)} \right) \end{aligned} \quad \dots (2.68)$$

and  $d'_{ns}(a)$  is given by equation (2.59).

In the special cases when  $k_3 \leq 0$  or  $k_3 \geq L_3$ ,  $j'_{ns}(\omega)$  has the simpler forms, for  $n+s$  even,

$$j'_{ns}(\omega) = \frac{4}{ns\pi^2} \cdot \frac{(1 - (-1)^n e^{-a_3 L_3})}{d'_{ns}(a_3)} \quad \text{for } k_3 \leq 0 \quad \dots (2.69)$$

$$= \frac{4}{ns\pi^2} \left( \frac{d(1 - (-1)^n e^{-a_4 L_3})}{d'_{ns}(a_4)} + c(1 - (-1)^n) \right) \quad \text{for } k_3 \geq L_3 \quad \dots (2.70)$$

## 2.5 Simplification for Acoustic Excitation

When the excitation is in the form of progressive acoustic plane waves, it is possible to simplify the forms of the acceptance terms. Assume that the acoustic waves are propagated in a direction such that the plane wave fronts make an angle  $\phi$  with the plane of the panel, and the direction of propagation of the trace wave over the panel is parallel to the  $x_1$  direction. The trace velocity will be  $U_c = \frac{C_0}{\sin \phi}$ , where  $C_0$  is the speed of sound. The excitation differs from the boundary layer pressure field for several reasons; the convection velocity  $U_c$  is independent of frequency, and the correlation coefficient is an undamped cosine in the longitudinal direction and unity in the lateral direction (i.e. along a wave front). Thus equations (2.53) and (2.54) reduce to

$$|\rho_p(\xi_1, 0, \tau; \omega)| = 1 = |\rho_p(0, \xi_3, \tau; \omega)| \quad \dots (2.71)$$

The joint acceptance terms can be modified by substituting  $a = 0$  in equation (2.56) and  $a_3 = 0$  in equation (2.60).

From equations (2.56) and (2.57), when  $a = 0$ , the longitudinal joint acceptance is

$$j_{mm}(\omega) = \frac{4(1 - (-1)^m \cos b L_1)}{m^2 \pi^2 (1 - (\frac{bL_1}{m\pi})^2)} \quad \text{for } \frac{bL_1}{m\pi} \neq 1 \quad \dots (2.72)$$

The solution given by equation (2.72) is not valid when  $(\frac{bL_1}{m\pi}) = 1$ , and  $j_{mm}(\omega)$  must be calculated directly from the definition of  $j_{mm}(\omega)$  in equation (2.42).

$$\text{Then } j_{mm}(\omega) = 1 \quad \text{for } \frac{bL_1}{m\pi} = 1 \quad \dots (2.73)$$

Similarly, when  $a_3 = 0$ , the lateral joint acceptance is, from equation (2.60)

$$j'_{nn}(\omega) = \frac{4(1 - (-1)^n)}{n^2 \pi^2} \quad \dots (2.74)$$

The cross acceptance terms can be reduced also. Putting  $a = 0$  in equation (2.64), or from the definition of  $j_{mr}(\omega)$ , in equation (2.42),

$$j_{mr}(\omega) = \frac{4(1 - (-1)^m \cos b L_1)}{mr\pi^2 (1 - (\frac{bL_1}{m\pi})^2)(1 - (\frac{bL_1}{r\pi})^2)} \quad \text{for } m+r \text{ even, } \frac{bL_1}{m\pi} \neq 1$$

$$\text{and } \frac{bL_1}{r\pi} \neq 1 \quad \dots (2.75)$$

$$= 0 \quad \text{for } m+r \text{ even and } \frac{bL_1}{m\pi} = 1, \text{ or } \frac{bL_1}{r\pi} = 1$$

$$= 0 \quad \text{for } m+r \text{ odd.}$$

From equation (2.65), with  $a = 0$ , or from the definition of  $k_{mr}(\omega)$  in equation (2.44),

$$k_{mr}(\omega) = \frac{4(-1)^m \sin b L_1}{mr\pi^2 (1 - (\frac{bL_1}{m\pi})^2)(1 - (\frac{bL_1}{r\pi})^2)} \quad \text{for } m+r \text{ odd, } \frac{bL_1}{m\pi} \neq 1$$

$$\text{and } \frac{bL_1}{r\pi} \neq 1$$

$$= \frac{2r}{\pi(m^2 - r^2)} \quad \text{for } m+r \text{ odd, } \frac{bL_1}{m\pi} = 1$$

$$= \frac{2m}{\pi(r^2 - m^2)} \quad \text{for } m+r \text{ odd, } \frac{bL_1}{r\pi} = 1 \quad \dots (2.76)$$

$$= 0 \quad \text{for } m+r \text{ even}$$

Finally, from equation (2.69) with  $a_3 = 0$ , or from the definition of  $j_{ns}(\omega)$  in equation (2.43)

$$j_{ns}(\omega) = \frac{2(1 - (-1)^n)^2}{ns\pi^2} \quad \text{for } n+s \text{ even}$$

$$\dots (2.77)$$

$$= 0 \quad \text{for } n+s \text{ odd}$$

## 2.6 Evaluation of Joint Acceptance Terms

### 2.6.1 Non-Dimensional Parameters

Computation of the joint and cross terms in equation (2.45) shows that in general, when the  $\alpha^{\text{th}}$  and  $\beta^{\text{th}}$  modes have well separated natural frequencies and the damping is light, the cross terms are small relative to the joint terms. Therefore it is of interest to study the effects of the excitation parameters on the joint acceptance terms as these will be of primary importance in the finally computed response spectra. From the boundary layer excitation correlation coefficients in Appendix A, the joint acceptance terms will depend on three parameters, boundary layer displacement thickness  $\delta^*$ , pressure field convection velocity  $U_c(\omega)$  and angular frequency  $\omega$ . The parameters  $U_c(\omega)$  and  $\omega$  can be usefully combined in terms of a frequency dependent narrow band excitation correlation length  $\zeta(\omega)$ . There are several ways of defining a typical correlation length, but the most appropriate one in this context is given by the separation distance to the first zero of the real part of  $S_p(\underline{x}', \underline{x}'', \omega)$  in equation (2.35). Thus, from equations (2.35) and (2.36),  $\zeta(\omega)$  is defined by

$$\cos \frac{\omega \zeta}{U_c(\omega)} = 0 \quad \dots (2.78)$$

$$\text{i.e.} \quad \zeta = \frac{\pi U_c(\omega)}{2\omega} = \frac{U_c}{4f} \quad \dots (2.79)$$

$$\text{Alternatively,} \quad \zeta = \frac{\lambda}{4} \quad \dots (2.80)$$

where  $\lambda$  is the excitation wavelength at frequency  $f$  defined by  $U_c = f\lambda$ .

Non-dimensional parameters  $\frac{L}{\zeta}$  and  $\frac{L}{\delta^*}$  can now be defined in terms of a typical panel length  $L$ , and

$$\frac{L}{\zeta} = \frac{2L\omega}{\pi U_c} = \frac{4Lf}{U_c} \quad \dots (2.81)$$

When the longitudinal or lateral joint acceptances are considered separately the typical length will be  $L_1$  or  $L_3$  respectively. When the full

panel is considered,  $L_1$  is used as the typical structural length and the panel aspect ratio  $\frac{L_1}{L_3}$  is introduced as a third non-dimensional parameter. From equation (2.81) the parameter  $\frac{L}{\zeta}$  can be considered as a non-dimensional length or frequency as required.

### 2.6.2 Longitudinal Joint Acceptance

Two forms of the longitudinal narrow band cross correlation coefficient are proposed in Appendix A for boundary layer excitation, but they both have the same general form :-

$$\rho_p(\xi_1, 0, \tau; \omega) = |\rho_p(\xi_1, 0, \tau; \omega)| \cos(\omega\delta - b\zeta) \quad \dots (2.82)$$

$$\text{where } b = \frac{\omega}{U_c(\omega)} \quad \text{and} \quad |\rho_p(\xi_1, 0, \tau; \omega)| = e^{-a|\xi_1|}$$

The two alternative forms of correlation coefficient apply to two ranges of the Strouhal number  $\frac{\omega\delta^*}{U_c}$ .

$$\text{When } \frac{\omega\delta^*}{U_c} \geq k_1, \quad \text{then } a = a_1 = \frac{\alpha_1\omega}{U_c} \quad \dots (2.83)$$

$$\text{and when } \frac{\omega\delta^*}{U_c} < k_1, \quad \text{then } a = a_2 = \frac{\alpha_2}{\delta^*} \quad \dots (2.84)$$

where  $\alpha_1, \alpha_2$  are constant coefficients.

Considering the upper Strouhal number range, the longitudinal joint acceptances can be calculated for the particular values associated with the boundary layer wind tunnel used in the experimental investigation, i.e.  $\alpha_1 = 0.1$  and  $U_c(\omega)$  is determined by equation (A.16). The limiting Strouhal number is given by  $k_1 = 0.37$ . With the assumption of simply supported mode shapes, equation (2.46), the longitudinal joint acceptance  $j_{\text{long}}(\omega)$  of equation (2.56) is shown in Figure 2.1 in terms of the non-dimensional parameter  $\frac{L_1}{\zeta}$  for modes of order  $m = 1$  to 7. The results are similar to those of Bozich (1964). The joint acceptance curve for each mode has a principal maximum, with the exception of  $m = 1$ , at  $\frac{L_1}{\zeta} = 2m$ , the approximation being most accurate for the higher order modes. This maximum

arises from the convective nature of the excitation field, and the condition  $\frac{L_1}{\zeta} = 2m$  implies that there is a matching between the excitation correlation length  $\zeta$  and the modal wavelength  $\lambda_m = \frac{2L_1}{m}$ . In terms of the excitation wavelength  $\lambda$  the condition becomes  $\lambda_m = \lambda$ . A similar result was obtained by Mercer (1965) for the response of the first order stringer torsional mode of a nine-bay beam. This mode, which can be compared with the mode  $m = 9$  for a simply supported single panel, showed a peak joint acceptance location close to  $\frac{L_1}{\zeta} = 2m$ .

Inspection of the curves in Figure 2.1 shows that, as  $m$  decreases, the location of the peaks for the low order modes progressively deviates from the condition  $\frac{L_1}{\zeta} = 2m$ . This effect is due to the finite size of the structure and is best exemplified by the limiting case of the fundamental mode  $m = 1$  where the peak occurs at  $\frac{L_1}{\zeta} = 0$ . There will be maximum response in this mode when there is uniform excitation over the structure and, in terms of a convected pressure field, this is satisfied when  $\zeta \rightarrow \infty$ . This condition will give peaks in all modes of odd order, and zero joint acceptances for the even order modes. The longitudinal joint acceptance is very similar, then, to the generalised force for deterministic loading of a beam.

The curves in Figure 2.1 contain secondary maxima and minima at values of  $\frac{L_1}{\zeta} < 2m$ , determined by subsidiary matching and mismatching of the modal wavelength and excitation correlation length. There is also slight evidence of maxima when  $\frac{L_1}{\zeta} > 2m$ , the acceptance curves showing slight "ripples".

The shape of the curves indicates that, when the excitation correlation length is varied by a change in frequency or convection velocity, no general statement can be made about the resultant variation in the longitudinal joint acceptance  $j_{\text{long}}(\omega)$ . In particular, when  $\frac{L_1}{\zeta}$  is in the neighbourhood of wavelength matching, and  $\frac{L_1}{\zeta} < 2m$ , an increase in  $\omega$  or a decrease in  $U_c$  will increase the longitudinal joint acceptance, but the same changes in  $\omega$  or  $U_c$  when  $\frac{L_1}{\zeta} > 2m$  will decrease the value of  $j_{\text{long}}(\omega)$ . The influence of the longitudinal joint acceptance on the panel response power spectral density

function can be determined from equation (2.45) but in general terms the response of mode  $\alpha$  is a function of the product

$$|H_{\alpha}(\omega)|^2 j_{mm}(\omega) j'_{nn}(\omega)$$

This product shows the well known resonance maximum given by  $|H_{\alpha}(\omega)|^2$  when  $\omega = \omega_{\alpha}$  but, from Figure 2.1, there will be further maxima in the modal response curve, particularly when there is wavelength matching at  $\frac{L_1}{\zeta} = 2m$ , that is when  $\omega = \frac{\pi m U_c}{L_1}$ . When conditions are such that  $\omega_{\alpha} = \frac{\pi m U_c}{L_1}$  there will be appreciable augmentation of the resonance peak. The matching in both the wavelength and frequency domains can be called "coincidence" by analogy with the coincidence effect in infinite panels excited by acoustic waves, and is of most importance when it occurs at a natural frequency.

The joint acceptance curves in Figure 2.1 were drawn for the particular value  $\alpha_1 = 0.1$  associated with the wind tunnel measurements of Bull (1963). Other investigations of the boundary layer pressure fluctuations in a zero pressure gradient have shown slightly different values of  $\alpha_1$ , so that the influence of  $\alpha_1$  on the longitudinal joint acceptance should be studied. Furthermore, recently published measurements by Schloemer (1966) in non-zero pressure gradients have shown that the decay rate of the narrow band longitudinal cross correlation coefficient depends on pressure gradient, the coefficient decaying more slowly in a favourable pressure gradient. The variation in  $\alpha_1$  shown by Schloemer is of the order of  $\pm 35\%$  about the zero gradient value.

The effect of  $\alpha_1$  on the longitudinal joint acceptance is shown in Figures 2.2 to 2.5 for modes of order  $m = 1$  to 4 respectively. The limiting case,  $\alpha_1 = 0$ , of zero spatial decay of the excitation longitudinal cross correlation coefficient represents the condition for plane wave acoustic excitation. When  $\alpha_1 = 0$  the acceptance curves show a series of well defined maxima and minima, the minima having zero value because there is a complete mismatch between the excitation narrow band waveform and the panel modal shapes. This complete cancellation occurs because the assumed



mode shape and the excitation correlation function have simple sinusoidal forms. When other mode shapes are assumed the joint acceptance will have non-zero minima. Similarly when the excitation has a non-zero value of  $\alpha_1$  complete cancellation will not be possible and the acceptance minima will be non-zero. Figures 2.2 to 2.5 show that, when  $\alpha_1$  is small, the shape of the acceptance curve changes rapidly as  $\alpha_1$  increases, and the maxima and minima are quickly blurred to give, first the "ripple" effect shown when  $\alpha_1 = 0.05$  and then the smooth curve shown when  $\alpha_1 = 0.3$ . Changes in  $\alpha_1$  of  $\pm 50\%$  about  $\alpha_1 = 0.1$  for the range of  $\frac{L_1}{\zeta}$  shown in the figures will give changes of up to  $\pm 50\%$  in the longitudinal joint acceptance curves.

The most important characteristic of the curves is the predominant peak which occurs when there is optimum matching between the mode shape and the excitation correlation pattern. It has been shown that this peak occurs in the neighbourhood of  $\frac{L_1}{\zeta} = 2m$ , but Figures 2.2 to 2.5 show that the position of the peak depends also on the value of  $\alpha_1$ . As  $\alpha_1$  increases, the maximum value of the joint acceptance occurs at lower values of  $\frac{L_1}{\zeta}$ . This indicates that, as the rate of decay of the excitation correlation function increases, the optimum matching occurs at convection velocities higher than those associated with wavelength matching.

The effect of  $\alpha_1$  on the magnitude of the longitudinal joint acceptance depends on the associated value of  $\frac{L_1}{\zeta}$ . In the neighbourhood of the peak value of the joint acceptance an increase in the excitation correlation decay rate causes a decrease in the joint acceptance. However, for values of  $\frac{L_1}{\zeta}$  away from the wavelength matching condition,  $\alpha_1$  has the converse effect and the value of  $j_{mm}(\omega)$  increases with  $\alpha_1$ . At large values of  $\alpha_1$  the main peak will have lost its prominence. It is apparent, therefore, that the effect of the excitation correlation decay rate on the panel response will depend on the value of the parameter  $\frac{L_1}{\zeta}$  at the frequency considered. At certain frequencies there will be an increase in response when  $\alpha_1$  increases whilst at other frequencies there will be a decrease in response.

Schloemer (1966) has shown that the presence of an adverse or favourable pressure gradient affects the convection velocity as well as the correlation

decay rate. In an adverse gradient the increased value of  $\alpha_1$  is associated with a lower convection velocity, and vice versa in a favourable gradient. Thus, in general, the net effect produces only small changes in the joint acceptance. The important exception is in the neighbourhood of wavelength matching, when  $\frac{L_1}{\zeta}$  is slightly greater than  $2m$ . In this case the changes in  $\alpha_1$  and  $U_c$  will increase the joint acceptance in a favourable gradient and decrease it in an adverse gradient. However, on the basis of Schloemer's results the changes should be less than  $\pm 50\%$  of  $j_{mm}(\omega)$ , unless there is a sharp pressure gradient.

The second form of the narrow band longitudinal cross correlation coefficient for  $\frac{\omega\delta^*}{U_c} < k_1$ , has an exponential decay term which is independent of frequency (equation (2.84)) and is inversely proportional to the boundary layer displacement thickness  $\delta^*$ . However, the non-dimensional parameter  $\frac{L_1}{\zeta}$  can be used because of the  $\cos \frac{\omega\zeta_1}{U_c}$  term in the correlation coefficient. The joint acceptance  $j_{mm}(\omega)$  can be calculated from equation (2.56) but, for each mode of order  $m$ , there will be a family of curves, with parameter  $\frac{L_1}{\delta^*}$ , which correspond to the single curve for mode  $m$  when  $\frac{\omega\delta^*}{U_c} \geq k_1$ . The curves for modes of order  $m = 1$  to 3 are shown in Figures 2.6 to 2.8 and it is seen that the effect of the parameter  $\frac{L_1}{\delta^*}$  is similar to that of  $\alpha_1$  in Figures 2.2 to 2.5. This is to be expected from the similar forms of the correlation coefficients. The effect of  $\alpha_2$  is not shown separately in this analysis but it can be included if the parameter  $\frac{L_1}{\delta^*}$  is replaced by  $(\frac{\alpha_2 L_1}{\delta^*})$ .

Figures 2.6 to 2.8 contain the curve for  $\frac{\omega\delta^*}{U_c} = 0.37$  which is the bounding value, from the results of Bull (1963), between the two forms of longitudinal cross correlation coefficient. The figures can be separated into two regions, region (1) where  $\frac{\omega\delta^*}{U_c} \geq 0.37$  is valid and region (2) where  $\frac{\omega\delta^*}{U_c} < 0.37$  is valid. The regions are marked in the figures, with vertical boundaries inserted at the points where the joint acceptance curves cross each other. In region (2) there are separate joint acceptance curves for each value of  $\frac{L_1}{\delta^*}$  but, as  $\frac{L_1}{\delta^*}$  decreases (for constant  $\frac{L_1}{\zeta}$ ) a stage is reached where  $\frac{\omega\delta^*}{U_c} = 0.37$ . The joint acceptance is then independent of further changes in  $\frac{L_1}{\delta^*}$  and retains the value given by the  $\frac{\omega\delta^*}{U_c} = 0.37$  curve.

For small values of  $\frac{L_1}{\zeta}$ , below the first vertical boundary line, the condition  $\frac{\omega \delta^*}{U_c} < 0.37$  is satisfied for most practical values of  $\frac{L_1}{\delta^*}$ . In the region of the wavelength matching the condition  $\frac{\omega \delta^*}{U_c} < 0.37$  is satisfied except in the thick boundary layer case when  $\frac{L_1}{\delta^*} < 30$ , approximately. At higher values of  $\frac{L_1}{\zeta}$  the condition  $\frac{\omega \delta^*}{U_c} \geq 0.37$  is valid for many values of  $\frac{L_1}{\delta^*}$ .

The data in Figures 2.6 to 2.8 can be presented in an alternative form, with  $\frac{L_1}{\zeta}$  as the curve parameter, to show the effect of boundary layer thickness. Typical curves for modes of order 1 and 2 are shown in Figures 2.9 and 2.10. The form of the correlation coefficient in equations (2.82) and (2.84) suggests that the boundary layer thickness  $\delta^*$ , which is present only in the exponential decay term, has less influence than the correlation length arising from the cosine term. This is borne out by the results in Figures 2.9 and 2.10 where, except for the  $m = 1$  mode and certain low value ranges of  $\frac{L_1}{\delta^*}$  in the  $m = 2$  mode, the curves vary slowly with  $\delta^*$ . Similar conclusions apply to the higher order modes. The results show that, depending on the value of  $\frac{L_1}{\zeta}$ ,  $j_{mm}(\omega)$  can either increase or decrease when  $\delta^*$  increases.

The curve of  $\frac{\omega \delta^*}{U_c} = 0.37$  is shown in Figure 2.9 and divides the figure into the two regions, described previously, in which the two forms of the cross correlation coefficient are valid.

### 2.6.3 Lateral Joint Acceptance

In the lateral direction the correlation coefficient is simplified by the absence of the convective (cosine) term but the computation of the joint acceptance is more difficult because the boundary between the two alternative forms of the lateral cross correlation coefficient is a function of separation distance. The two forms cannot be studied separately as in the longitudinal direction but the lateral joint acceptance can be investigated initially by assuming that the correlation coefficient has the form

$$|\rho_p(0, \xi_3, r; \omega)| = e^{-\frac{u_3 \omega |\xi_3|}{U_c}} \quad \dots (2.85)$$

for all values of  $\omega$ . This is the form which is valid when  $k_3 \leq 0$  and the lateral joint acceptance is given by equation (2.60). The joint acceptance curves for this approximate form can be compared with the acceptances calculated for the full cross correlation coefficient.

The lateral joint acceptance curves associated with the correlation coefficient of equation (2.85) are shown in Figures 2.11 and 2.12 for the modes of order  $m = 1$  to 4, and for three values of the coefficient  $\alpha_3$ . The curves are plotted in terms of the non-dimensional parameter  $\frac{L_3}{\zeta}$  for direct comparison with the longitudinal joint acceptance, and the form of the acceptance curves is seen to be different in the two directions. When the parameter  $\frac{L_3}{\zeta}$  is replaced by  $(\frac{\alpha_3 L_3}{\zeta})$  all the curves for a given mode  $m$  in Figure 2.11 or 2.12 will collapse onto a single curve. In the limit when  $\frac{\alpha_3 L_3}{\zeta} \rightarrow 0$ , the excitation is again similar to the case of a uniformly distributed load and the lateral joint acceptances for all even order modes tend to zero. The odd modes have non-zero joint acceptances for this limiting case and the maximum for the  $m = 1$  mode occurs at  $\frac{\alpha_3 L_3}{\zeta} = 0$ . In the higher order modes the joint acceptance increases to a maximum in the neighborhood of  $\frac{\alpha_3 L_3}{\zeta} = 2m$ , and then continuously decreases as  $\frac{\alpha_3 L_3}{\zeta}$  increases.

When the complete representation of the lateral cross correlation coefficient in equations (A.21) and (A.22) is used, the joint acceptance curves have the forms shown in Figure 2.13 for the first three modes,  $\frac{L_3}{\delta^*}$  being used as the curve parameter and the value of  $\alpha_3 = 0.715$  being taken from the boundary layer measurements. For comparison, the corresponding curves for the approximate correlation coefficient, equation (2.85), are also shown in the figure. At high values of  $\frac{L_3}{\zeta}$  when the condition  $k_3 \leq 0$  is satisfied, the approximate curve fully represents the joint acceptance. However, as  $\frac{L_3}{\zeta}$  decreases in value, the approximate curve diverges from the fully representative curves, the curves for the highest values of  $\frac{L_3}{\delta^*}$  showing the greatest divergence. The shape of the approximate curve is similar to those of the family of curves with parameter  $\frac{L_3}{\delta^*}$ , except at low values of  $\frac{L_3}{\delta^*}$  where  $k_3 \geq L_3$  and the approximation is no longer valid. The accuracy with which the lateral joint acceptance can be represented by the simple form depends on the value of  $\frac{L_3}{\delta^*}$ , but there is reasonable

accuracy, to within a factor of 2, for the range of  $\frac{L_3}{\delta^*}$  shown ( $\frac{L_3}{\delta^*} \leq 60$ ) except at very low values of  $\frac{L_3}{\zeta}$ .

The presence of the constant term  $c$  in the lateral correlation coefficient of equation (A.22), which was obtained from the measurements of Bull (1963), cannot be explained satisfactorily except as an interference effect due to background noise in the wind tunnel. It is probable that under ideal conditions the correlation coefficient would tend to zero at large separation distances and be of the form

$$|\rho_p(0, \xi_3, \tau; \omega)| = e^{-0.254 \frac{|\xi_3|}{\delta^*}} \quad \text{when } |\xi_3| < k_3 \quad \dots (2.86)$$

The correlation coefficient in equation (2.86) provides a reasonably good representation of the measurements of Bull (1963) at low separation distances but not at large separations (see Figure A.6). However, it is of interest to compare the lateral joint acceptance curves predicted from the two alternative correlation coefficients. A comparison on this basis is shown in Figure 2.14 for modes  $m = 1$  to 3, and  $\frac{L_3}{\delta^*} = 40$ . There is good agreement over most of the range of  $\frac{L_3}{\zeta}$ , the agreement being better than that obtained from the lateral correlation coefficient given by equation (2.85). The differences between the acceptance curves again occur primarily at low values of  $\frac{L_3}{\zeta}$  where the correlation coefficient form for  $|\xi_3| < k_3$  is the most important, but disagreement is never greater than a factor of 2. On this evidence it appears that the panel response estimated on the basis of a lateral correlation coefficient of the type shown in equations (A.21) and (A.22) would not differ greatly from that estimated from the modified correlation coefficient given by equations (A.21) and (2.85).

## 2.7 Direction of Convection of the Pressure Field

### 2.7.1 Joint Acceptance Terms

In equation (2.36), and in subsequent analysis, it was assumed that the pressure field was convected in the positive  $x_1$  direction. It is possible now to extend the analysis, under certain conditions, to include the convection directions which are inclined at an angle  $\theta$  to the  $x_1$  direction. This is of particular interest because practical structures are not

necessarily placed with one axis parallel to the direction of convection of the excitation field.

From Section 2.3, the total panel joint acceptance can be defined as

$$J_{\alpha\alpha}(\omega) = \frac{4}{A^2} \int_A \int_A \psi_{\alpha}(\underline{x}') \psi_{\alpha}(\underline{x}'') \rho_p(\xi_1, \xi_3, 0; \omega) d\underline{x}' d\underline{x}'' \quad \dots (2.87)$$

where the excitation cross correlation coefficient at zero time delay is

$$\rho_p(\xi_1, \xi_3, 0; \omega) = \frac{C_p(\xi_1, \xi_3, \omega)}{S_p(\omega)}.$$

The  $(x_1, x_3)$  rectangular Cartesian coordinates will be retained as the fixed ones of the panel and new Cartesian coordinates  $(y_1, y_3)$  will be introduced such that the pressure field convection velocity is in the positive  $y_1$  direction, and is inclined at an angle  $\theta$  to the positive  $x_1$  direction, for  $0 \leq \theta \leq \frac{\pi}{2}$ . In the new coordinate system the narrow band cross correlation coefficient is

$$\rho_p(\eta_1, \eta_3, 0; \omega) = |\rho_p(\eta_1, 0, \tau; \omega)| \cdot |\rho_p(0, \eta_3, \tau; \omega)| \cos b\eta_1 \quad \dots (2.88)$$

$$\text{where } \underline{\eta} \equiv (\eta_1, \eta_3) = \underline{y}'' - \underline{y}'$$

and where the assumed forms for the correlation coefficients in the  $y_1$  and  $y_3$  directions are

$$\begin{aligned} |\rho_p(\eta_1, 0, \tau; \omega)| &= e^{-a_1 |\eta_1|} \\ |\rho_p(0, \eta_3, \tau; \omega)| &= e^{-a_3 |\eta_3|} \end{aligned} \quad \dots (2.89)$$

Transforming to the  $(x_1, x_3)$  coordinates, the cross correlation coefficient becomes

$$\rho_p(\xi_1, \xi_3, 0; \omega) = e^{-a_1' |\xi_1|} e^{-a_3' |\xi_3|} \cos (b_1 \xi_1 + b_3 \xi_3) \quad \dots (2.90)$$

where

$$\begin{aligned}
 a_1' &= a_1 \cos \theta + a_3 \sin \theta \\
 a_3' &= a_1 \sin \theta + a_3 \cos \theta \\
 b_1 &= b \cos \theta \\
 b_3 &= b \sin \theta
 \end{aligned}
 \quad \dots (2.91)$$

Substituting equation (2.90) in equation (2.87), the joint acceptance is

$$\begin{aligned}
 J_{\alpha\alpha}(\omega) &= \frac{4}{A^2} \left( \int_0^{L_1} \int_0^{L_1} \psi_m(x_1') \psi_m(x_1'') e^{-a_1' |\xi_1|} \cos b_1 \xi_1 dx_1' dx_1'' \right. \\
 &\quad \times \left. \int_0^{L_3} \int_0^{L_3} \psi_n(x_3') \psi_n(x_3'') e^{-a_3' |\xi_3|} \cos b_3 \xi_3 dx_3' dx_3'' \right) \\
 &\quad - \frac{4}{A^2} \left( \int_0^{L_1} \int_0^{L_1} \psi_m(x_1') \psi_m(x_1'') e^{-a_1' |\xi_1|} \sin b_1 \xi_1 dx_1' dx_1'' \right. \\
 &\quad \times \left. \int_0^{L_3} \int_0^{L_3} \psi_n(x_3') \psi_n(x_3'') e^{-a_3' |\xi_3|} \sin b_3 \xi_3 dx_3' dx_3'' \right)
 \end{aligned}
 \quad \dots (2.92)$$

From arguments similar to those used in the derivation of equation (2.22), it can be shown that the double integrals in the second term of equation (2.92) are zero. Thus

$$\begin{aligned}
 J_{\alpha\alpha}(\omega) &= \frac{2}{L_1^2} \int_0^{L_1} \int_0^{L_1} \psi_m(x_1') \psi_m(x_1'') e^{-a_1' |\xi_1|} \cos b_1 \xi_1 dx_1' dx_1'' \\
 &\quad \times \frac{2}{L_3^2} \int_0^{L_3} \int_0^{L_3} \psi_n(x_3') \psi_n(x_3'') e^{-a_3' |\xi_3|} \cos b_3 \xi_3 dx_3' dx_3''
 \end{aligned}
 \quad \dots (2.93)$$

In Section 2.6, when the excitation pressure field was convected in the  $x_1$  direction, the excitation correlation function and the panel modal shape were assumed to have forms which were separable in the  $x_1$  and  $x_3$  directions, and the panel joint acceptance could be separated into components in the two coordinate directions. From equation (2.93), when the  $x_1$  axis is inclined at an angle  $\theta$  to the direction of convection, the panel joint

acceptance can be separated again into  $x_1$  and  $x_3$  components, but the associated excitation correlation functions (equation (2.91)) are combinations of the empirical longitudinal and lateral functions. The double integrals in equation (2.93) have the same form as equation (2.56), so that the general solutions of equation (2.56) are applicable.

The integrals in equation (2.93) show that the angle of convection influences the wavelength matching condition through the parameters  $b_1$  and  $b_3$ , and the effective correlation decay rate through the parameters  $a_1'$  and  $a_3'$ . From equation (2.91), for  $a_1 \geq 0$ ,  $a_3 \geq 0$  and  $0^\circ \leq \theta \leq 90^\circ$ ,  $a_1'$  and  $a_3'$  have a maximum value at  $\tan^{-1}(\frac{a_3}{a_1})$  and  $\tan^{-1}(\frac{a_1}{a_3})$  respectively, the maximum being  $\sqrt{(a_1^2 + a_3^2)}$  in each case.

The panel joint acceptance, equation (2.93), has been evaluated for cross correlation coefficients of the form shown in equation (2.89), where the coefficient in the  $y_3$  direction has, for boundary layer excitation, the simple form discussed in Section 2.6.3. The values of the joint acceptance calculated from equation (2.93) will not represent completely the response to boundary layer excitation but will give an indication of the effect of the direction of convection. Joint acceptance curves have been calculated for the conditions

$$a_1 = \frac{0.1\omega}{U_c} \quad \text{and} \quad a_3 = \frac{0.715\omega}{U_c},$$

and results for modes of order 1-1, 2-2 and 3-1 are shown in Figures 2.15 to 2.17 for a panel of aspect ratio 1.4545. This particular aspect ratio was chosen because it corresponded to the value for one of the experimental panels. The panel joint acceptance was calculated also for acoustic excitation, typical results for the panel of aspect ratio 1.4545 being shown in Figures 2.19 and 2.20. The assumed correlation function gives a better representation of the acoustic excitation field than it does for the boundary layer pressure field.

### 2.7.2 Discussion

The panel joint acceptance  $J_{aa}(\omega)$  can, from equation (2.93), be



expressed as the product of two functions each of which can be represented by a curve similar in shape to the curve for the appropriate mode order in Figure 2.1. Thus at all angles of convection the panel joint acceptance curves show the characteristic maxima and minima associated with the corresponding longitudinal joint acceptance curves in Figures 2.1 to 2.5, but the correlation length  $\zeta$  in Figure 2.1 is replaced by  $\frac{\zeta}{\cos \theta}$  in the  $x_1$  direction and  $\frac{\zeta}{\sin \theta}$  in the  $x_3$  direction. Hence the locations of the wavelength matching peaks in the curves will be at values of  $\frac{L_1}{\zeta}$  and  $\frac{L_3}{\zeta}$  which are lower than those associated with flow along the  $x_1$  and  $x_3$  axes respectively. The maxima will occur at positions such that

$$\frac{L_1}{\zeta} \leq 2m \quad \text{or} \quad \frac{L_3}{\zeta} \leq 2n$$

For the full panel joint acceptance  $J_{aa}(\omega)$ , the parameter  $\frac{L_3}{\zeta}$  is replaced by the aspect ratio  $\frac{L_1}{L_3}$ , and the peaks will occur at positions such that

$$\frac{L_1}{\zeta} \leq 2m \quad \text{or} \quad \frac{2nL_1}{L_3},$$

whichever is the larger. For example, in Figure 2.16, the wavelength matching peaks occur at values of  $\frac{L_1}{\zeta}$  where  $\frac{L_1}{\zeta} \leq 2.909n$ .

When the panel is considered as a complete unit, the mode shapes in the  $x_1$  and  $x_3$  directions combine to give a standing wave pattern which, for a simply supported mode of order  $(m-n)$ , is inclined at an angle  $\phi_{mn}$  to the  $x_1$  axis, where

$$\phi_{mn} = \tan^{-1} \left( \frac{L_1}{L_3} \cdot \frac{n}{m} \right)$$

The results of equation (2.93) for acoustic excitation, show that the panel joint acceptance is a maximum when the angle of convection  $\theta$  is equal to  $\phi_{mn}$ . Thus for plane wave excitation there is maximum panel response when the panel inclination to the direction of convection is such

that the excitation correlation pattern matches with the overall modal pattern of the panel. For the mode of order (2-2) in Figure 2.20, the maximum response occurs when

$$\theta = \phi_{mn} = 55^{\circ}30'.$$

Exceptions to this rule occur for modes of unit order in the  $x_1$  or  $x_3$  direction, but it has been shown in Figure 2.1 that the results for the unit order mode differ from the general results for the higher order modes.

In the case of boundary layer excitation, Figures 2.15 to 2.17 show that the maximum response occurs when  $\theta = 0^{\circ}$  or  $\theta = 90^{\circ}$ , but not, as in the acoustic case, when  $\theta = \phi_{mn}$ . The difference between the results for boundary layer and acoustic excitation arises from the exponential decay of the boundary layer correlation function. When  $0^{\circ} < \theta < 90^{\circ}$ ,  $a_1'$  and  $a_3'$  will be greater than  $a_1$  (assuming that  $a_1 < a_3$ ), and each will have a maximum value of  $\frac{0.723\omega}{U_c}$  for the assumed boundary layer correlation coefficient. The increased correlation decay rate reduces the acceptance peaks and thereby cancels the wavelength matching effect when  $\theta$  approaches  $\phi_{mn}$ .

If interest is centred on one particular value of  $\frac{L_1}{\zeta}$ , the results for both boundary layer and acoustic excitation show that the panel joint acceptance may have a maximum value when  $\theta$  has an intermediate value in the range  $0^{\circ}$  to  $90^{\circ}$ . The effect is of most importance for acoustic excitation, where there is no decay term in the excitation correlation function, particularly when the value of  $\frac{L_1}{\zeta}$  is associated with a zero of the joint acceptance at some value of  $\theta$ . In Figure 2.20, the (2-2) mode has zero joint acceptances when  $\theta = 0^{\circ}$  and  $90^{\circ}$ , and, when  $\frac{L_1}{\zeta} = 4$ , has a maximum in the neighbourhood of  $\theta = 50^{\circ}$ . Conversely the (3-1) mode has maximum values at  $\theta = 0^{\circ}$  and  $90^{\circ}$  and an intermediate minimum. The results for boundary layer excitation in Figures 2.15 to 2.17 show that, for low values of  $\frac{L_1}{\zeta}$ , the maximum response occurs usually when  $\theta = 0^{\circ}$  or  $\theta = 90^{\circ}$ , but at the higher values of  $\frac{L_1}{\zeta}$  the curves show a tendency to become

symmetrical about a maximum value at  $\theta = 45^\circ$ . This implies that, when the correlation lengths are small relative to the modal wavelengths, the aspect ratio effect becomes small and the panel is effectively square.

The effect of aspect ratio is illustrated in Figure 2.18 for the (3-1) mode of a series of panels having aspect ratios 1.0, 1.4545, 2.0 and 4.0, corresponding to the aspect ratios of the experimental panels. The figure contains panel joint acceptance curves for the limiting angles of convection  $\theta = 0^\circ$  and  $\theta = 90^\circ$ . When  $\theta = 0^\circ$  the aspect ratio has a small effect on the joint acceptance, the value of  $J_{\alpha\alpha}(\omega)$  increasing by a factor of approximately 2.5 for a four-fold increase in aspect ratio. When  $\theta = 90^\circ$  the effect is much greater, the same change in aspect ratio causing the joint acceptance to change by a factor of 25. Similar results will be found for intermediate values of  $\theta$ , the effect of aspect ratio being less than that shown when  $\theta = 90^\circ$ . The variation of panel joint acceptance with aspect ratio is fairly simple in the example shown but will be more complicated for higher order modes.

## 2.8 Cross Acceptance

The panel joint acceptance for boundary layer and acoustic excitation has been discussed in general terms in Sections 2.6 and 2.7, using the non-dimensional parameters  $\frac{L_1}{c}$ ,  $\frac{L_1}{\delta\delta}$ , and  $\frac{L_1}{L_3}$ . From equations (2.64) to (2.67), the longitudinal and lateral cross acceptances can be presented in a similar way. However it can be shown that the cross terms in the displacement power spectral density function are usually much smaller than the joint terms, as is shown by the results in Chapters 5 and 6, except under conditions of close natural frequencies and high damping in modes for which the sum of the lateral mode orders ( $n+s$ ) is even. Therefore a general study of the cross acceptance is of limited use and will not be undertaken in the present discussion, but the form of the cross acceptances can be illustrated by a comparison with the joint acceptance for particular conditions which apply to one of the experimental panels. The cross acceptance results in this chapter can be used in the case of heavy damping, when the cross acceptance becomes important, provided that due allowance is made for the assumptions of light damping which were made in the analysis.

In Figures 2.21 to 2.23, the acceptance curves are shown for the 4" x 2.75" panel when exposed to the turbulent boundary layer at a flow speed of  $U_0 = 329$  ft/sec. Differences between the joint and cross acceptances are immediately obvious and they are due to the dependence of the cross acceptance on the mode order pair (m,r) or (n,s), instead of the single mode order dependency of the joint acceptance. It has been shown that the joint acceptance is a positive function and in general exhibits a single predominant peak associated with the wavelength matching condition. Figures 2.21 to 2.23 show that the cross acceptance has a more complicated form. In Figure 2.21, the curves for the real part  $j_{mr}(\omega)$  of the longitudinal cross acceptance show the presence of two peaks of similar magnitude but of opposite sign. Curves for the imaginary part  $k_{mr}(\omega)$  of the longitudinal cross acceptance in Figure 2.22 also show changes in sign as the frequency changes. Further, from equation 2.44, it is seen that  $k_{mr}(\omega) = -k_{rm}(\omega)$ .

The joint and cross acceptance curves, in terms of either the non-dimensional parameters in Figures 2.1 to 2.20 or the frequency in Figures 2.21 to 2.23, show that the peaks are broad, the bandwidths being of the order of 70% of the centre frequencies. This is particularly noticeable when the acceptance curves are compared with the resonance peaks of the panel receptance. Thus the panel response will be only slightly lower than the maximum coincidence value if the panel natural frequency lies within a fairly broad frequency range centred on the wavelength matching frequency.

When the acceptance and impedance terms are combined, the cross term contributions to the displacement spectral density have the forms shown in Figures 2.24 and 2.25. The curves in Figure 2.24 are for mode pairs in which (m+r) is odd and (n+s) is even, and Figure 2.25 shows the form of the cross term when (m+r) and (n+s) are even. When (m+r) is odd, the cross term contains the product, given by equation (2.45), of

$$\frac{h_{\alpha\beta}}{g_{\alpha\beta}^2 + h_{\alpha\beta}^2} k_{mr}(\omega) j'_{ns}(\omega)$$

where  $g_{\alpha\beta}$ ,  $h_{\alpha\beta}$  are real and imaginary parts of the impedance product as defined in equation (2.24). If  $(n+s)$  is odd,  $j'_{ns}(\omega) = 0$  and the product is zero. From equation (2.51) the impedance term  $\frac{h_{\alpha\beta}}{g_{\alpha\beta}^2 + h_{\alpha\beta}^2}$  has

maxima, close to the natural frequencies  $\omega_\alpha$  and  $\omega_\beta$  of the mode pair, which are predominant in the curves in Figure 2.24. Secondary maxima are due to the cross acceptance terms. The sign of the cross term will depend on the sign of the acceptance terms, on the sign of the receptance term, and on the sign of the mode shape product of  $\psi_\alpha(\underline{x})\psi_\beta(\underline{x})$  at the position  $\underline{x}$  considered. For the range of frequencies shown in Figure 2.24 the cross term curve for the (2-1, 5-1) mode pair is positive and for the (1-2, 2-2) mode pair, is negative.

When  $(m+r)$  is even, the cross term contribution contains the product

$$\frac{g_{\alpha\beta}}{g_{\alpha\beta}^2 + h_{\alpha\beta}^2} j_{mr}(\omega) j'_{ns}(\omega)$$

As in the previous case,  $\frac{1}{g_{\alpha\beta}^2 + h_{\alpha\beta}^2}$  has maxima at, approximately,  $\omega = \omega_\alpha$  and  $\omega_\beta$ , but from equation (2.51)  $g_{\alpha\beta}$  has zero values close to the natural frequencies. Thus the cross term will not have the peaks shown in Figure 2.24, but will have zeros of the type shown in Figure 2.25 for a frequency close to 2030 c.p.s. In addition the cross acceptance term  $j_{mr}(\omega)$  will have a series of zeros shown in Figure 2.21, one of which, for the conditions considered, occurs in the neighbourhood of the natural frequency  $f = 1,300$  c.p.s. with the resultant complicated response curve in Figure 2.25. Finally a zero of  $j_{mr}(\omega)$  occurs in Figure 2.25 at approximately 450 c.p.s., well away from the natural frequencies of the modes considered. Whenever the cross term contribution passes through a zero there will be a change of sign, but Figure 2.25 shows only the amplitude of the contribution.

The relative magnitudes of the joint and cross term contributions to the panel displacement power spectral density function can be compared in Figures 2.24, 2.25 and 5.8. It is seen that the cross term contribution is

greatest for mode pairs where  $(m+r)$  is odd, but that the contribution is very small throughout the frequency range.

## 2.9 Summary

The response of plates to random excitation has been investigated theoretically under the general assumptions that :

- (a) there is no interaction between the plate and the excitation field;
- (b) the vibration can be adequately represented by a series of normal modes;
- (c) there is no modal coupling due to damping;
- (d) the mode shapes have an exact or approximate form which is separable in the  $(x_1, x_3)$  directions;
- (e) the excitation field is homogeneous and stationary;
- (f) the excitation cross power spectral density function can be represented in a form which is separable in the  $(x_1, x_3)$  directions.

In addition it was assumed that the panels were simply supported, and that the excitation narrow band cross correlation coefficient was of the exponential decay form. The excitation correlation coefficients for boundary layer excitation were expressed analytically from experimental data of Bull (1963) for zero pressure gradient conditions. A typical frequency dependent excitation correlation length  $\xi$  was defined in terms of the separation distance to the first zero of the excitation narrow band longitudinal space correlation coefficient.

The most important terms connecting the excitation and the structural modes are the joint and cross acceptances, and these have been studied in detail. Interest was centred on the joint acceptances because, except in cases of close natural frequencies and high damping, the cross terms are negligible relative to the joint terms.

The longitudinal joint acceptance has been studied for the two correlation forms associated with the Strouhal number regions bounded by

$\frac{\omega \delta^*}{U_c} = 0.37$ , using non-dimensional parameters  $\frac{L_1}{\zeta}$ ,  $\frac{L_1}{\delta^*}$ , and  $\frac{L_1}{L_3}$ . In each region the acceptance curves have a predominant peak in the neighbourhood of the wavelength matching condition  $\frac{L_1}{\zeta} = 2m$ , for a mode of order  $m$ . Thus as  $\frac{L_1}{\zeta}$  decreases, due to an increase in  $U_c$  or a decrease in  $\omega$ , the panel response will increase when  $\frac{L_1}{\zeta}$  is greater than  $2m$  and decrease when  $\frac{L_1}{\zeta}$  is less than  $2m$ .

When the excitation correlation decay coefficient  $\alpha_1$  is increased the joint acceptance decreases in the neighbourhood of the wavelength matching condition and increases for other values of  $\frac{L_1}{\zeta}$ . The value of  $\alpha_1$  affects also the position of the main peak of the joint acceptance curve, increases of  $\alpha_1$  moving the peak to lower values of  $\frac{L_1}{\zeta}$ . Thus, if the pressure field loses coherence very rapidly the maximum response occurs when the convection velocity is greater than that associated with the condition  $\frac{L_1}{\zeta} = 2m$ , or when the frequency is lower than that for  $\frac{L_1}{\zeta} = 2m$ . The condition  $\alpha_1 = 0$  is applicable to excitation by grazing incidence acoustic plane waves, and the joint acceptance has a series of well defined maxima and minima associated with wavelength matching and mismatching. When  $\alpha_1$  increases the maxima and minima become blurred into a smooth curve.

In the region  $\frac{\omega \delta^*}{U_c} < 0.37$ , a family of curves with parameter  $\frac{L_1}{\delta^*}$  replaces the single joint acceptance curve for a given value of  $\alpha_1$ . The parameter  $\frac{L_1}{\delta^*}$  has an effect similar to that of the coefficient  $\alpha_1$ . A range of values  $10 \leq \frac{L_1}{\delta^*} \leq 80$  was chosen, corresponding to the range experienced in the experimental work and to values which are typical of full scale aircraft.

In the lateral direction the joint acceptance curves do not exhibit the wavelength matching peak, because the convection velocity has no component in that direction. The two forms of lateral narrow band cross correlation coefficient are separated by a boundary which is a function of separation distance and not simply of Strouhal number as in the longitudinal direction. Thus the lateral joint acceptance has a single form which combines the two correlation coefficients. A simplified form of the cross correlation coefficient, strictly valid only when  $k_3 \leq 0$ , was used to

estimate the joint acceptance, for comparison with the full lateral joint acceptance. Good agreement was observed at high  $\frac{L_3}{\zeta}$  (i.e. when  $k_3 \leq C$ ) but as  $\frac{L_3}{\delta^*}$  decreased, the agreement deteriorated. For  $\frac{L_3}{\delta^*} \leq 60$ , there was agreement to within a factor of two except at the very low values of  $\frac{L_3}{\zeta}$ .

Closer agreement between the complete and approximate joint acceptances was achieved when an approximate cross correlation function was used in the region  $|\xi_3| < k_3$ . This function assumed that the correlation coefficient should tend to a zero value at large  $\frac{\xi_3}{\delta^*}$  instead of the non-zero value measured by Bull. It was shown that conclusions reached for the empirical correlation coefficients assumed in the analysis should not differ greatly from those applicable to conditions in which the correlation coefficient has a zero asymptote.

When the angle of convection  $\theta$  is changed, and  $\frac{L_1}{\zeta}$  does not have a fixed value, it is possible to obtain an optimum wavelength matching between the panel mode shape and the excitation correlation pattern. In the case of acoustic plane wave excitation, the panel response has a maximum value when  $\theta$  is equal to the angle  $\phi_{mm}$  which the modal standing wave makes with the  $x_1$  axis. For boundary layer excitation, however, the wavelength matching effect is cancelled by the increased effect of the correlation decay rate, and the maximum response occurs when  $\theta = 0^\circ$  or  $90^\circ$ . If  $\frac{L_1}{\zeta}$  has a fixed value, the response may be greater when the direction of convection is inclined to the panel axis. The effect is most pronounced for plane wave excitation, where order of magnitude changes were predicted for certain values of  $\frac{L_1}{\zeta}$ . When the correlation length is very small relative to the modal wavelength, the joint acceptance has values which tend to be symmetrical about the value for  $\theta = 45^\circ$ , and the panel is effectively square.

The cross acceptance has not been studied in terms of the non-dimensional parameters, but the form of the cross acceptance curves was illustrated for particular experimental conditions. The cross acceptance differs from the joint acceptance in that it has more than one peak and can be either positive or negative in sign, depending on the frequency. When the cross acceptances



and impedances are combined, the resulting cross terms will modify the spectrum shape determined from the joint terms alone. The cross term spectra can be complicated in shape, but the modification to the displacement spectra is small for the experimental conditions investigated.

## CHAPTER 3

### Experimental Equipment

#### 3.1 Wind Tunnel

The experimental investigation is concerned primarily with the vibration of panels exposed to turbulent boundary layer excitation, and vibration measurements were made when the specimens were mounted in the wall of a wind tunnel which was designed to have low noise and vibration characteristics. The wind tunnel is of the induced flow, non-return type driven by the injection of high pressure air downstream of the working sections. The running time is limited to two to three minutes by the storage capacity of the high pressure supply. The tunnel, whose general arrangement is shown in Figure 3.1, has two working sections, a subsonic section 10 feet long followed by a supersonic section 6 feet long, both of which have a rectangular cross-section with nominal dimensions 9 inches x 6 inches. The subsonic section is slightly divergent to compensate for boundary layer growth and to provide a zero pressure gradient. The flow velocity in the tunnel is determined by the throat area upstream of the supersonic section, and the use of two sets of tunnel liners resulted in two operating conditions which had nominal Mach numbers of  $M_0 = 0.3$  and  $0.5$  in the subsonic section.

To keep the vibration to a minimum the working sections are of massive steel construction and are mechanically isolated from the injector and from each other, being connected by flexible couplings. The working sections are carried on flexible mountings (see Plate 3.1) which isolate them from vibration transmitted through the laboratory floor. The extraneous sound field in the test section is kept to a minimum by heavily soundproofing the injector and diffuser, and the tunnel was always run in a choked condition so that injector and diffuser noise was not propagated internally into the subsonic section, except through the subsonic boundary layer in the sonic throat. The diffuser outlet is outside the laboratory building.

In spite of these precautions, measurements by Bull (1963) and Clark (1966) show that there is a significant low frequency noise field inside the working section. This noise field can influence the pressure spectrum on the wall of the wind tunnel, the effect being greater at the higher Mach number and thicker boundary layers. In Figure 3.2 the boundary layer spectra are compared with spectra of the background noise field measured along the tunnel centreline. At low frequencies the boundary layer and acoustic spectral densities are of similar magnitude and structural vibration will be due to a combination of the two excitation fields. Thus panel vibration measurements have been rejected for frequencies below 300 c.p.s.

Comprehensive measurements of the characteristics of the flow in the boundary layer wind tunnel have been made by Bull (1963) and it is necessary to summarise only the data which is of particular interest to the panel vibration investigation. Table 3.1 contains data for the four panel positions along the subsonic working section. The free stream velocity  $U_0$  and the dynamic pressure  $q_0$  of the airflow are essentially constant along the working section and, for each nominal Mach number  $M_0$ , the boundary layer thickness  $\delta$  increases from a value of approximately 0.4 inch at the upstream position to 1.42 inches at the downstream position, the positions being measured from the tunnel datum (Figure 3.1) at the upstream end of the subsonic working section. The boundary layer displacement thickness  $\delta^*$  is defined by

$$\delta^* = \int_0^{\infty} \left(1 - \frac{\rho U_1}{\rho_0 U_0}\right) dx_2$$

where  $\rho$  and  $U_1$  are the local density and mean velocity in the  $x_1$  direction, respectively. The overall root-mean-square pressure fluctuations are denoted by  $\sqrt{p^2}$ . Under operating conditions the static pressure in the tunnel working section is below the ambient pressure in the laboratory, the pressure differential being proportional, approximately, to the square of the free stream velocity in the tunnel. At a Mach number  $M_0 = 0.3$ , the pressure differential was approximately 1.0 lb/in<sup>2</sup> and, at  $M_0 = 0.5$ , approximately 2.35 lb/in<sup>2</sup>.

TABLE 3.1  
Summary of Experimental Conditions

Position	1	2	3	4
x inches	22.5	50.5	78.5	106.5
<u>M<sub>0</sub> = 0.3</u>				
U <sub>0</sub> ft/sec	329.4	329.4	329.4	329.4
q <sub>0</sub> lb/ft <sup>2</sup>	122.5	122.5	122.5	122.5
δ inches	0.38	0.72	1.06	1.40
δ* inch	0.055	0.096	0.138	0.179
√(p̄ <sup>2</sup> ) lb/ft <sup>2</sup>	0.692	0.668	0.655	0.650
<u>M<sub>0</sub> = 0.5</u>				
U <sub>0</sub> ft/sec	541.7	540.6	539.5	538.5
q <sub>0</sub> lb/ft <sup>2</sup>	306	305	304	303
δ inches	0.43	0.76	1.09	1.42
δ* inch	0.057	0.100	0.139	0.174
√(p̄ <sup>2</sup> ) lb/ft <sup>2</sup>	1.745	1.678	1.656	1.658

In the discussion of the experimental results the flow conditions will be referred to in terms of either the Mach number or the mean flow velocity.

### 3.2 Siren Tunnel

An alternative form of convected excitation field was provided by the siren tunnel, described by Clarkson and Pietrusewicz (1961). The tunnel consists of a 12 in x 14 in rectangular duct with an Altec Lansing Siren at one end and sound absorbing material at the other. The siren is coupled to the duct by means of an acoustic horn (Figure 3.3). The test section commences at a distance of 18 inches from the end of the horn and includes a 24 in x 47 in rectangular opening in one wall of the tunnel. Plane acoustic waves propagating from the horn will be convected at grazing incidence over a specimen mounted in the test section opening. The airflow through the siren orifice is controlled by a speaker coil modulator which, in turn, is controlled electronically by means of an oscillator or white noise generator. Within the limitations of the siren (Appendix A) the spectrum shape, for white noise generation, can be modified by suitable filters, and this form of excitation was used in the panel response investigation. Whilst the vibration measurements were in progress the sound field in the duct was monitored using a Bruel & Kjaer  $\frac{1}{2}$ -inch diameter microphone, and an overall level of 129 dB was maintained.

The duct and horn are heavily soundproofed, but the construction of the tunnel is less massive than the boundary layer tunnel. Thus the problem of background vibration was found to be more severe.

The siren requires a continuous air supply for its operation and there is an airflow along the duct. However, the velocity of the air is extremely low (approximately 2 ft/sec) and there is no possibility that it will cause any direct excitation of the panel. There will be the additional effect of jet noise described in Appendix A.

### 3.3 Experimental Panels

The size of the experimental panels was chosen as a compromise based on several considerations. The 9-inch walls of the working section were available for the positioning of experimental specimens but it was desirable that the panels should not extend into the regions of three-dimensional boundary layers in the corners of the duct. Thus the maximum permitted panel dimension in a direction perpendicular to the flow was 6 inches to 7 inches. In the longitudinal direction the panel dimensions were restricted so that the excitation conditions did not change significantly over the panel area. Further, the panel fundamental natural frequency should be well above the frequency limit of 300 c.p.s., below which measurements were rejected because of interference from the noise field in the tunnel. In the initial design of the boundary layer tunnel there were a series of 6 inch diameter ports along the length of the working section (see Plate 3.6). Thus panels, which satisfied the above conditions, could be mounted on 6 inch diameter plugs and inserted at desired positions along the working section. This method had the additional advantage that the panels could be rotated so that the major axes had any required angle of inclination to the flow direction. In particular the rectangular panels could be rotated through  $90^\circ$  so that the minor axes were parallel to the flow.

Thus, the experimental panels were formed by bonding thin steel sheets to 6 inch diameter circular plugs and the shape of each panel was determined by the dimensions of a hole cut through the plug. Four panels, shown in Plate 3.2, were constructed with basic dimensions

3.5 in x 3.5 in x 0.015 in ;  
4.0 in x 2.75 in x 0.015 in ;  
4.0 in x 2.0 in x 0.015 in ;  
4.0 in x 1.0 in x 0.015 in.

Thicker panels were not used because the reduced vibration amplitudes introduced measuring difficulties. Some experiments were carried out on

0.005 inch and 0.010 inch thick panels (Bull, Wilby and Blackman (1962)) but the panels were destroyed during initial tests. Replacement panels were not constructed, partly because the thinner panels showed a tendency to be affected by tensions introduced during construction, and the vibration measurements were made on panels of only one thickness.

The construction of a typical panel is shown in detail in Figure 3.4. The steel sheet was bonded to the carrier plug using Kodak-Eastman 910 Adhesive which set rapidly under pressure, and was cured at room temperature for 48 hours. To obtain a good bond the steel sheet was completely degreased by immersion for ten minutes in a 10% solution of sodium metasilicate and the brightness of the surface was then enhanced by immersion in an 85% phosphoric acid solution for two minutes. When the bond had cured the sheet was clamped to the plug along two sections of the periphery. The clamps did not determine the edge conditions of the experimental panel, but were added to prevent the panel from being carried into the tunnel in the event of a failure of the bond during tunnel operation. Surface irregularities around the clamping strips were filled with 'Araldite' resin so that the complete plug presented a flat surface, flush with the internal wall of the tunnel working section.

Some of the panels were modified to have static pressure holes inserted in the rigid face of the steel sheet but in other cases the tunnel static pressure was measured at plug positions adjacent to the panel position.

It was impossible to determine whether any panel tension was introduced during construction but every effort was made to reduce tensioning effects to a minimum. As a guide, the natural frequencies and mode shapes of the final panels were measured and compared with theoretical values. This comparison is shown in Appendix C and there is seen to be reasonably good agreement between the measured and estimated characteristics. The 0.015 inch thick panels did not display the "oil canning" effect observed in preliminary measurements on the thinner panels, and it was not necessary to use the stabilising static pressure differential employed by Ludwig (1962).

### 3.4 Displacement Measuring Probe

There are several ways of measuring the vibration of a structure but many of them require that transducers be attached to the vibrating body. In the case of the experimental panels the additional mass of the transducers would cause an appreciable change in the vibrational characteristics of the specimens. Therefore non-contacting capacitance probes, manufactured by Wayne Kerr Laboratories Limited, were used. Initially, the C probe, suitable for the measurement of vibration amplitudes of less than  $5 \times 10^{-3}$  inch was used but later the more sensitive B probe with a maximum amplitude limit of  $2.5 \times 10^{-3}$  inch was used, when it became available. A very sensitive probe was available for amplitude measurements of less than  $5 \times 10^{-4}$  inch but great difficulty was experienced in aligning the probe and panel surface with sufficient accuracy, the gap between the probe and panel being less than  $1 \times 10^{-3}$  inch. Slight distortion of the panel surface made the alignment impossible.

The probes consist of a flat, circular inner electrode which is surrounded by a guard ring. An insulating sleeve separates the electrode and guard ring. The outer radius of the guard ring is 0.125 inch for each probe but the effective radius of the B and C probes is 0.050 inch and 0.0707 inch respectively. The vibration meter acts on a high gain amplifier, connected to a 50 Kc/sec oscillator, with a feed back loop through a capacitance of approximately 0.5 pF between the probe and structure under test. The output of the amplifier is a 50 Kc/sec signal whose voltage amplitude is proportional to the distance between the probe and structure. The mean amplitude determines the mean distance between the probe and structure and the modulation amplitude is a measure of the displacement of the structure. The 50 Kc/sec carrier signal could be removed by filtering, and the meter output signal recorded on magnetic tape for detailed analysis did not contain the carrier signal. For small vibration amplitudes the amplification provided by the vibration meter can be increased by a factor of 5 by changing the output from "normal" setting to "x5" setting. This increased amplification was used when necessary.



The combined sensitivity of the probes and meter amplifier was calibrated before initial use and the calibration was repeated on several occasions during the period of the investigations to check for changes in amplifier characteristics. The calibration equipment can be seen in Plate 3.3 where the probe is rigidly mounted above a vibrator. Attached to the vibrator are an accelerometer and a small plate, the system being shown in greater detail in Figure 3.5. The movement of the plate was measured by the probe and monitored by means of a travelling microscope fitted with a vernier eyepiece, and by means of the accelerometer. At large amplitudes the probe was calibrated with reference to the microscope but at low amplitudes visual measurement was inaccurate and the accelerometer was used as the reference. The block diagram of the calibration apparatus is contained in Figure 3.6. The probes were calibrated for sinusoidal oscillations in the frequency range 200 c.p.s. to 1,000 c.p.s. and calibration curves for the Band C probes are shown in Figure 3.7. Within the accuracy of the method (approximately  $\pm 6\%$ ), the probe calibrations in terms of the r.m.s. displacement are :

Probe B:-	Normal Setting	$8.30 \times 10^{-5}$ inch displacement per volt.
	+5 Setting	$1.66 \times 10^{-5}$ inch displacement per volt.
Probe C:-	Normal Setting	$1.66 \times 10^{-4}$ inch displacement per volt.
	+5 Setting	$3.32 \times 10^{-5}$ inch displacement per volt.

The calibration measurements were made for a standard separation gap between the probe and plate of  $3.5 \times 10^{-3}$  inch for the B probe and  $7.0 \times 10^{-3}$  inch for the C probe. All vibration measurements were made with similar gap sizes but, in any case, variations of the separation distance have little effect on the probe calibration. In Figure 3.8, the calibration factor for the C probe, at frequencies of 250 c.p.s. and 500 c.p.s., changes by only  $\pm 2\%$  for variations in gap size of  $\pm 20\%$  from the standard of  $7.0 \times 10^{-3}$  inch.

The response of a capacitance probe can be in error if the probe face and vibrating surface are not parallel, but the errors will not be large

in general. From Figure 3.9, the capacitance based on the elemental area of the probe face, is

$$dC_v = \frac{k \ell dx}{y}$$

where  $k$  is a constant of proportionality and  $y$  is the distance between the probe face and the surface of the vibrating structure. The total capacitance, for a circular probe face of radius  $r$ , will be

$$C_v = \int_0^\pi \frac{2kr^2 \sin^2 \theta d\theta}{\bar{y} - r \cos \theta \tan \phi} \quad \dots (3.1)$$

where  $\bar{y}$  is the mean separation distance between the probe and the structure, and it is assumed that the vibrating structure is flat and inclined at an angle  $\phi$  to the probe face.

The solution of equation (3.1) is

$$C_v = \frac{2\bar{C}_v}{z^2} (1 - \sqrt{1 - z^2}) \quad \dots (3.2)$$

where  $\bar{C}_v = \frac{k\pi r^2}{\bar{y}}$  is the capacitance for parallel surfaces separated by a distance  $\bar{y}$  and

$$z = \frac{r \tan \phi}{\bar{y}} \quad \dots (3.3)$$

The effective separation  $y'$  between the probe and structure, as measured by the probe, can be defined by

$$C_v = \frac{k\pi r^2}{y'} \quad \dots (3.4)$$

From equations (3.2) and (3.4)

$$\bar{y} = \frac{2y'}{z^2} (1 - \sqrt{1 - z^2})$$

or, on rearrangement,

$$\bar{y} = y' (1 + (\frac{r \tan \phi}{2y'})^2) \quad \dots (3.5)$$

Thus the mean separation exceeds the measured value by a distance  $\Delta y = \bar{y} - y'$ , and from equation (3.5)

$$\frac{\Delta y}{y'} = \left( \frac{r \tan \phi}{2y'} \right)^2 \quad \dots (3.6)$$

Because of slight curvature of the experimental panels and small errors in aligning the measuring probe, it was impossible to position the probe so that the face was parallel to the panel surface. The angle  $\phi$  between the panel and the face of the probe could not be observed visually but it was estimated by advancing the probe until the guard ring touched the panel. This condition was indicated by a sudden loss of signal due to shorting of the measuring circuit.

When the probe guard ring just touches the panel

$$\tan \phi = \frac{\bar{y}_s}{R}$$

where  $R$  is the outer radius of the guard ring and  $\bar{y}_s$  is the value of  $\bar{y}$  when the probe is shorted out. Then, from equation (3.6)

$$\frac{\Delta y}{y'} = \left( \frac{\bar{y}_s}{2Ry'} \right)^2 \quad \dots (3.7)$$

For the Wayne Kerr C probe,  $\frac{\bar{y}_s}{R} = 8.768 y'_s$  where  $y'_s$  (measured in inches) is the separation distance indicated just before shorting occurs. Equation (3.7) now becomes

$$\frac{\Delta y}{y'} = 9.607 \left( \frac{y'_s}{y'} \right)^2 \% \quad \dots (3.8)$$

From equation (3.8) the error due to slight misalignment of the probe and panel is small and cannot exceed 9.607%, since  $\frac{y'_s}{y'}$  cannot exceed unity in practice. Further the value of  $\Delta y$  is always positive because the right hand side of equation (3.7) is positive definite. Thus the probe will always underestimate the mean separation distance.

In practice it was found that the C probe alignment could be adjusted to an optimum position for which the guard ring and panel touched at an indicated separation  $y'_s$  less than  $1 \times 10^{-3}$  inch, corresponding to an angle of inclination of approximately  $0^{\circ}35'$ . From equation (3.8), for  $y' = 7 \times 10^{-3}$  inch, the error due to the surfaces not being parallel is only 0.2%. For a system in which the vibrating system is rigid and moves so that the angle  $\phi$  between the probe face and vibrating surface is constant, then the above error will apply to the distance measurement only. The vibration amplitude is a measure of the difference between the maximum and minimum distances and both these distances are affected equally by the errors. Calibration checks confirmed that vibration measurements were not affected under these circumstances. In the present investigation, the vibration is in the form of distortion of the panel surface, and the angle between the panel and the face of the probe will not remain constant. However, for the displacements shown in Figure 5.2 and Table 6.1, the error is less than that estimated above for static misalignment. Thus errors due to the panel surface not being parallel to the probe face are negligible in the vibration measurements of the experimental panels.

For the panel vibration measurements the probe was carried in a holder which allowed fine adjustment of the probe face relative to the panel surface. The holder was attached to a rigid traverse gear which, when mounted on a boundary layer tunnel side plate as shown in Plate 3.4, allowed the probe to be moved over the full face of the panel. The traverse gear, whose dimensions are shown in Figure 3.10, was designed to minimise vibration interference. The combined system, of boundary layer tunnel side plate with attached traverse gear, could be used at several positions along the tunnel working section, or at positions away from the tunnel, for example in the siren tunnel and freely suspended from a gantry for damping measurements (Plate 4.1). When the side plate was placed in the siren tunnel, as shown in Plate 3.5, the remaining open area of the test section was covered with wooden boards.

### 3.5 Signal Analysis

The output signal from the Wayne Kerr vibration meter was recorded for a period of one minute on magnetic tape at a tape speed of 15 inches per second. At the end of each panel vibration recording, a 500 c.p.s. calibration signal of known amplitude was recorded to provide a datum when replaying for analysis.

An initial analysis of the vibration was made by an automatic frequency sweep to indicate the location of the peaks in the spectra. The sweep rates were too fast to provide statistically reliable information about the spectral density and a more detailed analysis was then carried out using the filters of either 1.2% or 2.0% bandwidth in the Muirhead-Pametrada Wave Analyser. The output signal from the filter was integrated for a period of 50 seconds to ensure statistical reliability (see Appendix B). The integration period was chosen after results had been compared for integration times of 10, 20 and 50 seconds. Taking the results for a 50 second integration period as reference, the measured spectral density obtained after 10 seconds integration was within  $\pm 22\%$  of the reference. After a 20 second integration period the scatter was reduced to  $\pm 15\%$ .

### 3.6 Pressure Equalising System

In many cases it was desirable that the panels should be unaffected by the static pressure differential between the tunnel working section and the laboratory. Thus the panel face external to the tunnel was enclosed in a box which could be evacuated to tunnel static pressure. Automatic equalisation was achieved by connecting the box to the tunnel working section at a point downstream of the experimental panel (see Plate 3.6). Final equalisation was carried out through the small radial holes, shown in Figure 3.4, in the plug carrying the panel. Unfortunately, this system created acoustic disturbances in the equalising system and the tunnel, which resulted in spurious vibration of the panels (Bull, Wilby and Blackman (1963)). Therefore an alternative system was adopted in which the small holes in the plug were sealed and the box was evacuated

by a vacuum pump. Because of air leakage through the adjustable carrier for the capacitance probe it was necessary to run the pump in a throttled condition whilst the panel vibration measurements were being made. To reduce the effects of a fluctuating airflow and pump noise, a large, baffled reservoir, with a volume approximately 450 times greater than that of the box, was connected between the box and the pump.

The pressure equalising box is shown, mounted on the plug, in Plate 3.7. The lid was attached to the box by two clamping strips, with a rubber sealing gasket between the box and the lid. A small pressure tapping hole was inserted in the lid, which also contained a large hole for the probe holder. A rubber 'O' ring formed the seal around the probe holder and the only air leak occurred along the screw threads for the probe adjustment. This leak was very difficult to seal completely because of the necessity for final adjustments to the distance between the probe and panel surface when the tunnel was operating. The detailed arrangement of the box and panel is shown in Figure 3.11, the internal dimensions of the box being 5.0 in x 3.5 in x 2.12 in, where the last dimension includes the rubber seals. The effective volume inside the box is increased by the addition of the volume of the rectangular hole in the carrier plug.

The complete pressure equalising system is shown in diagrammatic form in Figure 3.12. The box was connected to the reservoir by a flexible pipe of 1-inch diameter (internal) and 170 inches in length, with a control tap at a distance of 50 inches from the box. The reservoir was connected to the pump by a short length of flexible pipe. When panel vibration measurements were made in the boundary layer tunnel, the box was evacuated to approximately the tunnel operating static pressure, the box pressure being indicated on a large (7 feet) water manometer. When the tunnel airflow was turned on, the small manometer was opened and the pump controls adjusted until there was a zero pressure differential between the box and the tunnel. This method was sufficiently sensitive for equalisation to be achieved to within  $\pm 0.2$  inch of water in the short time available for adjustment.

### 3.7 Background Vibration and Equipment Noise

The side panels of the boundary layer wind tunnel and the traverse gear carrying the measuring probe were constructed so that the background vibration arising from relative movement between the probe and tunnel side plates would be a minimum. In spite of the precautions there was some relative movement which was measured by replacing the experiment panel with a 1.138 inches thick steel plug. The background vibration signal was recorded and analysed in the way described for panel vibration measurements. The recorded signals contained also contributions arising from electronic noise in the measuring equipment. For example, it was found that in certain acoustically noisy surroundings the Wayne Kerr vibration meters were subject to microphony. The positioning of the meters was restricted by the 10 feet length of low capacitance cable connecting the measuring probe to the meters. Thus it was often difficult to distinguish between background vibration and instrument noise.

Background noise spectra, containing background vibration and equipment noise contributions, are shown in Figures 3.13 and 3.14 for boundary layer and siren excitation. The probe calibration curve was used to convert the signal voltage into an "equivalent displacement"  $G_E(f)$  to give convenient comparison with the vibration spectra measured for the experimental panels. When the spectra in Figures 3.13 and 5.12 are compared, it is seen that the background signal can be neglected except at certain frequencies where a high peak in the noise spectrum coincides with a trough in the panel vibration spectrum. The background vibration spectra show little variation with position of the traverse gear along the tunnel working section and with tunnel airflow velocity, so that the most critical ratios of vibration signal to background noise occurred at the lower speed and the thinnest boundary layer. Even for these conditions the panel vibration spectra were affected only at certain frequencies where the panel vibration was a minimum, and corrections could be applied to the measurements.

Figure 3.13 compares background spectra measured in the absence, and in the presence, of boundary layer wind tunnel airflow. In both cases the vacuum pump was running in the condition used in panel vibration measurements.

It is seen that there is an increase in background spectrum level when the tunnel is running with large increases occurring at certain frequencies. These peaks could be due to mechanical resonances in the traverse gear or to microphonic resonances in the measuring circuitry. When the tunnel was in operation the background spectrum showed little change when the pump was switched off. The effect of the vacuum pump on the vibration of the experimental panels was checked in the absence of the airflow and was found to cause no significant vibration.

Measurements in the siren tunnel showed that the background signal was greater than that observed in the boundary layer wind tunnel, the corresponding spectra being compared in Figure 3.14. The increase could be attributed to the less rigid mounting of the boundary layer tunnel side plate, the siren tunnel not being designed to the same vibration free criteria as had been employed in the boundary layer wind tunnel, and to increases in traverse gear vibration and instrument microphony due to the increased noise level in the acoustic environment. However, the background equipment noise spectrum had a negligible effect on the panel vibration spectra in the frequency range of interest.



## CHAPTER 4

### Panel Damping

#### 4.1 Introduction

The prediction of panel response to random excitation, and the estimation of resolution loss corrections for measured response spectra, require a knowledge of the panel modal damping for the conditions of interest. Thus, in the present investigation, the effects of several parameters on panel damping have to be measured. For zero airflow, changes in modal damping due to the presence of the pressure equalising system and the tunnel working section have to be studied. The effect of airflow in the boundary layer and siren tunnels has to be measured also.

The zero and non-zero airflow conditions require different approaches to what are essentially the same methods of damping measurement. For zero airflow discrete frequency excitation was used, with possible methods of damping measurement being provided by the oscillation decay curve, the amplitude response curve, or the amplitude-phase response curve. The presence of the airflow requires the use of random excitation techniques, but the associated methods of response autocorrelation decay, power spectral analysis, and excitation-response cross power spectral analysis are basically similar to the above methods for discrete frequency excitation. The discrete frequency approach is well established, the advantages and disadvantages of the different experimental methods having been discussed in detail by Mead (1959) and Bishop and Gladwell (1963). Therefore only a brief outline is necessary. Random techniques have not been used widely and they will be discussed in greater detail.

The damping of the panel modes will be a combination of structural (hysteretic) and acoustic (viscous) damping where, by definition, a hysteretic damping force is proportional to displacement and in counterphase with velocity, and a viscous damping force is proportional to and in counterphase with velocity.

Measurements have shown that the damping of the panels is small, so that it can be represented adequately in most cases by considering it to be completely hysteretic or completely viscous. Thus it was not considered necessary to measure the relative magnitudes of the two forms of damping present in the panels. In general, the acoustic radiation will be smaller in the anti-symmetric modes than in the symmetric modes and will be of most importance in the lower order modes, particularly in the fundamental. When the pressure equalising box is placed over one face of the panel, the reverberant conditions in the box will reduce the acoustic damping, and this could be further reduced by the presence of the boundary layer tunnel working section where absorption is provided only by the open ends of the tunnel. Hence it was assumed that, under the experimental conditions, the panel damping was mainly hysteretic in nature. This assumption causes no problems for harmonically varying loads but difficulties arise in random excitation. These will be discussed in section 4.4. The term "loss factor" will be used for the hysteretic damping factor, to distinguish it from the viscous damping ratio or factor.

#### 4.2 Discrete Frequency Excitation Methods

##### 4.2.1 Amplitude-Phase Response Curve

Theoretically, the most suitable discrete frequency method for the panels is the amplitude-phase response curve. The method takes into account the amplitude and phase of the vibration and is basically more accurate than the direct amplitude methods. However, for reasons which will be discussed later, the method was found to be unsuitable for certain experimental conditions.

The use of the response amplitude-phase curve for the estimation of modal damping was developed by Kennedy and Pancu (1947) and the method has been applied to a wide variety of problems. The method has several advantages over direct amplitude methods and permits estimates of modal damping to be made when there are large off-resonant vibration amplitudes, and when two modes have close natural frequencies, provided that the damping is not too large.

For a single-degree of freedom system, when the hysteretic damping is expressed in terms of the complex stiffness, the equation of motion is

$$M_r \ddot{w} + K_r(1 + i v_r)w = F_p e^{i\omega t} \quad \dots (4.1)$$

for simple harmonic excitation, where  $v_r$  is the loss factor and  $M_r$ ,  $K_r$  are the modal mass and stiffness respectively.

Assuming a solution of the form  $w = \bar{w} e^{i\omega t}$ , then the displacement for unit force amplitude is

$$\frac{\bar{w}}{F_p} = \frac{1}{(K_r - M_r \omega^2) + i K_r v_r} = \frac{1}{M_r ((\omega_r^2 - \omega^2) + i v_r \omega_r^2)} = H_r(\omega) \quad \dots (4.2)$$

Thus the locus of  $\frac{\bar{w}}{F_p}$  in the Argand plane is a circle (this is only approximately true for viscous damping). For a multidegree of freedom system the amplitude-phase curve will be modified by off-resonant vibration and Kennedy and Pancu assume that the off-resonant contribution is constant in amplitude and phase in the neighbourhood of the natural frequency. The errors imposed by the assumption are smallest when the resonant loop in the response curve corresponds most closely to a circle, and the errors increase as the loop departs from a circular shape. It is assumed also that there is no modal coupling due to damping.

Kennedy and Pancu showed that, when the response curve of equation (4.2) is drawn, the natural frequency  $\omega_r$  is located at the point where the rate of change of arc length with frequency, or more accurately with  $(\text{frequency})^2$ , has a local maximum. The procedure for finding the modal damping is as follows. The natural frequency  $\omega_r$  is located as indicated above and the best circle is fitted to the experimental curve in the neighbourhood of  $\omega_r$ . A diameter drawn from the natural frequency will cut the circle at a second point which is the "displaced origin" for the mode. The vector associated with this point corresponds to the off-resonant vibration. Using the

displaced origin as a datum, the frequencies  $\omega_1$  and  $\omega_2$  ( $\omega_2 > \omega_1$ ) of the half-power points on the resonance circle can be located by geometrical construction, the half-power points being defined by

$$|w|^2 = \frac{|w_r|^2}{2}$$

where the amplitudes are measured from the displaced origin and  $|w_r|$  is the amplitude at  $\omega = \omega_r$ . The hysteretic loss factor is

$$\begin{aligned} v_r &= \frac{\omega_2^2 - \omega_1^2}{2\omega_r^2} \\ &\approx \frac{\omega_2 - \omega_1}{\omega_r} = \frac{\Delta\omega}{\omega_r} \text{ for small damping} \dots (4.3) \end{aligned}$$

When it is not possible to locate the half-power frequencies on the circle, as is often the case when modes are close together, or when the damping is high, the loss factor can be estimated from alternative formulae which apply to the frequency range close to the natural frequency.

#### 4.2.2 Amplitude Response Curve

The modal damping can be obtained directly from the amplitude response curve only in the case of a single degree of freedom system. For a multi-degree of freedom system, corrections have to be applied because of the off-resonant vibration in the other modes of the system. The loss factor is estimated from the frequency width of the resonant peak, and when this is measured at the half power points the loss factor  $v_r$  is again given by equation (4.3).

In a multi-degree of freedom system the amplitude of vibration in the neighbourhood of a natural frequency will include contributions from the off-resonant vibration of the other modes of the system.

Assume, as previously, that there is no modal coupling due to damping, and that there is a single damping factor associated with each mode. Further, assume that the effect of the off-resonant vibration on the amplitude of the response curve, in the neighbourhood of the resonance, is constant. Then

the amplitude of vibration, corresponding to equation (4.2) will be

$$|w'| = \frac{F_p}{M_r((\omega_r^2 - \omega^2)^2 + v_r^2 \omega_r^4)^{\frac{1}{2}}} + \chi \quad \dots (4.4)$$

where the dash denotes the "measured value" and where  $\chi$  is the contribution from the off-resonant vibration and is assumed to be constant. The assumption that  $\chi$  is constant will never be fully satisfied because it implies that the off-resonant vibration undergoes the same phase changes as the resonant vibration, an assumption which is not true. The validity of the assumption can be estimated from an inspection of the asymmetry of the measured peak.

Assuming the constant effect of the off-resonant vibration, Gladwell (1962) has obtained a revised loss factor. The method of calculating the revised value requires the location of the point of inflexion in the response curve, and the accuracy of estimation of the loss factor depends critically on the accuracy with which the curve can be drawn. If damping is small, the amplitude response curve has steep sides and cannot be plotted to a high degree of accuracy. Large errors can arise in the value of the revised loss factor. When the refined estimate was used in the experimental investigation there was a large scatter in the results. Thus an alternative method was used which reduced the scatter and was simpler to apply.

From equations (4.2) and (4.4), with  $\chi = \text{constant}$ ,

$$|w'| = |w| + \chi \quad \dots (4.5)$$

Expressing  $\chi$  in terms of the single degree of freedom resonant peak  $|w_r|$ , let

$$\chi = \epsilon |w_r| \quad \dots (4.6)$$

then  $|w'| = |w| + \epsilon |w_r|$

At the true half-power point  $|w| = \frac{|w_r|}{\sqrt{2}}$

and the measured amplitude will be

$$|w_1'| = |w_r| \left( \frac{1}{\sqrt{2}} + \epsilon \right) \quad \dots (4.7)$$

At the resonant frequency, the measured amplitude will be

$$|w_r'| = |w_r| (1 + \epsilon) \quad \dots (4.8)$$

From equations (4.7) and (4.8), the square of the measured amplitude is

$$|w_1'|^2 = \frac{(1 + \sqrt{2\epsilon})^2}{(1 + \epsilon)^2} \frac{|w_r'|^2}{2} \quad \dots (4.9)$$

Thus, instead of estimating the damping from the frequency bandwidth of the peak at

$$|w_1'|^2 = \frac{|w_r'|^2}{2} \quad \dots (4.10)$$

as is the case for a single-degree of freedom system, a revised estimate can be made from the bandwidth of the peak where the vibration amplitude is obtained from equation (4.9). The value of the correction term  $\left(\frac{1 + \sqrt{2\epsilon}}{1 + \epsilon}\right)^2$  is shown in Figure 4.1 as a function of  $\epsilon$ . The method of correction has the disadvantage that an estimate of the value of  $\epsilon$  has to be made first. This is often difficult in practice.

The method suffers from several practical disadvantages. The off-resonant vibration must be reduced to a minimum by suitable positioning of the exciter and probe. Also, in the case of small damping, the steep sides of the resonant peaks are difficult to measure accurately and a high degree of frequency stability is required for the exciting force.

### 4.3 Damping Measurements using Discrete Frequency Excitation

#### 4.3.1 Choice of Method

Two alternative methods have been proposed in Section 4.2 for the discrete frequency measurement of modal damping, the amplitude-phase response method being more accurate, in theory, than the amplitude response method. In practice it has been found that the amplitude response curve gave the more reliable results because there was an apparent instability of the resonant frequencies of the panels (see Bull, Wilby and Blackman (1963)). This instability may have been due partly to small irregularities in the frequency

of excitation but, from observation of the phenomenon in other circumstances, it was probably associated with slight temperature changes in the material of the panel. The temperature changes could be caused by the panel motion, eddy currents, or changes in local ambient temperature. The frequency changes were small when compared with the natural frequency (less than  $0.5\% f_r$ ), but could be of a similar order of magnitude to the frequency bandwidths of the resonant peaks. Thus, for a nominally constant input frequency, the response vector at frequencies very close to the natural frequency would drift over a large part of the resonance circle. It was difficult to correct for this instability in the amplitude-phase curves, and estimates of the damping showed large deviations from the mean. The amplitude response method had the advantage that frequency drift was immediately obvious and the associated damping measurements could be rejected. Thus the amplitude response method was often used in preference to the amplitude-phase method, although the latter was used in the siren tunnel measurements when the airflow was present but there was no activation of the speaker coil in the siren.

#### 4.3.2 Measuring Equipment

The panels, being of magnetic material, could be excited electromagnetically. The electromagnet was constructed with a 0.5 inch diameter permanent magnetic core which biased the magnetic field and minimised the possibility of panel vibration at twice the excitation frequency. The electromagnet was activated by a Muirhead-Wigan Decade Oscillator (Figure 4.2) which permitted the excitation frequency to be changed in 1 c.p.s. increments. The panel vibration was measured using the Wayne-Kerr Capacitance probe C and was monitored on an oscilloscope to ensure that the motion was linear. The square of the vibration amplitude was recorded automatically on a Moseley X-Y Recorder at a sweep rate of 0.1 inch/second. The frequency range in the neighbourhood of a resonance frequency was scanned manually at a rate of approximately one frequency increment per second, alternate sweeps being in the directions of frequency increasing and frequency decreasing. When applying the amplitude-phase response method the X-Y Recorder was replaced by a Solartron Resolved Components Indicator. The locations of

the exciter and probe on the panel surface were chosen to give optimum values for the resonant to off-resonant vibration ratio, and were on opposite panel faces. In general the gap between the panel surface and the end face of the magnetic core of the exciter was 0.625 inch. For smaller gaps the permanent magnetic field produced small increases in the panel natural frequencies and at larger distances considerable increases in the supply power to the electromagnet were required. At the high natural frequencies it was necessary to reduce the panel-exciter gap, but measurements showed that within the limits used, 0.25 to 0.625 inch, the size of the gap did not affect the measured damping.

The panel damping was measured under free space conditions by mounting the panel in a tunnel side-plate which was suspended from a gantry in the laboratory (Plate 4.1). The effect of the presence of the pressure equalising system was measured by repeating the free space measurements when the pressure equalising box, with the reservoir tank connected, was attached to the carrier plug. Further measurements under zero airflow conditions were carried out when the panels were mounted in the boundary layer and siren tunnels, the exciter being mounted inside each tunnel. This method was also possible in the presence of the airflow in the siren tunnel because the airspeed was very low. The pressure equalising system was not required for the siren tunnel measurements but the box and pipe were fitted to provide conditions similar to those in the boundary layer tunnel, although the reservoir tank was disconnected.

#### 4.3.3 Measured Loss Factors

Mean values of the measured loss factors are shown in Table 4.1 for three conditions, viz. both faces free, one face free and one enclosed by the pressure equalising box, and one face in the boundary layer tunnel and one enclosed by the box. The values are in the uncorrected form obtained from the frequency bandwidth of the amplitude response curve at the measured half power point (equation (4.10)). Results marked with an asterisk were obtained from response curves which had a high degree of skewness and the results have a reduced accuracy. In certain cases the skewness was so large that no reliable damping estimate could be made, and



the results are omitted. The measurements show that the damping is small, with loss factors in the range  $0.0017 \leq \nu_r \leq 0.012$ .

The error in the above loss factors, caused by the presence of off-resonant vibration, was estimated using the method described in Section 4.2.2. The magnitude of the off-resonant contribution was estimated by measuring the panel vibration at frequencies away from the resonant peaks. It was assumed that the off-resonant vibration in the mode considered, and the off-resonant vibration of the interfering modes were equal in amplitude but differed in phase. Thus it was assumed that, if the measured amplitude at the off-resonant frequency was  $\chi_m$ , then the amplitude contribution from the interfering modes was  $\frac{\chi_m}{\sqrt{2}}$ . The vibration amplitude was measured on each side of the resonant peak and the mean value  $\bar{\chi}_m$  taken. Then  $\frac{\bar{\chi}_m}{\sqrt{2}} = \bar{\chi}$

Based on this procedure, corrections to the measured loss factor are shown in Table 4.1. For many of the modes, the estimated loss factor corrections are less than 10% but they are much larger in certain cases. In the complex Argand plane it can be shown that the above simple theory will overestimate the required corrections, so that the values shown in Table 4.1 will be upper limits for the errors in the measurements.

For each mode, the frequency sweep was repeated several times and, after rejecting unreliable plots where frequency drift had occurred, the mean values of the loss factors (shown in Table 4.1) were obtained. It was found that the measured values were generally within  $\pm 10\%$  of the mean values. During the measurements the excitation force was controlled so that the maximum vibration amplitude of the panel did not exceed  $2 \times 10^{-3}$  inch. This limit exceeded the vibration amplitudes encountered in the boundary layer and siren tunnel measurements, and within the limit the vibration remained linear and the damping remained constant. However, it was observed that there was a reduction in the frequency stability of the high amplitude vibration, which supported the suggestion that the instability was due to small temperature changes in the panel, induced by the panel motion.

The results in Table 4.1 show no general variation of damping with

panel environment. The most important changes are observed in the (1-1) order modes which show decreases in damping when one or both panel faces are enclosed. These modes, where the panel motion is everywhere in phase, are the modes which are most likely to be affected when one face of the panel is enclosed in a cavity, because there is maximum volume displacement of the air adjacent to the panel. The presence of the cavity will affect the free field noise radiation and, when this is reduced, there will be a corresponding reduction in the acoustic contribution to the total modal damping. The (1-1) mode of the 4 in x 2.75 in panel was particularly sensitive to the presence of the pressure equalising system, and the measured damping varied appreciably when the components of the system were changed. The magnitudes of the variations were shown in Table 4.2. In all damping measurements this mode was found to depend on the environment more critically than did any other mode. From the results in Table 4.2 it is apparent that the variations in damping coefficient are caused by a resonant condition in the pressure equalising system as a whole rather than in the box alone.

In general, the higher order modes show no significant variation with the surrounding conditions, the exceptions showing a slight reduction in damping due to the presence of the pressure equalising system. The effect of the boundary layer tunnel is small because the tunnel enclosure is much less restrictive on acoustic radiation than is the pressure equalising system. Bozich (1965) has estimated the radiation damping for panels mounted in a duct. He assumed that the generalised motion of the panel could be replaced by the equivalent motion of a rigid piston in a baffle, and the results showed that there was a significant change in radiation damping when the panel area was larger than the duct cross-sectional area. The change was restricted to the fundamental modes, the effect on the higher modes being negligible. The assumed representation of the panel motion may not be very accurate for the higher modes but should be satisfactory for the fundamental modes. In the present investigation the ratio of panel area to duct cross-sectional area did not exceed 0.34, so the presence of the duct would be expected to have a negligible effect.

Table 4.1

Mean Measured Loss Factors for Zero Airflow

3.5in x 3.5in x 0.015in Panel

Face I	Wind Tunnel	Free	Free	Wind Tunnel	Free	Free
Face II	Box	Box	Free	Box	Box	Free
Mode	Uncorrected Loss Factor			Correction <sup>+</sup> from Section 4.2.2		
1-1	0.00968	0.00592	0.01025	- 7	- 5	- 16
1-2	0.00281	0.00301	0.00259	- 7	- 5	- 8
2-1	0.00251	0.00277	0.00262	- 9	- 8	- 9
2-2	0.00213	0.00218	0.00213	- 12	- 9	- 9
1-3	0.00237	0.00247	-	- 10	- 13	-
3-1	0.00335	0.00335	0.00529*	- 7	- 13	- 10
2-3	0.00252	0.00185*	0.00211*	- 7	- 6	- 14
3-2	0.00172	0.00211	0.00196	- 10	- 13	- 19
3-3	0.00200	0.00250	-	- 17	- 23	-
4-1	0.00248	-	-	- 12	-	-

+ Correction expressed as a percentage change.

\* Results from response curves with a high degree of skewness.

Table 4.1 (cont'd)

Panels: 4.0in x 2.75in x 0.015in ; 4.0in x 2.0in x 0.015in.

Face I	Wind Tunnel	Free	Free	Wind Tunnel	Free	Free
Face II	Box	Box	Free	Box	Box	Free
Mode	Uncorrected Loss Factor			Correction <sup>+</sup> from Section 4.2.2		
<u>Panel: 4.0in x 2.75in x 0.015in.</u>						
1-1	0.00431	0.00709	0.01066	- 4	- 7	- 10
1-2	0.00292	0.00320*	0.00421	- 5	- 17	- 13
2-1	0.00338	0.00328	0.00360	- 7	- 7	- 7
2-2	0.00218	0.00213*	0.00259*	- 11	- 12	- 10
1-3	0.00269	0.00641	0.00530	- 12	- 36	- 28
3-1	0.00312	0.00385	0.00766	- 4	- 10	- 18
2-3	0.00248	0.00323	0.00480	- 12	- 31	- 37
3-2	0.00208	0.00310*	0.00358*	- 10	- 17	- 25
4-1	0.00330	0.00297*	0.00362	- 9	- 29	- 13
4-2	0.00248	0.00256	0.00261*	- 12	- 21	- 17
<u>Panel: 4.0in x 2.0in x 0.015in.</u>						
1-1	0.00813	0.00913	0.01203	- 8	- 11	- 12
1-2	-	0.00945	0.01060	-	- 18	- 18
2-1	0.00904	0.00851	0.00593	- 16	- 16	- 12
2-2	0.00492	0.00483	0.00518	- 23	- 27	- 27
3-1	0.00418	0.00411	0.00636	- 8	- 15	- 14
3-2	-	0.00419	0.00457	-	- 24	- 25
4-1	0.00421	0.00422	0.00627	- 7	- 13	- 19
5-1	0.00235	0.00274	0.00331	- 13	- 22	- 20

Table 4.2

Effect of Pressure Equalising System on  
4.0in x 2.75in x 0.015in.

Components of System attached to Panel*	Damping Loss Factor $\nu_{\alpha}$
Pressure equalising box alone	0.00447
Box + 55.5in pipe with tap open	0.00982
Box + 55.5in pipe with tap closed at end of pipe	0.00710
Box + 55.5in pipe with tap open + 116in pipe	0.00710
Box + full system	0.00413

\*second face of panel free to atmosphere

Under similar conditions, but with an incomplete pressure equalising system (Section 4.3.2), damping measurements were made in the siren tunnel. The measured values, shown in Table 4.3, are similar to those in Table 4.1 when one face was free. Also, loss factors were measured in the siren tunnel in the presence of the airflow. The airflow was extremely small and it was anticipated that there would be no significant changes in the damping. The results in Table 4.3 show that, except for the (1-1) mode of the 4 in x 2.75 in panel, the assumption was justified within the experimental accuracy. In the absence of airflow the loss factors were measured with an experimental scatter of less than  $\pm 12\%$ , but in the presence of the airflow the experimental scatter increased to  $\pm 25\%$ .

#### 4.4 Random Excitation Methods

##### 4.4.1 General Problem

When an airflow is introduced over one surface of a panel, random vibration is induced which masks any discrete frequency excitation, except when the airflow is very small, as in the siren tunnel. In the presence of random vibration, the estimation of panel damping using discrete frequency methods is not possible, but the damping can be measured if random excitation techniques are applied to methods which are similar to those used for discrete frequency excitation. Additional factors have to be considered when the random excitation has a spatial distribution over the structural surface.

The assumption has been made in Section 4.1 that the damping in the panel modes is mainly hysteretic and this caused no problems in the analysis of the discrete frequency methods where the excitation was harmonic. However, the concept of hysteretic damping is valid, strictly, only for harmonically varying loads and care has to be exercised in conditions of random excitation.

One of the basic properties of random analysis is the equivalence of the time and frequency domains and the ability to transform from one to the other by means of the Fourier transformation. When the analysis is applied to structural vibrations it is assumed that the complex response function or

Table 4.3

Mean Loss Factors Measured in the Siren Tunnel

Panel Condition	5.5in x 3.5in		4.0in x 2.75in		4.0in x 2.0in	
	Without Air	With Air	Without Air	With Air	Without Air	With Air
Mode: 1-1	0.00477	0.00591	0.00983	0.01429	0.00819	0.00845
1-2	0.00249	0.00269	0.00516	0.00476	0.00912	0.00946
2-1	0.00248	0.00308	0.00532	0.00541	0.00990	0.00859
2-2	0.00202	0.00177	0.00438	0.00483	0.00435	0.00386
1-3	0.00320	0.00317	0.00651	0.00645	-	-
3-1	0.00331	0.00326	0.00557	0.00575	0.00401	0.00459
2-3	0.00169	0.00186	0.00456	0.00437	-	-
3-2	0.00169	0.00186	0.00441	0.00342	0.00368	0.00373
3-3	0.00203	0.00193	-	-	-	-
1-4	0.00367	0.00367	-	-	-	-
4-1	0.00221	0.00210	0.00394	0.00459	0.00381	0.00358
4-2	-	-	0.00311	0.00329	-	-
5-1	-	-	0.00517	0.00608	-	-

Note: One face of panel is covered by pressure equalising box.

receptance  $H_a(\omega)$  and its Fourier transform, the real impulse function  $h_a(\tau)$ , exist and have valid forms. The difficulties associated with hysteretic damping, for which the impulse response function is not clearly defined, can be illustrated by the Fourier transform pair  $H_a(\omega)$  and  $h_a(\tau)$ .

For viscous damping the equation of motion can be written, as in equation (2.3),

$$M_a \ddot{q}_a(t) + C_a \dot{q}_a(t) + K_a q_a(t) = L_a(t)$$

and the receptance is  $H_a(\omega) = \frac{1}{Y_a(\omega)} = \frac{1}{M_a((\omega_a^2 - \omega^2) + 2i\delta_a \omega \omega_a)}$

where  $\omega_a = \sqrt{\frac{K_a}{M_a}}$  and  $\delta_a = \frac{C_a}{2\sqrt{M_a K_a}}$

The Fourier transform of  $H_a(\omega)$  is

$$h_a(t) = \frac{1}{2\pi} \int_{-\infty}^{\infty} H_a(\omega) e^{-i\omega t} d\omega \quad \dots (4.11)$$

$$= \frac{e^{-\delta_a \omega_a t}}{M_a \omega_a \sqrt{1 - \delta_a^2}} \sin(\omega_a t \sqrt{1 - \delta_a^2})$$

which satisfies the conditions for a real impulse function.

However, for hysteretic damping the Lagrange equation can be written in terms of a complex stiffness,  $M_a \ddot{q}_a(t) + K_a(1 + i\nu_a)q_a(t) = L_a(t)$  and the receptance is

$$H_a(\omega) = \frac{1}{M_a((\omega_a^2 - \omega^2) + i\nu_a \omega \omega_a^2)}$$

The Fourier transform of  $H_a(\omega)$  is now

$$h_a(t) = \frac{e^{-i\omega_a \sqrt{1 + i\nu_a} t}}{2iM_a \omega_a \sqrt{1 + i\nu_a}}$$

which is complex and does not satisfy the conditions of an impulse function.

To overcome this problem in random analysis it is suggested that the hysteretic damping is expressed in terms of an effective viscous damper by



writing the Lagrange equation in the form

$$M_{\alpha} \ddot{q}_{\alpha}(t) + C_{ae} \dot{q}_{\alpha}(t) + K_{\alpha} q_{\alpha}(t) = L_{\alpha}(t)$$

where  $C_{ae} = \frac{K_{\alpha} v_{\alpha}}{\omega}$  is the effective viscous damping. The analysis is then performed in terms of viscous damping and the hysteretic damping reinstated in the final equation when  $C_{ae}$  is replaced by  $\frac{K_{\alpha} v_{\alpha}}{\omega_{\alpha}}$  i.e.  $\delta_{\alpha}$  is replaced by  $\frac{v_{\alpha}}{2}$ .

Three methods are proposed in the following sections for the measurement of modal damping. The methods concern the use of the response power spectrum, the excitation-response cross power spectrum and the response autocorrelation function respectively, but, for practical reasons, only the autocorrelation method was employed finally.

#### 4.4.2 Power Spectrum Analysis Method

The random vibration of a structure can be analysed to obtain the displacement power spectrum, which will contain a series of resonance peaks similar to those obtained from discrete frequency excitation sweeps. Damping estimates can be made from measurements of the frequency bandwidths of the resonance peaks, in the same manner as that described for the amplitude response curve method (Section 4.2.2). However, in addition to the errors occurring in the discrete frequency case, further errors will arise if the analysing filters do not possess bandwidths which are smaller than the resonant peak bandwidths. It has been shown by Forlifer (1964) that ideally the bandwidths of the peaks should be at least four times larger than the filter bandwidths, (see also Appendix C).

For single point random excitation, with spectral density  $S_p(\omega)$ , the displacement spectral density at point  $\underline{x}$  is given by

$$S_d(\omega) = \int |H_{\alpha}(\omega)|^2 S_p(\omega) \psi_{\alpha}^2(\underline{x}) \quad \dots (4.12)$$

and, for constant input spectral density, the response is directly proportional to  $|H_{\alpha}(\omega)|^2$ . When the excitation force has a spatial distribution over the structure, the displacement power spectrum has the

modified form given by

$$S_d(\omega) = \sum_{\alpha} \sum_{\beta} \psi_{\alpha}(\underline{x}) \psi_{\beta}(\underline{x}) H_{\alpha}^*(\omega) H_{\beta}(\omega) \int_A \int_A \psi_{\alpha}(\underline{x}') \psi_{\beta}(\underline{x}'') S_p(\underline{x}', \underline{x}'', \omega) d\underline{x}' d\underline{x}''$$

Thus the resonance peaks in the response spectra will give reliable estimates of the damping only when the cross acceptance terms ( $\alpha \neq \beta$ ) are small, and when the joint acceptance and the excitation cross power spectral density vary only slowly with frequency. These conditions are usually satisfied in lightly damped structures.

#### 4.4.3 Cross Power Spectrum Method

The discrete frequency determination of modal damping from the amplitude-phase curve method has a parallel in random excitation where the damping is estimated from the excitation-response cross power spectrum. As in the discrete frequency case, the method has advantages over other methods in which only the power spectral density function is used.

The cross power spectral density can be measured directly if a suitable pair of matched filters is available, and the resultant experimental errors are directly dependent on the loss of resolution due to the filter bandwidth. Alternatively, the excitation-response cross correlation function can be measured, and the Fourier transform computed to determine the cross power spectral density. Errors will arise due to truncation of the correlation function before transformation, but the magnitude of the truncation error can be estimated theoretically for an ideal system.

The cross correlation function for an excitation  $p(\underline{x}', t)$  at  $\underline{x}'$  and the associated response  $w(\underline{x}'', t)$  at  $\underline{x}''$  is defined as

$$R(p(\underline{x}'), w(\underline{x}''), \tau) = \lim_{T \rightarrow \infty} \frac{1}{2T} \int_{-T}^T p(\underline{x}', t) w(\underline{x}'', t + \tau) dt \quad \dots (4.13)$$

and the cross correlation and spectral density functions are related

$$\begin{aligned} \text{by } S(p(\underline{x}'), w(\underline{x}''), \omega) &= \frac{1}{2\pi} \int_{-\infty}^{\infty} R(p(\underline{x}'), w(\underline{x}''), \tau) e^{-i\omega\tau} d\tau \\ R(p(\underline{x}'), w(\underline{x}''), \tau) &= \int_{-\infty}^{\infty} S(p(\underline{x}'), w(\underline{x}''), \omega) e^{i\omega\tau} d\omega \end{aligned} \quad \dots (4.14)$$

As before, assume that the response can be represented by the summation of a series of normal modes

$$w(\underline{x}, t) = \sum_{\alpha} q_{\alpha}(t) \psi_{\alpha}(\underline{x}) \quad \dots (4.15)$$

and the equation of motion for the  $\alpha^{\text{th}}$  mode is

$$\begin{aligned} M_{\alpha} \ddot{q}_{\alpha} + C_{\alpha} \dot{q}_{\alpha} + K_{\alpha} q_{\alpha} &= L_{\alpha}(t) \\ &= \int_A \psi_{\alpha}(\underline{x}) p(\underline{x}, t) d\underline{x} \end{aligned} \quad \dots (4.16)$$

The solution to equation (4.16) can be written in terms of the impulse response function  $h_{\alpha}(\tau)$

$$\begin{aligned} q_{\alpha}(t) &= \int_{-\infty}^{\infty} L_{\alpha}(t - \tau_1) h_{\alpha}(\tau_1) d\tau_1 \\ &= \int_{-\infty}^{\infty} \int_A \psi_{\alpha}(\underline{x}) p(\underline{x}, t - \tau_1) h_{\alpha}(\tau_1) d\underline{x} d\tau_1 \end{aligned} \quad \dots (4.17)$$

From equations (4.13), (4.14) and (4.17)

$$\begin{aligned} R(p(\underline{x}'), w(\underline{x}''), \tau) &= \sum_{\alpha} \psi_{\alpha}(\underline{x}'') \int_{-\infty}^{\infty} \int_A \psi_{\alpha}(\underline{x}) h_{\alpha}(\tau_1) \\ &\quad \times \lim_{T \rightarrow \infty} \frac{1}{2T} \int_{-T}^T p(\underline{x}', t) p(\underline{x}, t + \tau - \tau_1) dt d\underline{x} d\tau_1 \\ &= \sum_{\alpha} \psi_{\alpha}(\underline{x}'') \int_{-\infty}^{\infty} \int_A \psi_{\alpha}(\underline{x}) h_{\alpha}(\tau_1) R_p(\underline{x}', \underline{x}, \tau - \tau_1) d\underline{x} d\tau_1 \end{aligned} \quad \dots (4.18)$$

Transforming equation (4.18), the cross power spectral density is

$$S(p(\underline{x}'), w(\underline{x}''), \omega) = \sum_{\alpha} \psi_{\alpha}(\underline{x}'') H_{\alpha}(\omega) \int_A \psi_{\alpha}(\underline{x}) S_p(\underline{x}, \underline{x}', \omega) d\underline{x} \quad \dots (4.19)$$

If it is assumed that  $S_p(\underline{x}, \underline{x}', \omega)$  is independent of frequency  $\omega$ , for a frequency range  $\omega_1 \leq \omega \leq \omega_2$ , then within this range

$$S(p(\underline{x}'), w(\underline{x}''), \omega) = \sum_{\alpha} \psi_{\alpha}(\underline{x}'') \Lambda_{\alpha}(\underline{x}') H_{\alpha}(\omega)$$

$$\text{where } \Lambda_{\alpha}(\underline{x}') = \int_A \psi_{\alpha}(\underline{x}) S_p(\underline{x}, \underline{x}', \omega) d\underline{x} \quad \text{for } \omega_1 \leq \omega \leq \omega_2$$

$$\text{Then } S(p(\underline{x}'), w(\underline{x}''), \omega) = \sum_{\alpha} \kappa_{\alpha}(\underline{x}', \underline{x}'') H_{\alpha}(\omega) \quad \text{for } \omega_1 \leq \omega \leq \omega_2 \quad \dots (4.20)$$

$$\text{where } \kappa_{\alpha}(\underline{x}', \underline{x}'') = \psi_{\alpha}(\underline{x}'') \Lambda_{\alpha}(\underline{x}')$$

a result which is similar to equation 4.2 for the discrete frequency amplitude-phase curve method of Kennedy and Pancu.

In practice it is not possible to measure  $R(p(\underline{x}'), w(\underline{x}''), \tau)$  for an infinitely long time delay  $\tau$ , and the function must be measured for a finite range of  $\tau$ ,  $-\tau_1 \leq \tau \leq \tau_2$ . The computed cross power spectrum is then, by analogy with equation (4.14),

$$S'(p(\underline{x}'), w(\underline{x}''), \omega) = \frac{1}{2\pi} \int_{-\infty}^{\infty} D(\tau) R(p(\underline{x}'), w(\underline{x}''), \tau) e^{-i\omega\tau} d\tau \quad \dots (4.21)$$

where  $D(\tau)$  is a weighting function such that

$$D(\tau) = 0 \quad \text{for } \tau < -\tau_1 \quad \text{and } \tau > \tau_2$$

Substituting for  $R(p(\underline{x}'), w(\underline{x}''), \tau)$  in equation (4.21), the measured cross power spectral density can be expressed in terms of the true cross power spectrum,

$$\text{i.e. } S'(p(\underline{x}'), w(\underline{x}''), \omega) = \frac{1}{2\pi} \int_{-\infty}^{\infty} \phi_D(\omega - \omega') S(p(\underline{x}'), w(\underline{x}''), \omega') d\omega' \quad \dots (4.22)$$

$$\text{where } \phi_D(\omega - \omega') = \int_{-\infty}^{\infty} D(\tau) e^{-i(\omega - \omega')\tau} d\tau \quad \dots (4.23)$$

is the "spectral window". The effect of  $\phi_D(\omega - \omega')$  is similar to that of a

filter and produces errors which are equivalent to the filter bandwidth effect in direct cross power spectral analysis. With the assumption of constant excitation spectral density, equation (4.22) gives the modified form of equation (4.20), for single point excitation.

$$S'(p(\underline{x}'), w(\underline{x}''), \omega) = \sum_{\alpha} \kappa_{\alpha}(\underline{x}', \underline{x}'') \frac{1}{2\pi} \int_{-\infty}^{\infty} \phi_D(\omega - \omega') H_{\alpha}(\omega') d\omega' \quad \dots (4.24)$$

There are several well established forms of  $D(\tau)$  which are discussed in detail by Blackman and Tuckey (1958) and the simplest, but the least reliable statistically, is

$$D(\tau) = 1 \quad -\tau_1 \leq \tau \leq \tau_2 \quad \dots (4.25)$$

Using the form of  $D(\tau)$  given by equation (4.25), and the form of  $H_{\alpha}(\omega)$  applicable to viscous damping, Clarkson and Mercer (1965) have shown that the truncation of the cross correlation function distorts the circular response curve in the Argand plane. They have computed a series of corrections by which the true damping can be estimated from measured values of the radius of curvature  $\rho_l$  of the response curve, and the rate of change of arc length  $l$  with frequency at the natural frequency of the mode. For small values of the viscous damping coefficient and for practical time delays the corrections are very sensitive to changes in the parameter  $\frac{1}{\rho_l} \frac{dl}{df}$ .

#### 4.4.4 Response Autocorrelation Method

The response autocorrelation method is similar to the response decay method for discrete frequency excitation and suffers from the same disadvantages. For a single-degree of freedom system the exponential decay rate of the autocorrelation function is proportional to the damping ratio, but the correlation function for one mode of a multi-degree of freedom system is distorted by vibration in the other modes. Thus only in special cases can the equivalent single-degree of freedom decay rate be measured.

It has been shown in equation (2.13) that, under certain specified conditions, the response autocorrelation function is

$$R_d(\tau) = \sum_{\alpha} \sum_{\beta} \psi_{\alpha}(\underline{x}) \psi_{\beta}(\underline{x}) \int_A \int_A \psi_{\alpha}(\underline{x}') \psi_{\beta}(\underline{x}'') \\ \times \int_{-\infty}^{\infty} \int_{-\infty}^{\infty} h_{\alpha}(\tau_1) h_{\beta}(\tau_2) R_p(\underline{x}', \underline{x}'', \tau + \tau_1 - \tau_2) d\tau_1 d\tau_2 d\underline{x}' d\underline{x}'' \quad \dots (4.26)$$

From physical reasons  $R_p(\underline{x}', \underline{x}'', \tau)$  and  $h_{\alpha}(\tau)$  are real functions and, therefore, each term in the summation series is real. Alternatively the response autocorrelation function can be expressed in terms of the excitation cross-power spectral density

$$R_d(\tau) = \sum_{\alpha} \sum_{\beta} \psi_{\alpha}(\underline{x}) \psi_{\beta}(\underline{x}) \int_A \int_A \psi_{\beta}(\underline{x}') \psi_{\alpha}(\underline{x}'') \\ \int_{-\infty}^{\infty} H_{\beta}^*(\omega) H_{\alpha}(\omega) S_p(\underline{x}', \underline{x}'', \omega) e^{i\omega\tau} d\omega d\underline{x}' d\underline{x}'' \quad \dots (4.27)$$

where, comparing with equation (4.26), each pair of terms  $(\alpha, \beta)$  and  $(\beta, \alpha)$  must have a real sum.

Consider the integral

$$I'_{\alpha\beta}(\underline{x}', \underline{x}'') = \int_{-\infty}^{\infty} H_{\beta}^*(\omega) H_{\alpha}(\omega) S_p(\underline{x}', \underline{x}'', \omega) e^{i\omega\tau} d\omega \quad \dots (4.28)$$

For viscous damping it has been shown that

$$H_{\alpha}(\omega) = \frac{1}{M_{\alpha}((\omega_{\alpha}^2 - \omega^2) + 2i\delta_{\alpha}\omega\omega_{\alpha})} \quad \dots (4.29)$$

with poles at  $\omega = \pm\omega_{\alpha} \sqrt{1 - \delta_{\alpha}^2} + i\delta_{\alpha}\omega_{\alpha}$

Equation (4.28) can be evaluated by contour integration in the upper half of the complex frequency plane, provided that  $S_p(\underline{x}', \underline{x}'', \omega)$  is of order less than  $\omega^3$ , with the result

$$I'_{\alpha\beta}(\underline{x}', \underline{x}'') = \frac{2\pi e^{-\delta_{\alpha}\omega_{\alpha}\tau}}{M_{\alpha}M_{\beta}\omega_{\alpha}\sqrt{1-\delta_{\alpha}^2}} \frac{1}{D_{\alpha\beta}^* D_{\alpha\beta}^*} \{ S_{\alpha}^r (D_{\alpha\beta}^i \cos(\omega_{\alpha}\tau\sqrt{1-\delta_{\alpha}^2}) - D_{\alpha\beta}^r \sin(\omega_{\alpha}\tau\sqrt{1-\delta_{\alpha}^2})) \\ + S_{\alpha}^i (D_{\alpha\beta}^i \sin(\omega_{\alpha}\tau\sqrt{1-\delta_{\alpha}^2}) + D_{\alpha\beta}^r \cos(\omega_{\alpha}\tau\sqrt{1-\delta_{\alpha}^2})) \} \quad \dots (4.30)$$

where

$$\begin{aligned}
 S_p(\underline{x}', \underline{x}'', (1-\delta_\alpha^2 + i\delta_\alpha)\omega_\alpha) &= S_\alpha^r(\underline{x}', \underline{x}'', (1-\delta_\alpha^2 + i\delta_\alpha)\omega_\alpha) - iS_\alpha^i(\underline{x}', \underline{x}'', (1-\delta_\alpha^2 + i\delta_\alpha)\omega_\alpha) \\
 &= C_p(\underline{x}', \underline{x}'', \omega_\alpha) - iQ_p(\underline{x}', \underline{x}'', \omega_\alpha) \text{ for small damping} \\
 &= S_p(\underline{x}', \underline{x}'', \omega_\alpha) \quad \omega_\alpha \delta_\alpha \ll 1 \quad \dots (4.31)
 \end{aligned}$$

which is the excitation cross power spectral density at  $\omega = \omega_\alpha$

$$\begin{aligned}
 D_{\alpha\beta} &= D_{\alpha\beta}^r + iD_{\alpha\beta}^i \\
 &= (\omega_\alpha^2 - \omega_\beta^2) - 2\omega_\alpha \delta_\alpha (\omega_\alpha \delta_\alpha + \omega_\beta \delta_\beta) + 2i\omega_\alpha (1-\delta_\alpha^2) (\omega_\alpha \delta_\alpha + \omega_\beta \delta_\beta) \\
 &= (\omega_\alpha^2 - \omega_\beta^2) - 2\omega_\alpha \delta_\alpha (\omega_\alpha \delta_\alpha + \omega_\beta \delta_\beta) + 2i\omega_\alpha (\omega_\alpha \delta_\alpha + \omega_\beta \delta_\beta) \text{ for small damping} \\
 &\dots (4.32)
 \end{aligned}$$

$$D_{\alpha\beta} D_{\alpha\beta}^* = (\omega_\alpha^2 - \omega_\beta^2) + 4\omega_\alpha \omega_\beta (\omega_\alpha \delta_\alpha + \omega_\beta \delta_\beta) (\omega_\alpha \delta_\beta + \omega_\beta \delta_\alpha) \quad \dots (4.33)$$

From equation (4.31), equation (4.27) contains integrals of the form

$$\int_A \int_A \psi_\beta(\underline{x}') \psi_\alpha(\underline{x}'') C_p(\underline{x}', \underline{x}'', \omega_\alpha) d\underline{x}' d\underline{x}''$$

and

$$\int_A \int_A \psi_\beta(\underline{x}') \psi_\alpha(\underline{x}'') Q_p(\underline{x}', \underline{x}'', \omega_\alpha) d\underline{x}' d\underline{x}''$$

which have been evaluated in Section 2.3.2. In particular, for the case  $\alpha=\beta$  it has been shown that

$$\int_A \int_A \psi_\alpha(\underline{x}') \psi_\alpha(\underline{x}'') Q(\underline{x}', \underline{x}'', \omega) d\underline{x}' d\underline{x}'' = 0 \quad \dots (4.34)$$

From equations (4.32) and (4.33) it can be shown that, for  $\alpha=\beta$

$$\frac{D_{\alpha\alpha}^r}{|D_{\alpha\alpha}|^2} = \frac{-1}{4\omega_\alpha^2} \quad \text{and} \quad \frac{D_{\alpha\alpha}^i}{|D_{\alpha\alpha}|^2} = \frac{-1}{4\omega_\alpha^2 \delta_\alpha} \quad \dots (4.35)$$

Equation (4.27) can now be written:

$$\begin{aligned}
 R_d(\tau) = & \int_{\alpha} \psi_{\alpha}^2(\underline{x}) \frac{\pi e^{-\delta_{\alpha} \omega_{\alpha} \tau}}{2M_{\alpha}^2 \omega_{\alpha}^2 \delta_{\alpha}} (\cos \omega_{\alpha} \tau + \delta_{\alpha} \sin \omega_{\alpha} \tau) \int_A \int_A \psi_{\alpha}(\underline{x}') \psi_{\alpha}(\underline{x}'') C_p(\underline{x}', \underline{x}'', \omega_{\alpha}) d\underline{x}' d\underline{x}'' \\
 & + \int_{\alpha} \int_{\beta} \psi_{\alpha}(\underline{x}) \psi_{\beta}(\underline{x}) \frac{2\pi e^{-\delta_{\alpha} \omega_{\alpha} \tau}}{M_{\alpha} M_{\beta} \omega_{\alpha} |D_{\alpha\beta}|} \{ (D_{\alpha\beta}^i \cos \omega_{\alpha} \tau - D_{\alpha\beta}^r \sin \omega_{\alpha} \tau) \int_A \int_A \psi_{\beta}(\underline{x}') \psi_{\alpha}(\underline{x}'') C_p(\underline{x}', \underline{x}'', \omega_{\alpha}) \\
 & \quad d\underline{x}' d\underline{x}'' \\
 & + (D_{\alpha\beta}^i \sin \omega_{\alpha} \tau + D_{\alpha\beta}^r \cos \omega_{\alpha} \tau) \int_A \int_A \psi_{\beta}(\underline{x}') \psi_{\alpha}(\underline{x}'') Q(\underline{x}', \underline{x}'', \omega_{\alpha}) d\underline{x}' d\underline{x}'' \} \\
 & \dots (4.36)
 \end{aligned}$$

When the resonant peaks associated with modes  $\alpha$  and  $\beta$  are well separated in frequency and, say,  $\omega_{\alpha} \gg \omega_{\beta}$  then

$$\frac{D_{\alpha\beta}^r}{|D_{\alpha\beta}|^2} \approx \frac{1}{\omega_{\alpha}^2} \quad \text{and} \quad \frac{D_{\alpha\beta}^i}{|D_{\alpha\beta}|^2} \approx \frac{2\delta_{\alpha}}{\omega_{\alpha}^2} \quad \dots (4.37)$$

From equations (4.35) and (4.37) it can be shown that, for  $\delta_{\alpha} \ll 1$ , the coefficient  $\frac{D_{\alpha\alpha}^i}{|D_{\alpha\alpha}|^2}$  is large compared with the coefficients  $\frac{D_{\alpha\alpha}^r}{|D_{\alpha\alpha}|^2}$ ,  $\frac{D_{\alpha\beta}^r}{|D_{\alpha\beta}|^2}$  and  $\frac{D_{\alpha\beta}^i}{|D_{\alpha\beta}|^2}$ . Then equation (4.36) can be reduced further to:

$$R_d(\tau) \approx \int_{\alpha} \psi_{\alpha}^2(\underline{x}) \frac{\pi e^{-\delta_{\alpha} \omega_{\alpha} \tau}}{2M_{\alpha}^2 \omega_{\alpha}^2 \delta_{\alpha}} \cos \omega_{\alpha} \tau \int_A \int_A \psi_{\alpha}(\underline{x}') \psi_{\alpha}(\underline{x}'') C_p(\underline{x}', \underline{x}'', \omega_{\alpha}) d\underline{x}' d\underline{x}'' \quad \dots (4.38)$$

When the frequencies  $\omega_{\alpha}, \omega_{\beta}$  are close together the coefficients

$$\frac{D_{\alpha\alpha}^r}{|D_{\alpha\alpha}|^2}, \quad \frac{D_{\alpha\alpha}^i}{|D_{\alpha\alpha}|^2}, \quad \frac{D_{\alpha\beta}^r}{|D_{\alpha\beta}|^2} \quad \text{and} \quad \frac{D_{\alpha\beta}^i}{|D_{\alpha\beta}|^2}$$

have similar orders of magnitude and the simple form of  $R_d(\tau)$  in equation (4.38) is not valid. Any simplification in that case will depend on the relative magnitudes of the spatial double integrals for the particular excitation considered.

If  $R_d(\tau)$  can be expressed in the form of equation (4.38), then the value of  $\delta_{\alpha}$  can be determined experimentally. With  $\tau$  as the independent variable, equation (4.38) has the form

$$R_d(\tau) = \sum_{\alpha} Z_{\alpha} e^{-\delta_{\alpha} \omega_{\alpha} \tau} \cos \omega_{\alpha} \tau \quad (Z_{\alpha} = \text{constant})$$



which is a series of exponentially decaying cosines. If it is assumed that the contribution from the  $\alpha^{\text{th}}$  mode is due mainly to the response in the frequency range in the close neighbourhood of  $\omega_\alpha$ , and that the contributions from the other modes are negligible in this frequency range, then

$$(R_d(\tau))_{\omega_\alpha} = \sum_{\alpha} e^{-\delta_\alpha \omega_\alpha \tau} \cos \omega_\alpha \tau$$

where  $(R_d(\tau))_{\omega_\alpha}$  denotes the autocorrelation function obtained from the filtered response signal, with the filter centre frequency at  $\omega_\alpha$ . This can be measured experimentally to determine  $\delta_\alpha$ , if the filter response is flat in the frequency range of interest. In practice the contributions from other modes will distort the correlation function and will introduce inaccuracies.

In the special case of single point random excitation the response autocorrelation function has a much simpler form than equation (4.36). The real part  $C_p(\underline{x}', \underline{x}'', \omega)$  of the cross power spectral density function reduces to the power spectral density function  $S_p(\omega)$  and the terms for  $\alpha \neq \beta$  in equation (4.36) are zero. Thus equation (4.36) reduces immediately to

$$R_d(\tau) = \sum_{\alpha} \psi_{\alpha}^2(\underline{x}) S_p(\omega_{\alpha}) \frac{\pi e^{-\delta_{\alpha} \omega_{\alpha} \tau}}{2 M_{\alpha}^2 \omega_{\alpha}^2 \delta_{\alpha}} (\cos \omega_{\alpha} \tau + \delta_{\alpha} \sin \omega_{\alpha} \tau)$$

#### 4.5 Damping Measurements using Random Techniques

##### 4.5.1 Choice of Method

Theoretically the excitation-response power spectral density method provides the most accurate estimate of the modal damping but in practice this is not always true, and it has been found that in certain circumstances a better estimate of the damping is given by the autocorrelation decay method. However, the autocorrelation methods suffer from the disadvantage that it can be used for only a limited number of modes. The cross spectrum and autocorrelation methods were applied to the experimental panels and the latter method was chosen as the more accurate for the conditions of the investigation. Damping loss factors for the panels, determined from the cross- and autocorrelation techniques, have been compared with discrete frequency results by Richards, Wilby and McNulty (1965) and a detailed comparison is not necessary in this discussion.

#### 4.5.2 Measuring Equipment

In the cross power spectrum method it is necessary to record simultaneously the excitation and response. Because of practical difficulties the boundary layer pressure field on the panel could not be measured and a second excitation was introduced. This was provided by an electromagnet which, in association with a white noise generator, produced a randomly varying magnetic field. The experimental system is shown diagrammatically in Figure 4.3. The probe, designed by McNulty (see Richards, Wilby and McNulty (1965)), consisted of two coils wound on a core which was a specially constructed capacitance probe for use with the Wayne Kerr Vibration Meter. This design was adopted because of the limited space available in the pressure equalising box. The core had no permanent magnetism, and one of the coils carried a D.C. current to provide the permanent magnetic field necessary to bias the alternating field. The D.C. current was controlled by a variable resistance to give a predetermined D.C.:A.C. current ratio. The voltage input to the A.C. coil and the voltage output from the Wayne Kerr Vibration Meter were recorded simultaneously on a twin track tape recorder. The panel response contained vibration due to boundary layer excitation and electromagnetic excitation, both of which were random in nature. However, the boundary layer induced vibration had zero correlation with the electromagnetic excitation and was eliminated when the two recorded signals were correlated. Correlation was carried out on the correlator developed by Allcock, Tanner and McLachlan (1962) at the University of Southampton. For each time delay selected, the signals were integrated for a period of 10 seconds and the correlation coefficient was computed.

The effect of the D.C. field is shown in Figure 4.4. The 3.5in x 3.5in panel was excited, in zero airflow conditions, at a frequency  $f = \frac{1}{2}f_{1,1} = 245$  c.p.s., where  $f_{1,1}$  is the natural frequency of the (1-1) mode. This is the most severe condition for the frequency doubling effect because there is a natural frequency in the neighbourhood of  $2f$  but not at  $f$ . When there is no D.C. field the vibration is essentially at a frequency  $2f$  and there is poor correlation with the excitation, which has a frequency  $f$ . Also the shape of the correlation function is distorted. When the D.C.:A.C. current

ratio is increased the correlation at the excitation frequency increases and the correlation curve assumes a true cosine form. Under normal conditions for damping measurement the excitation is selected to be narrow band white noise centred at the natural frequency concerned, and the effect of the D.C. field will be much smaller.

The autocorrelation function for the response was obtained directly from the measurements of vibration due to boundary layer excitation. When autocorrelation functions are measured for lightly damped structures it may be necessary to use long time delays, with associated errors arising from speed fluctuations on the recording system. The most important speed variations in this context are the rapid changes due to eccentric drive capstans, bearing friction and uneven driving torque, and the replay frequency is modulated by the ratio of the replay to record speeds

$$f(\text{replay}) = f(\text{record}) \cdot \frac{v(\text{replay})}{v(\text{record})}$$

For a high quality recording system the speed variations should be small in amplitude and will have a negligible effect on spectral analysis, but there could be a significant effect on the auto- and cross-correlation functions when long time delays are used.

To measure the amplitude of the errors for the particular tape recorder used in the panel response measurements, sinusoidal signals were recorded, for a tape speed of 15 inches/second, at frequencies of 500, 1,000 and 2,000 c.p.s. which covered the range of interest for the damping measurements. The autocorrelation coefficients for the calibration signals were determined. Ideally the autocorrelation curve should have the form of an undamped cosine

$$\rho(\tau) = \cos \omega \tau$$

but in practice, because of the speed variations, it has the form of a decaying cosine. The decay rate can be easily determined if the autocorrelation coefficients are measured for successive peaks of the autocorrelation curve, determined by  $\cos \omega \tau = 1$ . The decay curves for the three calibration signals are shown in Figure 4.5. When the time delay is

expressed directly in seconds the autocorrelation decay rate has a strong dependency on frequency (figure 4.5(a)), but when the delay is expressed in terms of the number of periods  $N$  of the autocorrelation function,  $N = ft$ , the decay rate is only weakly dependent on frequency (Figure 4.5(b)). From Figure 4.5, corrections were made to the damping measurements, but in general the vibration autocorrelation decay was measured over time delays for which  $N \leq 16$ , and the corrections were small ( $<2\%$ ).

It has been shown in Section 4.4.3 that, in certain circumstances, the vibration signal can be filtered to provide an approximation to a single-degree of freedom system, with the associated simple form of the autocorrelation function. This was achieved in practice by the use of either the one-third-octave filters of a Bruel and Kjaer Spectrometer or the one-third-octave filters of a Muirhead-Pametrada Wave Analyser. The choice of filter was dictated by the mode under investigation. The Bruel and Kjaer filters had good octave discrimination but had fixed centre frequencies at one-third octave intervals. Thus they could be used only when one of the filter centre frequencies was close to the natural frequency of the mode under investigation. For other modes the Muirhead-Pametrada Wave Analyser, which had variable filter centre frequencies but poor octave discrimination, was used. Filters with one-third octave bandwidths were used so that the maximum information could be obtained for a single mode. The narrower filter bandwidths available (4.5%, 2.0% and 1.2%) had characteristics which varied over frequency ranges which were close to the natural frequency of the mode. Thus they might modify the single mode response and introduce further inaccuracies.

#### 4.5.3 Results from Cross Power Spectrum Method

Measurements under zero airflow conditions showed that, in order to achieve a significant cross correlation coefficient, the excitation should have a narrow frequency distribution, as in the case of narrow band white noise. The effect of the bandwidth of the white noise on the cross correlation coefficient is shown in Figure 4.6. The measurements show that even when the excitation energy is restricted to the range 500 c.p.s. to 1,000 c.p.s. the energy is distributed over too wide a frequency band and

the response contains too many natural frequencies. The maximum correlation coefficient is less than 0.2 and the signals quickly decrease to values which are of the same order of magnitude as the correlator instrument error. Thus narrow excitation bandwidths of 4.5% were used in the majority of the measurements. However, when using the 4.5% bandwidth excitation, care had to be taken to centre the excitation frequency band at the natural frequency of the mode under consideration, so that the excitation would satisfy the condition that the spectral density was independent of frequency, at least in the immediate neighbourhood of the natural frequency.

Using 4.5% bandwidth white noise excitation, damping loss factors were estimated for several modes under zero airflow conditions and the values were compared with those obtained from the decay of the autocorrelation coefficient. The cross power spectra were computed using the weighting function  $D(\tau) = 1$  (equation 4.25) and the corrections of Clarkson and Mercer (1965) for the truncation effect were applied to all results. In all cases the loss factors estimated from the cross-power spectrum were considerably larger than those estimated from the autocorrelation function or from discrete frequency excitation. In Figure 4.7, a typical excitation-response cross-correlation curve and the associated computed cross power spectrum are shown for the (2-2) mode of the 3.5in x 3.5in x 0.015in panel. For the transformation, the cross-correlation curve was truncated at a time delay of 16 milliseconds. The cross correlation coefficient in Figure 4.7 decays quickly and for time delays greater than 10 milliseconds the values of the coefficient never exceed the level of the errors inherent in the correlator. Thus at the longer time delays the correlation coefficients are probably spurious and the transformation is in error. However, if the correlation coefficient is truncated at a time delay of 10 milliseconds the estimated loss factor would require excessive correction with the possibility of large errors. In the example chosen the estimated loss factor was an order of magnitude greater than the values estimated from the autocorrelation method or from the discrete frequency amplitude response curve.

From the zero-airflow investigation the cross spectrum method was found to be unsuitable for very lightly damped structures and was not used when

the airflow was present. Limited experience with specimens having higher loss factors indicates that the method might be of value in such cases.

#### 4.5.4 Results from Autocorrelation Method

It has been shown theoretically in Section 4.4 that the autocorrelation technique can be applied only to modes whose natural frequencies are well separated from the neighbouring peaks so that, when the response signal is passed through a filter centred at the natural frequency, the filtered signal contains a negligible contribution from the neighbouring peaks. Further, the method cannot be used if the peak is small relative to the neighbouring peaks because there will be a significant contribution from these modes to the vibration at the natural frequency under consideration. This contribution cannot be eliminated by filtering. It is obvious from these restrictions that the method can be applied to only a very limited number of natural frequencies.

The above conditions were applied to the measured vibration spectra and several modes were selected for investigation. The appropriate one-third octave filter was chosen to minimise the effect of the vibration in neighbouring modes. For each of the modes considered, the shape of the autocorrelation curve was inspected at a representative measuring condition. When the curve did not have the shape of a decaying cosine the corresponding modes were rejected. Thus the modes finally selected satisfied the condition that the vibration could be adequately represented by a single degree of freedom system. Figure 4.8(a) shows the autocorrelation curve for a mode (1-1 mode of the 2.0in x 4.0in panel) finally chosen for investigation and it can be compared with the autocorrelation curve in Figure 4.8(b), for the 2-1 mode of the 2.0in x 4.0in panel, which is distorted by low frequency modulation. Applying simplified arguments to two neighbouring sinusoidal signals at frequencies  $f'$  and  $f''$ , it can be shown that the resultant autocorrelation function will contain components modulated at frequencies  $\frac{f' - f''}{2}$  and  $\frac{f'' + f'}{2}$ . On this basis the 1-1 ( $f_{1,1} = 1070$  c.p.s.) and 2-1 ( $f_{2,1} = 1280$  c.p.s.) modes would provide low frequency modulation at a frequency of 105 c.p.s. which is comparable to the modulation frequency of approximately 90 c.p.s. present in Figure 4.8(b).

Although the full autocorrelation curve was used for sample cases when checking the validity of the single-degree of freedom assumption, the full curve is not required for the decay measurements where only the peak values of the autocorrelation coefficient are of use. The positions of the peaks were located approximately from the Lissajous figure for the two correlated signals, when displayed on an oscilloscope, and the peak values were then found from detailed correlation measurements around each peak. It was not possible in this method to identify any frequency drift in the panel vibration and the experimental scatter was expected to be of a similar order of magnitude ( $\pm 25\%$ ) to that experienced in the amplitude-phase method for discrete frequency excitation. Thus loss factor variations of less than  $\pm 25\%$  of the mean values cannot be considered as significant.

Damping loss factors for the selected modes were measured for the four panel positions along the tunnel working section. The results in Figures 4.9 and 4.10 show that the damping is essentially independent of panel position. This conclusion agrees with the results of a limited number of measurements using discrete frequency excitation under zero airflow conditions, and indicates that damping is not affected by boundary layer thickness nor by panel-tunnel resonances at the panel positions. The results in Figures 4.9 and 4.10 show that the measurements do lie within the predicted limits of  $\pm 25\%$  of the mean values.

The effect of airflow on the radiation damping of panels in a duct has been investigated theoretically by Fahy and Pretlove (1965) who considered the case of a panel spanning one wall of the duct. The effects of the airflow were most important at the panel fundamental natural frequency but in the example shown by the authors, for a panel with an area to duct cross sectional area ratio of 9, there was little variation of damping with air-speed, for frequencies greater than 500 c.p.s., in the Mach number range  $M=0$  to 0.5. In the measurements of panel response to boundary layer excitation the panel to duct area ratio was less than 0.34 and the maximum panel length was only 45% of the duct wall dimension. Thus the results of Fahy and Pretlove suggest that the airflow in the boundary layer tunnel would

have a small effect on the experimental panels.

Mean values of the measured loss factor are shown in Table 4.4, where the results for the two flow speeds,  $U_0 = 329 \text{ ft/sec.}$  and  $540 \text{ ft/sec.}$  are compared with the zero airflow measurements. The loss factors are associated with modes which are well separated in frequency from neighbouring modes, except in the case of the (1-2) and (2-1) modes of the  $3.5 \text{ in} \times 3.5 \text{ in}$  panel. By suitable positioning of the measuring probe on panel nodal lines it was possible to obtain response spectra which had contributions from only one of the two modes. Thus the loss factors for the two modes could be estimated. Results for the rectangular panels are shown for two panel orientations, with the major axis parallel and perpendicular to the flow direction. Within the experimental accuracy the results show no significant effect of panel orientation.

The results in Table 4.4 indicate that there is an increase in damping due to the presence of the airflow, but that there is no general variation which is applicable to all the panels. In the case of the square panel the damping is greatest for a flow velocity of  $540 \text{ ft/sec.}$  but the rectangular panels have maximum damping when  $U_0 = 329 \text{ ft/sec.}$  The measured damping increases are not very large for the  $3.5 \text{ in} \times 3.5 \text{ in}$  panel, being less than 30% of the zero airflow value, and except for the (1-1) mode, the changes are not much greater for the  $4.0 \text{ in} \times 2.0 \text{ in}$  panel ( $\leq 46\%$ ). It should be noted that in general the experimental errors will increase the apparent damping so that the mean values in Table 4.4 will tend to overestimate the true damping. However, very large increases were measured for the  $4.0 \text{ in} \times 2.75 \text{ in}$  panel, the two modes (1-1) and (2-1) showing damping factors which are up to 3.25 times larger than the zero airflow values. These large changes are difficult to explain because the panel dimensions and modal natural frequencies are similar to the corresponding values for the  $3.5 \text{ in} \times 3.5 \text{ in}$  panel. The mode showing the largest changes in damping is the (1-1) mode of the  $4.0 \text{ in} \times 2.75 \text{ in}$  panel, which, as has been discussed in Section 4.3.3 and Table 4.2, was very sensitive to the arrangement of the pressure equalising system. Thus there may be additional effects which contribute to the changes in damping for this mode, but it was not possible to identify them.



Table 4.4

Effect of Airflow on Damping Loss Factor (Mean Values)

Flow Velocity ft/sec.		0	329	540		
Panel	MODE	v(0)	v(329)	v(540)	$\frac{v(329)}{v(0)}$	$\frac{v(540)}{v(0)}$
3.5in x 3.5in	1-1	0.00968	0.00798	0.01159	0.82	1.20
	1-2	0.00281	0.00318	-	1.13	-
	2-1	0.00281	0.00291	0.00356	1.05	1.27
	2-2	0.00213	0.00246	0.00264	1.15	1.24
	3-1	0.00335	0.00300	-	0.90	-
4.0in x 2.75in	1-1	0.00431	0.01097	0.01001	2.54	2.32
	2-1	0.00338	0.00715	0.00453	2.11	1.34
2.75in x 4.0in	1-1	0.00431	0.0140	0.00851	3.25	1.98
	1-2	0.00338	0.00708	0.00537	2.09	1.59
4.0in x 2.0in	1-1	0.00813	0.01563	0.00909	1.92	1.12
	2-1	0.00904	0.01315	-	1.46	-
	3-1	0.00418	0.00585	0.00487	1.40	1.16
2.0in x 4.0in	1-1	0.00813	0.01063	0.00869	1.31	1.07
	1-3	0.00418	0.00506	0.00420	1.21	1.01

#### 4.6 Summary

The modal damping of the experimental panels has been measured in zero airflow conditions, using discrete frequency excitation and the amplitude response method. The response amplitude-phase method was found to be unsuitable for the experimental conditions. The panel damping was measured under free field conditions, and under conditions for which one or both of the faces of the panels were enclosed. In many cases the damping was reduced by the presence of the enclosure, but in all conditions the damping was light, with loss factors in the range  $0.0017 \leq \nu_r \leq 0.012$ . The change in damping due to the presence of an enclosure was attributed to the decrease in acoustic radiation, and hence in acoustic damping, because of the reverberant conditions in the enclosure. A method was proposed for estimating the experimental error arising from the presence of off-resonant vibration in multi-degree of freedom systems, but the method was crude and gave only an indication of the magnitude of error.

In the presence of an airflow, random techniques can be used to measure modal damping, the choice of method being determined by the available analysing equipment and the experimental conditions. The damping can be estimated from the bandwidth of the resonant peaks in the response spectra if suitable filters are available. Alternatively the loss factor can be estimated from the excitation-response cross power spectrum, but corrections for truncation errors will be necessary if the spectrum is obtained by transformation of the cross correlation coefficient. Both of the above methods were found to be inaccurate in the experimental conditions of the present investigation and the autocorrelation decay method was used. This method can be applied to only a limited number of modes, where the natural frequencies are well spaced, the damping is light, and the resonant peak is not small relative to the neighbouring peaks. The results showed a general increase in modal damping in the presence of an airflow, the damping for the square panel being greatest at a flow speed of 540ft/sec., whilst the damping for the rectangular panels was greatest at a flow speed of 329ft/sec. The largest changes in damping occurred in the (1-1) mode of each panel.

## CHAPTER 5

### Measured Response to Boundary Layer Excitation

#### 5.1 Introduction

##### 5.1.1 Method of Presentation of Results

The four panels used in the experimental programme have been described in Chapter 3. One panel was of square planform but the other three were rectangular in shape and could be placed in the wall of the tunnel working section so that the major axis was either parallel or perpendicular to the direction of the airflow. Thus each rectangular panel could be used effectively as two panels, one with aspect ratio  $L_1/L_2$  greater than unity and one with an aspect ratio less than unity. For ease of reference, the panels will be denoted by the planform dimensions, the first dimension quoted being that in the flow direction. Thus the 4.0in x 2.0in panel is placed with the 4.0inch sides parallel to the flow direction, and the 2.0in x 4.0in panel has the 2.0inch sides parallel to the flow. The full range of experimental panels is shown in Table 5.1 in order of increasing aspect ratio.

In the theoretical investigation the mode order (m-n) refers to a mode having m half-wavelengths in a direction parallel to the airflow and n half-wavelengths perpendicular to the flow. This notation will be used again and it should be noted that, for example, the (1-2) mode of the 4.0in x 2.0in panel is physically the same mode as the (2-1) mode of the 2.0in x 4.0in panel.

Rectangular Cartesian co-ordinate axes were chosen as shown in Figure 5.1 with the undisturbed neutral plane of the panel lying in the  $(x_1, x_3)$  co-ordinate plane, and the tunnel airflow in the negative  $x_1$  direction. A probe position which was one quarter of the way along a panel diagonal was chosen for most of the vibration measurements, but supplementary measurements were made at other positions. When the rectangular panels were used, vibration measurements were usually made at the same physical positions on the panel

Table 5.1

Dimensions of the Experimental Panels

Panel	Planform Dimensions	Aspect Ratio $L_1/L_3$
1	1.0in x 4.0in	0.25
2	2.0in x 4.0in	0.50
3	2.75in x 4.0in	0.6875
4	3.5in x 3.5in	1.00
5	4.0in x 2.75in	1.4545
6	4.0in x 2.0in	2.00
7	4.0in x 1.0in	4.00

surface for the two aspect ratio cases. Thus, measuring positions were chosen as shown in Figure 5.1, to minimise the effect of any asymmetry in the panel vibrational characteristics.

The panel response is expressed directly in terms of the root mean square (r.m.s) displacement and the displacement power spectral density  $G_d(f)$ , or it is expressed in terms of the response to unit excitation when it is desirable to exclude the effect of the excitation power spectral density. In the latter case the displacement power spectral density at a frequency  $f$  is divided by the excitation pressure power spectral density for the same frequency  $f$ , to give the ratio  $G_d(f)/G_p(f)$ . The power spectral density functions  $G_d(f)$  and  $G_p(f)$  are the single sided functions ( $0 \leq f < \infty$ ) which are measured in practice (see Section A.3.2).

#### 5.1.2 Errors due to Theoretical Assumptions

The measured panel natural frequencies and mode shapes in Appendix C indicate that the experimental panels have boundary conditions which are intermediate between those of simply supported and fully fixed panels, but which approach the conditions associated with a fully fixed panel. In the theoretical analysis it has been assumed that the mode shapes could be represented by those associated with a simply supported panel, although the measured natural frequencies and modal damping applicable to the fully fixed panels were used. Before the theoretical and experimental results are compared, the effect of the above assumption on the displacement power spectral density function can be discussed by comparing theoretical results for simply supported and fully fixed panels. The theoretical comparison will include only the effect of the mode shape, and will not include the natural frequencies associated with simply supported and fully fixed modes of vibration.

The mode shapes will influence the displacement power spectral density function in equation (2.45) through three terms: the generalised mass  $M_n$ ; the panel acceptance  $J_{ns}(\omega)$ ; and the modal displacement  $\psi(\underline{x})$  at the position  $\underline{x}$  considered on the panel. The generalised mass and the acceptance depend on the integrated effect of the mode shape over the panel surface, and their

influence is independent of the position on the panel. In Section 2.3.3 the generalised mass for a simply supported panel is shown to be greater than that for a fully fixed panel, and in equation (2.45)  $M_a$  appears in the denominator of the displacement power spectral density function. Thus the use of simply supported mode shapes in the determination of the generalised mass will reduce the displacement power spectral density function by a factor of 2.1 for the (1-1) mode, the factor falling to a value of 1.7 for the higher order modes.

The joint acceptance terms, also, are larger for simply supported mode shapes than for fully fixed mode shapes, and Bozich (1964) has shown that for some conditions of acoustic excitation the difference is a factor of 2, approximately. However, the changes in  $M_a$  and  $J_{\alpha\beta}(\omega)$  will act in opposition in the response function of equation (2.45), so that the combined effect should exhibit only a small variation with panel boundary conditions.

The effect of the  $\psi(\underline{x})$  term will depend on the location  $\underline{x}$  of the point of interest, and a comparison between simply supported and fully fixed modes is available directly from Figures C.2 to C.4. For some positions the simply supported mode shape will give larger deflections than the fully fixed modes, whereas the converse will be true at other positions. It is seen that the choice of mode shape will be important when  $\underline{x}$  is chosen to lie on, or close to, a nodal line of one of the mode shapes. When the displacement is estimated for the quarter point of the diagonal, the point of interest lies on a nodal line of the simply supported modes for which  $m$  or  $n$  is equal to 4, and theoretical estimates will predict a zero displacement in these modes. Use of fully fixed mode shapes would give a non-zero response, which is in better agreement with experiment (Figure 5.9). For this position on the panel surface, the term  $\psi_a^2(\underline{x})$  for a simply supported panel exceeds that for a fully fixed panel by a factor of approximately 2.7 for the (1-1) mode, 1.2 for the (2-2) mode, 0.4 for the (3-3) mode and 6.6 for the (5-1) mode. In particular, the results for panels 3 and 5 show a large difference between the theoretical and measured spectral densities in the 5<sup>th</sup> order modes.

From the above discussion it is seen that the effect of mode shape on the panel displacement power spectral density function arises mainly from the modal displacement  $\psi_\alpha(\underline{x})$  for the position  $\underline{x}$  considered, but an additional contribution due to the net effect of the acceptance and generalised mass terms will be present also.

The mean measured natural frequencies in Table C.2 were used in the calculation of the theoretical spectra, but in some cases the measured and predicted resonant peaks are displaced slightly in the frequency domain. This shift is of little significance because the panel natural frequencies changed slightly with ambient temperature. Zero airflow damping has been used in the prediction of the displacement spectra and in the estimation of the resolution loss due to the finite filter bandwidth, except for the (1-1) and (1-2) modes of panel 3 and the (1-1) and (2-1) modes of panel 5 where mean damping values measured in the presence of the airflow were used. A comparison of theoretical and measured spectra will show the relative shapes of the spectra in terms of the relative importance of the modes of vibration, and will not be concerned with the frequencies of the peaks in the theoretical and experimental spectra.

The theoretical spectra include data at the panel natural frequencies, and in some cases at the spectral troughs (Figure 5.8), to show the effect of including the cross terms in the calculation of the panel response. For the panels investigated it is seen that the cross terms have a negligible effect, and they have been excluded from the general comparisons between the theoretical and measured results.

## 5.2 Root Mean Square Displacement

### 5.2.1 Overall Displacement

The determination of the panel overall and modal r.m.s. displacements at the probe measuring positions is discussed in Appendix D, theoretical and experimental modal displacements being presented in detail in Tables D.1 to D.8 for measuring positions at a quarter point on a panel diagonal. The overall r.m.s. displacements associated with these measuring positions are shown in Figure 5.2, the experimental values being determined directly from

the measurements, and the theoretical values by summation over the lower order modes. Data for the 1.0in x 4.0in and 4.0in x 1.0in panels have been omitted because the levels were found to be very low and were affected by background vibration. It is seen from the figure that in all cases the predicted displacement exceeds the measured value, but the experimental and theoretical results show similar variations with the boundary layer thickness. The largest measured response shown in the results is an r.m.s. displacement of  $1.45 \times 10^{-4}$  inch for the square panel (4). This displacement is approximately 1% of the panel thickness.

In Figure 5.2(a) the theoretical and experimental results for panel 2 (2.0in x 4.0in) and panel 6 (4.0in x 2.0in) show that at the lower Mach number,  $M_0=0.3$ , the vibration levels are greater in panel 2 than in panel 6, but the converse is true at the higher Mach number. This effect is present in the results for panels 3 and 5 in Figure 5.2(b), but it is less marked because the panel aspect ratios are closer to unity.

#### 5.2.2 Modal Displacement

Modal r.m.s. displacements have been measured for the experimental panels, an approximation to the response in the individual modes being obtained by the use of 2% bandwidth filters in the analysis of the displacement signals. The results are compared in the Tables D.1 to D.8 with theoretical values predicted by the method shown in Appendix D. Typical results for panels 2, 4 and 6, and a Mach number  $M_0=0.3$ , are shown in Figures 5.3 and 5.4 where it is seen that, although the theory overestimates the magnitude of the measured response, it provides a reliable estimate of the variation of response with boundary layer thickness. The results show that there is a general increase in the modal r.m.s. displacement with boundary layer thickness until a maximum displacement is reached at a boundary layer thickness which depends on the mode order. Further increases in the boundary layer thickness will result in a decrease of the modal r.m.s. displacement. Inspection of the results shows that, as the boundary layer increases in thickness, the modal maxima occur first in the modes with the highest natural frequencies, and at the lower flow velocity.



Thus the phenomenon can be attributed, at least in part, to the concentration of excitational energy at lower frequencies as the boundary layer thickness increases. Figure A.2 shows that, at the lower Mach number, the excitation spectral density at a given frequency in the range 2,000 c.p.s. to 3,000 c.p.s. reaches a maximum at a boundary layer thickness in the experimental range. Thus modes with natural frequencies in this range could be expected to have associated displacement maxima. A more detailed investigation of the effect of boundary layer thickness will be postponed until Section 5.4, when the effect of excitation spectral density can be excluded if necessary.

The presence of a maximum displacement is not indicated in the total response results in Figure 5.2, except in the case of panel 6, for a flow speed  $M_0 = 0.3$ . The variation of the total response with boundary layer thickness will be determined by the corresponding variation of the dominant modes. In Figures 5.3 and 5.4 the dominant modes of panels 2 and 4 do not have a displacement maximum in the range of boundary layer thicknesses considered, and this is reproduced in the total results in Figure 5.2. However the results for panel 6 in Figure 5.4 show that the dominant modes are approaching maximum displacement values at the upper limit of the boundary layer thickness range considered. This is particularly true for the experimental results, and the associated total response in Figure 5.2 indicates the presence of a displacement maximum at the thicker boundary layers considered.

### 5.3 Displacement Spectra

A series of measured response spectra are shown for panels 2 to 6 in Figures 5.5 to 5.9 respectively. The measurements were made at a flow velocity of  $U_0 = 329 \text{ ft/sec}$  ( $M_0 = 0.3$ ) and a boundary layer thickness of  $\delta = 1.4 \text{ inches}$ , the probe position being at a quarter point on the panel diagonal. The response spectral density is expressed in terms of the displacement to unit excitation, and the peak values have been corrected for resolution loss due to the finite bandwidth of the analysing filters (Appendix B). The effect of the filters is negligible except in the regions very close to the natural frequencies. In each figure the measured spectrum is compared with the corresponding theoretical spectrum estimated

from equation (2.45), using joint acceptance terms only. The natural frequencies in the theoretical spectra were taken as the mean values from the measured spectra and are given in Table C.2.

A comparison of the theoretical and experimental spectra shows that the shapes are similar, in terms of the relative importance of the normal modes, but the theory overestimates the peak values and underestimates the values in the troughs. However, close agreement of the magnitude of the spectral density is not expected because of the errors and assumptions present in the experimental and theoretical analysis. In addition to the errors in the theoretical analysis which are discussed in Section 5.1.2, experimental errors occur because of the experimental scatter inherent in random analysis, and because of errors in the measurement of the damping ratios and in the estimation of the resolution loss.

The best agreement between theory and experiment is found in the results for panels 2, 4 and 6. In the case of panels 3 and 5 the agreement is good at the two lowest natural frequencies where damping values measured in the presence of the airflow were used, but is less good at higher frequencies where zero airflow damping was used in the calculations.

When the spectra for panels 2 and 3 are compared with the results for panels 5 and 6, the relative importance of the modes is obvious. The theoretical and experimental spectra for the 2.0in x 4.0in and 2.75in x 4.0in panels show that the greatest response at the measuring position occurs in the (1-1) fundamental mode, but the (2-1) mode is predominant in the 4.0in x 2.75in and 4.0in x 2.0in panels. This change in relative magnitude is more noticeable when comparing the (2-1) and (1-3) modes of panel 3 with the (1-2) and (3-1) modes of panel 5. These modes have very close natural frequencies and, because of filter effects, the presence of the secondary peak is observed only as a distortion in the shape of the measured primary peak. In Figure 5.6 the response in the (2-1) mode is an order of magnitude greater than that in the (1-3) mode, but in Figure 5.8 the (3-1) mode peak is considerably greater than the (1-2) mode peak. Direct comparisons of spectra for the above four panels have been presented by Wilby (1964) and Wilby and Richards (1965).

Response spectra for the 1.0in x 4.0in and 4.0in x 1.0in panels are shown in Figure 5.10 but, because of the high natural frequencies and low response, little information can be deduced from the figure. Also the results are influenced by the presence of background vibration. However, it can be seen that the experimental and theoretical response in the fundamental mode is much smaller in the case of the 4.0in x 1.0in panel than it is for the 1.0in x 4.0in panel.

In Figures 5.11 to 5.13 response spectra are presented for panels 3, 4 and 5, with an airflow velocity of 540ft/sec. The spectra are again shown in terms of the response to unit excitation so that a comparison of the results for the two flow speeds in Figures 5.6 to 5.8 and Figures 5.11 to 5.13 will not include the effect of changes in excitation spectral density. The comparison will show only the effect of the acceptance curves and, for the two lowest frequency modes of the 4.0in x 2.75in and 2.75in x 4.0in panels, the effect of modal damping. The agreement between theory and experiment at a flow speed of 540ft/sec is not as good as at the lower speed but there is still fairly good agreement in the relative shapes of the spectra. Figures 5.11 and 5.13 show changes in the relative magnitudes of the modes which are similar to those observed between Figures 5.6 and 5.8.

When results for the two airspeeds are compared it is seen that the theoretical and measured high frequency response increases more rapidly with air velocity than does the low frequency response. Thus at the higher speed the fall-off of the response spectra with increasing frequency is less rapid than at the lower speed. This change in spectrum shape becomes more obvious when the direct response spectra are compared, as in Figure 5.14 for panel 5, where changes in excitation spectral density (see Figure A.2) further emphasise the changes in the shape of the response spectra. Figure A.2 shows that for the higher flow velocity there is relatively more excitational energy at the higher frequencies. Further discussion of the effect of airflow velocity on the panel response at the natural frequencies is contained in Section 5.5.

The effect of boundary layer thickness on the shape of the response spectra is not illustrated in this chapter but spectra have been compared by Wilby and Richards (1965) for the 3.5in x 3.5in panel. At the lower

frequencies there is a general increase in the response, due to the change in the excitation spectral density and in the panel joint acceptance. The trend can be reversed, however, at the higher frequencies. In the following section the effect of boundary layer thickness on the modal response at the panel natural frequencies will be investigated.

#### 5.4 Effect of Boundary Layer Thickness

It has been shown in the previous section that the measured and predicted spectra are similar in shape, and it is possible now to study in greater detail the effect of boundary layer thickness on the panel response. In Appendix D and Section 5.2.2 measured and predicted modal r.m.s. displacements are presented and the effect of boundary layer thickness is shown in Figures 5.3 and 5.4. Similar comparisons can be made when the displacement spectral density at the panel natural frequencies is considered, and the response can be associated with the excitation power spectral density and cross correlation functions at the corresponding frequencies. In the case of the r.m.s. displacement the response can be associated with the same excitation functions, if it is assumed that the r.m.s. displacement is due mainly to the response in the neighbourhood of the modal natural frequency. This assumption was used in the estimation of the r.m.s. displacement from the displacement spectral density in Section D.2. The choice of r.m.s. displacement or displacement spectral density as the function of interest will have little effect on the conclusions to be drawn, but any errors present in the r.m.s. displacement comparison will be magnified in the displacement spectral density function. However the latter function can be related directly to the spectra in Figures 5.5 to 5.14 and, therefore, has been chosen for investigation. If necessary the effect of flow velocity and boundary layer thickness on the r.m.s. displacement can be studied from the data available in Tables D.1 to D.8.

Figure 5.15 shows the measured spectral density  $G_d(f)$  at the natural frequencies of the (1-1), (1-2), (2-1) and (2-2) modes of the 3.5in x 3.5in panel, for four boundary layer thicknesses along the tunnel working section. The measurements are compared with theoretical curves calculated from equation (2.45) when the cross terms,  $\alpha\beta$ , are neglected.

The estimated values exceed the measured values throughout the range of boundary layer thickness, but the variation of response with boundary layer thickness is similar in the two cases. The data in the figure can be compared with data in Figure 5.3 where the same information is presented in terms of the r.m.s. displacement. The agreement between experiment and theory in Figure 5.15 appears to be worse than in Figure 5.3 but this is due mainly to the effective squaring of the information presented in Figure 5.3. For the same reason the effect of boundary layer thickness on the displacement power spectral density function appears to be stronger than the effect on the r.m.s. displacement.

Reasons for the discrepancies between theory and experiment have been discussed in Section 5.1.2, and in future comparisons it will be of interest to consider only the variation of the response with the various parameters. To obtain a convenient comparison the measured values for a given mode and measuring position can be multiplied by an arbitrary factor so that the experimental points are superposed on the theoretical curve. The factor, which is the mean ratio of the theoretical power spectral density to the measured spectral density, will indicate the extent by which the predicted values exceed the measured results.

On the above basis a comparison of the theoretical and experimental results is shown in Figures 5.16 to 5.20 for panels 2 to 6, and a flow velocity of 329ft/sec. The results are presented directly in terms of the displacement power spectral density function  $G_d(f)$ , and include the effect of changes in excitation power spectral density with boundary layer thickness. The measurements show a certain amount of experimental scatter but in general the effect of the boundary layer thickness is predicted well for all panels. The principal exceptions are the (1-1) modes of panels 5 and 6, where the measured rate of change of response with boundary layer thickness is greater than that predicted. Figures 5.21 to 5.23 contain similar data for panels 3 to 5, and a flow velocity of 540ft/sec. The experimental scatter is greater than at the lower speed but the results again show similar trends for the measurements and estimates. The (1-1) mode of the 4.0in x 2.75in panel exhibits the divergence between theory and experiment which was shown at

$U_0 = 329 \text{ ft/sec.}$ , and a similar divergence is observed in the results for the (1-1) mode of the 3.5in x 3.5in panel.

The ratio of the predicted to measured displacement power spectral densities at the panel natural frequencies is shown in Table 5.2, the measured values having been corrected for resolution loss, and the theoretical values calculated using zero airflow damping unless otherwise indicated. The theoretical spectral densities were estimated using joint terms only, but it has been shown that the error due to this simplification is negligible. For reasons given earlier, close agreement cannot be expected for the magnitudes of the theoretical and experimental displacement power spectral densities, and Table 5.2 indicates the extent of the discrepancy. The results in the table do not follow a consistent pattern but in 65% of the cases the factor is less than 5. This result is similar to that of section D.3, that the ratio of theoretical to measured modal r.m.s. displacement was mainly in the range 1.0 to 2.0. There is close agreement between theory and experiment for the 3.5in x 3.5in panel at a flow velocity of 329ft/sec., but there is a general increase in the ratio at the higher velocity. A similar trend with velocity is observed for the 2.75in x 4.0in panel but not for the 4.0in x 2.75in panel. When damping measured in the presence of the airflow is used for modes (1-1) and (2-1) of panel 5 and modes (1-1) and (1-2) of panel 3, the agreement between experiment and theory is much closer. Large differences between predicted and measured results for other modes of panels 3 and 5 may be influenced by changes in modal damping with airspeed.

Considering now the response to unit excitation, experimental and theoretical results for several modes, and both airflow velocities, are presented in Figure 5.24 for panel 4 and Figure 5.25 for panel 5. The experimental values are multiplied by the factors obtained from Table 5.2. The rate of change of response with boundary layer thickness is generally less than in the previous figures where the rate of change was amplified by the effect of the excitation power spectral density function. The experimental scatter has now become more significant, in terms of the total change in response for the boundary layer thickness range considered, but the measured and predicted results again show similar dependencies on boundary layer thickness.

Table 5.2

Ratio of Theoretical to Measured Displacement Power Spectral Density  
(Boundary Layer Excitation)

Mode Order	(m-n)	1-1	1-2	2-1	2-2	1-3	3-1	2-3	3-2	3-3
Panel	Mach No.	Theoretical $G_d(f)$ /Experimental $G_d(f)$								
3.5in x 3.5in	0.3	1.8	1.5	2.0	1.5	5.5	1.0	-	1.9	9.0
	0.5	6.4	4.6	6.1	3.4	6.2	5.2	-	2.0	2.4
4.0in x 2.75in	0.3	9.9	7.0	4.2	13.7	11.1	7.1	10.5	3.8	-
	0.5	2.2*	-	1.6*	5.2	0.7	2.1	1.0	4.8	-
2.75in x 4.0in	0.3	8.3	2.5	-	3.6	-	2.4	5.2	4.5	-
	0.5	1.8*	1.0*	-	6.2	-	4.1	12.5	3.9	-
4.0in x 2.0in	0.3	13.8	3.8	-	-	-	-	-	-	-
	0.5	5.3*	2.3*	-	-	-	-	-	-	-
2.0in x 4.0in	0.3	5.7	48.2	3.1	-	-	1.0	-	-	-
	0.3	1.6	2.0	1.0	3.6	1.3	-	-	-	-

\*Calculated using damping measured in the presence of the airflow.

In Chapter 2 the longitudinal joint acceptance terms are shown to have one of two alternative forms, the choice of form being determined by the value of the Strouhal number  $\frac{\omega \delta^*}{U_c}$ . When  $\frac{\omega \delta^*}{U_c} \geq 0.37$ , the excitation longitudinal narrow band cross correlation coefficient is independent of the boundary layer thickness  $\delta$  (or displacement thickness  $\delta^*$ ) except indirectly through the convection velocity  $U_c$  (equation (A.16)), and when  $\frac{\omega \delta^*}{U_c} < 0.37$ ,  $\delta^*$  is present in the correlation exponential decay term (equation (A.11)). In Figure 5.26 the regions of validity for the two forms of excitation correlation function are shown in relation to the modes of panels 4, 5 and 6. For a given measuring position, the condition  $\frac{\omega \delta^*}{U_c} \geq 0.37$  is satisfied at the natural frequencies of all the modes shown above the associated horizontal broken line. The condition  $\frac{\omega \delta^*}{U_c} < 0.37$  is satisfied at the lowest natural frequencies of panels 4 and 5 for all experimental conditions but at higher frequencies the condition  $\frac{\omega \delta^*}{U_c} \geq 0.37$  is satisfied in certain conditions.

The variation of modal response with boundary layer thickness can now be investigated with reference to Figure 5.26 and the non-dimensional curves in Chapter 2. Values of the non-dimensional parameter  $L_1/\zeta$ , averaged over the four boundary layer thicknesses in the experimental range, are given in Table 5.3 for frequencies  $f = f_{mn}$ . The variation of  $L_1/\zeta$  with  $\delta$  is approximately  $\pm 1.5\%$  about the mean value for the (1-1) mode, increasing to  $\pm 6\%$  at the highest natural frequencies considered.

For panel 4, it is seen from Figure 5.26 that at the natural frequencies of the (1-2) and (2-1) modes  $\frac{\omega \delta^*}{U_c} < 0.37$  for all the measuring conditions. Thus the change in spectral density with boundary layer thickness is a combination of the change in the longitudinal joint acceptance as shown in Figures 2.6 and 2.7, and the change in the lateral joint acceptance in Figure 2.16. Considering the (1-2) mode, the longitudinal joint acceptance  $j_{mm}(\omega)$  increases as  $\delta^*$  increases, when  $M_o = 0.5$  ( $L_1/\zeta = 2.45$ ), and decreases as  $\delta^*$  increases when  $M_o = 0.3$  ( $L_1/\zeta = 4.10$ ). In the lateral direction  $j'_{nn}(\omega)$  increases by approximately the same amount as  $\delta^*$  increases at the two airspeeds. Thus the combined effect of  $J_{nn}(\omega) = j_{mm}(\omega) \mp j'_{nn}(\omega)$  shows an increase in response with boundary layer thickness at the higher speed, and essentially no change at the lower speed where the increase in  $j'_{nn}(\omega)$  is cancelled by



Table 5.3  
Value of Non-Dimensional Panel Length at Natural Frequencies  
(Boundary Layer Excitation)

Mode Order (m-n)	1-1	1-2	2-1	2-2	1-3	3-1	2-3	3-2	3-3	1-5	5-1
Panel	Mean Value of $L_1/\tau_{mn}$										
	Mach No.										
3.5in x 3.5in	0.3	2.04	4.10	3.70	5.56	7.30	6.84	8.70	8.66	11.82	-
	0.5	1.23	2.45	2.22	3.31	4.31	4.05	5.12	5.10	6.87	-
4.0in x 2.75in	0.3	2.62	6.30	3.92	7.80	12.69	6.56	14.30	10.16	-	14.82
	0.5	1.58	3.75	2.38	4.62	7.43	3.90	8.34	5.98	-	8.63
2.75in x 4.0in	0.3	1.80	2.70	4.34	5.36	4.51	8.73	6.99	9.83	10.19	-
	0.5	1.09	1.63	2.58	3.18	2.69	5.11	4.12	5.73	5.93	-
4.0in x 2.0in	0.3	5.18	12.98	6.20	14.36	-	8.61	-	16.57	-	-
	0.5	3.10	7.59	3.69	8.36	-	5.09	-	9.61	-	-
2.0in x 4.0in	0.3	2.69	3.10	6.49	7.18	4.31	-	8.29	-	-	-
	0.5	1.55	1.85	3.80	4.19	2.55	-	4.81	-	-	-

Note:  $\tau_{mn}$  is the value of  $\tau$  at  $f=f_{mn}$

the decrease in  $j_{nn}(\omega)$ . The measurements show response variations with boundary layer thickness which are closely similar to the predicted variations. In the case of the (3-2) mode,  $\frac{\omega \delta^*}{U_c} < 0.3$ ; at the first three measuring positions for  $M_o = 0.5$ , but only at the first position for  $M_o = 0.3$ . From Figures 2.8 and 2.13,  $j_{nn}(\omega)$  and  $j'_{nn}(\omega)$  both increase with  $\delta^*$  at  $M_o = 0.5$  ( $L_1/\zeta = 5.10$ ). When  $M_o = 0.3$  ( $L_1/\zeta = 8.66$ )  $j'_{nn}(\omega)$  shows an increase with  $\delta^*$  but, from Figure 2.1 and  $m=3$ , the change in  $U_c$  with  $\delta^*$  results in a decrease of  $j_{nn}(\omega)$  which exceeds the increase in  $j'_{nn}(\omega)$ . Thus the combined effect results in an increase in modal response with boundary layer thickness at a flow speed of 540ft/sec., but there is a decrease in response as the boundary layer thickness increases at a flow speed of 329ft/sec. Again, the variation in the measured results is in agreement with the predictions.

In Figure 5.25, containing the results for panel 5, the natural frequency of mode (1-3) satisfies the condition  $\frac{\omega \delta^*}{U_c} \geq 0.37$  for most measuring conditions, and the theoretical and experimental results indicate that the response has a similar dependence on boundary layer thickness at both airflow velocities. From Figures 2.1 and 2.7 it is seen that  $j_{nn}(\omega)$  decreases as  $\delta^*$  increases, and  $j'_{nn}(\omega)$  increases with  $\delta^*$ , the changes at each Mach number being approximately the same.

Arguments similar to the above can be repeated for other modes and in all cases, regardless of whether  $\frac{\omega \delta^*}{U_c} \geq 0.37$  or  $\frac{\omega \delta^*}{U_c} < 0.37$ , the theory predicts response variations with boundary layer thickness which are similar to the measured changes.

### 5.5 Effect of Flow Velocity

The flow velocity will influence the panel response through the pressure power spectral density function, the pressure narrow band correlation length and the narrow band cross correlation decay. When an increase in flow velocity is achieved for constant dynamic pressure, the total energy of excitation will remain constant but there will be a redistribution of energy in the frequency domain, the distribution being made over a wider frequency range as is the case when the boundary layer thickness is decreased. However,

if, as is generally true, there is an increase in dynamic pressure associated with the velocity increase, then there will also be a general rise in the pressure power spectral density.

The pressure narrow band correlation length is directly proportional to the convection velocity and so will increase with the free stream velocity. This implies that, when the flow velocity is increased, the excitation wavelength which is associated with a frequency  $\omega$  by a fixed observer must increase also. Thus at a given instant in time the pressure field is correlated over a larger area for the higher flow velocity. Also the increase in flow velocity will decrease the cross correlation decay rate in the Strouhal number regions where this is inversely proportional to the convection velocity.

The response of the experimental panels to boundary layer excitation was measured for two flow velocities,  $U_0 = 329 \text{ ft/sec.}$  and  $540 \text{ ft/sec.}$  The measurements were restricted to these two velocities by the design of the boundary layer wind tunnel and although some conclusions can be drawn from the experimental results, it is not possible to predict with confidence the general trend of the measurements with flow velocity. A change in flow velocity can affect the panel response in several ways. The excitation power spectral density at a given frequency will change with flow velocity, and the change in the pressure field convection velocity will affect the excitation correlation function and the acceptance terms. The change in flow velocity may also affect the panel damping.

When the measured displacement spectra were compared in Figure 5.14 it was shown that there was a general increase in vibration when the flow velocity was increased. If the vibration is expressed in terms of the response to unit excitation, Figures 5.24 and 5.25, there is still an increase with flow velocity, except for certain modes or boundary layer thickness ranges. The preceding discussion has shown, also, that the theory overestimates the magnitude of the panel response, and that the extent of the overestimation, shown in Table 5.2 is different at the two Mach numbers. From table 5.2 it can be deduced that the variation of response with flow velocity, predicted from the theoretical analysis,

differs from that measured in practice.

In Figures 5.27 to 5.29 the displacement power spectral density at the natural frequencies of several panel modes is expressed as the ratio of the response at Mach number  $M_0=0.5$  to the response at  $M_0=0.3$ . Thus a ratio greater than unity indicates an increase in the displacement power spectral density function  $G_d(f)$  with velocity, the effect of a change in excitation power spectral density being included. The results in Figures 5.27 to 5.29 show that, theoretically and experimentally, the ratio, and hence the effect of the flow velocity, increases with mode order. For example, the measured response ratios for panel 4 are approximately 1.2 in the (1-1) mode, 2.5 in the (2-2) mode and 120 in the (3-3) mode, the theoretical values being 4.0, 5.5 and 40 respectively. One reason for this change with mode order or frequency is the variation, particularly at the higher frequencies, of the excitation power spectral density function with velocity. This is shown in Figure A.2.

The form of presentation used in Figures 5.27 to 5.29 is very susceptible to experimental error, the error in the measurements being the combined error of the results at the two Mach numbers. Thus the scatter in the experimental results in the three figures is large. "Average" curves have been drawn through the measured data, the curves being based on the theoretical results multiplied by the corresponding factors in Table 5.2. The figures do not show very good agreement between the predicted and measured variation with Mach number. This may be due partly to changes in panel damping when the airflow velocity changes. In the calculation of the response, zero airflow damping was assumed for all the modes except the (1-1) and (2-1) modes of the 4.0in x 2.75in panel and the (1-1) and (1-2) modes of the 2.75in x 4.0in panel. In the measurement of the modal damping there was experimental scatter of approximately  $\pm 25\%$  and changes of this order with Mach number were not considered significant. However, such changes result in errors of  $\pm 60\%$  in the displacement power spectral density, errors which are of a similar magnitude to the differences between theory and experiment shown for several modes in Figures 5.27 to 5.29.

In addition to the possibility of errors of the above nature, there appears to be a general divergence of results as the natural frequency increases. At low natural frequencies the theory predicts a greater change with Mach number than is measured, whilst the converse is true at higher natural frequencies. Thus the measured change in spectrum shape with flow velocity, illustrated in Figure 5.14, is more pronounced than would be predicted. From the available data it is possible to estimate the approximate frequency below which the theory overestimates the vibration and above which the theory underestimates the vibration. The results indicate that the frequency boundary decreases as the panel aspect ratio increases, the frequency being, approximately, 2,700 c.p.s. for panel 3, 1,900 c.p.s. for panel 4, and 1,500 c.p.s. for panel 5. Recently, Maestrello (1966) has published experimental and theoretical data for a panel of aspect ratio 5.54, and for the modes shown the experimental results have a much larger variation with Mach number than do the theoretical results. The panel aspect ratio is approximately four times larger than that for panel 5, so that the present results and those of Maestrello are not inconsistent.

#### 5.6 Angle of Convection

The effect of the angle of convection of the pressure field has been discussed theoretically in Chapter 2 and it was shown that, for a given value of  $L_1/\zeta$ , the displacement spectral density in certain modes would be higher at angles in the range  $0^\circ < \theta < 90^\circ$  than at the limiting angles  $\theta = 0^\circ$  and  $90^\circ$ . Thus, vibration measurements were carried out on the 4.0in x 2.75in panel, for a flow velocity of 329 ft/sec., a boundary layer thickness of 1.40 inches, and a series of angles of inclination of the major axis to the direction of flow in the boundary layer tunnel. The results are shown in Figure 5.30, where they have been multiplied by arbitrary factors to provide convenient comparisons with the predicted variation with angle of convection, the angle  $\theta = 0^\circ$  indicating that the flow is parallel to the panel major axis.

The theoretical curves were calculated from equations (2.93), with  $a_1 = \frac{0.1\omega}{U_c}$  and  $a_2 = \frac{0.715\omega}{U_c}$ , and are shown in terms of the panel joint

acceptance. The values of  $a_1$  and  $a_3$  used in the calculations assume that the condition  $\frac{\omega \delta^*}{U_c} \geq 0.37$  is valid for all the modes, and that the simplified form of the lateral cross correlation coefficient is valid also. The errors arising from these assumptions should not be large for the conditions considered. From Figure 5.26 it is seen that for all modes of panel 5, except the (1-1) and (2-1) modes,  $\frac{\omega \delta^*}{U_c} \geq 0.37$  at the panel position chosen. In the lateral direction the non-dimensional parameters have to be considered in greater detail but it can be shown from Figures 2.16 and 2.17 that the differences in joint acceptance terms for the simplified and complete forms of the excitation correlation coefficient are small.

In general Figure 5.30 shows that predicted and measured spectral densities have a similar dependency on the angle of convection of the pressure field. Modes (1-1), (2-1), (2-2) and (3-1) have the largest response at either  $\theta=0^\circ$  or  $90^\circ$ . Modes (4-1) and (4-2), however, have a maximum value at an intermediate value of  $\theta$ . In the case of the (4-1) mode, the maximum of the experimental results occurs at a much higher angle than predicted, but inspection of the non-dimensional curves shows that in this mode and for values of  $L_1/\zeta$  in the neighbourhood of the value considered small changes of  $L_1/\zeta$  can produce large changes in the angle for maximum response. It is noted however that the estimated and measured results differ in one aspect. For modes with order  $n=1$  along the minor axis the theory predicts a larger variation of response with  $\theta$  than that shown in the measurements, whilst for modes with  $n=2$  the converse is true.

### 5.7 Effect of Static Pressure Differential

Under normal operating conditions the static pressure in the boundary layer wind tunnel working section is below atmospheric pressure, but a pressure equalising system, described in Chapter 3, was used to balance the pressure across the experimental panels. However, conditions in the equalising box could be maintained at any desired pressure between the limiting values of atmospheric and tunnel pressure. Thus the panel vibration could be measured over a range of static pressure differentials.

When a panel is subjected to a static pressure differential there is an associated increase in the effective stiffness of the system which can

affect the panel response in three ways. For any loading distribution, there will be an increase in panel stiffness which will decrease the panel deflection to a given load. In addition, when the response spectrum is considered, there will be changes in spectrum shape due to the increase in the panel natural frequencies. When the excitation spectral density changes with frequency, the excitation and response at a natural frequency will vary with the natural frequency. Also, when the excitation is randomly distributed in space, as in the case of a turbulent boundary layer pressure field, and the static pressure differential is altered, there will be changes on the acceptance terms at the natural frequencies. It is possible to separate these three effects in the analysis of the experimental results.

The effect of static pressure differential  $\Delta p$  on the response spectra for two panels is shown in Figure 5.31 and 5.32 for a Mach number of 0.5 and a boundary layer thickness of 0.43 inch. The spectra are shown for the limiting values of the pressure differential, the maximum value at the Mach number being approximately 2.41 lb/in<sup>2</sup>. No corrections have been applied for resolution loss. The increases of the natural frequencies with pressure differential are clearly shown, and there is a general decrease in the displacement power spectral density.

The variation of the natural frequencies with the pressure differential is shown in Figures 5.33 and 5.34 for the two panels, the frequencies for the 3.5 in x 3.5 in panel being measured at two panel positions in the tunnel working section. Within the pressure differential range shown there is a linear increase of the natural frequency of each mode with pressure differential, the rate of change being greatest for the lowest order modes. The 3.5 in x 3.5 in panel has a frequency rate of change of 140 c.p.s./lb/in<sup>2</sup> for the (1-1) mode, decreasing to a rate of 80 c.p.s./lb/in<sup>2</sup> for the (3-3) mode.

The experimentally determined natural frequencies in Figures 5.33 and 5.34 can be used to predict the effect of a static pressure differential on the random vibration of the panels. The response was calculated from equation (2.45), in terms of the displacement for unit excitation so that the effect of the excitation spectral density could be eliminated. It

was assumed that the cross terms in equation (2.45) could be neglected, and that the damping was constant for each mode. This latter assumption may be invalid in certain cases, for example for the (1-1) mode of the 4.0in x 2.75in panel, where the effect of the pressure equalising system on the damping of the panel may vary significantly with frequency in the neighbourhood of an acoustic resonance in the system. The variation of the panel displacement power spectral density with pressure differential is shown in Figures 5.35 and 5.36 at the natural frequencies of several modes of the panels. To provide a comparison between the theoretical and experimental values, the measured results have again been multiplied by factors as in previous comparisons. It is seen that in some cases there is a fairly large scatter in the experimental values, but this may be due partly to changes in modal damping discussed above. In general the predicted and measured values show similar dependencies on the static pressure differential, the important exceptions being the fundamental (1-1) modes of the panels where the predicted rate of change of spectral density is greater than the measured value.

Figures 5.35 and 5.36 contain also a series of curves which show the change in panel vibration under the assumption that the joint acceptance remains constant. The curves represent the change in spectral density due only to a change in panel stiffness, the displacement power spectral density at the natural frequency being inversely proportional to the fourth power of the natural frequency. In most cases the differences between the curves for variable and constant joint acceptance terms are small and less than the experimental scatter, but for the previously noted exceptions of the (1-1) modes, the curves for constant joint acceptance give the better approximation to the measured rate of change of spectral density.

The changes in the joint acceptance terms can be studied by reference to the appropriate general curves in Chapter 2. When the pressure differential increases, the parameter  $L_1/\zeta_{mn}$ , where  $\zeta_{mn}$  is the excitation correlation length associated with the (m-n) modal natural frequency, will increase at a rate proportional to the change in the natural frequency. The values of  $L_1/\zeta_{mn}$  for  $\Delta p=0$  are given in Table 5.3. Taking the (1-1)



and (2-2) modes of the 3.5in x 3.5in panel as an example, it is seen from Figures 5.26 that the condition  $\frac{\omega \delta^*}{U_c} < 0.37$  is satisfied at all pressure differentials. From Figures 2.2 and 2.16, the longitudinal joint acceptance  $j_{1,1}(\omega)$  and the lateral joint acceptance  $j'_{1,1}(\omega)$  decrease in value as  $\Delta p$  increases. Thus the total predicted change of displacement power spectral density with pressure differential is greater than that due to a stiffness change only. This is shown by the corresponding curves in Figure 5.35. In the case of the (2-2) mode,  $j_{2,2}(\omega)$  shows a decrease as the pressure differential increases (Figure 2.3) but  $j'_{2,2}(\omega)$  shows a larger increase, the product  $j_{2,2}(\omega) \cdot j'_{2,2}(\omega)$  being greater than unity. Thus the combined effect of the joint acceptance and stiffness terms gives a rate of change of spectral density which is less than that predicted on a stiffness basis alone. However, for the pressure differential range available and for the modes investigated, the changes in the panel joint acceptance are small and the spectral density changes depend mainly on the effective stiffness of the panel. In some early experiments, Bull, Wilby and Blackman (1963), it was shown that the static pressure differential had a significant effect on a panel of 0.005 inch thickness but the panel was damaged before the measurements could be concluded.

### 5.8 General Discussion

In the comparison of theoretical and experimental results it was seen that the theory overestimates the magnitude of the vibration, for reasons already stated, but predicts with reasonable accuracy the variation of the response with the parameters considered. However, there are one or two exceptions to the general rule, and these occur mainly at low mode orders. In particular the (1-1) modes are found to experience the greatest divergence between theory and experiment. This is not unexpected because the errors due to the assumed mode shape will be most significant in the (1-1) mode. It has been assumed that the difference between the joint acceptance terms for simply supported and fully fixed modes remains constant when the excitation parameters are varied, but this may not be valid for the low order modes.

Errors may arise because of inadequacies in the representation of the excitation pressure field. The response in the (1-1) mode will depend, more than in any other mode, on the excitation cross correlation measurements for large separation distances and low values of  $\frac{\omega \xi}{U_c}$ , ranges where the experimental data is not very reliable. Further the assumption for separability of the excitation narrow band cross correlation coefficient in the  $x_1$  and  $x_3$  directions,

$$|\rho_p(\xi_1, \xi_3, \tau; \omega)| = |\rho_p(\xi_1, 0, \tau; \omega)| \cdot |\rho_p(0, \xi_3, \tau; \omega)|$$

is not well substantiated in the low frequency range. However, in spite of the possible sources of error, the theory gives a good approximation of the response variation in the fundamental modes.

The divergence between theory and experiment is more difficult to explain when considering the effect of flow velocity. In this case the most important change in the excitation cross correlation coefficient will probably be that associated with the correlation length  $\zeta$ , which is directly proportional to the convection velocity. Inspection of the results suggests that the theory tends to overestimate the effect of flow velocity when  $L_1/\zeta$  is in the neighbourhood of the coincidence value but underestimates the effect when  $L_1/\zeta$  is much greater than  $2\pi$ , that is when the convection velocity is well below that required for coincidence in the mode considered. Unfortunately the limited amount of data prevents this explanation from being presented with much confidence, but the discrepancy may be due to the different shapes of the joint acceptance curves for simply supported and fully fixed modes.

## 5.9 Summary

The vibration of the experimental panels has been measured, in general at a quarter point on a diagonal, and under all the experimental conditions the total r.m.s. displacement at the measuring point did not exceed 1% of the panel thickness. After making allowances for the position on the panel surface and for the possible peak to r.m.s. displacement ratio, it could be assumed that the vibration was essentially linear. Total and modal root

mean square displacements show that the theory overestimates the response at all boundary layer thicknesses and flow velocities, but predicts quite accurately the variation of the response with boundary layer thickness.

Spectral analysis of the measurements, in the frequency range 300 - 3,000 c.p.s., showed that the measured and predicted displacement power spectra were similar in shape, although the predictions overestimated the spectral density at the panel natural frequencies. This difference is explained partly by the assumption of simply supported mode shapes in the theoretical analysis, but close agreement is not expected in random vibration investigations. The theoretical results predict with reasonable accuracy the relative importance of the modes, the fundamental mode being the most important for panels with aspect ratio less than unity and, at the diagonal quarter point position, the mode of order (2-1) being predominant for panels with aspect ratio equal to or greater than unity.

Considering the panel response at the panel natural frequencies, the measured variation of displacement power spectral density with boundary layer thickness was predicted closely by the theory. In general the response increases with boundary layer thickness for the experimental conditions, the change being due partly to the increase in excitation power spectral density for the frequency range of interest, and partly to the change in the excitation correlation pattern. In the higher order modes, a response maximum is reached at the boundary layer thickness at which the excitation spectral density, for the frequency associated with the mode, reaches a maximum. Further increases in the boundary layer thickness cause a decrease in the modal response. When the effect of the excitation spectral density was eliminated it was found that the change in the excitation correlation pattern could produce either an increase or a decrease in the panel displacement power spectral density function for unit excitation, the rate of change of response being determined by the values of the non-dimensional parameters  $L_1/\zeta$ ,  $L_3/\zeta$  and  $L_1/\delta^*$ . Thus some modes showed an increase in  $G_d(f)/G_p(f)$  with boundary layer thickness at one Mach number and a decrease at the other Mach number. In all cases

the rate of change of response to unit excitation with boundary layer thickness were small, the estimated changes for the experimental conditions being less than  $\pm 3$ dB for a two-fold increase in boundary layer thickness.

The response of the panels increased when the airflow velocity was increased from 329ft/sec to 540ft/sec. Theoretically it was shown that the change was due to an increase in the excitation power spectral density and a change in the excitation correlation pattern. Considering the response to unit excitation at the panel natural frequencies, measured and predicted results showed an increase in response with Mach number for the majority of the modes. However, there was a marked difference between the experimental and theoretical results, because the theory predicted larger changes with Mach number than those measured for the lower order modes, and smaller changes than those measured for the higher order modes. Tentative explanations of this discrepancy have been proposed but it was not possible to extend the investigation because of the limited performance of the wind tunnel.

It has been shown theoretically in Chapter 2, using a simplified form of the excitation and correlation function, that the response in certain modes would be a maximum when the direction of convection  $\theta$  of the pressure field had a value in the range  $0^\circ < \theta < 90^\circ$ , whilst other modes would have a maximum response at  $\theta = 0^\circ$  or  $90^\circ$ . This has been confirmed by experiment at a Mach number of 0.3, the direction of convection being changed by rotation of the experimental panel. Thus the orientation of a structure relative to the flow direction may be of importance in determining the response in certain frequency ranges.

The majority of the panel vibration measurements were made in the absence of a static pressure differential across the panel. When a static pressure differential, to a maximum of 2.4lb/in<sup>2</sup>, was introduced there was an increase in the panel natural frequencies and a decrease in the displacement power spectral density. It was shown that, for the experimental conditions, the change in panel response was due mainly to the change in effective stiffness of the structure, the changes in natural frequency causing only small changes in the associated excitation cross correlation

functions. However, when larger pressure differentials, or structures with lower basic stiffness, are considered, changes in the joint acceptance at the natural frequencies may become significant.

## CHAPTER 6

### Measured Response to Acoustic Excitation

#### 6.1 Introduction

When the vibration of large scale structures is being investigated it is often not possible to expose more than a small area of structure to turbulent boundary layer excitation. Thus alternative forms of random excitation are used, and it is necessary to be able to extrapolate the experimental results to include the case of boundary layer excitation. The experimental panels used in the present investigation could be exposed to random acoustic excitation in the form of grazing incidence plane waves in a siren tunnel, or inclined plane waves in the far field of a small cold air jet, and the results could be compared with those for boundary layer excitation. Initial measurements, presented by Bull, Wilby and Blackman (1963), showed that the responses to siren and air jet excitation were similar, and only siren excitation was used in later measurements.

#### 6.2 Root Mean Square Displacement

The response of the panels to random acoustic excitation was measured when the specimens were placed in the siren tunnel. The panels were positioned so that the direction of propagation of the plane waves was in the negative  $x_1$  direction, and the vibration was measured at the positions on the panel surface which were used in the boundary layer measurements. The panel total r.m.s. displacements at the measuring positions are shown in Table 6.1. Comparison with the results in Figure 5.2 shows that the vibration is greater than that due to boundary layer excitation, due partly to the increase in the excitation power spectral density at the lower frequencies, shown in Figures A.2 and A.9. The maximum r.m.s. displacement ( $5.8 \times 10^{-4}$  inch) again occurs in the 3.5 inches square panel, and is approximately 4% of the panel thickness. The vibration should be linear even for the peak displacements and no non-linear vibration was observed on the monitoring oscilloscope.

Table 6.1

Total Root Mean Square Displacement at  
the Probe Measuring Position  
(Siren Excitation)

Panel	Measuring Position		r.m.s. Displacement (inch)
	$x_1$ (inches)	$x_2$ (inches)	
3.5in x 3.5in	0.88	0.88	$5.8 \times 10^{-4}$
4.0in x 2.75in	1.00	1.375	$5.5 \times 10^{-4}$
	1.00	0.688	$3.2 \times 10^{-4}$
2.75in x 4.0in	0.688	3.00	$3.0 \times 10^{-4}$
4.0in x 2.0in	1.00	1.00	$6.7 \times 10^{-5}$
	1.00	0.50	$5.4 \times 10^{-5}$
2.0in x 4.0in	0.50	3.00	$4.5 \times 10^{-5}$

### 6.3 Displacement Spectra

Measured response spectra for panels 2 to 6 are shown in Figures 6.1 to 6.5. The spectra are presented for the frequency range to 3,000 c.p.s. used in the boundary layer measurements but, as discussed in Section A.4, the excitation in the frequency range above (approximately) 1,100 c.p.s. is a poor representation of grazing incidence plane waves propagating in a direction parallel to the tunnel axis. Thus experimental results in the frequency range above 1,100 c.p.s. should be treated with reserve because the excitation correlation function deviates from the ideal form. Because of this upper limit on the frequency range the useful information is restricted to a small number of low order modes. The measured spectra have been corrected for loss of resolution at the natural frequencies of the low order modes, using the method of Appendix B.

Panel displacement spectra have been calculated, from the theoretical analysis in Section 2.5, and they are shown in Figures 6.1 to 6.5 for comparison with the measurements. The spectra were calculated on the assumption that the cross terms could be neglected, but the combined effect of the joint and cross terms is shown at the panel natural frequencies. The cross terms are seen to have a very small effect on the estimated response but the contribution is greater than that for boundary layer excitation. In Figure 6.4 the effect of the cross terms is shown at two of the troughs in the estimated spectrum. At these frequencies the cross terms have a greater effect on the spectrum than at the natural frequencies and the correction is much larger than was shown in Figure 5.8 for boundary layer excitation. The reason for the difference is due to changes in the joint terms rather than in the cross terms. Under siren excitation the response in the (3-1) mode, estimated from the joint term contribution only, is small because  $L_1/\ell$  is close to a value associated with a joint acceptance minimum. Thus the cross term contribution has a larger value relative to the joint terms than it does in the boundary layer case when the joint term contribution is much larger.

Because of the assumption of unit correlation in the lateral direction, the estimated response is zero for all modes (m-n) where n is even. These



modes do appear in the measured spectra and their presence indicates the divergence between the ideal and the actual lateral correlation functions, or the existence of slight asymmetry in the panel mode shapes. At high frequencies where the excitation does not conform to the ideal model, the differences between the theoretical and experimental spectra are large but at low frequencies the measured response in the (1-2) modes of panels 2 and 3 does not show a large deviation from the theoretical spectra. However, there is a large difference between theory and experiment in the vibration of the (1-2) mode of the 3.5in x 3.5in panel. The natural frequencies of the (1-2) and (2-1) modes of the square panel are close together and modal interaction might be expected, but this was not observed in the discrete frequency measurements presented in Appendix C. Thus the presence of the measured response in the (1-2) mode must be due to differences between the actual and assumed lateral correlation functions for the excitation field, and to slight irregularities in the panel mode shape.

Apart from the above exceptions when  $n$  is even, the predicted spectral density exceeds the measured value, as was found for boundary layer excitation. The ratio of the estimated spectral density to the measured spectral density is shown in Table 6.2 for the modes of interest. The values of the ratio are similar to those for boundary layer excitation and they do not show a continuation of the apparent increase of the ratio with flow or convection velocity which was observed in the results in Table 5.2. The change from the boundary layer to acoustic excitation results in an increase in convection velocity by a factor of approximately 2.5.

The results in Figures 6.1 to 6.5 are presented in terms of the response to unit excitation so the spectra can be compared directly with the response spectra for boundary layer excitation contained in Figures 5.5 to 5.13, without the necessity of correcting for differences in excitation spectral density. The spectra show one obvious difference between the response to boundary layer excitation and the response to acoustic excitation. The displacement spectra for acoustic excitation are dominated by the vibration in the fundamental (1-1) mode, whereas at the corresponding positions on the panels, the boundary layer induced

Table 6.2

Ratio of Theoretical to Experimental  
Displacement Power Spectral Density

(Siren Excitation)

Panel	Mode Order (m-n)	$\frac{\text{Theoretical } G_d(f)}{\text{Measured } G_d(f)}$
3.5in x 3.5in	1-1	3.4
	2-1	2.1
4.0in x 2.75in	1-1	2.9
	2-1	8.3
	3-1	0.5
2.75in x 4.0in	1-1	4.0
	2-1	5.8
4.0in x 2.0in	1-1	1.5
	2-1	11.5
2.0in x 4.0in	1-1	1.7

vibration shows that the response of some of the higher order modes is of a similar magnitude to that of the (1-1) mode. This is due partly to the low or zero response to the acoustic field in the low frequency (1-2) and (2-2) modes, particularly in the response spectra for the 2.0in x 4.0in and 2.75in x 4.0in panels, but it is due also to changes in the relative magnitudes of the acceptances of the other modes.

The relative importance of the modes for which  $n$  is odd depends mainly on the joint acceptance terms, and the effect on these terms of the change from boundary layer to acoustic excitation can be estimated from the non-dimensional curves in Chapter 2. If, as in the present investigation, the turbulent boundary layer is associated with subsonic flow, there will be an increase in convection velocity at a given frequency if acoustic excitation is substituted for the boundary layer. There will be a corresponding decrease in the non-dimensional parameter  $L_1/\zeta_{mn}$  ( $= \frac{4L_1 f_{mn}}{U_c}$ ) with associated changes in the joint acceptance. Also there will be a change in the exponential decay rate of the pressure narrow band cross correlation coefficient and, from Figures 2.2 to 2.5, this can have a very strong effect on the joint acceptance. The influence of the boundary layer thickness on the response to boundary layer excitation has to be considered but the effect will probably be less important than the first two changes.

Values of  $L_1/\zeta_{mn}$  for the lower order modes are shown in Table 6.3 and can be compared with the corresponding values in Table 5.3 for the boundary layer excitation, the values for acoustic excitation being approximately 0.4 times the values at  $M_0=0.5$  in the boundary layer case. In the (1-1) mode  $L_1/\zeta_{mn}$  has values less than unity for all panels exposed to the acoustic field and there will be an increase in the vibration in this mode for any of the experimental panels when the convection velocity increases due to the change from boundary layer to acoustic excitation. In the (2-1) mode,  $L_1/\zeta_{mn}$  changes from values in the range 2.0 to 4.0 for the boundary layer to values of 1.0 to 1.6 for the acoustic excitation. Thus from Figures 2.3 and 2.7 the longitudinal joint acceptance for acoustic excitation is less than in the boundary layer case. These variations in the joint acceptance explain the spectrum change from a shape in which the (1-1) and (2-1) modes

Table 6.3

Value of Non-Dimensional Panel Length at  
Natural Frequencies.

(Siren Excitation)

Panel	Mode Order (m-n)	$L_1/\zeta_{mn}$
3.5in x 3.5in	1-1	0.53
	2-1	1.03
	1-3	1.12
	3-1	1.69
	2-3	2.07
4.0in x 2.75in	1-1	0.68
	2-1	1.01
	3-1	1.63
2.75in x 4.0in	1-1	0.47
	2-1	1.09
	1-3	1.05
	2-3	1.68
4.0in x 2.0in	1-1	1.30
	2-1	1.54
	3-1	2.10
2.0in x 4.0in	1-1	0.65
	1-3	1.65

are of similar importance for boundary layer excitation to one in which the (1-1) mode is predominant, under acoustic excitation. The extent of the change will depend on the value of  $L_1/\zeta_{mn}$  for the modes considered. If the natural frequency of the (1-1) mode, or the panel length, is large so that  $L_1/\zeta_{1,1}$  is in the neighbourhood of a zero of the joint acceptance  $j_{1,1}(\omega)$  (when  $\alpha_1=0$ ) then the relative effects of the boundary layer and acoustic pressure fields on the panel vibration will differ from those associated with the experimental panels.

Figures 2.2 to 2.5 can be used to estimate the effect, on panel response, of deviations of the longitudinal excitation cross correlation coefficient from the ideal of an undamped cosine. From Table 6.3 and Figures 2.2 and 2.3 it is seen that variations of  $\alpha_1$  will have a negligible effect on the (1-1), (1-3), (2-1) and (2-3) modes shown in the table, but from Figure 2.4 there will be a significant effect on the (3-1) modes. In the latter case the values of  $L_1/\zeta_{mn}$  lie in the neighbourhood of a zero of the longitudinal joint acceptance when  $\alpha_1=0$  and the theory will underestimate the vibration in the mode, particularly for the 4.0in x 2.0in panel where the value of  $L_1/\zeta_{mn}$  is very close to the zero condition. In Figures 6.3 to 6.5 it is seen that the vibration in the (3-1) mode is underestimated by the theory, and part of the discrepancy can now be attributed to the deviation of the pressure field from the ideal. In the lateral direction it is possible that small deviations of the pressure cross correlation coefficient from the ideal value of unity will have a small effect, except in the case of modes with  $n$  even, when the response will be sensitive to changes in the pressure correlation function. However changes in the pressure correlation decay rate will make only a small contribution to the difference between theory and experiment for the modes in Table 6.2.

#### 6.4 Angle of Convection

Because of the limited useful frequency range, an investigation into the effects of the angle of convection on the panel response does not have a great value. However, the response of the (1-1) and (2-1) modes of the 4.0in x 2.75in panel was measured for a range of values of the angle of convection  $\theta$ ,  $0^\circ \leq \theta < 90^\circ$ , and the results are shown in Figure 6.6, the

displacement spectral density for  $\theta=0^\circ$  being used as a datum. The angle  $\theta=0^\circ$  indicates that the major axis of the panel is parallel to the direction of convection.

The theoretical displacement power spectral density, calculated from equation (2.93) at the panel natural frequencies, is shown in Figure 6.6 and the curves closely predict the measured variation with angle of convection. As in the case of boundary layer excitation (Figure 5.30), convection direction has only a small effect on the vibration in the (1-1) mode. The response in the (2-1) mode varies markedly with angle of convection for acoustic excitation, the displacement being theoretically zero when  $\theta=90^\circ$ , and the variation is considerably larger than for boundary layer excitation.

#### 6.5 Summary

To provide a comparison with the boundary layer induced vibration, the experimental panels were exposed to grazing incidence random acoustic plane waves. Measured overall root mean square displacements were greater than those for the boundary layer excitation, but, at the quarter point along a panel diagonal, they did not exceed 4% of the panel thickness. The results showed good agreement with the estimated spectra in the frequency range below 1,100 c.p.s., the range in which the experimental conditions satisfied the theoretical assumptions of freely propagating acoustic plane waves, but showed a wide divergence at higher frequencies. This divergence could be explained in part by modification of the theoretical assumptions.

The vibration occurred predominantly in the (1-1) mode, the measured displacement power spectral density for unit excitation at the natural frequency of the mode being greater, as predicted, than that for boundary layer excitation. There was negligible measured response in the modes of order (m-n) where n is even, the theoretical response in these modes being zero. Exceptions arose at the higher frequencies when the excitation deviated from the ideal. Limited measurements showed that the effect of the direction of convection on the modal response could be closely predicted.

## CHAPTER 7

### Conclusions

The response of simple structures to random excitation, in the form of a naturally developed turbulent boundary layer or acoustic plane waves, has been discussed on the basis of theoretical and experimental results. Summaries of the detailed discussion have been given at the end of each chapter and it is possible now to draw several general conclusions.

- (1) Under assumptions of separability of the excitation and response functions in the co-ordinate directions, the joint acceptance can be separated into longitudinal and lateral components. In general the longitudinal acceptance is more important than the lateral acceptance, which is a slowly varying function. The lateral acceptance depends on the boundary layer pressure lateral correlation function which often is not known with confidence. However, in many cases it will be sufficiently accurate to use only a simplified form of the correlation function.
- (2) For boundary layer excitation, the response cross terms due to the statistical coupling of the normal modes, are negligible when the damping is light. In any case, when the pressure field is convected along the longitudinal axis of the structure, the cross terms for modes  $(m-n)$  and  $(r-s)$  are zero when  $n+s$  is odd.

When the structure is exposed to acoustic excitation and the damping is light, the cross terms are negligible at the natural frequencies but may be significant off-resonance, at spectral troughs close to the natural frequencies of modes for which the joint acceptance is small. However, the off-resonance case is of little importance in practice.

- (3) When the response of fully fixed panels to random excitation is estimated using the simplifying assumptions of simply supported mode shapes in the analysis, the predictions exceed the measured values. However in most cases the difference is similar to that expected due to the assumptions. The theory predicts reasonably accurately the variations of the response with boundary layer thickness, static pressure differential, angle of convection and aspect ratio, but discrepancies can occur in the (1-1) mode, which is the mode most likely to be affected by assumptions concerning the edge conditions of the panel. When predicting the effect of flow velocity the theory is less reliable because it overestimates the effect in the neighbourhood of coincidence and underestimates the effect away from coincidence.
- (4) The boundary layer thickness affects the excitation pressure power spectral density function and hence the response spectrum. It affects also the decay rate of the narrow band pressure cross correlation at low Strouhal numbers, but this has only a secondary effect. The modal response at a natural frequency increases with boundary layer thickness until the pressure power spectral density reaches a maximum. Thereafter further increases in the boundary layer thickness will reduce the structural vibration. The concentration of the excitational energy at the lower frequencies, as the boundary layer thickness increases, means that the higher order modes reach a maximum response first, and the response spectra become biased towards the lower order modes.
- Because the total response depends on the vibration in the predominant modes, and these have low natural frequencies, the total root mean square displacement does not reach a maximum until the thicker boundary layers are reached.
- (5) The flow velocity affects the response through the pressure power spectral density function and the excitation correlation length. As the velocity increases there is a general increase in the vibration but, because the excitational energy is distributed over a wider



frequency range, the vibration spectral density increases more quickly at the higher frequencies. Above coincidence, further increases in the flow velocity may reduce the vibration in the associated modes, the change depending on the net effect of excitation spectral density and correlation length changes. The joint acceptance terms do not change very rapidly with flow velocity in the neighbourhood of coincidence, so that the convection velocity must be well separated from the coincidence value if the vibration is to be reduced significantly.

- (6) When the structure is allowed to vibrate in the presence of a static pressure differential, there is a general decrease in the structural response, and an increase in the natural frequencies. The change in the displacement power spectral density function is due mainly to the change in the effective stiffness of the structure, there being little change in the panel joint acceptance as this changes relatively slowly with frequency.
- (7) For a given mode order, and an infinite range of values of the non-dimensional panel length, the maximum response to acoustic excitation will occur at coincidence when the convection direction is parallel to the overall standing wave system in the structure, at a convection angle  $\theta$  where  $0^\circ < \theta < 90^\circ$ .

In the case of boundary layer excitation, the maximum response occurs when  $\theta = 0^\circ$  or  $90^\circ$ , because at other values of  $\theta$  the improved matching between the excitation correlation length and the modal wavelength is cancelled by the increased effective decay rate of the excitation correlation function.

For a fixed value of the non-dimensional panel length, the modal response to either form of excitation may be a maximum for a value of  $\theta$  in the range  $0^\circ < \theta < 90^\circ$ , but the fundamental mode is affected little by changes in the angle of convection.

- (8) Under boundary layer excitation the response spectra of panels with aspect ratios less than unity are dominated by the vibration in the fundamental mode. Panels with aspect ratios greater than unity have displacement spectra which have a relatively greater contribution from the higher order modes.

The total root mean square displacement increases more rapidly with flow velocity when the panel aspect ratio is greater than unity, than when it is less than unity.

- (9) For the structures considered, the vibration in the fundamental mode was greater for acoustic excitation than for boundary layer excitation. However, this conclusion may not be applicable when the panel length is much greater than the acoustic wavelength at the resonance frequency. When comparing the response to boundary layer and acoustic excitation, the correlation decay rate may become more important than the convection velocity. In particular this is true for a mode when the ratio of the panel length to the excitation correlation length at the natural frequency has a value close to that associated with a joint acceptance zero for acoustic excitation. Thus the relative effect of boundary layer and acoustic excitation can depend critically on the associated non-dimensional panel length.
- (10) It is known that, when random techniques are used in the analysis of experimental data, certain corrections may be necessary when the spectrum has a series of resonance peaks. In the present investigation a series of correction curves have been determined and, for the measured power spectral density at a natural frequency to be less than 30% in error, the filter bandwidth must be less than the bandwidth of the spectral peak.
- (11) There are several ways of applying random techniques to the measurement of the damping of structures, but difficulties can arise which limit the use of each of the alternative methods. The

investigation has shown that direct spectral analysis methods are of value only when the filter bandwidth is less than one-quarter of the bandwidth of the resonance peaks. Measurements have shown that the excitation-response cross correlation method is unsatisfactory for very lightly damped structures and that the response autocorrelation decay method is more accurate, provided that the natural frequencies are well separated and the modal response is not small relative to that in neighbouring modes.

- (12) The presence of an airflow increases the damping of the low order structural modes, the largest effect being shown in the fundamental mode. The damping was unaffected by boundary layer thickness.

The results of the present investigation have extended the range of information concerning the response of structures to boundary layer excitation, but further work is required before a complete understanding of the problem is possible. Several aspects of the problem require investigation and some of these can be outlined briefly as a guide to future research work.

(a) Published results, and those of the present investigation, show that there is a discrepancy between the measured and predicted effects of the flow velocity on the structural vibration. In comparisons of theoretical and experimental results it has been assumed that the joint acceptance curves for simply supported and fully fixed panels are similar in shape. The assumption may not be sufficiently accurate for large changes in velocity, and differences in the curves could contribute to the observed discrepancy. Thus it may be necessary to consider more accurate representations of the panel vibrational characteristics.

(b) The majority of the available results refer to single panels and, for use in practical structures, the results have to be extrapolated

to the case of panel-stiffener arrays. Measurements of the vibration of panel arrays are required under laboratory and full scale conditions to establish the circumstances under which the extrapolation is valid. Also, alternative methods have to be determined for the estimation of the vibration of the arrays.

In association with this investigation it may be necessary to obtain in greater detail pressure correlation measurements for small values of frequency, and large separation distances.

(c) In the present investigation it has been assumed that the structural vibration could be represented by a series of normal modes and the vibration is dominated by standing waves, which can be considered to be composed of running and reflected waves. Conditions can arise in which there is no reflected wave, and the panel vibration is represented by a series of running waves without the presence of standing waves. The occurrence of standing and running waves has been investigated by Baroudi (1964) and Maestrello (1965,b,c) but the work could be extended to panel arrays and typical practical structures.

## APPENDIX A

### Excitation Fields

#### A.1 Type of Excitation

The measurements of panel vibration have been restricted to two types of convected random excitation. Interest has been centred mainly on the response to turbulent boundary layer excitation but acoustic plane wave excitation has been used for comparison. The acoustic field can be defined readily but the random characteristics of the boundary layer pressure field require more detailed study based on experimental results. The pressure field under a turbulent boundary layer has been measured by several investigators using flush mounted transducers but the results of particular interest to this investigation were obtained by Bull (1963) in the wind tunnel used for the panel response measurements. The results are in agreement with those of other investigators and include narrow band correlation measurements. Empirical curves can be fitted to the measured boundary layer statistical characteristics and the equations to the curves can be used in the prediction of panel response.

#### A.2 Narrow Band Cross Correlation Coefficient

Assuming that the pressure field is stationary and homogeneous, a narrow band cross correlation function can be defined as

$$R_{p,\Delta\omega}(\xi_1, \xi_2, \tau; \omega_F) = \lim_{T \rightarrow \infty} \frac{1}{2T} \int_{-T}^T p_{\Delta\omega}(\underline{x}, t; \omega_F) p_{\Delta\omega}(\underline{x} + \underline{\xi}, t + \tau; \omega_F) dt \quad \dots (A.1)$$

where  $p_{\Delta\omega}(\underline{x}, t; \omega_F)$  is the filter output when the pressure signal  $p(\underline{x}, t)$  is passed through a filter of bandwidth  $\Delta\omega$  and centre frequency  $\omega_F$ .

It can be shown, using a method similar to that for the derivation of equation (4.27), that the narrow band cross correlation function is

$$R_{p,\Delta\omega}(\xi_1, \xi_3, \tau; \omega_F) = \int_{-\infty}^{\infty} Z_1^*(\omega) Z_2(\omega) S_p(\xi_1, \xi_3, \omega) e^{i\omega\tau} d\omega \quad \dots (A.2)$$

where  $S_p(\xi_1, \xi_3, \omega)$  is the pressure cross power spectral density function and  $Z_1(\omega), Z_2(\omega)$  are the frequency response functions of two filters centred at  $\omega_F$ . Assume that the two filters are identical,

$$Z_1^*(\omega) Z_2(\omega) = |Z(\omega)|^2, \quad ,$$

and that they have ideal rectangular pass band characteristics

$$\begin{aligned} |Z(\omega)|^2 &= 1 & \text{for } \omega_F - \frac{\Delta\omega}{2} < |\omega| < \omega_F + \frac{\Delta\omega}{2} \\ &= 0 & \text{for all other } \omega \end{aligned}$$

Then equation (A.2) becomes

$$R_{p,\Delta\omega}(\xi_1, \xi_3, \tau; \omega_F) = S_p(\xi_1, \xi_3, \omega_F) e^{i\omega_F\tau\Delta\omega} + S_p(\xi_1, \xi_3, -\omega_F) e^{-i\omega_F\tau\Delta\omega}$$

that is, dropping the suffix F,

$$\begin{aligned} R_{p,\Delta\omega}(\xi_1, \xi_3, \tau; \omega) &= 2(C_p(\xi_1, \xi_3, \omega) \cos \omega\tau + Q_p(\xi_1, \xi_3, \omega) \sin \omega\tau) \Delta\omega \\ &= 2|S_p(\xi_1, \xi_3, \omega)| \cos(\omega\tau - B) \Delta\omega \quad \dots (A.3) \end{aligned}$$

$$\begin{aligned} \text{where } S_p(\xi_1, \xi_3, \omega) &= C_p(\xi_1, \xi_3, \omega) - iQ_p(\xi_1, \xi_3, \omega) \\ &= |S_p(\xi_1, \xi_3, \omega)| e^{-iB} \quad \dots (A.4) \end{aligned}$$

A narrow band cross correlation coefficient can now be defined as

$$\begin{aligned} \rho_p(\xi_1, \xi_3, \tau; \omega) &= \frac{R_{p,\Delta\omega}(\xi_1, \xi_3, \tau; \omega)}{R_{p,\Delta\omega}(0, 0, 0; \omega)} \\ &= \frac{|S_p(\xi_1, \xi_3, \omega)| \cos(\omega\tau - B)}{S_p(\omega)} \quad \dots (A.5) \end{aligned}$$

where  $S_p(\omega) = S_p(0, 0, \omega)$  is the excitation power spectral density.

When the pressure field has the form of convected turbulence, the simplest case is that of frozen turbulence convected with velocity  $U_c$  in the positive  $x_1$  direction. The cross correlation function has the property

$$\begin{aligned} R_p(\xi_1, \xi_3, \tau) &= R_p(0, \xi_3, \tau - \tau_0) \text{ where } \tau_0 = \frac{\xi_1}{U_c} \\ &= R_p(\xi_1 - U_c \tau, \xi_3, 0) \end{aligned} \quad \dots (A.6)$$

The cross power spectral density function becomes, from equation (A.6),

$$\begin{aligned} S_p(\xi_1, \xi_3, \omega) &= \frac{1}{2\pi} \int_{-\infty}^{\infty} R_p(\xi_1, \xi_3, \tau) e^{-i\omega\tau} d\tau \\ &= \frac{e^{-\frac{i\omega\xi_1}{U_c}}}{2\pi U_c} \int_{-\infty}^{\infty} R_p(\xi_1, \xi_3, 0) e^{\frac{i\omega\xi_1}{U_c}} d\xi_1 \quad \dots (A.7) \\ &= \frac{\Omega(\frac{-\omega}{U_c}, \xi_3, 0)}{U_c} \cdot e^{-\frac{i\omega\xi_1}{U_c}} \end{aligned}$$

where  $\Omega(\frac{-\omega}{U_c}, \xi_3, 0) = \frac{1}{2\pi} \int_{-\infty}^{\infty} R_p(\xi_1, \xi_3, 0) e^{\frac{i\omega\xi_1}{U_c}} d\xi_1$ , and is real, because

$R_p(\xi_1, \xi_3, 0) = R_p(-\xi_1, \xi_3, 0)$ . Comparing equations (A.4) and (A.7),

$$B = \frac{\omega\xi_1}{U_c}.$$

Thus for frozen turbulence convected with velocity  $U_c$  in the  $x_1$  direction

$$\rho_p(\xi_1, \xi_3, \tau; \omega) = \frac{|S_p(\xi_1, \xi_3, \omega)|}{S_p(\omega)} \cos \omega(\tau - \frac{\xi_1}{U_c}) \quad \dots (A.8)$$

For decaying turbulence, Bull (1960) following Harrison (1958), has shown that the correlation coefficient may be expected to have the form

$$\rho_p(\xi_1, \xi_3, \tau; \omega) = F\left(\frac{\omega\xi_1}{U_c}, \frac{\omega\xi_3}{U_c}\right) \cos \omega(\tau - \frac{\xi_1}{U_c}) \quad \dots (A.9)$$

except at very small values of  $\frac{\omega\xi_1}{U_c}$  and  $\frac{\omega\xi_3}{U_c}$  when  $\xi_1, \xi_3$  are non zero.

It was assumed initially that  $U_c$  was constant, but frequency dependent convection velocities can be used. Correlation coefficients similar to the form shown in equation (A.9) were used to describe the measured results.

### A.3 Boundary Layer Excitation

#### A.3.1 Nature of Pressure Field

The measurements of Bull (1963) can provide an insight into the nature of the pressure field which arises from natural transition from laminar to turbulent flow on a flat wall.

The turbulence can be considered to be composed of pressure eddies of different sizes or wave number. The eddies are convected in the free stream direction, with a range of convection velocities associated with each wave number. However the experimental results indicate that the range of convection velocities is sufficiently narrow for a unique value of the convection velocity to be associated with each wave number. In the evolution of the pressure field the smallest eddies predominate initially, but they decay fairly quickly and the large scale eddies are then of importance. The large eddies decay relatively slowly at a rate which is independent of frequency. This division into small and large scale turbulence is associated with two forms of narrow band cross correlation coefficient.

#### A.3.2 Statistical Properties

The statistical properties of the pressure field can be measured in either the time or frequency domain, and, theoretically, these are equivalent through the Wiener-Khinchin relationships. In practice it is often easier to measure the cross correlation function than the cross power spectral density function, which can then be obtained by Fourier transformation. Alternatively the narrow band cross correlation function, as defined in equation (A.1), can be measured, and this was the method adopted by Bull(1963).

The measured boundary layer pressure power spectral density is shown in Figure A.1, non-dimensionalised in terms of the boundary layer thickness  $\delta$ ,



mean square pressure  $\langle p^2 \rangle$ , and free stream velocity  $U_0$ . The power spectral density is expressed in terms of the measurable single sided function  $G_p(\omega)$  where  $\omega \geq 0$ , and  $G_p(\omega) = 2S_p(\omega)$ .  $G(\omega)$  is defined by

$$G(\omega) = \frac{2}{\pi} \int_0^{\infty} R(\tau) \cos \omega \tau d\tau$$

The spectrum is smooth and has a broad maximum in the region of  $\frac{\omega \delta}{U_0} = 2$ . From the tunnel characteristics in Table 3.1, Figure A.1 gives the excitation spectra shown in Figure A.2 for the panel positions in the tunnel working section, where, for convenience, the spectral density is expressed as  $G_p(f) = 2\pi G_p(\omega)$ . The spectra were estimated for positions corresponding to the centres of the panels and it is assumed that the spectral densities are effectively constant over the panel area. The measurements in Figure A.1 were carried out on a rigid wall but, in the absence of information, it has been assumed that the boundary layer pressure field is unchanged by the presence of the flexible panel. The vibration amplitudes of the panel are very small relative to the boundary layer displacement thickness  $\delta^*$ , so distortion of the pressure field should be small. The spectral shapes in Figure A.2 assume that there is no interference from the acoustic field in the tunnel. It is shown in Chapter 3 that this can occur at low frequencies and corrections have to be made where necessary. The overall hydrodynamic pressure in the boundary layer is approximately 124dB re  $2 \times 10^{-3}$  dynes/sq.cm for a flow velocity  $U_0 = 329$  ft/sec., and 132 dB for  $U_0 = 540$  ft/sec.

The amplitude of the measured narrow band cross correlation coefficient in the longitudinal direction is shown in Figure A.3 and, except at low values of  $\frac{\omega \xi_1}{U_c}$ , the results can be represented approximately by the single exponential function

$$|\rho_p(\xi_1, 0, \tau; \omega)| = e^{-\frac{0.1\omega|\xi_1|}{U_c}} \dots (A.10)$$

At low values of  $\frac{\omega \xi_1}{U_c}$  the measurements diverge from the fitted curve, the divergence occurring at a higher value of  $\frac{\omega \xi_1}{U_c}$  for a higher value of  $\frac{\xi_1}{\delta^*}$ . In Figure A.4 the correlation amplitude at low  $\frac{\omega \xi_1}{U_c}$  is shown as a function of

$\frac{\xi_1}{\delta^*}$  and a single exponential function

$$|\rho_p(\xi_1, 0, \tau; \omega)| = e^{-\frac{0.037|\xi_1|}{\delta^*}} \quad \dots (A.11)$$

has been fitted. The data in Figure A.3 can now be separated into two regions, the boundary between the regions being given approximately by the condition  $\frac{\omega \delta^*}{U_c} = 0.37$ . When  $\frac{\omega \delta^*}{U_c} \geq 0.37$  the correlation coefficient can be expressed as a function of  $\omega$ , equation (A.10), and when  $\frac{\omega \delta^*}{U_c} < 0.37$ , the coefficient is independent of frequency and is a function of  $\frac{\xi_1}{\delta^*}$  only, equation (A.11). Curves of constant  $\frac{\xi_1}{\delta^*}$  are represented by the broken lines in Figure A.3.

The narrow band cross correlation measurements in the lateral direction can be similarly divided into two regions as indicated in Figure A.5. The measured correlation amplitude can be represented again by a single exponential function, given by

$$|\rho_p(0, \xi_3, \tau; \omega)| = e^{-\frac{0.715\omega|\xi_3|}{U_c}} \quad \dots (A.12)$$

except at low values of  $\frac{\omega \xi_3}{U_c}$  when the results diverge from the fitted wave. Comparing Figures A.3 and A.5, or equation (A.10) and (A.12), the correlation amplitude decays more rapidly with distance in the lateral direction than in the longitudinal direction.

In Figure A.6, an empirical curve has been fitted to the measured correlation coefficients at small  $\frac{\omega \xi_3}{U_c}$ . The data in the figure differs from that in the preceding three figures because the results have a non-zero asymptote at large  $\frac{\xi_3}{\delta^*}$  and the equation for the curve is

$$|\rho_p(0, \xi_3, \tau; \omega)| = 0.28 + 0.72 e^{-\frac{0.547|\xi_3|}{\delta^*}} \quad \dots (A.13)$$

The correlation amplitude curves derived from equation (A.13) are shown in Figure A.5 as broken lines. Physically it is difficult to explain the presence of the non-zero values of the cross correlation coefficient at large  $\frac{\xi_3}{\delta^*}$  and they may result from low frequency acoustic disturbances in the wind tunnel. Under free conditions it is probable that the lateral cross correlation coefficient will approach zero for small  $\frac{\omega \xi_3}{U_c}$  and large  $\frac{\xi_3}{\delta^*}$ .

However, equation (A.13) represents the excitation field in the wind tunnel and will be used in the estimation of the panel vibration. The effect of the constant term in equation (A.13) on the panel response is discussed in Section 2.6.3. The boundary between the regions of validity of equations (A.12) and (A.13) is not well defined in the lateral direction and, from Figure A.5, is given by the condition

$$|\xi_3| = k_3 = \left( 9.1 \log_e \left( \frac{U_c}{\omega \delta^*} \right) - 5.45 \right) \delta^* \quad \dots (A.14)$$

Thus, when  $|\xi_3| \geq k_3$  the amplitude of the narrow band lateral cross correlation coefficient is given by equation (A.12) and when  $|\xi_3| < k_3$ , by equation (A.13).

The measurements of Bull (1963) indicate that, at least for high values of  $\frac{\omega \xi_1}{U_c}$ , the amplitude of the cross correlation coefficient can be represented fairly accurately by

$$|\rho_p(\xi_1, \xi_3, \tau; \omega)| = |\rho_p(\xi_1, 0, \tau; \omega)| \cdot |\rho_p(0, \xi_3, \tau; \omega)| \quad \dots (A.15)$$

At low  $\frac{\omega \xi_1}{U_c}$  equation (A.15) is less accurate but, from the limited data available, it still seems to be a reasonable approximation.

The frequency dependent convection velocity for the turbulent pressure field is shown in Figure A.7 and the measurements are found to be fairly well represented by the equation

$$U_c = U_c(\omega) = \left( 0.59 + 0.30 e^{\frac{-0.89 \omega \delta^*}{U_0}} \right) U_0 \quad \dots (A.16)$$

The value of the convection velocity given by the above equation is assumed to be associated with a unique pressure eddy wave number.

#### A.4 Acoustic Excitation

The grazing incidence acoustic field in the siren tunnel has a restricted frequency range with lower and upper cut-off frequencies determined by the design of the tunnel and siren. The low frequency limit occurs at approximately 100 c.p.s., in the neighbourhood of the theoretical cut-off frequency of the

acoustic horn. At high frequencies the acoustic output of the siren is limited by the response of the modulator coil and the spectrum falls off sharply at frequencies greater than 800 c.p.s. The shape of the noise spectrum can be controlled, within the limited frequency range, by the use of electronic filters in the excitation circuit of the modulator coil. A typical third octave spectrum for the acoustic excitation field is shown in Figure A.8. The figure contains also the spectrum of the noise field due to the jet noise effect of the air flowing through the siren orifices when the airflow modulator is not operating. Comparing the two spectra in Figure A.8 it is seen that at frequencies greater than 1,500 c.p.s. the noise is essentially that due to the jet noise effect. The excitation pressure power spectral density curve, corresponding to Figure A.8, is presented in Figure A.9 and the data can be used to determine the measured panel vibration in terms of the response to unit excitation.

The pressure distributions and correlation coefficients in the siren tunnel are contained in the calibration charts of Clarkson and Pietrusewicz (1961). Over the panel area the overall noise level will be constant to within 0.5 dB, and in narrow frequency bands, to within 1.0 dB. The calibration charts show that, for frequencies below 1,100 c.p.s. and for separation distances equal to the maximum panel dimension, the lateral narrow band cross correlation coefficient has a value which is within 5% of unity, but there is a greater divergence, of the order of 15%, from the ideal of an undamped cosine correlation form in the longitudinal direction. As the frequency increases the acoustic field is distorted by reflections from the tunnel walls and the correlation coefficient diverges from the ideal of freely propagating plane waves. However, in the prediction of the panel vibration it is assumed that the narrow band cross correlation coefficient is an undecaying cosine in the longitudinal direction and has a value of unity in the lateral direction. Within experimental accuracy, and for the limited frequency range considered, a comparison of the theoretical and experimental vibration spectra, based on the above assumption, should be valid.

### A.5 Summary

From the measurements of the statistical properties of the boundary layer pressure field, the narrow band cross correlation coefficient can be expressed in a general form which can be modified to fit other types of convected excitation. The cross correlation coefficient has the form

$$\rho_p(\xi_1, \xi_3, \tau; \omega) = |\rho_p(\xi_1, \xi_3, \tau; \omega)| \cos \omega(\tau - \frac{\xi_1}{U_c}) \quad \dots (A.17)$$

for convection with velocity  $U_c$  in the positive  $x_1$  direction.

The coefficient amplitude can be written in separable form

$$|\rho_p(\xi_1, \xi_3, \tau; \omega)| = |\rho_p(\xi_1, 0, \tau; \omega)| \cdot |\rho_p(0, \xi_3, \tau; \omega)| \quad \dots (A.18)$$

The amplitude of the longitudinal narrow band cross correlation coefficient is

$$|\rho_p(\xi_1, 0, \tau; \omega)| = e^{-a_1 |\xi_1|} \quad \frac{\omega \delta^*}{U_c} \geq k_1 \quad \dots (A.19)$$

$$= e^{-a_2 |\xi_1|} \quad \frac{\omega \delta^*}{U_c} < k_1 \quad \dots (A.20)$$

where  $a_1 = \frac{a_1 \omega}{U_c}$ ,  $a_2 = \frac{a_2}{\delta^*}$  and  $a_1, a_2$  are constants.

The amplitude of the lateral narrow band cross correlation coefficient is

$$|\rho_p(0, \xi_3, \tau; \omega)| = e^{-a_3 |\xi_3|} \quad |\xi_3| \geq k_3 \quad \dots (A.21)$$

$$= c + d e^{-a_4 |\xi_3|} \quad |\xi_3| < k_3 \quad \dots (A.22)$$

where  $a_3 = \frac{a_3 \omega}{U_c}$ ,  $a_4 = \frac{a_4}{\delta^*}$  and  $a_3, a_4$  are constants.

The convection velocity  $U_c$  is a function of angular frequency  $\omega$  and is given by

$$U_c = U_c(\omega) = \left( \kappa_1 + \kappa_2 e^{-\frac{\kappa_5 \omega \delta^*}{U_0}} \right) U_0 \quad \dots (A.23)$$

The particular values of the coefficients associated with the boundary layer measurements of Bull (1963) are :-

$$\begin{array}{ll} \alpha_1 = 0.1 & c = 0.28 \\ \alpha_2 = 0.037 & d = 0.72 \\ \alpha_3 = 0.715 & \kappa_1 = 0.59 \\ \alpha_4 = 0.547 & \kappa_2 = 0.30 \\ \alpha_5 = 0.89 & \end{array}$$

and the ranges of validity of the correlation coefficients in equations (A.19) to (A.22) are

$$k_1 = 0.37, \quad k_3 = \left( 9.1 \log_e \left( \frac{U}{\omega \delta^*} \right) - 5.45 \right) \delta^*$$

For a convected pressure field which is not a boundary layer, the terms containing the boundary layer displacement thickness  $\delta^*$  do not appear and the correlation coefficient forms reduce to equations (A.19) and (A.21). The convection velocity  $U_c$  will be given by equations which differ from equation (A.23), and may be independent of frequency as in the case of an acoustic field. Theoretically, for acoustic plane waves propagating in the  $x_1$  direction,  $a_1 = a_3 = 0$  and

$$|\rho_p(\xi_1, 0, \tau, \omega)| = 1 = |\rho_p(0, \xi_3, \tau, \omega)|.$$

## APPENDIX B

### Effects of Filter Bandwidth in Spectral Analysis

#### B.1 Introduction

In the measurement of power spectral density, one of the important sources of error is the finite bandwidth of the analysing filter. The choice of filter is usually controlled by two requirements. The bandwidth must be narrow so that there is no loss of spectral resolution but, conversely, the bandwidth must be wide so that the statistical uncertainty error is small. When the data record is short and there is an unlimited choice of filter bandwidth, an optimum must be achieved to obtain a balance between spectral resolution and statistical reliability. Alternatively when the record is sufficiently long, and the only criterion is the required spectral resolution, there may be only a limited number of filter bandwidths available. In such circumstances the filter bandwidths used may be significantly greater than the bandwidths of the spectral peaks, and corrections have to be applied if more accurate estimates of the power spectrum are required.

Under the assumptions of ergodicity it has been shown by Morrow (1958) that the standard deviation error  $\epsilon_s$  for the power spectral density function  $G(f)$  is

$$\epsilon_s = \frac{1}{\sqrt{\Delta f \cdot T}} G(f)$$

where  $\Delta f$  is the filter bandwidth and  $T$  is the averaging time. In the panel vibration analysis the narrowest filter used had a 1.2% bandwidth which, at a frequency of 500 c.p.s. is equivalent to  $\Delta f = 6$  c.p.s., and the integrating time was 50 seconds. The statistical error was  $\epsilon_s = 6\%$ , indicating good statistical reliability. However the filter bandwidths were large relative to the bandwidths of the resonance peaks, and corrections had to be made to the measured spectra.

## B.2 Single-degree of Freedom System

If the spectral density function is expressed in terms of frequency  $f$ , the Wiener-Khinchin relations are :

$$\begin{aligned} G(f) &= 4 \int_0^{\infty} R(\tau) \cos 2\pi f \tau d\tau \\ R(\tau) &= \int_0^{\infty} G(f) \cos 2\pi f \tau df \end{aligned} \quad \dots (B.1)$$

where  $G(f) = 2S(f) = 4\pi S(\omega)$  is the spectral density function which is measured in practice.

For a system with one degree of freedom, the displacement spectral density function is

$$G_d(f) = |H_1(f)|^2 G_p(f) \quad \dots (B.2)$$

where  $H_1(f)$  is the complex response function and can be expressed in terms of viscous or hysteretic damping.  $G_p(f)$  is either the direct excitation spectral density function for single point excitation or has a form similar to a generalised force for distributed loading.

When the vibration is analysed with a filter of bandwidth  $\Delta f_F$  and characteristic  $H_2(f)$ , the measured spectral density function is

$$\begin{aligned} G'_d(f) &= \frac{1}{\Delta f_F} \int_0^{\infty} |H_2(f)|^2 G_d(f) df \\ &= \frac{1}{\Delta f_F} \int_0^{\infty} |H_1(f)|^2 |H_2(f)|^2 G_p(f) df \end{aligned} \quad \dots (B.3)$$

where the dash denotes a "measured" value.

Within the accuracy of the measurements, the filter can be assumed to have the characteristics of an ideal rectangular filter.



$$\begin{aligned} \text{Thus } |H_2(f)|^2 &= 1 & f_F - \frac{\Delta f_F}{2} \leq f \leq f_F + \frac{\Delta f_F}{2} \\ &= 0 & \text{for all other } f \end{aligned} \quad \dots (B.4)$$

where  $f_F$  is the centre frequency of the filter.

If it can be assumed that the excitation spectral density is constant within the range of integration, i.e. within the filter bandwidth, then

$$G_p(f) = \text{constant} = K' \quad \dots (B.5)$$

This is valid for most forms of random excitation.

Substituting equations (B.4) and (B.5) into equation (B.3) gives

$$G_d'(f) = \frac{K'}{\Delta f_F} \int_{f_F - \frac{\Delta f_F}{2}}^{f_F + \frac{\Delta f_F}{2}} |H_1(f)|^2 df \quad \dots (B.6)$$

Assume that the damping is hysteretic and that  $|H_1(f)|^2$  has the normalised form

$$|H_1(f)|^2 = \frac{\nu_r^2 f_r^4}{(f_r^2 - f^2)^2 + \nu_r^2 f_r^4} \quad \dots (B.7)$$

with a maximum value of unity at  $f = f_r$ . Then, from equations (B.6) and (B.7)

$$G_d'(f) = \frac{K'}{\Delta f_F} \int_{f_F - \frac{\Delta f_F}{2}}^{f_F + \frac{\Delta f_F}{2}} \frac{\nu_r^2 f_r^4}{(f_r^2 - f^2)^2 + \nu_r^2 f_r^4} df \quad \dots (B.8)$$

When the definite integral in equation (B.8) is evaluated, and the filter centre frequency  $f_F$  is replaced by  $f$  for convenience, then

$$G'_d(f) = \frac{v_r^2 K'}{2T_r \left(\frac{\Delta f_F}{f_r}\right)} \left( \frac{\log_e \left(\frac{\psi+\phi}{\psi-\phi}\right)}{2 \sqrt{2(T_r+1)}} + \frac{\tan^{-1} \theta}{\sqrt{2(T_r-1)}} \right) \dots (B.9)$$

where  $T_r^2 = 1 + v_r^2$

$$\theta(f) = \frac{\sqrt{2(T_r-1)} \left(\frac{\Delta f_F}{f_r}\right) \left(T_r + \left(\frac{f}{f_r}\right)^2 - \left(\frac{\Delta f_F}{2f_r}\right)^2\right)}{\left(1 - \left(\frac{f}{f_r}\right)^2 + \left(\frac{\Delta f_F}{2f_r}\right)^2\right) - T_r \left(\frac{\Delta f_F}{f_r}\right)^2 + v_r^2}$$

$$\psi(f) = \left(1 - \left(\frac{f}{f_r}\right)^2 + \left(\frac{\Delta f_F}{2f_r}\right)^2\right)^2 + T_r \left(\frac{\Delta f_F}{f_r}\right)^2 + v_r^2 \dots (B.10)$$

$$\phi(f) = \sqrt{2(T_r+1)} \left(\frac{\Delta f_F}{f_r}\right) \left(T_r - \left(\frac{f}{f_r}\right)^2 + \left(\frac{\Delta f_F}{2f_r}\right)^2\right)$$

Evaluation of equation (B.9) for  $\frac{f}{f_r} = 1$  gives the measured peak spectral density  $G'_d(f_r)$ .

For comparison with equation (B.9), the true response spectral density is, from equations (B.2), (B.5) and (B.7),

$$G_d(f) = \frac{K' v_r^2 f_r^4}{(f_r^2 - f^2)^2 + v_r^2 f_r^4} \dots (B.11)$$

and the reduction in resolution at a given frequency  $f$  is given from equations (B.9) and (B.11) by the ratio

$$\frac{G'_d(f)}{G_d(f)} = \frac{(f_r^2 - f^2)^2 + v_r^2 f_r^4}{2T_r f_r^4 \left(\frac{\Delta f_F}{f_r}\right)} \left( \frac{\log_e \left(\frac{\psi+\phi}{\psi-\phi}\right)}{2 \sqrt{2(T_r+1)}} + \frac{\tan^{-1} \theta}{\sqrt{2(T_r-1)}} \right) \dots (B.12)$$

The loss of resolution due to filter bandwidth effects is illustrated in Figures B.1 and B.2 where the measured response peaks for two single degree of freedom systems are predicted from equation (B.9) and compared with the true curve given by equation (B.11). It is assumed in all cases that the excitation has unit spectral density, i.e.  $K' = 1$ , so that the peak of the true curve is unity. The filters used in the calculations have bandwidths of 1.2% and 2.0%, corresponding to the filters available for the vibration analysis. In Figure B.1, where the loss factor  $\nu_r = 0.012$  implies a resonance curve bandwidth which is similar in size to the filter bandwidths, the distortion of the true peak is not large, but the predicted curves show the general trend of reduced peak spectral density and increased resonance curve bandwidth. For the lower loss factor of  $\nu_r = 0.002$  in Figure B.2, there is considerable distortion by both filters and there is a large reduction in resolution. In the neighbourhood of the natural frequency, the measured peak is considerably lower than the true peak, but a reversal occurs close to the natural frequency and the measured spectral density exceeds the true value at all other frequencies. However, it should be observed that the filter bandwidth effect is restricted to a narrow frequency range in the neighbourhood of the natural frequency of the peak, and that there is only a small difference between the true and measured spectra in the lower regions of the resonance curve. For the conditions of Figure B.2, the true and measured values of the spectral density function are approximately equal when the frequency differs from  $f_r$  by more than 2% of  $f_r$ .

Equation (B.12), which predicts the loss of resolution due to filter bandwidth, can be used to correct the measured spectral peaks and corrections of this form have been computed for filters with 1.2% and 2.0% bandwidths. The corrections are shown in Figures B.3 and B.4 for a series of damping loss factors covering the range encountered in the experimental measurements. It is seen that, even for the 1.2% filter bandwidth, there can be large resolution corrections at the natural frequency when the damping loss factor is less than  $\nu_r = 0.004$ . These curves can be used to correct the measured response of a single degree of freedom system or the

response of a multi-degree of freedom system when the vibration can be considered to be due to motion in only one mode. The disadvantage of the method is that the value of the damping loss factor is required before resolution corrections can be estimated. It will be shown in Section B.4 that, in principle, the true damping can be estimated from the measured bandwidth of the spectral peaks but that in practice the results have an unacceptably low degree of accuracy. Thus alternative methods of estimating the damping have to be used before resolution loss corrections can be applied.

### B.3 Multi-degree of Freedom System

In some circumstances the assumption of one degree of freedom is not valid and the method of correction for reduced resolution must be modified. A simple, but rather crude, modification which is suggested here is similar to the corrections proposed in the amplitude response curve method for the discrete frequency determination of modal damping.

In the neighbourhood of a natural frequency of a multi-degree of freedom system, the displacement power spectral density function can be represented as the sum of the spectral density function  $G_d(f)$  for a single degree of freedom system and the background vibration spectral density function  $G_b(f)$  associated with the off-resonant vibration in the other degrees of freedom. The true spectral density function will be

$$G_T(f) = G_d(f) + G_b(f) \quad \dots (B.13)$$

where, for single point excitation,  $G_d(f)$  is given by equation (B.11).

For simplicity, and without much loss of generality, assume that  $G_b(f)$  is independent of frequency, and that

$$G_b(f) = \text{constant} = K'' G_d(f_r) \quad \dots (B.14)$$

where  $G_d(f_r)$  is the peak value of  $G_d(f)$ , i.e. from equation (B.11),  
 $G_d(f_r) = K'$ .

The assumption that the off-resonant vibration has a constant contribution to the spectral density function is similar to the assumption of constant amplitude contribution in the amplitude response curve method for the determination of modal damping, but it has greater validity because there is no problem of phase matching between the resonant and off-resonant contributions in random vibration.

Following the arguments of Section B.2, the true spectral density for unit excitation is

$$G_T(f) = \frac{v_r^2 f_r^4}{(f_r^2 - f^2)^2 + v_r^2 f_r^4} + K'' \quad \dots (B.15)$$

and the measured spectral density is

$$G_T'(f) = \frac{v_r^2}{2T_r \left( \frac{\Delta f}{f_r} \right)} \left( \frac{\log_e \left( \frac{\psi + \phi}{\psi - \phi} \right)}{2\sqrt{2}(T_r + 1)} + \frac{\tan^{-1} \theta}{\sqrt{2}(T_r - 1)} \right) + K'' \quad \dots (B.16)$$

Equations (B.15) and (B.16) have been used to calculate the errors in the measured peak values and these are shown in Figures B.5 and B.6 for the 1.2% and 2.0% bandwidth filters respectively. It can be seen from the figures that in most cases the effect of the background vibration is negligible when the background spectral density is less than 10% of the peak value, i.e. when  $K'' < 0.1$ .

In practice the value of  $K''$  is estimated from the spectral troughs adjacent to the peak under investigation and Figures B.5 and B.6 are used to predict the true spectral peaks from the measured values. However the correction can be applied only if the modal damping is known, from either the measured bandwidth of the resonant peak, or from other sources. An example of the use of the corrections is shown in Table B.1 where data are taken from measurements of panel response to siren excitation, the spectral analysis being carried out with filters of 1.2% and 2.0% bandwidths.

Table B.1

The Effect of Filter Bandwidth on the Measured Peaks in the Displacement Spectra

Mode	Damping Loss Factor $\nu_r$	Uncorrected Spectral Density*			Corrected Spectral Density		
		$\Delta f_F=1.2\%$ (1)	$\Delta f_F=2.0\%$ (2)	$\frac{Col.(1)}{Col.(2)}$	$\Delta f_F=1.2\%$ (3)	$\Delta f_F=2.0\%$ (4)	$\frac{Col.(3)}{Col.(4)}$
<u>Panel: 3.5" x 3.5"</u>							
1-1	0.00477	0.381	0.254	1.50	0.810	0.794	1.02
2-1	0.00248	0.0354	0.0244	1.47	0.122	0.133	0.92
<u>Panel: 4.0" x 2.75"</u>							
1-1	0.00983	0.0706	0.0541	1.31	0.096	0.0985	0.97
1-1	0.00983	0.288	0.220	1.44	0.395	0.364	1.08
2-1	0.00532	0.0268	0.0196	1.37	0.0515	0.0545	0.95
<u>Panel: 4.0" x 2.0"</u>							
1-1	0.00819	0.0163	0.0114	1.43	0.0245	0.0233	1.05
1-1	0.00819	0.0424	0.0285	1.48	0.0637	0.0582	1.09

$\Delta f_F$  = Filter bandwidth

\* Uncorrected for loss of resolution.

Before corrections for loss of resolution were applied, the 1.2% filter gave peak spectral densities which were 30% to 50% greater than those obtained with the 2.0% filter. When the corrections were applied from Figures B.5 and B.6, the spectral densities increased by factors of 2 to 5, and the results for the two filters agreed to within  $\pm 9\%$ .

#### B.4 Bandwidth of Resonant Peaks

The preceding discussion, particularly with respect to Figures B.1 and B.2, has shown that the bandwidth of the filter has an effect on the bandwidth of the response resonant peaks as well as on the spectral density of the resonance curve. The difference between the true and measured bandwidths of the spectral peaks is important in the estimation of modal damping, and the relationship between the two bandwidths can be determined theoretically.

Assume that the system has only one degree of freedom and that the measured spectral density function is given by equation (B.9). Denoting the measured bandwidth of the resonant peak by  $\Delta f_M$  at the half power point, then  $\Delta f_M$  satisfies the equation

$$G_d' \left( d_r + \frac{\Delta f_M}{2} \right) = \frac{1}{2} G_d' (f_r) \quad \dots (B.17)$$

which can be solved numerically. The resulting relationship between the measured and true resonance bandwidths,  $\Delta f_M$  and  $\Delta f_T$  (where  $\Delta f_T = v_r f_r$ ) is shown in Figure B.7 for two filter bandwidths  $\Delta f_F = 0.1 f_r$  and  $0.01 f_r$ . The results are seen to be virtually independent of the filter bandwidth  $\Delta f_F/f_r$ , and are similar to results which Forlifer (1964) obtained, with certain approximations, for viscous damping. Figure B.7 can now be used to predict the value of  $\Delta f_T$ , and hence the modal damping, when the measured bandwidth  $\Delta f_M$  is known.

For practical cases the values of  $\Delta f_T$  estimated by this method may be subject to large errors, and the method is useful in a very limited range of conditions. As an example, consider a system with a hysteretic loss factor  $v_r = 0.006$  and an analysing filter with a 1.2% bandwidth. Then  $\frac{\Delta f_F}{\Delta f_T} = 2.0$

and, from Figure B.7,  $\frac{\Delta f_E}{\Delta f_M} = 0.895$ . When the vibration of this system is analysed,  $\Delta f_M$  will be measured to an accuracy of, at best,  $\pm 10\%$ . Inspection of Figure B.7 shows that the resultant accuracy of estimation of  $\Delta f_T$  will be of the order of  $-35\%$  to  $+235\%$ , which is quite unacceptable. Therefore only when  $\frac{\Delta f_E}{\Delta f_T} < 0.5$  (or  $\frac{\Delta f_E}{\Delta f_M} < 0.45$ ) can this method be used with reasonable accuracy. It could not be used for the vibration analysis of the panels used in these experiments, and other methods (Chapter 4) were used.

#### B.5 Summary.

The effect of the finite bandwidth of the analysing filters on the resolution of peaks in measured spectra has been studied theoretically and found to be large for the conditions in the present experimental investigations. Corrections to the measured spectral density have been derived, to compensate for the loss of resolution. Theoretically it is possible to estimate modal damping from the measured spectra but it has been shown that in practice the errors will be unacceptably large in the present experimental analysis. Ideally the filter bandwidth should be less than one quarter of the resonant peak bandwidth.



## Appendix C

### Panel Natural Frequencies and Mode Shapes

#### C.1 Material Properties

The panel natural frequencies and mode shapes are required for two reasons. A comparison of measured and estimated frequencies and mode shapes will indicate the type of boundary conditions which exist in the experimental panels. Also the true natural frequencies are required for the prediction of the response of the panels to boundary layer and acoustic excitation.

The panels were made from mild steel which showed the grain pattern associated with rolled metal sheet. The presence of a grain pattern suggested that the panels would not possess isotropic elastic properties and this was confirmed by measurements of Young's modulus. The modulus was measured in directions parallel and perpendicular to the grain direction using standard methods, the measurements being repeated for several specimens to reduce the errors due to misalignment of the very thin specimens. The results in Table C.1 show that the elastic modulus differs by up to 15% in the two directions, the suffix m in  $E_m$  denoting the value of the Young's modulus in the direction of the major axis of the panel, and the suffix n the value along the minor axis.

It was not possible to measure Poisson's ratio  $\nu$  with a reasonable degree of accuracy, so a value  $\nu = 0.3$  was assumed for all cases. The error incurred by this assumption is negligible because Poisson's ratio has only a small effect on the predicted natural frequency. The panel density was measured using standard methods.

#### C.2 Estimation of Natural Frequencies and Mode Shapes

There are well established techniques for the estimation of natural frequencies and mode shapes of rectangular panels with various boundary

Table C.1

Properties of the Panel Materials

Panel (Inches)	3.5 x 3.5	4.0 x 2.75	4.0 x 2.0	4.0 x 1.0
Thickness (Inch)	0.015	0.015	0.015	0.015
Density (lb/cu.in)	0.27	0.27	0.27	0.27
Young's Modulus (lb/sq.in)				
$E_m$	$31.4 \times 10^6$	$31.4 \times 10^6$	$32.1 \times 10^6$	$32.1 \times 10^6$
$E_n$	$36.0 \times 10^6$	$36.0 \times 10^6$	$30.0 \times 10^6$	$30.0 \times 10^6$
Mean $E$	$33.7 \times 10^6$	$33.7 \times 10^6$	$31.0 \times 10^6$	$31.0 \times 10^6$
Poisson's Ratio $\sigma$ (Assumed)	0.30	0.30	0.30	0.30

conditions, and the method of Warburton (1954) has been used to predict the vibrational characteristics of the experimental panels.

Warburton assumes that the plates are isotropic, elastic and of a uniform thickness which is small relative to the wavelength of the vibration. The analysis is based on the ordinary theory of thin plates. He assumes further that the waveforms of the vibrating plate can be represented, only approximately in many conditions, by the waveforms for beams with directions parallel to the plate axes. The characteristic beam function assumed by Warburton for a beam freely supported at  $x = 0$  and  $x = L$  is

$$\psi_m(x) = \sin \frac{m\pi x}{L} \quad \dots (C.1)$$

where  $m = 1, 2, \dots$  is the mode order given by the number of modal half wavelengths.

For a beam with fixed end conditions at  $x = 0, L$

$$\psi_m(x) = \cos \frac{\gamma_1'}{2} \left( \cosh \frac{\gamma_1' x}{L} - \cos \frac{\gamma_1' x}{L} + \tan \frac{\gamma_1'}{2} (\sinh \frac{\gamma_1' x}{L} - \sin \frac{\gamma_1' x}{L}) \right) \quad \dots (C.2)$$

for  $m = 1, 3, 5, \dots$

where  $\tan \frac{\gamma_1'}{2} + \tanh \frac{\gamma_1'}{2} = 0$ .

and

$$\psi_m(x) = \sin \frac{\gamma_2'}{2} \left( \cosh \frac{\gamma_2' x}{L} - \cos \frac{\gamma_2' x}{L} - \cot \frac{\gamma_2'}{2} (\sinh \frac{\gamma_2' x}{L} - \sin \frac{\gamma_2' x}{L}) \right) \quad \dots (C.3)$$

for  $m = 2, 4, 6, \dots$

where  $\tan \frac{\gamma_2'}{2} - \tanh \frac{\gamma_2'}{2} = 0$ .

The panel natural frequencies are determined from the beam functions and the equation of motion of the plate, using Rayleigh's method. For the experimental panels, natural frequencies were estimated for simply supported and fully fixed edge conditions, using the mean value of Young's modulus

shown in Table C.1. The predicted frequencies are shown in Table C.2. Under ideal conditions the (r-s) and (s-r) modes of the square panel will combine to give modal patterns having nodes which are not parallel to the panel edges. However very small deviations from the ideal will separate the natural frequencies of the (r-s) and (s-r) modes sufficiently for the interaction to be prevented. Warburton shows that after a 2% change in panel aspect ratio the interaction is negligible. Small irregularities in the structure of the material will have similar effects, especially when the panels are thin.

The work of Warburton was extended by Hearmon (1959) to include the case of orthotropic plates which have three mutually perpendicular axes of elastic symmetry, two of which lie in the plane of the plate and are parallel to the respective sides. The third axis is perpendicular to the plane of the plate and, for thin plates and small deflections, can be ignored. Hearmon considered characteristic functions similar to those assumed by Warburton but expressed them in the combined form

$$\psi_m(x) = \cosh \frac{\gamma'_3 x}{L} - \cos \frac{\gamma'_3 x}{L} - k' \left( \sinh \frac{\gamma'_3 x}{L} - \sin \frac{\gamma'_3 x}{L} \right) \quad \dots (C.4)$$

$$\text{for } m \geq 1$$

$$\text{where } k' = 0.982; \quad \gamma'_3 = 4.730 \quad \text{when } m = 1$$

$$k' = 1; \quad \gamma'_3 = (m + \frac{1}{2})\pi \quad \text{when } m \geq 2$$

From Hearmon's results the panel natural frequencies were estimated using the measured values of Young's modulus in the directions of the panel axes, and they are contained in Table C.2.

When a panel is backed by a rectangular cavity the vibrational characteristics differ from those estimated for "in vacuo" conditions. The effect of a cavity has been studied theoretically by Pretlove (1965) for the volume displacing modes, the modes which are most likely to be affected by the change in the surroundings. The effect will be greatest in the case of the fundamental natural frequency. Pretlove shows that, if

the "in vacuo" fundamental frequency is less than the open ended acoustic mode frequency of the cavity, and if there is no acoustic coupling of the panel modes, then the fundamental frequency of the panel is increased. At higher order modes Pretlove shows that a decrease in the panel natural frequencies can occur, but suggests that the presence of slight air leaks could destroy the cavity effect at all frequencies.

### C.3 Measured Natural Frequencies

The natural frequencies and mode shapes of the experimental panels were measured using discrete frequency excitation methods described in Chapter 4. The exciting force was provided by an electromagnetic coil wound on a permanent magnetic core. The presence of the permanent magnetic field produced a static deflection of the panel as shown in Figure C.1, the deflection increasing as the gap between the exciter and panel surface decreased, but the associated changes in the natural frequencies were less than 0.8%. The natural frequencies were determined with an exciter-panel gap of 0.625 inch for the lower order modes, decreasing to 0.25 inch at the higher frequencies, so that the presence of the exciter had a negligible effect on the magnitude of the natural frequencies. During the measurement of the natural frequencies, the vibration amplitude did not exceed 0.001 inch and the ratio of vibration amplitude to panel thickness did not exceed 6.7%. Thus, from the work of Hu-Nan Chu and Herrmann (1956) on simply supported plates, the vibration should be essentially linear, and this was confirmed by monitoring the vibration on an oscilloscope.

The natural frequencies of the experimental panels are shown in Table C.2 for the environments used in the modal damping measurements. The free-free surface condition, when the panel was suspended away from noise reflecting bodies, represents most closely the theoretical "in vacuo" condition. Comparing the results with the frequency estimates using Warburton's method, the measured frequencies are much closer to those predicted for fully-fixed boundary conditions than those for simply supported edges, which suggests that the panel has essentially fully-fixed edges. In the lower modes, the square panel has frequencies  $f_{rs}$  and  $f_{sr}$  which are fairly well separated

Table C.2

Panel Natural Frequencies: 3.5in x 3.5in x 0.015in.

Method	Estimated Frequency (c/s)			Measured Frequency (c.p.s.)				
	Warburton		Hearmon	Discrete Frequency Excitation		Zero Airflow		Random
	S.S.*	Clamped	Clamped					Airflow <sup>+</sup>
Edge Conditions								
Face I	Free	Free	Free	Free	Free	Wind Tunnel	Siren Tunnel	Wind Tunnel
Face II	Free	Free	Free	Free	Box	Box	Box	Box
Mode:								
1-1	255	467	470	482	499	498	490	500
1-2	637	952	979	966	972	969	963	980
2-1	637	952	939	871	885	885	873	890
2-2	1020	1405	1412	1290	1303	1300	1289	1310
1-3	1274	1711	1768	1670	1673	1666	1658	1690
3-1	1274	1711	1674	1570	1581	1584	1570	1590
2-3	1657	2142	2181	1954	1965	1965	1954	1990
3-2	1657	2142	2124	1949	1971	1967	1954	1980
3-3	2294	2853	2868	-	2593	2592	2585	2630
1-4	2167	2729	2825	-	-	2525	2559	-
4-1	2167	2729	2660	-	-	-	2506	-

\* S.S denotes simply supported boundaries.

+ Mean values for 320 ft/sec and 540 ft/sec.

**Table C.2 (cont.)**

Panel Natural Frequencies: 4.0in x 2.75in x 0.015in.

		Estimated Frequency (c/s)		Measured Frequency (c.p.s.)					
Method		Warburton		Hearmon	Discrete Frequency Excitation			Random	
Edge Conditions		S.S.*	Clamped	Clamped	Zero Airflow				Airflow <sup>+</sup>
Face I		Free	Free	Free	Free	Free	Wind Tunnel	Wind Tunnel	
Face II		Free	Free	Free	Free	Box	Box	Box	
<u>Mode:</u>	1-1	304	575	586	541	569	581	537	560
	1-2	923	1396	1439	1307	1333	1347	1314	1300
	2-1	597	908	904	833	853	851	808	830
	2-2	1216	1706	1730	1567	1594	1607	1554	1590
	1-3	1956	2636	2726	2498	2492	2552	2442	2490
	3-1	1085	1467	1443	1351	1376	1381	1321	1350
	2-3	2248	2941	3010	2747	2759	2782	2712	2770
	3-2	1704	2230	2228	2008	2022	2068	1997	2030
	3-3	2736	3445	3488	-	-	-	-	-
	4-1	1768	2236	2186	2047	2020	2042	1943	2010
	4-2	2387	2972	2939	2646	2662	2675	2603	2640
	5-1	2646	3206	3124	-	-	-	2819	2860

\*S.S. denotes simply supported boundaries; + mean values for 320ft/sec and 540ft/sec.

Table C.2 (cont.)

Panel Natural Frequencies: 4.0in x 2.0in x 0.015in  
4.0in x 1.0in x 0.015in.

Method	Estimated Frequency (c/s)			Measured Frequency (c.p.s.)					
	Warburton		Hearmon	Discrete Frequency		Excitation		Random	
	S.S.*	Clamped	Clamped	Free	Free	Wind Tunnel	Siren Tunnel	Airflow <sup>+</sup>	Wind Tunnel
Edge Conditions									
Face I	Free	Free	Free	Free	Free	Box	Box	Box	Box
Face II	Free	Free	Free	Free	Free	Box	Box	Box	Box
Panel: 4.0in x 2.0in.									
Mode:									
1-1	-	938	925	1058	1073	1064	1062	1080	
1-2	-	2442	2409	2495	2510	-	2512	2540	
2-1	-	1216	1215	1265	1275	1272	1273	1280	
2-2	-	2717	2689	2742	2757	2761	2746	2780	
3-1	-	1711	1727	1723	1739	1723	1733	1740	
3-2	-	3181	3165	3140	3155	-	3147	3160	
4-1	-	2422	2456	2403	2417	2401	2411	2425	
5-1	-	3338	3392	3321	3341	3322	-	3330	
Panel: 4.0in x 1.0in.									
Mode:									
1-1	-	3477	3402	3457	-	-	3360	-	
2-1	-	3686	3623	3665	-	-	3648	-	
3-1	-	4056	4014	+	-	-	3963	-	

\*S.S. denotes simply supported boundaries;  
+ mean values for 320ft/sec and 540ft/sec.



and this can be explained partly, from Hearmon (1959), by the orthotropic Young's modulus. When the measured frequencies are compared with estimates using Hearmon's method, the experimental values are generally lower, but the difference is less than 10%. It is to be expected that the theoretical methods might overestimate the true frequency to a small degree but the larger discrepancy suggests that the panels do not conform completely to fully-fixed conditions, or that the effective boundary, because of small irregularities in the bonding, does not lie accurately on the boundary formed by the edge of the rectangular hole in the carrier plug. However, the discrepancy is not large since slight irregularities in the material will have an appreciable effect on the thin panels.

When one face of the panel was enclosed by the pressure equalising box, the measured natural frequencies showed a small increase, the change being most significant at the fundamental frequency, where increases as large as 5% were observed. The box is similar to the rectangular enclosure discussed by Pretlove but has a large leak to the vacuum pump. The open ended acoustic mode frequency for the combined depth of the plug and the box is approximately 1,020 c.p.s., which is greater than the fundamental natural frequencies of the 3.5in x 3.5in and 4.0in x 2.75in panels, but the acoustic natural frequencies of the complete pressure equalising system are more difficult to predict. However, the measurements suggest that the presence of the box increases the effective stiffness of the panel, but by only a small amount.

Table C.2 contains mean values of the natural frequencies which were obtained from the spectral analysis of the panel response to boundary layer excitation for flow velocities of 329 ft/sec and 540 ft/sec. The values agree closely with the discrete frequency measurements, the small differences in some modes being due, possibly, to slight changes in panel temperature in the presence of the airflow.

#### C.4 Measured Mode Shapes

The panel mode shapes were measured by traversing the capacitance probe across the face of the panel, and measuring the vibration amplitude

at each position. The finite diameter of the probe did not permit the displacement to be measured close to the boundaries but, as the main aim was to establish that the panels had no peculiar characteristics, it was not considered necessary to use other methods to measure the vibration close to the edges. The measured mode shapes are shown in Figures C.2 to C.4 for three of the panels, and they are compared with theoretical shapes for simply supported (equation (C.1)) and fully fixed (equation (C.2) and (C.3)) boundary conditions.

Every effort was made, by suitable positioning of the exciter and probe, to eliminate the effects of off-resonance vibration in other modes but several modes shown in the figures suffer from distortion which can be attributed to this type of interference. The distortion could be reduced if the resonant vibration amplitude was obtained from the complex response plane but, for reasons discussed in Chapter 4, this alternative method suffered from other disadvantages.

The modal patterns for the panels were observed visually from the Chladni figures and they are shown in Plates C.1 to C.3. The patterns were displayed using aluminium filings, and the discrete frequency exciter was positioned to minimise the off-resonance vibration in other modes. The modal patterns are clearly formed for all panels except the 4.0in x 1.0in panel, but some of the modes of the 4.0in x 2.75in panel (Plate C.2) have distorted nodal lines. In particular the modes of order (1-2) and (3-1) have very close natural frequencies and it was impossible to position the single exciter so that undistorted nodal lines could be obtained. Because of elastic anisotropy and slight irregularities in the panel material, the modal patterns of the 3.5in x 3.5in panel show no trace of the modal interaction associated with ideal square panels, and the analysis of the random vibration of the square panel presents no problems additional to those for a rectangular plate.

#### C.5 Summary

The panel natural frequencies, mode shapes and modal patterns have been measured using discrete frequency excitation. The natural frequencies

were found to lie within the frequency range determined by simply supported and fully fixed edge conditions, but the values were close to those estimated for the fully fixed boundaries. On this evidence, and that provided by the measured mode shapes, it is concluded that the boundary conditions of the experimental panels approximate to those for fully fixed structures. In general the vibrational characteristics of the panel showed no irregularities and, partly because of the orthotropic elastic properties of the panel material, the square panel did not possess diagonal or circular modes.

The panel natural frequencies were affected to only a small extent by the presence of the pressure equalising box, but the frequencies were influenced by the ambient temperature.

## APPENDIX D

### Panel Root Mean Square Displacement

#### D.1 Introduction

The theoretical analysis in Chapter 2 has provided a means of estimating the panel displacement power spectral density function. From Equation (2.45) the complete spectrum is obtained from a double summation over the mode orders  $\alpha$ ,  $\beta$  or, if the cross terms can be neglected, the analysis can be reduced to a single summation of the joint terms. In the experimental investigation, narrow band analysis of the panel response gives the measured displacement power spectrum which can be compared directly with the theoretical predictions. However, the comparison suffers from the disadvantage that the magnitude of the spectral density depends critically on the accuracy of estimation of the modal damping and of the loss of resolution due to the finite filter bandwidth. When the vibration is compared in terms of the mean square or root mean square (r.m.s.) displacement associated with a broad frequency band, the experimental errors become less important. Thus a response comparison in terms of root mean square displacement may give a more useful indication of the accuracy of the method of estimation. Also, in some circumstances the mean modal response may be required in place of the spectral density.

#### D.2 Theoretical R.M.S. Displacement

For a single degree of freedom system, the displacement power spectral density function  $G_d(\omega)$ , in terms of the angular frequency  $\omega$ , is given by

$$G_d(\omega) = |H(\omega)|^2 G_p(\omega)$$

where  $H(\omega)$  is the complex response function. The mean square displacement is then :

$$\begin{aligned}\bar{v}^2(t) &= \int_0^\infty G_d(\omega) d\omega \\ &= \int_0^\infty |H(\omega)|^2 G_p(\omega) d\omega\end{aligned}$$

In a multi-degree of freedom system with single point loading, the mean square displacement can be determined in a similar way, and the mean square response in mode  $r$  is

$$\overline{w_r^2}(t) = \int_0^\infty |H_r(\omega)|^2 G_p(\omega) d\omega \quad \dots (D.1)$$

where  $H_r(\omega)$  is the complex response function for the mode of order  $r$ .

Now assume that  $G_p(\omega) = \text{constant} = K_p$ , and  $|H_r(\omega)|^2$  has the form applicable to hysteretic damping with loss factor  $v_r$

$$\text{i.e. } |H_r(\omega)|^2 = \frac{1}{M_r^2((\omega_r^2 - \omega^2)^2 + v_r^2 \omega_r^4)} \quad \dots (D.2)$$

Then equation (D.1) becomes, on integration,

$$\begin{aligned} \overline{w_r^2}(t) &= \frac{\pi K_p}{M_r^2 \omega_r^3 v_r} (1 - \frac{3}{8} v_r^2 + \dots) \\ &\approx \frac{\pi K_p}{M_r^2 \omega_r^3 v_r} \quad \text{for } v_r \ll 1 \quad \dots (D.3) \end{aligned}$$

For a lightly damped panel the main contribution to  $\overline{w_r^2}(t)$  comes from the frequency range in the neighbourhood of  $\omega_r$ . Thus the assumption that  $G_p(\omega) = K_p$ , for all  $\omega_r$ , can be relaxed to apply only to frequencies close to  $\omega_r$ , provided that  $G_p(\omega)$  does not increase by several orders of magnitude at frequencies away from  $\omega_r$ .

In equation (D.3),  $K_p$  can be expressed in terms of the maximum displacement spectral density  $G_d(\omega_r)$  in mode  $r$ , where, from equation (D.2)

$$K_p = M_r^2 v_r^2 \omega_r^4 G_d(\omega_r) \quad \dots (D.4)$$

Substituting equation (D.4) into equation (D.3) yields

$$\begin{aligned}\overline{w_r^2}(t) &= \frac{\pi}{2} v_r \omega_r G_d(\omega_r) \\ &= \frac{\pi}{2} v_r f_r G_d(f_r) \quad \dots (D.5)\end{aligned}$$

so that the modal mean square displacement can be estimated from the resonant displacement power spectral density.

For distributed random loading, as in the case of panels excited by a boundary layer pressure field, assume that conditions exist such that the cross terms in equation (2.45) can be neglected (see Section 2.8). Then equation (D.1) can be replaced, from equation (2.45) by

$$\overline{w_a^2}(\underline{x}, t) = \frac{A}{4} \psi_a^2(\underline{x}) \int_0^\infty |H_a(\omega)|^2 J_{aa}(\omega) G_p(\omega) d\omega \quad \dots (D.6)$$

Assuming that the major contribution to  $\overline{w_a^2}(\underline{x}, t)$  comes from the frequency range in the neighbourhood of  $\omega_r$ , and that in this range  $G_p(\omega)$  and  $J_{aa}(\omega)$  are effectively constant (as is the case for boundary layer excitation and lightly damped structures) then, from equation (D.5), the modal mean square displacement is given by

$$\overline{w_a^2}(\underline{x}, t) = \frac{\pi}{2} v_a f_a G_d(f_a) \quad \dots (D.7)$$

where  $G_d(f_a)$  is the peak displacement power spectral density in the mode of order  $a$ , measured at the position  $\underline{x}$  on the panel surface. The total mean square displacement at position  $\underline{x}$  is obtained from the summation of equation (D.7) over all  $a$ .

Comparing equations (D.3) and (D.4) it is seen that the displacement power spectral density at the natural frequency is inversely proportional to the square of the loss factor whereas the modal mean square displacement is inversely proportional to the loss factor. Thus errors in the determination of the loss factor will result in smaller errors in the mean

square displacement than in the displacement power spectral density at the natural frequency.

The modal r.m.s. displacements have been estimated from equation (D.7) for the experimental panels, the position  $\underline{x}$  being the quarter point on a panel diagonal,  $\underline{x} = (\frac{L_1}{4}, \frac{L_3}{4})$ . The results are shown in Tables D.1 to D.8. The theoretical overall r.m.s. displacements were estimated from the modal data shown. This implies that the mean square displacement was integrated over an effective frequency range of 0 - 3,000 c.p.s. for panels 3, 4 and 5, and over a range 0 - 3,500 c.p.s. for panels 2 and 6. Thus the results shown in Figure 5.2 as a function of boundary layer thickness may be smaller than the true total r.m.s. displacements, but the excluded contributions from the higher order modes will be small.

### D.3 Measured R.M.S. Displacement

The total panel r.m.s. displacement was obtained directly from the measured overall displacement signal, and the results are shown in Figure 5.2.

The modal r.m.s. displacements have to be measured using narrow band filters which are chosen so that sufficient energy is included for the given mode, whilst energy from the other modes is excluded as much as possible. In the analysis of the experimental results, the modal r.m.s. displacement was estimated using filters with a 2% bandwidth, and the results are contained in Tables D.1 to D.8. The filter bandwidth may appear to be narrow but it is considerably wider than the bandwidth of many of the resonant peaks in the displacement spectra. Further the filtered signal contains a negligible contribution from the neighbouring resonance peaks, except in a small number of cases. The effect of filter bandwidth was observed by comparing results obtained using filters with bandwidths of 1.2% and 2.0%. For a flow Mach number  $M_0 = 0.3$ , the r.m.s. displacements determined by the two filters differed by less than 12%, except for the results of several modes, identified by asterisks in Tables D.1 to D.4. This difference can be compared with a theoretical difference of 30% for a signal of constant spectral density. When the two filters gave results which differed by more than 12%, the larger difference was not necessarily

due to the use of filters with too narrow a bandwidth. In some cases the difference occurred because the 2% bandwidth filters allowed the inclusion of contributions from very close resonant peaks. Three of the panels had mode pairs whose natural frequencies were so close together that the r.m.s. displacements in the individual modes could not be measured. For these modes the r.m.s. displacement was measured for each mode pair and, in the Tables, the results are associated with the mode which has the larger theoretical response of the pair. Such mode pairs are the modes (2-1) and (1-3) of panel 3, (2-3) and (3-2) of panel 4, and (1-2) and (3-1) of panel 5.

A comparison of the results in Tables D.1 to D.8 shows that in general the theory overestimates the response, the ratio of theoretical to measured modal r.m.s. displacement being mainly in the range of 1.0 to 2.0. The difference will be due partly to the practical impossibility of measuring the full modal displacement, and partly to the use of simply supported mode shapes in the theoretical investigation (see Section 5.1.2). A detailed inspection of the results shows that the theory predicts quite closely the variation of modal r.m.s. displacement with boundary layer thickness (Figures 5.3 and 5.4), but that the estimate change of response with Mach number is slightly greater than that measured. However, the effect of Mach number cannot be assessed with confidence because results are available for only two flow velocities.



TABLE D.1

Modal R.M.S. Displacement  $M_0 = 0.3$

Panel 3 : 2.75in x 4.0in x 0.015in.

$x_1 = 0.688in$   $x_3 = 3.00in$

		R.M.S. DISPLACEMENT 1 (INCH)							
		Theoretical				Experimental			
Position <sup>2</sup>		1	2	3	4	1	2	3	4
Mode									
1-1	-5	1.99	3.16	-5	5.32	-5	1.25*	-5	3.14
1-2	-5	1.15	1.91	-5	3.13	-5	1.17	-5	2.69
2-1	-5	1.26	2.04	-5	2.69	-5	6.61	-6	1.52
2-2	-5	1.22	1.87	-5	2.19	-5	6.61	-6	1.18
1-3	-6	3.74	5.40	-6	6.62	-6	-	-	-
3-1	-6	2.17	2.44	-6	2.05	-6	1.58	-6	1.45
2-3	-6	3.61	4.35	-6	4.29	-6	1.57	-6	2.30*
3-2	-6	2.04	2.16	-6	1.54	-6	1.08*	-6	1.19*
1-5	-7	5.69	6.51	-7	6.38	-7	-	-	-

Notes: 1. R.M.S. Displacement  $w \times 10^{-2}$  inch is written in the form (w, -n)

2. See Table 3.1

\* See Section D.3.

TABLE D.2

Modal R.M.S. Displacement  $M_0 = 0.3$

Panel 4 : 3.5in x 3.5in x 0.015in.

$x_1 = 0.88\text{in}$   $x_3 = 0.88\text{in}$

R.M.S. DISPLACEMENT 1 (INCH)																
Theoretical					Experimental											
Position2	1	2	3	4	1	2	3	4								
Mode																
1-1	2.74	-5	4.36	-5	5.83	-5	7.39	-5	1.67	-5	2.49	-5	3.04	-5	5.03	-5
1-2	1.20	-5	1.86	-5	2.35	-5	2.59	-5	1.05	-5	1.58	-5	1.93	-5	2.41	-5
2-1	2.94	-5	5.01	-5	7.04	-5	8.38	-5	2.31	-5	4.15	-5	4.65	-5	5.18	-5
2-2	1.56	-5	2.77	-5	3.20	-5	3.40	-5	1.29	-5	2.31	-5	2.59	-5	2.86	-5
1-3	2.04	-6	2.49	-6	2.79	-6	2.84	-6	1.89*	-6	2.91*	-6	3.90*	-6	3.74*	-6
3-1	6.49	-6	1.05	-5	1.26	-5	1.26	-5	6.17	-6	1.02	-5	1.21	-5	1.24	-5
2-3	2.60	-6	2.98	-6	3.32	-6	3.29	-6	-	-	-	-	-	-	-	-
3-2	5.94	-6	7.79	-6	8.13	-6	7.58	-6	4.71	-6	6.23	-6	7.07	-6	6.47	-6
3-3	1.23	-6	1.39	-6	1.40	-6	1.31	-6	6.11	-7	8.56	-7	9.26	-7	9.17	-7

Notes : See Table D.1

TABLE D.3

Modal R.M.S. Displacement  $M_o = 0.3$ 

Panel 5 : 4.0in x 2.75in x 0.015in.

 $x_1 = 1.00\text{in.}$   $x_3 = 0.688\text{in.}$ 

R.M.S. DISPLACEMENT 1 (INCH)																
		Theoretical				Experimental										
Position <sup>2</sup>		1	2	3	4	1	2	3	4							
Mode																
1-1	1.75	-5	2.78	-5	3.80	-5	4.60	-5	7.17	-6	1.59	-5	2.23	-5	2.41	-5
1-2	4.77	-6	6.02	-6	6.43	-6	6.96	-6	2.76	-6	-	-	-	-	-	-
2-1	1.87	-5	3.19	-5	4.50	-5	5.41	-5	1.41	-5	2.35	-5	3.14	-5	3.26	-5
2-2	7.50	-6	9.45	-6	1.02	-5	1.04	-5	1.87	-6	3.52	-6	3.11	-6	3.35	-6
1-3	6.72	-7	7.67	-7	8.04	-7	7.79	-7	-	-	4.88*	-7	4.80*	-7	5.60*	-7
3-1	9.41	-6	1.61	-5	2.08	-5	2.21	-5	3.65	-6	7.44	-6	8.44	-6	9.60	-6
2-3	8.98	-7	1.02	-6	1.04	-6	9.85	-7	5.18*	-7	5.78*	-7	5.15*	-7	5.50*	-7
3-2	1.17	-6	4.22	-6	4.51	-6	4.34	-6	1.94	-6	2.57	-6	2.54	-6	2.62	-6
5-1	1.20	-6	1.25	-6	1.20	-6	1.07	-6	-	-	-	-	-	-	-	-

Notes : See Table D.1

TABLE D.4

Modal R.M.S. Displacement  $M_0 = 0.3$ Panel 2 : 2.0in x 4.0in x 0.015in.  $x_1 = 0.50in$   $x_3 = 3.00in$ .6 : 4.0in x 2.0in x 0.015in.  $x_1 = 1.00in$   $x_3 = 0.50in$ .

		R.M.S. DISPLACEMENT 1 (INCH)													
		Theoretical					Experimental								
Position <sup>2</sup>		1	2	3	4	1	2	3	4						
Mode		Panel 2													
1-1	8.86	-6	1.38	-5	1.80	-5	2.00	-5	5.95	-6	9.80	-6	-	1.27	-5
1-2	6.25	-6	9.78	-6	1.23	-5	1.33	-5	3.44	-6	6.64	-6	-	7.92	-6
2-1	1.80	-6	2.10	-6	2.02	-6	1.82	-6	1.56*	-6	1.77*	-6	-	1.69*	-6
2-2	2.26	-6	2.45	-6	2.32	-6	2.08	-6	1.15*	-6	1.29	-6	-	1.23	-6
1-3	2.56	-6	3.46	-6	3.89	-6	3.85	-6	2.12*	-6	3.05	-6	-	3.20	-6
2-3	9.30	-7	9.92	-7	9.58	-7	8.87	-7	-	-	-	-	-	-	-
1-5	4.47	-7	5.04	-7	5.03	-7	4.72	-7	-	-	-	-	-	-	-
	Panel 6														
1-1	6.04	-6	8.12	-6	9.25	-6	9.26	-6	1.76	-6	3.25	-6	3.82	4.54	-6
1-2	6.49	-7	7.34	-7	7.66	-7	7.38	-7	-	-	-	-	-	4.52	-7
2-1	7.45	-6	1.13	-5	1.35	-5	1.43	-5	2.74	-6	5.84	-6	7.96	6.98	-6
2-2	1.12	-6	1.26	-6	1.28	-6	1.21	-6	2.79*	-7	3.80*	-7	3.29*	2.84*	-7
3-1	4.61	-6	6.30	-6	6.78	-6	6.47	-6	4.11	-6	6.54	-6	6.40	5.82	-6
3-2	6.86	-7	8.88	-7	7.51	-7	7.00	-7	-	-	-	-	-	-	-
5-1	9.59	-7	9.97	-7	9.34	-7	8.42	-7	-	-	-	-	-	-	-

Notes : See Table D.1

TABLE D.5

Modal R.M.S. Displacement  $M_0 = 0.5$ 

Panel 3 : 2.75in x 4.0in x 0.015in.

 $x_1 = 0.688\text{in}$   $x_3 = 3.00\text{in}$ .

		R.M.S. DISPLACEMENT 1 (INCH)														
		Theoretical				Experimental										
Position <sup>2</sup>		1	2	3	4	1	2	3	4							
Mode																
1-1	5.21	-5	7.29	-5	1.05	-4	1.30	-4	1.66	-5	2.65	-5	4.64	-5	4.78	-5
1-2	2.31	-5	4.36	-5	6.35	-5	8.15	-5	1.75	-5	2.25	-5	3.85	-5	5.24	-5
2-1	3.00	-5	4.76	-5	6.41	-5	7.80	-5	1.13	-5	1.59	-5	2.65	-5	2.16	-5
2-2	2.76	-5	4.69	-5	6.37	-5	7.75	-5	1.86	-5	1.86	-5	2.98	-5	3.02	-5
1-3	8.69	-6	1.54	-5	2.11	-5	2.58	-5	-	-	-	-	-	-	-	-
3-1	7.90	-6	1.25	-5	1.50	-5	1.61	-5	6.37	-6	8.22	-6	1.04	-5	7.96	-6
2-3	3.45	-6	5.94	-6	7.73	-6	8.80	-6	5.31	-6	1.06	-5	8.22	-6	7.76	-6
3-2	8.94	-6	1.40	-5	1.64	-5	1.71	-5	6.90	-6	9.02	-6	1.19	-5	9.28	-6
1-5	1.76	-6	2.06	-6	2.30	-6	2.39	-6	-	-	-	-	-	-	-	-

Notes : See Table D.1

TABLE D.6

Modal R.M.S. Displacement  $M_o = 0.5$ 

Panel 4 : 3.5in x 3.5in x 0.015in.

 $x_1 = 0.88\text{in}$   $x_3 = 0.88\text{in}$ 

		R.M.S. DISPLACEMENT $l$ (INCH)							
		Theoretical				Experimental			
Position <sup>2</sup>		1	2	3	4	1	2	3	4
Mode									
1-1	6.34 -5	9.60 -5	1.29 -4	1.62 -4	1.53 -5	3.85 -5	5.31 -5	5.64 -5	
1-2	2.38 -5	4.40 -5	6.28 -5	7.93 -5	1.46 -5	2.79 -5	3.45 -5	4.38 -5	
2-1	5.89 -5	9.08 -5	1.24 -4	1.56 -4	2.39 -5	3.98 -5	5.98 -5	6.31 -5	
2-2	3.14 -5	5.63 -5	8.05 -5	1.01 -4	2.12 -5	4.14 -5	4.65 -5	4.98 -5	
1-3	5.81 -6	8.91 -6	1.09 -5	1.21 -5	-	7.42 -6	8.62 -6	8.83 -6	
3-1	1.31 -5	2.07 -5	2.78 -5	3.38 -5	6.63 -6	1.19 -5	1.79 -5	1.56 -5	
2-3	8.63 -6	1.48 -5	1.91 -5	2.17 -5	-	-	-	-	
3-2	1.53 -5	2.67 -5	3.55 -5	4.15 -5	1.33 -5	2.12 -5	3.32 -5	2.85 -5	
3-3	5.49 -6	9.06 -6	1.07 -5	1.13 -5	5.84 -6	6.63 -6	7.69 -6	8.29 -6	

Notes : See Table D.1

TABLE D.7

Modal R.M.S. Displacement  $M_0 = 0.5$

Panel 5 : 4.0in x 2.75in x 0.015in

$x_1 = 1.00in$   $x_3 = 0.688in$ .

R.M.S. DISPLACEMENT <sup>1</sup> (INCH)																
Experimental																
Theoretical																
Position <sup>2</sup>	1	2	3	4	1	2	3	4								
Mode																
1-1	4.69	-5	7.30	-5	9.98	-5	1.25	-4	1.06	-5	3.98	-5	4.25	-5	4.45	-5
1-2	1.28	-5	2.01	-5	2.56	-5	3.00	-5	-	-	-	-	-	-	-	-
2-1	4.50	-5	7.15	-5	9.88	-5	1.25	-4	2.12	-5	4.65	-5	5.58	-5	6.64	-5
2-2	2.22	-5	3.91	-5	5.30	-5	6.38	-5	1.19	-5	2.32	-5	2.39	-5	2.79	-5
1-3	1.99	-6	2.41	-6	2.64	-6	2.84	-6	3.19	-6	5.98	-6	3.32	-6	3.45	-6
3-1	1.81	-5	2.84	-5	3.92	-5	4.73	-5	1.33	-5	2.25	-5	2.86	-5	3.12	-5
2-3	3.26	-6	3.87	-6	4.24	-6	4.40	-6	3.72	-6	6.64	-6	5.98	-6	4.65	-6
3-2	1.29	-5	2.27	-5	3.01	-5	3.42	-5	9.82	-6	1.66	-5	1.86	-5	1.63	-5
5-1	7.24	-6	1.15	-5	1.38	-5	1.47	-5	-	-	-	-	-	-	-	-

Notes : See Table D.1.

TABLE D.8

Modal R.M.S. Displacement  $M_0 = 0.5$ Panel 2 : 2.0in x 4.0in x 0.015in.  $x_1 = 0.50$ in  $x_3 = 3.00$  in.6 : 4.0in x 2.0in x 0.015in.  $x_1 = 1.00$ in  $x_3 = 0.50$  in.

		R.M.S. DISPLACEMENT 1 (INCH)							
		Theoretical				Experimental			
Position <sup>2</sup>		1	2	3	4	1	2	3	4
Mode									
1-1	Panel 2 2.31 -5	3.49 -5	4.68 -5	5.70 -5	1.14 -5	1.81 -5	2.91 -5	3.02 -5	
1-2	1.38 -5	2.27 -5	3.11 -5	3.84 -5	5.58 -6	9.29 -6	1.16 -5	1.80 -5	
2-1	6.75 -6	1.02 -5	1.21 -5	1.29 -5	4.78 -6	6.90 -6	-	1.19 -5	
2-2	9.14 -6	1.45 -5	1.67 -5	1.72 -5	3.98 -6	6.63 -6	7.46 -6	9.30 -6	
1-3	6.54 -6	1.09 -5	1.44 -5	1.69 -5	5.31 -6	9.55 -6	1.11 -5	1.56 -5	
2-3	4.87 -6	7.00 -6	7.65 -6	7.70 -6	-	-	-	-	
1-5	5.15 -6	6.02 -6	6.50 -6	6.45 -6	-	-	-	-	
1-1	Panel 6 1.84 -5	2.78 -5	3.67 -5	4.41 -5	1.11 -5	1.49 -5	2.39 -5	2.35 -5	
1-2	2.02 -6	2.40 -6	2.61 -6	2.81 -6	6.50 -6	9.29 -6	1.05 -5	1.23 -5	
2-1	2.04 -5	3.40 -5	4.71 -5	5.84 -5	9.29 -6	1.43 -5	1.58 -5	2.23 -5	
2-2	4.09 -6	5.02 -6	5.45 -6	5.62 -6	-	-	-	-	
3-1	1.29 -5	2.19 -5	2.95 -5	3.55 -5	1.11 -5	1.75 -5	2.65 -5	2.73 -5	
3-2	3.40 -6	3.94 -6	4.17 -6	4.10 -6	-	-	-	-	
5-1	6.50 -6	9.71 -6	1.04 -5	1.04 -5	-	-	-	-	

Notes : See Table D.1.



## REFERENCES

- |  |  |
|--|--|
| Allcock, G.A. (1962)<br>Tanner, P.L.<br>McLachlan, K.R.    | A general purposes analogue correlator for the analysis of random noise signals. University of Southampton Report AASU 205.  |
| Barnoski, R.L. (1965)                                      | Response of elastic structures to deterministic and random excitation. United States Air Force Report AFFDL-TR-64-199 (May 1965).  |
| Baroudi, M.Y. et al (1964)                                 | Turbulence-induced panel vibration. University of Toronto UTIA Report 98 (February 1964).  |
| Baroudi, M.Y. et al (1963)<br>Ludwig, G.R.<br>Ribner, H.S. | An experimental investigation of turbulence-excited panel vibration and noise (boundary layer noise) A.G.A.R.D. Report 465 (April 1963)  |
| Bies, D.A. (1965)  | A wind tunnel investigation of panel response to boundary layer pressure fluctuations at Mach 1.4 and Mach 3.5. Bolt, Beranek & Newman Inc. Report No.1264 (October 1965) or N.A.S.A. CR.501 (May 1966)            |
| Bishop, R.E.D. (1963)<br>Gladwell, G.M.L.                  | An investigation into the theory of resonance testing. Phil.Trans.Roy.Soc.London A <u>255</u> , 1055 pp.241-280. (January 1963).   |
| Blackman, R.D. (1958)<br>Tukey, J.W.                       | The measurement of power spectra. Dover Publications.  |
| Bozich, D.J. (1964)  | Spatial correlation in acoustic-structural coupling. J.Acoust.Soc.Amer. <u>36</u> , 1, pp.52-58 (January 1964).  |
| Bozich, D.J. (1965)  | Radiation damping of panels mounted in ducts Wyle Laboratories Report WR.64-4. (Huntsville, Alabama).  |
| Bull, M.K. (1960)  | Instrumentation for and preliminary measurement of space-time correlations and convection velocities of the pressure field of a turbulent boundary layer. University of Southampton Report AASU 149 (August 1960). |

# REFERENCES (Cont.)

- Bull, M.K. (1963) Wall pressure fluctuations associated with subsonic turbulent boundary layer flow.  
University of Southampton Ph.D. Thesis (June 1963)
- Bull, M.K. (1962)  
Wilby, J.F.  
Blackman, D.R. Research in boundary layer oscillations and noise. Summary report.  
University of Southampton Report AASU 220 (June 1962)
- Bull, M.K. (1963)  
Wilby, J.F.  
Blackman, D.R. Wall pressure fluctuations in boundary layer flow and response of simple structures to random pressure fields.  
University of Southampton Report AASU 243 (July 1963).
- Clark, D.M. (1966) Wind tunnel noise.  
University of Southampton M.Sc. thesis (April 1966).
- Clarkson, B.L. (1965)  
Mercer, C.A. Use of cross correlation in studying the response of lightly damped structures to random forces.  
A.I.A.A. Journal 3, 2, pp.2287-2291. (December 1965).
- Clarkson, B.L. (1961)  
Pietruszewicz, S.A. The University of Southampton random siren facility.  
University of Southampton Report AASU 204 (December 1961).
- Corcos, G.M. (1956)  
Liepmann, H.W. On the contribution of turbulent boundary layers to the noise inside a fuselage.  
NACA TM.1420 (September 1956).
- Davies, D.E. (1964) The radiation sound field of a rectangular panel set in an infinite wall and excited by a turbulent boundary layer.  
R.A.E. Tech.Note Structures 335 (April 1964).
- Dyer, I. (1958) Sound radiation into a closed space from boundary layer turbulence.  
Bolt, Beranek & Newman Inc. Report 602. (December 1958).
- Eringen, A.C. (1957) Response of beams and plates to random loads.  
J.App.Mech. 24, pp.46-52. (March 1957).
- Fahy, F.J. (1965)  
Pretlove, A.J. Acoustic forces on the vibrating wall of a duct which carries airflow.  
Paper K24, 5th International Congress of Acoustics, Liege (September 1965).

# REFERENCES (Cont.)

- Ffowcs Williams, J.E. (1963)  
Lyon, R.H. The sound radiated from turbulent flows near flexible boundaries. Bolt, Beranek & Newman Inc. Report 1054. (August 1963).
- Forlifer, W.R. (1964) The effects of filter bandwidth in spectrum analysis of random vibration. Shock, Vibration and Associated Environments Bulletin No.33, Pt.2, pp.273-278. (February 1964).
- Gladwell, G.M.L. (1962) A refined estimate for the damping coefficient. J.R.Ae.Soc. 66, 614, pp.124-125 (February 1962) Errata, J.R.Ae.Soc. 66, 621, pp.589 (September 1962).
- Harrison, M. (1958) Pressure fluctuations on the wall adjacent to a turbulent boundary layer. David Taylor Model Basin (U.S.A.) Report 1260.
- Hearmon, R.F.S. (1959) The frequency of flexural vibration of rectangular orthotropic plates with clamped or supported edges. J.App.Mech. 26, pp.537-540. (December 1959)
- Hun Nan Chu (1956)  
Herrmann, R. Influence of large amplitudes on free flexural vibrations of rectangular elastic plates. J.App.Mech. 23, pp.532-540.
- Kennedy, C.C. (1947)  
Pancu, C.D.P. Use of vectors in vibration measurement and analysis. J.Aero.Sci. 14, 11, pp.603-625. (November 1947).
- Kraichnan, R.H. (1957). Noise transmission from boundary layer pressure fluctuations. J.Acoust.Soc.Amer. 29, 1, pp.65-80. (January 1957).
- Ludwig, G.R. (1962) An experimental investigation of the sound generated by thin steel panels excited by turbulent flow (Boundary layer noise). University of Toronto, U.T.I.A. Report 87, (November 1962).
- Lyon, R.H. (1956) Response of strings to random noise fields. J.Acoust.Soc.Amer. 28, 3, pp.391-398. (May 1956).

#### REFERENCES (Cont.)

- Maestrello, L. (1964) Test results from the boundary layer facility (Noise radiated by the panel) Volume I. Boeing Co. Document No. D6-9944, Vol.I. (January 1964)
- Maestrello, L. (1965a) Measurement of noise radiated by boundary layer excited panels. J.Sound Vib., 2, 2, pp.100-115. (April 1965).
- Maestrello, L. (1965b) Measurement and analysis of the response field of turbulent boundary layer excited panels. J.Sound Vib., 2, 3, pp.270-292. (July 1965).
- Maestrello, L. (1965c) The effect of length and thickness on the panel response due to turbulent boundary layer excitation. Paper L.28, 5th International Congress of Acoustics, Liege (September 1965).
- Maestrello, L. (1966) Test results from the boundary layer facility. (Noise radiated by the panel) Volume III. Boeing Co. Document No. D6-9944, Vol.III. (May 1966).
- Maidanik, G. (1960) The use of delta function for the correlations of pressure fields. Bolt, Beranek & Newman Inc. Report 772. (October 1960).
- Mead, D.J. (1959) The internal damping due to structural joints and techniques for general damping measurement. A.R.C. Tech.Rep. C.P.452.
- Mercer, C.A. (1965) Response of a multi-supported beam to a random pressure field. J.Sound Vib., 2, 3, pp.293-306. (July 1965).
- Morrow, C.T. (1958) Averaging time and data-recording time for random vibration spectra. J.Acoust.Soc.Amer. 30, pp.456-461. (May 1958).

# REFERENCES (Cont.)

- Nash, W.A. (1961) Response of an elastic plate to a distributed random pressure characterized by a separable cross correlation.  
United States Air Force Report AFOSR-TN-61-1215. (September 1961).
- Powell, A. (1958a) On the fatigue failure of structures due to vibrations excited by random pressure fields.  
J.Acoust.Soc.Amer. 30, 12, pp.1130-1135. (December 1958).
- Powell, A. (1958b) On the response of structures to random pressures and to jet noise in particular. Chapter 8 of Random Vibration.  
Edited by S.H. Crandall. John Wiley & Sons Inc.
- Pretlove, A.J. (1965) Free vibrations of a rectangular panel backed by a closed rectangular cavity.  
J.Sound Vib., 2, pp.197-209, (July 1965).
- Rechtien, R.D. (1965) The autocorrelation function of structural response measurements.  
NASA TN-D.2578. (January 1965).
- Ribner, H.S. (1956) Boundary-layer-induced noise in the interior of aircraft.  
University of Toronto, U.T.I.A. Report 37.
- Richards, E.J. (1965)  
Wilby, J.F.  
McNulty, G.J. Research in boundary layer oscillations and noise.  
University of Southampton Report ISAV 137. (December 1965).
- Schloemer, H.H. (1966) Effects of pressure gradients on turbulent boundary-layer wall-pressure fluctuations.  
U.S. Navy Underwater Sound Laboratory, U.S.L.Report 747. (July 1966).
- Stevenson, M. (1961)  
Saltus, D.W.  
Taggart, R. An experimental study of acoustic excitation of flat plates by unsteady flow.  
Robert Taggart Inc. (Virginia, U.S.A.) Report RT.1101 (July 1961).
- Tack, D.H. (1962)  
Lambert, R.F. Response of bars and plates to boundary-layer turbulence.  
J.Aerospace Sci., 29, pp.311-322 (March 1962).

## REFERENCES (Cont.)

- Warburton, G.B. (1954) The vibration of rectangular plates.  
Proc.Inst.Mech.Eng., 168, pp.371-384.
- Webb, D.R.B. (1962) Surface pressures and structural strains  
Keeler, A.R. resulting from fluctuations in the  
Allen, G.R. turbulent boundary layer of a Fairey  
Delta 2 Aircraft.  
R.A.E. Tech.Note Structures 313.  
(May 1962).
- White, P.H. (1962) Response of a flexibly supported string  
to a convected random pressure field.  
University of California Repor. No.62-43.
- Wilby, J.F. (1963) Random excitation of a simple panel:  
some experimental results.  
University of Southampton Report AASU 231  
(January 1963).
- Wilby, J.F. (1964) Turbulent boundary layer pressure  
fluctuations and their effect on  
adjacent structures.  
1964 Yearbook of Wissenschaftlichen  
Gesellschaft für Luft- und Raumfahrt (WGLR).
- Wilby, J.F. (1965) Panel response and its relation to the  
Richards, E.J. type of excitation.  
Chapter 16 in Acoustical Fatigue in  
Aerospace Structures. Edited by W.J. Trapp  
and D.M. Forney, Jr. Syracuse Univ. Press.



Plate 3-1 Boundary layer wind tunnel.



Plate 3.2 Experimental panels.



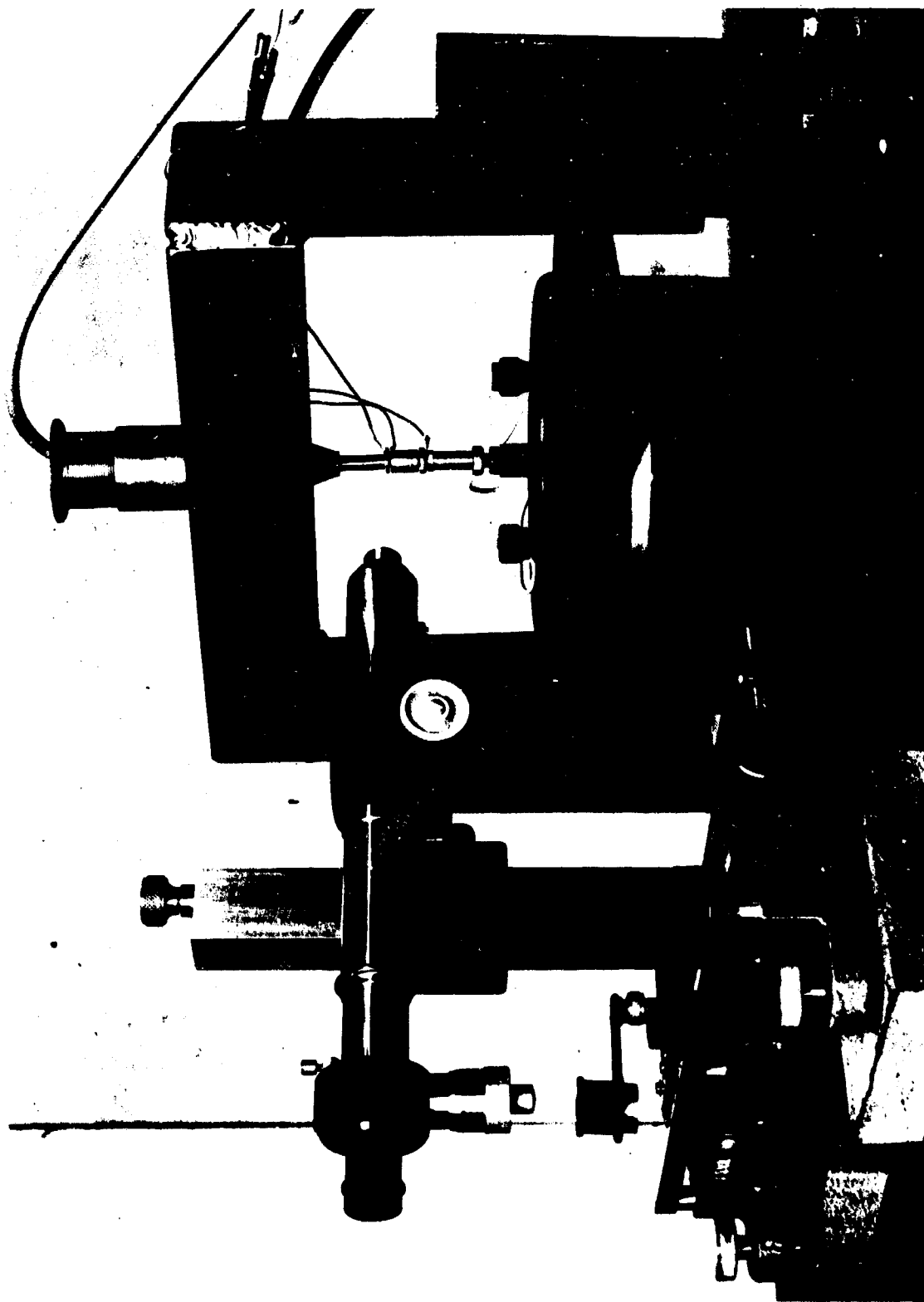


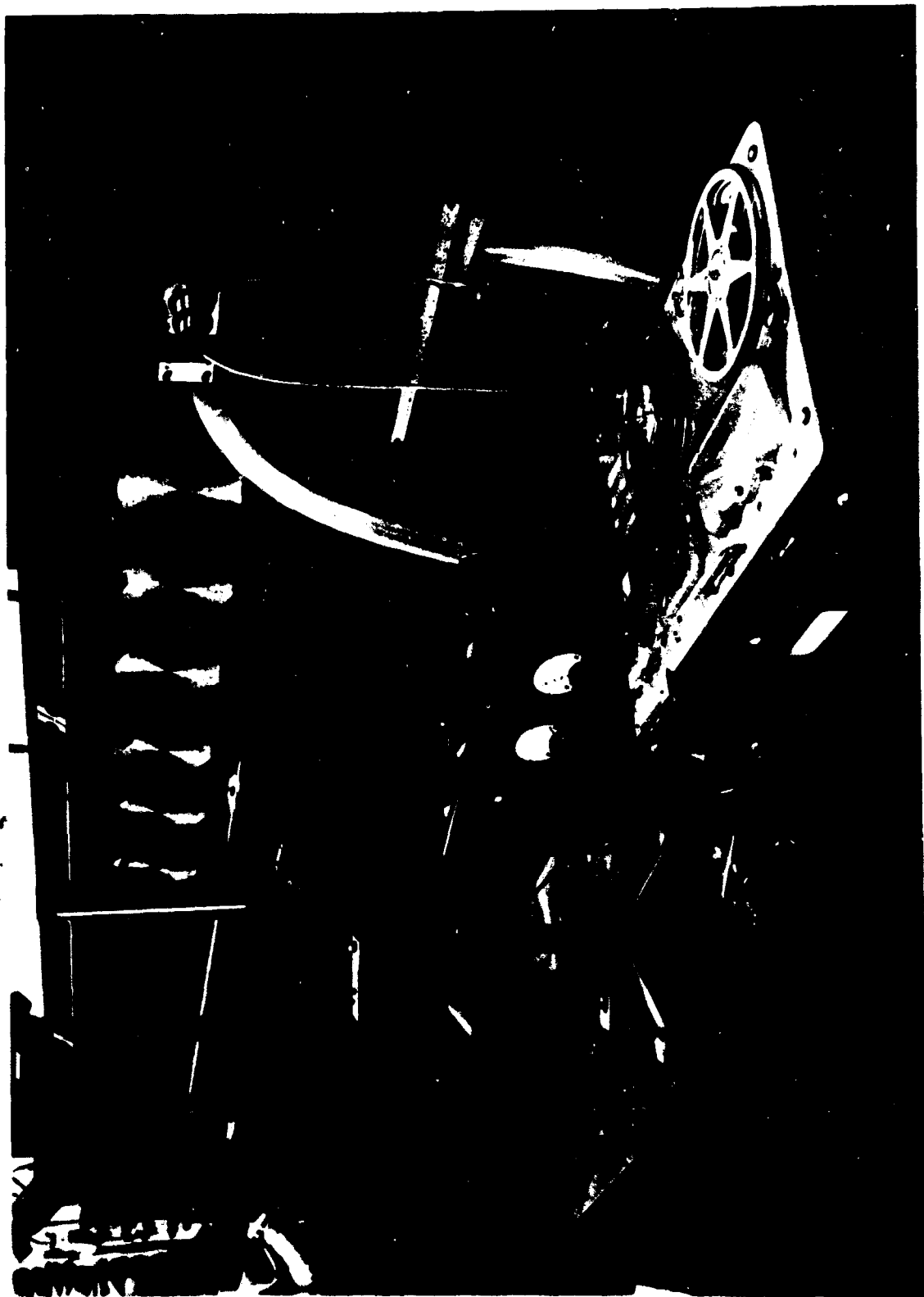
Plate 3.3 Capacitance probe calibration equipment.



Plate 3-4 Traversing unit and wind tunnel side plate.



Plate 3-5 Wind tunnel side plate in the siren tunnel .



**Plate 3-6** Traversing unit mounted on the wind tunnel.

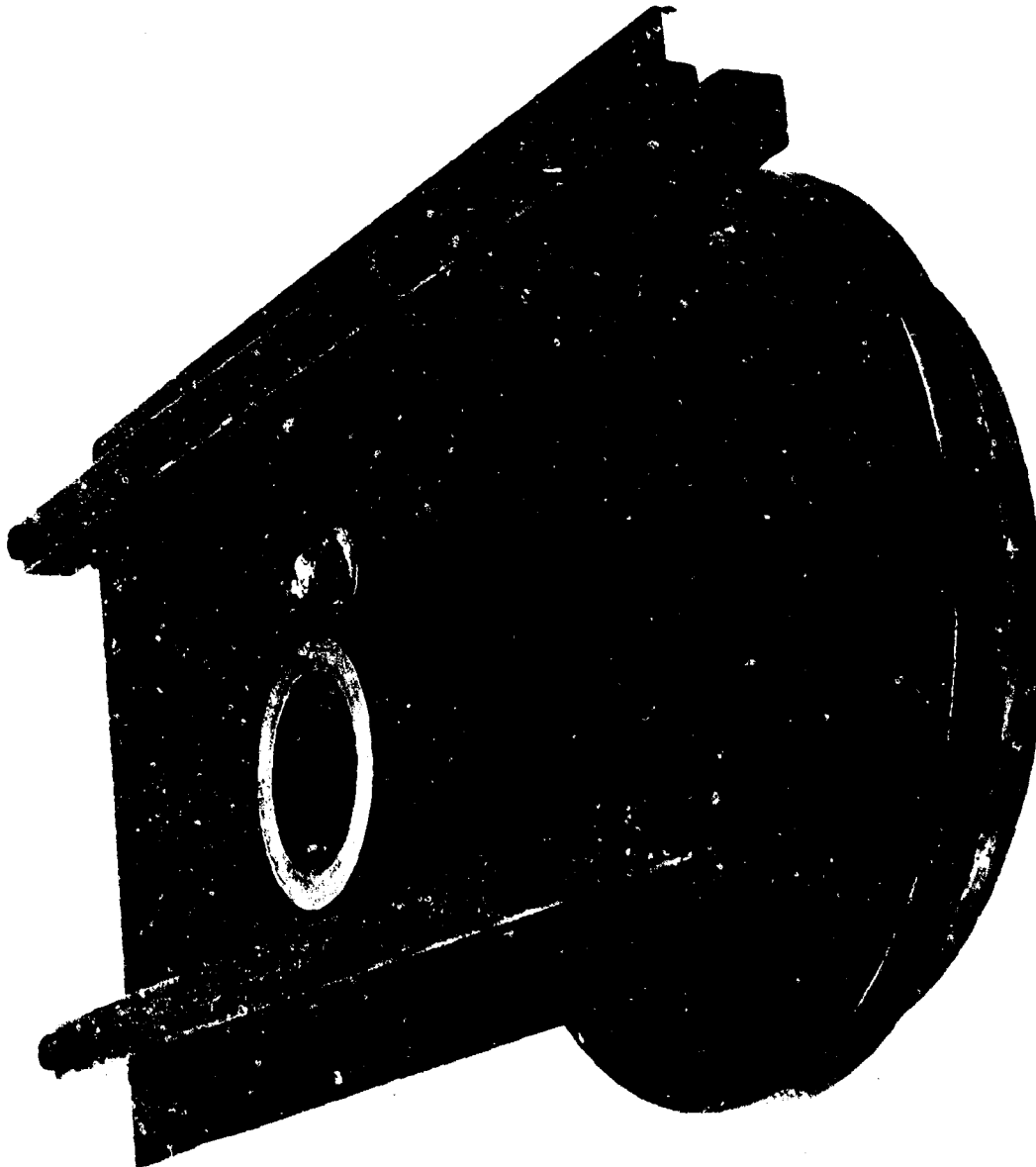


Plate 3-7 Carrier plug with pressure equalising box .

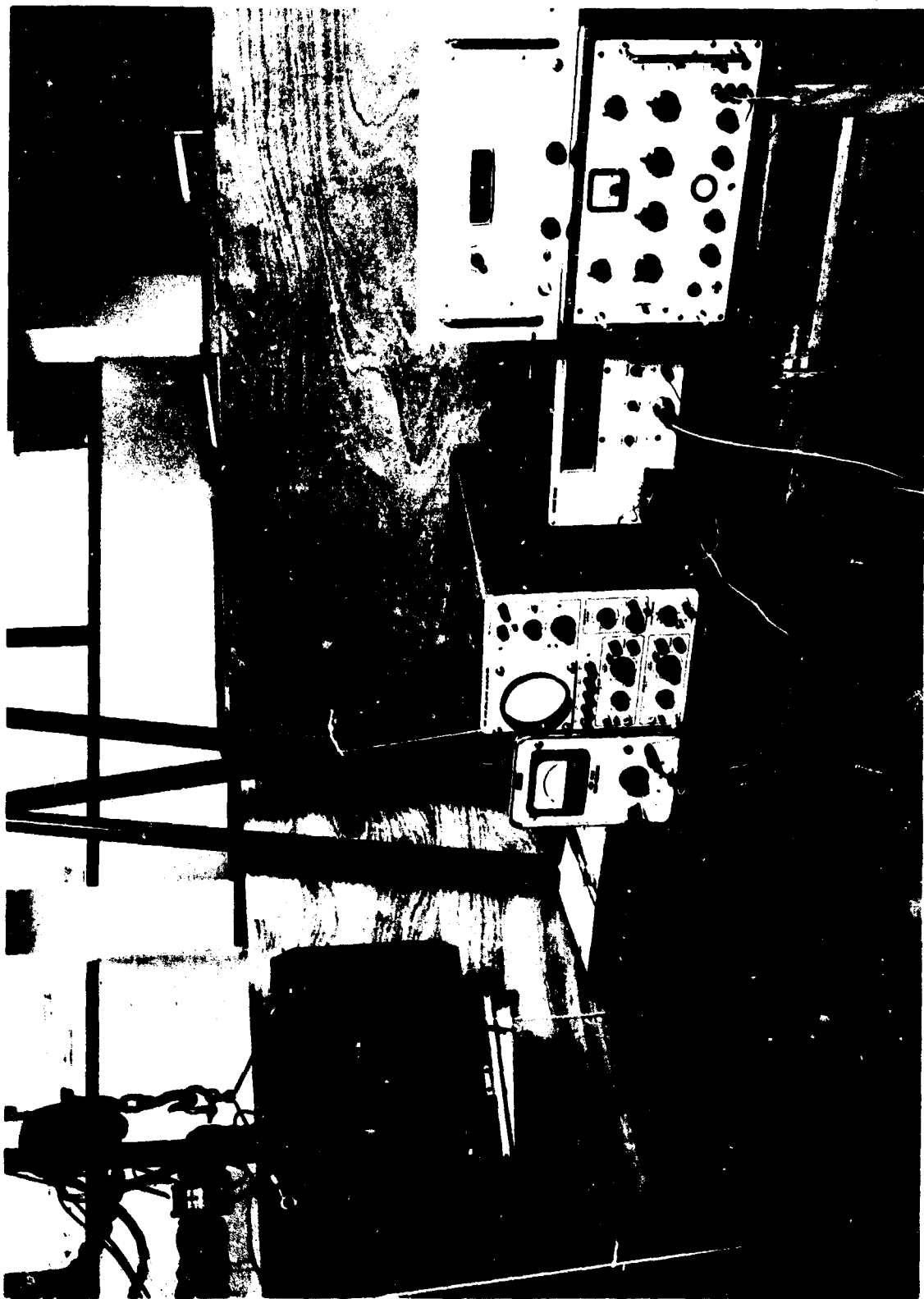


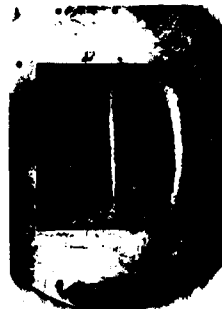
Plate 4.1 Equipment for free-space damping measurements.



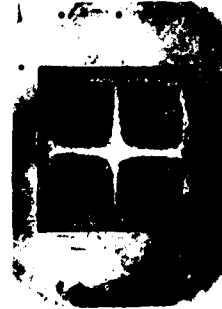
1-1



1-2



2-1



2-2



1-3



3-1



2-3



3-2



3-3



1-4



4-1

PLATE C.1 MODAL PATTERNS FOR THE 3.5 IN. x 3.5 IN. PANEL.



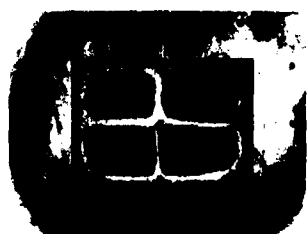
1-1



1-2



2-1



2-2



1-3



3-1



2-3



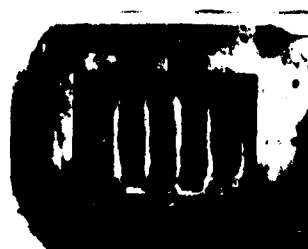
3-2



4-1



4-2



5-1

PLATE C.2 MODAL PATTERNS FOR THE 4.0 IN. x 2.75 IN. PANEL.

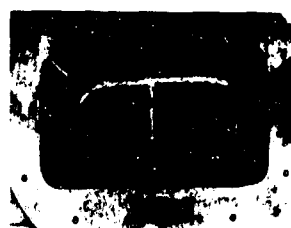




1-1



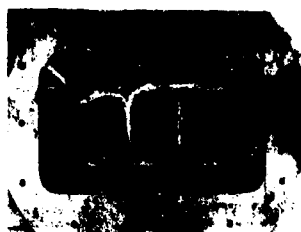
1-2



2-1



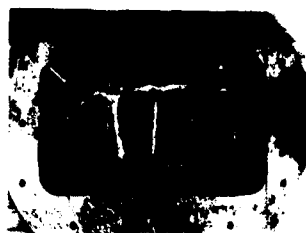
2-2



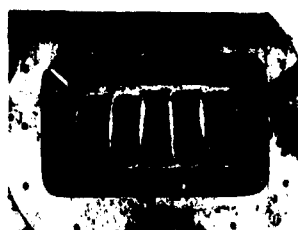
3-1



3-2

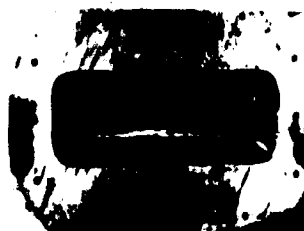


4-1



5-1

40 IN. x 20 IN. PANEL



1-1



2-1

40 IN. x 10 IN. PANEL

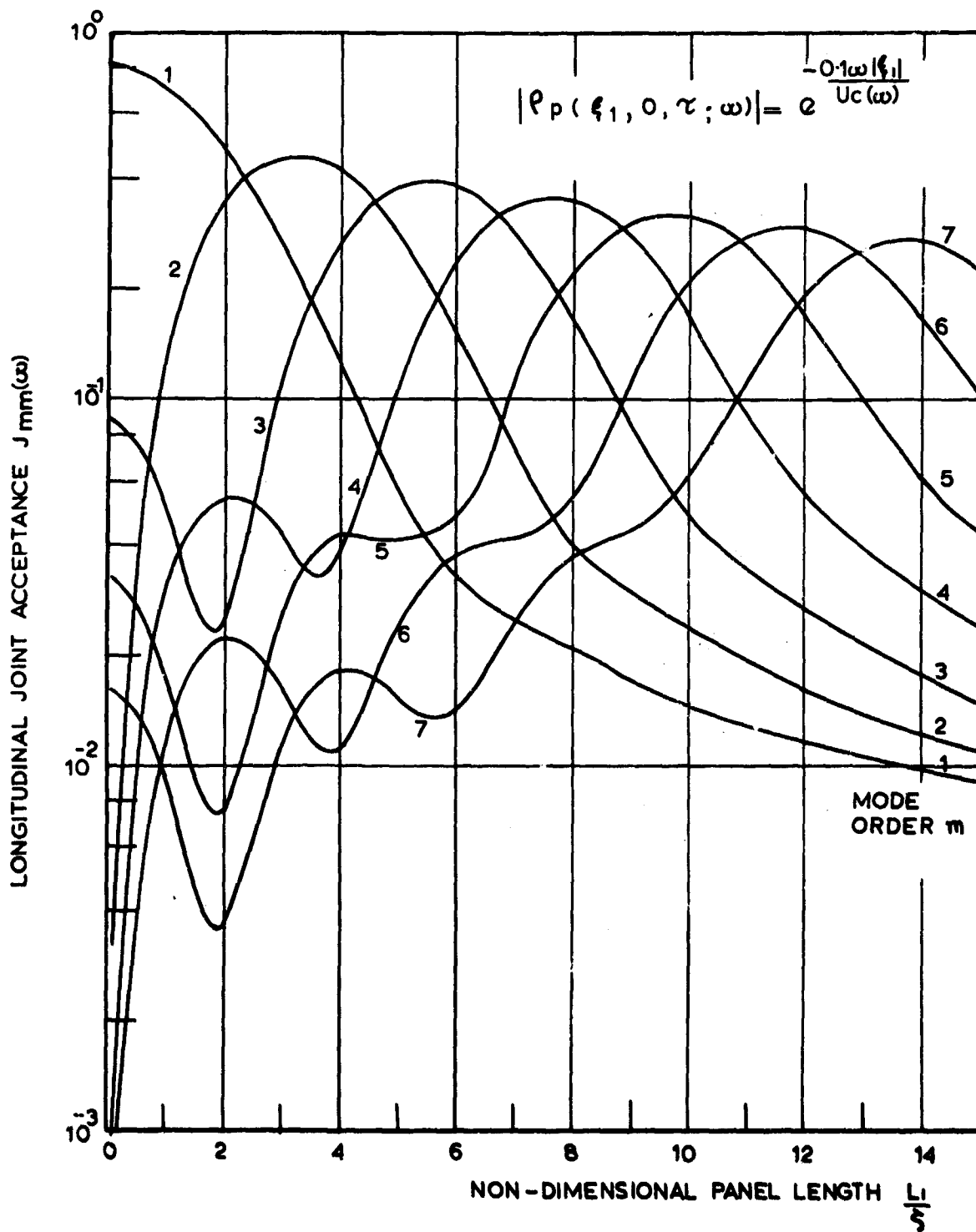


Figure 2.1. Longitudinal joint acceptance valid for  $\frac{\omega\delta^*}{U_c(\omega)} \geq 0.37$ .

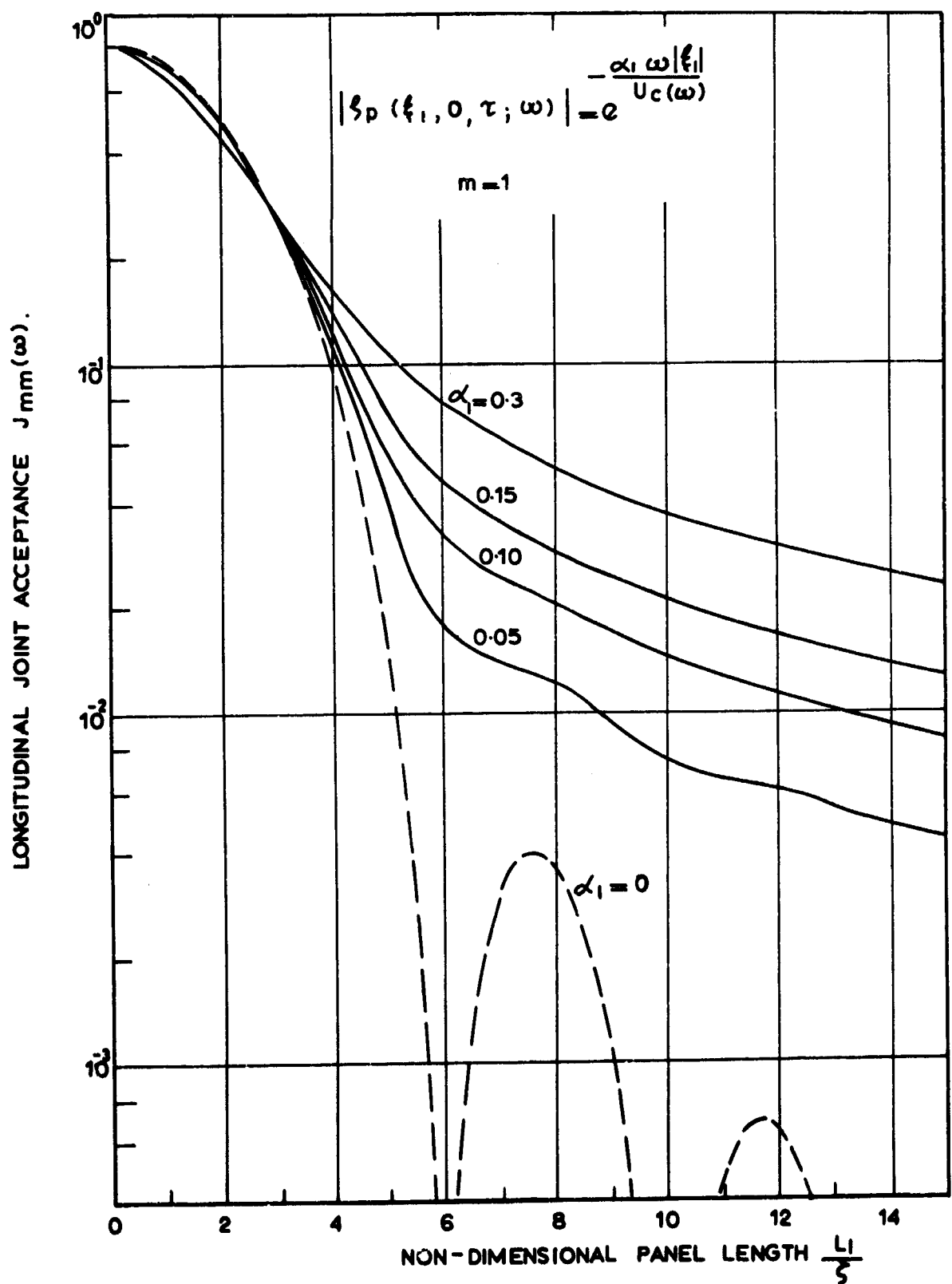


Fig. 22 Effect of  $\alpha_1$  on joint acceptance :  $m=1$

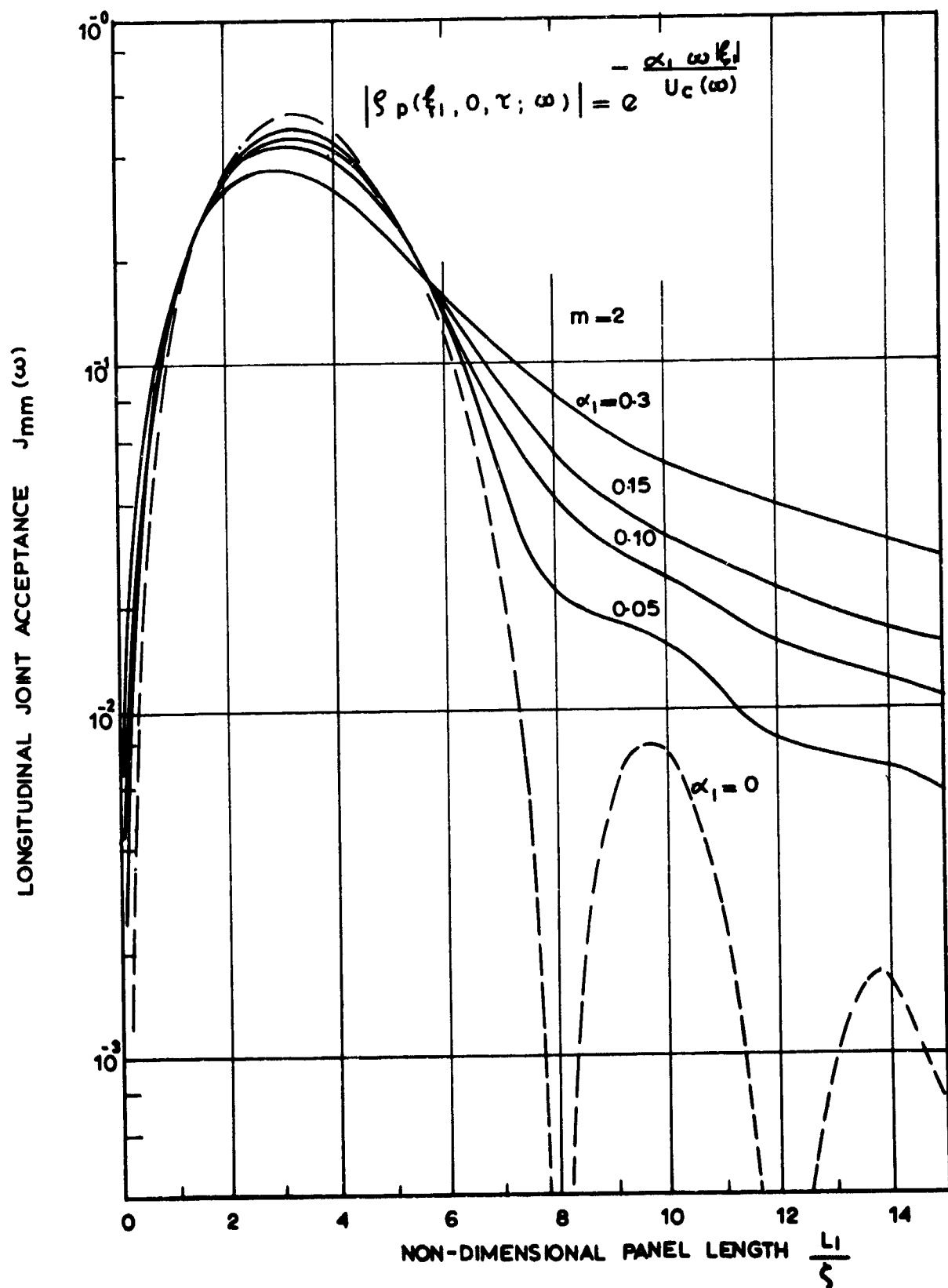


Fig. 2-3 Effect of  $\alpha_1$  on joint acceptance :  $m=2$

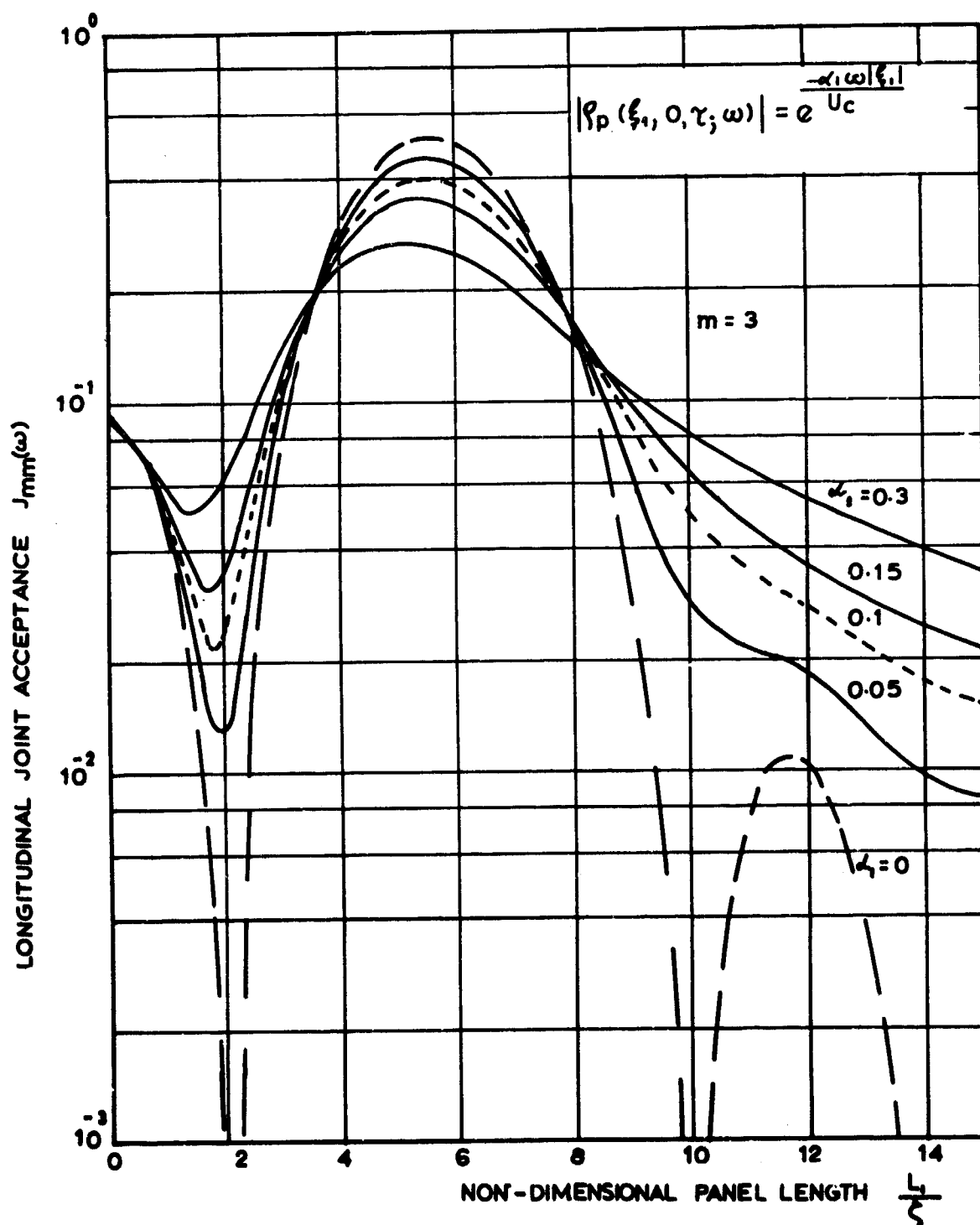


Figure 2.4 Effect of  $\gamma_1$  on joint acceptance,  $m=3$ .

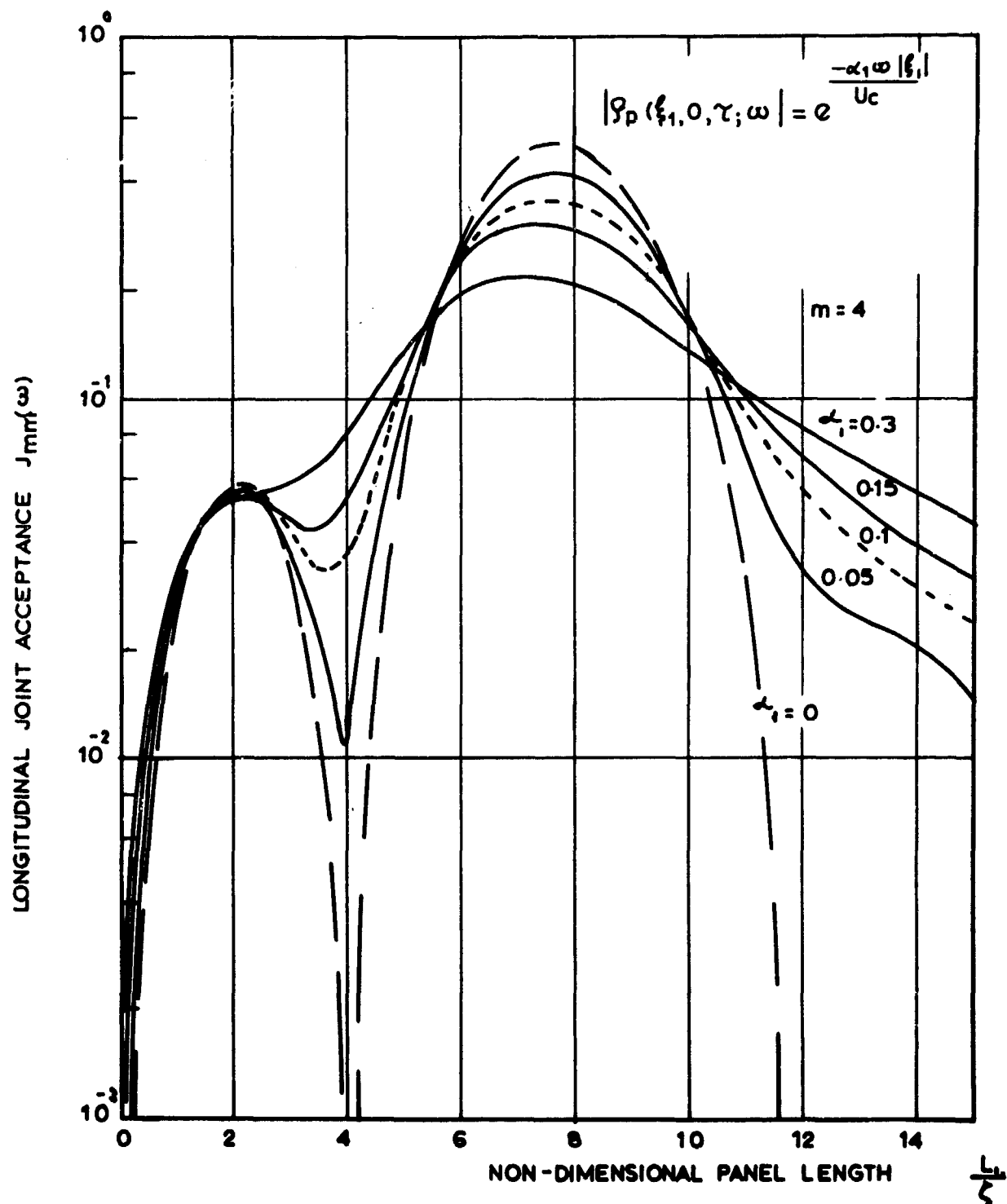


Figure 2.5 Effect of  $\alpha_1$  on joint acceptance,  $m=4$ .

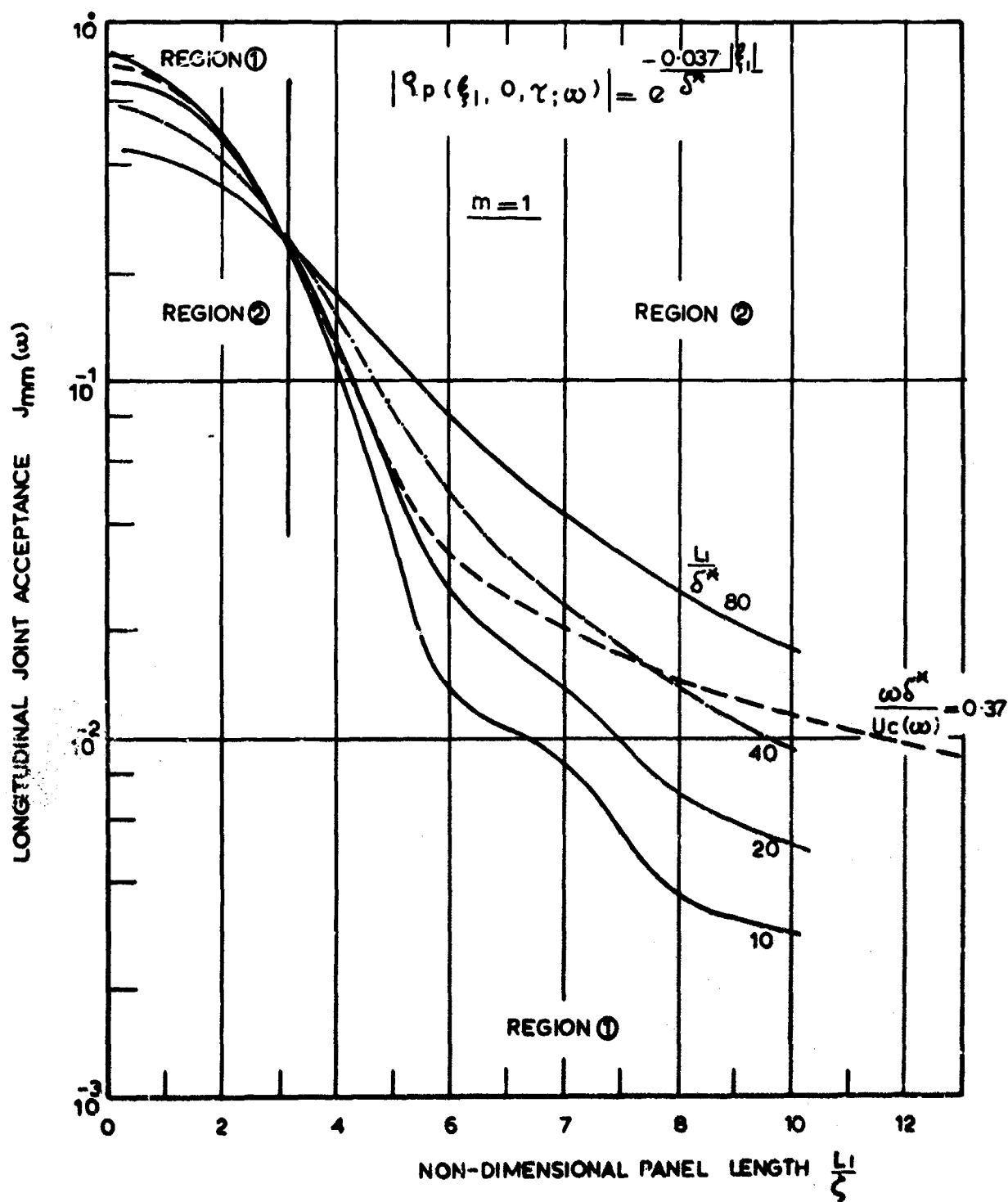


Fig. 2-6 Longitudinal joint acceptance as function of boundary layer displacement thickness .Mode  $m=1$

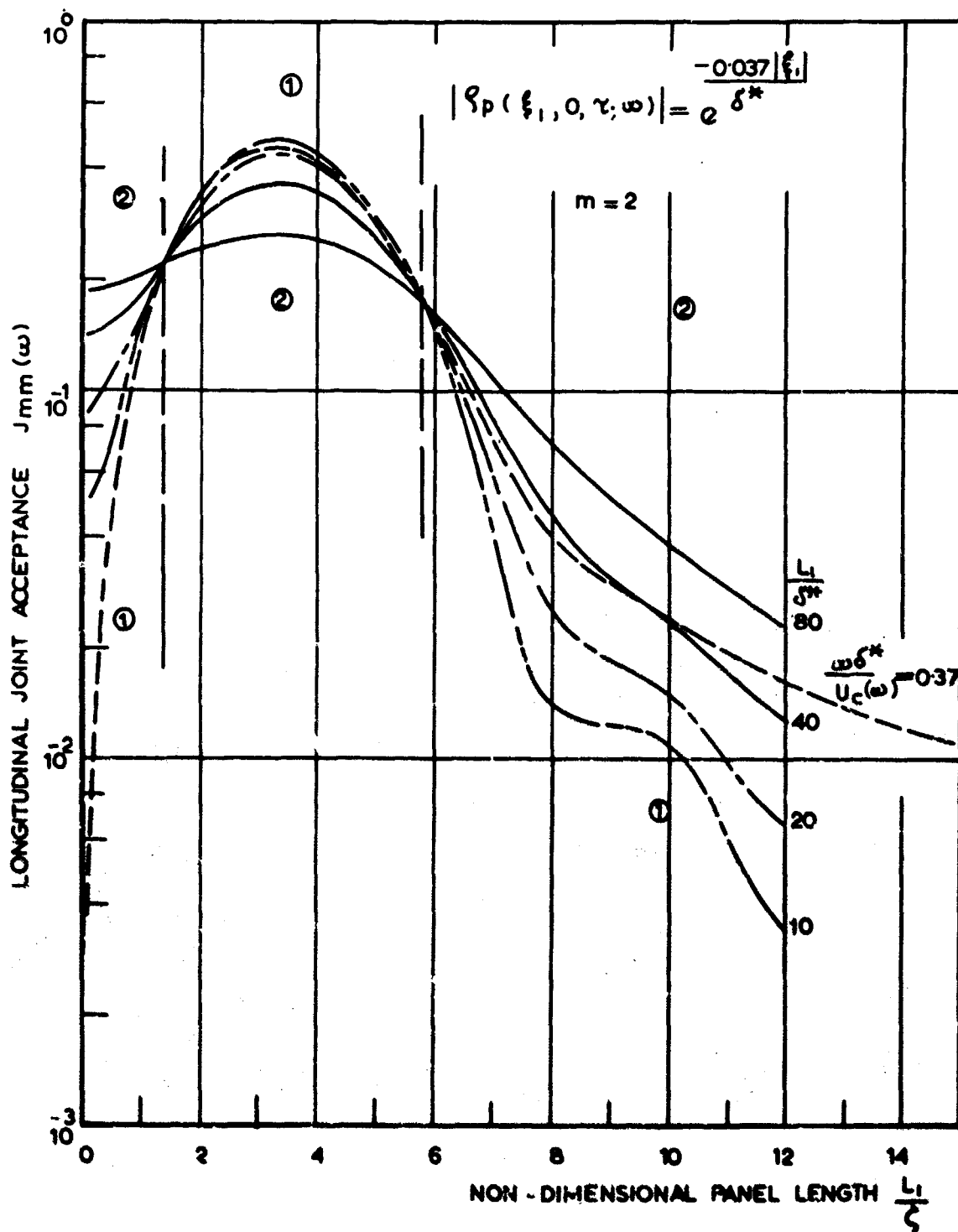


Fig 27 Longitudinal joint acceptance as function of boundary layer displacement thickness. Mode  $m = 2$



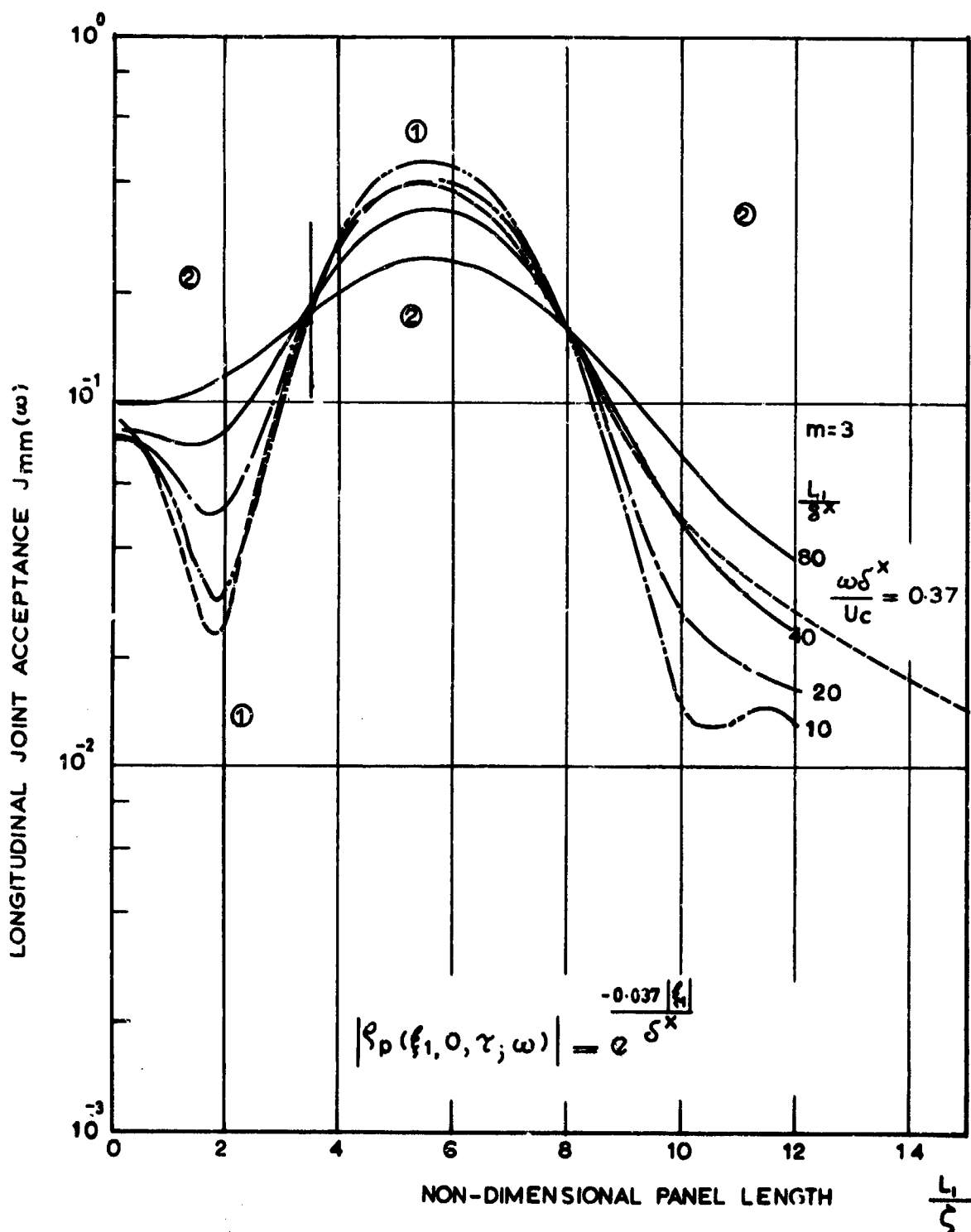


Figure 2.8 Longitudinal joint acceptance as a function of boundary layer displacement thickness. Mode  $m = 3$

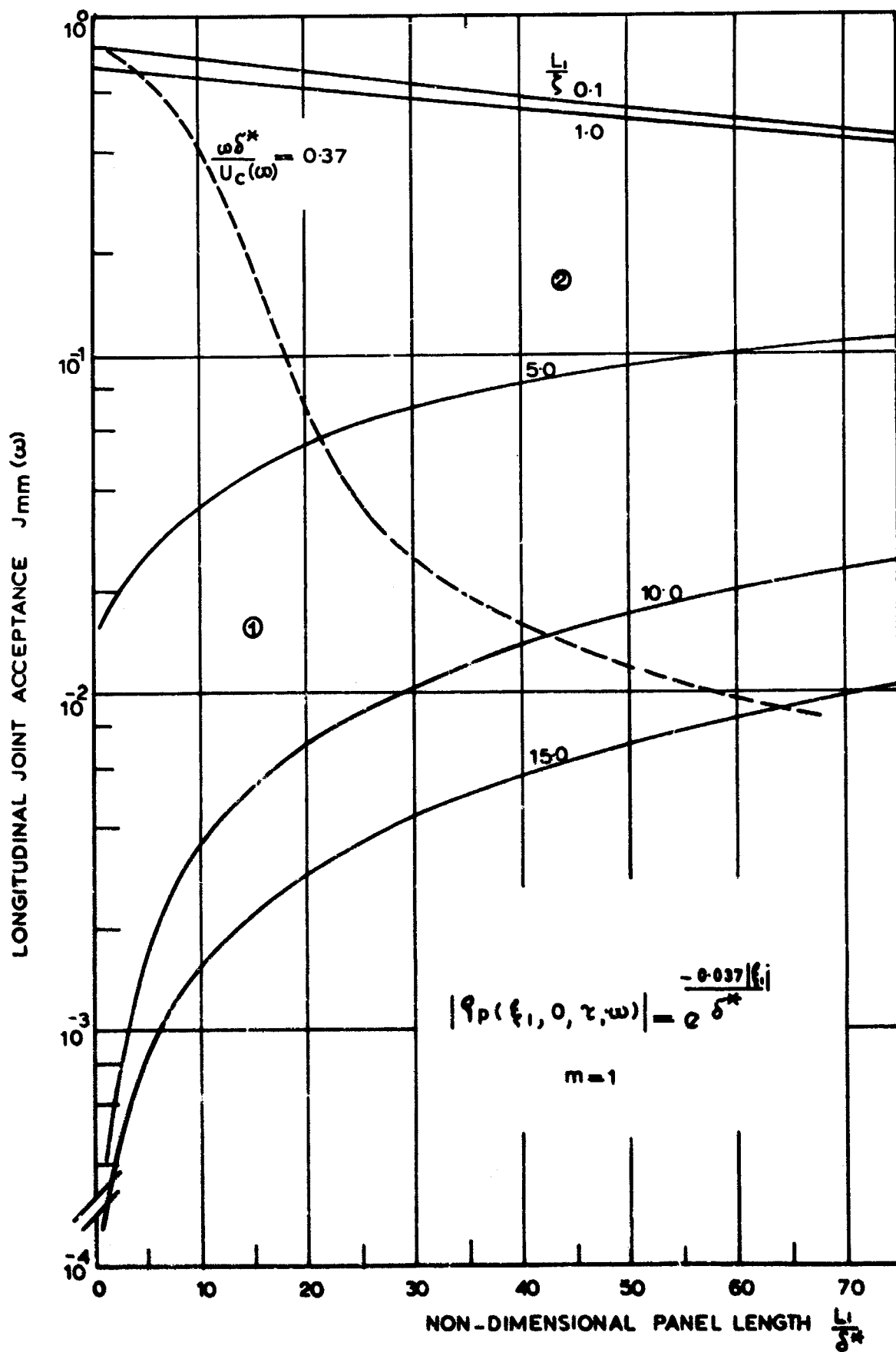


Fig.29 Longitudinal joint acceptance as function of boundary layer displacement thickness. Mode  $m=1$

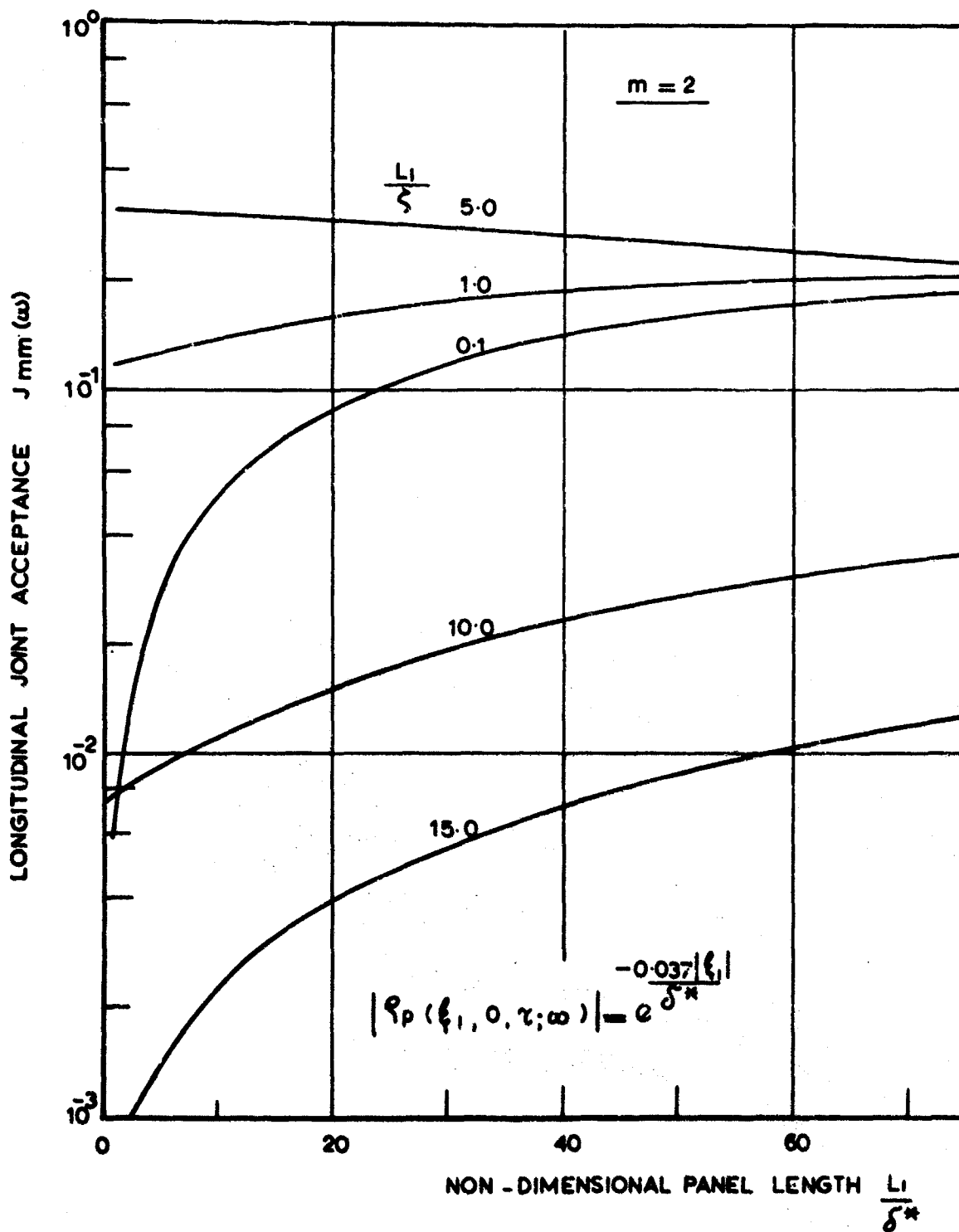


Fig. 2-10 Longitudinal joint acceptance as function of boundary layer displacement thickness. Mode  $m = 2$

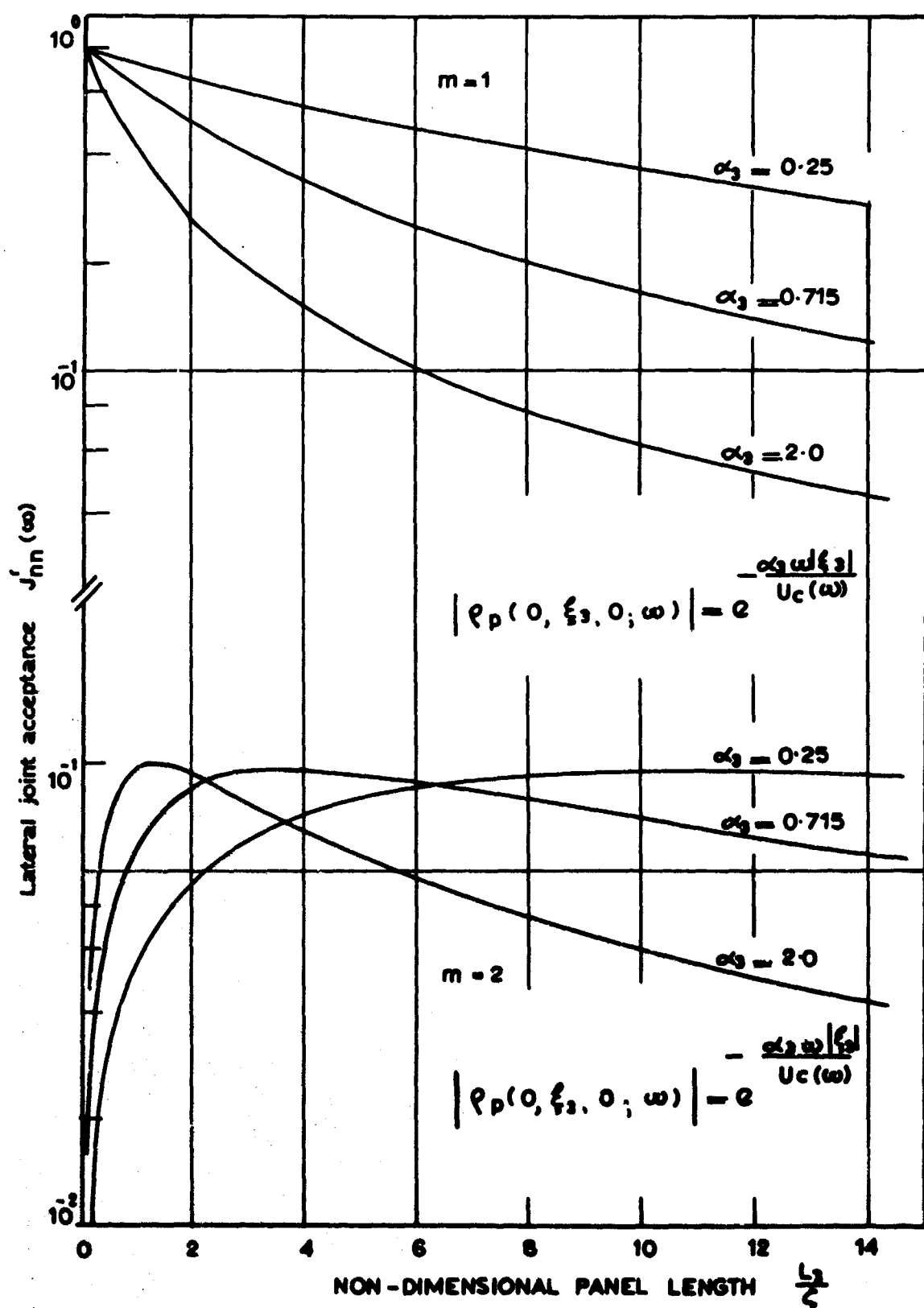


Figure 2-11. Effect of lateral correlation coefficient on panel joint acceptance . Simple form ( $m = 1, 2$ )

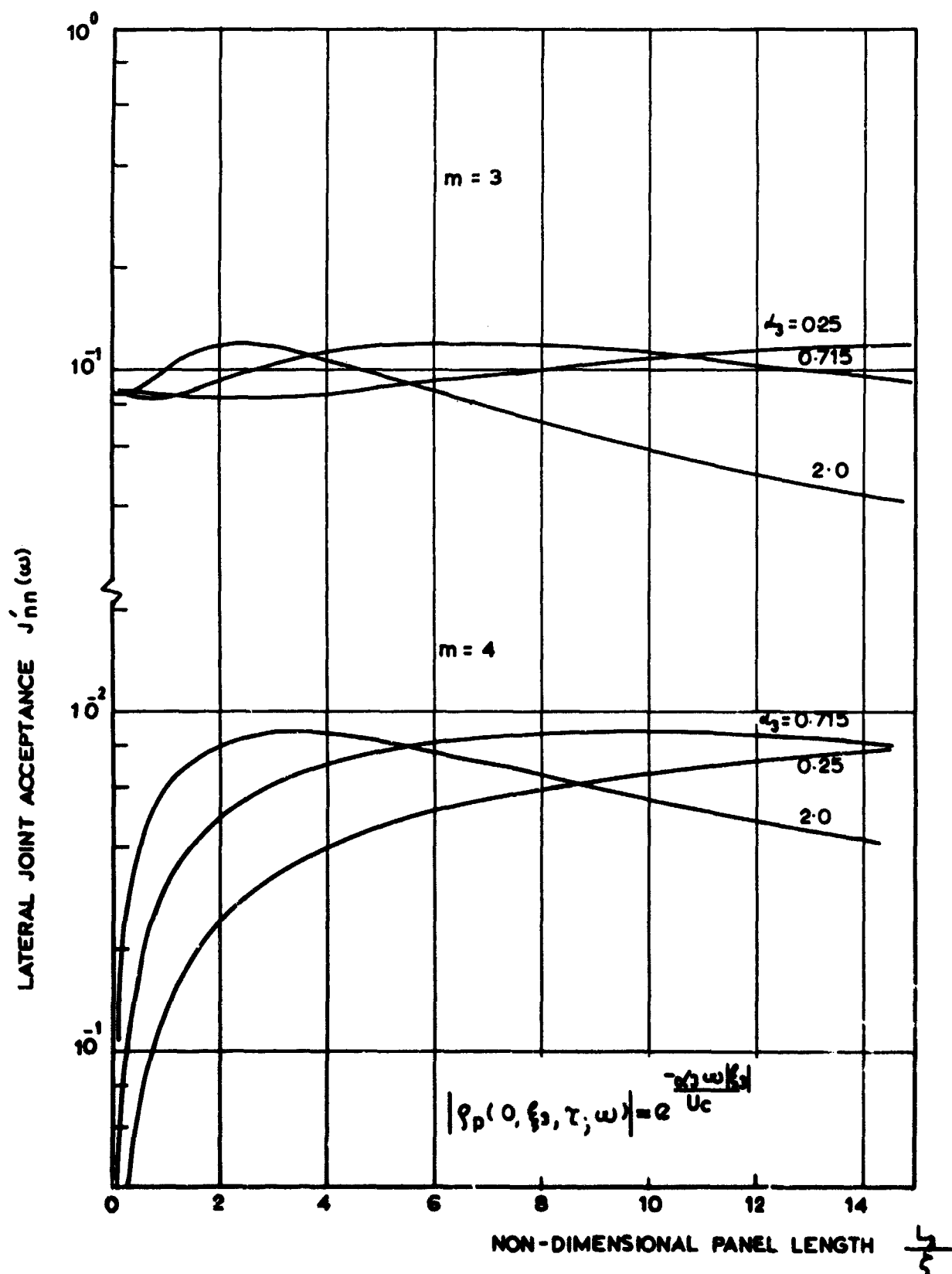


Figure 2.12 Effect of lateral correlation coefficient on panel joint acceptance.  
Simple form:  $m = 3.4$ .

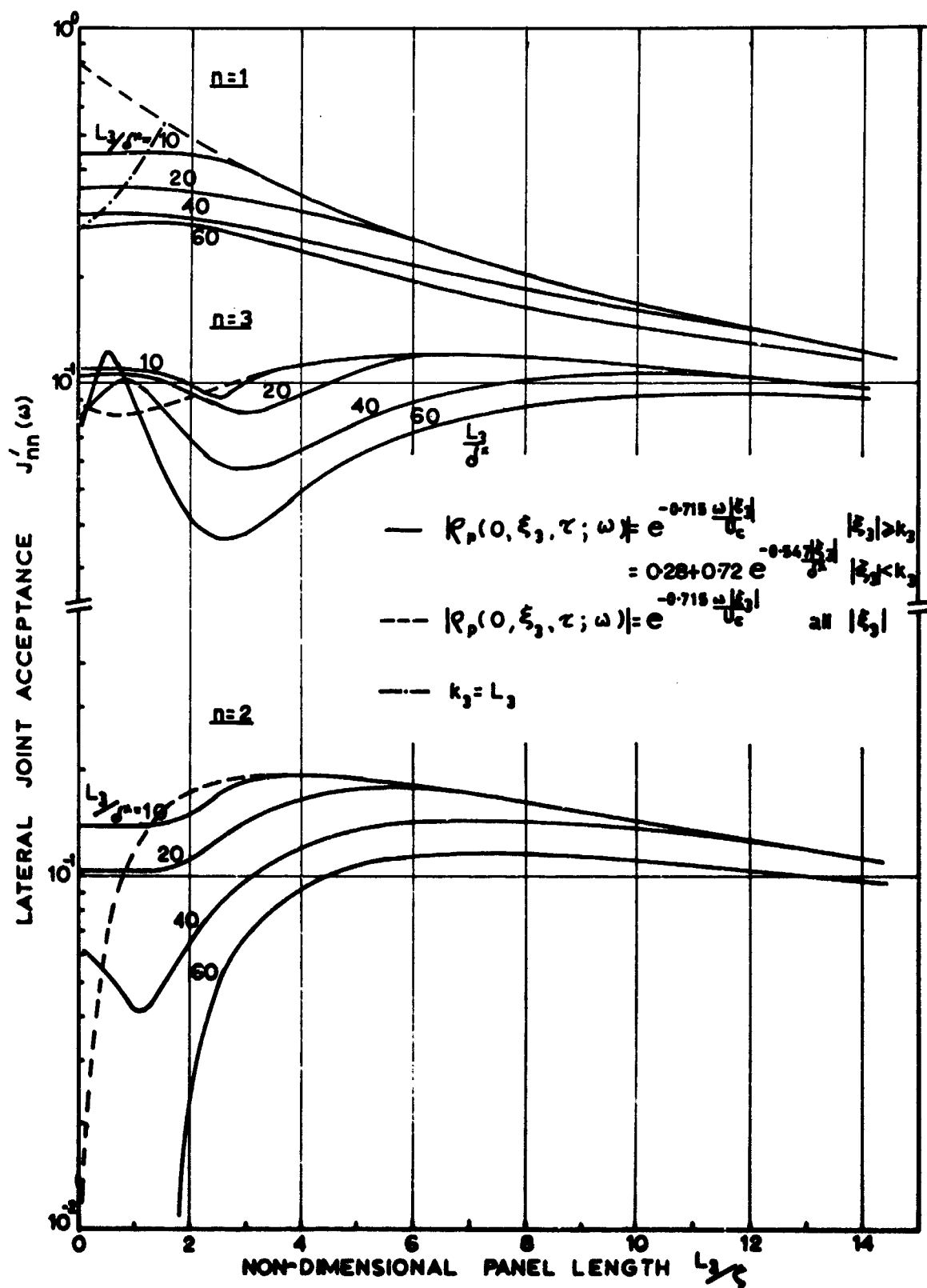


Figure 2.13 Lateral joint acceptance for boundary layer excitation.

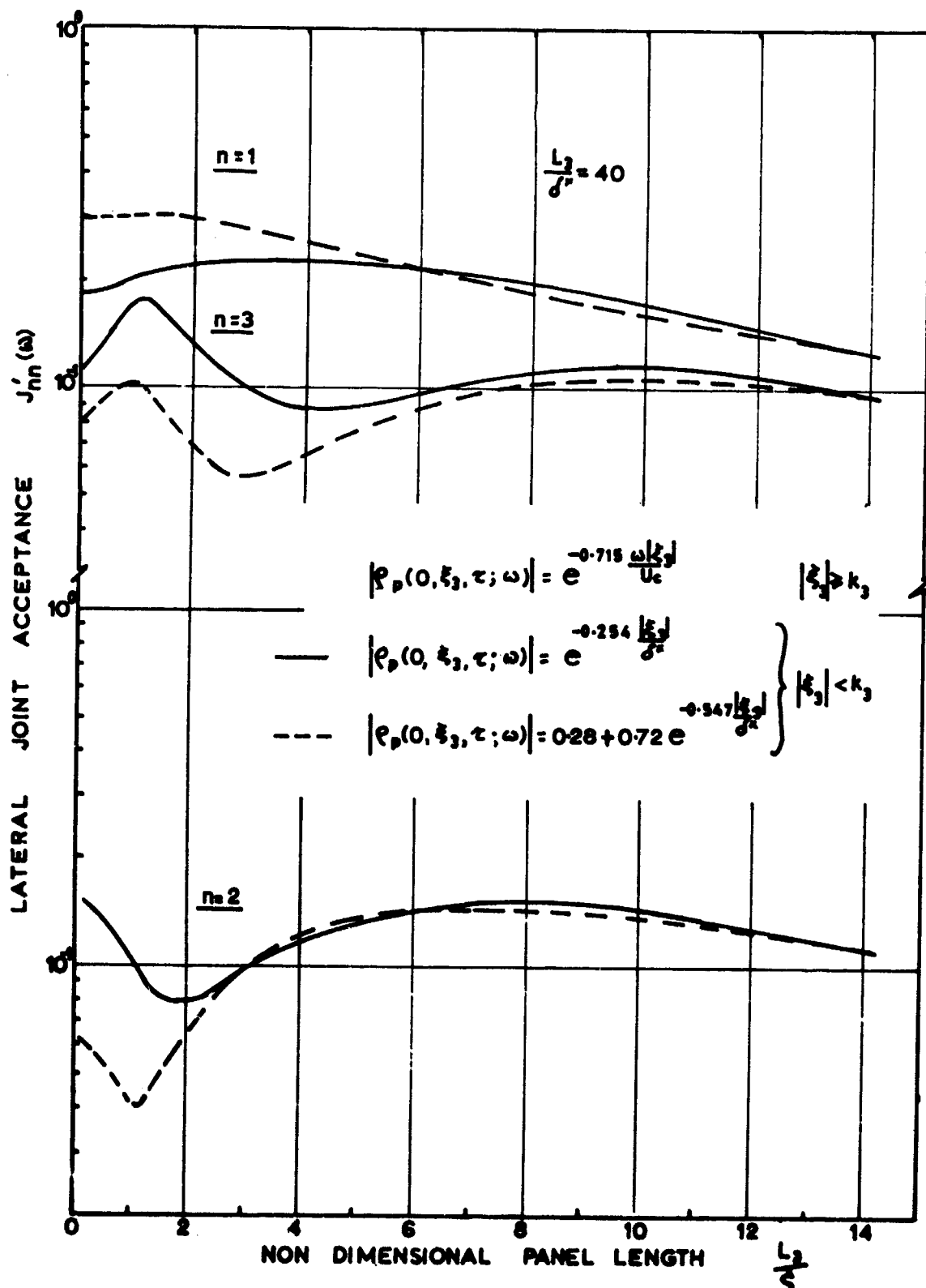


Figure 2-14 Lateral joint acceptances for different forms of correlation coefficient.

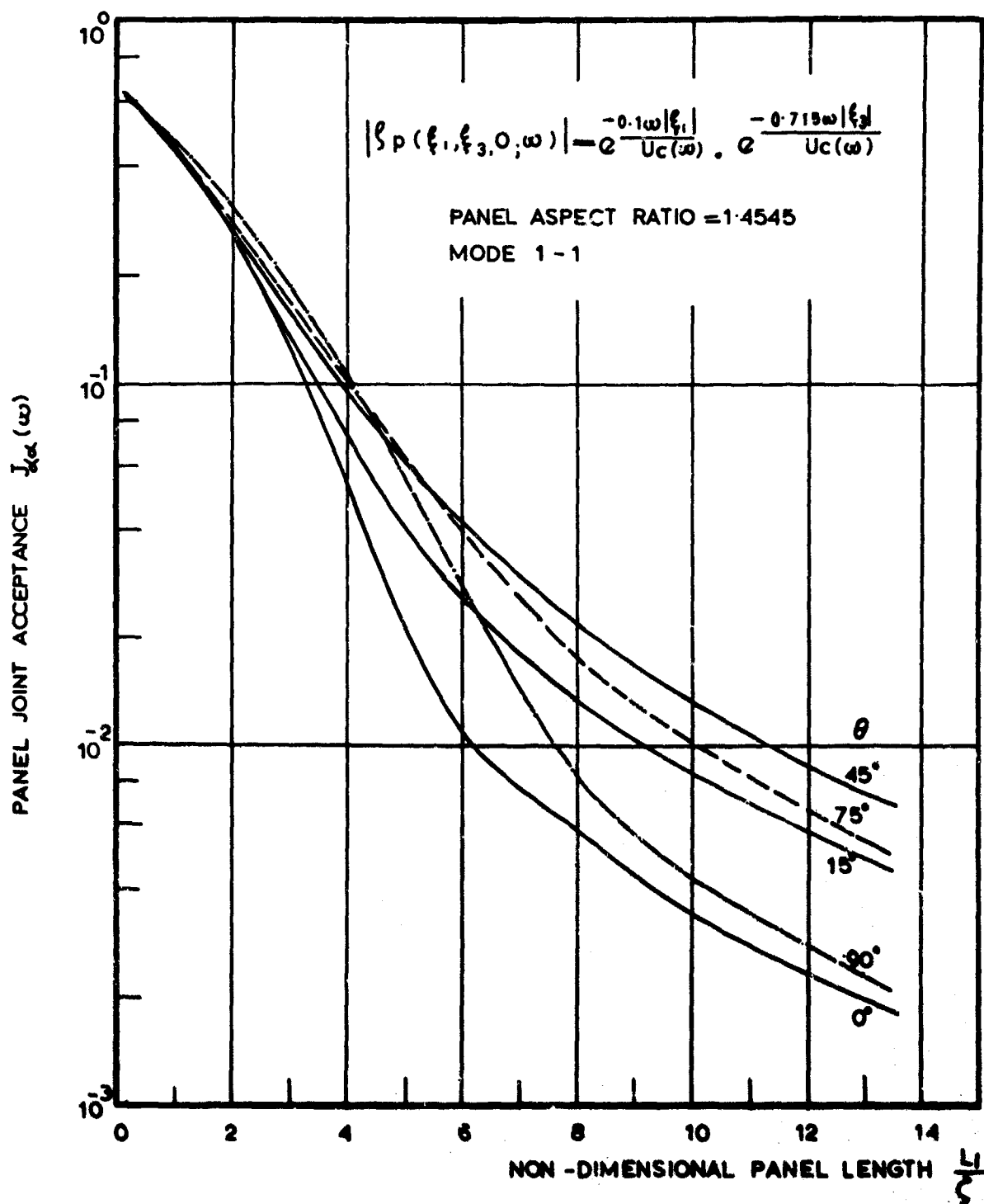


Fig. 215 Effect of pressure field convection direction  $\theta$  on panel joint acceptance. Mode 1-1



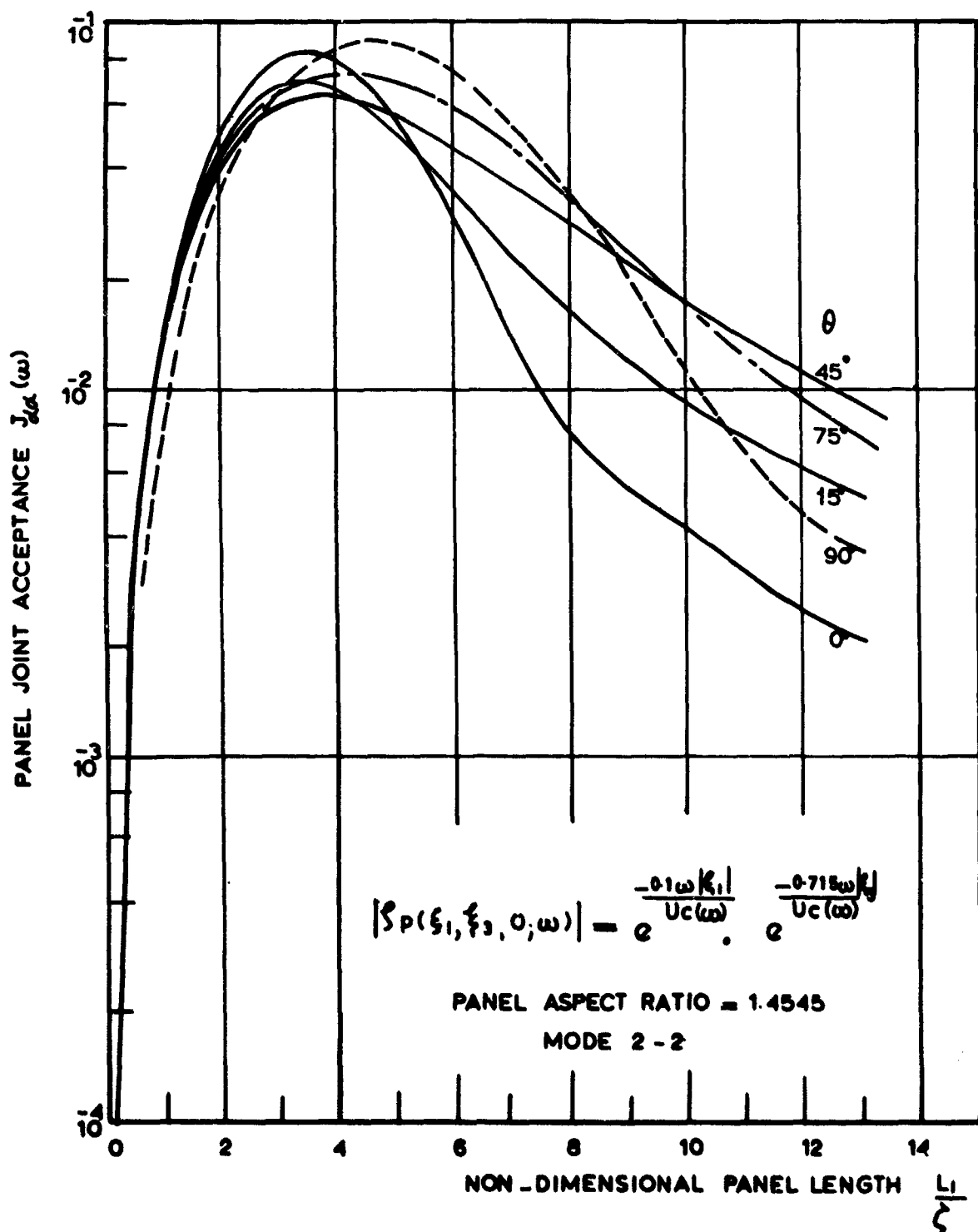


Fig. 216 Effect of pressure field convection direction  $\theta$  on panel joint acceptance. Mode 2-2

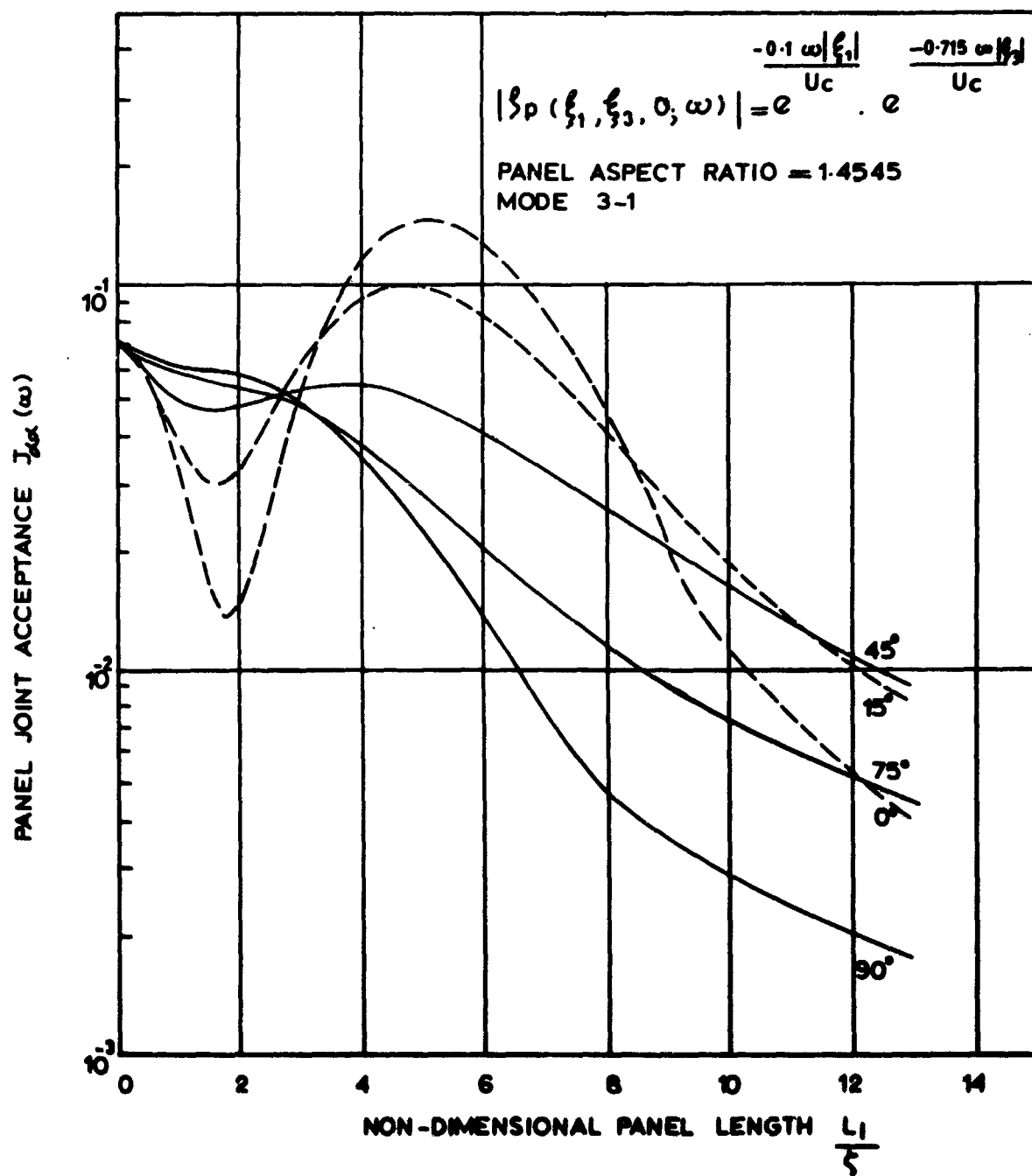


Fig. 2-17 Effect of pressure field convection direction  $\theta$  on panel joint acceptance Mode 3-1

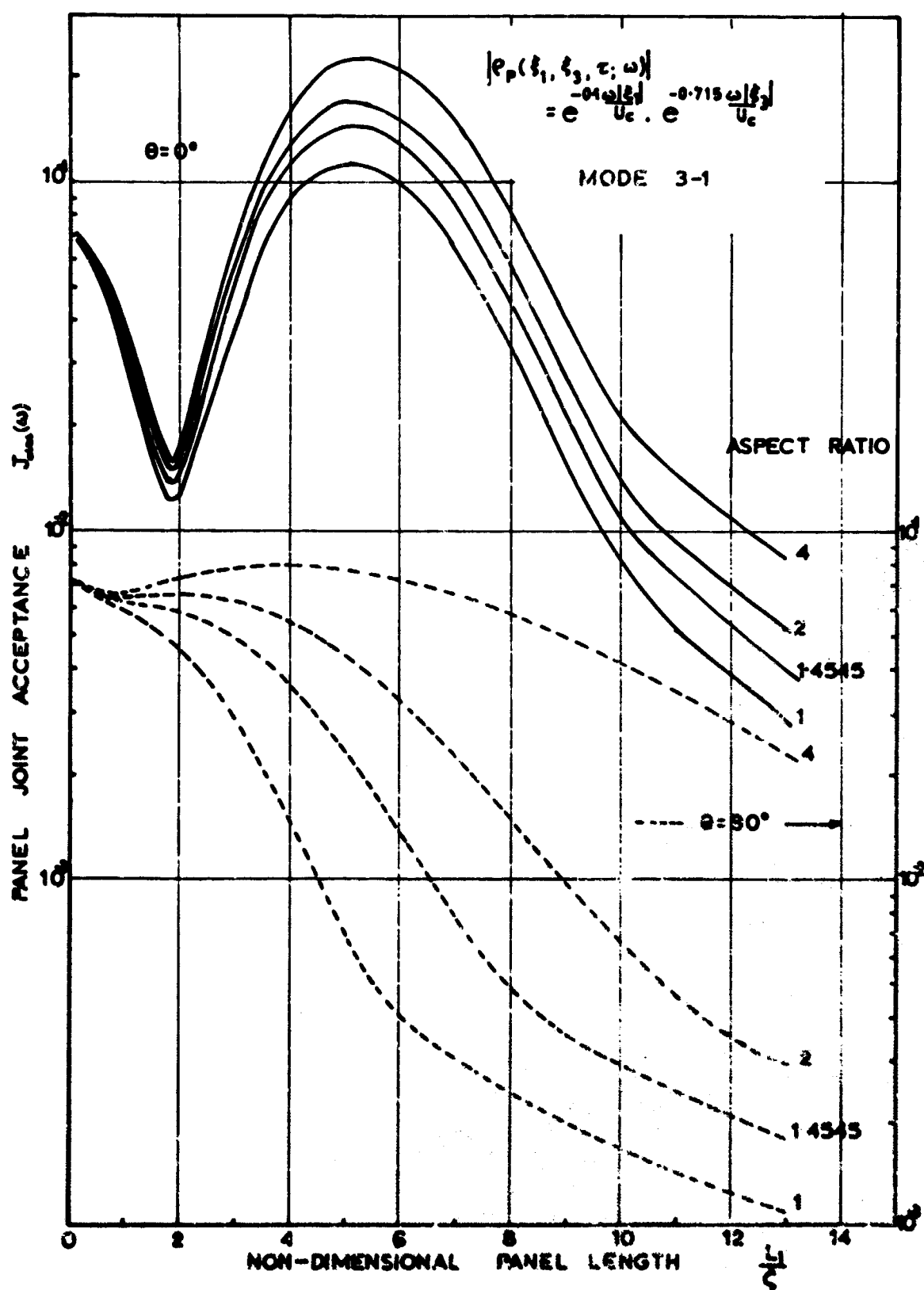


Figure 2-18 Effect of pressure field convection direction and panel aspect ratio on the joint acceptance.

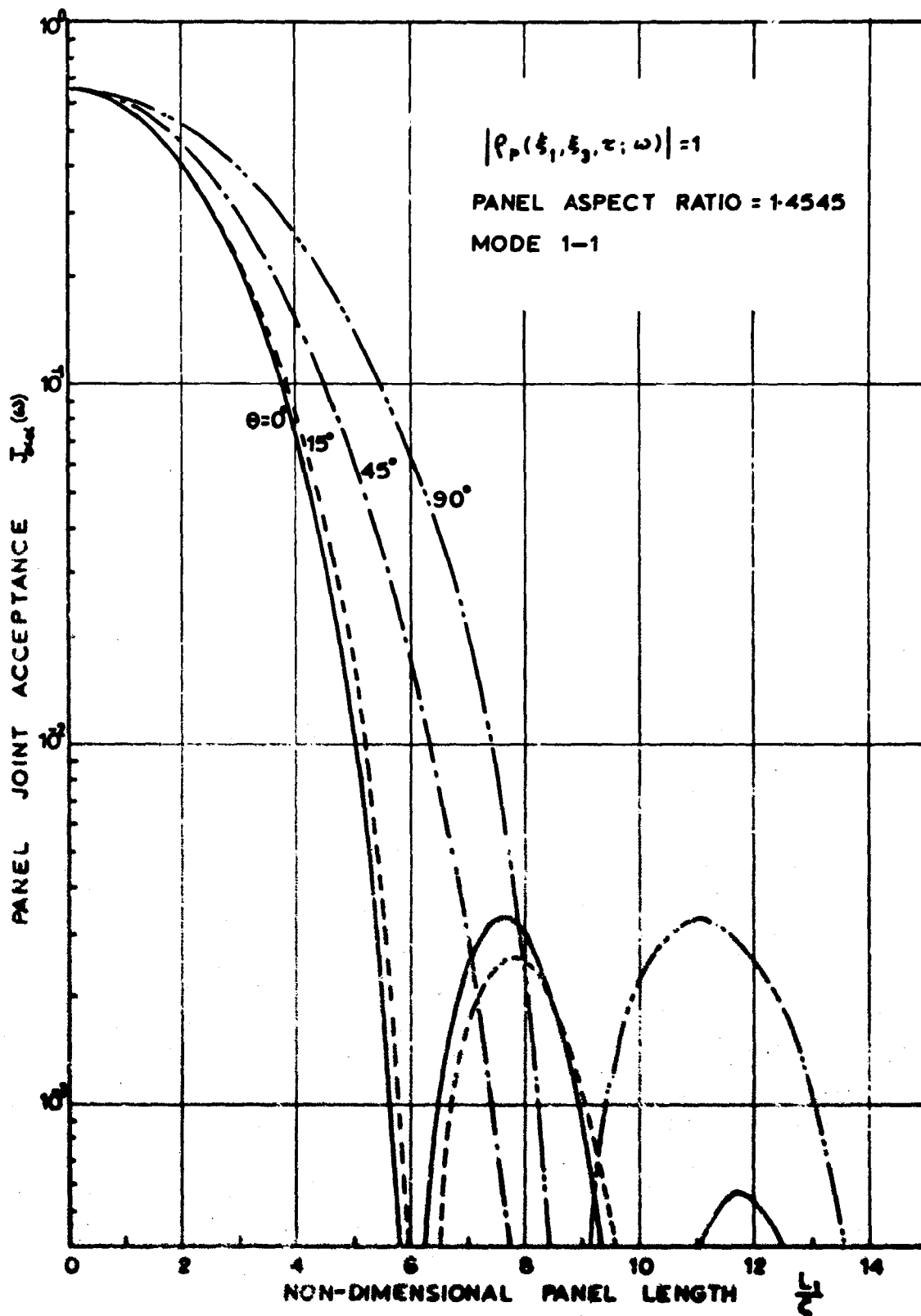


Figure 2-19 Effect of acoustic wave direction on panel joint acceptance.

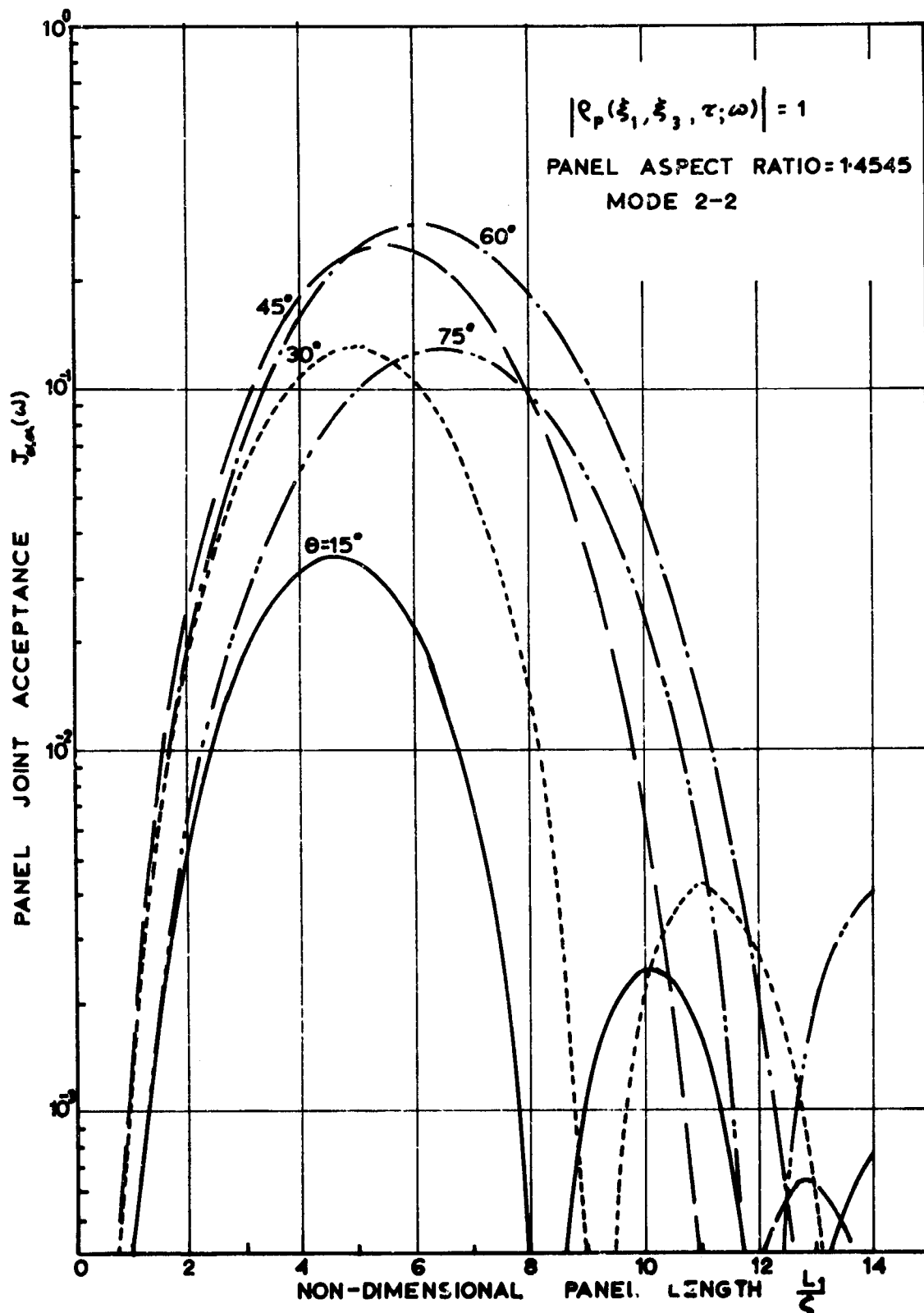


Figure 2-20 Effect of acoustic wave propagation direction on panel joint acceptance.

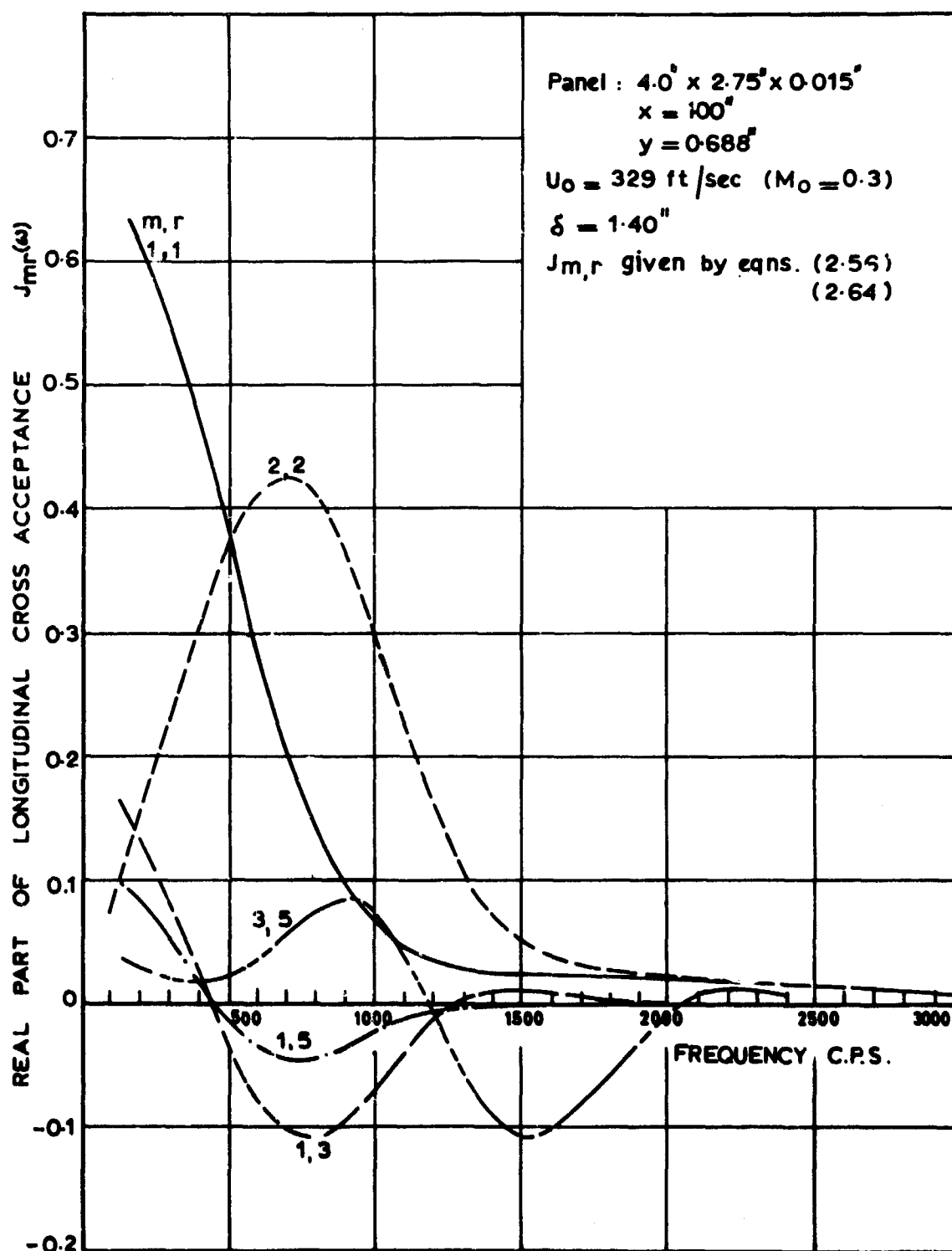


Fig.2-21 Real part of longitudinal cross acceptance calculated for panel 5 under boundary layer excitation.

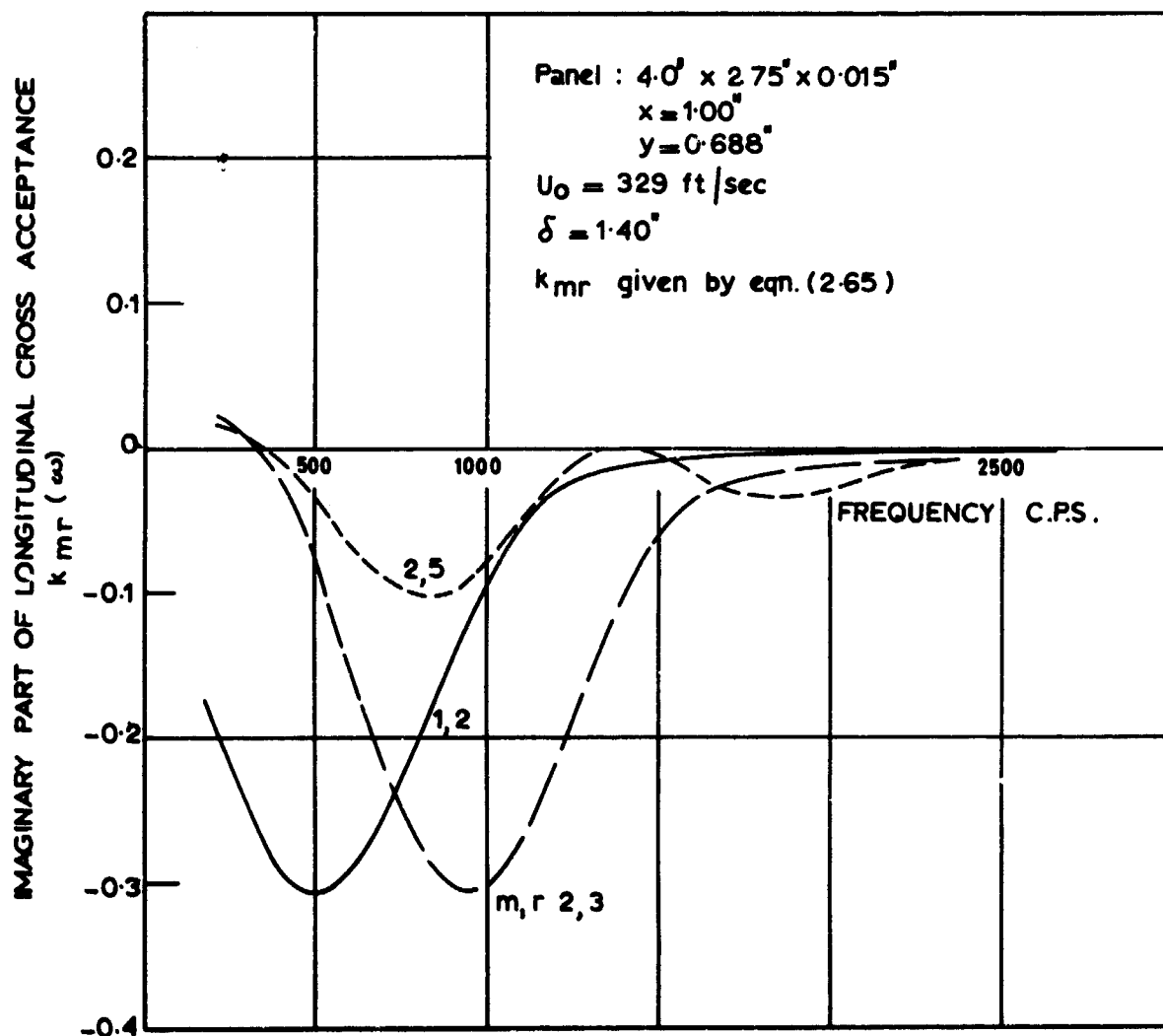


Fig.2.22 Imaginary part of longitudinal cross acceptance calculated for panel 5 under boundary layer excitation.

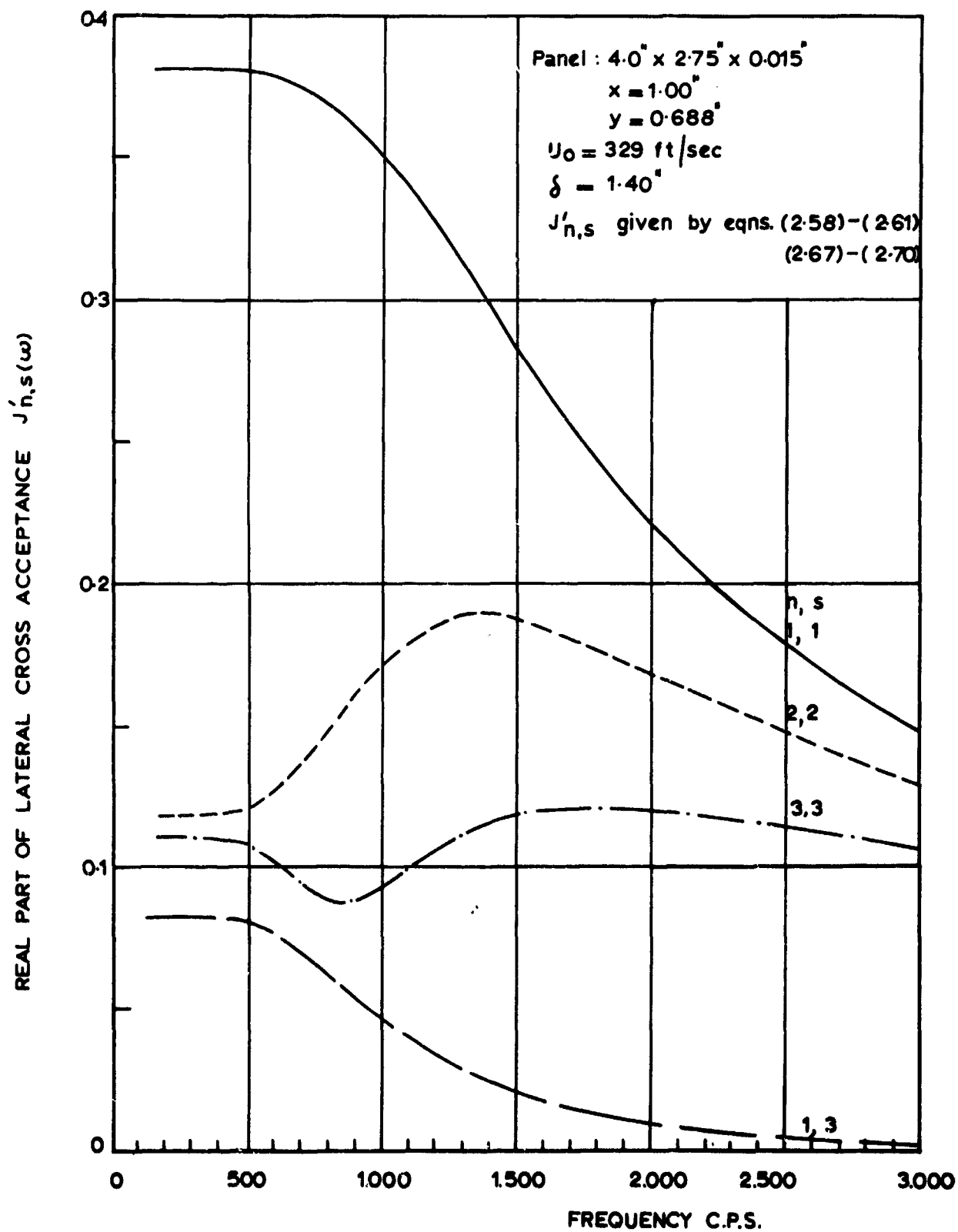


Fig.2.23 Real part of lateral cross acceptance calculated for panel 5 under boundary layer excitation .



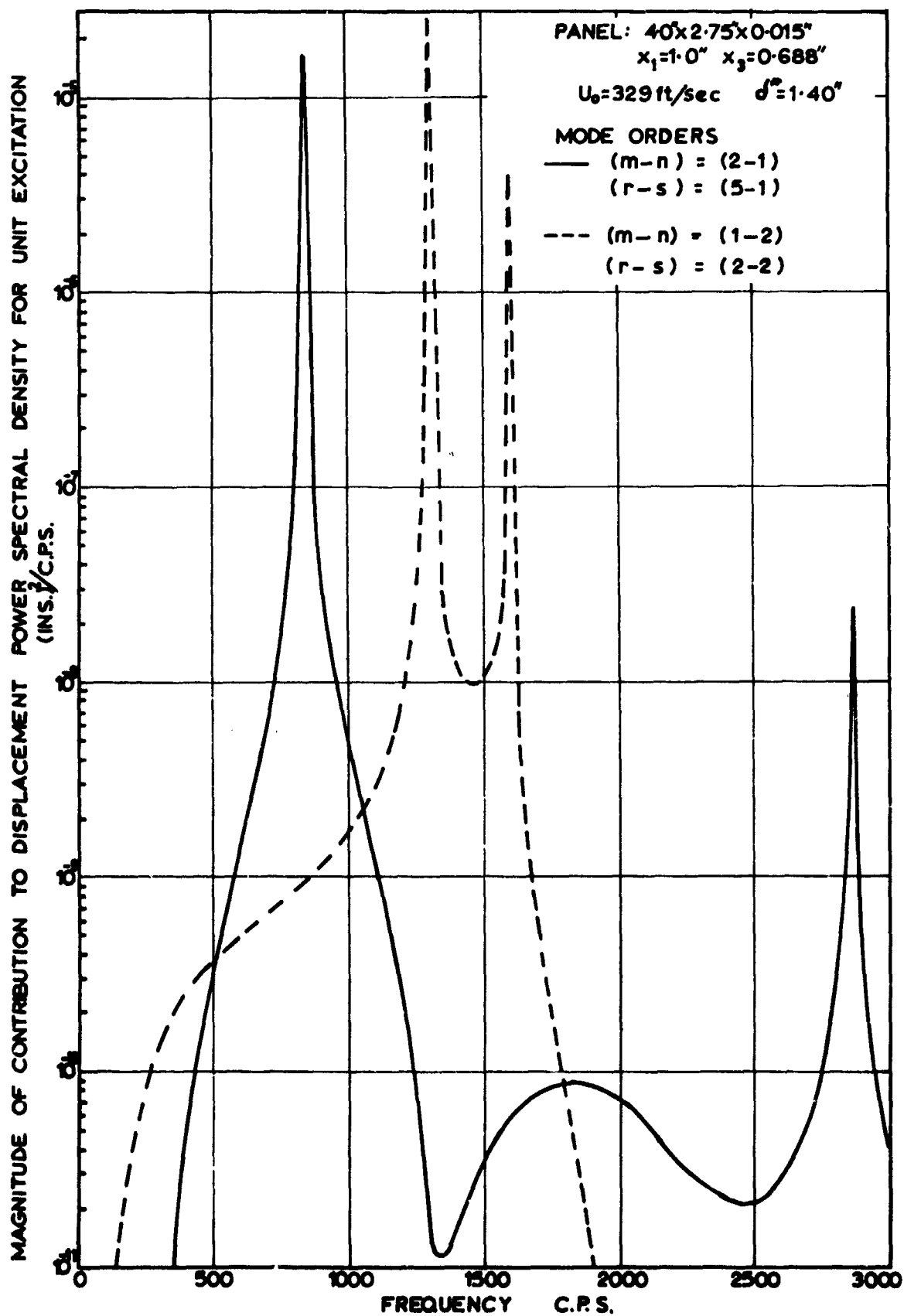


Figure 2.24 Predicted contribution of cross terms to response spectrum for boundary layer excitation: (m+r)odd.

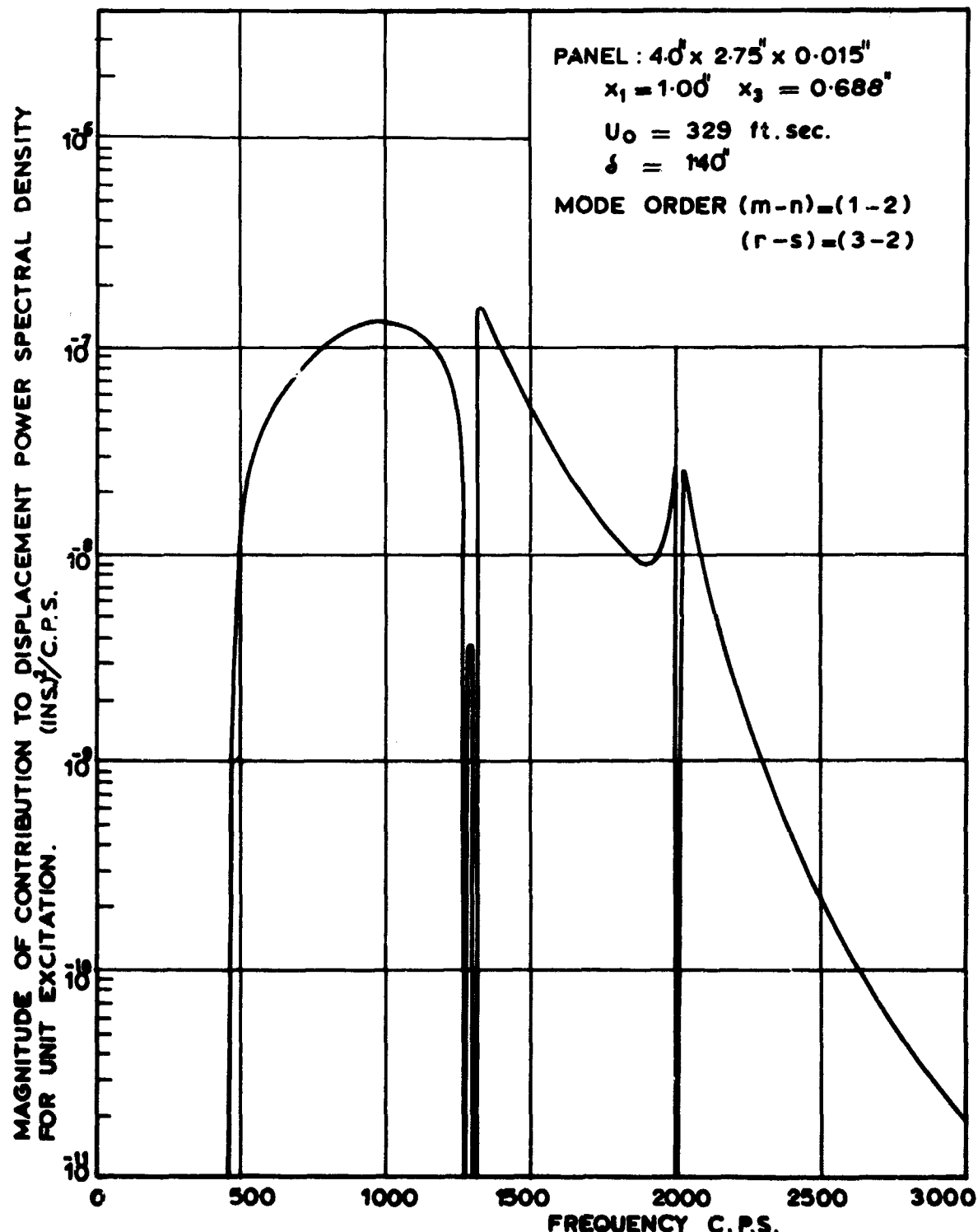


Fig.2-25. Predicted contribution of cross terms to response spectrum of panel 5 for boundary layer excitation. (m+r) even.

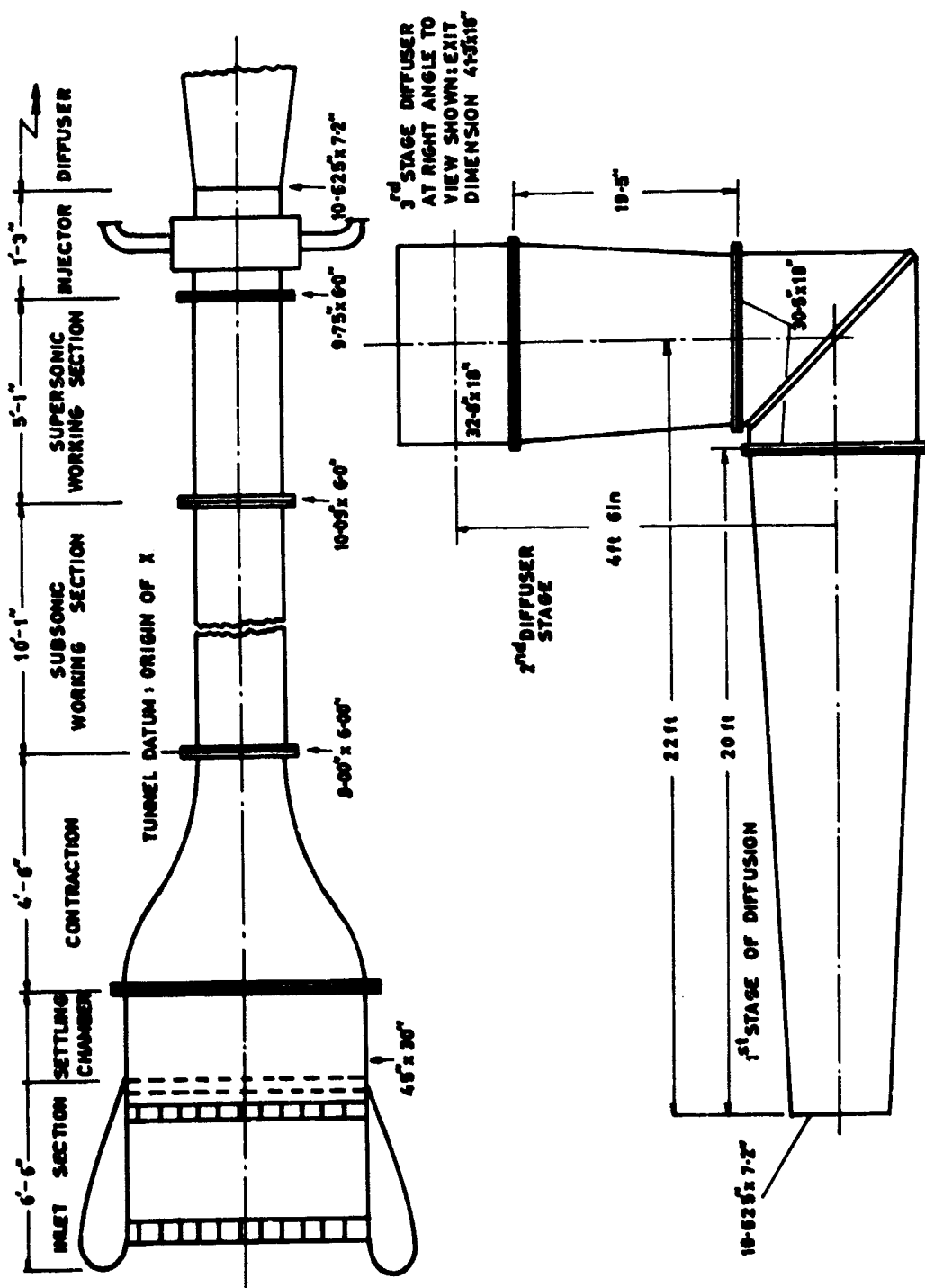


Figure 3-1 General arrangement of 9 in x 6 in boundary layer wind tunnel.

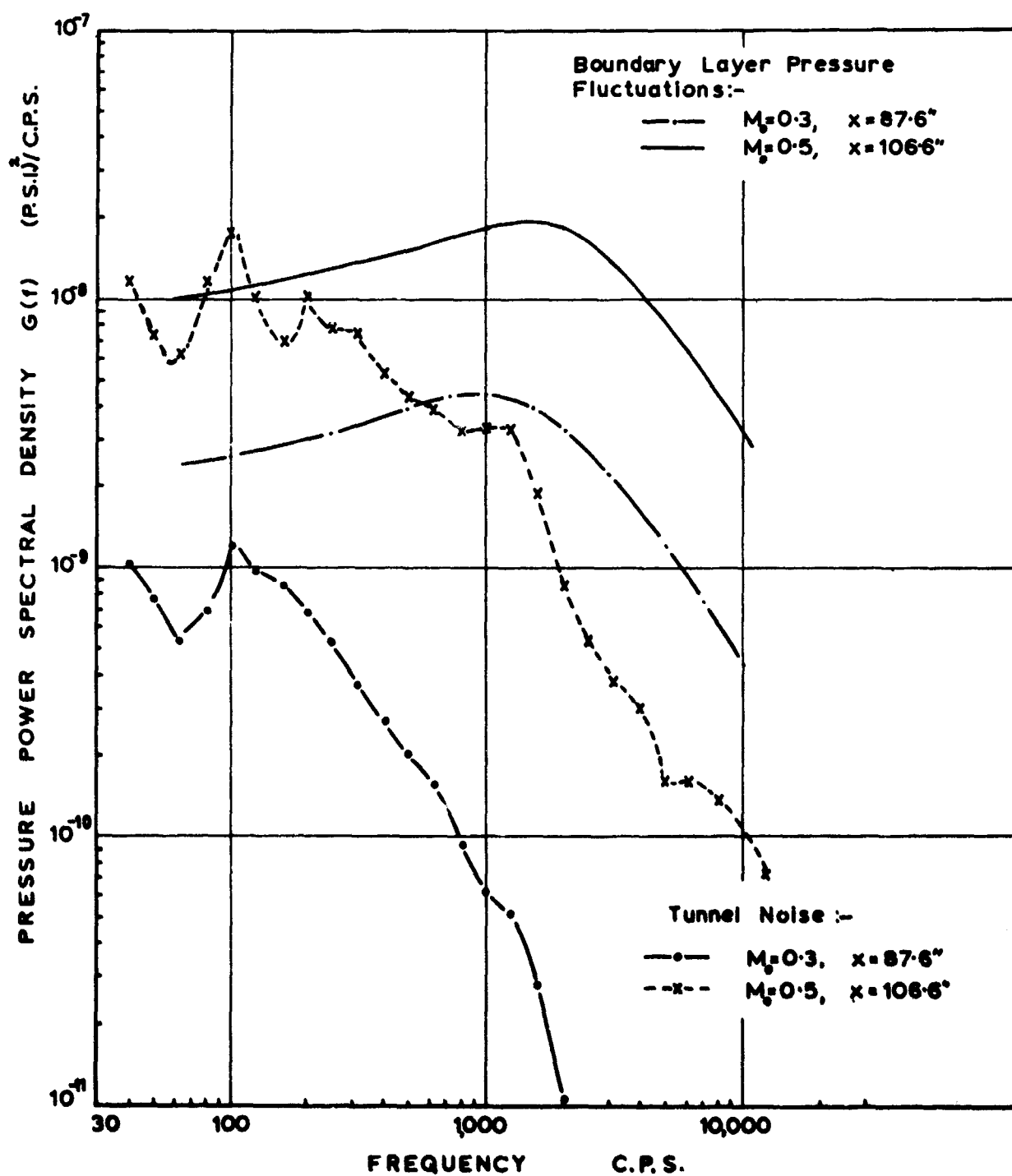


Figure 3.2 Background noise in the boundary layer wind tunnel.

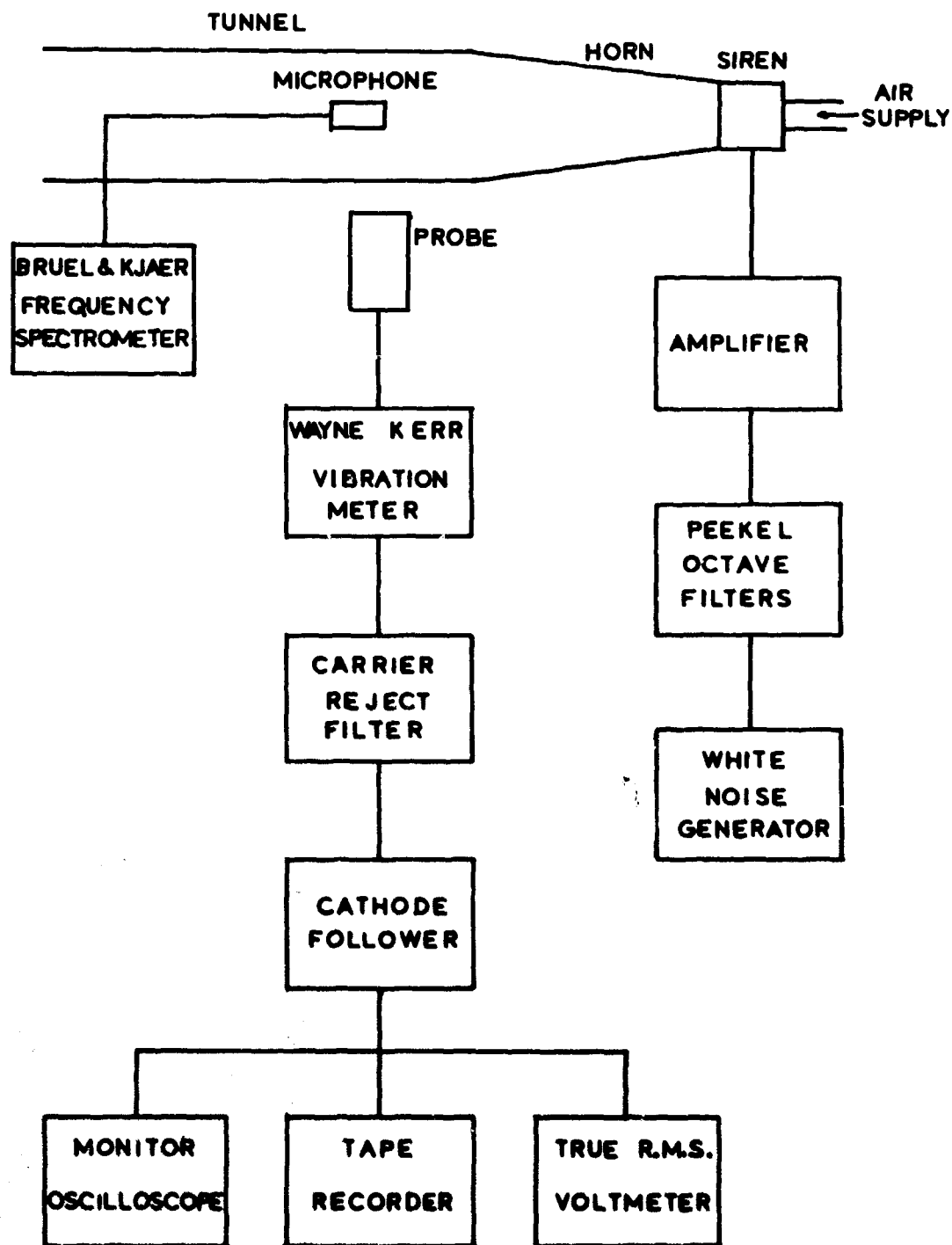


Figure 3-3 Block diagram of the apparatus for the measurement of panel response to acoustic excitation.

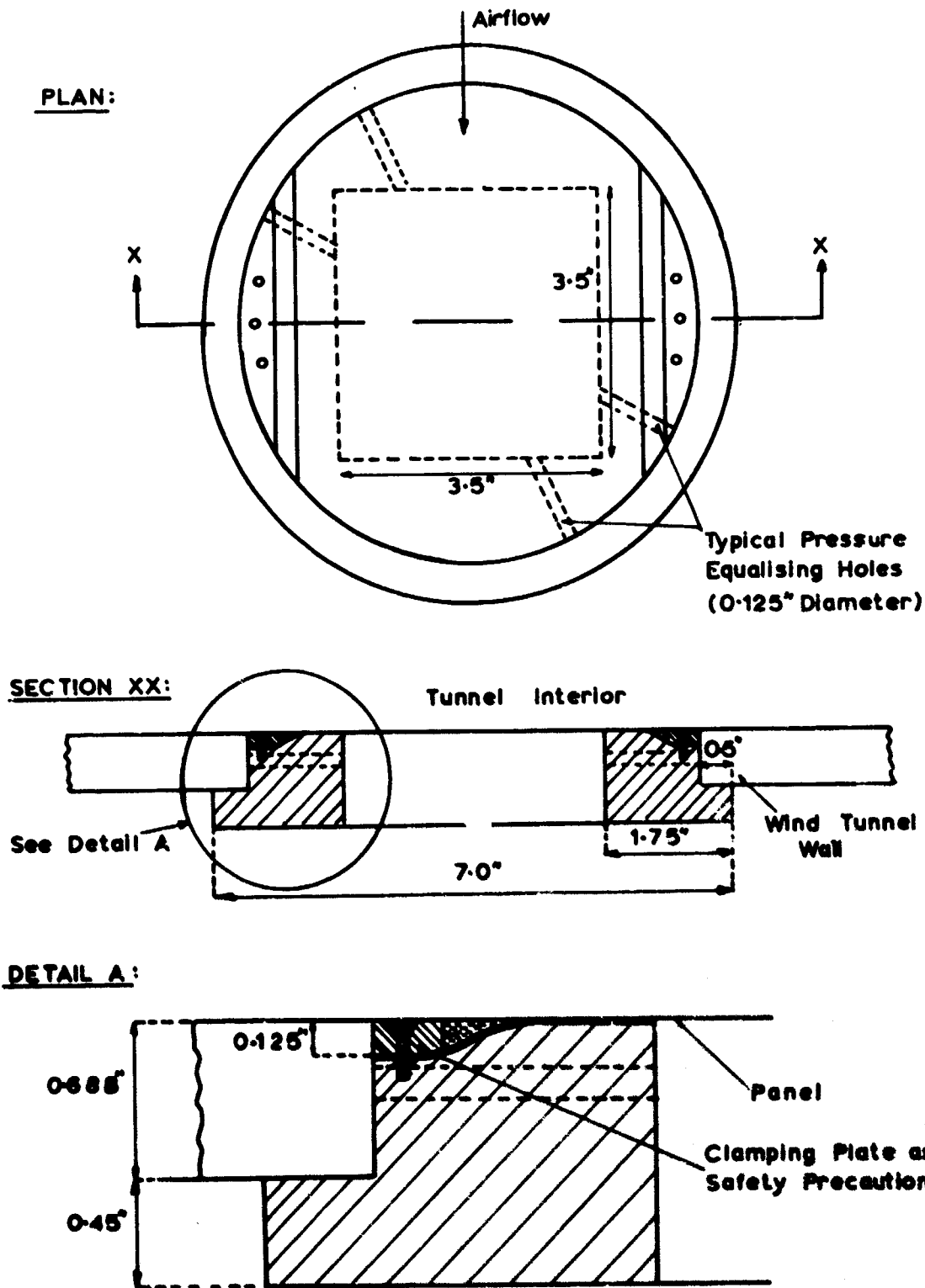
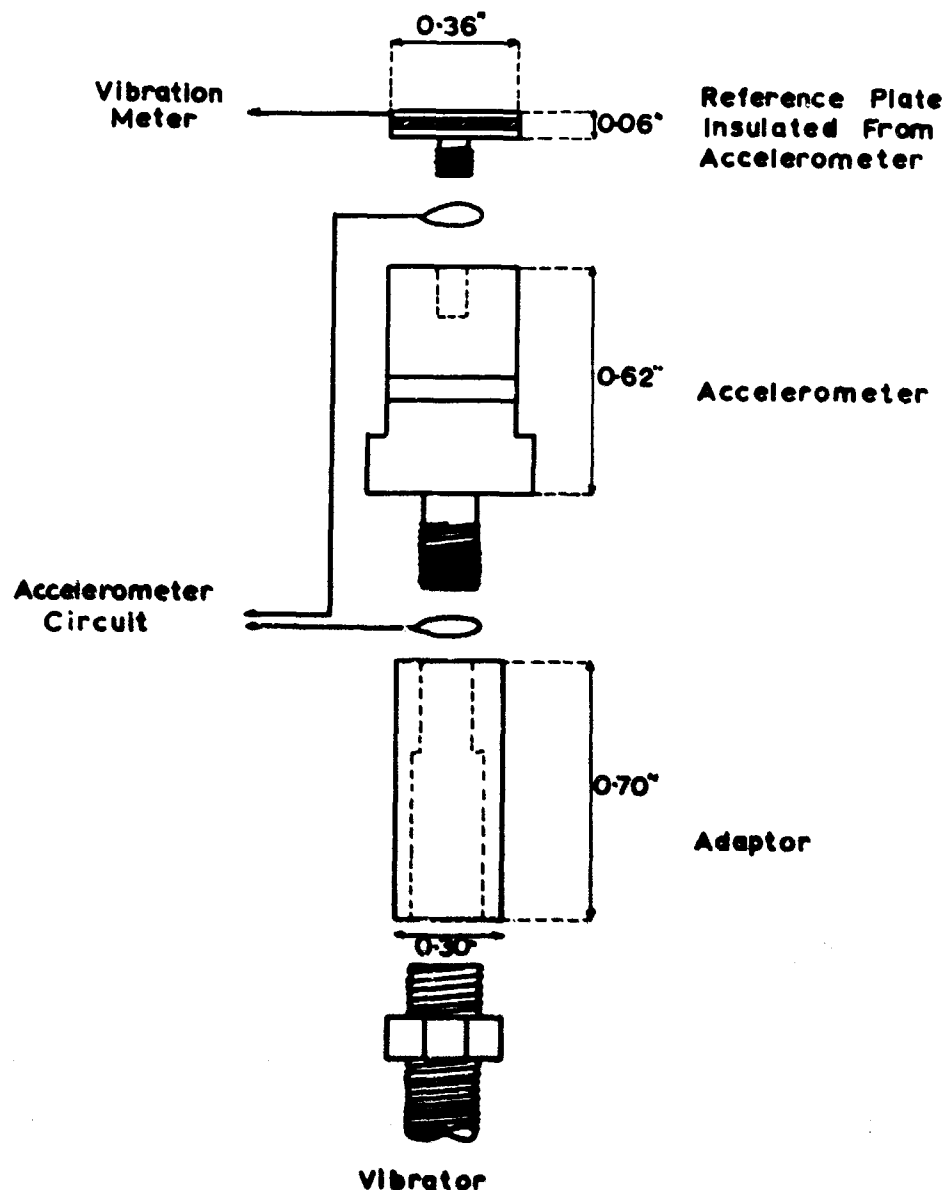


Figure 3.4 Construction of an experimental panel.



Scale: 2 x Full Size

**Figure 3-5** Details of construction of the equipment for the calibration of the Wayne Kerr capacitance probes.

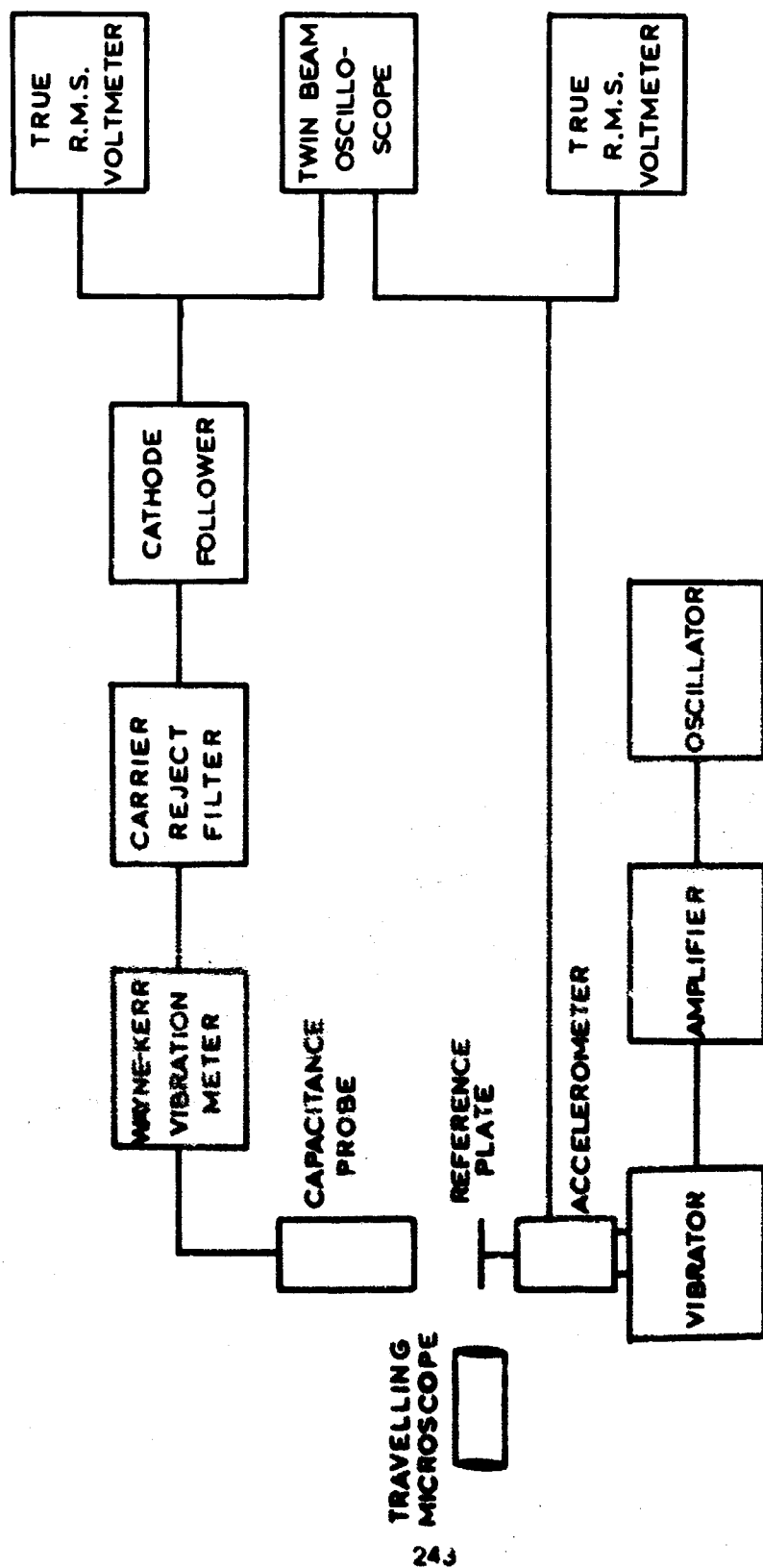


Figure 3-6 Block diagram of the apparatus for the calibration of the Wayne Kerr capacitance probes.



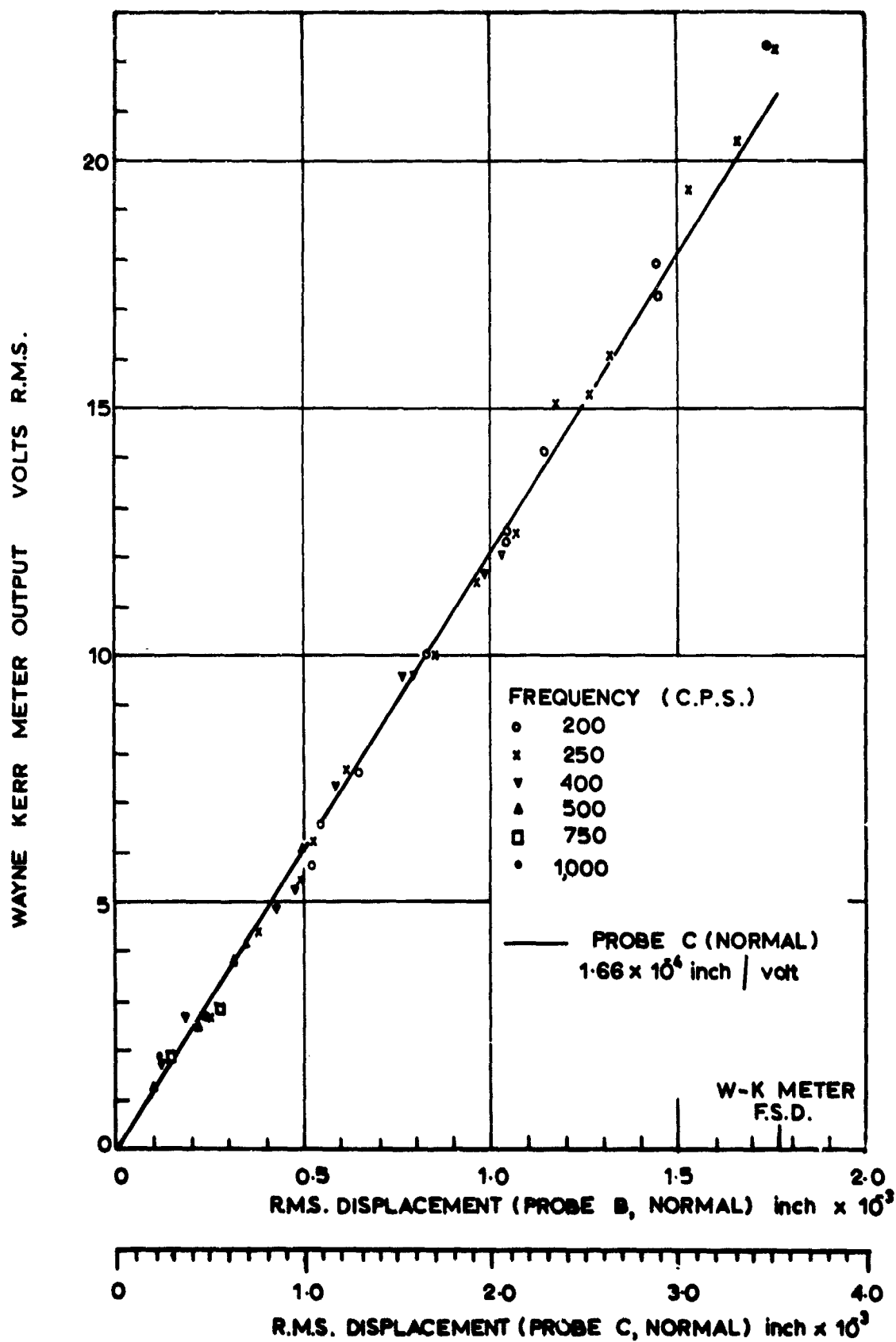


Figure 3.7 Calibration curve for Wayne Kerr capacitance probes.

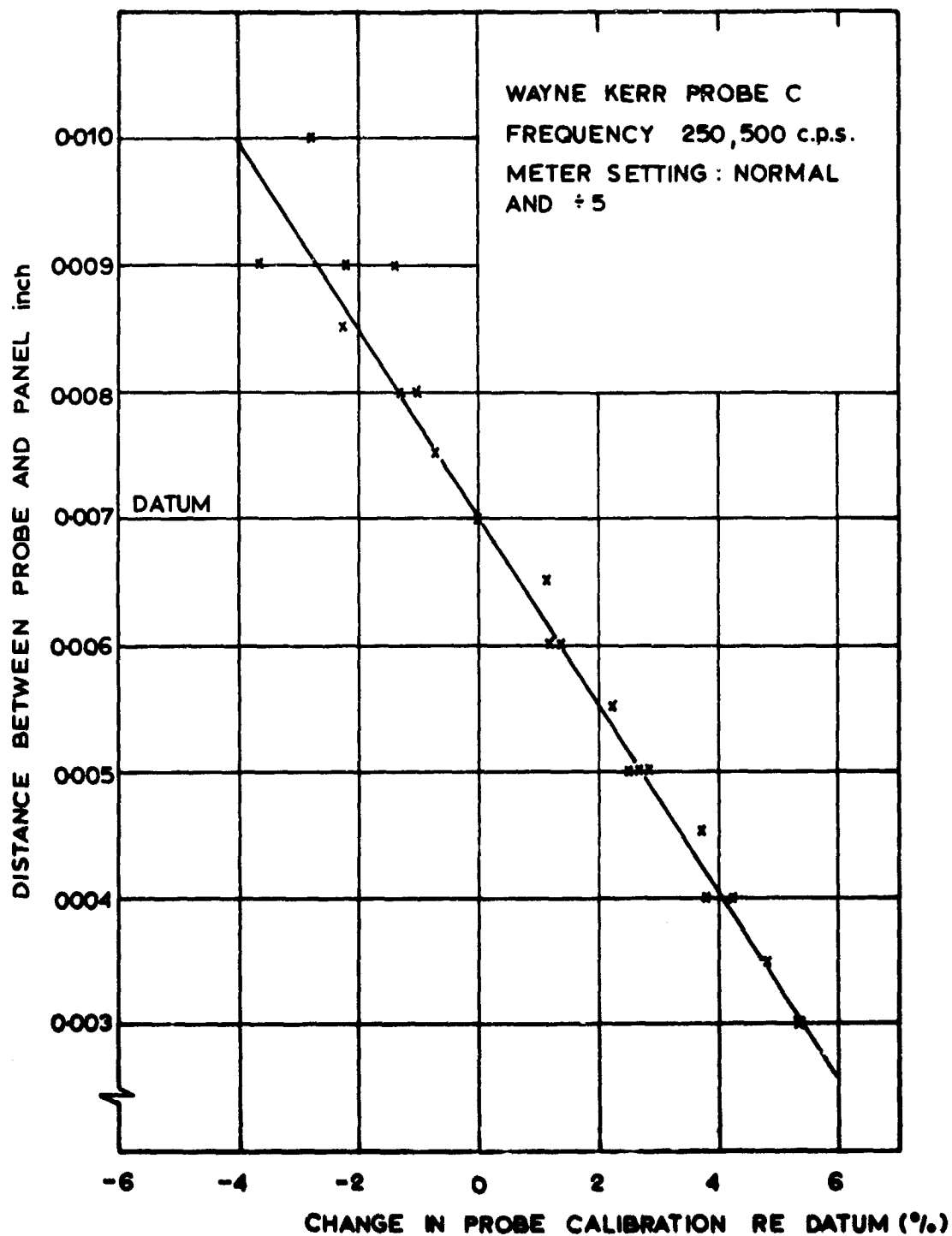


Figure 3-8 Effect of distance between probe and panel on Wayne Kerr probe calibration.

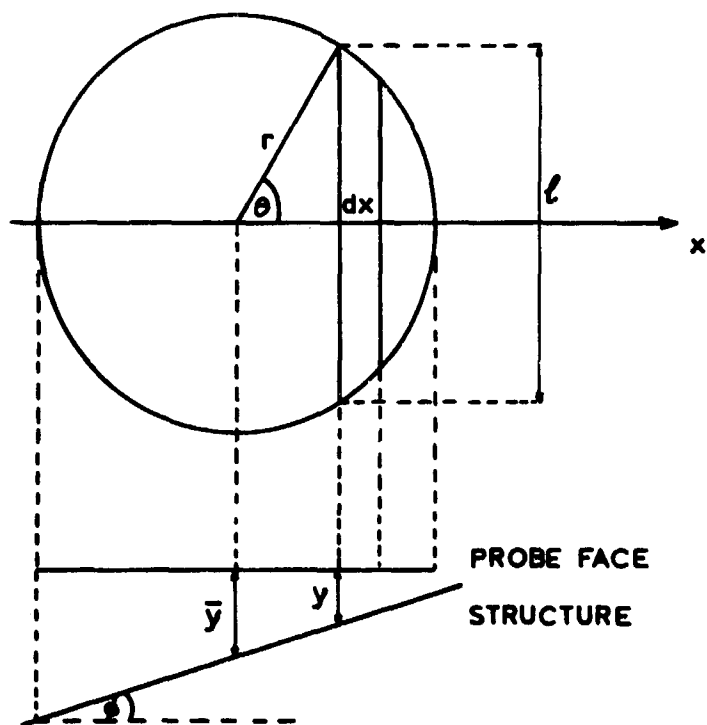


Figure 3-9 Vibrating surface Inclined to probe face.

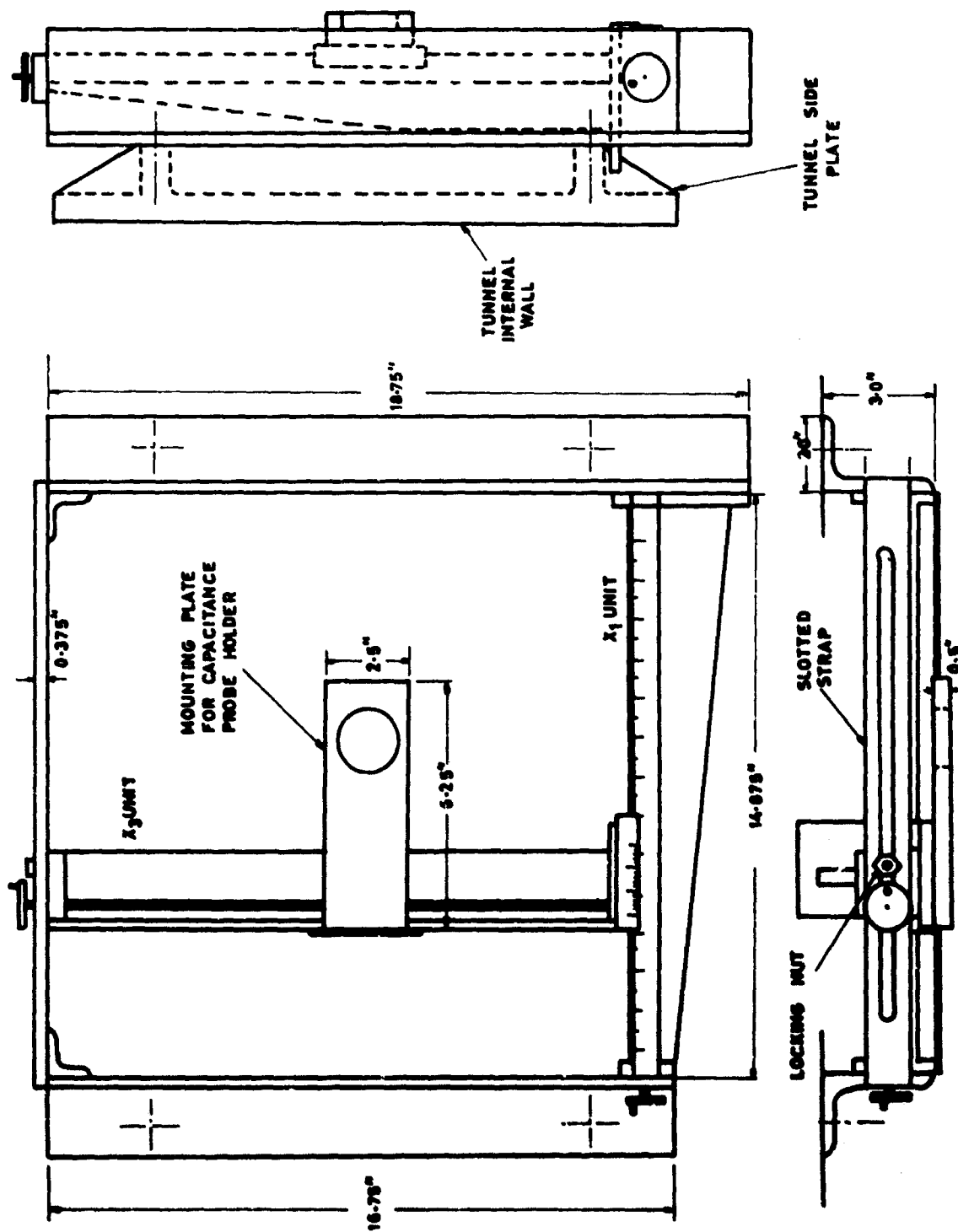
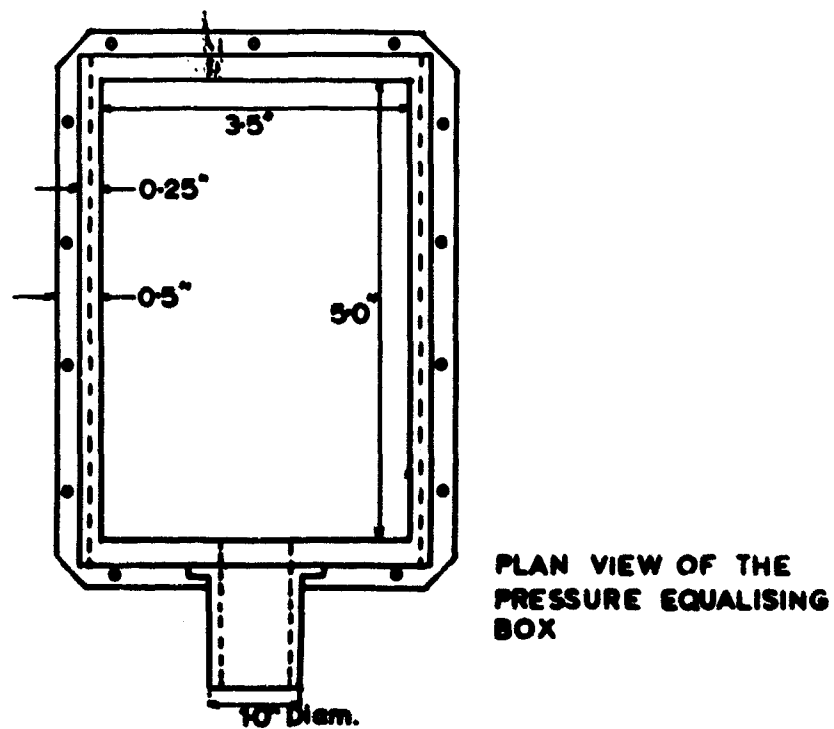
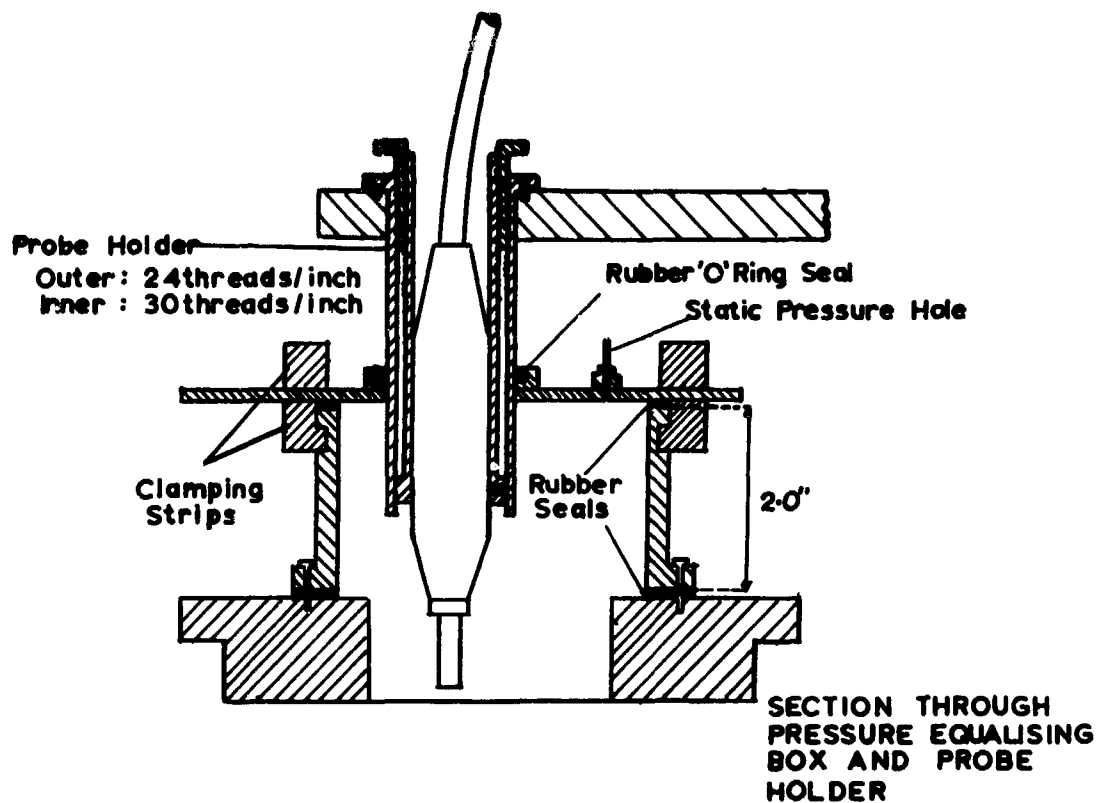
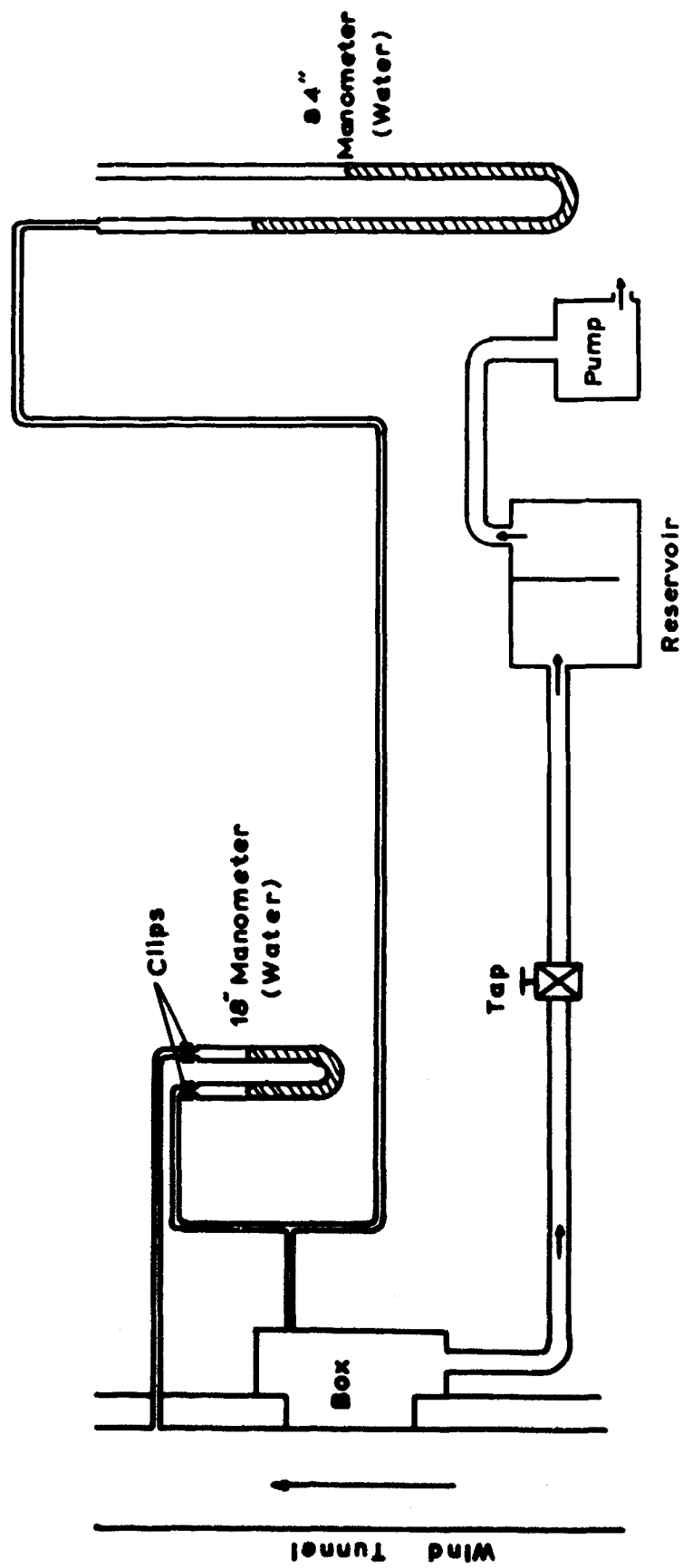


Figure 3-10 Traversing unit for the vibration-measuring probe



**Figure 3-11 Details of the pressure equalising box and probe holder.**



**Figure 3.12** Diagram of pressure equalising system .

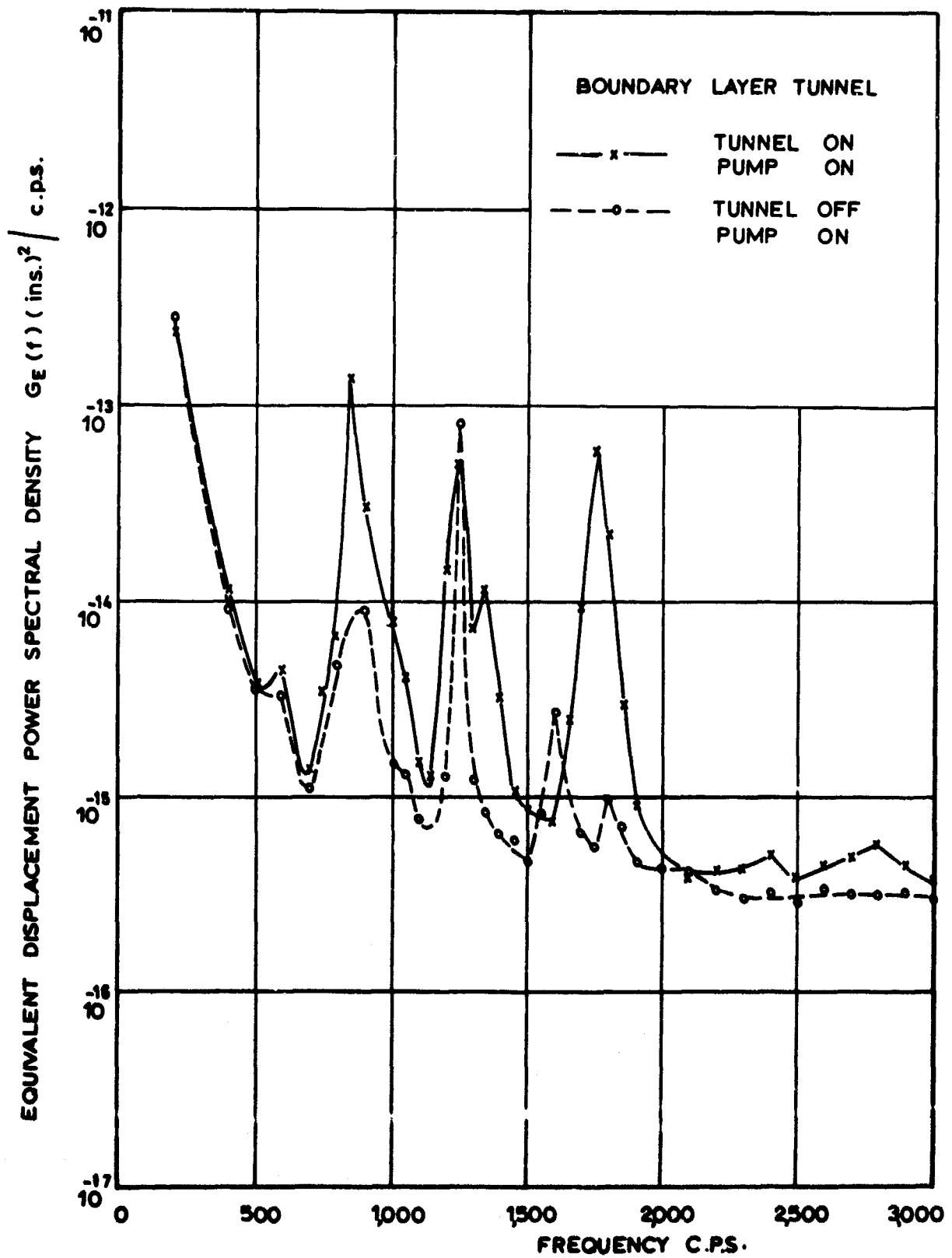


Fig.3·13 Background vibration and equipment noise :  
boundary layer excitation.

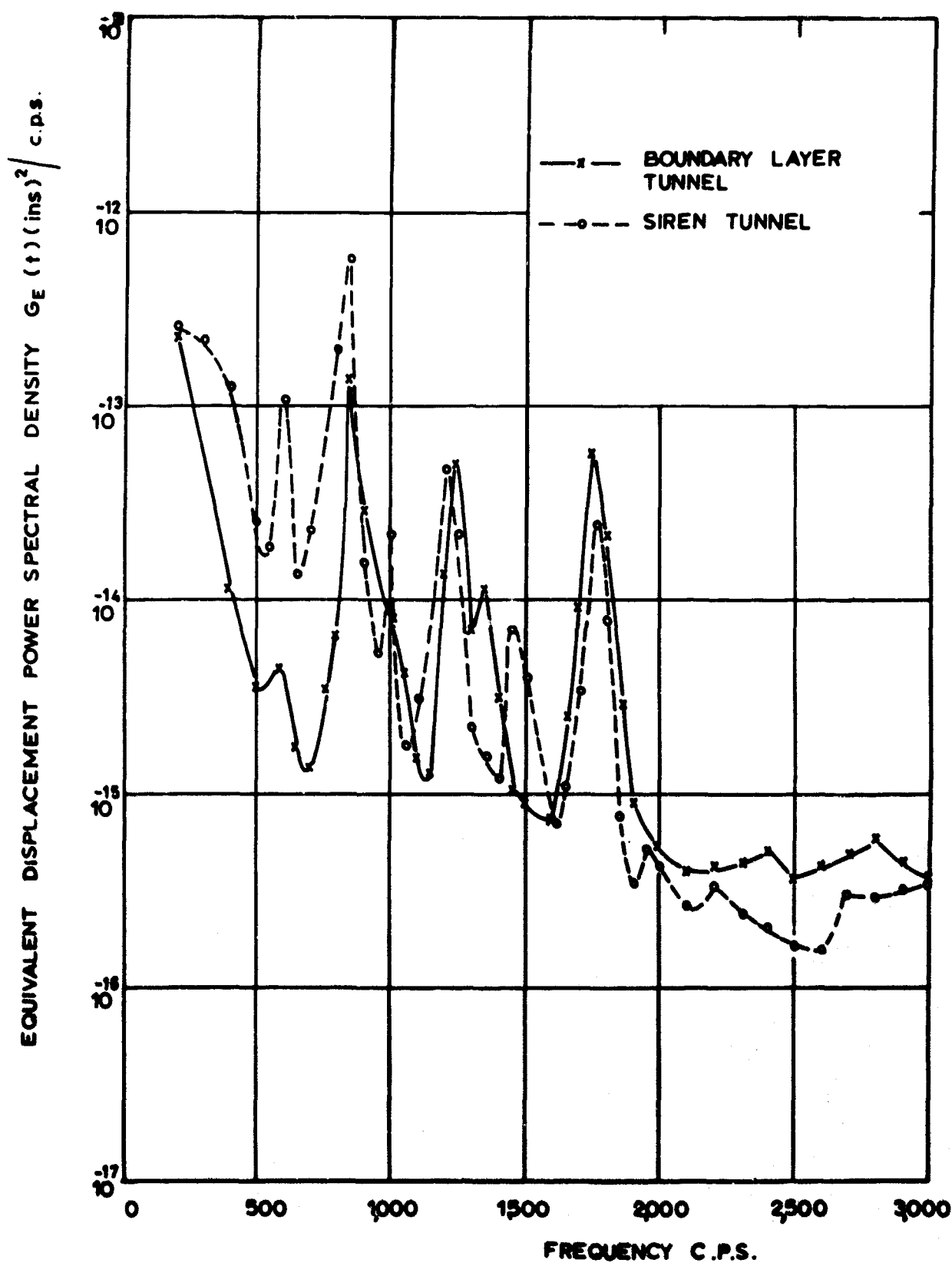


Figure 3-14 Background vibration and equipment noise :  
 boundary layer and siren excitations.



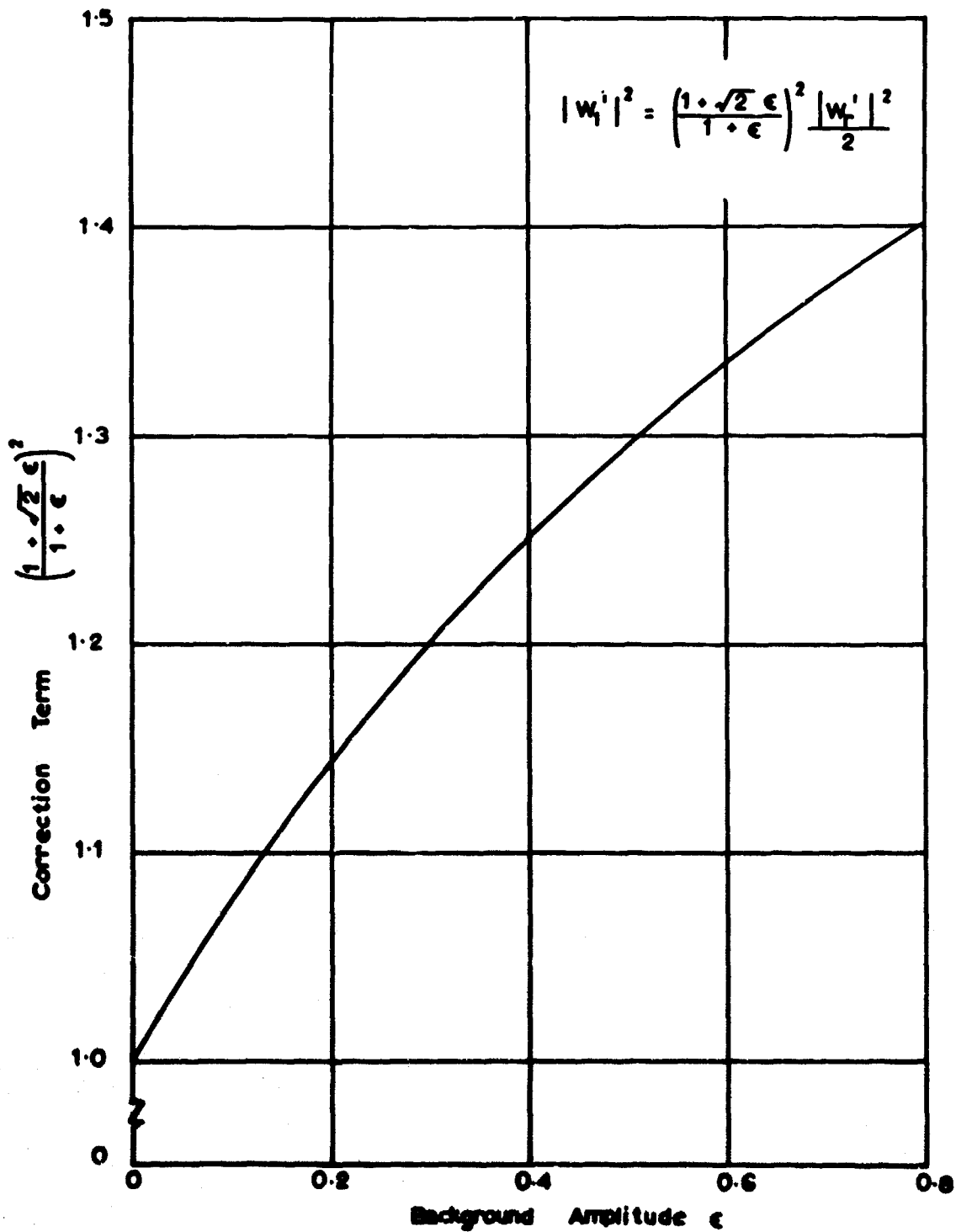


Figure 4.1 Correction term for estimation of true half power point.

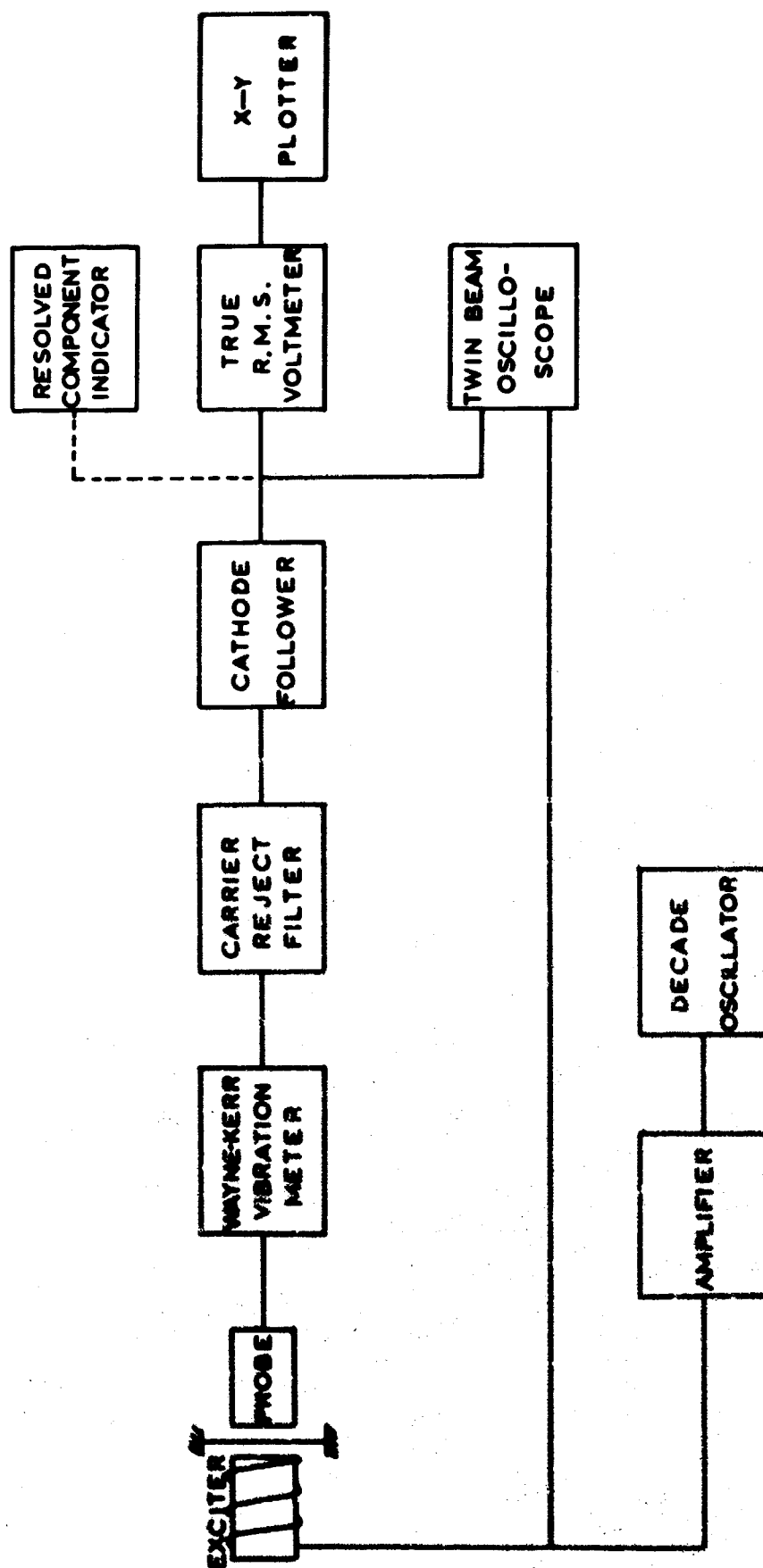
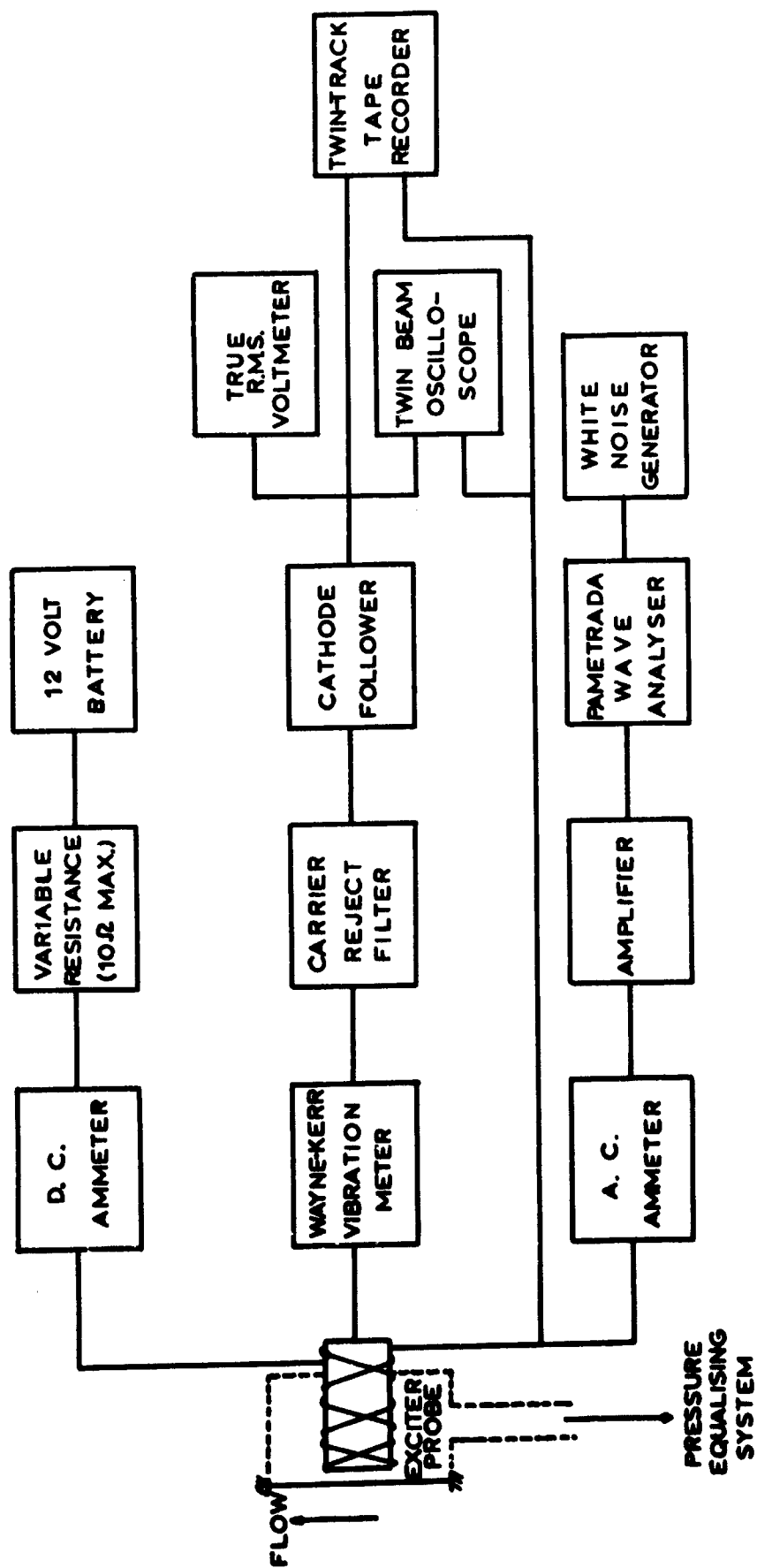


Figure 42 Block diagram of the apparatus for the measurement of panel damping using discrete frequency excitation.



**Figure 4-3** Block diagram of the apparatus for the measurement of panel damping using cross correlation techniques.

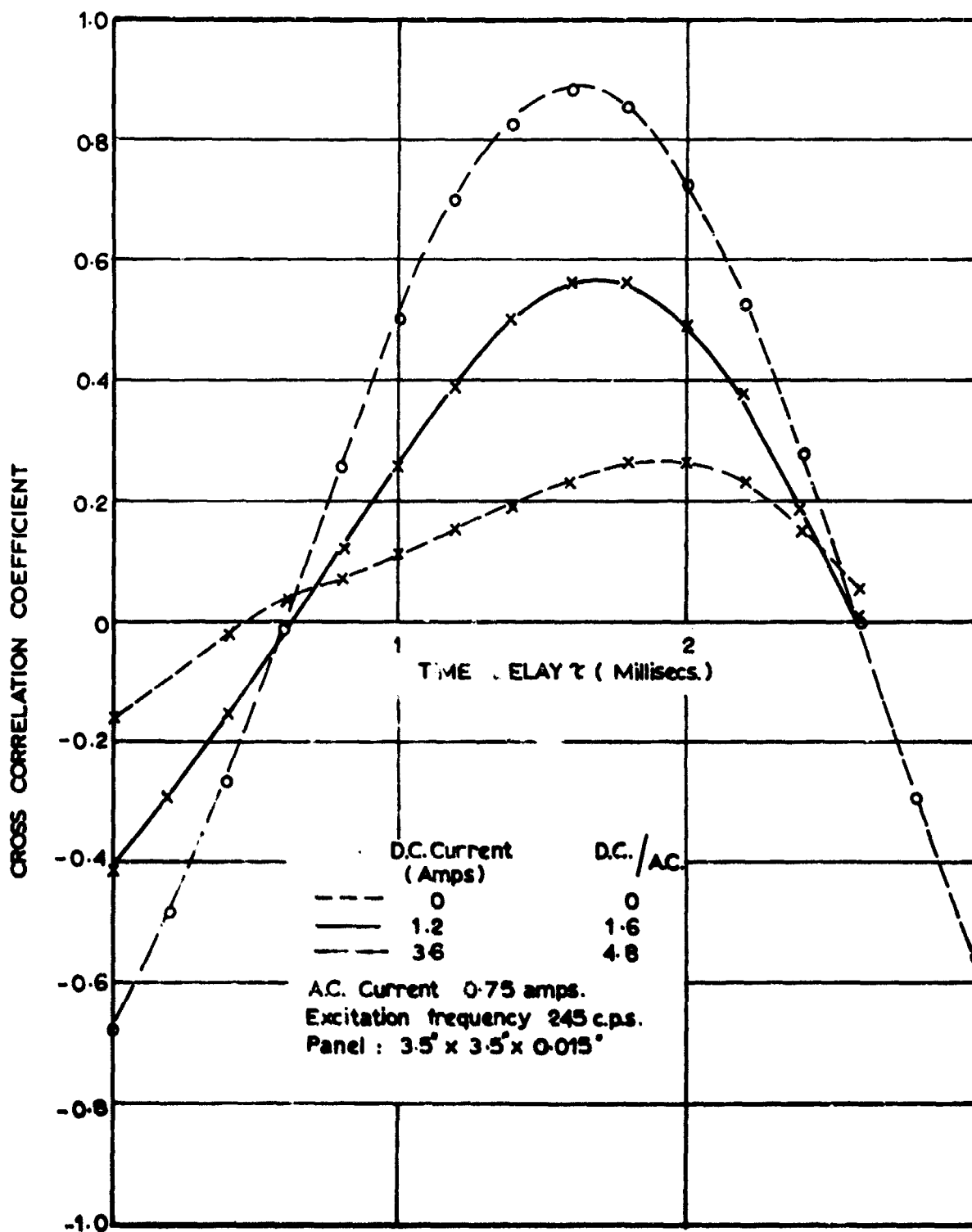


Figure 4.4 Effect of D.C. current on excitation - response cross correlation coefficient.

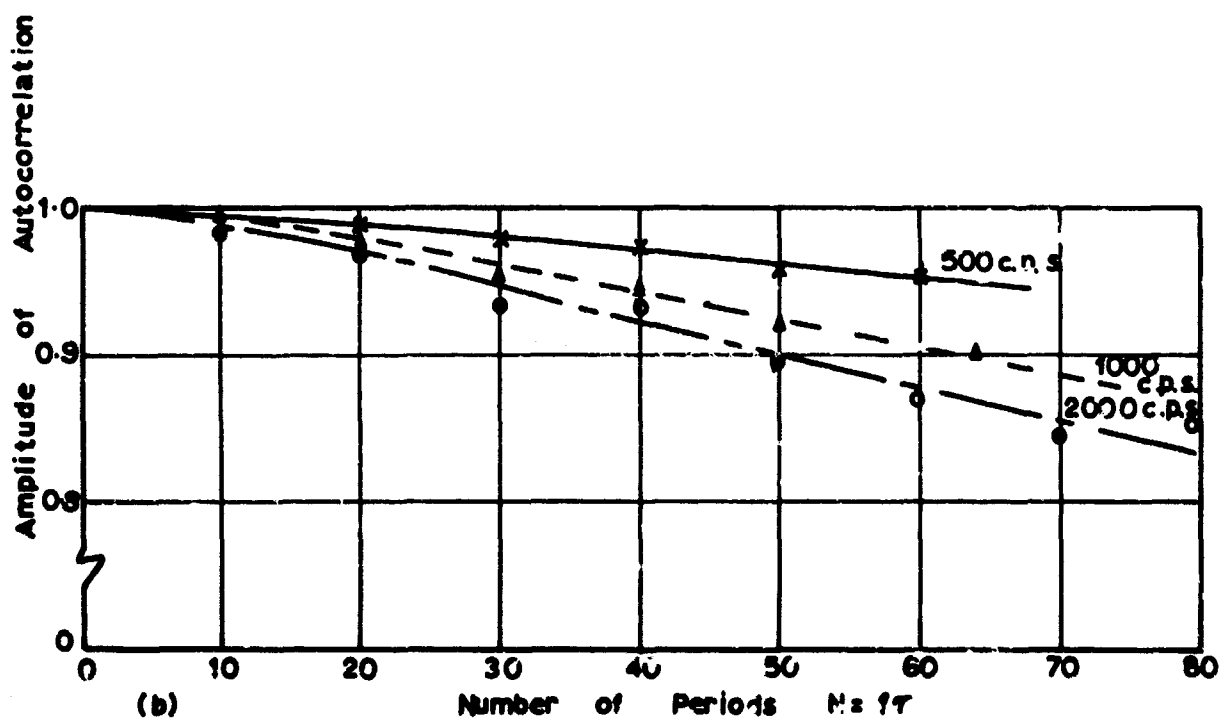
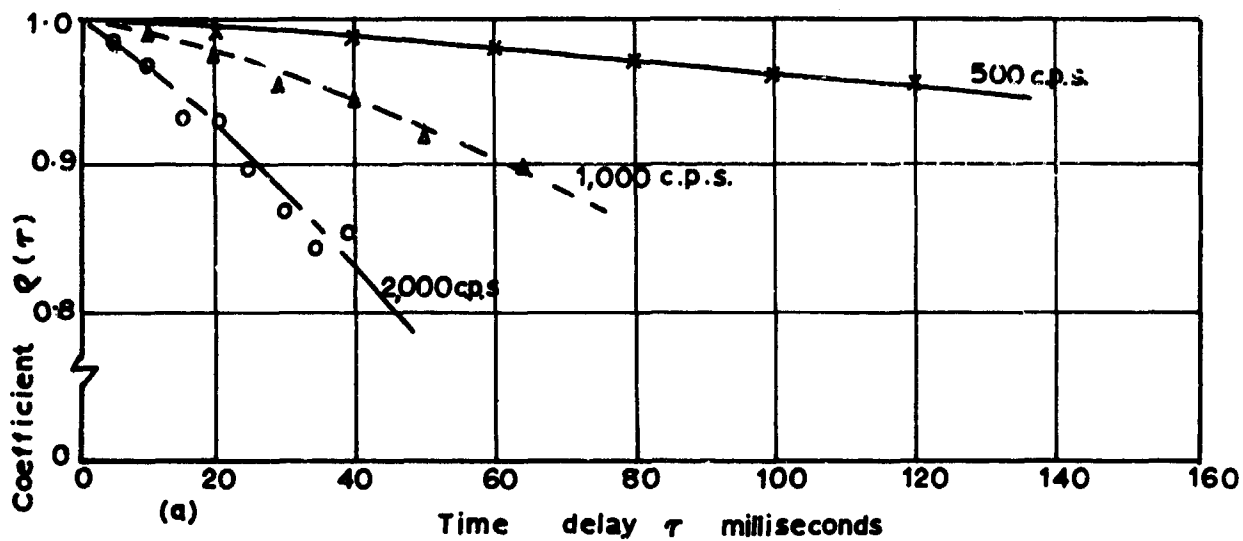


Figure 4.5 Autocorrelation Decay Caused by Tape Recorder Speed Variations.

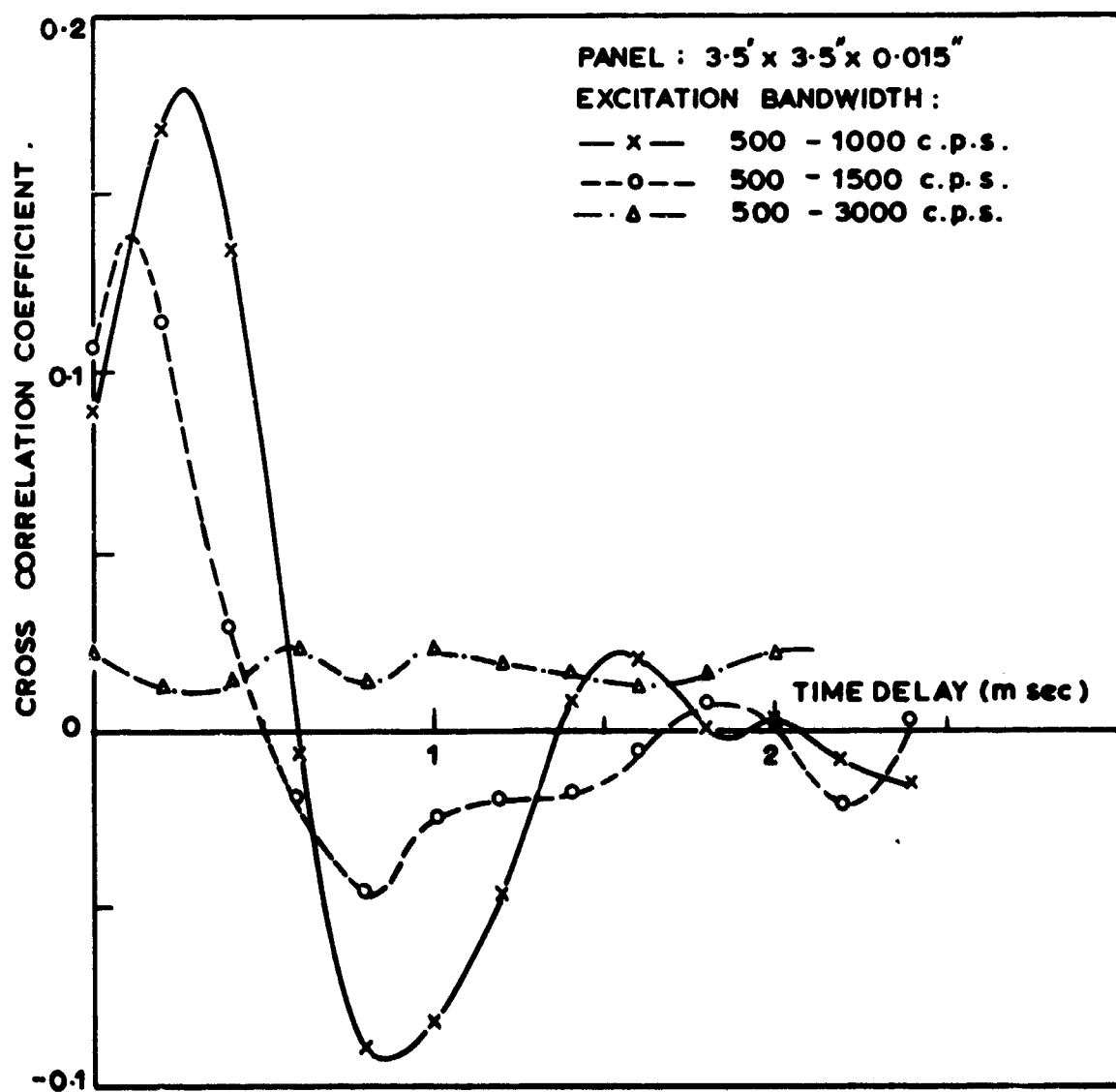
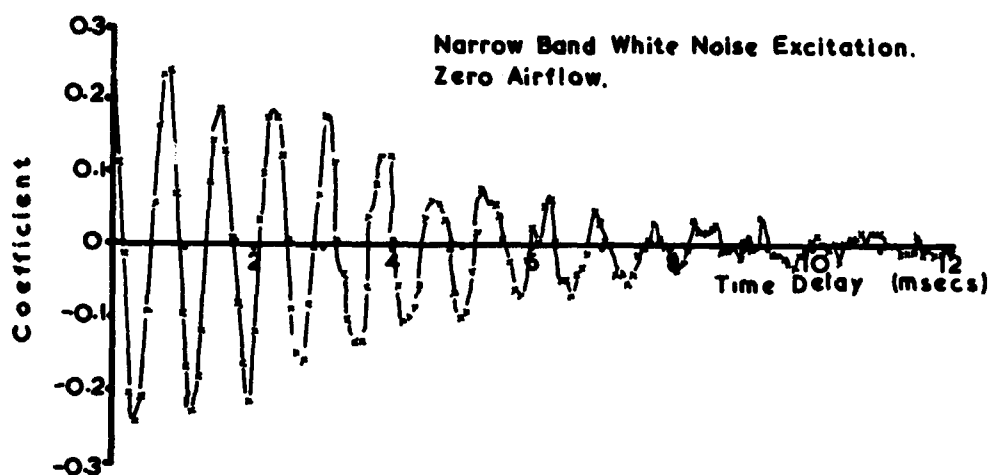


Fig. 4.6 Effect of excitation bandwidth on cross correlation between excitation and response .

(a) CROSS CORRELATION COEFFICIENT.



(b) CROSS POWER SPECTRUM,

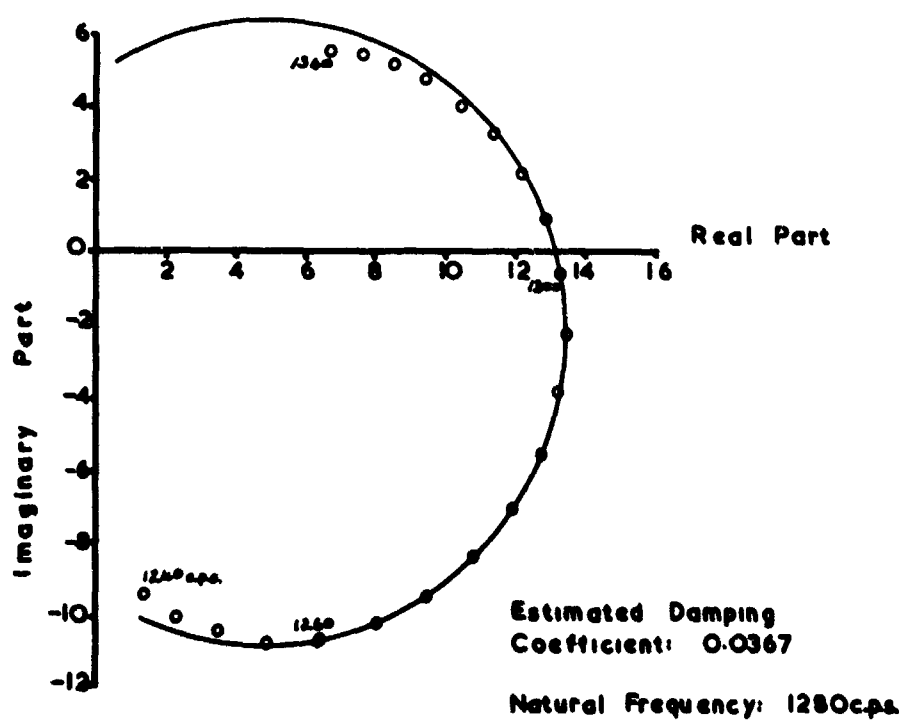
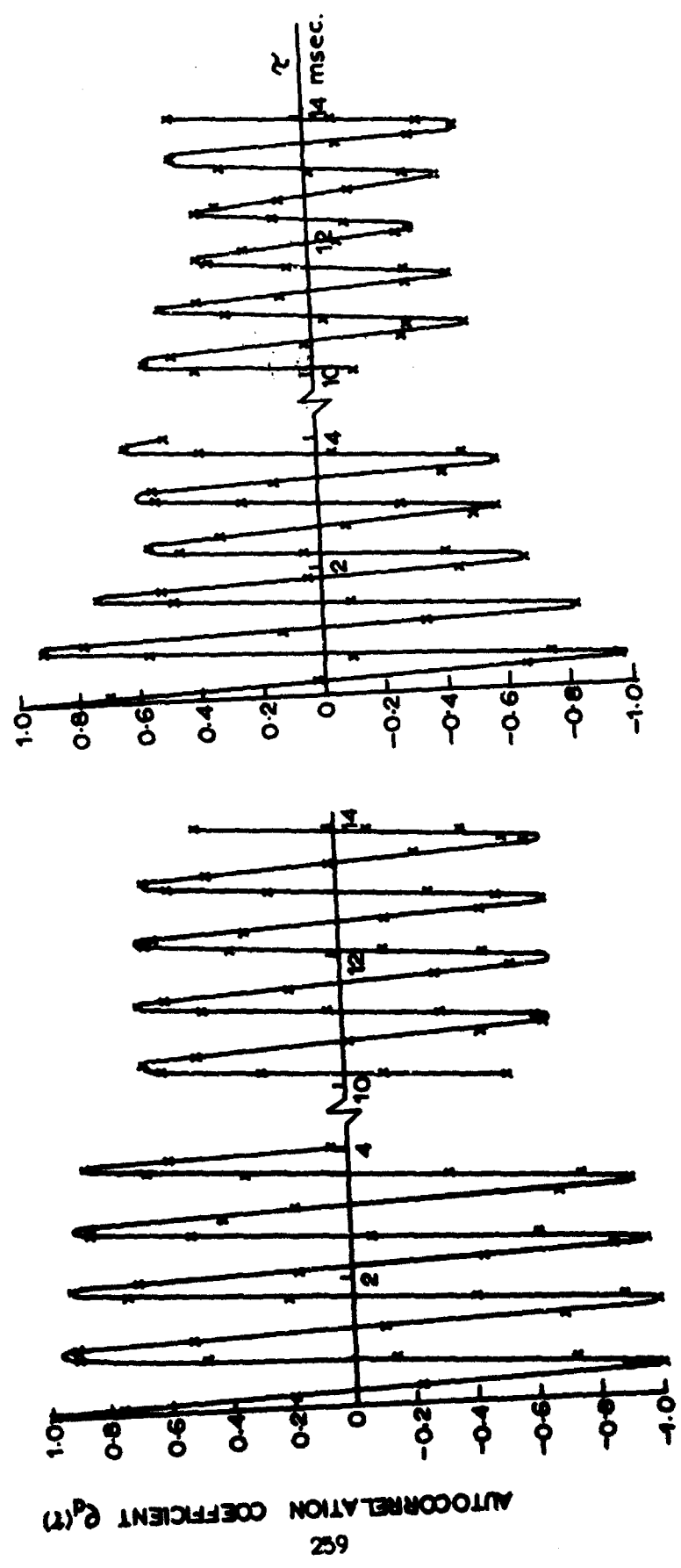


FIG. 4-7 CROSS CORRELATION BETWEEN EXCITATION AND RESPONSE FOR LIGHTLY DAMPED MODE.

PANEL 2.0 x 4.0 x 0.015

MODE 2-1

MODE 1-1



(a) COSINE FORM.

(b) MODULATED COSINE FORM.

Figure 4.8 Typical panel response autocorrelation coefficients.



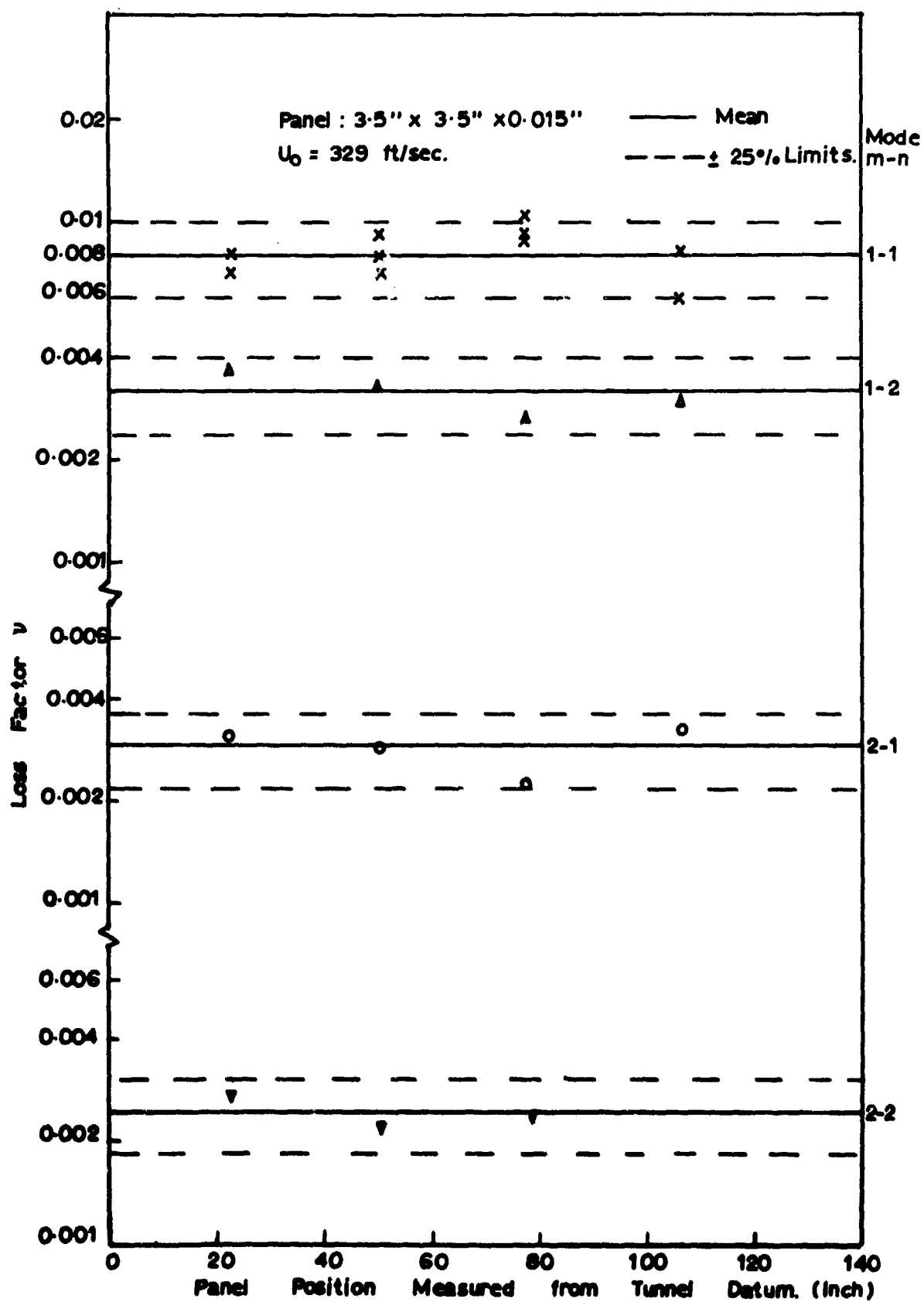


Figure 4.9 Panel Damping in the Presence of Airflow.

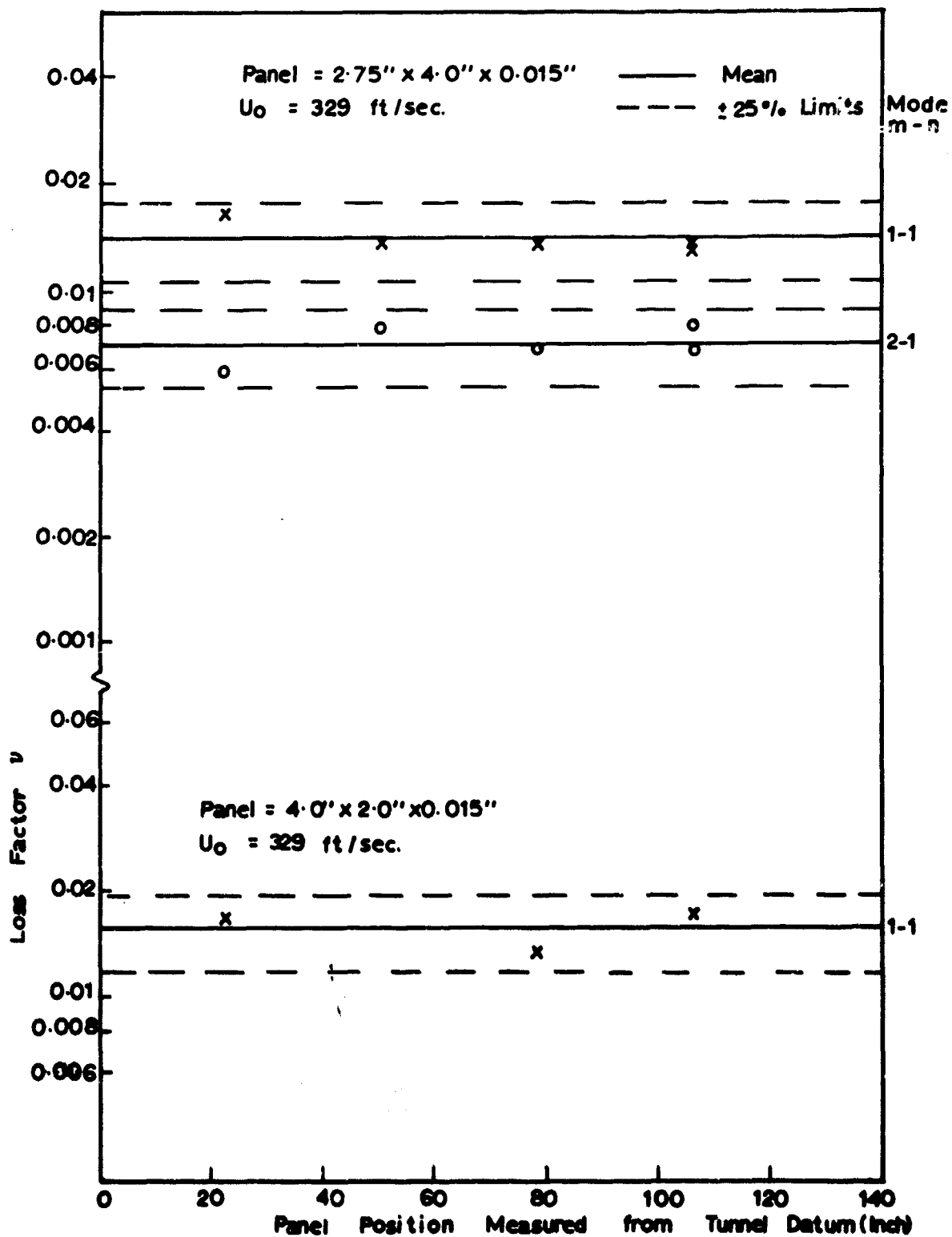
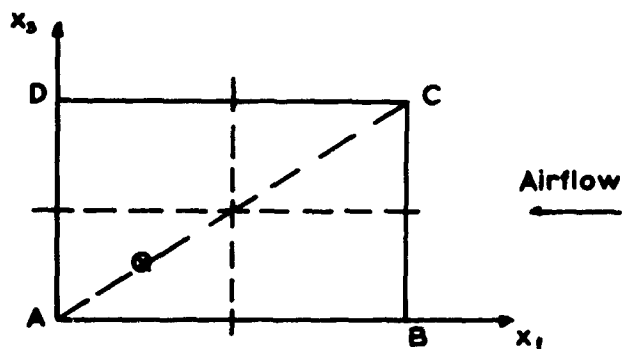
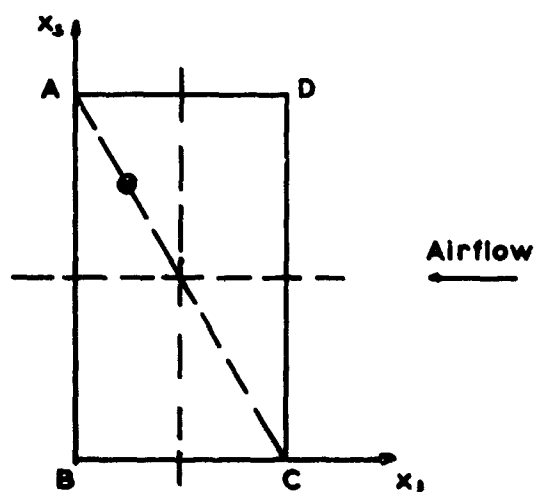


Figure 4.10 Panel Damping in the presence of Airflow.



(a) ASPECT RATIO  $\geq 1.0$



(b) ASPECT RATIO  $< 1.0$

● Measuring position at a quarter point on a diagonal

Figure 5.1 Coordinate system for panels in the boundary layer and siren tunnels.

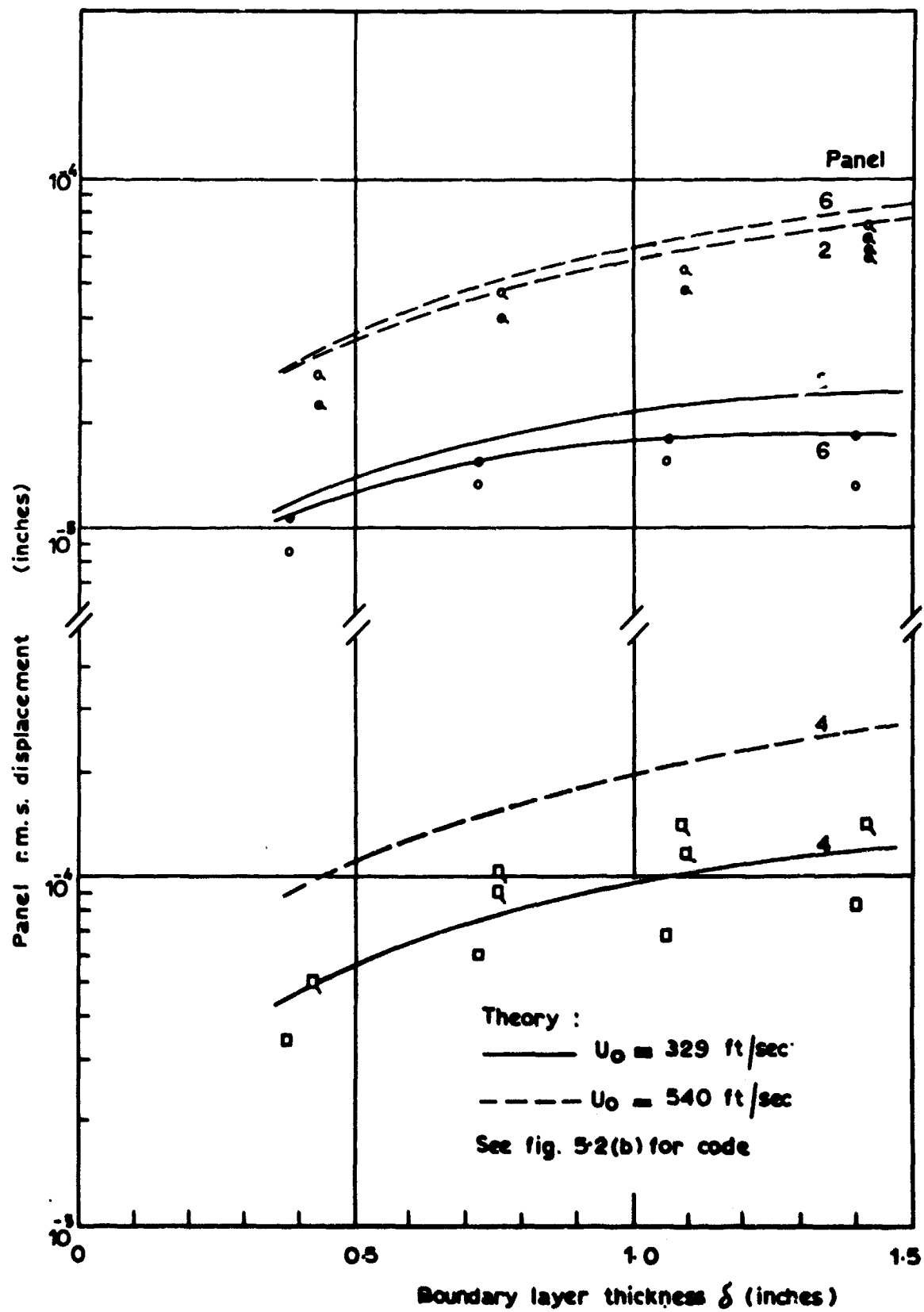


Fig. 5-2 (a) Panel r.m.s. displacement at measuring positions.

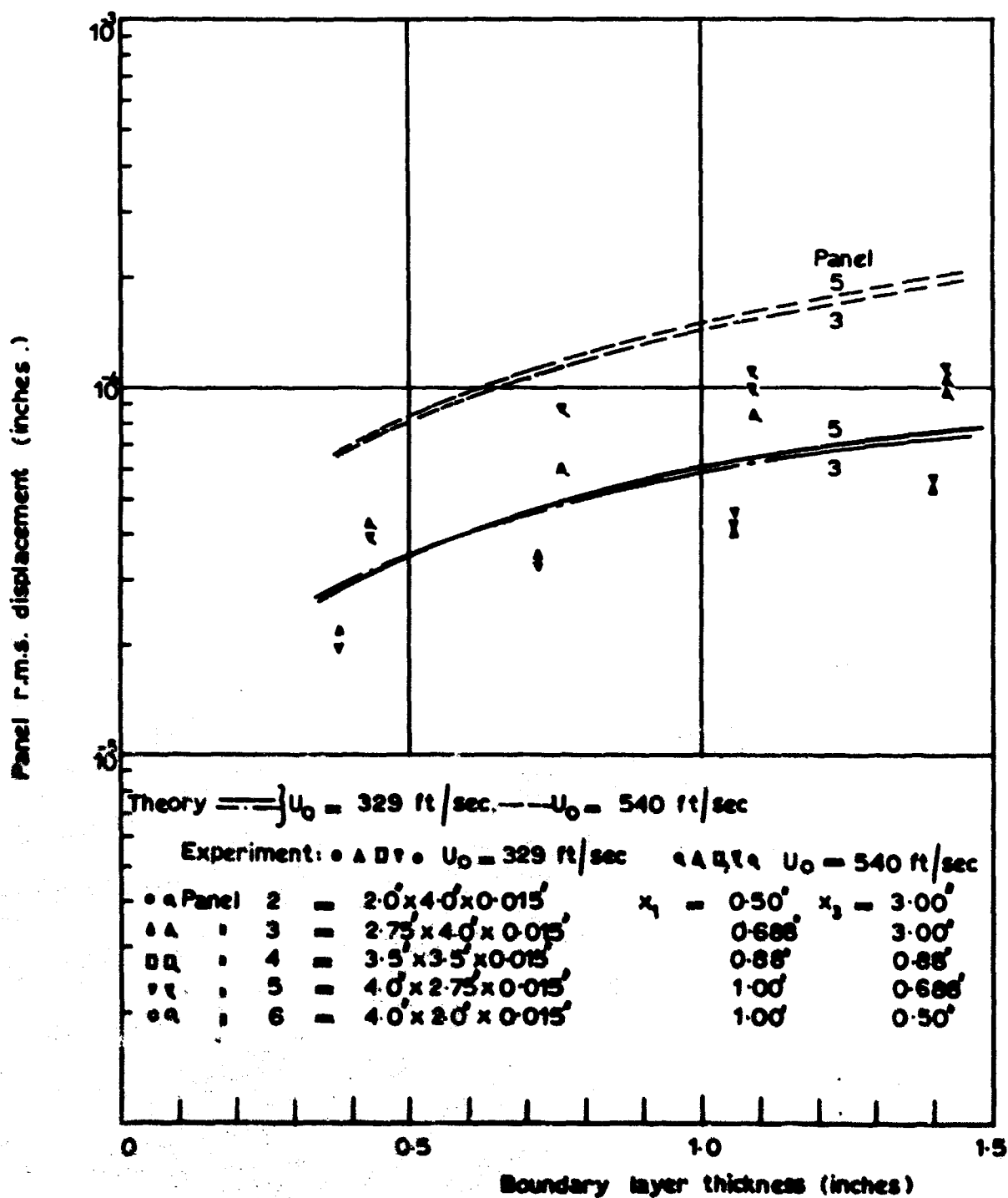


Fig 5-2(b) Panel r.m.s. displacement at measuring positions.

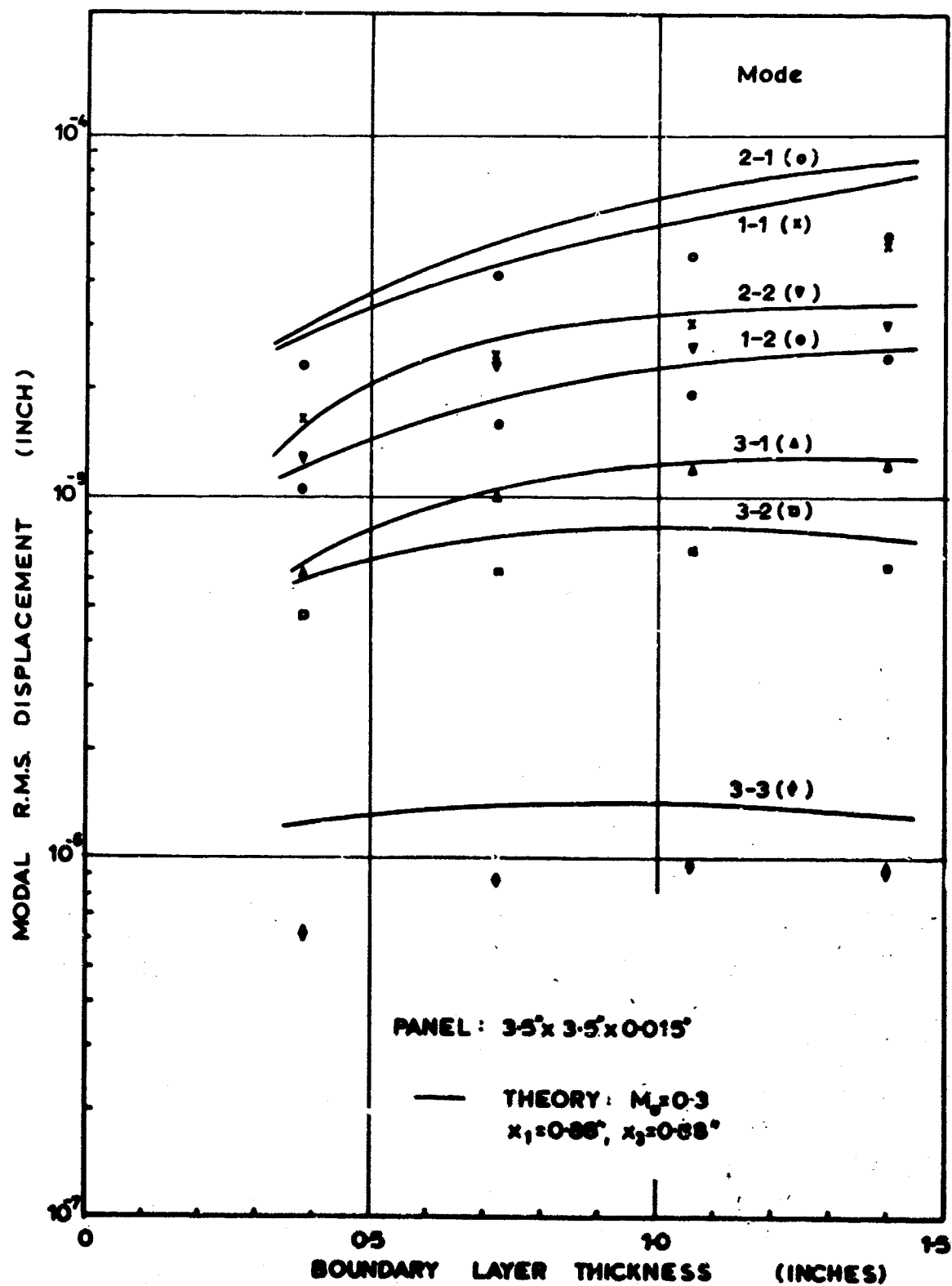


Figure 5-3 Root mean square displacement in individual modes.

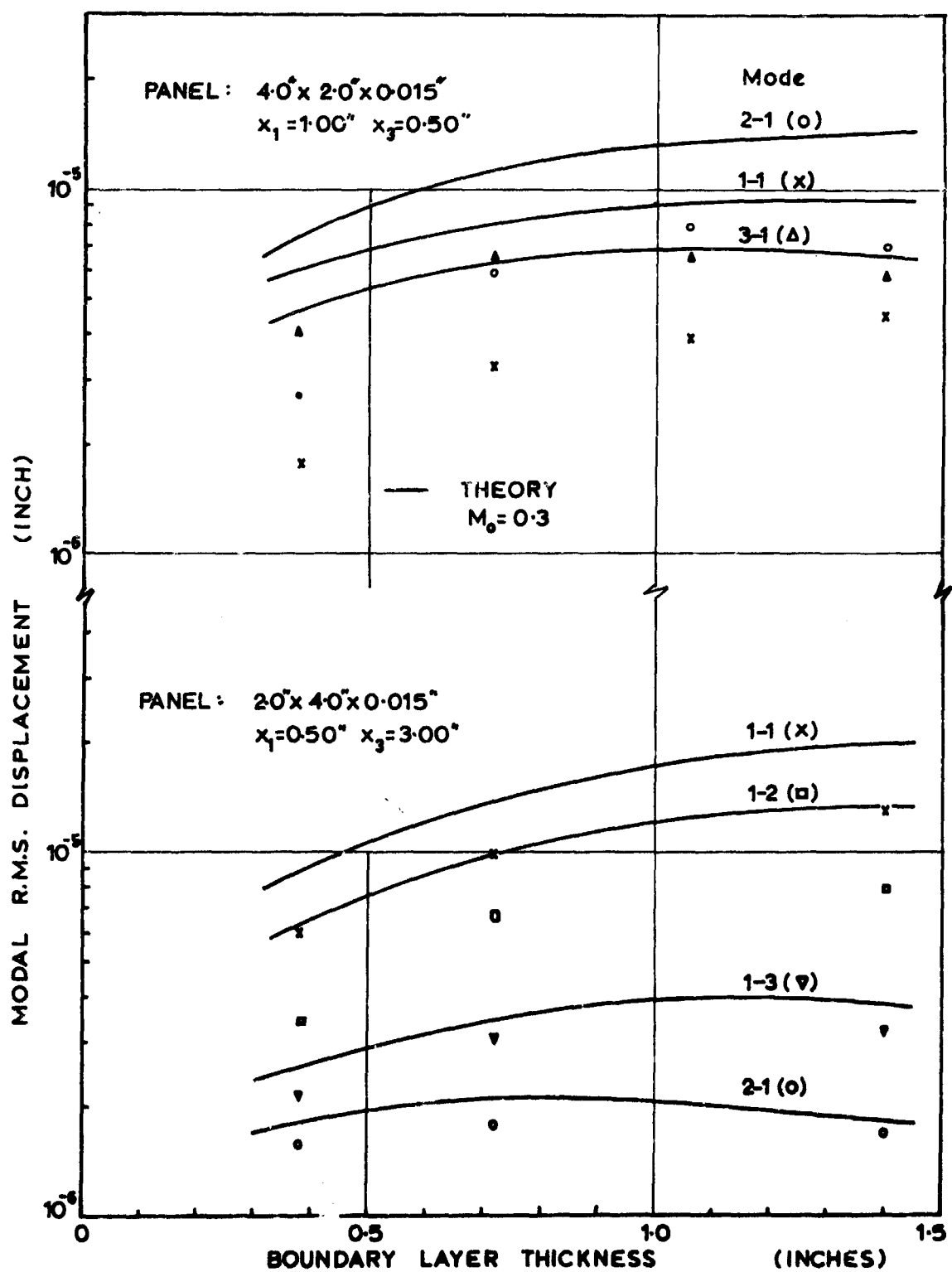


Figure 5.4 Root mean square displacement in individual modes.

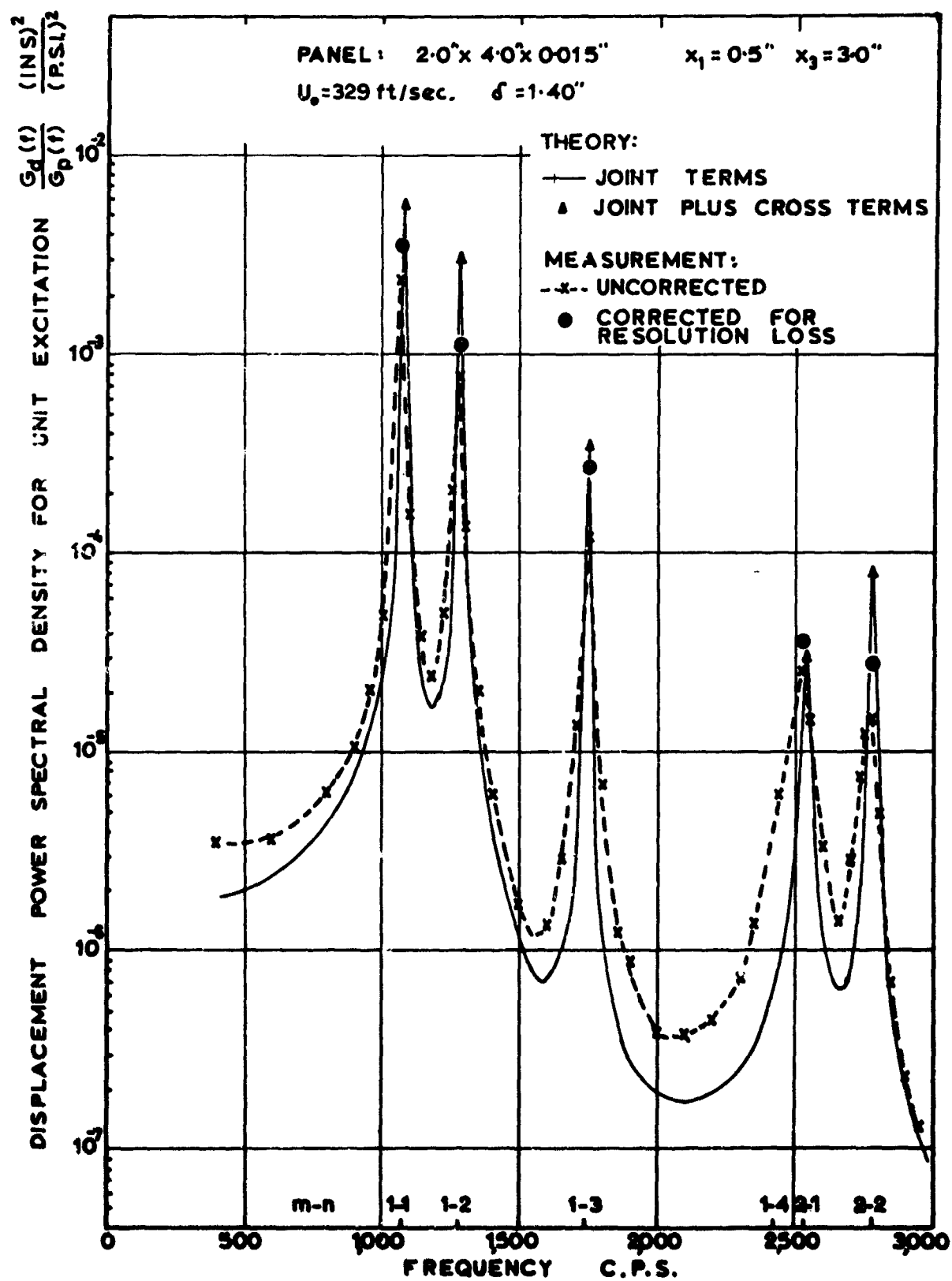


Figure 5-5 Response of panel 2 to boundary layer excitation. ( $M_\infty = 0.3$ )



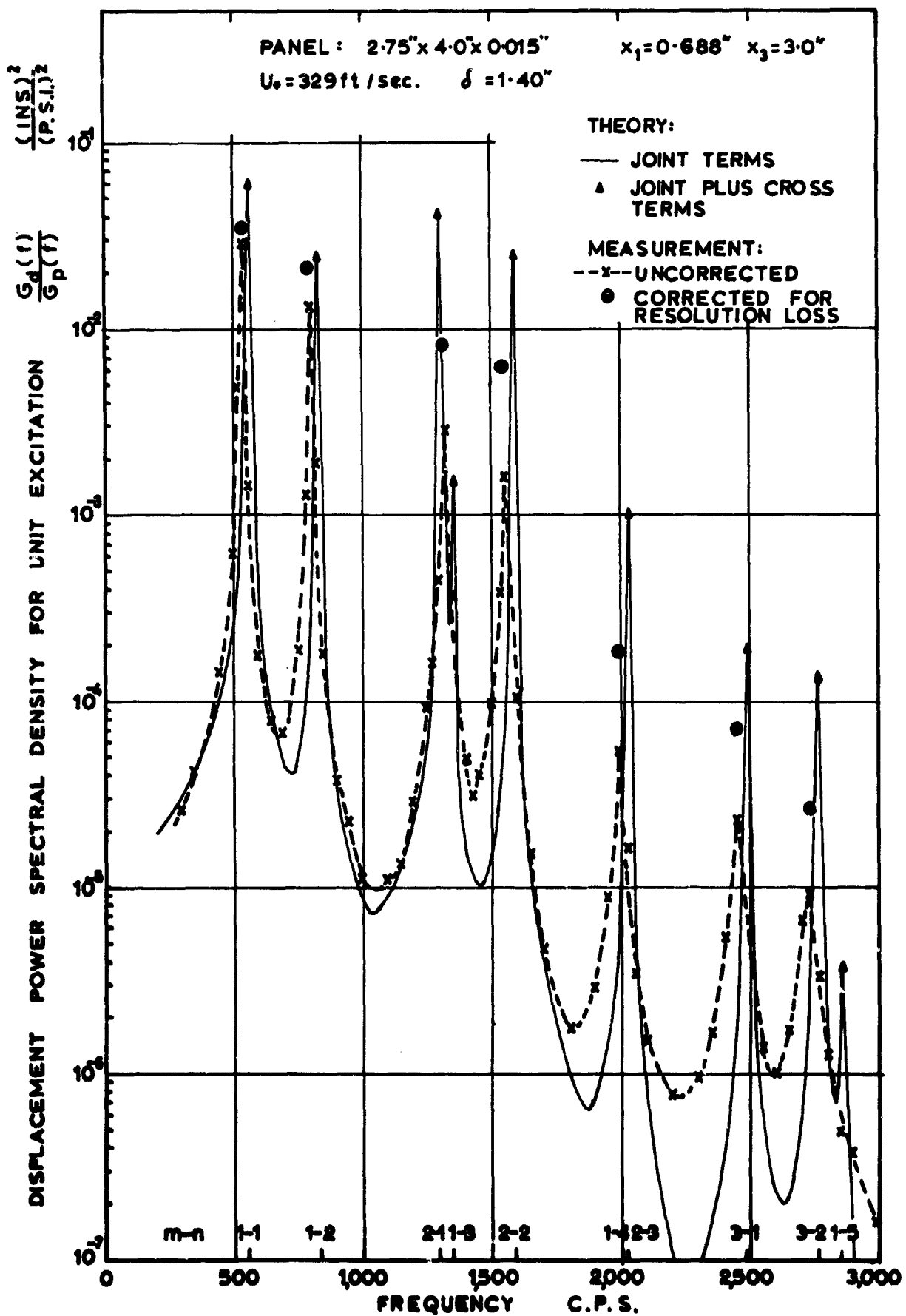


Figure 5-6 Response of panel 3 to boundary layer excitation.

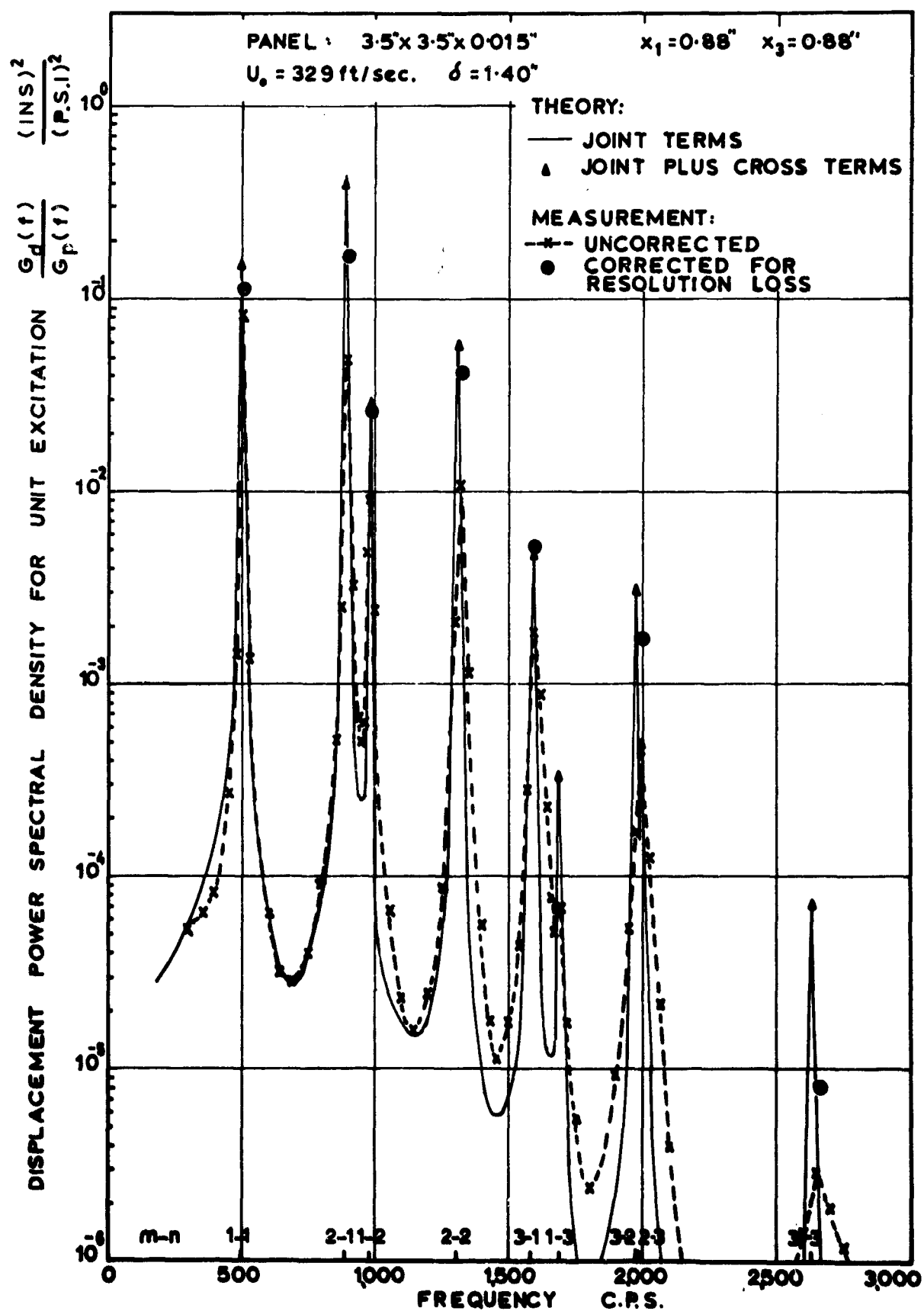


Figure 5.7 Response of panel 4 to boundary layer excitation, ( $M_0 = 0.3$ )

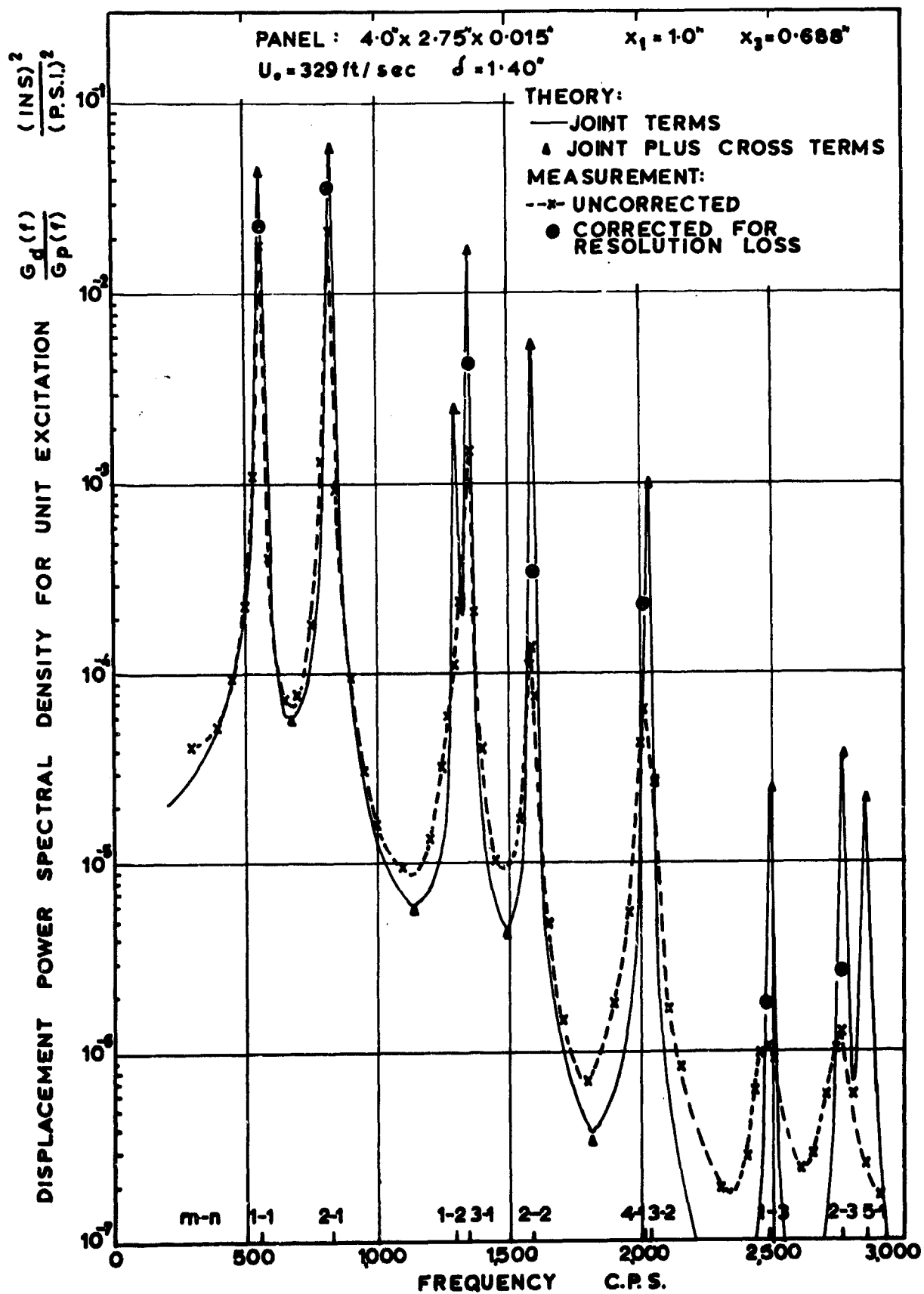


Figure 5-8 Response of panel 5 to boundary layer excitation. ( $M_\infty = 0.3$ )

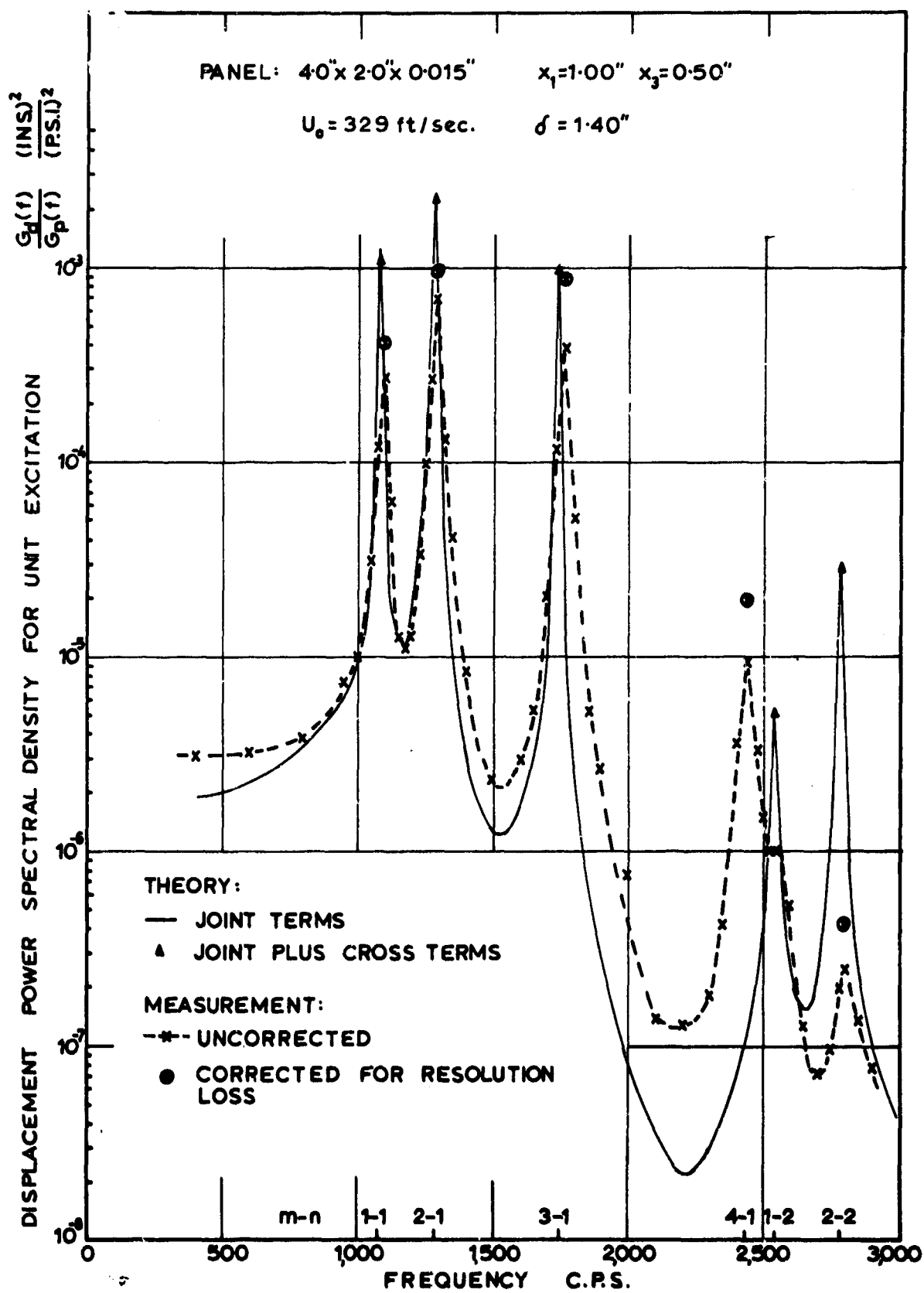


Figure 5.9 Response of panel 6 to boundary layer excitation. ( $M_0=0.3$ )

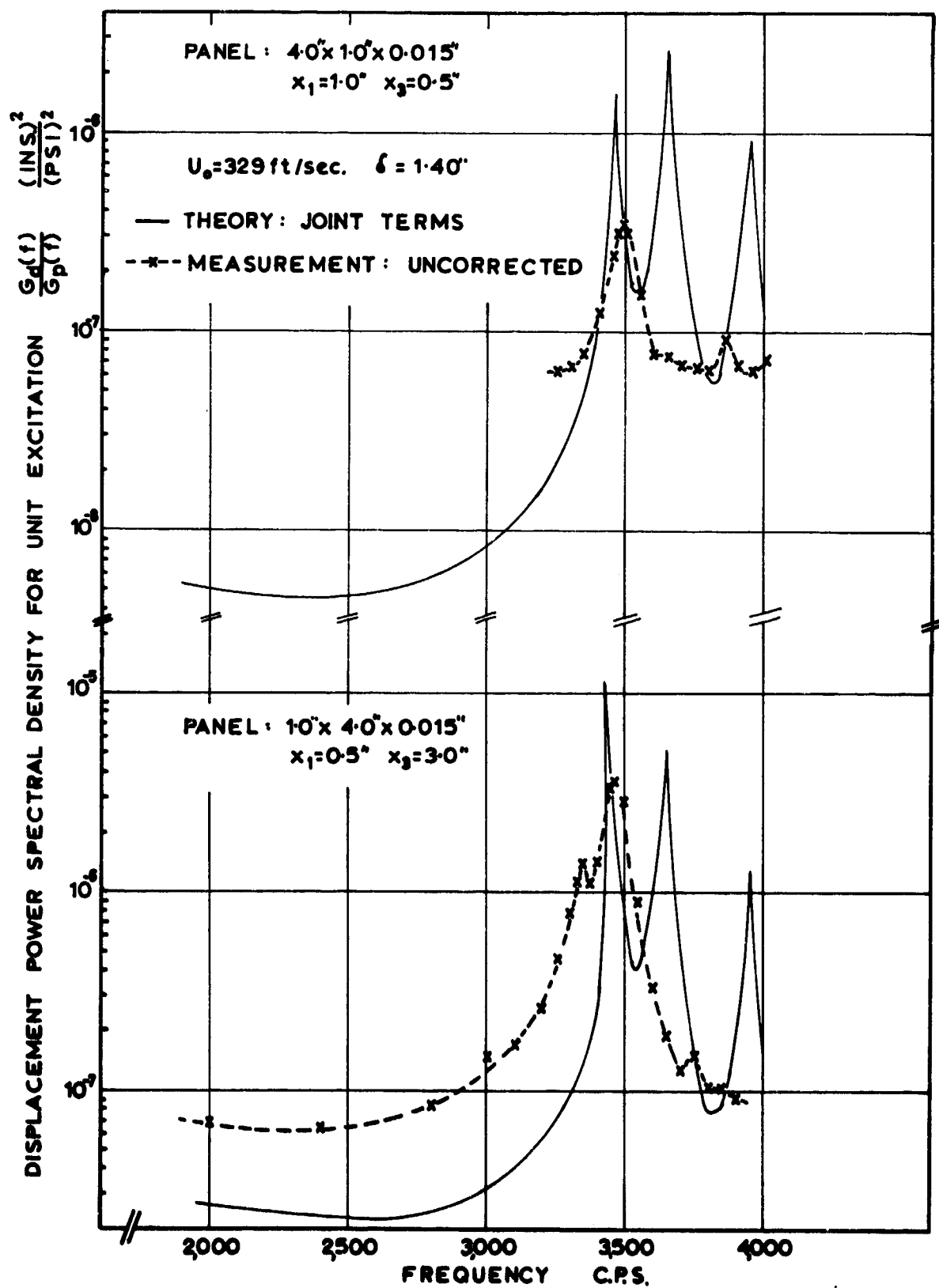


Figure 5.10 Response of panels 1 and 7 to boundary layer excitation. ( $M_0=0.3$ )

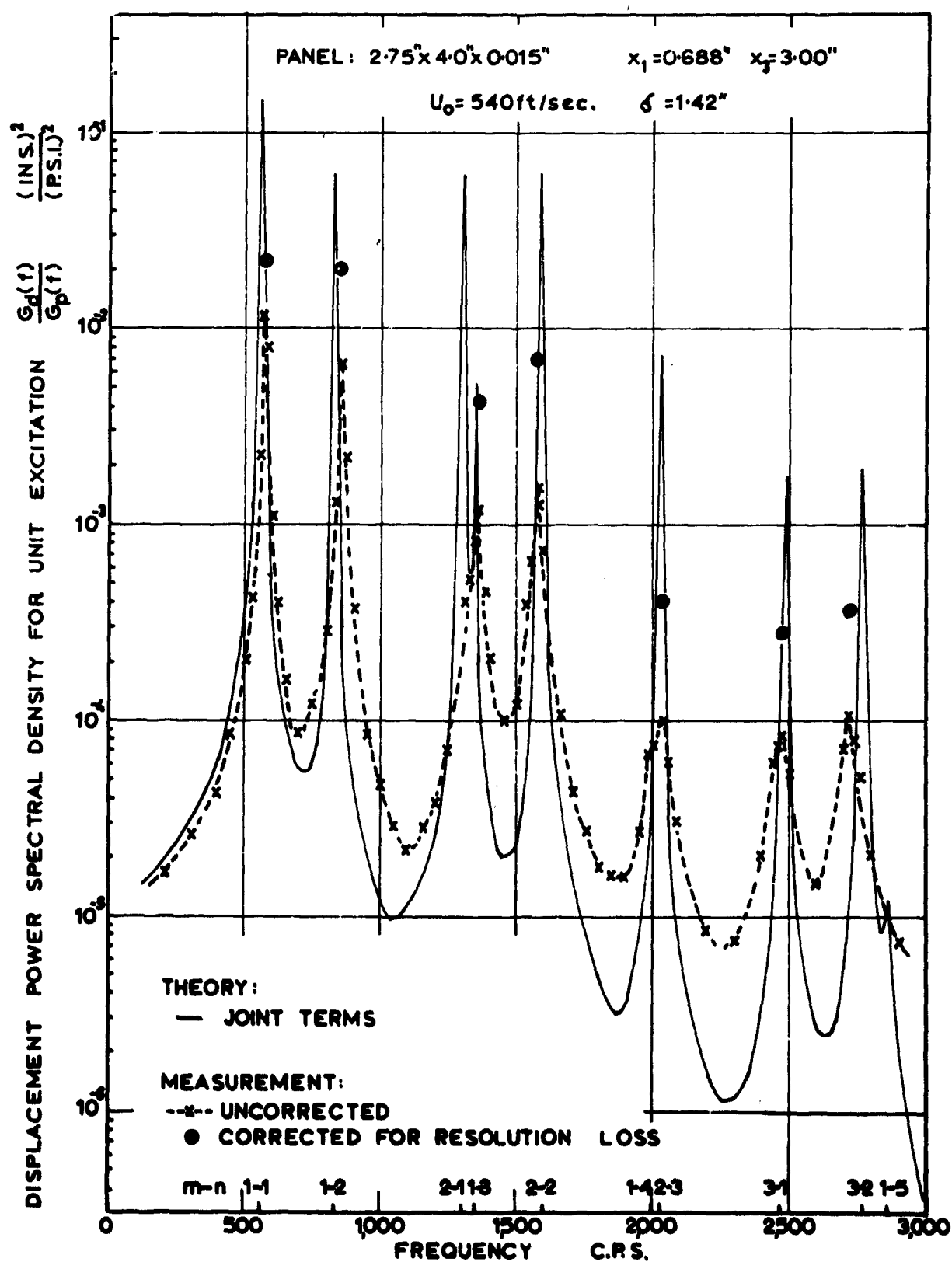


Figure 5-11 Response of panel 3 to boundary layer excitation. ( $M_0 = 0.5$ )

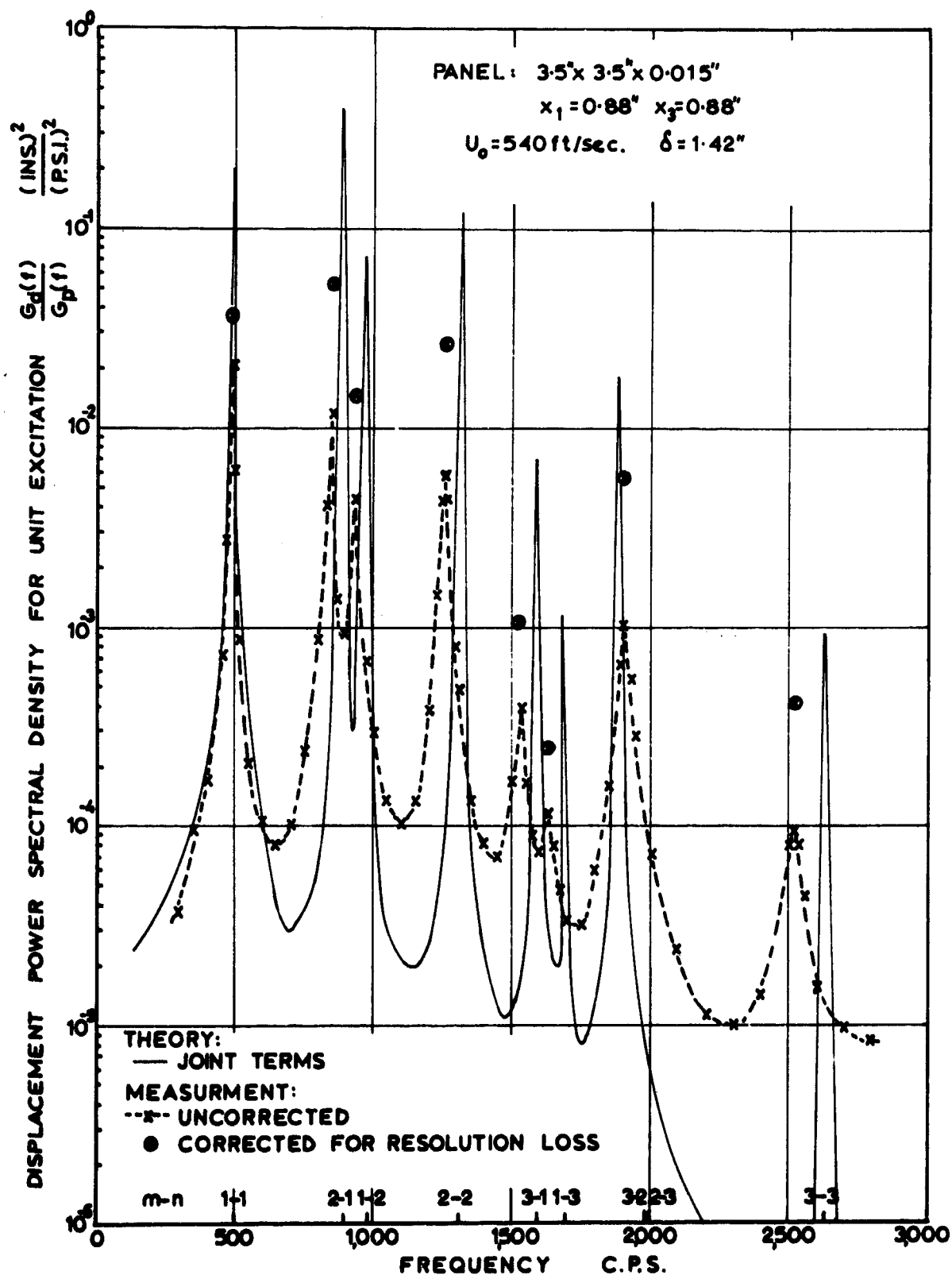


Figure 5-12 Response of panel 4 to boundary layer excitation. ( $M_0 = 0.5$ )

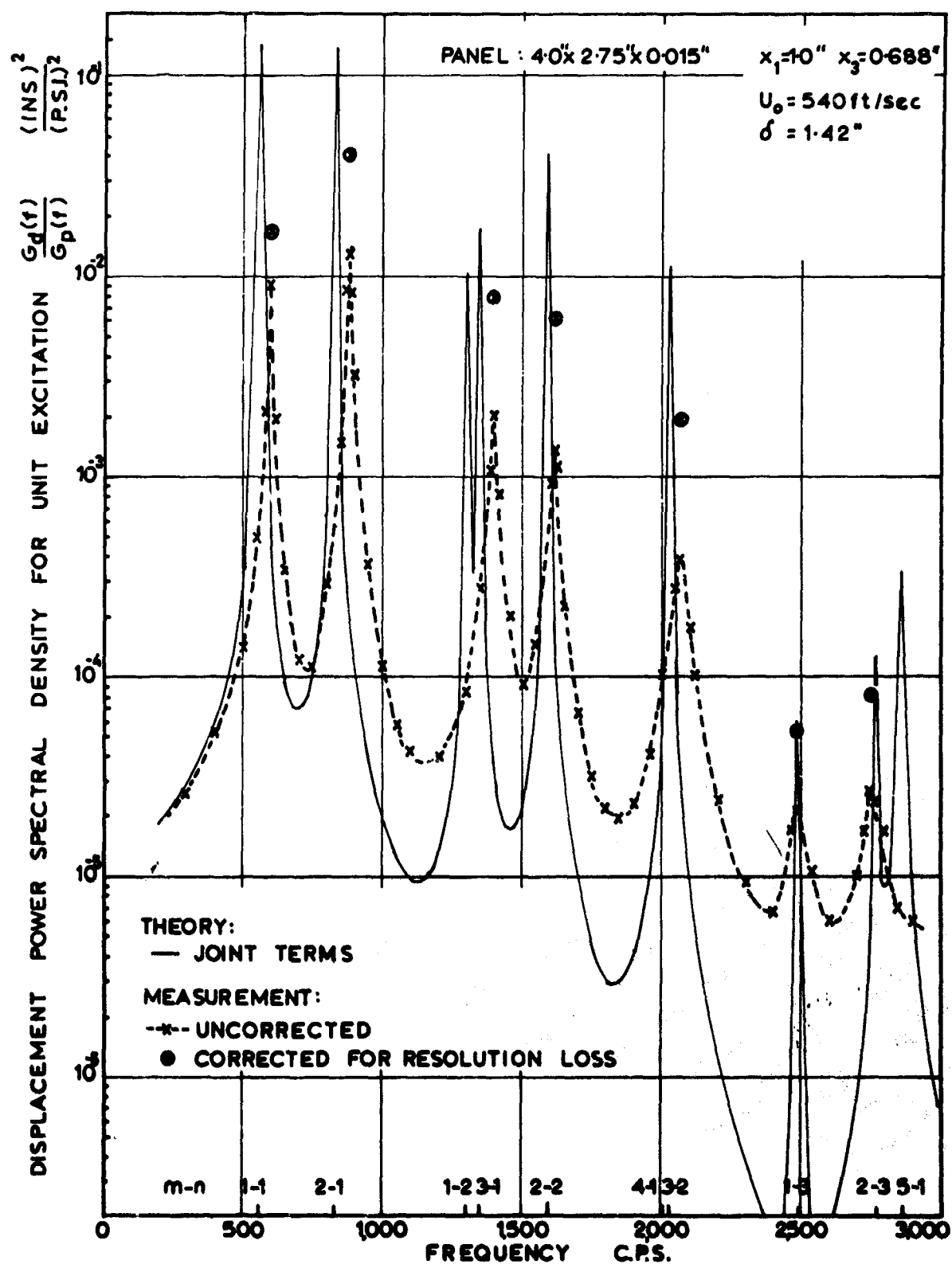


Figure 5-13 Response of panel 5 to boundary layer excitation. ( $M_0=0.5$ )



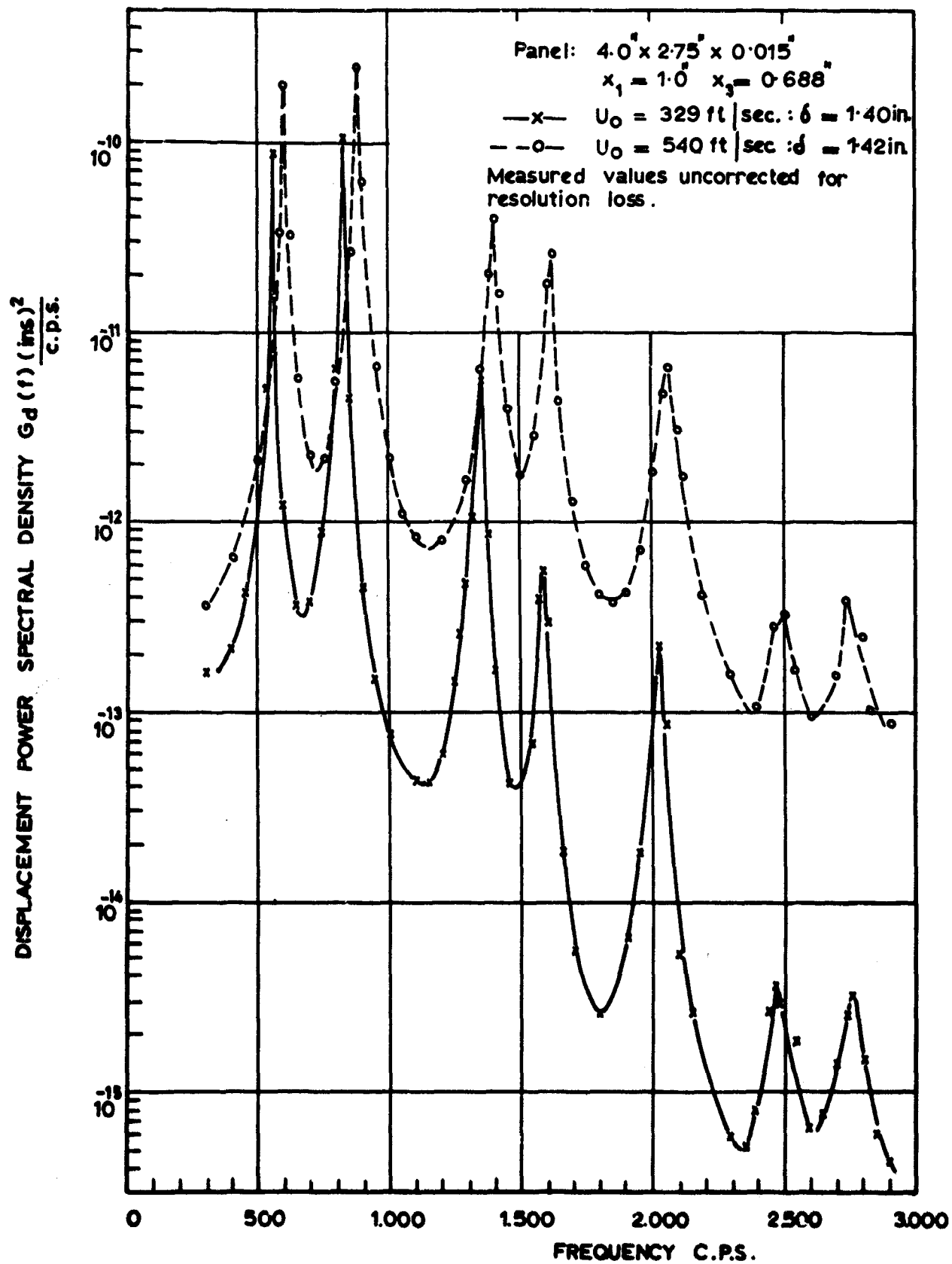


Figure 5.14 Effect of flow velocity on panel response spectra.

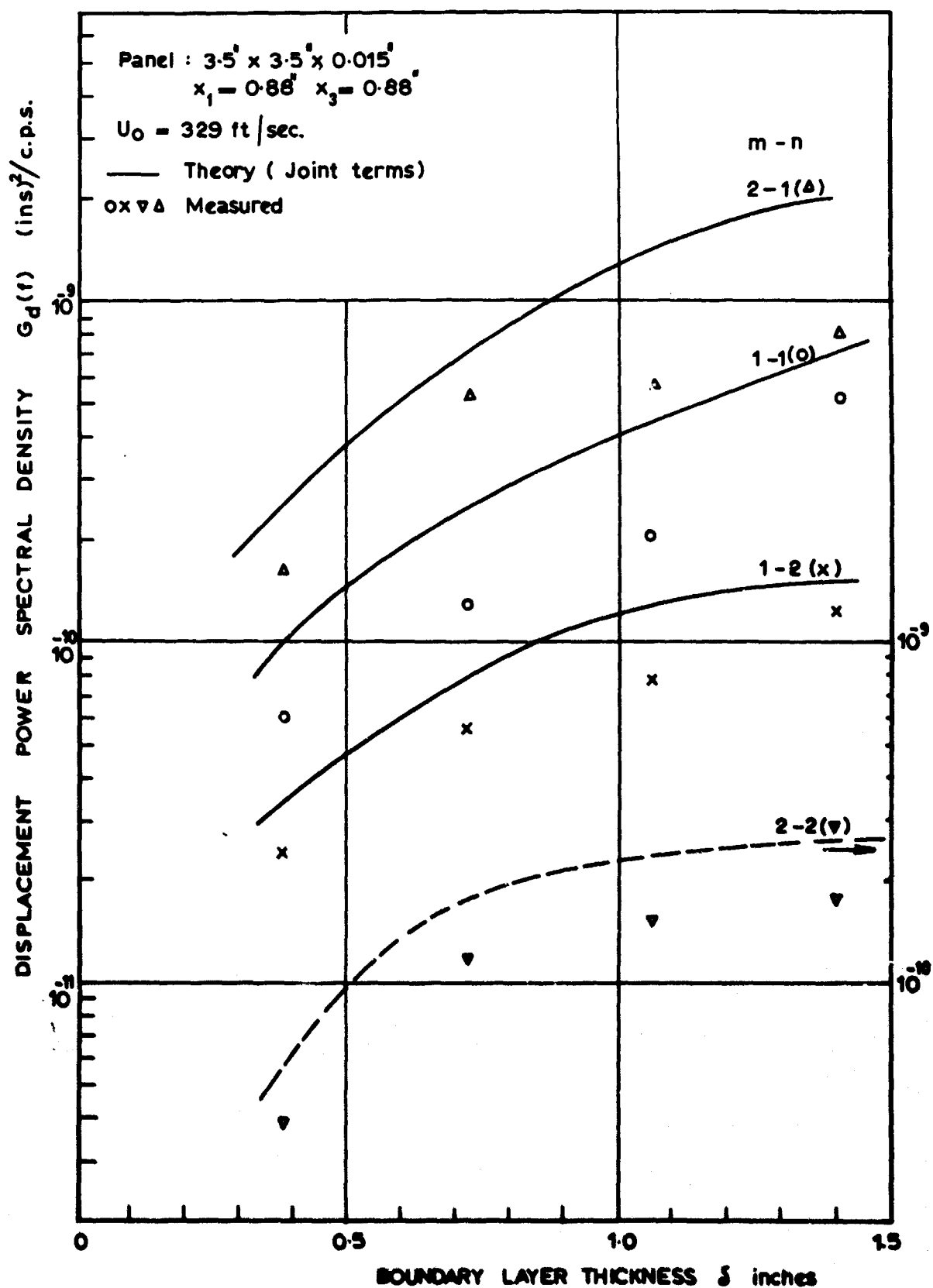


Figure 5-5 Variation of modal response at natural frequencies with boundary layer thickness. (Panel 4,  $M_0 = 0.3$ )

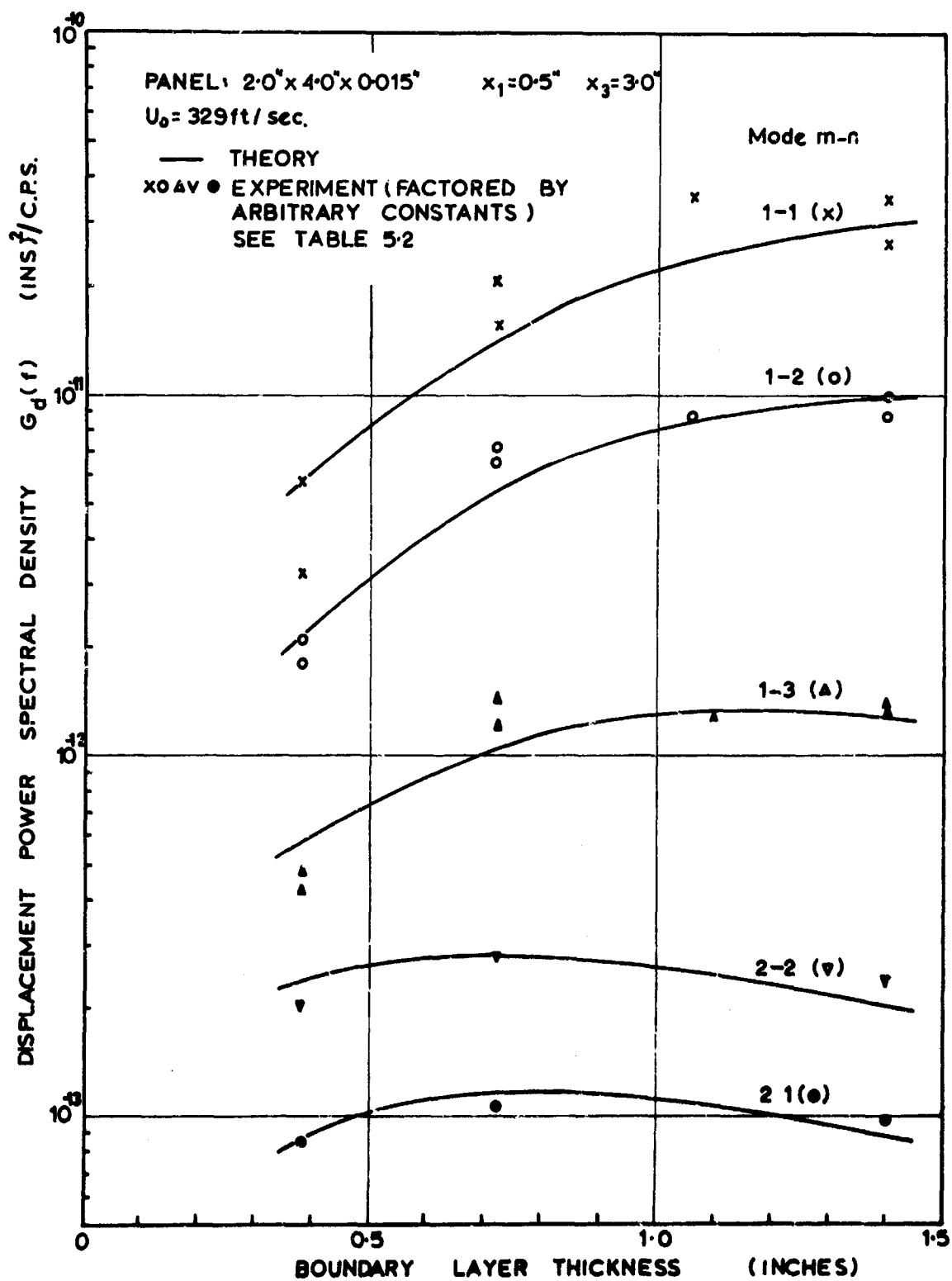


Figure 5-16 Variation of modal response at natural frequencies with boundary layer thickness. (Panel 2,  $M_0=0.3$ )

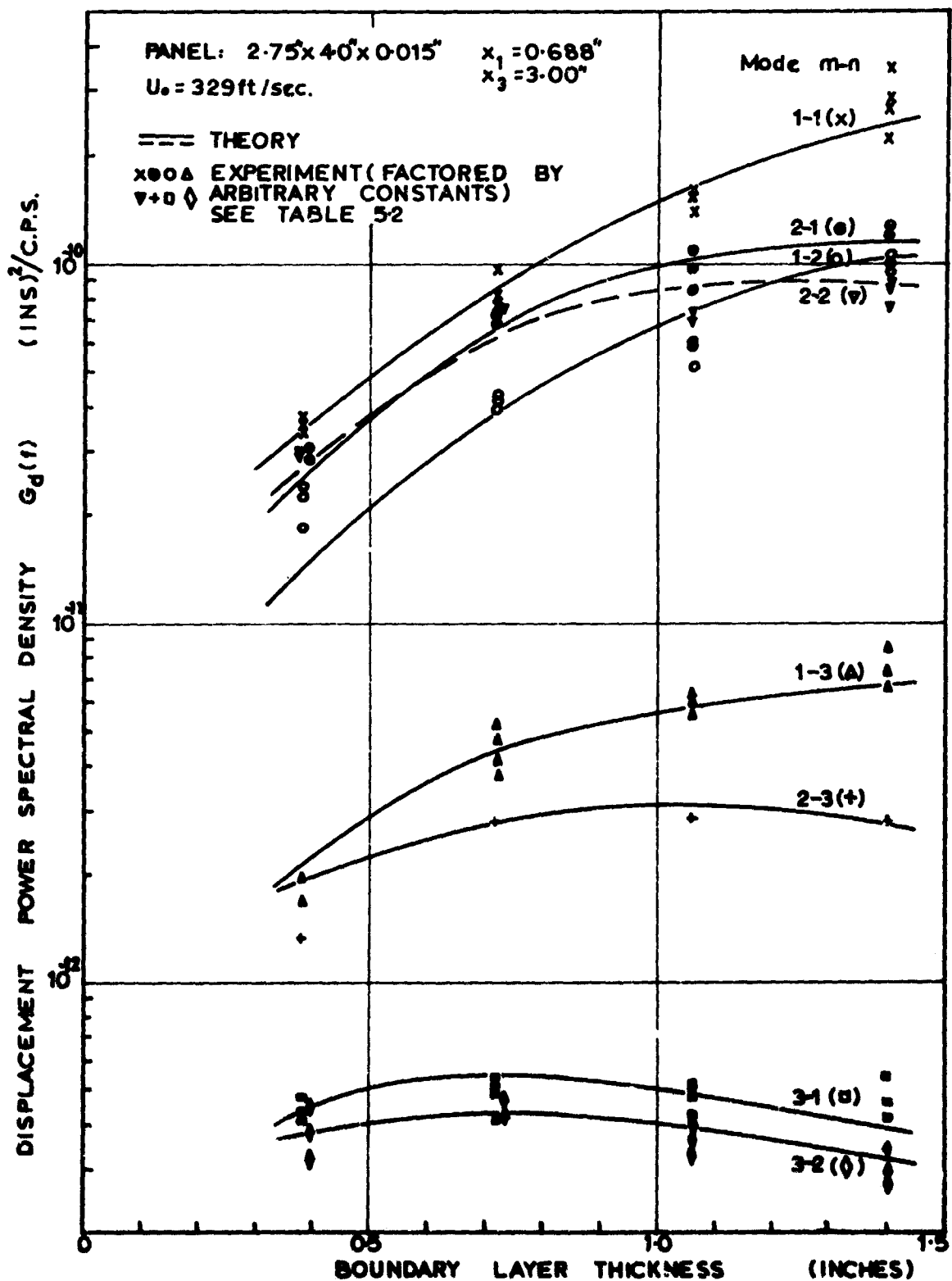


Figure 5-17 Variation of modal response at natural frequencies with boundary layer thickness. (Panel 3,  $M_0 = 0.3$ )

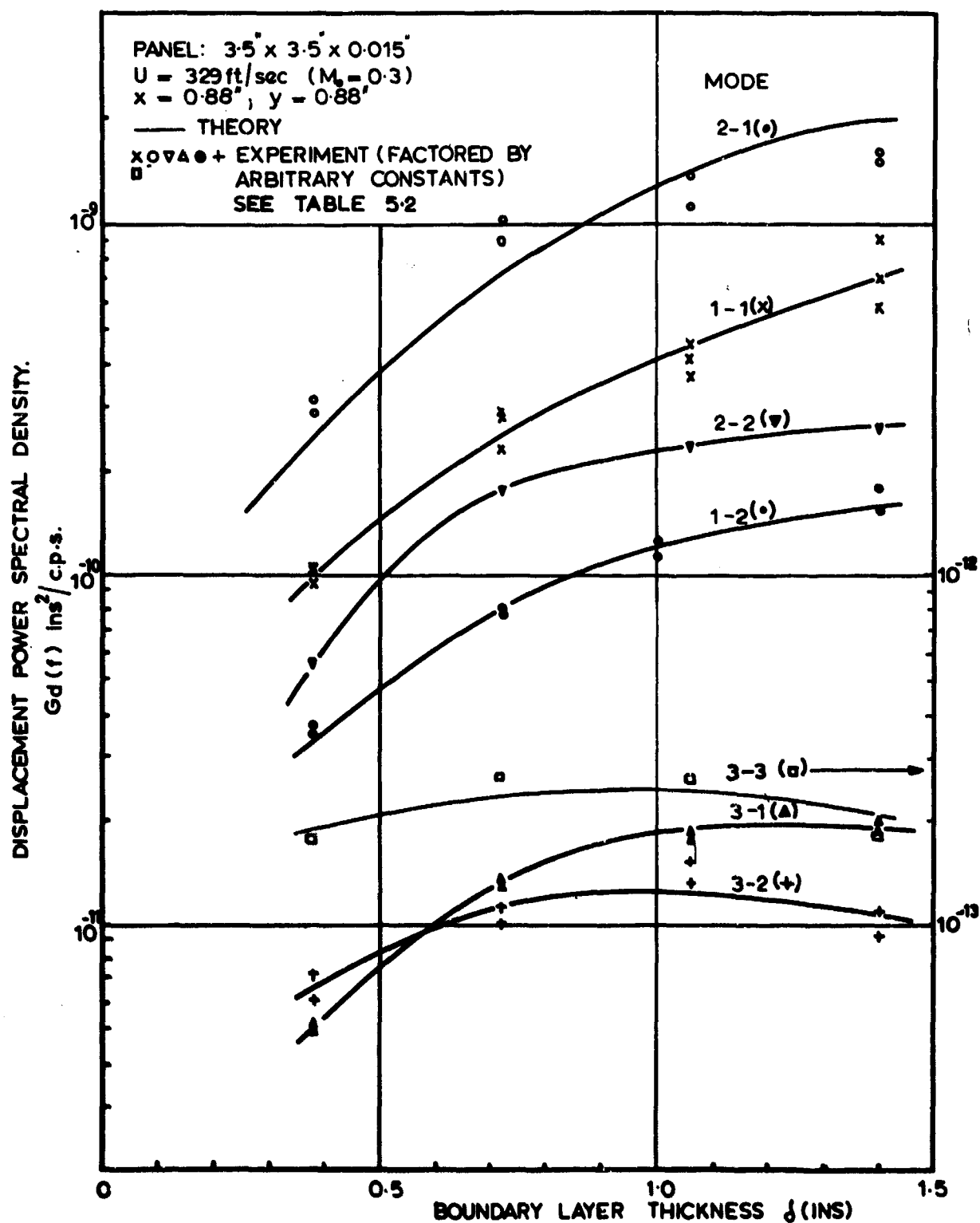


Figure 5.18 Variation of modal response with boundary layer thickness (Panel 4,  $M_0 = 0.3$ )

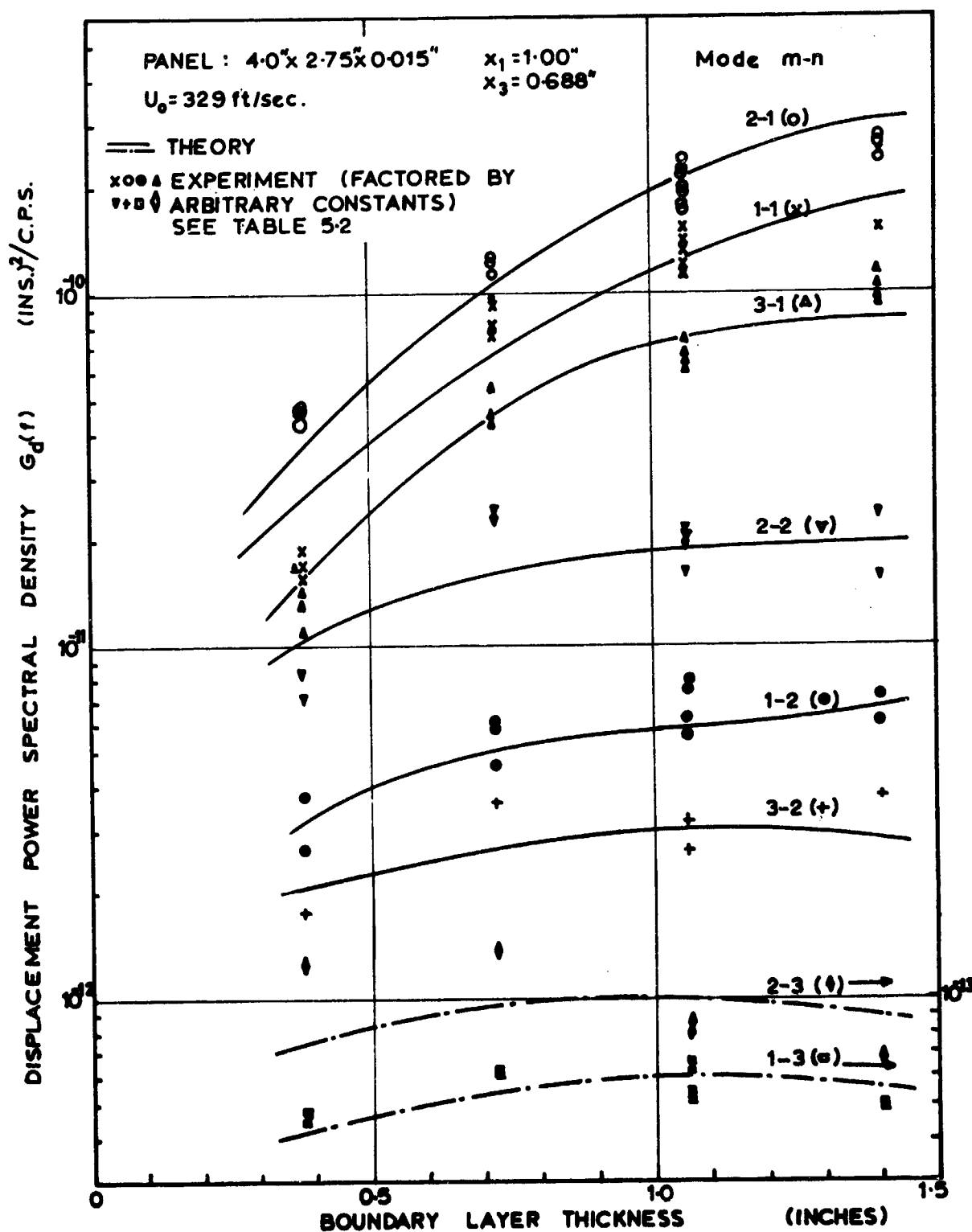


Figure 5-19 Variation of modal response at natural frequencies with boundary layer thickness. (Panel 5,  $M_0 = 0.3$ )

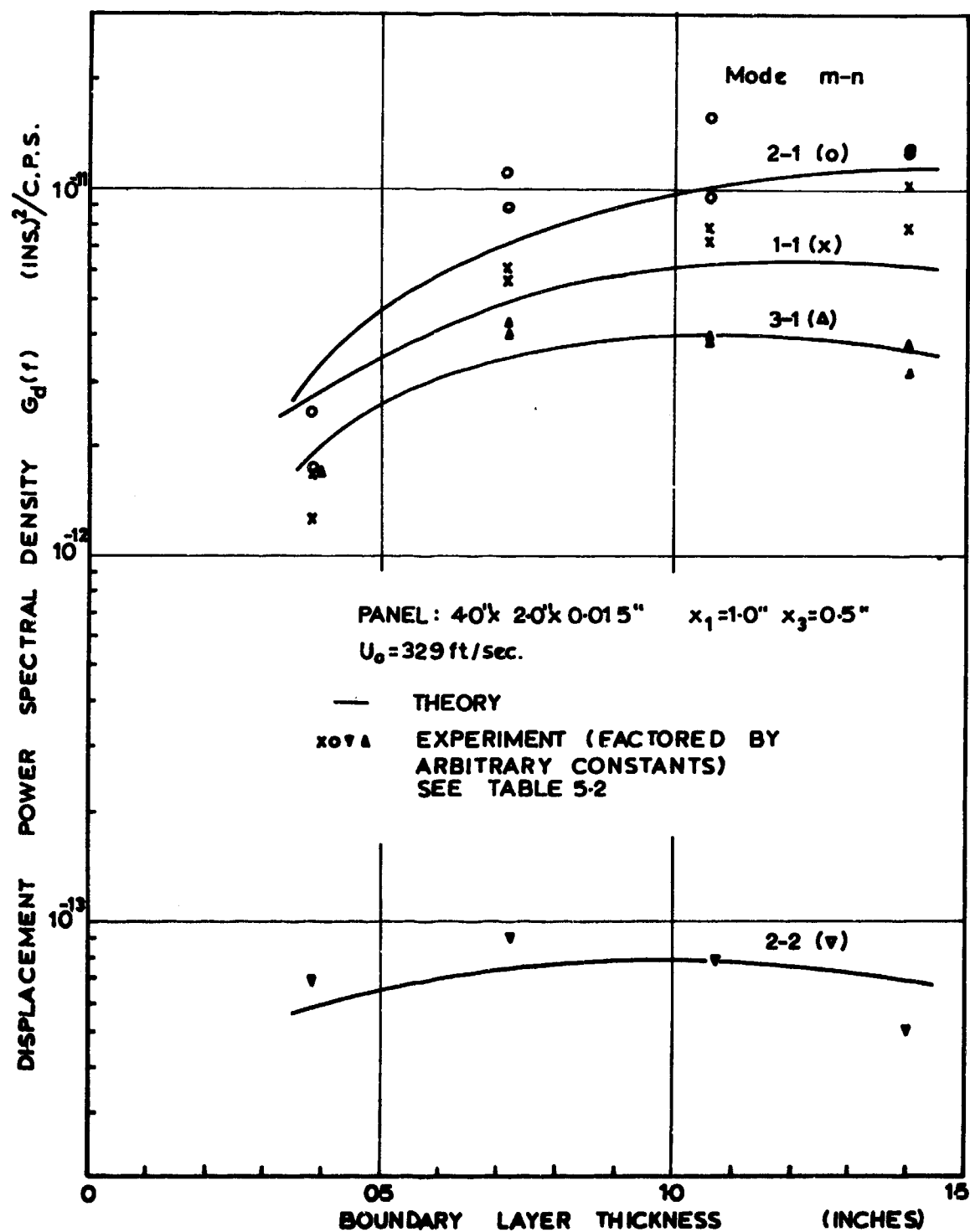


Figure 5-20 Variation of modal response at natural frequencies with boundary layer thickness. (Panel 6,  $M_0=0.3$ )

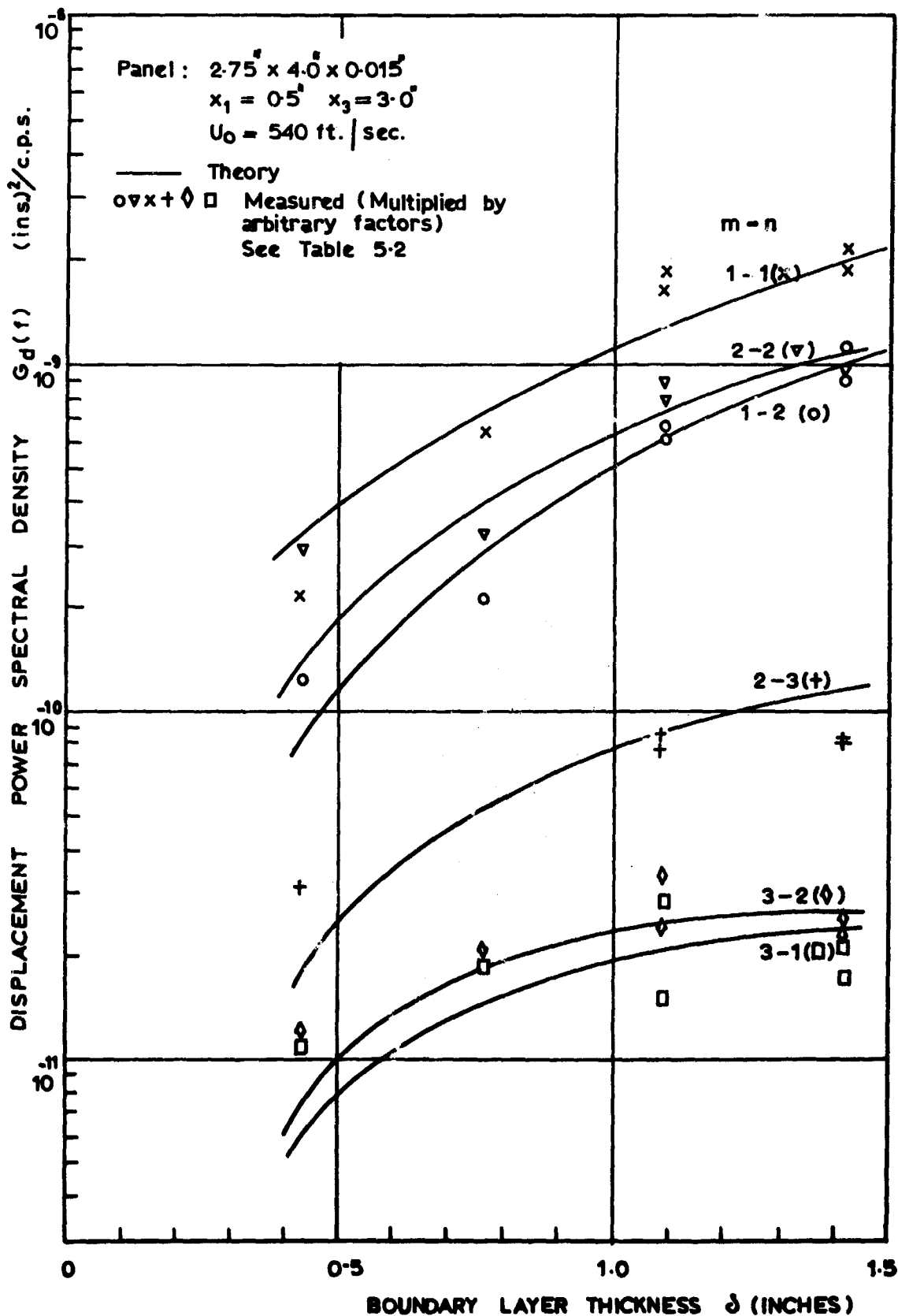


Figure 521 Variation of modal response at natural frequencies with boundary layer thickness. (Panel 3,  $M_0 = 0.5$ )



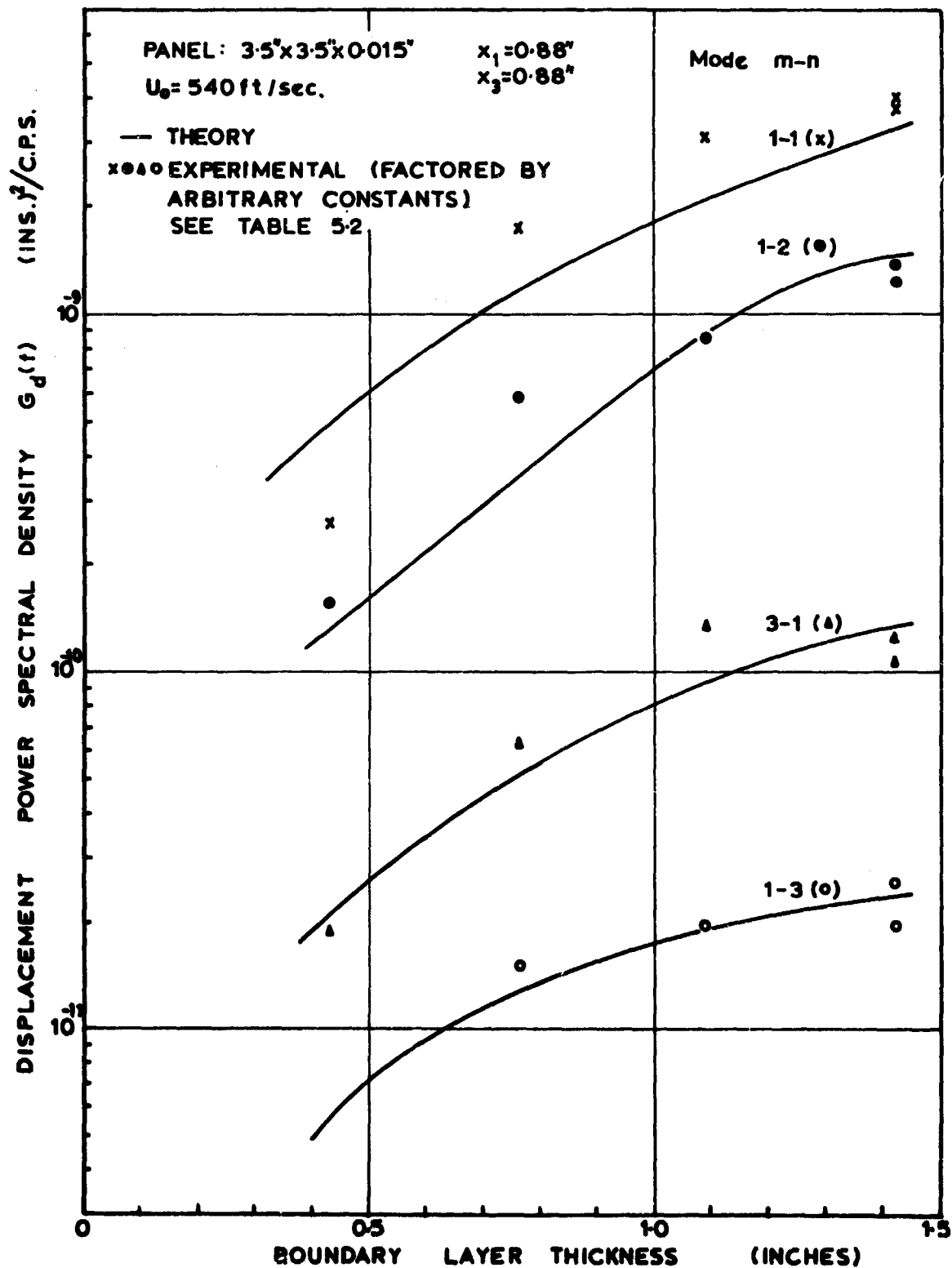


Figure 5-22(a) Variation of modal response at natural frequencies with boundary layer thickness. (Panel 4,  $M_0=0.5$ )

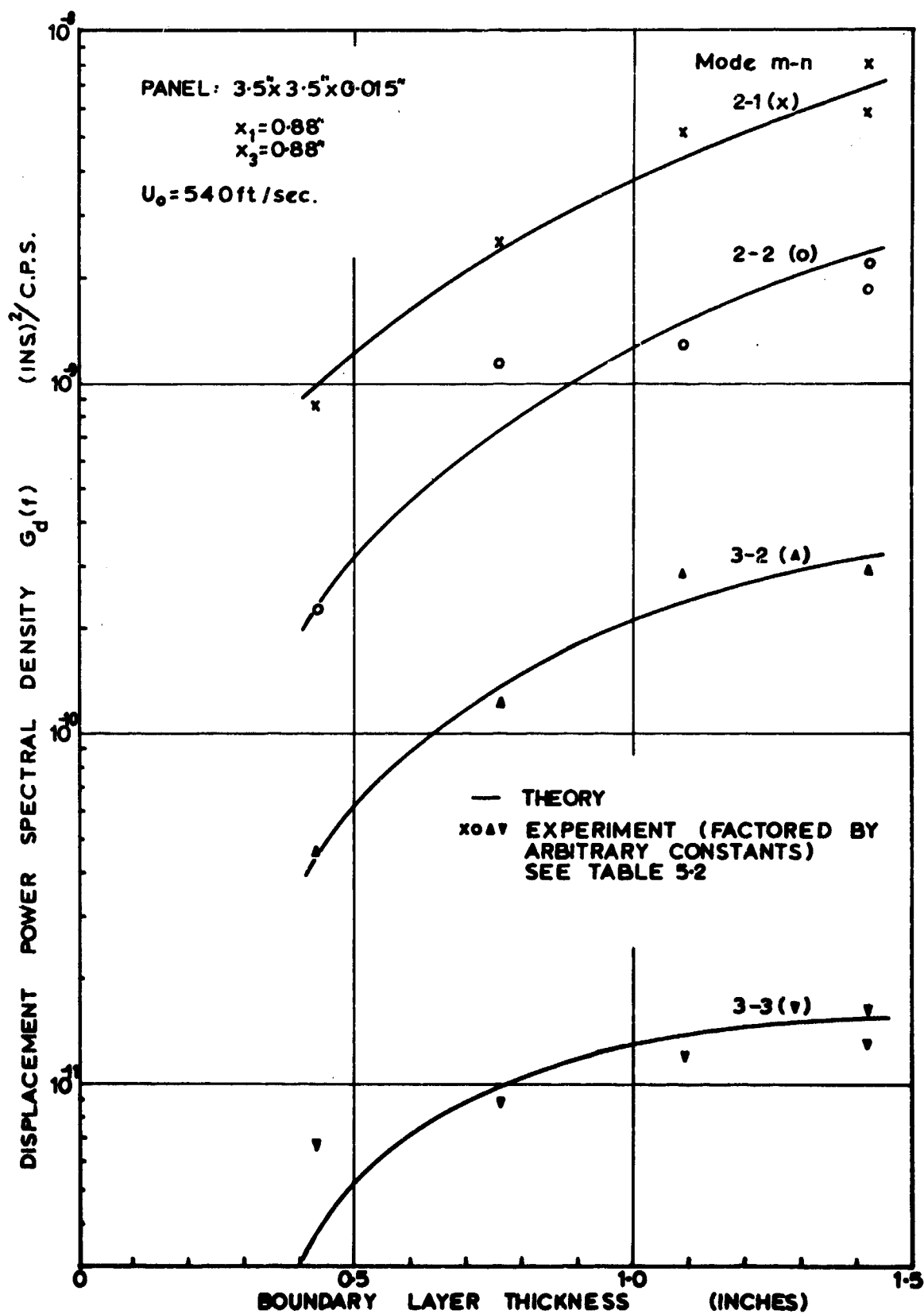


Figure 522(b) Variation of modal response at natural frequencies with boundary layer thickness. (Panel 4,  $M=0.5$ )

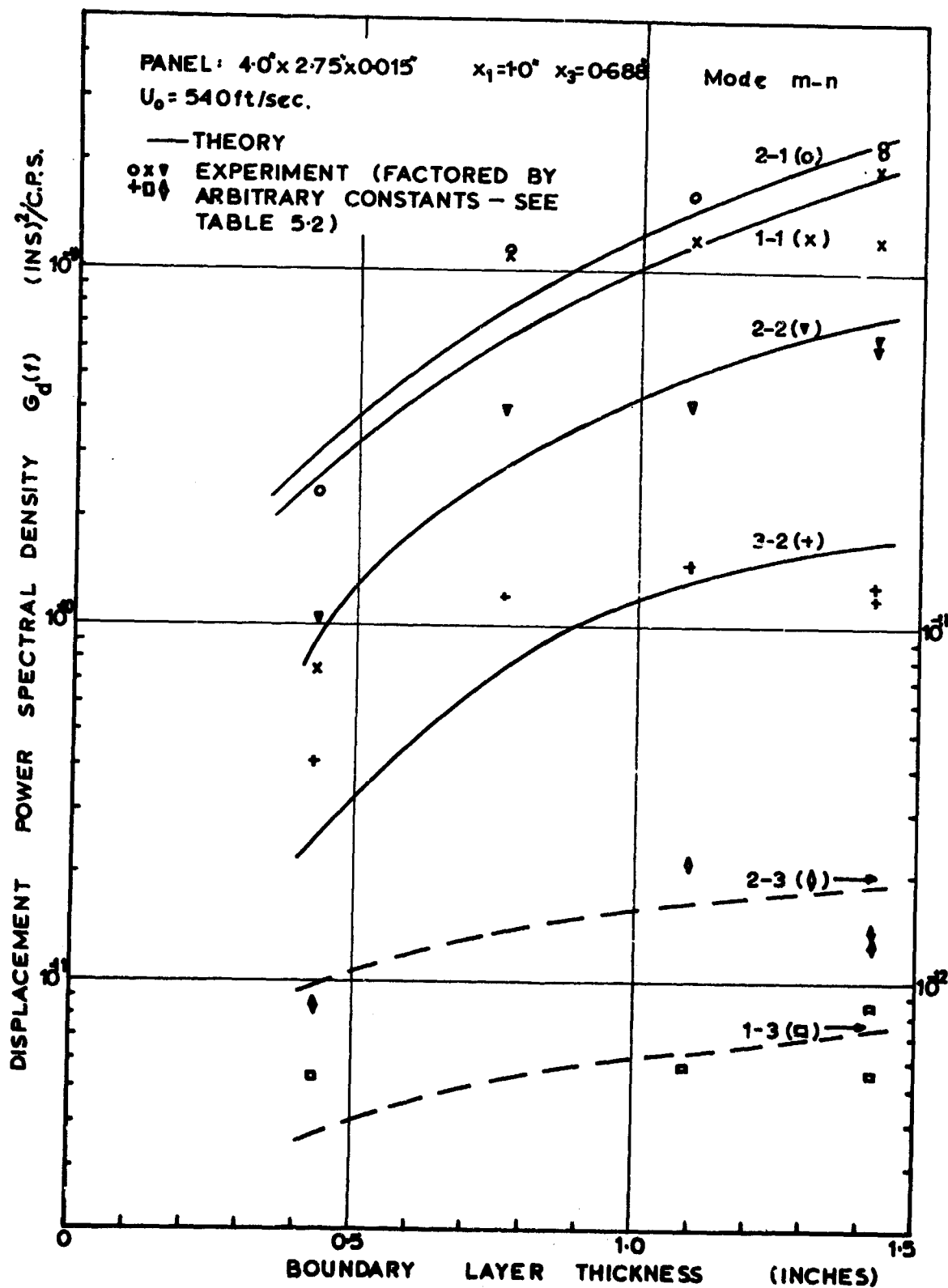


Figure 5-23 Variation of modal response at natural frequencies with boundary layer thickness. (Panel 5,  $M_0=0.5$ )

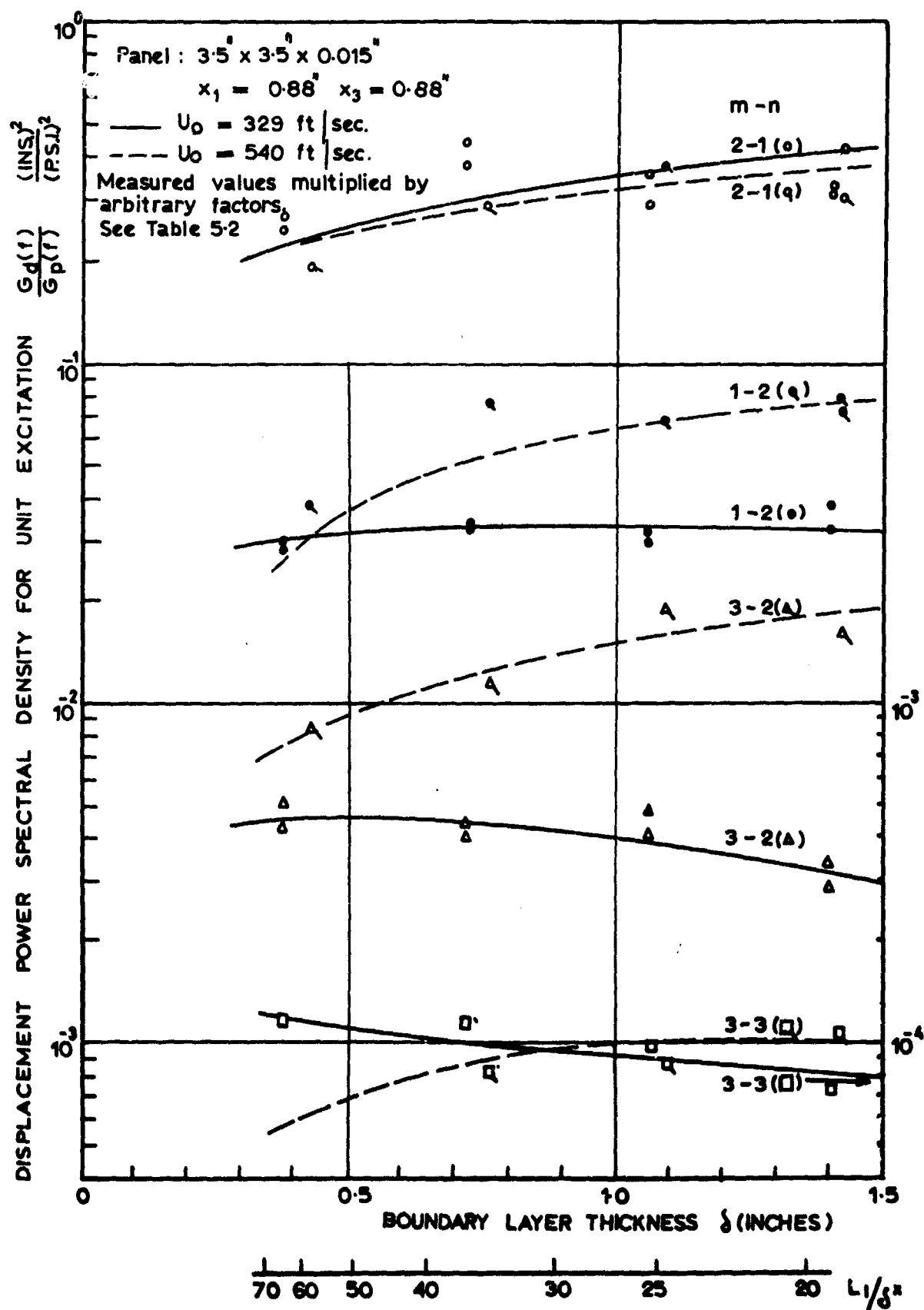


Fig. 524 Response to unit excitation at natural frequencies as a function of boundary layer thickness.  
 (Panel 4,  $M_0 = 0.3, 0.5$ )

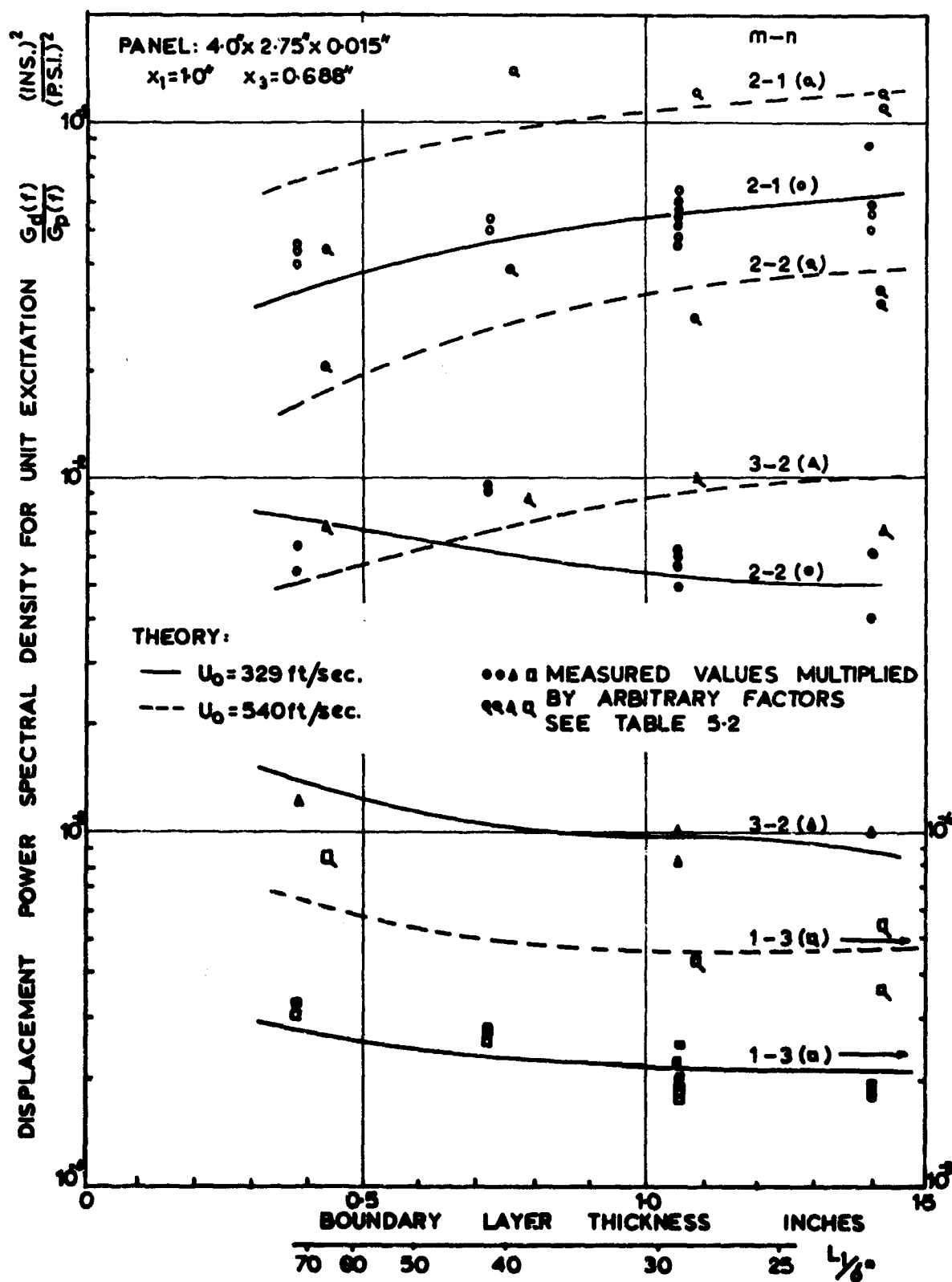


Figure 5-25 Response to unit excitation at natural frequencies as a function of boundary layer thickness.  
 (Panel 5,  $M_0 = 0.3, 0.5$ )



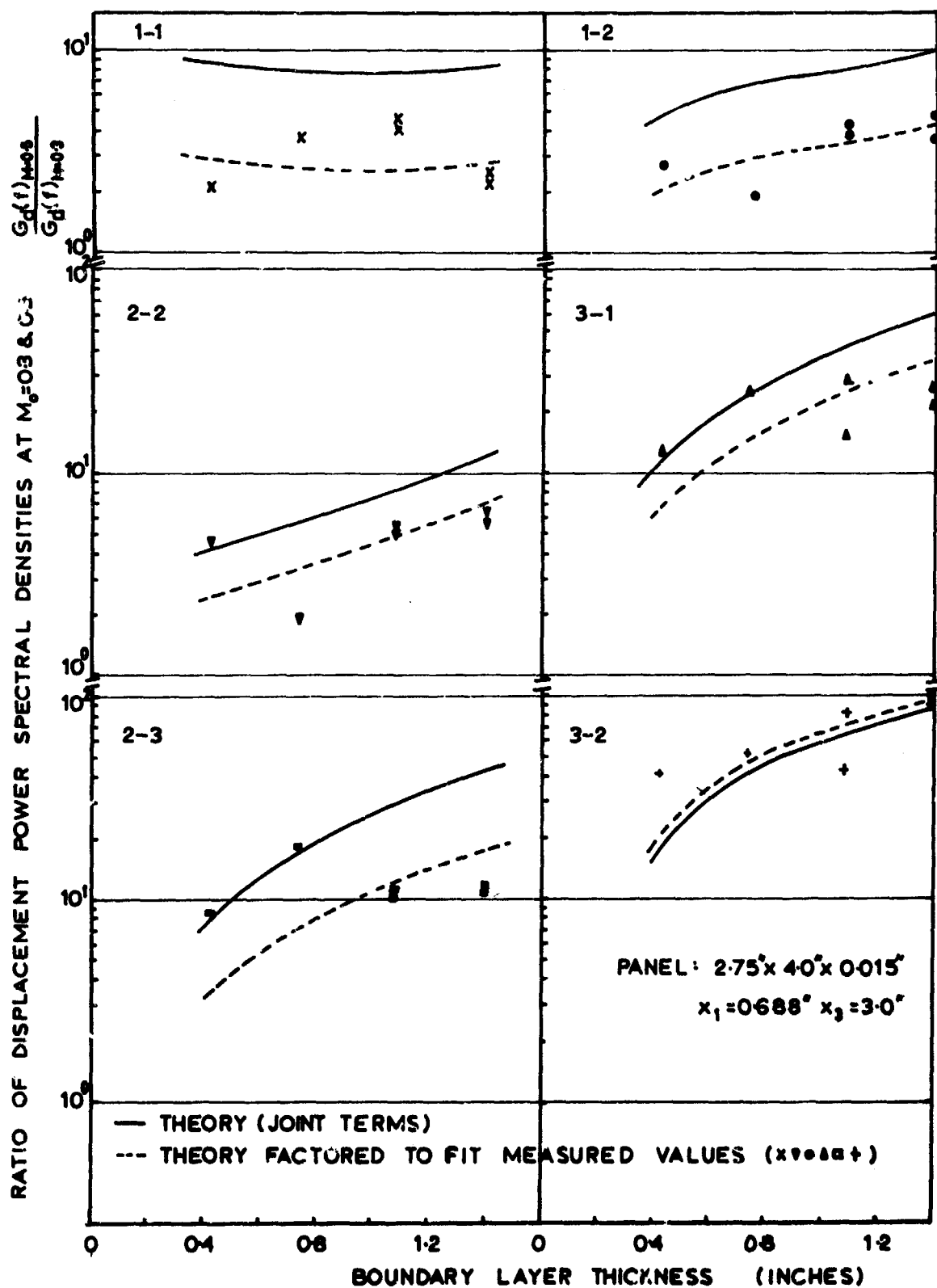


Figure 5.27 Variation of modal response at natural frequencies with flow velocity (Panel 3).

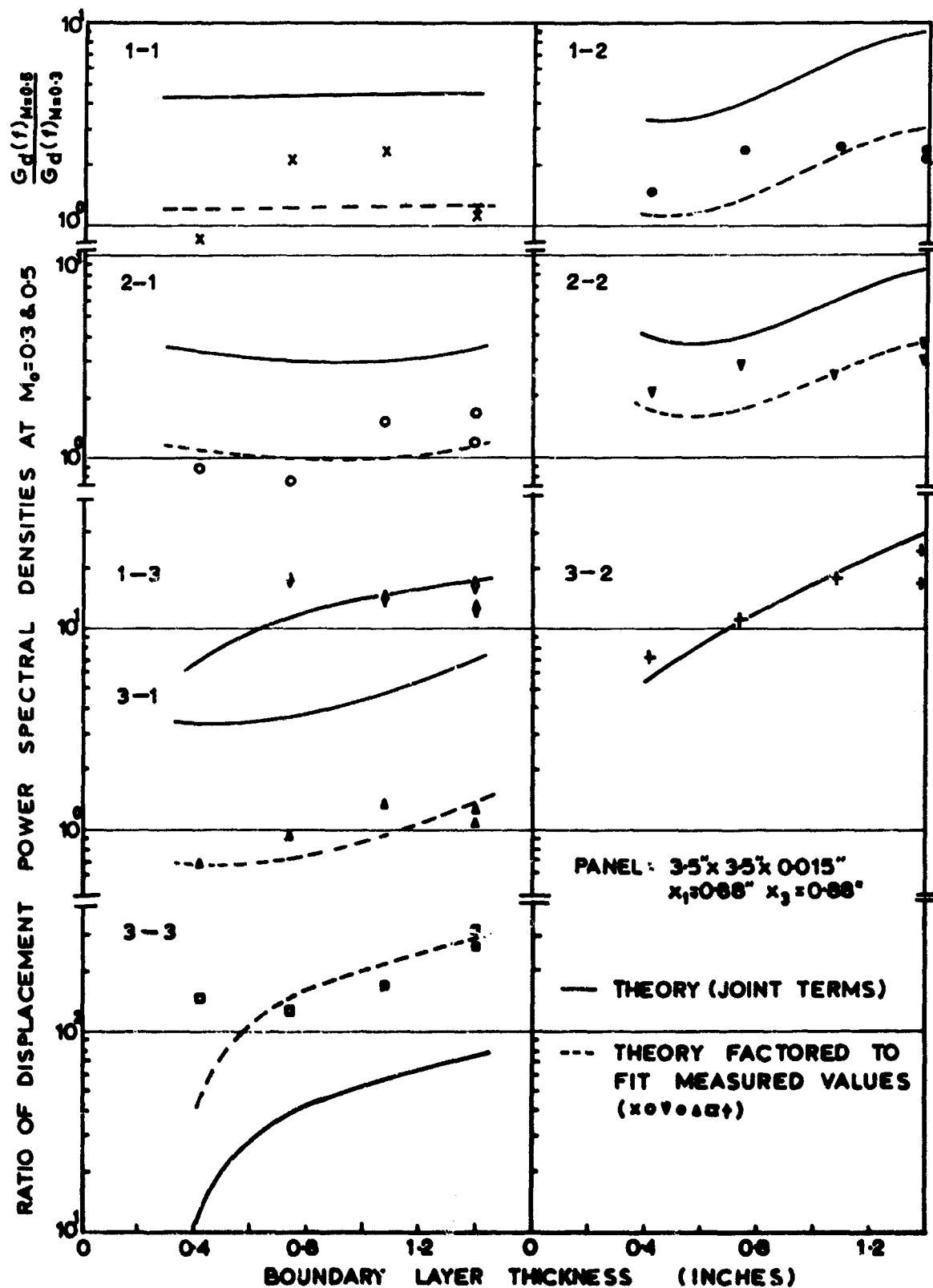


Figure 5-28 Variation of modal response at natural frequencies with flow velocity (Panel 4).



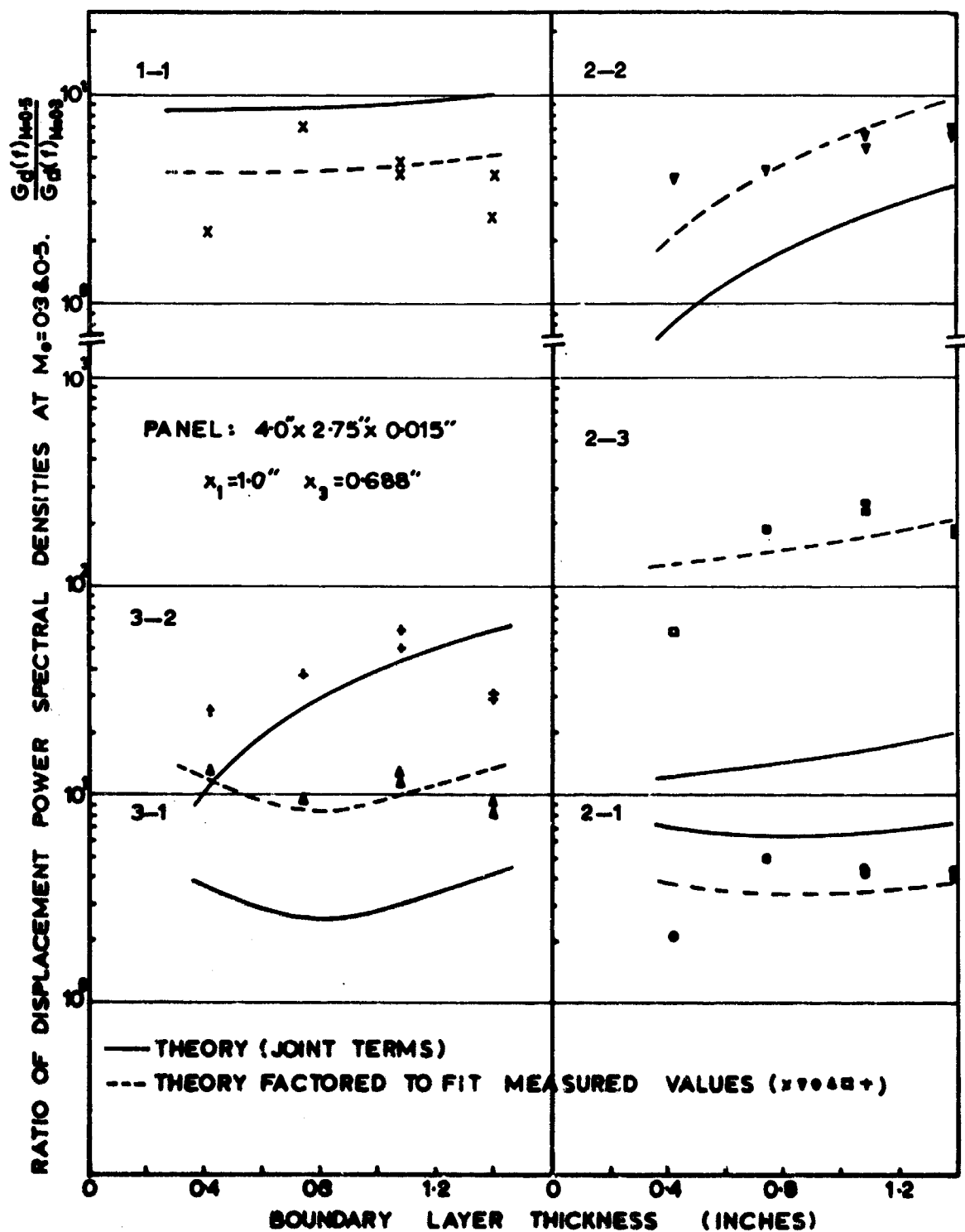


Figure 5-29 Variation of modal response at natural frequencies with flow velocity (Panel 5).

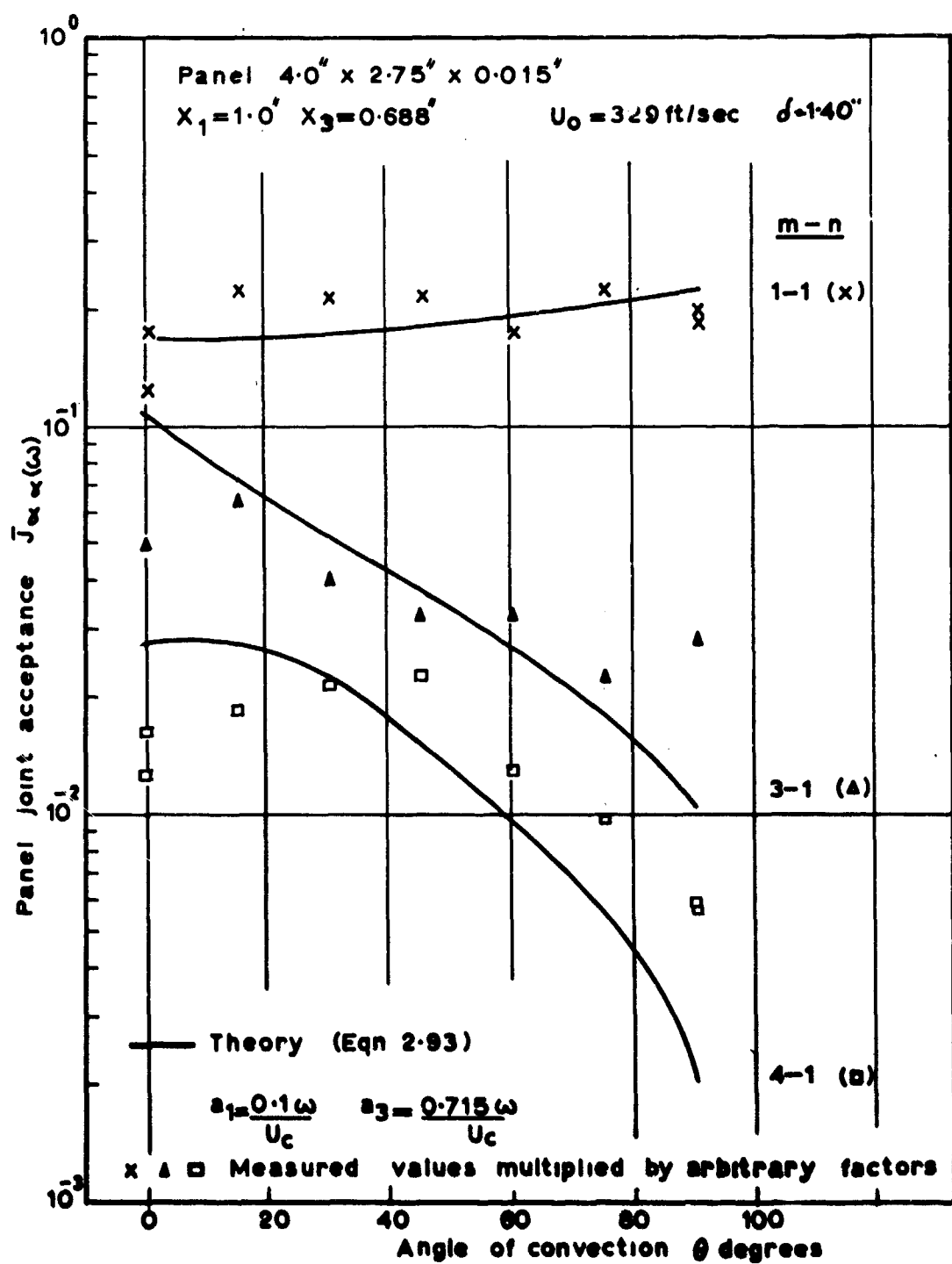


Figure 5.30(a) Effect of angle of convection on response of panel 5 to boundary layer excitation.

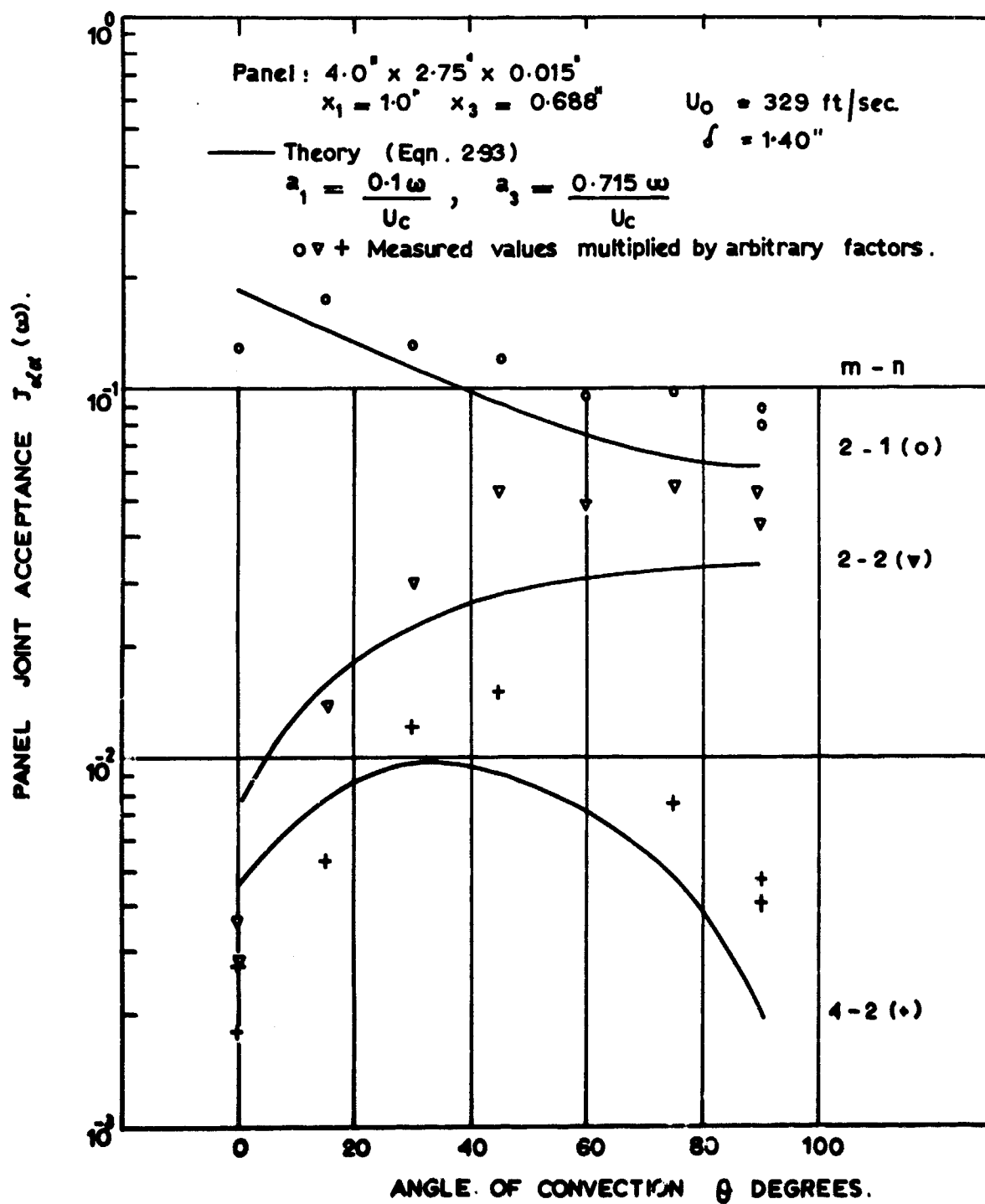


Figure 5-30(b) Effect of angle of convection on response of panel 5 to boundary layer excitation.

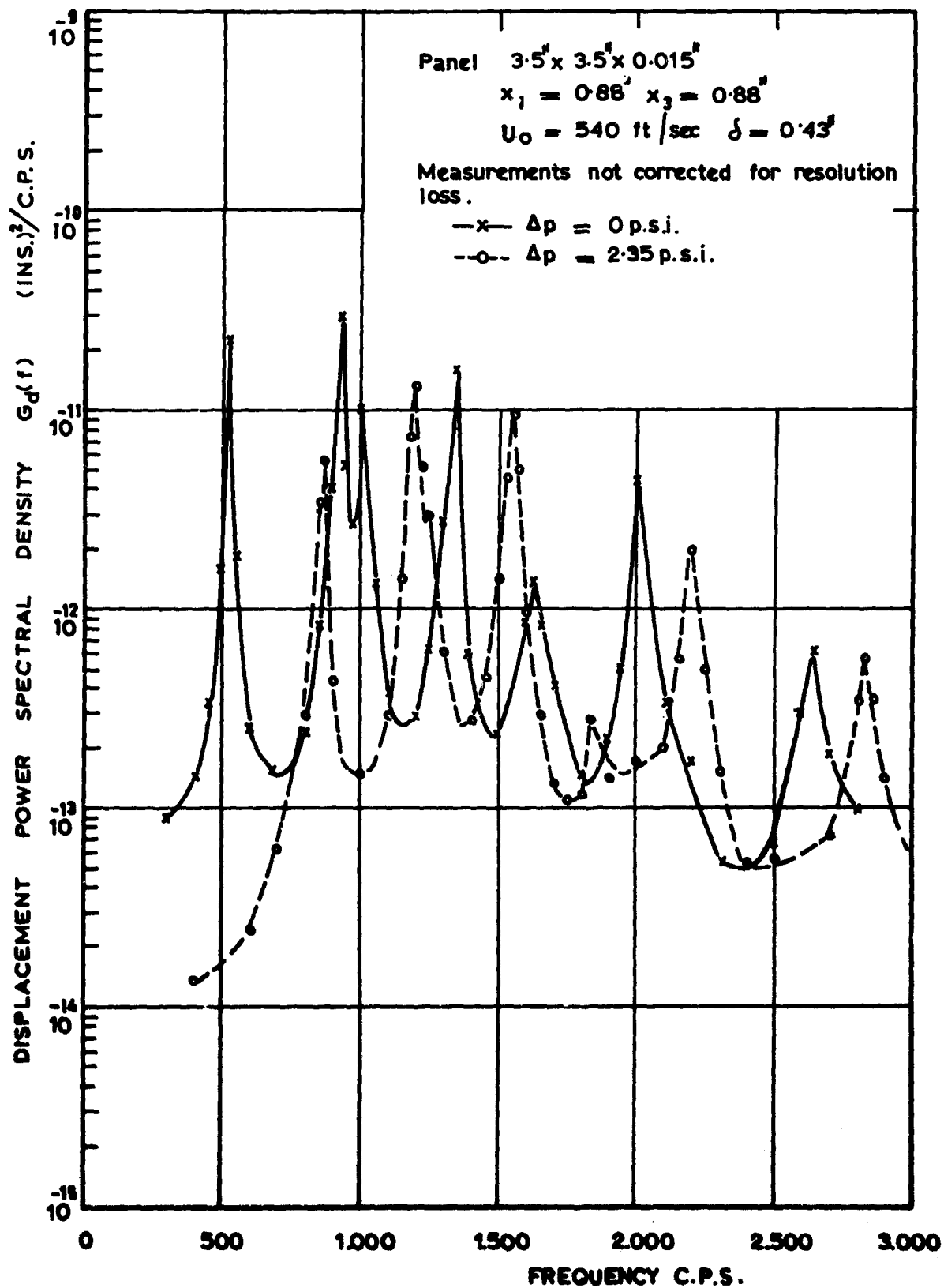


Fig.5.31 Effect of static pressure differential on measured response of panel 4 to boundary layer excitation.

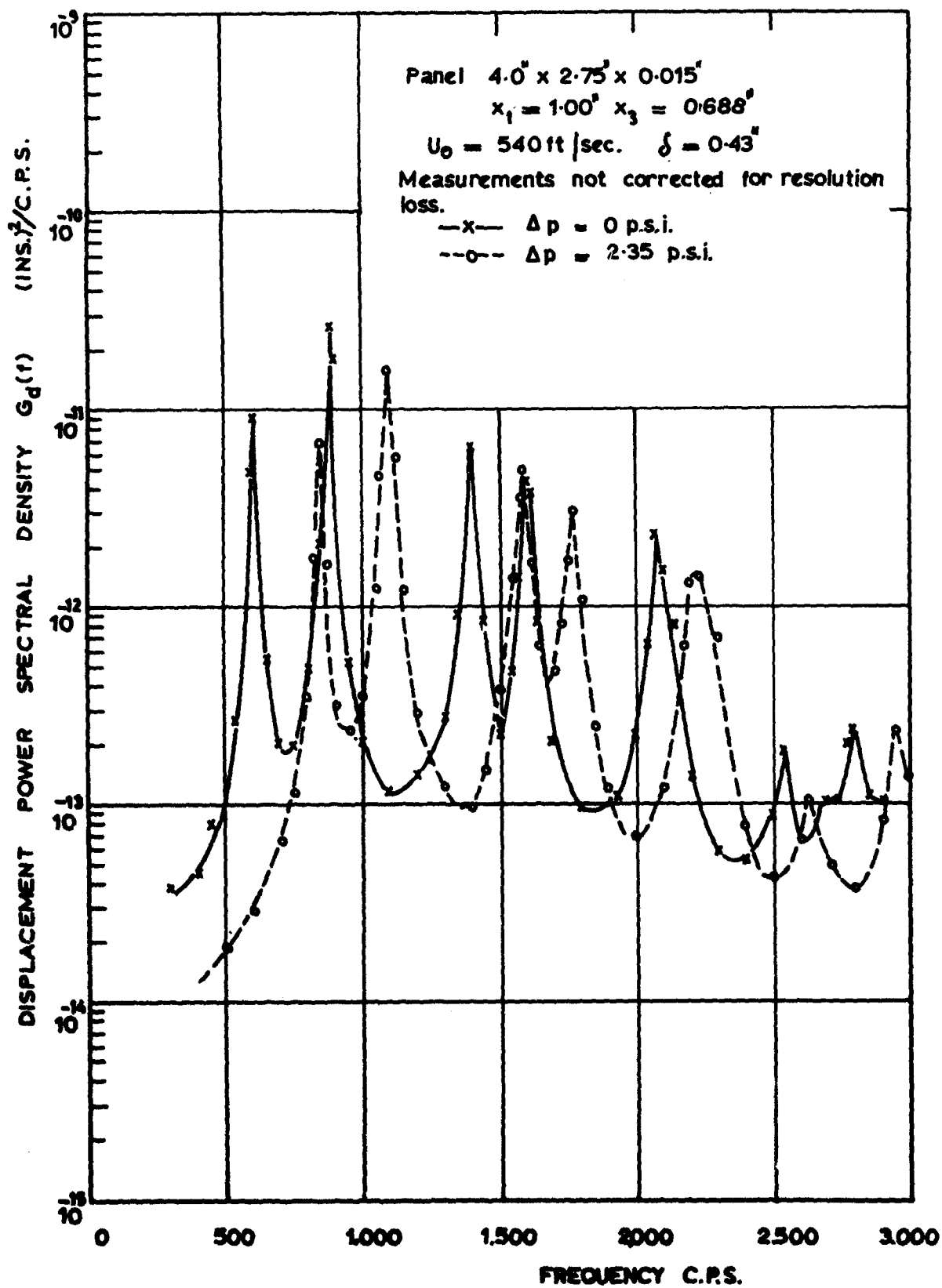


Fig. 5-32 Effect of static pressure differential on measured response of panel 5 to boundary layer excitation.

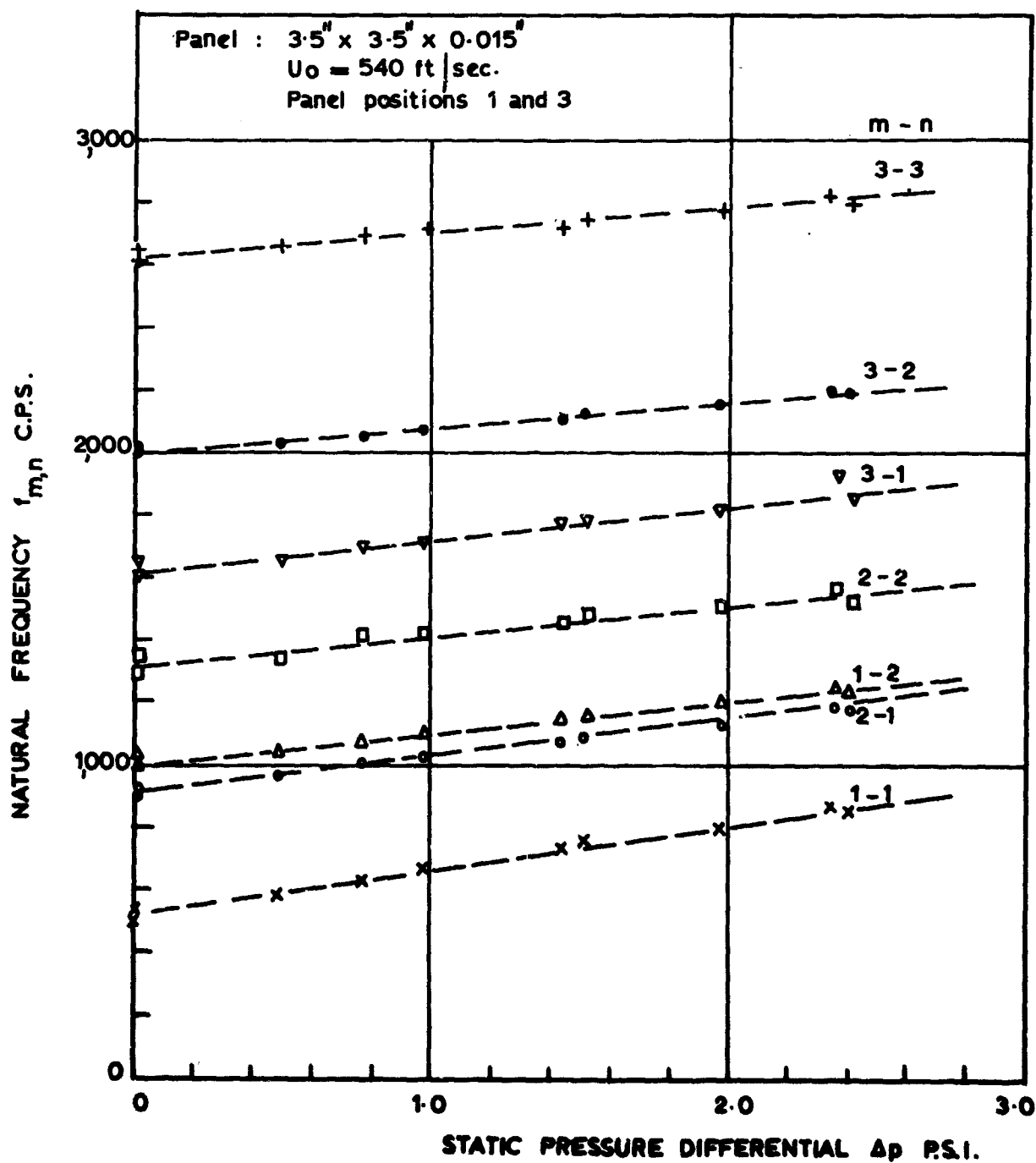


Figure 5-33 Effect of pressure differential in wind tunnel on natural frequencies of panel 4.

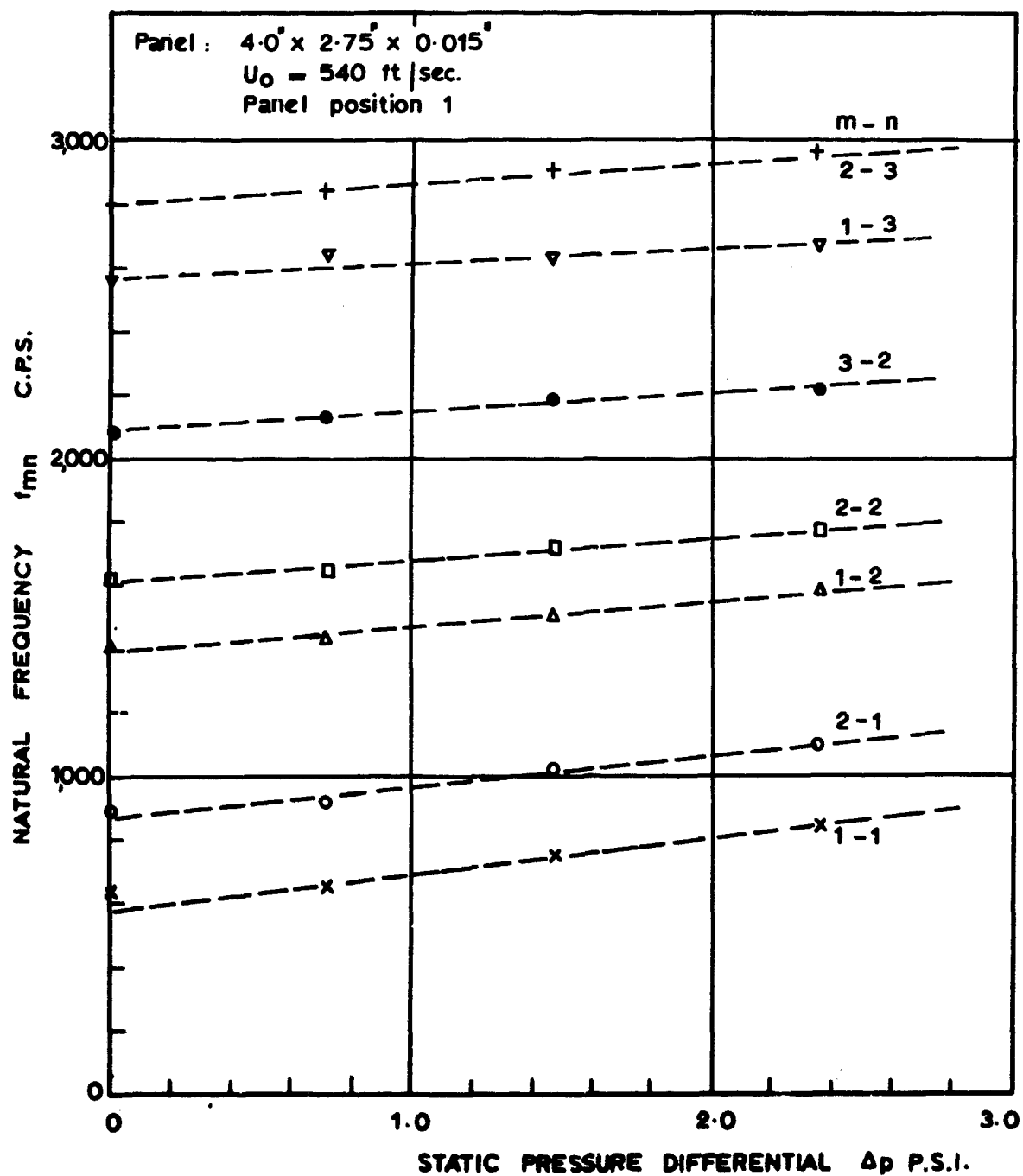


Figure 5.34 Effect of pressure differential in wind tunnel on natural frequencies of panel 5.

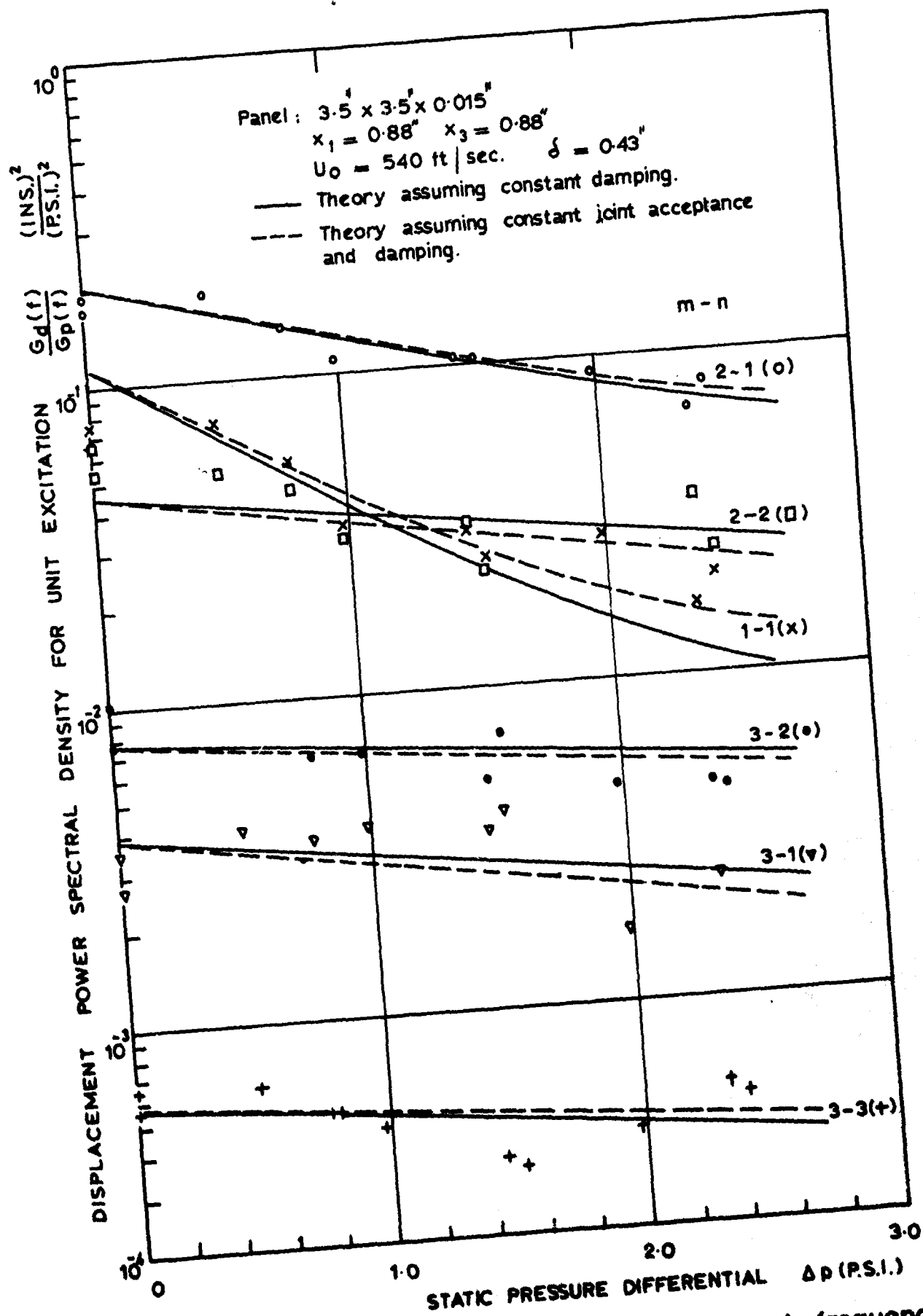


Fig. 5.35 Variation of modal response at natural frequencies with static pressure differential (Panel 4)



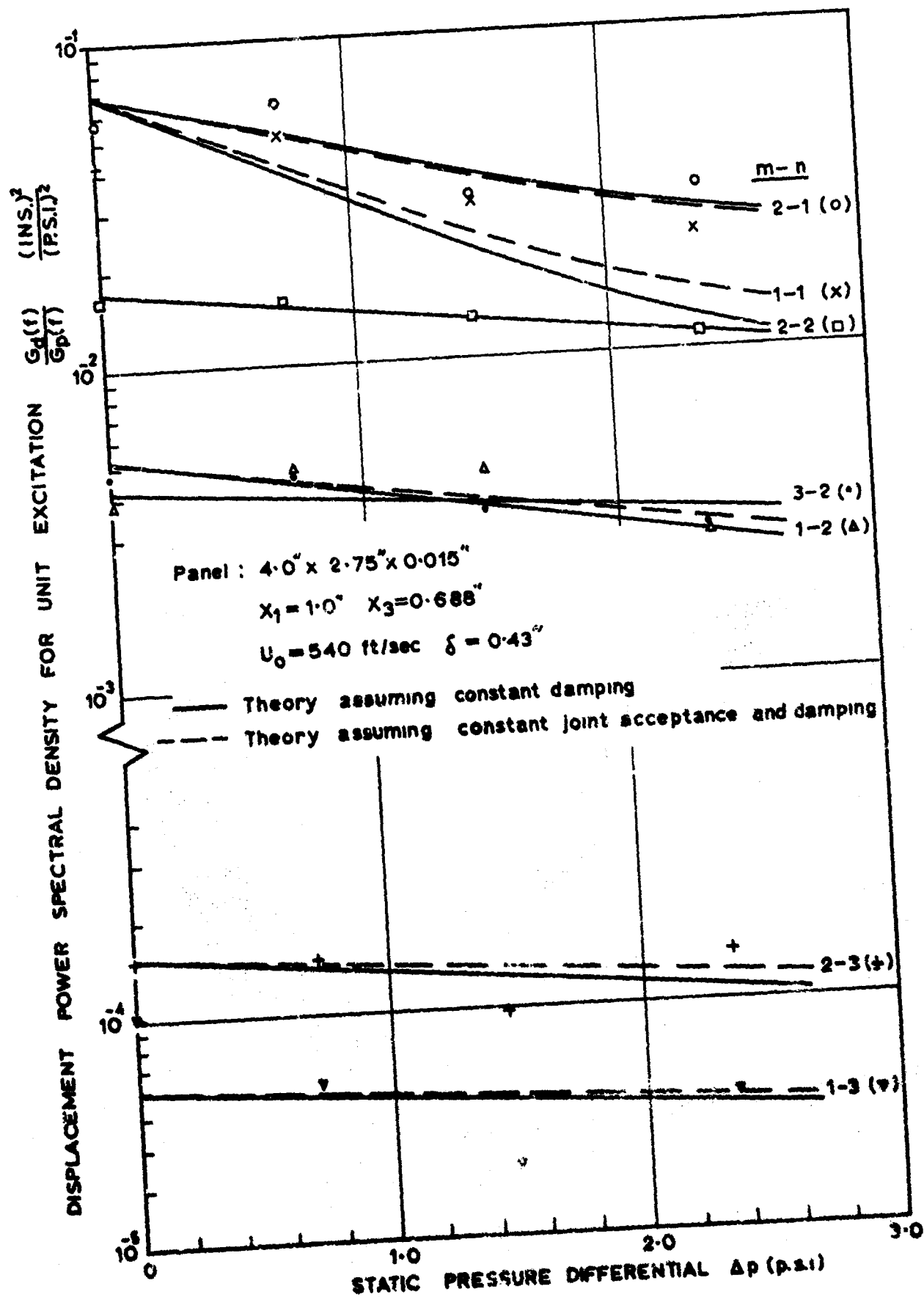


Figure 5.36 Variation of modal response at natural frequencies with static pressure differential

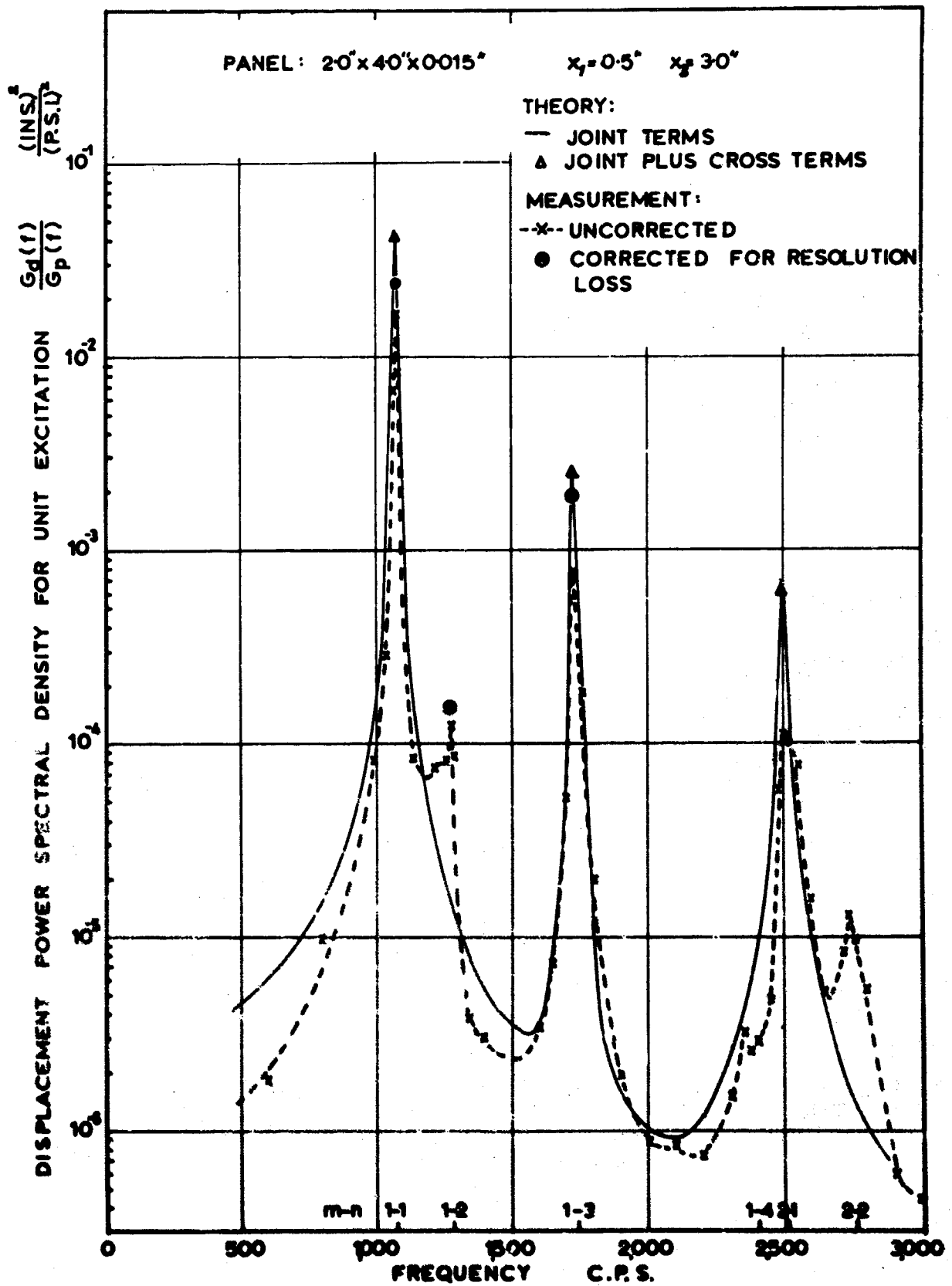


Figure 6-1 Response of panel 2 to acoustic excitation.

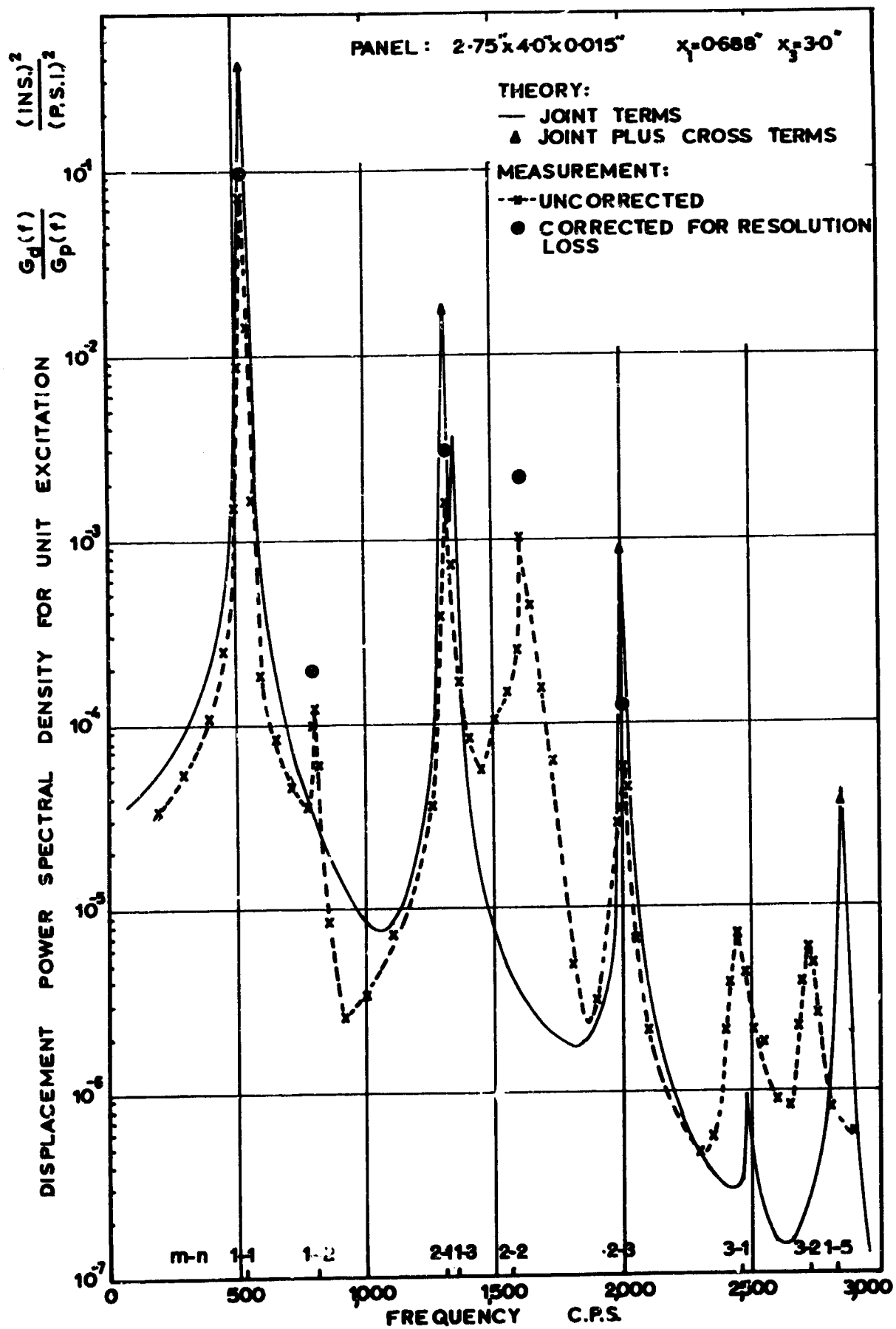


Figure 6-2 Response of panel 3 to acoustic excitation.

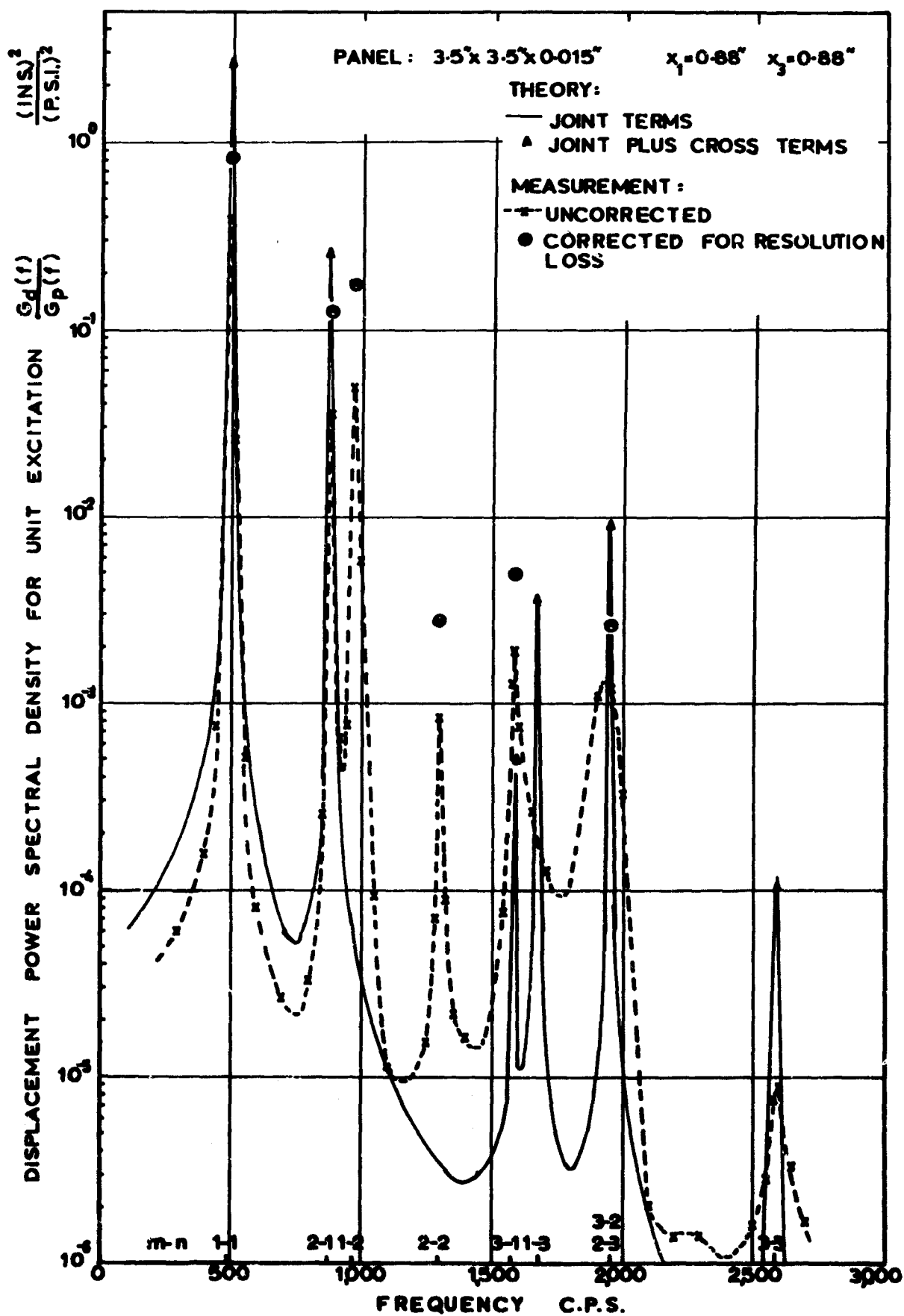


Figure 6.3 Response of panel 4 to acoustic excitation

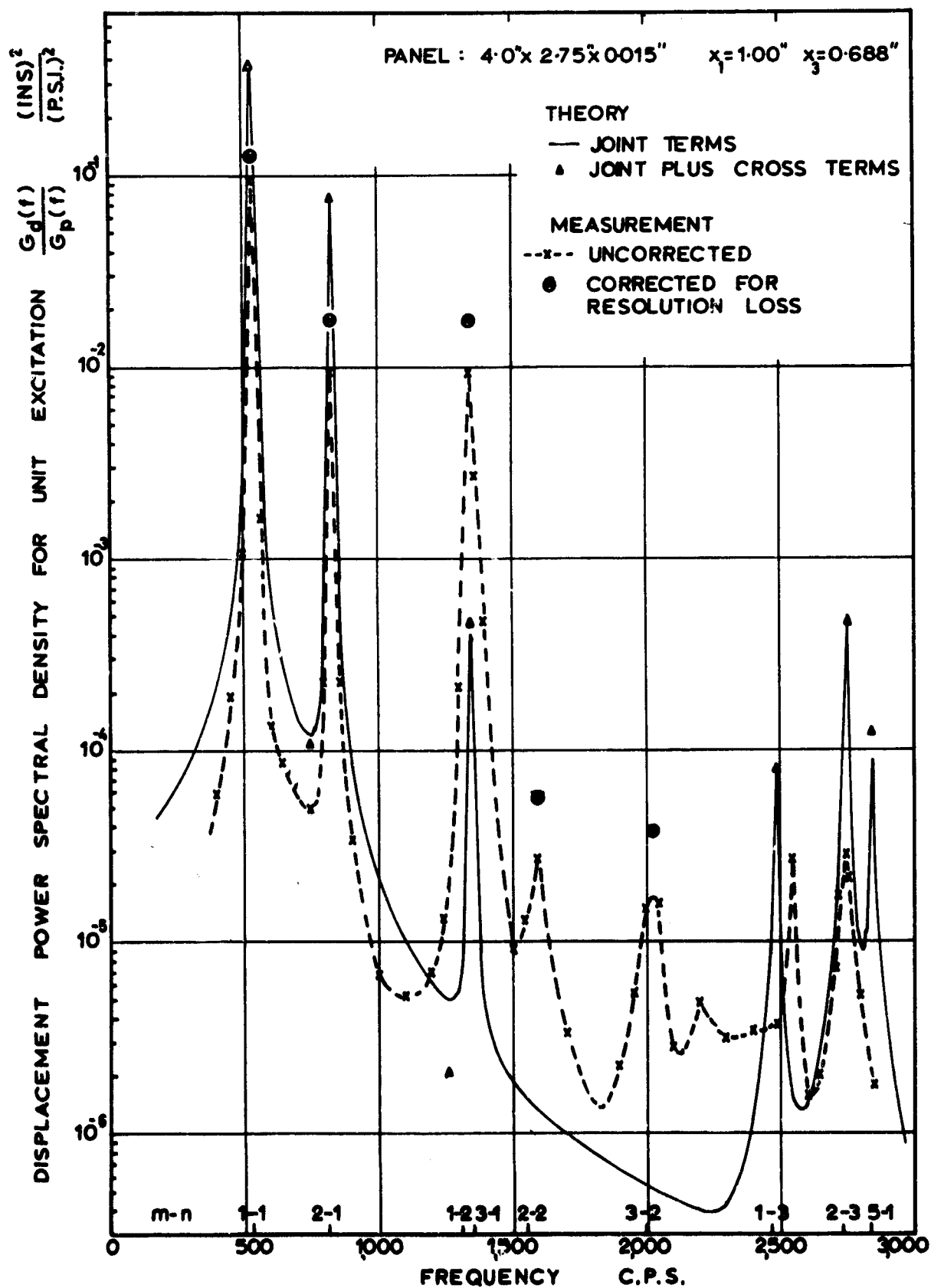


Figure 6.4 Response of panel 5 to acoustic excitation.

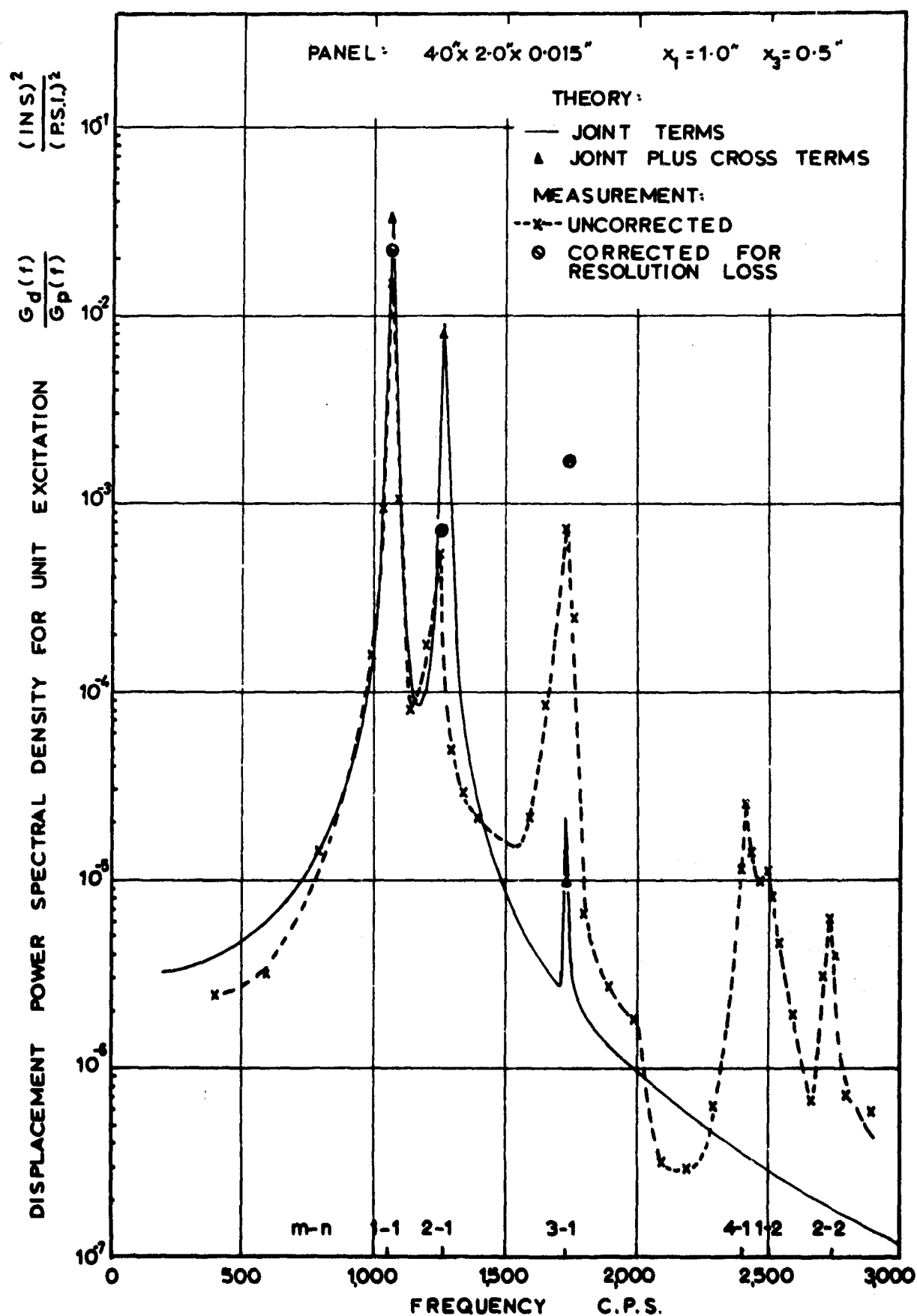


Figure 6-5 Response of panel 6 to acoustic excitation.

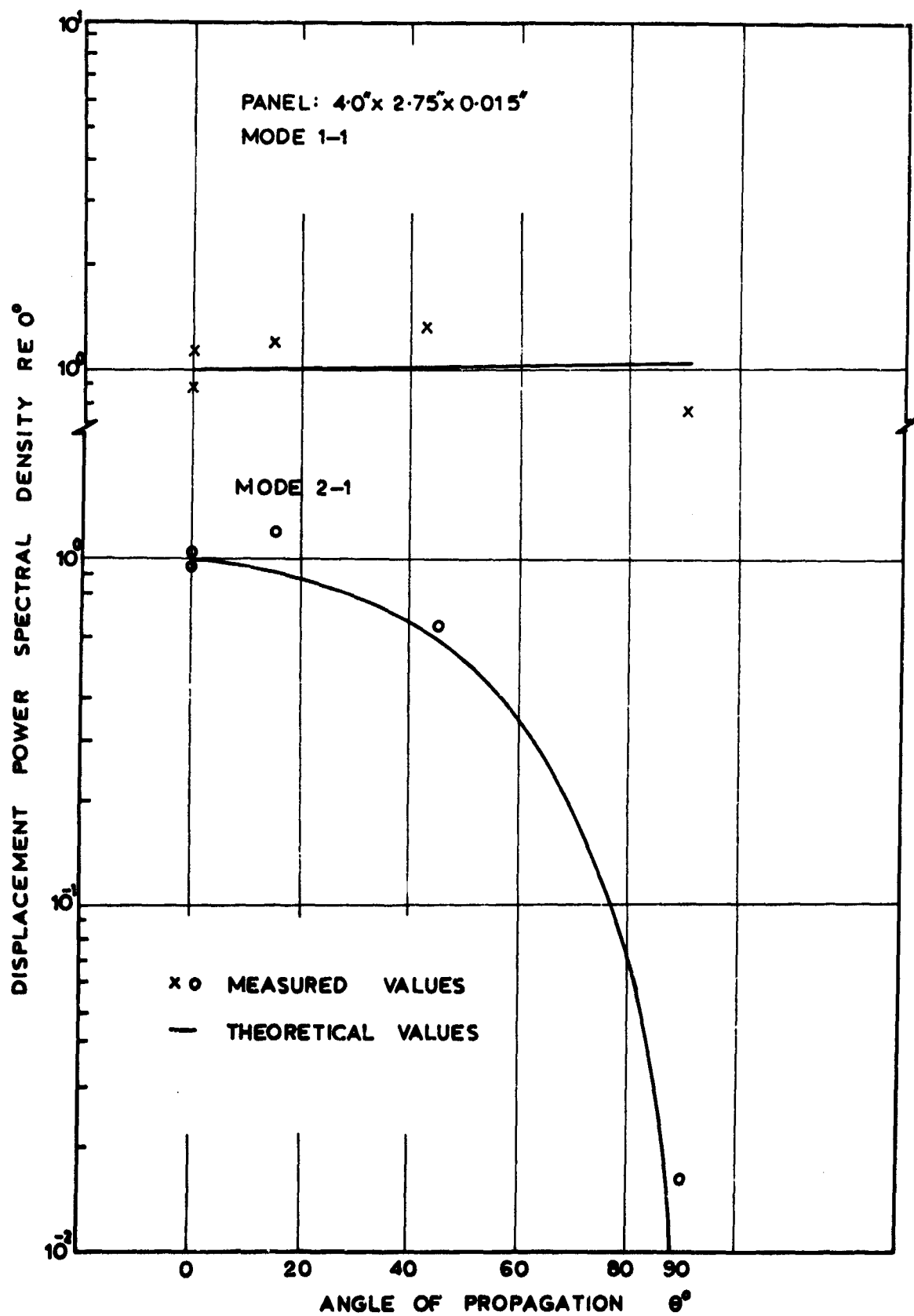


Figure 6-6 Response to siren excitation: effect of angle of propagation.

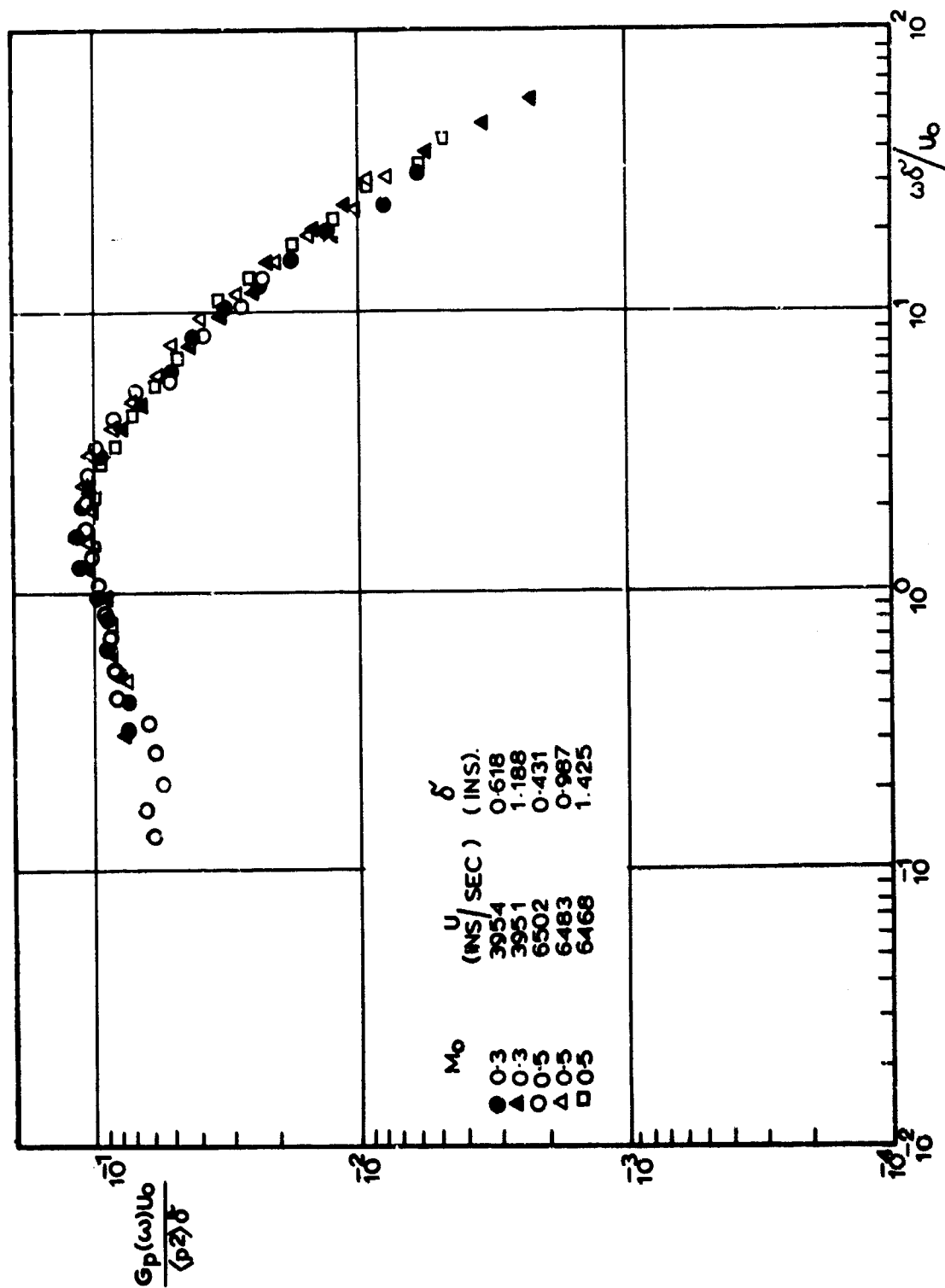


Figure A.1. Similarity of corrected frequency spectra of wall pressure fluctuations under various flow conditions. FROM BULL (1963)



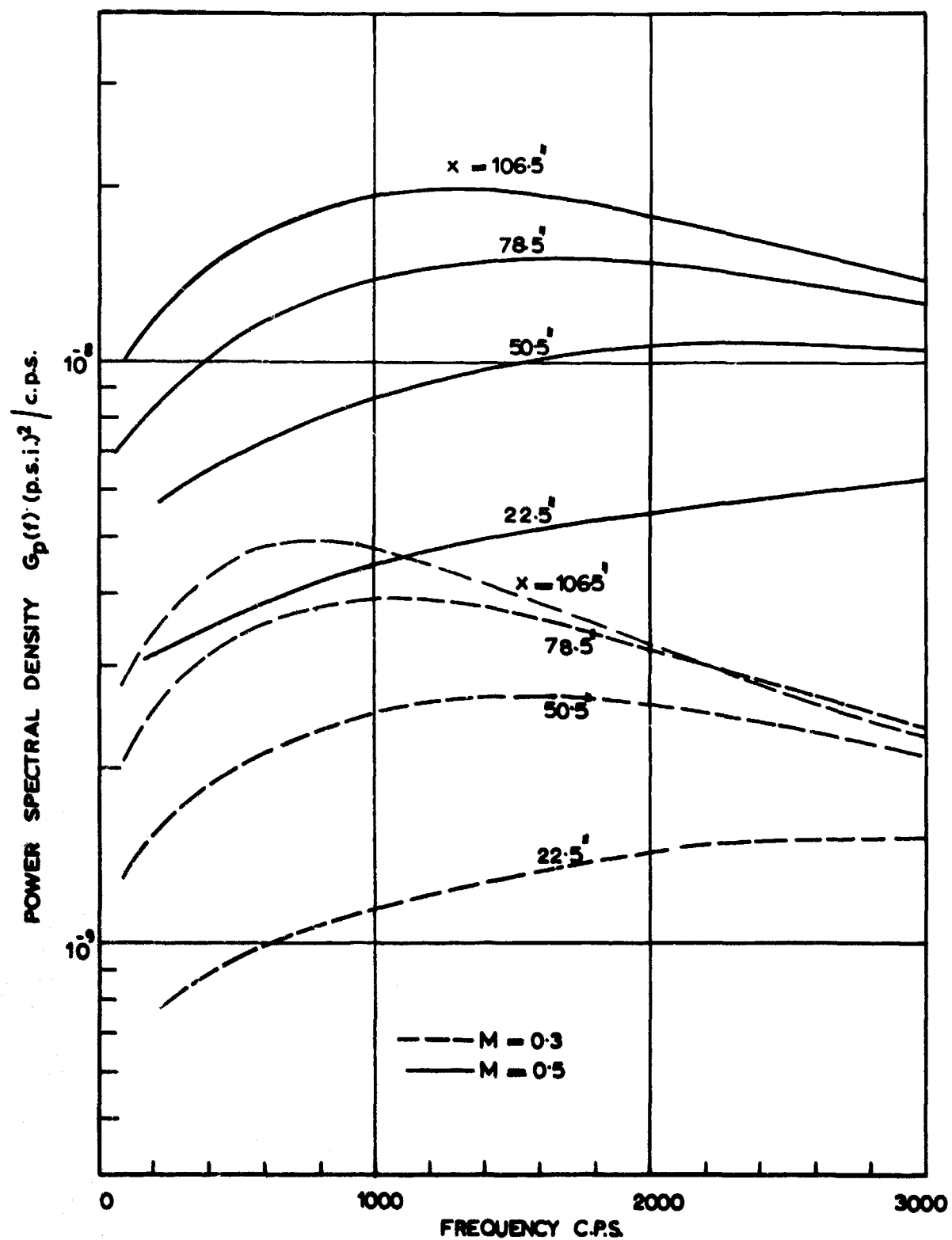


Figure A2. Turbulent boundary layer spectra at panel positions.

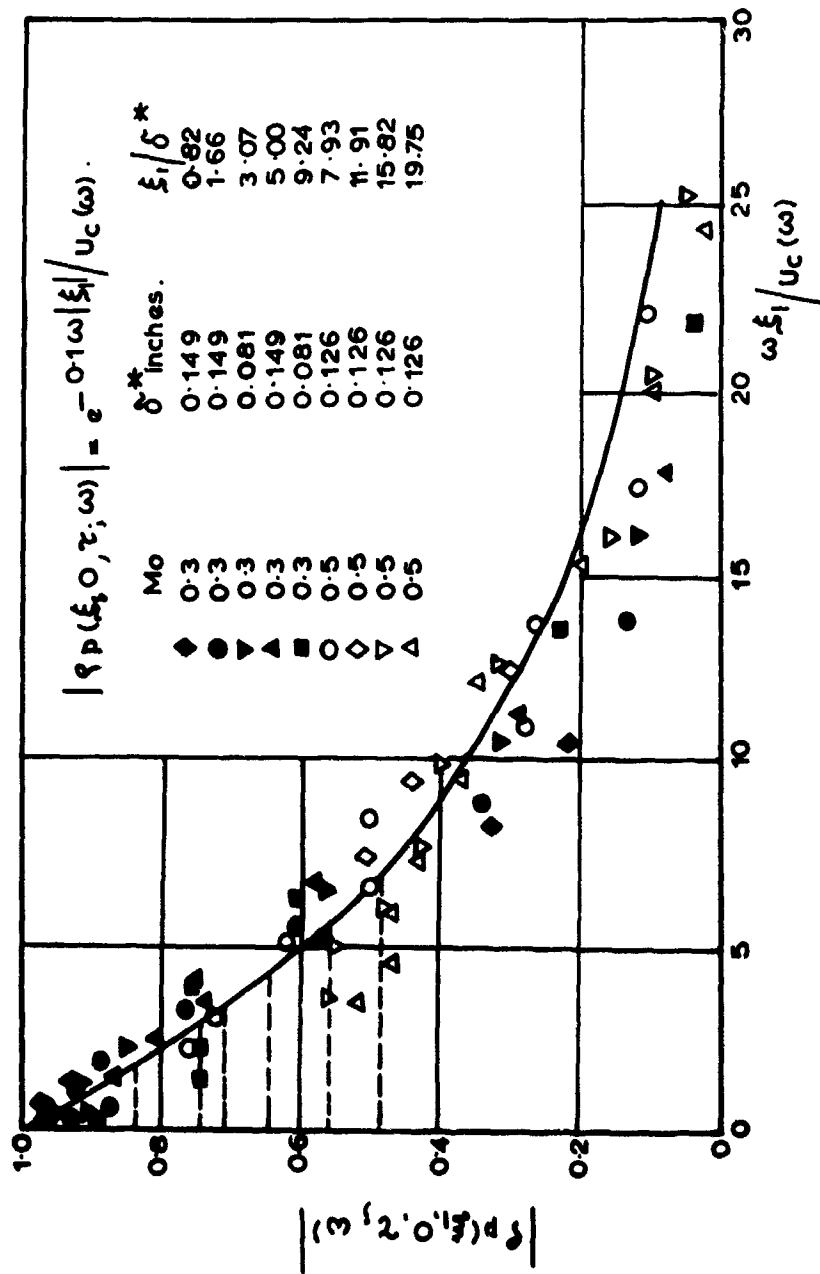


Figure A3. Amplitude of narrow band longitudinal space time correlations of the wall pressure field FROM BULL (1963)

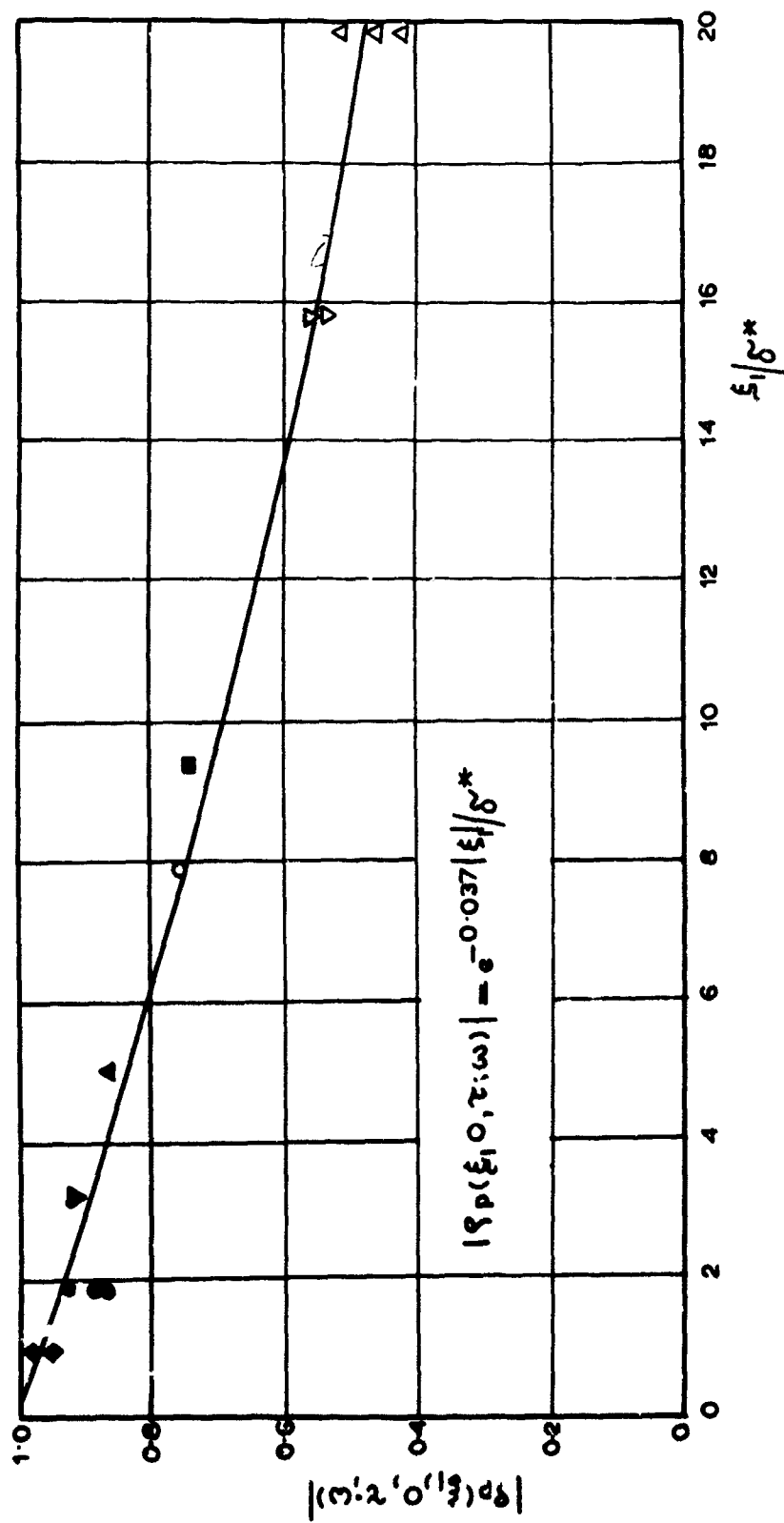


Figure A.4. Low frequency value of narrow band longitudinal pressure correlation amplitudes. FROM BULL (1963)

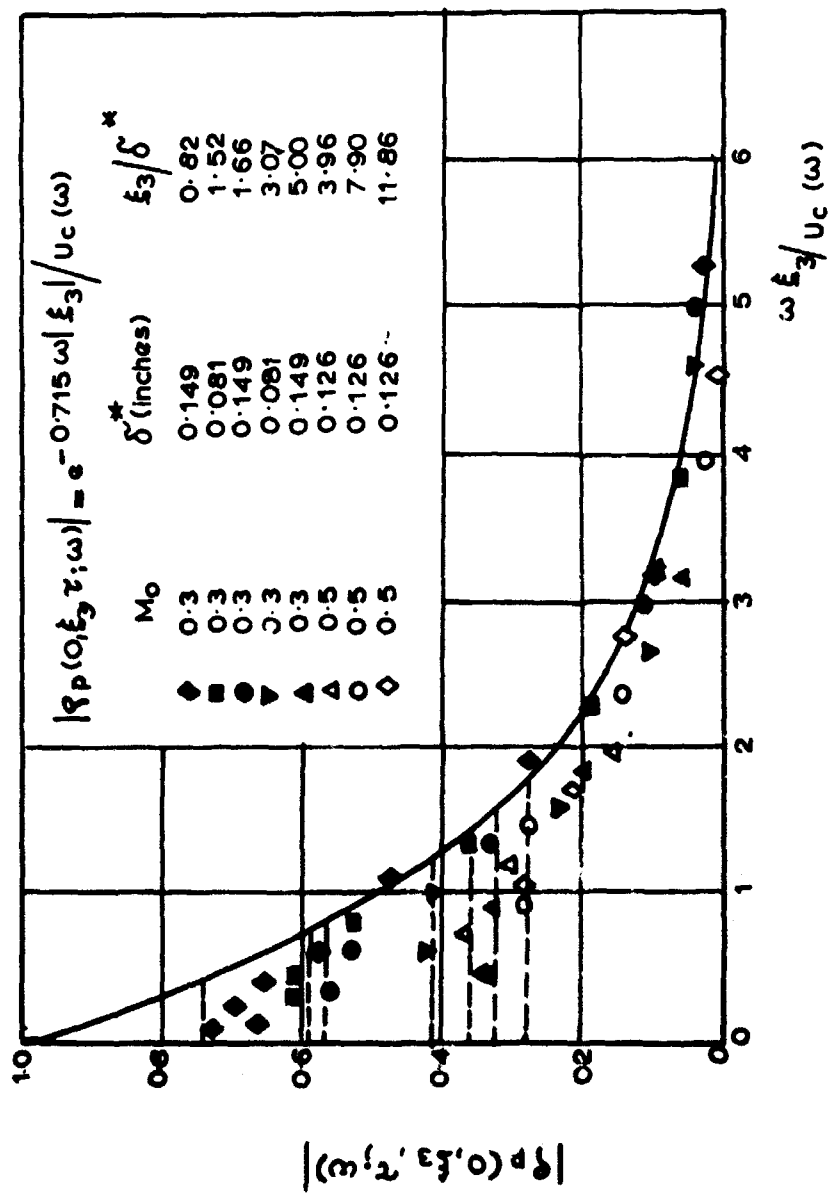


Figure A5. Amplitude of narrow band lateral space-time correlation of the wall pressure field. FROM BULL (1963)

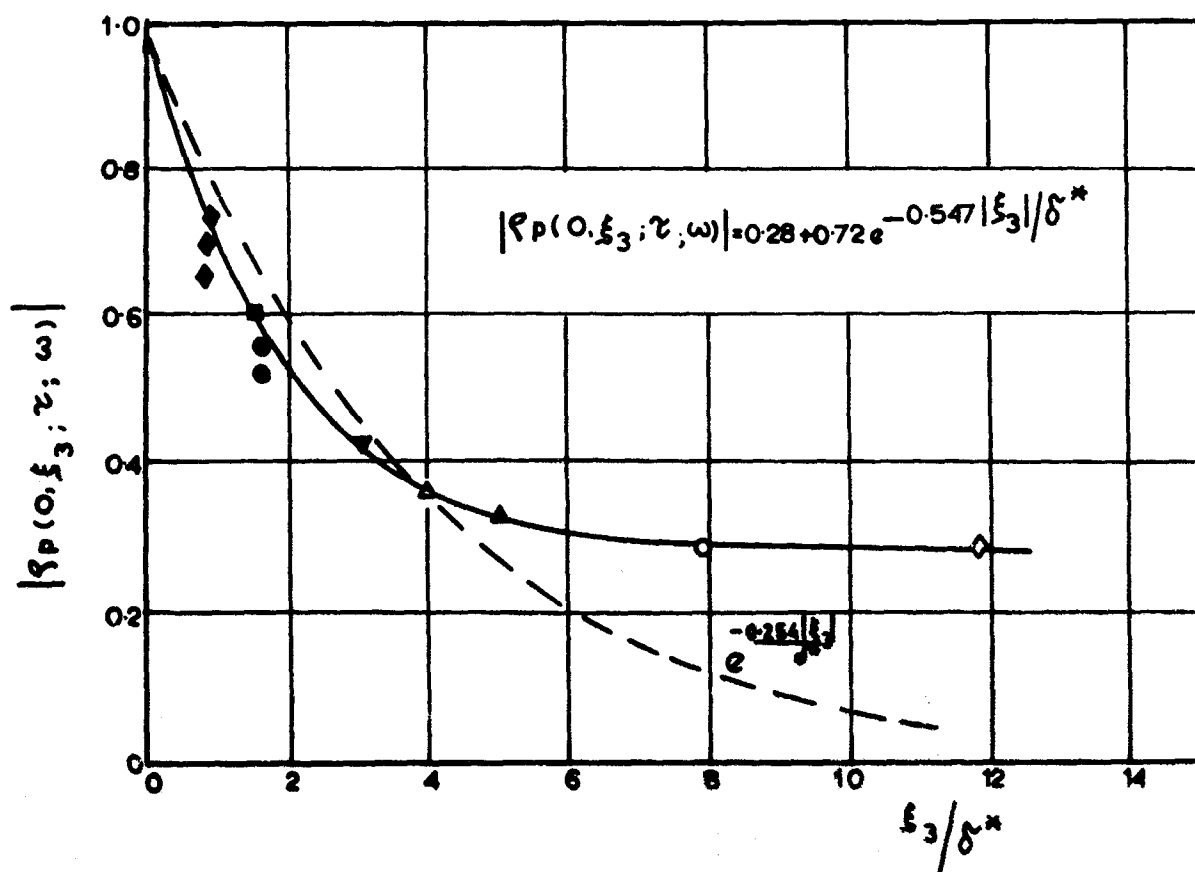


Figure A6 Low frequency values of narrow-band lateral pressure correlation amplitudes. FROM BULL (1963)

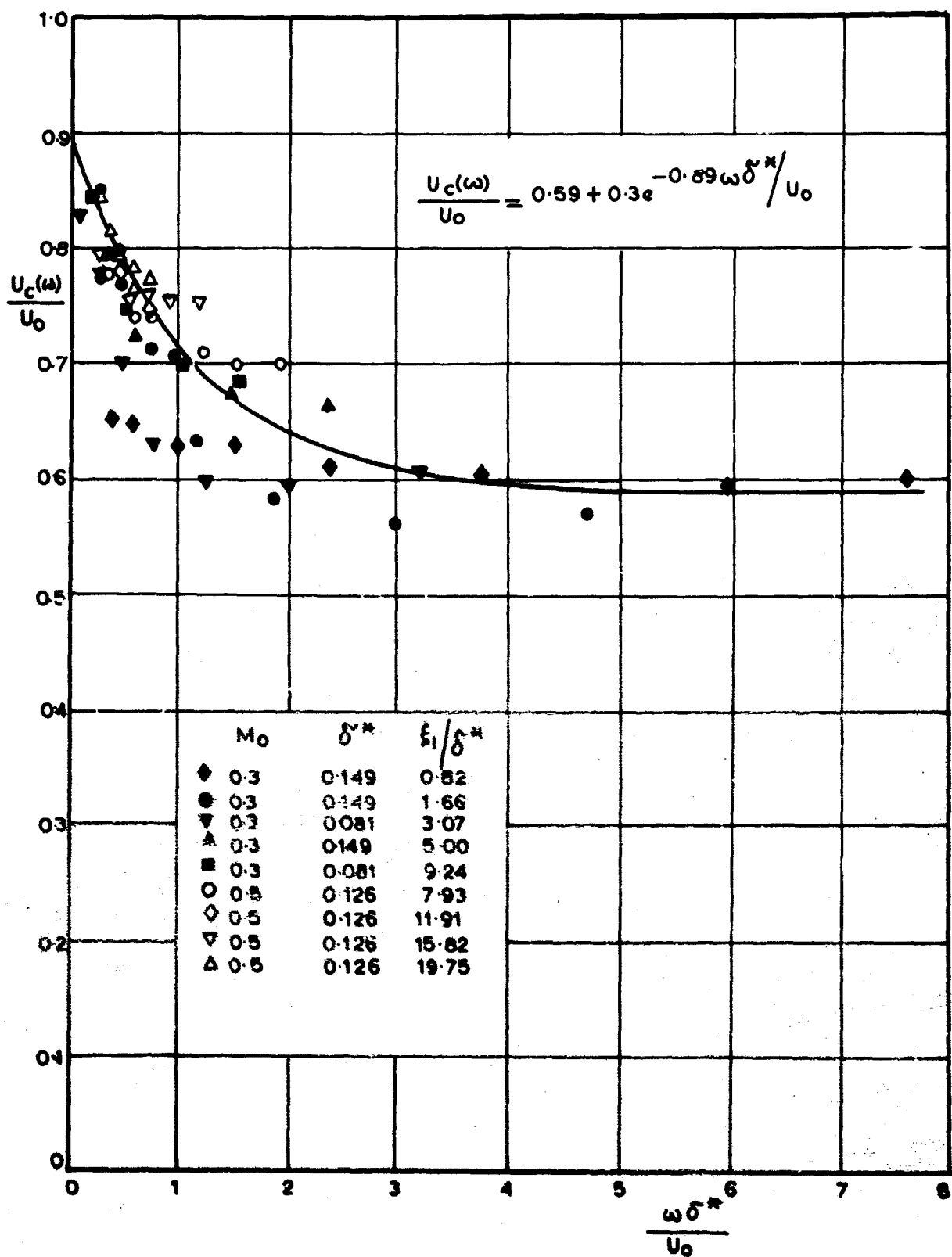


Figure A.7. Convection velocities derived from narrow band longitudinal space-time correlations of the wall pressure field. FROM BULL (1963).

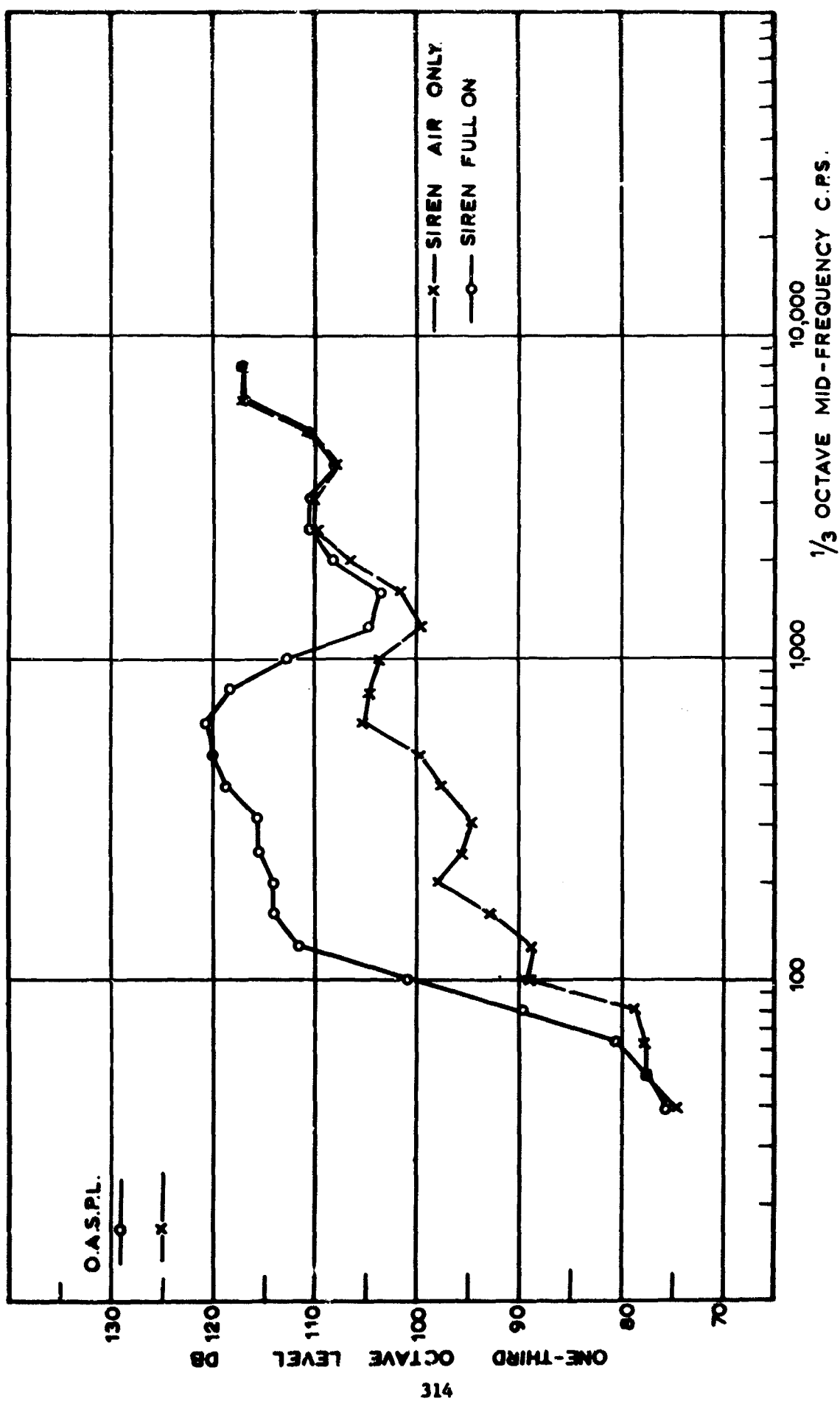


Figure A.8 Siren tunnel noise spectra.

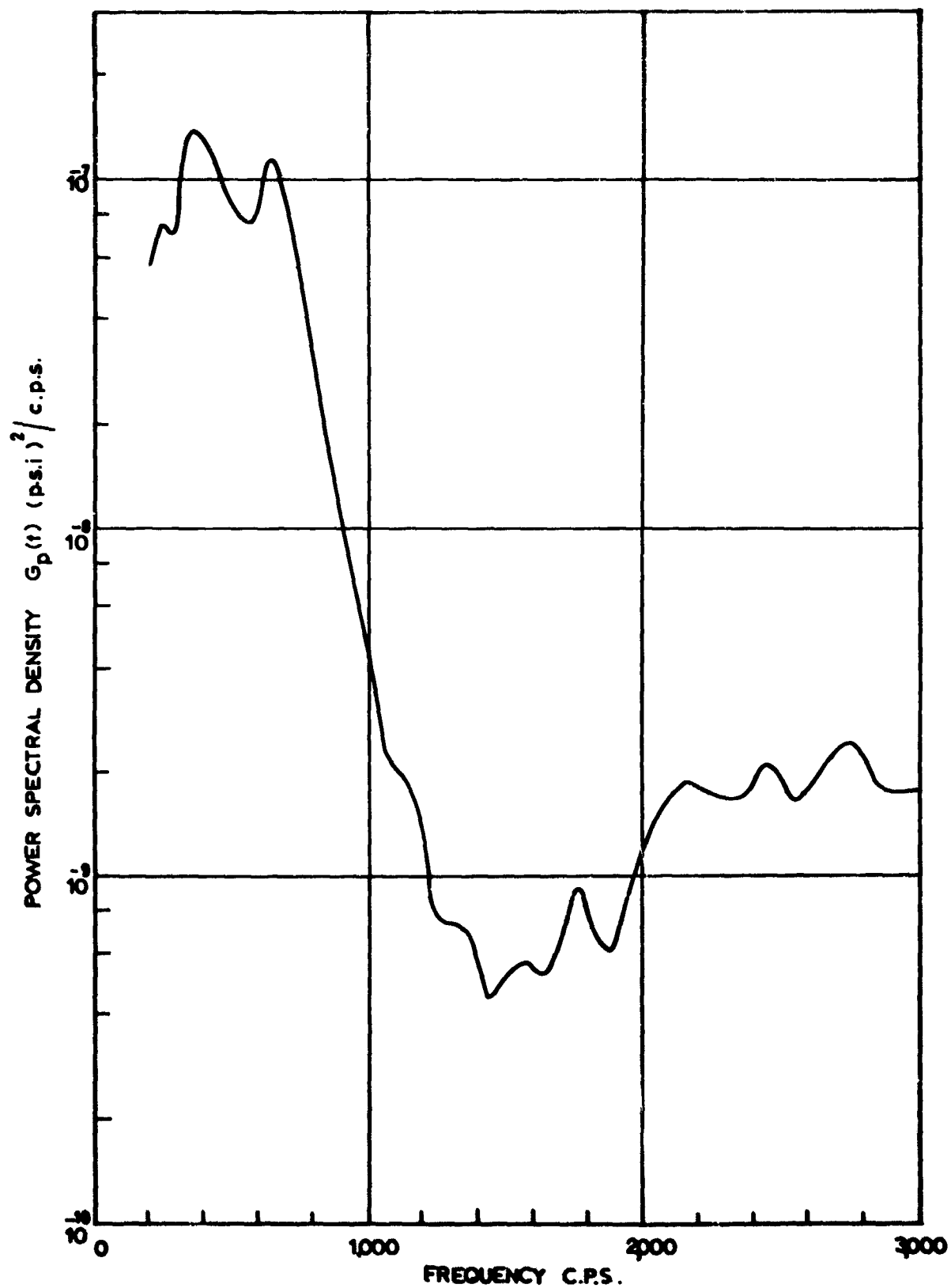


Figure A9. Excitation spectrum in the siren tunnel.



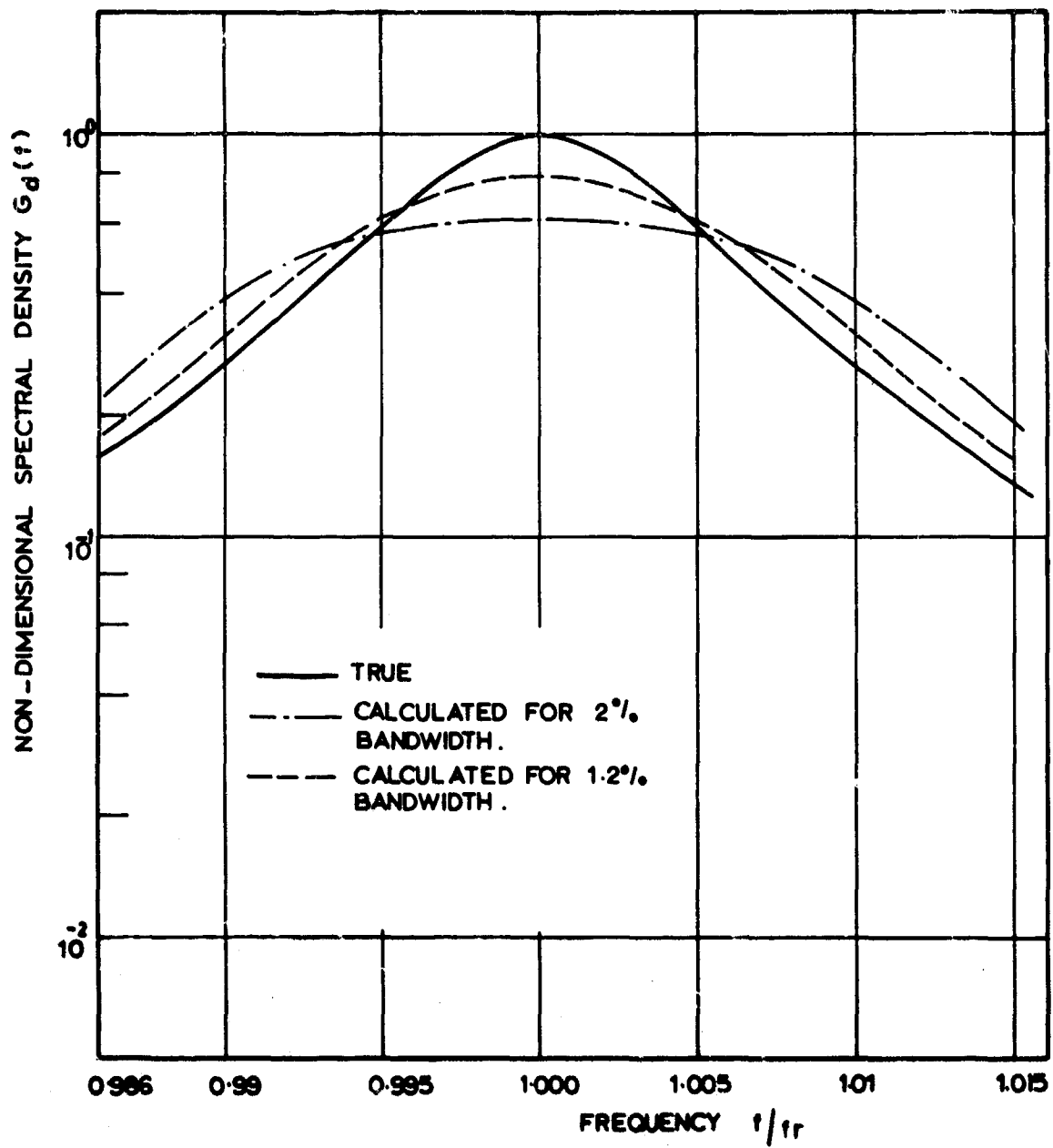


Figure B1. Effect of filter bandwidth on response spectra.  
(Loss factor = 0.012)

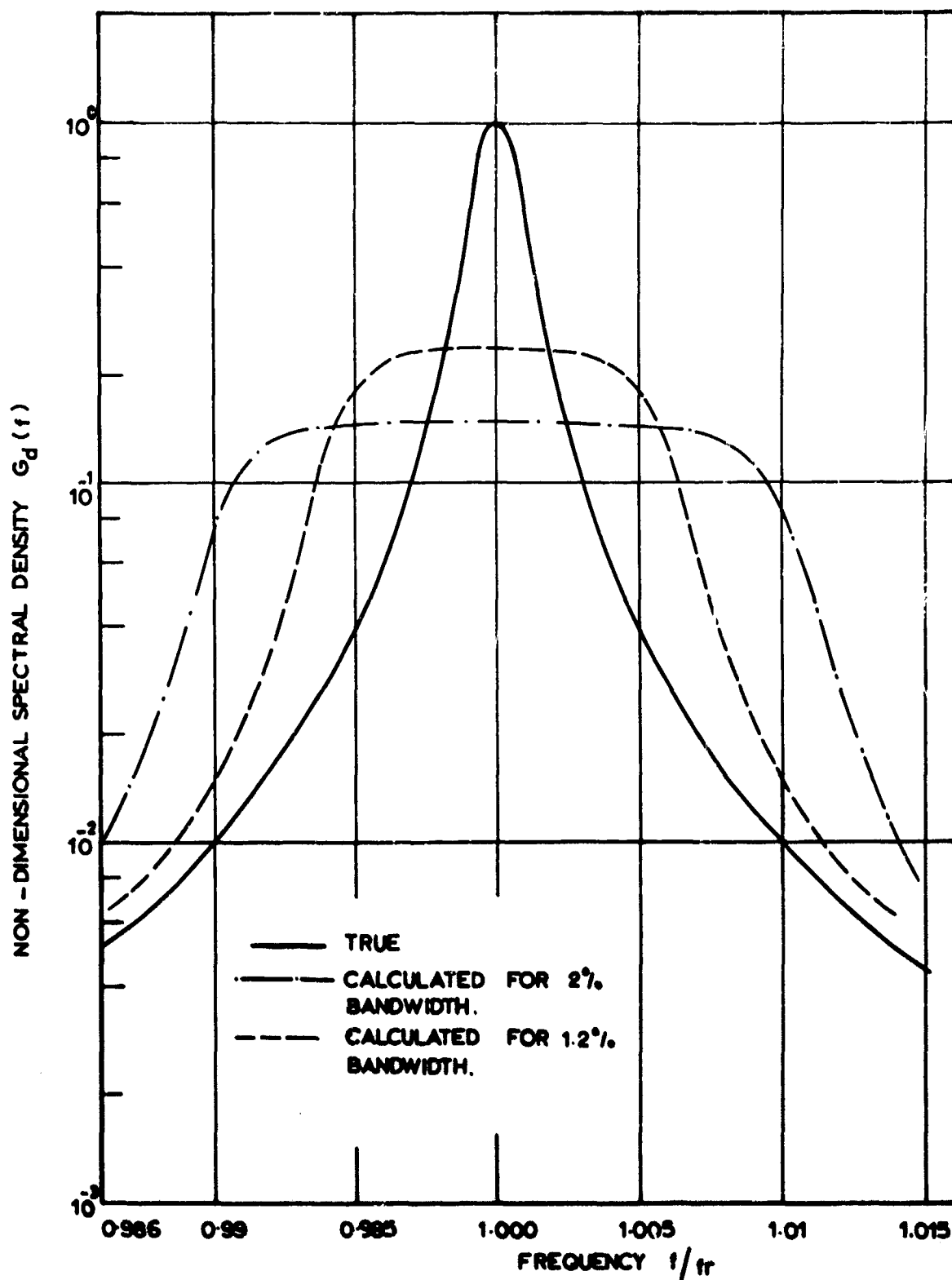


Figure B2 Effect of filter bandwidth on response spectra.  
(Loss factor = 0.002)

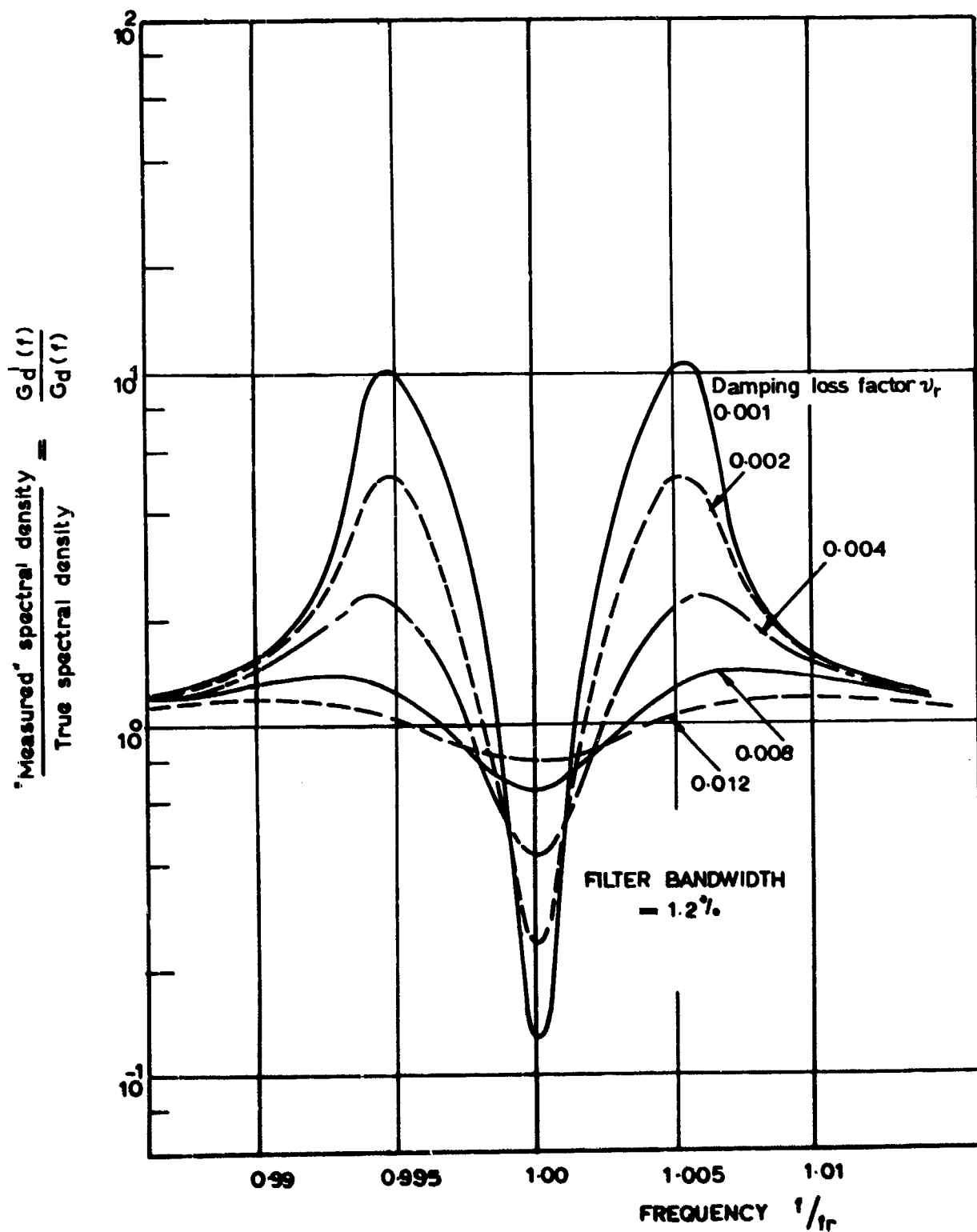


Figure B3. Spectrum resolution corrections for filter with 1.2% bandwidth.

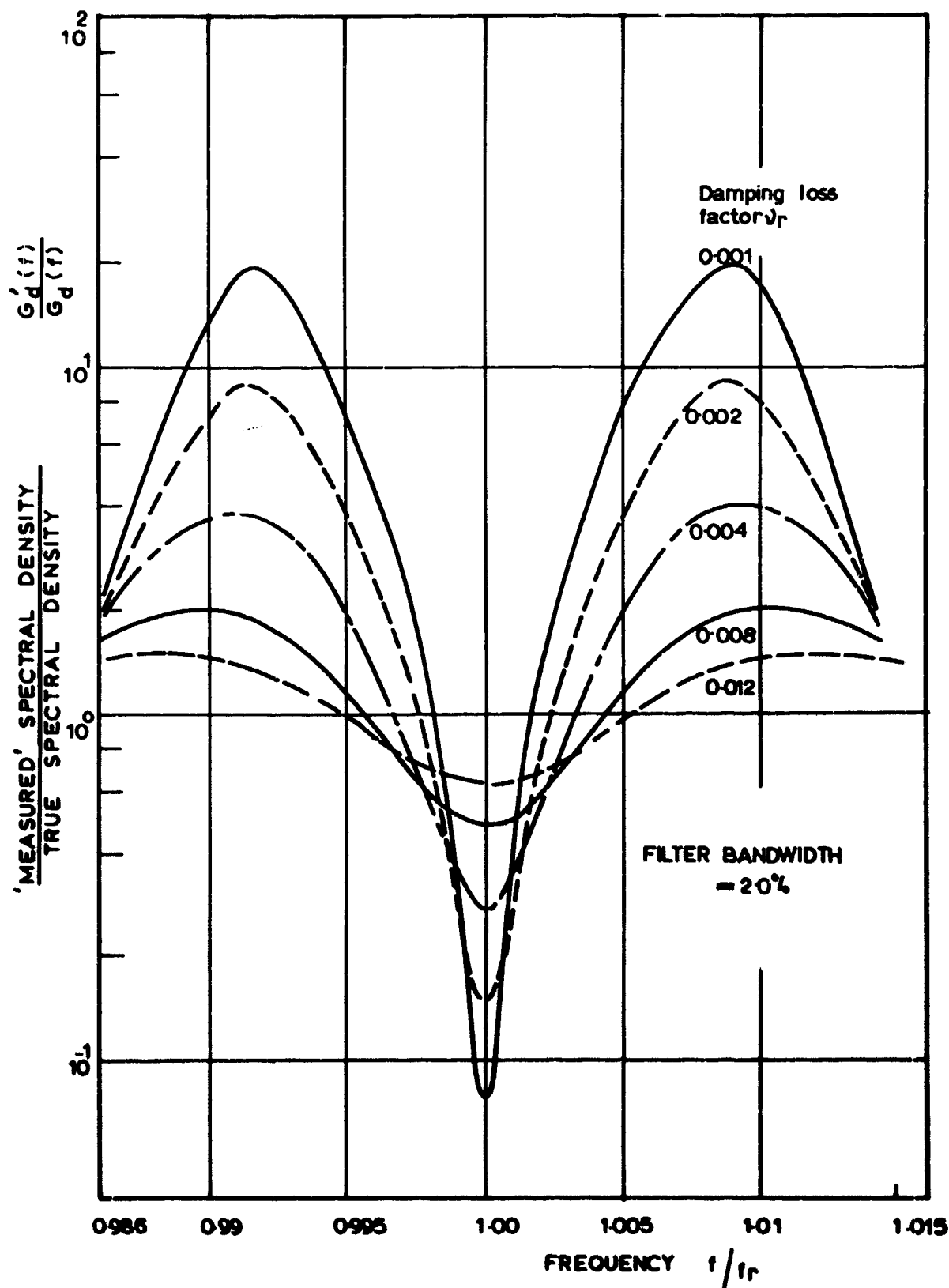


Fig. B.4. Spectrum resolution corrections for filter with 2.0% bandwidth

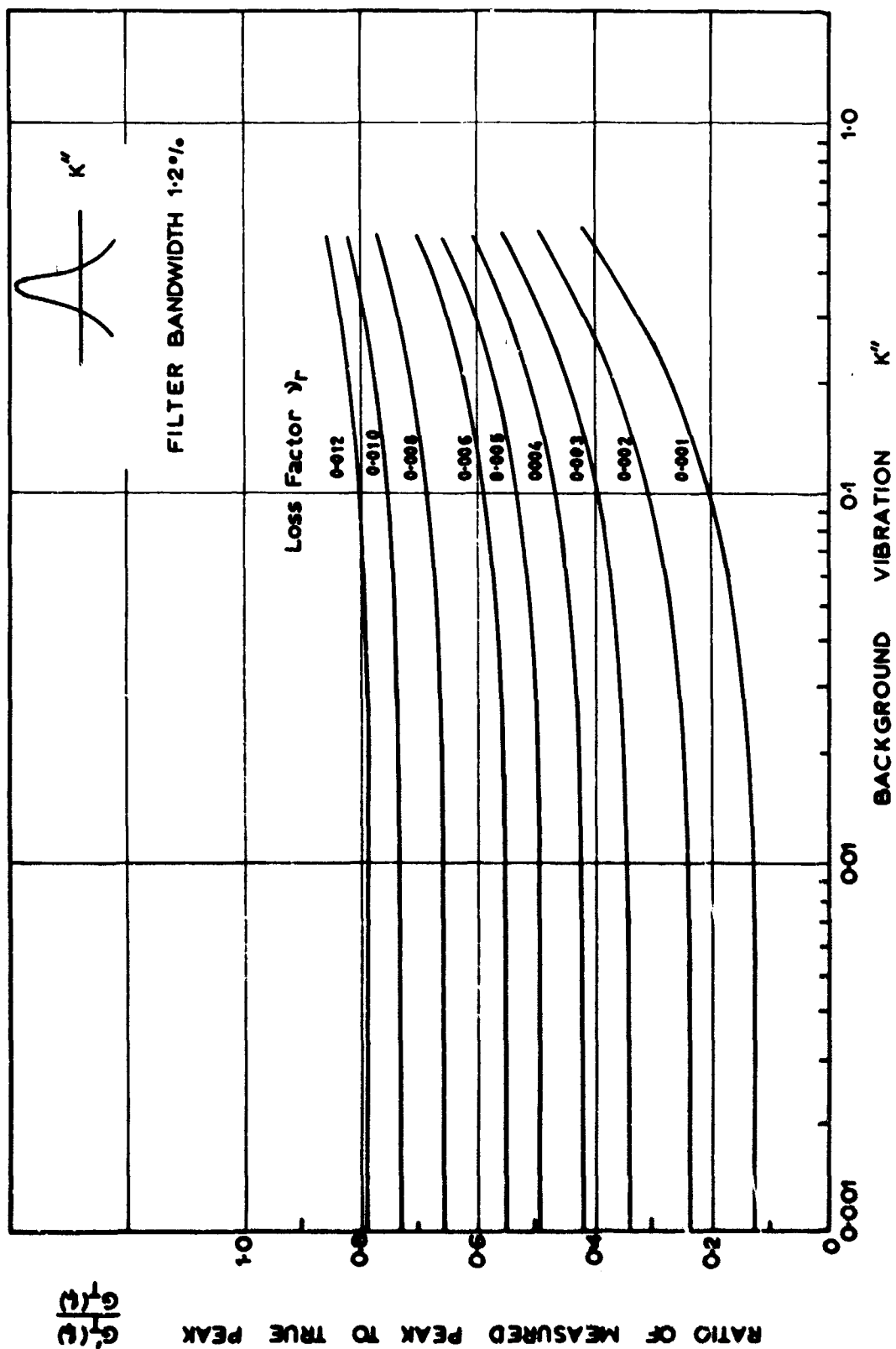


Figure B 5 Spectrum resolution correction at the natural frequency of a system in presence of background vibration (Filter bandwidth 1.2%).

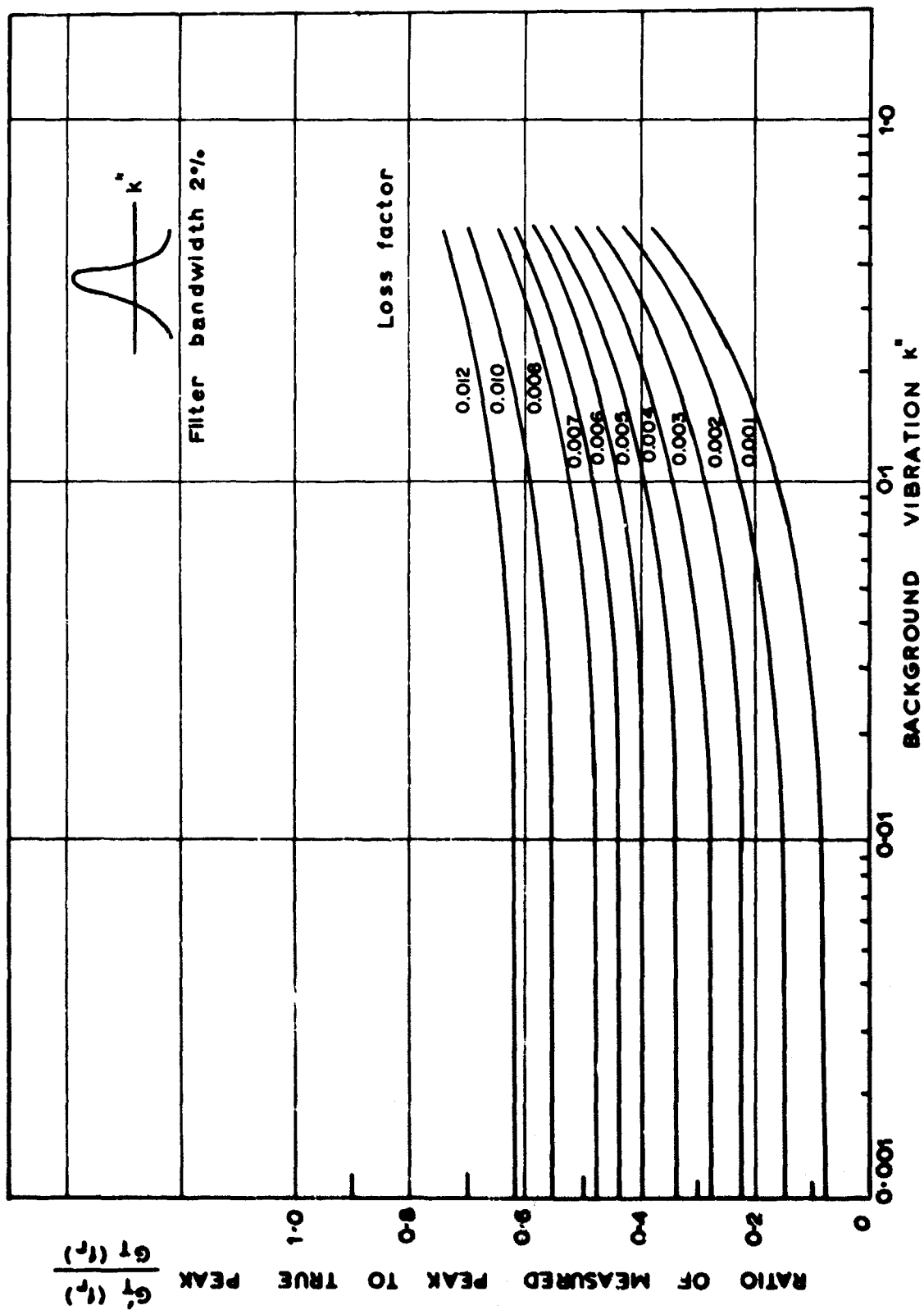


Figure B6 Spectrum resolution correction at the natural frequency of a system in presence of background vibration. (Filter bandwidth 2.0%)

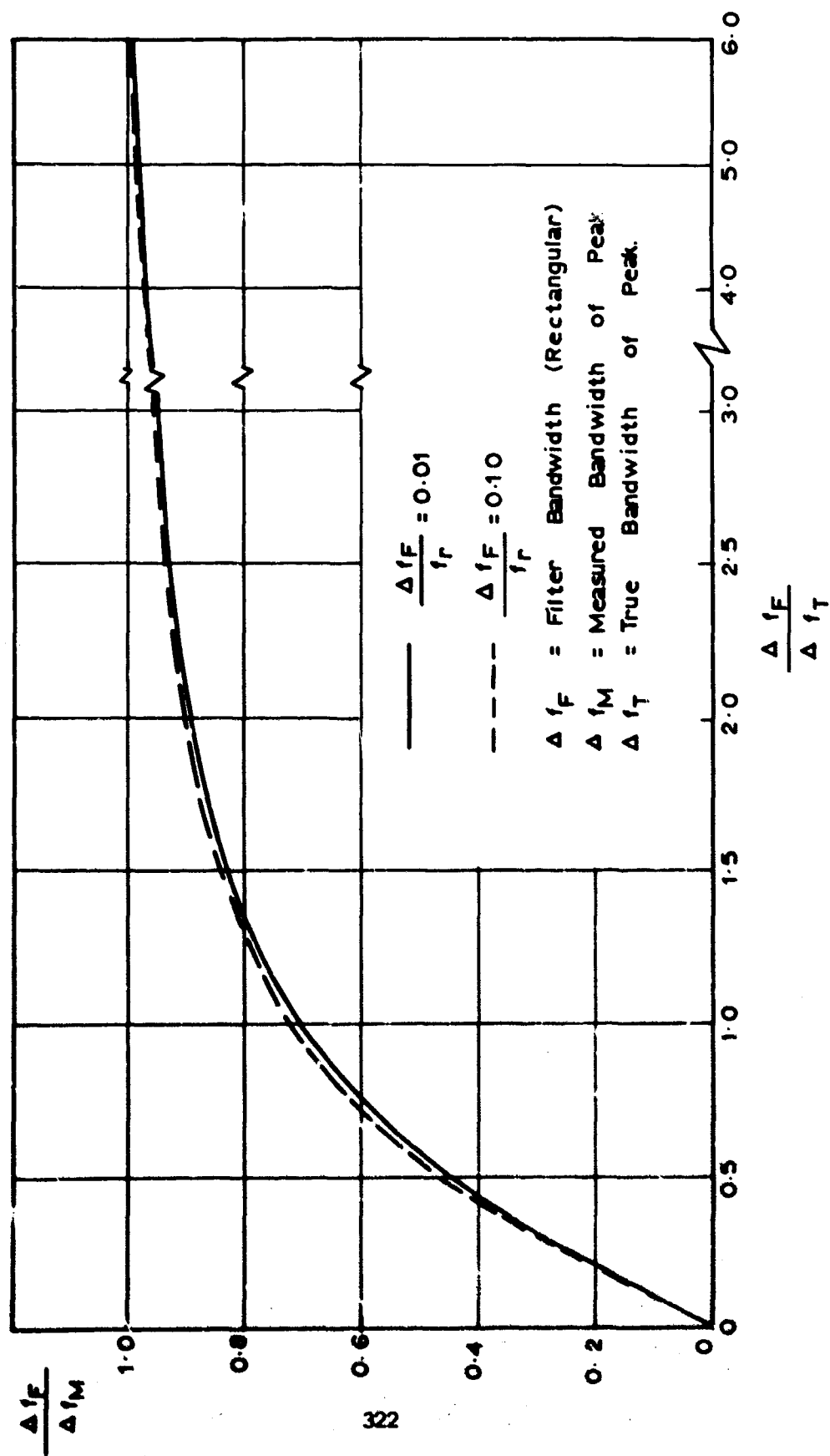


Figure B7. Relationship between true and measured bandwidths at half power point.

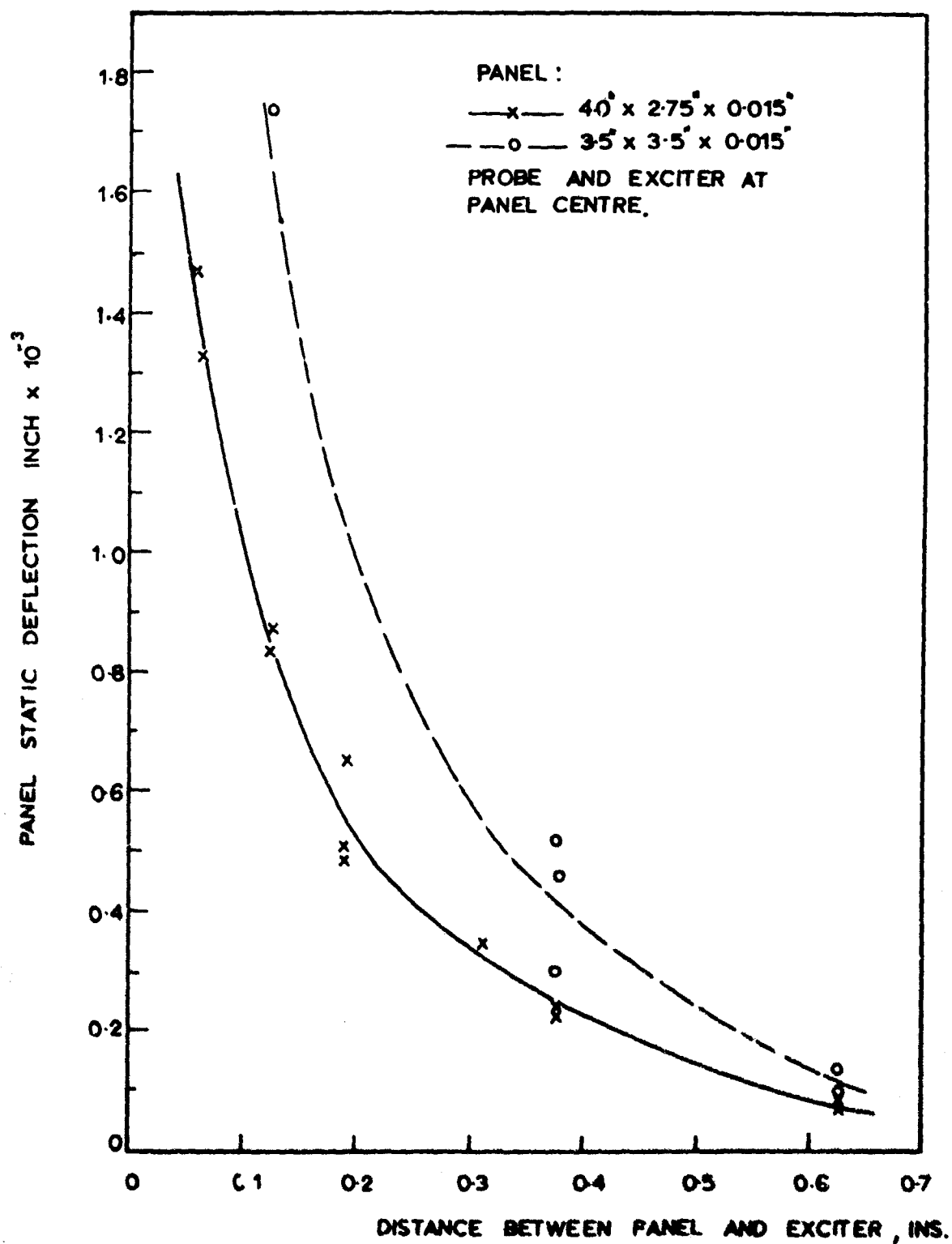
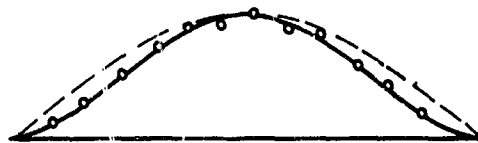


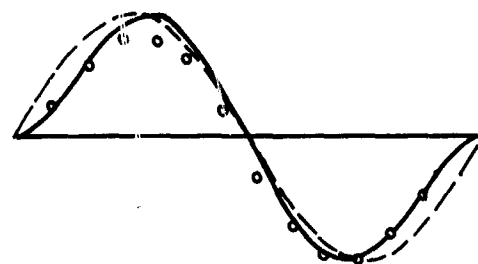
Figure C.1. Panel static deflection due to permanent magnetism of the exciter.



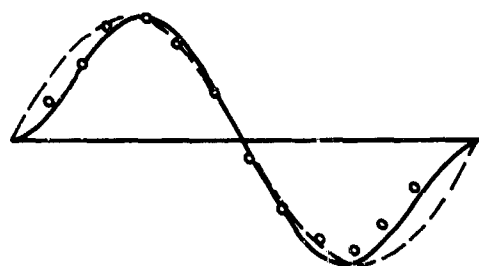
MODE m n  
1-1



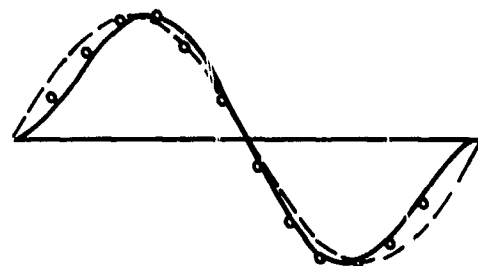
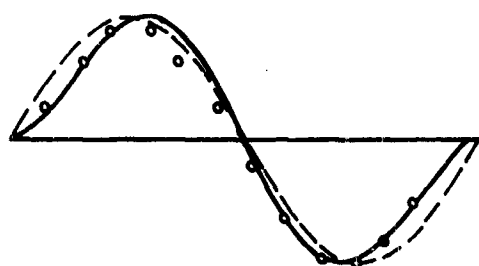
1-2



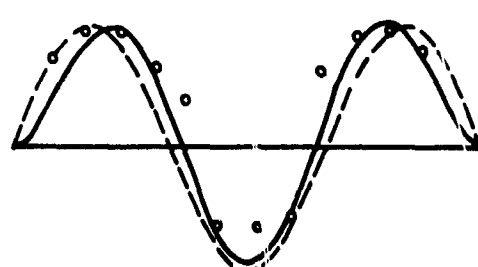
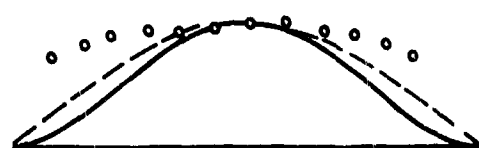
2-1



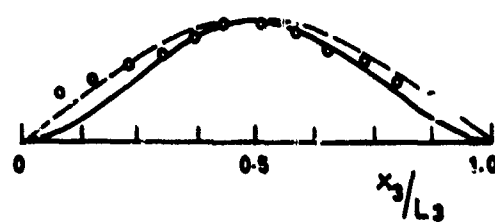
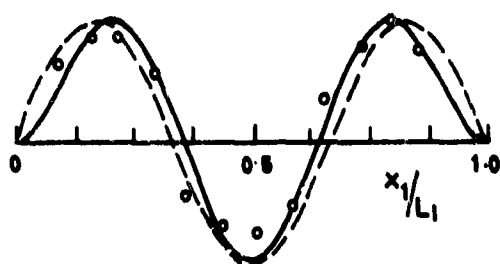
2-2



1-3



3-1

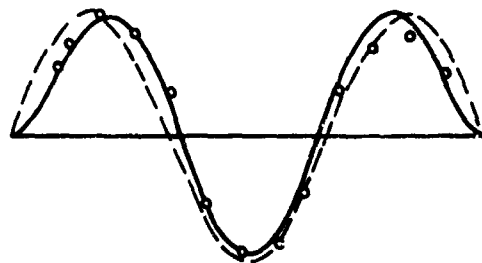
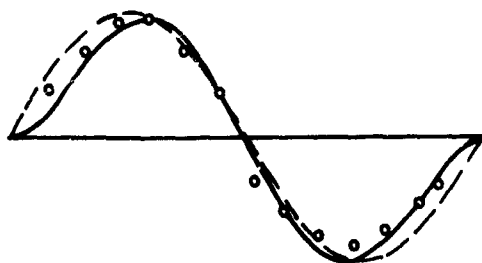


— FULLY FIXED EQNS. (C2)(C3)  
- - - SIMPLY SUPPORTED EQN. (C1)  
• MEASURED

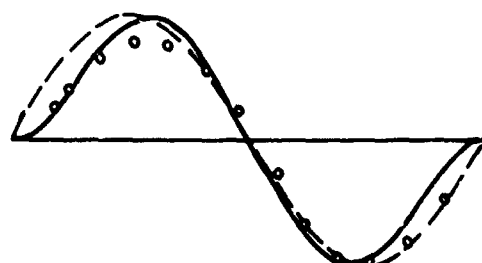
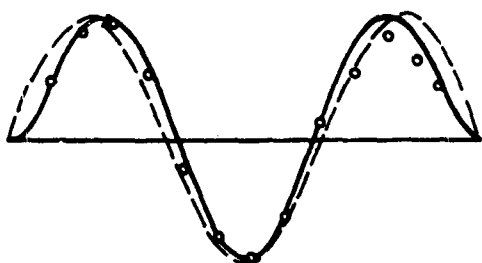
Figure C.2(a) Mode shapes for 3.5' x 3.5' x 0.015' panel.

MODE  $m-n$

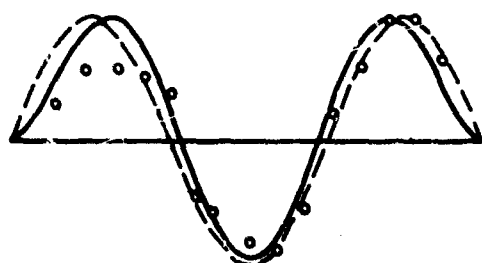
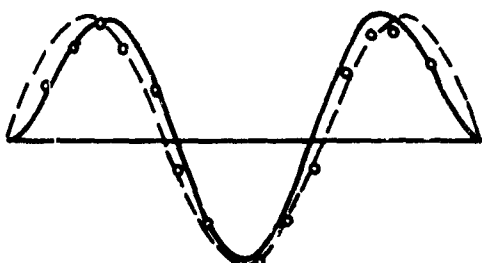
2-3



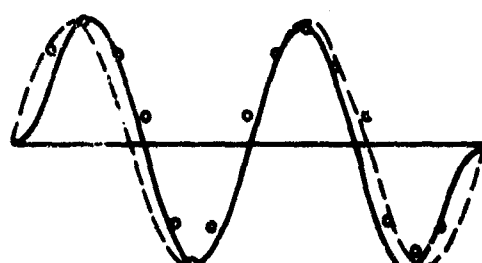
3-2



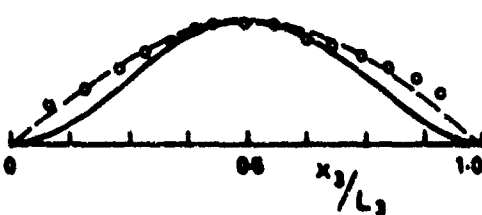
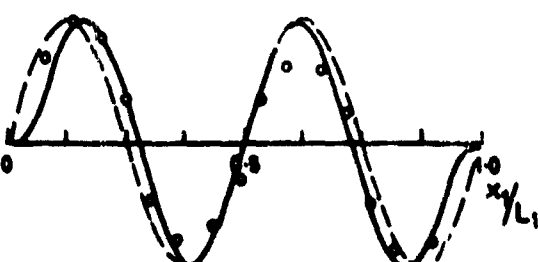
3-3



1-4



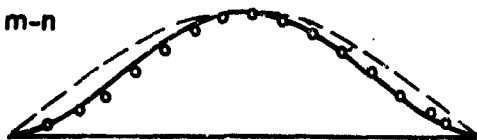
4-1



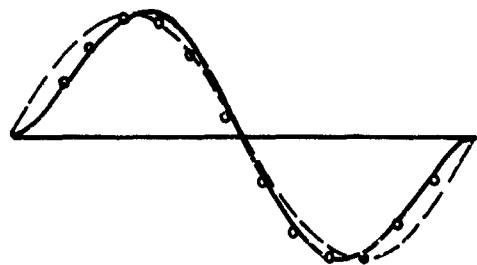
— FULLY FIXED EQNS (C.2)(C.3)  
 --- SIMPLY SUPPORTED EQN.(C.1)  
 • MEASURED

Figure C.2(b) Mode shapes for  $3.5'' \times 3.5'' \times 0.015''$  panel.

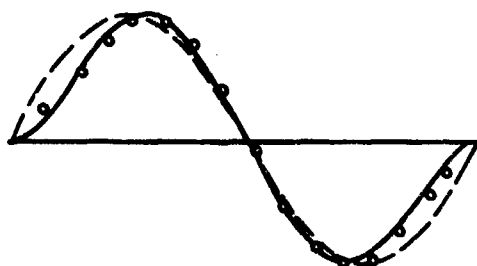
MODE m-n  
1-1



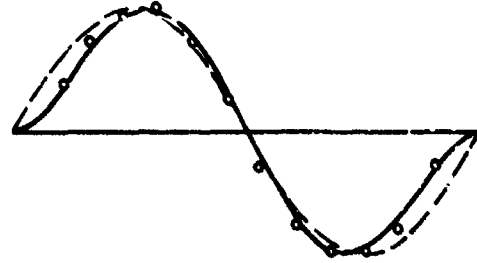
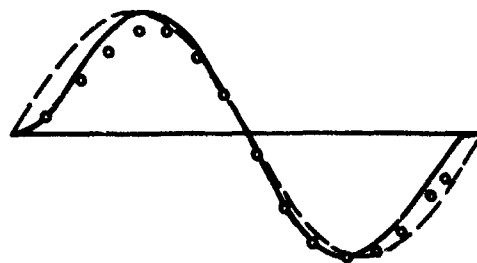
1-2



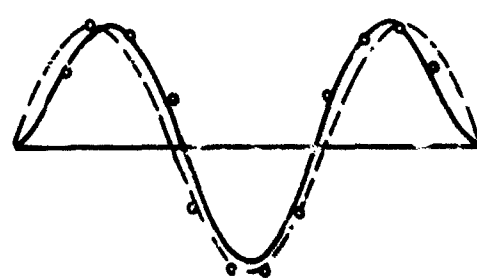
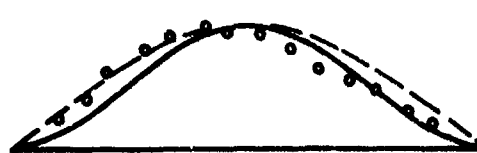
2-1



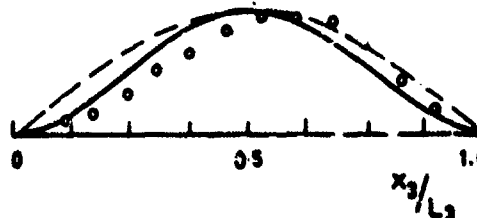
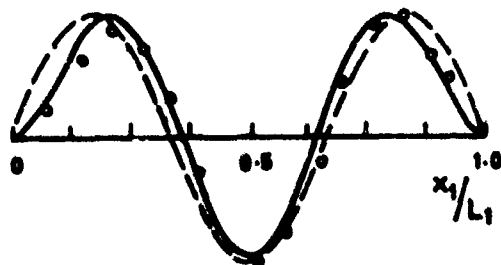
2-2



1-3



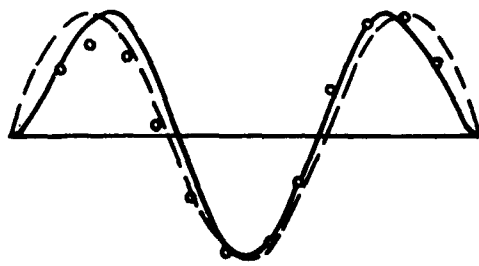
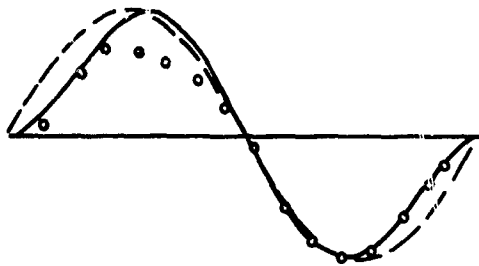
3-1



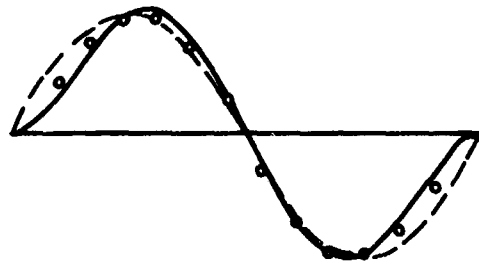
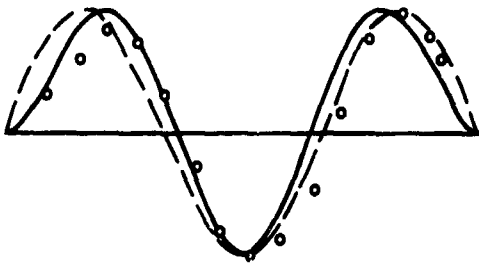
— FULLY FIXED EONS. (C.2)(C.3)  
- - - SIMPLY SUPPORTED EGN. (C.1)  
• MEASURED

Figure C.3.(a) Mode shapes for  $4.0' \times 2.75' \times 0.015'$  panel.

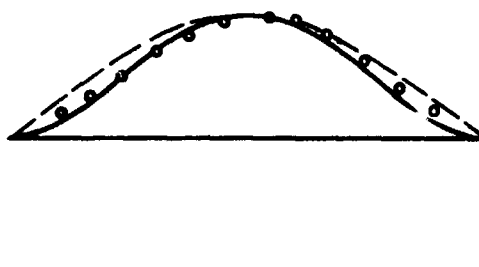
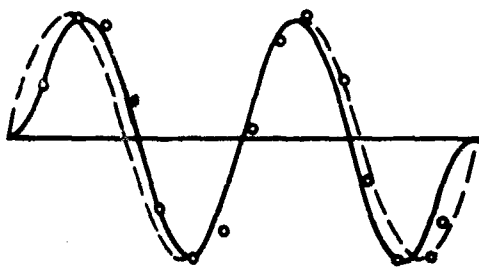
MODE  $m-n$   
2-3



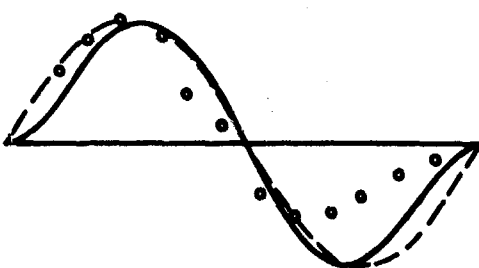
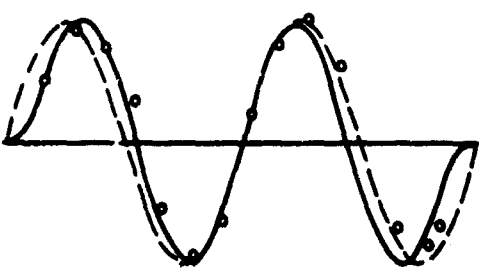
3-2



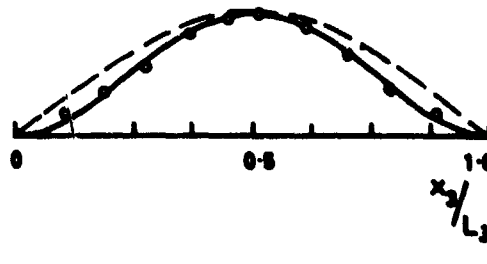
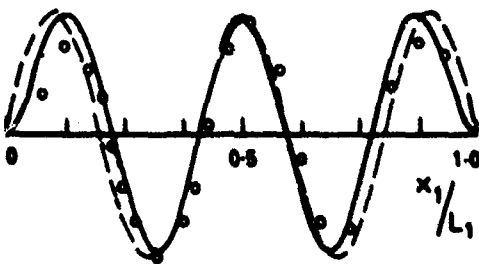
4-1



4-2



5-1



— FULLY FIXED EQNS. (C.2)(C.3)  
- - - SIMPLY SUPPORTED EQN. (C.1)  
• MEASURED

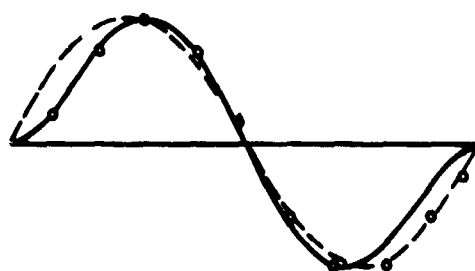
Figure C.3(b) Mode shapes for 4.0' x 2.75' x 0.015' panel.

MODE m-n

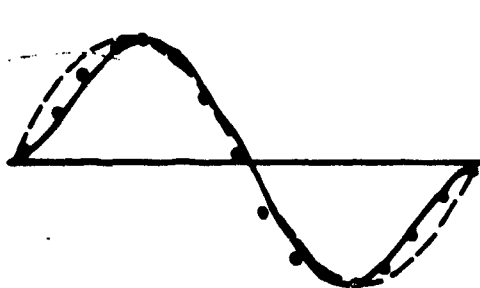
1-1



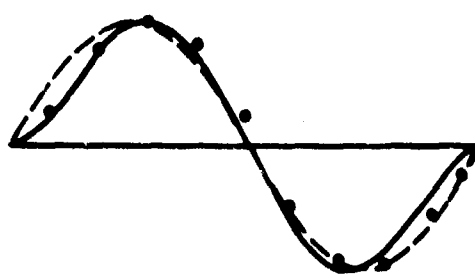
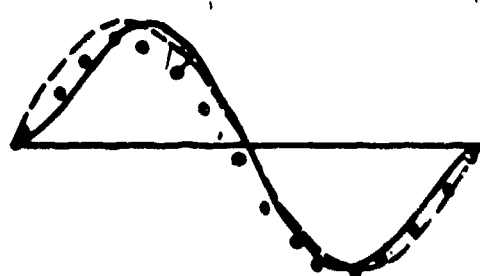
1-2



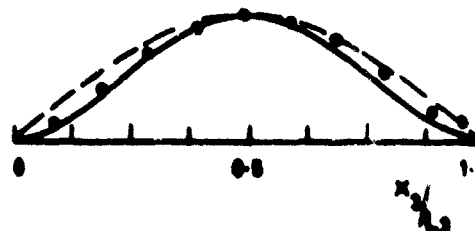
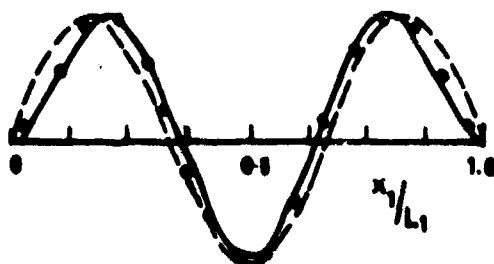
2-1



2-2



3-1

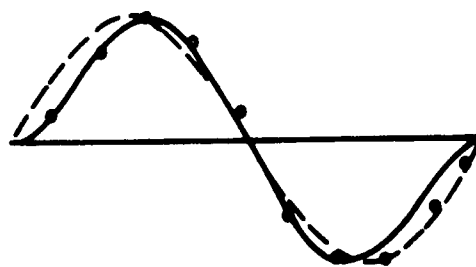
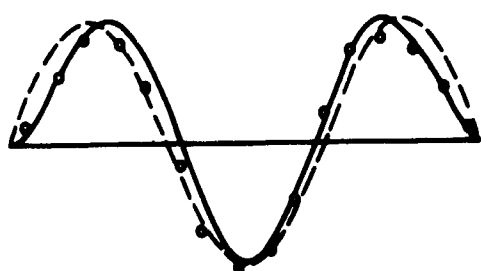


— FULLY FIXED EONS. (C.2) (C.3)  
 --- SIMPLY SUPPORTED EON. (C.1)  
 • MEASURED.

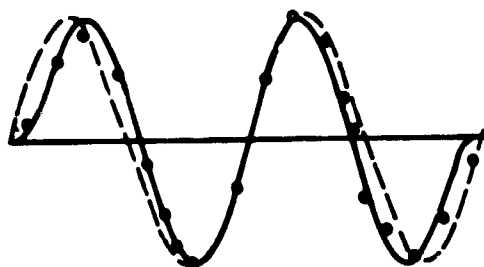
Figure C.4(a) Mode shapes for  $4.0 \times 2.0 \times 0.015$  panel.

MODE  $m-n$

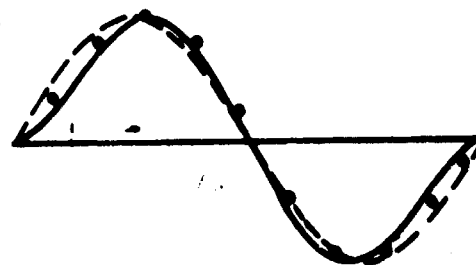
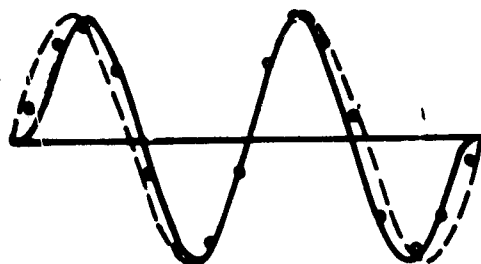
3-2



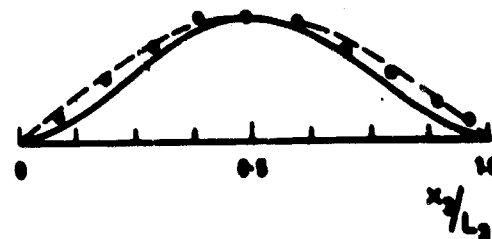
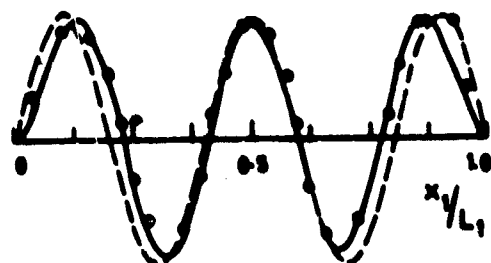
4-1



4-2



5-1



— FULLY FIXED EONS. (C.2) (C.3)  
 --- SIMPLY SUPPORTED EONS. (C.1)  
 • MEASURED

Figure C.4(b) Mode shapes for  $4.0' \times 20' \times 0.015'$  panel.

Unclassified  
Security Classification

DOCUMENT CONTROL DATA - R&D		
(Security classification of title, body of abstract and indexing annotation must be entered when the overall report is classified)		
1. ORIGINATING ACTIVITY (Corporate author) Institute of Sound and Vibration Research, University of Southampton, Southampton, England.		2a. REPORT SECURITY CLASSIFICATION Unclassified
		2b. GROUP
3. REPORT TITLE THE RESPONSE OF SIMPLE PANELS TO TURBULENT BOUNDARY LAYER EXCITATION		
4. DESCRIPTIVE NOTES (Type of report and inclusive dates) Final Scientific Report November 1963-November 1966.		
5. AUTHOR(S) (Last name, first name, initial) Wilby, John F.		
6. REPORT DATE October 1967	7a. TOTAL NO OF PAGES 350	7b. NO OF REFS 56
8a. CONTRACT OR GRANT NO Contract AF61(052)-756 A. PROJECT NO. 1471 Task 147102		8b. ORIGINATOR'S REPORT NUMBER(S) AFFDL-TR-67-70
		8c. OTHER REPORT NO(S) (Any other numbers that may be assigned this report)
10. AVAILABILITY/LIMITATION NOTICES This document is subject to special export controls and each transmittal to foreign government or foreign nationals may be made only with prior approval of AF Flight Dynamics Laboratory (FDDA) WPAFB, Ohio		
11. SUPPLEMENTARY NOTES		12. SPONSORING MILITARY ACTIVITY Air Force Flight Dynamics Laboratory Wright-Patterson AFB, Ohio 45433
13. ABSTRACT <p>The response of a series of panels to turbulent boundary layer excitation has been measured for flow velocities of 329 ft./sec. and 540 ft./sec., and boundary layer thicknesses in the range 0.4 inch to 1.4 inches. The effects of boundary layer thickness, pressure field convection direction, panel aspect ratio and static pressure differential are well predicted. The effect of flow velocity is not predicted accurately, the theory over-estimating the effect near coincidence and under-estimating the effect elsewhere.</p> <p>The boundary layer thickness affects the panel vibration mainly through the pressure spectrum. Static pressure affects the vibration mainly through the change in stiffness.</p> <p>Random techniques are used to measure panel damping in the presence of an airflow and the results show an increase in damping due to the flow. The increase is small in general.</p> <p>Distribution of this Abstract is Unlimited.</p>		

DD FORM 1473  
1 JAN 64

Unclassified  
Security Classification

Unclassified

Security Classification

14. KEY WORDS	LINK A		LINK B		LINK C	
	ROLE	WT	ROLE	WT	ROLE	WT
Structures Random Vibration Boundary Layer Pressure Field Damping Flow Velocity Boundary Layer Thickness Static Pressure Differential Convection Direction						

#### INSTRUCTIONS

1. **ORIGINATING ACTIVITY:** Enter the name and address of the contractor, subcontractor, grantee, Department of Defense activity or other organization (corporate author) issuing the report.

2a. **REPORT SECURITY CLASSIFICATION:** Enter the overall security classification of the report. Indicate whether "Restricted Data" is included. Marking is to be in accordance with appropriate security regulations.

2b. **GROUP:** Automatic downgrading is specified in DoD Directive 5200.10 and Armed Forces Industrial Manual. Enter the group number. Also, when applicable, show that optional markings have been used for Group 3 and Group 4 as authorized.

3. **REPORT TITLE:** Enter the complete report title in all capital letters. Titles in all cases should be unclassified. If a meaningful title cannot be selected without classification, show title classification in all capitals in parentheses immediately following the title.

4. **DESCRIPTIVE NOTES:** If appropriate, enter the type of report, e.g., interim, progress, summary, annual, or final. Give the inclusive dates when a specific reporting period is covered.

5. **AUTHOR(S):** Enter the name(s) of author(s) as shown on or in the report. Enter last name, first name, middle initial. If military, show rank and branch of service. The name of the principal author is an absolute minimum requirement.

6. **REPORT DATE:** Enter the date of the report as day, month, year, or month, year. If more than one date appears on the report, use date of publication.

7a. **TOTAL NUMBER OF PAGES:** The total page count should follow normal pagination procedures, i.e., enter the number of pages containing information.

7b. **NUMBER OF REFERENCES:** Enter the total number of references cited in the report.

8a. **CONTRACT OR GRANT NUMBER:** If appropriate, enter the applicable number of the contract or grant under which the report was written.

8b, 8c, & 8d. **PROJECT NUMBER:** Enter the appropriate military department identification, such as project number, subproject number, system numbers, task number, etc.

9a. **ORIGINATOR'S REPORT NUMBER(S):** Enter the official report number by which the document will be identified and controlled by the originating activity. This number must be unique to this report.

9b. **OTHER REPORT NUMBER(S):** If the report has been assigned any other report numbers (either by the originator or by the sponsor), also enter this number(s).

10. **AVAILABILITY/LIMITATION NOTICE:** Enter any limitations on further dissemination of the report, other than those

imposed by security classification, using standard statements such as:

- (1) "Qualified requesters may obtain copies of this report from DDC."
- (2) "Foreign announcement and dissemination of this report by DDC is not authorized."
- (3) "U. S. Government agencies may obtain copies of this report directly from DDC. Other qualified DDC users shall request through \_\_\_\_\_."
- (4) "U. S. military agencies may obtain copies of this report directly from DDC. Other qualified users shall request through \_\_\_\_\_."
- (5) "All distribution of this report is controlled. Qualified DDC users shall request through \_\_\_\_\_."

If the report has been furnished to the Office of Technical Services, Department of Commerce, for sale to the public, indicate this fact and enter the price, if known.

11. **SUPPLEMENTARY NOTES:** Use for additional explanatory notes.

12. **SPONSORING MILITARY ACTIVITY:** Enter the name of the departmental project office or laboratory sponsoring (paying for) the research and development. Include address.

13. **ABSTRACT:** Enter an abstract giving a brief and factual summary of the document indicative of the report, even though it may also appear elsewhere in the body of the technical report. If additional space is required, a continuation sheet shall be attached.

It is highly desirable that the abstract of classified reports be unclassified. Each paragraph of the abstract shall end with an indication of the military security classification of the information in the paragraph, represented as (TS), (S), (C), or (U).

There is no limitation on the length of the abstract. However, the suggested length is from 150 to 225 words.

14. **KEY WORDS:** Key words are technically meaningful terms or short phrases that characterize a report and may be used as index entries for cataloging the report. Key words must be selected so that no security classification is required. Identifiers, such as equipment model designation, trade name, military project code name, geographic location, may be used as key words but will be followed by an indication of technical content. The assignment of links, roles, and weights is optional.

Unclassified

Security Classification